University of Windsor
Scholarship at UWindsor

Electronic Theses and Dissertations | Theses, Dissertations, and Major Papers

2015

Development of Novel Nano - Single Si Phase Cast Hypereutectic Al-Si Alloys

Peter Guba
University of Windsor

Follow this and additional works at: https://scholar.uwindsor.ca/etd

Recommended Citation
Guba, Peter, "Development of Novel Nano - Single Si Phase Cast Hypereutectic Al-Si Alloys" (2015). *Electronic Theses and Dissertations*. 5694.
https://scholar.uwindsor.ca/etd/5694

This online database contains the full-text of PhD dissertations and Masters' theses of University of Windsor students from 1954 forward. These documents are made available for personal study and research purposes only, in accordance with the Canadian Copyright Act and the Creative Commons license—CC BY-NC-ND (Attribution, Non-Commercial, No Derivative Works). Under this license, works must always be attributed to the copyright holder (original author), cannot be used for any commercial purposes, and may not be altered. Any other use would require the permission of the copyright holder. Students may inquire about withdrawing their dissertation and/or thesis from this database. For additional inquiries, please contact the repository administrator via email (scholarship@uwindsor.ca) or by telephone at 519-253-3000ext. 3208.

Development of Novel Nano – Single Si Phase Cast Hypereutectic Al-Si Alloys

By

Peter Guba

A Dissertation
Submitted to the Faculty of Graduate Studies
through the Department of
Mechanical, Automotive and Materials Engineering
in Partial Fulfillment of the Requirements for the Degree of
Doctor of Philosophy
at the
University of Windsor

Windsor, Ontario, Canada

2015

© 2015 Peter Guba

Development of Novel Nano – Single Si Phase Cast Hypereutectic Al-Si Alloys

by

Peter Guba

APPROVED BY:

_____
W. Misiolek, External Examiner
Lehigh University

_____
R. Bowers, Outside Program Reader
Mechanical, Automotive and Materials Engineering

_____
B. Zhou, Program Reader
Mechanical, Automotive and Materials Engineering

_____
A. Fartaj, Program Reader
Mechanical, Automotive and Materials Engineering

_____
F. A. Conle, Special Committee Member

_____
A. Sobiesiak, Co-Advisor
Mechanical, Automotive and Materials Engineering

_____
J. H. Sokolowski, Co-Advisor
Mechanical, Automotive and Materials Engineering

April 29, 2015

Declaration of Co-Authorship

I hereby declare that this PhD dissertation incorporates material that is the result of joint research.

This PhD dissertation incorporates the outcomes of joint research in the field of Thermal Analysis, in collaboration with Dr. Adam Gesing, and is covered in Section 4.3.3 and in the field of Process Parameters Programming, Control and some Results Analysis, in collaboration with Dr. Al Conle, covered in Section 4.3. The hypothesis and deliverables, experimental design, data interpretation were addressed by the author, and the contributions of the Collaborators were primarily through the provision of deconvolution of first derivative curves by Dr. Adam Gesing and the creation of SC/HPDC UMSA software by Dr. Al Conle.

Other collaborative project contributions were made by Dr. Jerry Sokolowski, Dr. Marcin Kasprzak, Mohammad Alam, Andy Jenner and Joe Giovanatto and a patent is pending. The author is one of the Co-Inventors.

I am aware of the University of Windsor's Senate Policy on Authorship and I certify that I have properly acknowledged the contribution of other researchers to my PhD dissertation, and have obtained written permission from each of the Collaborators to include the above material(s) in my PhD dissertation.

I certify that, with the above qualification, this PhD dissertation, and the research to which it refers, is the product of my own work.

Four (4) refereed journal publications are pending.

I declare that, to the best of my knowledge, my PhD dissertation does not infringe upon anyone's copyright nor violates any proprietary rights and that any ideas, techniques, quotations, or any other material from the work of other people included in my PhD dissertation, published or otherwise, are fully acknowledged in accordance with the standard referencing practices. Furthermore, to the extent that I have included copyrighted material that surpasses the bounds of fair dealing within the meaning of the Canada Copyright Act, I certify that I have obtained a written permission from the copyright owner(s) to include such material(s) in my PhD dissertation.

I declare that this is a true copy of my PhD dissertation, including any final revisions, as approved by my PhD Committee and the Graduate Studies office, and that this PhD dissertation has not been submitted for a higher degree to any other University or Institution.

ABSTRACT

The research presented in this PhD dissertation renders a novel nano and ultra-fine structured cast industrial grade hypereutectic Al-Si-Cu engineering material and processing technologies capable of maximizing its functional characteristics. This development will allow for further engineering of exceptionally lightweight and near net-shape components for aerospace and transportation applications. The research outcomes offer the design and casting communities with new capabilities enabling gains in component properties, productivity, rapid component design and manufacturing procedures. These procedures include industrial melt chemical and physical treatments and an ultra rapid Solution and Artificial Aging Heat Treatments. These approaches were not feasible due to problems such as the lack of scientific knowledge on industrial grades of nano Al-Si-X alloys, limited solid solubility of elements, inadequate wear resistance in extreme environments and the lack of physical simulation engineering tools. The patented Universal Metallurgical Simulator and Analyzer (UMSA) Technology Platforms' capabilities were further developed to expedite Squeeze Casting (SC), Liquid and Semi-Solid melt processing using various pressure profiles for rapid physical simulations of these complex experimental industrial alloys. SC/HPDC UMSA experiments address: liquid and semi-solid chemical and dynamic physical treatments for structure control and elimination of solidification issues; neutralization of impurity elements; high temperature Solution Treatment and Artificial Aging; and elimination of the grain boundary precipitate-free zone that contributes to corrosion. The novel melt's physical treatments include impact pressure, monotonic pressure and cyclic pressure loading profiles. Several

novel as-cast and heat treated structures were developed and comprehensively characterized. Extensive UMSA Platform(s) processing and Thermal Analysis capabilities were enhanced, allowing for significant gains in understanding the link between processing parameters, Thermal Analysis data, and as-cast and heat treated material characteristics. The project utilized leading edge scientific methodologies for development of new cost effective nano and ultra-fine structured cast aluminum materials that will satisfy future fuel economy and emission targets.

DEDICATION

I dedicate my dissertation to my lovely wife Zuzana and to my sons Jurko and Peter.

My accomplishments are a measure of their love and support and their words of encouragement have carried me through the long process of developing a PhD dissertation.

I have a special feeling of gratitude for my loving mother, my sister Paulina, and for my father who passed away when I was 11 years old. Their impact on my success started long before I immigrated to Canada and began working on my thesis and I am forever thankful to them.

ACKNOWLEDGEMENTS

I would like to take this opportunity to thank my Co-Supervisors, Dr. Jerry H. Sokolowski and Dr. Andrzej Sobiesiak for their support and guidance during my PhD program and during the writing of this PhD dissertation.

I am grateful to Dr. Al Conle for his help with the development of the integrated Instron Hydraulic Testing Frame into the SC/HPDC UMSA Technology Platform and to Dr. Adam Gesing for his help with the deconvolution of the UMSA thermal data and with the SEM/EDS analysis.

I appreciate the help provided by Dr. Marcin Kasprzak, from the Silesian University of Technology, in Poland, regarding automation of the SC-UMSA Platform.

Many thanks to Sharon Lackie, from the Great Lakes Institute for Environmental Research and to Dr. Leszek Dobrzanski, from the Silesian University of Technology, for their assistance with SEM analysis. Thanks to Andy Jenner, Bruce Durfy and the members of the Technical Support Centre (TSC) for manufacturing the mini melting furnace, the die and the plunger.

I appreciate the support provided by CanmetMATERIALS, in Hamilton, in the area of comprehensive TEM analysis of the experimental test samples.

I also want to express my thanks to Dr. John Bonnen from the Ford Research and Innovation Center, in Michigan, for allowing me to have access to the microhardness and macrohardness testers.

Thanks to Dan Edelstein from the Leddy Library for assistance with the statistical analysis of the experimental data.

To the current and former members of the Metal Casting and Post-Processing (MCPT) Group thank you for your friendship and for assistance with various demanding tasks. I also want to thank Ellen Moosberger for her assistance with the review and editing of this PhD dissertation.

Initial work on development of the die in the frame was carried out by AUTO21 Master's students, Joe Giovanatto and Paul Marchwica and by the Capstone students. The author, Brandon Hooper, Dr. Al Conle, Dr. Marcin Kasprzak and Mohammad Alam, under the supervision of Dr. Jerry Sokolowski, worked on the modification and upgrading of the die settings, the new plunger design, slide gating, thermocouple settings and on the improvement of data collection as well as on software development for successful operation of the SC-UMSA Technology Platform.

The Displacement Pin Technology developed in the framework of the AUTO21 program, with various dynamic pressure profile capabilities will be patented and industrially commercialized by the MCPT Group and by the University of Windsor.

TABLE OF CONTENTS

DECLARATION OF CO-AUTHORSHIP..... iii

ABSTRACT….....….....……. …….iv

DEDICATION……..…....…….vi

ACKNOWLEDGEMENTS……..…..…..…vii

LIST OF TABLES……..….….xiv

LIST OF FIGURES……..….……...xvi

LIST OF APPENDICES……..……...xxxvii

LIST OF ABBREVIATIONS/SYMBOLS…….……..xxxviii

CHAPTER 1: OBJECTIVES……..…….……..…1

CHAPTER 2: LITERATURE REVIEW……..… 4

2.1 Cast Aluminum Alloys……... ……..……4

2.1.1 Aluminum-Silicon Equilibrium Phase Diagram and Structure Characteristics……..…..5

2.1.2 Cast Aluminum and Aluminum Alloy Designation System……...……..7

2.1.3 Selected Alloying Elements of Al-Si Alloys…….....…...7

2.1.4 Selected Silicon Modifying Elements…….11

2.1.5 Selected Grain Refining Elements……..12

2.1.6 Selected Impurity Elements……...13

2.1.7 Silicon Crystal Growth……...13

2.2 Melt Treatment of Al-Si Alloys..... ……...28

2.2.1 Chemical Modification of Hypoeutectic Al-Si Alloys……29

2.2.2 Chemical Modification of Hypereutectic Al-Si Alloys……...34

2.2.3 Melt Thermal Treatment of Al-Si Alloys (Quench Modification)……..43

2.2.4 Physical Treatment of Al-Si Alloys…….…50

2.3 Squeeze Casting….....……..…..……..64

2.3.1 Squeeze Casting Technology……..….…64

2.3.2 Effect of Pressure on Solidification of Al-Si Alloys……..……65

2.4 Solid State Heat Treatment of Al-Si Alloys..... ……..… ….…70

2.4.1 Solution Heat Treatment 72
2.4.2 Quenching 73
2.4.3 Artificial Aging (AA) and Natural Aging (NA) of Al-Si Alloys 73
2.4.4 Heat Treatment of Hypereutectic Al-Si Alloys 76
2.5 Thermal Analysis (TA) of Hypereutectic Al-Si Alloys.....80
2.5.1 Overview of Thermal Analysis Techniques.....80
2.5.2 Thermal Analysis using the Universal Metallurgical Simulator and Analyzer (UMSA) Technology Platform.....83
2.5.3 UMSA Thermal Analysis of the Hypereutectic Al-20Si-3Cu Alloy.....86
2.6 Silicon Equivalency.....91
2.7 Literature Review Conclusions.....93
2.8 Development Status of Nano and Ultra-fine Structed Cast Alloys – Scientific Research Hypothesis.....95
CHAPTER 3: EXPERIMENTAL METHODOLOGIES.....98
3.1 Experimental Materials.....98
3.1.1 Chemical Composition and Si_{EQ} of the Experimental Ingot.....98
3.1.2 Experimental Sr Master Alloy, Pure Calibration Metals and BN Die Lubricoat.....100
3.2 High Temperature (HT) UMSA Technology Platform.....101
3.3 SC/HPDC UMSA Technology Platform.....104
3.3.1 Background.....104
3.3.2 SC/HPDC UMSA Technology Platform's Functional Design.....105
3.3.3 SC/HPDC UMSA Die.....106
3.3.4 SC/HPDC UMSA Test Sample.....108
3.3.5 Processing Parameters for Programmable SC/HPDC UMSA Experiments.....108
3.3.6 Test Control Software and Data Collection Procedure for SC/HPDC UMSA Experiments.....114
3.3.7 Procedure(s) used for the SC/HPDC UMSA Experiments.....117
3.3.8 Thermal Analysis, Testing of Analytical Characteristics and Data Interpretation Methodologies.....122

3.4 Calibration of Thermocouples and Data Acquisition Systems for the HT and SC/HPDC UMSA Platform Experiments.....123

3.4.1 Thermocouple Selection and Calibration Requirements.....123

3.4.2 Calibration Procedures for the Experimental Thermocouples and Data Acquisition Systems.....124

3.4.3 Effect of SC/HPDC UMSA Process Parameters on Average Solidification Temperature of Pure Aluminum.....129

3.5 Metallographic Sample Preparation.....130

3.6 Light Optical Microscopy (LOM) Analysis.....131

3.7 Microhardness and Hardness Measurements.....131

3.8 Scanning Electron Microscopy (SEM) Analysis.....132

3.9 Focused Ion Beam (FIB) Microscopy.....133

3.9.1 S/TEM Sample Preparation.....133

3.10 Scanning/Transmission Electron Microscopy (S/TEM) Analysis….....134

3.11 Design of HT and SC/HPDC UMSA Experiments…….....135

CHAPTER 4: EXPERIMENTAL RESULTS and DATA ANALYSIS.....138

4.1 Thermal and Microstructural Analysis of Experimental Alloy, Sample #0808 – Unmodified Melt Solidified at 0.1MPa and ASR=0.4°C/s.....138

4.1.1 HT UMSA Thermal Characteristics for Sample #0808.....138

4.1.2 Microstructural Characterization of Sample #0808.....149

4.1.3 HT UMSA Thermal Characteristics of Sample #0618.....152

4.1.4 Microstructural Characterization of Sample #0618.....161

4.1.5 Summary of Thermal and Microstructural Analysis for the Unmodified and 0.15wt.%Sr Modified Experimental Alloys Solidified under Atmospheric Pressure and at an ASR of 0.4°C/s.....165

4.2 SC/HPDC UMSA Thermal and Microstructural Analysis of #0717, #0508 and #0925 Experimental Alloys Solidified at an ASR ≈ 10°C/s.....168

4.3 Effect of Various Pressure Loading Modes on the Thermal Characteristics and Microstructure of the Experimental Alloy Processed in the SC/HPDC UMSA Die.....178

4.3.1 Development of Novel Al-Si Sandwich (Shell) Dendritic Structure Unmodified Alloy Sample #0429.....179
4.3.2 Thermal Data and Microstructure for the 0.04 wt.%Sr Modified Alloy Sample #1009 processed in the SC/HPDC UMSA Platform..... 191
4.3.3 Thermal and Microstructural Analysis for the 0.15 wt.%Sr Modified Alloy Samples processed in the SC/HPDC UMSA Die using Impact and Cyclic Pressure Loadings.....195
4.4 As-Cast Structure Categories for the 0.15wt%Sr Modified Test Samples processed in the SC/HPDC UMSA..... 243
4.4.1 Analysis of the Best Category #1, SC/HPDC UMSA processed 0.15wt% Sr Modified Test Samples #0925b, #1002b, #0919..... 248
4.4.2 Sample #0925/Category #4, 0.15wt.%Sr Modified, Naturally Solidified in the SC/HPDC UMSA Die.....249
4.4.3 Summary of the Process Parameters, TA Data and Resultant As-cast Structure Categories.....250
4.5 Statistical Analysis of As-cast Structure Categories, TA Data and Process Parameters of Test Samples Presented in Sections 4.3 and 4.3.3.....254
4.6 Ultra-Rapid Si Spheroidization and $Al_5Cu_2Mg_8Si_6$ and Al_2Cu Phases Dissolution Heat Treatment.....259
4.7 Microhardness and Macrohardness for Selected Experimental Samples vs. the Yamaha Engine Block.....271
4.8 Wear Performance of Selected Test Samples.....275
4.9 Comparison of the Yamaha Engine Block Structure vs. the SC/HPDC UMSA Sample (Category 1.1)(# 0925b-AA2 Heat Treated).....278
4.10 Development of Nano and Ultra-Fine Structured Aluminum Alloys and Composites that are not reported in this Dissertation.....280
CHAPTER 5: DISCUSSION REGARDING SELECTED EXPERIMENTAL OUTCOMES AND COMPARISON WITH THE LITERATURE INFORMATION.....282
CHAPTER 6: MAIN FINDINGS and CONCLUSIONS.....287
CHAPTER 7: RECOMMENDATIONS FOR FUTURE RESEARCH……291

APPENDIX - S/TEM/EDS Analysis of the Yamaha Engine Block……319
REFERENCES/BIBLIOGRAPHY……294
VITA AUCTORIS……...…329

LIST OF TABLES

Table 1. Cast Aluminum and Aluminum Alloy Designation System [3, 4]. 7
Table 2. Mechanical Properties vs. Silicon Crystal Growth Velocity for Hypoeutectic and Near Eutectic Al-Si Alloys. 14
Table 3. Thermal Characteristics obtained during the Melting and Solidification Processes for the Al-20Si-3Cu Alloy [248]. 88
Table 4. UMSA Cooling Cycle Thermal Characteristics for the Test Sample taken from the Al-20Si-3Cu Ingot [241]. 89
Table 5. Comparison of the Chemical Compositions for Selected Hypereutectic Alloys 91
Table 6. Reactions during Solidification of the B390.1 Alloy at different SR[251]. 91
Table 7. Nominal Chemical Composition of the Experimental Alloy [6]. 98
Table 8. T_{liq}, $T^{AlSi}_{E, NUC}$ and Si_{EQ} for unmodified experimental alloy solidified in the HT UMSA Platform at ASR = (0.4 to 1.1) °C. 100
Table 9. Thermocouple Characteristics [258]. 124
Table 10. Matrix for Calibration of the Thermocouples, HT and SC/HPDC UMSA Data Acquisition Systems using Pure Aluminum and Zinc. 125
Table 11. Effect of SC/HPDC UMSA Process Parameters on Average Solidification Temperature for Pure Aluminum. 129
Table 12. HT UMSA Tests for the Experimental Alloy used for Comprehensive TA Data and Microstructure Analysis. 136
Table 13. SC/HPDC UMSA Test Processing Parameters for the Development of Novel Structures. 136
Table 14. HT UMSA Processing Parameters using Ultra Rapid Two and Three Step Solution Heat Treatment Tests for the Sr Modified Experimental Alloy. 137
Table 15. HT UMSA Processing Parameters for Ultra Rapid Artificial Aging Tests for the Sr Modified Experimental Alloy. 137

Table 16. Thermal Analysis Events during Solidification of the Unmodified Experimental Alloy in the HT UMSA Platform under Atmospheric Pressure, ASR = 0.4 °C/s, ref. #0808.....145
Table 17. Thermal Analysis Events during Solidification for the 0.15 wt.%Sr modified experimental alloy in the HT UMSA Platform under atmospheric pressure, ASR = 0.4 °C/s, ref. #0618. 157
Table 18. Selected Thermal Characteristics for Test Samples #0717, #0508 and #0925.....175
Table 19. Summary of Subsurface As-cast Structure Data associated with the As-Cast Structure Categories.....245
Table 20. Subsurface and Center Characteristics for Eight Test Sample Structure Categories. 246
Table 21. Summary of the Process Parameters and Resultant As-Cast Structure Categories. 251
Table 22. Summary of Thermal Analysis Data and Resultant As-Cast Structure Categories. 252
Table 23. Summary of Novel Structures for the Experimental Alloy. 253
Table 24. Structure Category vs. Procee Parameters.....257
Table 25. D_{avg}Si-WA vs. Process Parameters.....257
Table 26. MCRn vs. Process Parameters.....257
Table 27. Structure Category vs. TA Data & Process Parameters.....257
Table 28. D_{avg}Si-WA vs. Process Parameters & TA Data.....257
Table 29. D_{max}AlSi-Co vs. Process Parameters & TA Data 257
Table 30. Comparison between literature references, the Yamaha engine block and experimental sample # 0925b's phase stochiometries and sizes of its structural features.....269
Table 31. Comparison of the Chemical Composition (wt.%) of the Main Phases between the Yamaha Engine Block and Sample # 0925b under As-cast and Heat Treated Conditions. 270

LIST OF FIGURES

Figure 1. Aluminum-Silicon equilibrium phase diagram and chemical compositions for the a-hypoeutectic (from 1.65 wt.%Si to 12.6 wt.%Si), b-eutectic (12.6 wt.%Si), c-hypereutectic (> 12.6 wt.%Si) phases [2], [3]. Note: The pure Al liquidus temperature according to the NIST standard is 660.323 °C..... 5

Figure 2. Silicon morphology after directional solidification of an Al-Si near-eutectic alloy (Al-12Si) at velocities of (20, 250 and 950) m/s. These structures represent a) flakes, b) mixed flakes/fibers and c) fiber morphologies. The Al-rich phase has been chemically removed [48], [49]..... 14

Figure 3. The crystal structure of stable Si nuclei created by the assembly of two tetrahedrals [47]..... 15

Figure 4. Twin Plane Re-entrant Edge Mechanism. a) The equilibrium form of a germanium crystal, an octahedron bounded by {111} surfaces. The solid is to be twinned about the plane indicated by the dotted line, b) Crystal with a single twin, c) Closure of twins due to ridge formation, d) A crystal containing two twin planes, with six equivalent {211} preferred growth directions, e) Creation of extra re-entrant corners I and II, f) Crystal with two twins, g) Propagation of crystal due to re-entrant corners [51]..... 17

Figure 5. a) SEM deep etched Star-like dendritic morphology of primary silicon [57], [58]. b) SEM micrograph five-fold branched primary Si particle surrounded by Al-halo and Al-Si eutectic, [52], [54], [55]..... 18

Figure 6. Diagram of the Al–Si alloys microstructure vs. Si concentration and Solidification Rates. I) Fiber-like structures with a primary α–phase. II) A fine-grained eutectic-like structure. III) A flake structure with primary Si crystals. IV) A flake structure with a primary α-phase [59]..... 18

Figure 7. Primary Silicon morphology as a function of undercooling and Si concentration [52], [60]..... 19

Figure 8. Feathery type Silicon in the hypereutectic Al-17wt.%Si alloy, a) LOM micrograph,..... 19
Figure 9. A schematic illustration of the polygonal outline of octahedral primary silicon in the sectioning planes (two dimensional observations), a) triangular outline, b) square outline, c) trapezoidal outline and d) hexagonal outline [66], [67]..... 20
Figure 10. Schematic illustration of growth sequence of octahedral primary Si [66]..... 21
Figure 11. SEM micrographs for the Al-20Si alloy, a) shapes of polygons, b) magnified micrograph of the indicated region (see arrow) in a) - imperfect octahedral primary Si [66], [68]..... 21
Figure 12. SEM micrograph of dendrite Silicon morphology, the Al-50 at.%Si droplet solidified at the onset of undercooling at 10 °C [69]..... 22
Figure 13. Micrographs of the spherical primary silicon crystal in an Al-16Si alloy treated with Sodium [72]; a) BSE image; b) Electron Probe Microanalysis for SiKα radiation; c) Electron Probe Microanalysis for NaKα radiation. Note: that the contrast in a) matches the Sodium segregated region revealed in the NaKα micrograph c)..... 23
Figure 14. a) SEM micrograph showing the plate-like primary silicon crystals formed at low undercooling, b) SEM micrograph of the growth front of extracted primary Si showing multiple twin traces in the Al-16Si alloy [69], [72]. 24
Figure 15. LOM micrograph of the Al-12Si alloy cooled in furnace and quenched after 50 % of the structure has solidified. Flake Silicon eutectic nodules and “Wheat Sheaf” morphology, 240x [75]..... 25
Figure 16. SEM micrographs, deep-etched Al-14Si-0.18Sr alloy, longitudinal section, growth direction bottom to top. V = 89 μm/s. a) Modified eutectic silicon, 242x.b) enlargement of the marked area in a) 1760x [75]..... 25
Figure 17. SEM micrograph showing primary Silicon Dendrites in the Aluminum Matrix for the Strontium modified hypereutectic Al-20Si-3Cu Alloy [78]. 27
Figure 18. SEM microstructure showing nano blocky primary silicon crystals, which grow like primary silicon in the 0.15 wt.%Sr modified hypereutectic Al-20Si-3Cu alloy, solidified at a MCR of ≈ 400 °C/s [78]..... 28

Figure 19. Schematic representation for adsorption of impurity atoms at monolayer steps on a growth interface. Where ξ is the spacing between added atoms, $2r_c$ is a critical dimension for layer extension [89]..... 30
Figure 20. Schematic representation of (011) plane projection of the eutectic Si phase: a) Type I, Sr–Al–Si co-segregation which promotes twinning by changing the stacking sequence. b) Type II, Sr–Al–Si co-segregation within the eutectic Si phase at the re-entrant edges or growing surfaces. A, B and C – represents Si crystals with different orientations [96]..... 31
Figure 21. The influence of casting conditions on the properties of the unmodified and 0.05 wt.%Sr modified Al-11Si alloy, a) Elongation, b) Yield (R_{02}) and Ultimate Tensile Strength (R_m) [108]..... 33
Figure 22. LOM micrographs for the hypereutectic Al-18Si alloy, a) re-melted and cast without melt treatment, b) treated with 0.2 wt.%$SrCl_2$ [83]..... 36
Figure 23. Si dendrite in the hypereutectic Al-18Si alloy modified with 0.01 wt.%Sr [129]..... 36
Figure 24. Influence of Sr addition on Average Particles Size and Volume Fraction of the Primary Silicon [129]..... 37
Figure 25. LOM micrographs of the Al-30Si alloy; a) unmodified, b) modified by 0.06 wt.%P and 0.07 wt.%Sr combined [130]..... 38
Figure 26. Microstructure of the Al-18Si alloy: a) conventionally cast without additions, b) with the addition of 0.005 wt.%P + 0.02 wt.%Sr and processed by the solid-liquid duplex casting process [131]..... 39
Figure 27. SEM micrographs, deep-etched shape cast Al-17Si-3Ba alloy, a) longitudinal and b) transverse section. Star-like (Points A and C), FishBone (Point B) morphologies of the Si crystal. Point (C) shows the Divergence of Si flakes from a point of origin located at the center of the star-like assembly of the Si crystal [133]..... 40
Figure 28. Schematic of the liquidus lines and a eutectic point shift due to the solid solution of Ba in Si as imposed in the Al-Si phase diagram according to reference [135]..... 40

Figure 29. Effect of the RE addition to the Al-21Si alloy on: a) primary Si size and at a different CR (the CR is calculated between the primary reaction and the eutectic reaction temperature), b) Temperature of metallurgical reactions at a CR of 2 °C/min [138]..... 42
Figure 30. LOM micrographs: a) Al-17Si alloy + 3 wt.%$A1_2O_3$, A-Al_2O_3 particles, B-partially modified primary silicon, b) Al-17Si alloy + 3 wt.%$A1_2O_3$ + 0.5 wt.%Na modified primary and eutectic silicon [139]..... 42
Figure 31. SEM micrographs of the deep-etched Al-20Si alloy, a) unmodified and b) modified with 0.5 wt.% γ-$A1_2O_3$ nanoparticles [140]..... 43
Figure 32. SEM micrographs of the morphology of the Al-13Si, a) without the Thermal Rate Treatment, b) with the Thermal Rate Treatment [50]..... 44
Figure 33. The mean atomic density-ρ_o and coordination number of the alloy-n_c vs. the superheating temperature of the alloy [50]..... 44
Figure 34. LOM micrographs of the Al-16Si alloy cast into a metal mold at different superheating temperatures and cooling rates, a) The superheating temperature of 720 °C cooled at 60 °C/s, b) 720 °C and 150 °C/s, c) 1050 °C and 150 °C/s [87]..... 45
Figure 35. Comparison of the effect of the melt superheating temperature on the Si particle size for the Al–16Si alloy at different CR and SR (sand or metal mold); S-cooled at 60 °C/s and cast into a sand mold, M-cooled at 60 °C/s and cast into a metal mold, MC-cooled at 150 °C/s and cast into a metal mold [87]..... 46
Figure 36. SEM micrographs for the Al–20Si alloy, a) as-cast (SR = 50 °C/s), b) melt spun ribbon at the free surface (SR = 1.11×10^6 °C/s) [142]..... 46
Figure 37. LOM micrographs, hypereutectic Al-20Si-3Cu alloy UMSA test samples superheated to various temperatures (735, 785 and 850) °C solidified under various SR (1. 3, 4. 5 and 35) °C/s..... 50
Figure 38. Effect of ultrasonic treatment on the size of primary silicon particles in an Al–17Si alloy without refining additions [173]..... 52

Figure 39. Microstructure of the Al-20Si alloy, a) as-cast by squeeze casting at 760 °C indicating formation of non-equilibrium α-aluminum dendrites, b) semi-solid rheo squeeze casting after USV treatment [162]..... 53
Figure 40. Schematic presentation of vibrating force, developed by the interaction of alternating electric and stationary magnetic fields [175], [176]..... 54
Figure 41. LOM micrographs for the Al-17Si alloy, a) without the magnetic field-electric current (0 T, approximately 60 A, 100 Hz), b) vibrated specimens (1.6 T, approximately 60 A, and frequencies of 1 kHz) [179] . 56
Figure 42. The average size of the primary Silicon particles vs. a) magnetic field intensity and b) holding time at 710 °C (f = 1 kHz, J = 60 A) [179]..... 56
Figure 43. SEM micrographs, morphologies of primary Silicon in the hypereutectic Al-17Si alloy cast at 675 °C, a) without PECT, b) with PECT input voltage 2 kV, frequency 4 Hz [182]..... 57
Figure 44. SEM micrographs for the Al-25Si alloy, a) untreated alloy, b) alloy treated by electric pulse (800 V, 22 Hz, at 760 °C, for 2 min.) [183]..... 58
Figure 45. LOM micrographs for the A390 alloy, a) Rheocast, quenched directly from the semi-solid region at 561.5 °C, b) Thixocast, reheated to the semi-solid region at 561.5 °C, and quenched [185]..... 59
Figure 46. Schematic illustration of the MC - HPDC process [186]..... 60
Figure 47. LOM micrographs for the Al-17Si alloy, a) unmodified and conventional HPDC, b) 0.01 wt.%Sr modified and conventional HPDC, c) 0.01 wt.%Sr modified and MC-HPDC [186]. 60
Figure 48. Comparison of the HPDC and MC HPDC technologies applied to the Al-17Si alloy, a) tensile properties, b) Primary Si particle size distribution [187]..... 60
Figure 49. SEM micrographs for the Al-20Si alloy treated by HCPEB, 23 kV, 25 pulses, 25 J/m^2 a) the cross section image after etching, b) local enlargement of a) [191]..... 62
Figure 50. SEM micrographs of the cross section of the laser remelted layer for the Al–30Si cast alloy, a) Cross section of the parent sample and of the remelted layer (F: fully remelted layer, P: partially remelted layer, BM:

as-cast structure), b) primary and eutectic Si particles within the fully remelted layer [194]..... 63
Figure 51. Schematic diagram of the Squeeze Casting Technology [198]..... 65
Figure 52. The effect of rapid cooling and the application of 100 MPa pressure on the Al-Si phase diagram [199]..... 66
Figure 53. Change of Liquidus and Solidus lines in the binary Al-Si phase diagram following rapid solidification at ambient pressure [212]..... 68
Figure 54. As-cast microstructures for the Al-20Si alloy solidified under: (a, e) ambient pressure, (b, f) 1 GPa, (c, g) 2 GPA and (d, h) 3 GPa. Processed melt temperature: (727 to 877) °C, pressure: kept for 5 minutes, cooling rate 20 °C/s..... 69
Figure 55. SEM micrographs of Si precipitates in the primary α-Al phase solidified under 3GPa after heating at 5°C/min to (a) 160°C, (b) 230°C and (c) 300°C..... 70
Figure 56. Equilibrium binary solid solubility as a function of the temperature for alloying elements most frequently added to aluminum alloys [5]..... 71
Figure 57. Dissolution process for a) eutectic Al_2Cu and b) blocky Al_2Cu particles [225]..... 73
Figure 58. Precipitation hardening curves for binary Al-Cu alloys quenched in water at 100 °C and artificially aged at 150 °C[5]..... 75
Figure 59. Precipitation Heat Treatment or Artificial Aging curves for the Solution Heat Treated 6061 Aluminum Alloy [5]..... 76
Figure 60. a) Hardness Change vs. Aging Time for the alloys aged at 180 °C, b) Effect of Copper and c) Effect of Silicon content on hardness in the samples aged at 180 °C for 15 hr [227]..... 77
Figure 61. LOM microstructure for the Al–12Si–Cu–Mg Alloy, a) As-cast structure without modification and heat treatment and b) Sodium modified structure after solution heat treatment at 490 ºC/4 hr [227]..... 78
Figure 62. Temperature vs. time heat treatment plots of the UMSA experiments performed for the Al-20Si engine block and test samples: a) T6 Conventional - solution at 490 °C for 4 hr, air quenching and AA at 200

°C for 4hr, b) T6 Modified - rapid solidification arrested at 380 °C, followed by solution at 510 °C for 0.5 hr, air quenching and continuous AA at 200 °C for 4 hr [7]..... 79
Figure 63. LOM micrographs of the Al-20Si alloy: a) test sample solidified at 20 °C/s, represents the thick section of the HPDC engine block, b) test sample subjected to the Solution Treatment operation at 510 °C for 0.5 hr [6]..... 80
Figure 64. Cooling Curve (TA) and its first derivative (ATD) for the AlSi6 alloy after AlSr10 modification [237]..... 82
Figure 65. a) The cooling, first and second derivative curves of the alloy containing Bi showing the TA characteristics, b) correlation between the first and the second derivative curves in the Al dendrite arrest region showing the points of interest [110]..... 83
Figure 66. Photograph of the Environmental UMSA Technology Platform's main components..... 85
Figure 67. First derivative of the Cooling Curves vs. Temperature for the hypereutectic Al-20Si-3Cu Yamaha alloy solidified in: a) a low thermal mass cup at MCR = 5.5 ºC/s, b) a low thermal mass cup at MCR = 15 ºC/s , c) a high thermal mass cup at MCR = 75 ºC/s..... 85
Figure 68. UMSA Time vs. Temperature Heating and Cooling Curves for the Hypereutectic Al-20Si-3Cu Ingot. The test samples were melted at a heating rate of 0.75 °C/s and solidified under controlled conditions at (1, 2.8 and 4.4) °C/s cooling rates, respectively [241]. The numbers correspond to various metallurgical reactions as shown in Table 3 below [248]..... 88
Figure 69. UMSA First Derivative of the Heating and Cooling Curves for the Hypereutectic Al-20Si-3Cu Ingot [241]..... 89
Figure 70. Fraction Solid vs. Temperature Curve for the SR = 1 °C/s for the Al-20Si-3Cu Alloy [248].....90
Figure 71. a) Experimental ingot, b) location of the SC/HPDC UMSA and HT UMSA test samples..... 99

Figure 72. Photograph of the HT UMSA Technology Platform's main components. 102
Figure 73. a) HT UMSA test sample drawing and b) picture..... 103
Figure 74. High Temperature UMSA test sample and TA cup assembly..... 103
Figure 75. Overall view of the SC/HPDC UMSA Technology Platform..... 106
Figure 76. Details of the SC/HPDC UMSA Die assembly..... 107
Figure 77. The transparent 3D model assembly for the plunger, melting chamber and die..... 107
Figure 78. SC/HPDC UMSA test sample; a) picture before SC processing, b) drawing with dimensions (mm) before SC processing, c) UMSA processed as-cast sample..... 108
Figure 79. SC/HPDC UMSA processing parameters for the pressure profile, load and stroke curves vs. time..... 110
Figure 80. Cumulative energy input expressed as work done by the plunger under impact and cyclic pressure (38 - 81) MPa/10 c applied to the 0.15 wt.%Sr modified experimental alloy processed in the SC/HPDC UMSA die, ref. #0925b..... 112
Figure 81. SC/HPDC UMSA test setup, data recording and data collection devices.... 115
Figure 82. Schematic diagram of SC/HPDC-UMSA data collection..... 117
Figure 83. Desktop view of four channels Labview software for monitoring and recording temperatures of thermocouples in HP computer..... 122
Figure 84. Comparison of calibrated and uncalibrated cooling curves and uncalibrated first derivative curve vs. time for pure Aluminum, solidified in the HT UMSA platform under atmospheric pressure (0.1 MPa)..... 127
Figure 85. Comparison of calibrated and uncalibrated cooling curves and uncalibrated first derivative curve vs. time for pure Zinc solidified in the HT UMSA die under atmospheric pressure and lower SR ≈ 0.25 ^{o}C/s..... 127
Figure 86. Relationship between UMSA measured solidification temperature and NIST calibrated solidification temperature at 0.1 MPa and ASR ≈ 0.4 ^{o}C/s..... 128
Figure 87. Cooling curves, first derivative curves and cyclic pressure profile curves vs. time for Pure Aluminum processed in the SC/HPDC UMSA die..... 129

Figure 88. Preparation of the samples for S/TEM analysis; a) the area of interest is marked as a red rectangle, b) deposited platinum strip, c) the bulk material around the Pt strip was removed allowing for formation of the specimen slice, d) the Pt needle welded to the specimen slice allows for cutting and removal from the bulk sample, e) the sample slice was thinned by the ion beam, f) perpendicular view of the thin membrane having a thickness of 200 nm. The thinned specimen was welded to the copper grid for further S/TEM analysis..... 134

Figure 89. (a, b). a) Cooling/Solidification Curve superimposed with the First Derivative and Dynamic Baseline vs. Time and b) Fraction Solid Curve vs. Time for the unmodified experimental alloy, solidified under atmospheric pressure in the HT UMSA Platform, ASR = 0.4 °C/s, ref. #0808..... 140

Figure 90. First derivative of the Cooling/Solidification Curve and Fraction Solid Curve vs. Temperature for the unmodified experimental alloy, solidified under atmospheric pressure in the HT UMSA Platform, ASR = 0.4 °C/s, ref. #0808..... 141

Figure 91. Cooling/Solidification and First Derivative Curves (region of primary Si and β-Fe phase nucleation and growth) vs. Time for the unmodified experimental alloy, solidified under atmospheric pressure in the HT UMSA Platform, ASR = 0.4 °C/s, ref. #0808..... 142

Figure 92. First derivative of the Cooling/Solidification Curve (region of primary Si and β-Fe phase nucleation and growth) vs. Temperature for the unmodified experimental alloy, solidified under atmospheric pressure in the HT UMSA Platform, ASR = 0.4 °C/s, ref. #0808..... 142

Figure 93. Solidification and First Derivative Curves (region of β-Fe phase and Al-Si Eutectic nucleation and growth) vs. Time for the unmodified experimental alloy solidified under atmospheric pressure in the HT UMSA Platform, ASR = 0.4 °C/s, ref. #0808..... 143

Figure 94. First derivative of the Cooling/Solidification Curve (region of β-Fe phase and Al-Si Eutectic nucleation and growth) vs. Temperature for the

unmodified experimental alloy, solidified under atmospheric pressure in the HT UMSA Platform, ASR = 0.4 °C/s, ref. #0808..... 143

Figure 95. Solidification and First Derivative Curves (regions: Al-Si eutectic, α-Fe, π, Q, Θ phases and (Q+Θ) eutectic nucleation and growth and Solidus temperature) vs. Time for the unmodified experimental alloy, solidified under atmospheric pressure in the HT UMSA Platform, ASR = 0.4°C/s, ref. #0808..... 144

Figure 96. First derivative of the Solidification/Cooling Curve (Regions: Al-Si Eutectic, α-Fe, π, Q, Θ phases & (Q+Θ) eutectic growth and Solidus temperature) vs. Temperature for the unmodified experimental alloy, solidified under atmospheric pressure in the HT UMSA Platform, ASR =0.4 °C/s, ref. #0808..... 144

Figures 97. The as-cast micrographs for the unmodified experimental alloy solidified in the HT UMSA Platform under atmospheric pressure and at ASR = 0.4 ^{o}C/s; a,e,f) LOM micrographs/polished, b) SEM micrographs/deep-etched, c,d) SEM micrographs/polished, ref.#0808..... 150

Figure 98. a) LOM and b) SEM micrographs of the polished test sample for the unmodified experimental alloy solidified in the HT UMSA Platform under atmospheric pressure and at ASR = 0.4 ^{o}C/s, ref. #0808..... 151

Figure 99. a) Cooling/Solidification Curve superimposed with the First Derivative and the Dynamic Baseline and b) Fraction Solid Curves vs. Time for the 0.15 wt.%Sr modified experimental alloy, solidified under atmospheric pressure in the HT UMSA Platform, ASR = 0.4 °C/s, ref. #0618..... 153

Figure 100. First Derivative of the Cooling/Solidification Curve and Fraction Solid and the DBL Curves vs. Temperature for the 0.15 wt.%Sr modified experimental alloy, solidified under atmospheric pressure in the HT UMSA Platform, ASR = 0.4 °C/s, ref. #0618..... 154

Figure 101. Cooling/Solidification and First Derivative Curves (region of Liquidus and Recalescence and Undercooling Temperatures associated with α-Al Phase Nucleation and Growth) vs. Time for the 0.15 wt.%Sr modified

experimental alloy, solidified in the HT UMSA Platform under atmospheric pressure and ASR = 0.4 °C/s, ref. #0618..... 154
Figure 102. First Derivative Curve (region of liquidus and recalescence and undercooling temperatures associated with α-Al phase nucleation and growth) vs. Temperature for the 0.15 wt.%Sr modified experimental alloy, solidified in the HT UMSA Platform under atmospheric pressure and ASR = 0.4 °C/s, ref. #0618..... 155
Figure 103. Solidification/Cooling and First Derivative Curves (region of recalescence associated with π, Q, Θ phases & Q+Θ eutectic nucleation and growth and solidus temperature) vs. Time for the 0.15 wt.%Sr modified experimental alloy, solidified in the HT UMSA Platform under atmospheric pressure and ASR = 0.4 °C/s, ref. #0618..... 155
Figure 104. First Derivative Curve (region of recalescence associated with π, Q, Θ phases and Q+Θ eutectic nucleation and growth and Solidus Temperature) vs. Temperature for the 0.15 wt.%Sr modified experimental alloy, solidified in the HT UMSA Platform under atmospheric pressure and ASR = 0.4 °C/s, ref. #0618..... 156
Figure 105. The as-cast micrographs for the 0.15 wt.%Sr modified experimental alloy solidified in the HT UMSA Platform under atmospheric pressure and at ASR = 0.4 ^{o}C/s. b-e) LOM micrographs/polished, a, f) SEM micrographs/polished, ref. #0618..... 163
Figure 106. The as-cast micrographs for the 0.15 wt.%Sr modified experimental alloy solidified in the HT UMSA Platform under atmospheric pressure and at ASR = 0.4 ^{o}C/s. a-d) LOM micrographs/polished, e, f) SEM micrographs/polished, ref. #0618..... 164
Figure 107. Cooling/Solidification Curves and First Derivative Curves vs. Time for the unmodified and 0.15 wt.%Sr modified experimental alloy solidified in the HT UMSA SS cup under atmospheric pressure, ASR = 0.4 ^{o}C/s, ref. #0808 and #0618..... 166

Figure 108. First Derivative Curves vs. Temperature for the unmodified and 0.15 wt.%Sr modified experimental alloy solidified in the HT UMSA SS cup under atmospheric pressure, ASR = 0.4 ^{o}C/s, ref. #0808, #0618..... 166
Figure 109. Fraction Solid Curves vs. Temperature for the unmodified and 0.15 wt.%Sr modified experimental alloy solidified in the HT UMSA SS cup under atmospheric pressure, ASR = 0.4 ^{o}C/s, ref. #0808 and #0618..... 167
Figure 110. Selected Thermal Characteristics for the unmodified and 0.15 wt.%Sr modified experimental alloy solidified in the HT UMSA SS cup under atmospheric pressure, ASR = 0.4 ^{o}C/s, ref. #0808 and #0618..... 167
Figure 111. a) Cooling/Solidification Curve superimposed with the First Derivative and the Dynamic Baseline Curve and b) Fraction Solid Curve vs. Time for the unmodified experimental alloy, solidified under atmospheric pressure in the SC/HPDC UMSA die, ASR = 10.2 °C/s, ref. #0717.....170
Figure 112. First derivative of the Cooling Curve, Dynamic Baseline Curve and Fraction Solid Curve vs. Temperature for the unmodified experimental alloy, solidified under atmospheric pressure in the SC/HPDC UMSA die, ASR = 10.2 °C/s, ref. #0717..... 171
Figure 113. a) Cooling/Solidification Curve superimposed with the First Derivative and the Dynamic Baseline Curve and b) Fraction Solid Curve vs. Time for the 0.1 wt.%Sr modified experimental alloy solidified in the SC/HPDC UMSA die under atmospheric pressure, ASR = 15.3 °C/s, ref. #0508..... 172
Figure 114. First Derivative of the Cooling Curve and Fraction Solid Curve vs. Temperature for the 0.1wt.%Sr modified experimental alloy solidified in the SC/HPDC UMSA die under atmospheric pressure, ASR = 15.3 °C/s, ref. #0508..... 173
Figure 115. a) Cooling/Solidification Curve superimposed with the First Derivative and the Dynamic Baseline Curve and b) Fraction Solid Curve vs. Time for the 0.15 wt.%Sr modified experimental alloy solidified in the SC/HPDC UMSA die under atmospheric pressure, ASR = 9.3 °C/s, ref. #0925..... 174

Figure 116. First derivative of the Cooling Curve, Dynamic Baseline Curve and Fraction Solid Curve vs. Temperature for the 0.15 wt.%Sr modified experimental alloy solidified in the SC/HPDC UMSA die under atmospheric pressure, ASR = 9.3 °C/s, ref. #0925..... 175
Figure 117. LOM micrographs for the experimental alloy solidified in the SC/HPDC UMSA die under atmospheric pressure: a, b) unmodified, ref. #0717; c, d) 0.1 wt.%Sr modified, ref. #0508; e, f) 0.15 wt.%Sr modified, ref. #0925..... 176
Figure 118 (a - f). SEM micrograph, deep-etched (the α-Al matrix was etched out), 0.1 wt.%Sr modified experimental alloy, solidified in the SC/HPDC UMSA die under atmospheric pressure, ASR = 15.3 ^{o}C/s, ref. #0508..... 177
Figure 119. a) Cooling/Solidification Curve superimposed with the First Derivative and Dynamic Baseline and Stroke Curve vs. Time, b) Fraction Solid Curve vs. Time for the unmodified experimental alloy, solidified under impact and cyclic pressure (48-72) MPa/10c in the SC/HPDC UMSA die, ASR = 20.1 °C/s, ref. #0429..... 186
Figure 120. First Derivative Curve, Fraction Solid Curve and Dynamic Baseline vs. Temperature for the unmodified experimental alloy, solidified under impact and cyclic pressure (48-72) MPa/10c, in the SC/HPDC UMSA die, ASR = 20.1 °C/s, ref. #0429.....187
Figure 121. Cooling/Solidification Curve superimposed with the First Derivative and Dynamic Baseline, Fraction Solid and Stroke Curve vs. Time for the unmodified experimental alloy, solidified under impact and cyclic pressure (48-72)MPa/10c in the SC/HPDC UMSA die, ASR=20.1°C/s, ref. #0429..... 187
Figure 122. a - c) LOM polished and d - f) SEM deep-etched microstructures for the unmodified experimental alloy processed in the SC/HPDC UMSA die under impact and cyclic pressure (48-72) MPa/10c at ASR = 20.1 ºC/s, ref. #0429..... 188
Figure 123. LOM micrographs, (subsurface of the samples) for the unmodified experimental alloy solidified; a - d) SC/HPDC UMSA die under a

different ASR and different pressure conditions; e, f) HT UMSA SS cup, ref. #0429, #0717, #0808..... 189
Figure 124. Comparison between the as-cast phases Average Size unmodified experimental alloy, solidified; (Red) in the HT UMSA SS cup under atmospheric pressure at ASR = 0.4 ºC/s, ref. #0808; (Blue) in the SC/HPDC UMSA die under atmospheric pressure at ASR = 10.2 ºC/s, ref. #0717 and (Green) in the SC/HPDC UMSA die under impact and cyclic pressure (48-72) MPa/10c at ASR = 21.9 ºC/s, ref. #0429..... 190
Figure 125. a) Cooling/Solidification Curve superimposed with the First Derivative, Dynamic Baseline, Stroke amd Pressure Profile Curves vs. Time, b) Fraction Solid Curve vs. Time for the 0.04wt.%Sr modified experimental alloy, processed under impact and cyclic pressure (38-82) MPa/10c in the SC/HPDC UMSA die, ASR = 19.5 °C/s, ref. #1009..... 192
Figure 126. First Derivative Curve, Fraction Solid Curve and Dynamic Baseline vs. Temperature for the 0.04wt.%Sr modified experimental alloy, solidified under impact and cyclic pressure (38-82) MPa/10c, in the SC/HPDC UMSA die, ASR = 19.5 °C/s, ref. #1009..... 193
Figure 127. LOM micrographs showing the experimental alloy, processed in the SC/HPDC UMSA die under impact and cyclic pressure (38-81) MPa/10c: a, b) unmodified, ref. #0429, c, d) 0.04 wt.%Sr modified, ref. #1009..... 194
Figure 128. a) Cooling/Solidification Curve superimposed with the First Derivative, Dynamic Baseline, Stroke and Pressure Profile Curves vs. Time, b) Fraction Solid Curve vs. Time for the 0.15 wt.%Sr modified experimental alloy, solidified under impact and cyclic pressure (38-81) MPa/10c in the SC/HPDC UMSA die, ASR = 18.3 °C/s, ref. #0925b..... 199
Figure 129. First Derivative Curve, Fraction Solid Curve and Dynamic Baseline vs. Temperature for the 0.15 wt.%Sr modified experimental alloy, solidified under impact and cyclic pressure (38-81) MPa/10c, in the SC/HPDC UMSA die, ASR = 18.3 °C/s, ref. #0925b..... 200
Figure 130. Cooling/Solidification Curve superimposed with the First Derivative Curve, Pressure Profile Curve, Stroke and Cumulative Energy Curve vs.

Time for the 0.15 wt.%Sr modified experimental alloy, processed using impact pressure and cyclic pressure (38-81) MPa/10c in the SC/HPDC UMSA die, ASR = 18.3 °C/s, ref. #0925b..... 200
Figure 131. First Derivative Curve and the Calculated Polynomial DBL vs. Temperature for the 0.15 wt.%Sr modified experimental alloy, solidified under impact and cyclic pressure (38-81) MPa/10c, in the SC/HPDC UMSA die, ASR = 18.3 °C/s, ref. #0925b..... 202
Figure 132. Deconvoluted First Derivative Curves for Individual Thermal Events vs. Time for the 0.15 wt.%Sr modified experimental alloy, solidified under impact and cyclic pressure (38-81) MPa/10c, in the SC/HPDC UMSA die, ASR = 18.3 °C/s, ref. #0925b..... 202
Figure 133. Deconvoluted First Derivative Curves for Individual Thermal Events vs. Temperature for the 0.15 wt.%Sr modified experimental alloy, solidified under impact and cyclic pressure (38-81) MPa/10c, in the SC/HPDC UMSA die, ASR = 18.3 °C/s, ref. #0925b..... 203
Figure 134. Deconvoluted Fraction Solid Curves for Individual Thermal Events vs. Temperature for the 0.15 wt.%Sr modified experimental alloy, solidified under impact and cyclic pressure (38-81) MPa/10c, in the SC/HPDC UMSA die, ASR = 18.3 °C/s, ref. #0925b..... 203
Figure 135. LOM micrographs for the 0.15 wt.%Sr modified experimental alloy, solidified in the SC/HPDC UMSA die, under impact and cyclic pressure (38-81) MPa/10c; a) Subsurface of the sample, b) center of the sample, ref.#0925b, mag. 100x..... 205
Figure 136. a - d) LOM and e, f) SEM micrographs for the 0.15 wt.%Sr modified experimental alloy, solidified in the SC/HPDC UMSA die under impact and cyclic pressure (38-81) MPa/10c, ref. #0925b..... 210
Figure 137. a) LOM and b-f) SEM micrographs for the 0.15 wt.%Sr modified experimental alloy, solidified in the SC/HPDC UMSA die under impact and cyclic pressure (38-81) MPa/10c, ref. #0925b..... 211

Figure 138. a - f) SEM deep-etched micrographs for the 0.15 wt.%Sr modified experimental alloy, solidified in the SC/HPDC UMSA die under cyclic pressure (38-81) MPa/10c, ASR = 18.3 °C/s, ref. #0925b..... 212
Figure 139. a) HAADF image, b - g) superimposed with HAADF and EDS elemental maps, for the 0.15 wt.%Sr modified experimental alloy, solidified in the SC/HPDC UMSA die, under impact and cyclic pressure (38-81) MPa/10c. TEM foil was extracted from the subsurface of the sample (the distance from the edge of the sample is 20 μm), ref. #0925b..... 214
Figure 140. a) HAADF image, b-f) superimposed with HAADF and EDS elemental maps, for the 0.15 wt.%Sr modified experimental alloy, solidified in the SC/HPDC UMSA die, under impact and cyclic pressure (38-81) MPa/10c. TEM foil was extracted from the center of the sample. (the distance from the edge of the sample is ≈ 9 mm), ref. #0925b..... 215
Figure 141. a) Cooling/Solidification Curve with superimposed First Derivative, Dynamic Baseline, Stroke and Pressure Profile Curves vs. Time, b) Fraction Solid Curve vs. Time for the 0.15 wt.%Sr modified experimental alloy, processed under impact pressure (0-22) MPa/1c in the SC/HPDC UMSA die, ASR = 14.1 °C/s, ref. #0916..... 217
Figure 142. First Derivative Curve, Fraction Solid Curve and Dynamic Baseline vs. Temperature for the 0.15 wt.%Sr modified experimental alloy, solidified under impact pressure (0-22) MPa/1c in the SC/HPDC UMSA die, ASR = 14.1 °C/s, ref. #0916..... 218
Figure 143. Cooling/Solidification Curve with superimposed First Derivative Curve, Pressure Profile Curve, Stroke and Cumulative Energy Curve vs. Time for the 0.15 wt.%Sr modified experimental alloy, processed under impact pressure (0-22) MPa/1c in the SC/HPDC UMSA die, ASR = 14.1 °C/s, ref. #0916..... 218
Figure 144. a) Cooling/Solidification Curve with superimposed First Derivative, Dynamic Baseline, Stroke and Pressure Profile Curves vs. Time, b) Fraction Solid Curve vs. Time for the 0.15 wt.%Sr modified experimental alloy, processed under impact/cyclic pressure

(0-27) MPa/2c in the SC/HPDC UMSA die, ASR = 16.3 °C/s, ref. #0916b..... 219
Figure 145. First Derivative Curve, Fraction Solid Curve and Dynamic Baseline vs. Temperature for the 0.15 wt.%Sr modified experimental alloy, solidified under impact/cyclic pressure (0-27) MPa/2c, in the SC/HPDC UMSA die, ASR = 16.3 °C/s, ref. #0916b..... 220
Figure 146. a) Cooling/Solidification Curve superimposed with the First Derivative and Dynamic Baseline, Stroke and Pressure Profile Curves vs. Time, b) Fraction Solid Curve vs. Time for the 0.15 wt.%Sr modified experimental alloy, solidified under impact and cyclic pressure (39-82) MPa/45c in the SC/HPDC UMSA die, ASR = 17.0 °C/s, ref.#0628b..... 224
Figure 147. First Derivative Curve, Fraction Solid Curve and Dynamic Baseline vs. Temperature for the 0.15 wt.%Sr modified experimental alloy, solidified under impact and cyclic pressure (39-82) MPa/45c, in the SC/HPDC UMSA die, ASR = 17.0 °C/s, ref. #0628b..... 225
Figure 148. Cooling/Solidification Curve superimposed with the First Derivative Curve, Pressure Profile Curve, Stroke and Cumulative Energy Curve vs. Time for the 0.15 wt.%Sr modified experimental alloy, solidified under impact and cyclic pressure (39-82) MPa/45c in the SC/HPDC UMSA die, ASR = 17.0 °C/s, ref. #0628b..... 225
Figure 149. a) Cooling Curves, First Derivative Curves and Pressure Profile Curves for the 0.15 wt%Sr modified experimental alloy processed in the SC/HPDC UMSA die under impact and cyclic pressure (38-82) MPa/10c, at different initial die temperatures; 273 ºC (Blue -ref. #0919), 262 ºC (Green -ref. #0925b) and 267 ºC (Red -ref. #1002b); b) Details for Figure a - undercooling region)..... 228
Figure 150. a) SC/HPDC UMSA die temperature profile for #0919, #1002b and #0925b experiments, b) cooling water temperature profile for #0919 and #0925b experiments..... 229

Figure 151. a) Cooling/Solidification Curve superimposed with the First Derivative and Dynamic Baseline, Stroke and Pressure Profile Curves vs. Time, b) Fraction Solid Curve vs. Time for the 0.15 wt.%Sr modified experimental alloy, processed under impact and cyclic pressure (38-82) MPa/10c in the SC/HPDC UMSA die, ASR = 13.6 °C/s, ref. #0919.....230
Figure 152. First Derivative Curve, Fraction Solid Curve and Dynamic Baseline vs. Temperature for the 0.15 wt.%Sr modified experimental alloy, solidified under impact and cyclic pressure (38-82) MPa/10c in the SC/HPDC UMSA die, ASR = 13.6 °C/s, ref. #0919..... 231
Figure 153. a - f) SEM deep-etched micrographs for the 0.15 wt.%Sr modified experimental alloy, solidified in the SC/HPDC UMSA die under impact and cyclic pressure (38-82) MPa/10c, ASR = 13.6°C/s, ref. #0919..... 232
Figure 154. a) Cooling/Solidification Curve superimposed with the First Derivative and Dynamic Baseline, Stroke and Pressure Profile Curves vs. Time, b) Fraction Solid Curve vs. Time for the 0.15 wt.%Sr modified experimental alloy, solidified under impact and cyclic pressure (38-82) MPa/10c in the SC/HPDC UMSA die, ASR = 14.6 °C/s, ref. #1002b..... 233
Figure 155. First Derivative Curve, Fraction Solid Curve and Dynamic Baseline vs. Temperature for the 0.15 wt.%Sr modified experimental alloy, solidified under impact and cyclic pressure (38-82) MPa/10c in the SC/HPDC UMSA die, ASR = 14.6 °C/s, ref. #1002b..... 234
Figure 156. a - f) SEM deep-etched micrographs for the 0.15 wt.%Sr modified experimental alloy, solidified in the SC/HPDC UMSA die under impact and cyclic pressure (38-82) MPa/10c, ASR = 14.6 °C/s, ref. #1002b..... 235
Figure 157. a) Cooling/Solidification Curve superimposed with the First Derivative, Dynamic Baseline, Stroke and Pressure Profile Curves vs. Time, b) Fraction Solid Curve vs. Time for the 0.15 wt.% Sr modified experimental alloy, processed under impact and cyclic pressure (0-30) MPa/1.5c in the SC/HPDC UMSA die, ASR = 13.9 °C/s, ref. #0517..... 239

Figure 158. First Derivative Curve, Fraction Solid Curve and Dynamic Baseline vs. Temperature for the 0.15 wt.%Sr modified experimental alloy, solidified under impact and cyclic pressure (0-30) MPa/1.5c, in the SC/HPDC UMSA die, ASR = 13.9 °C/s, ref. #0517..... 240

Figure 159. SEM, deep-etched microstructure for the 0.15 wt.%Sr modified experimental alloy, solidified in the SC/HPDC UMSA die under impact and cyclic pressure (0-30) MPa/1.5c; a) Transition from the edge to the center of the sample, b) order of Si dendrite(s) development on the subsurface of the sample; c, d) Si dendrites; e, f) Novel Hexagonal Si Whiskers, ref. #0517..... 241

Figure 160. SEM micrograph of the deep etched structure of the (Q+Θ) eutectic for the 0.15 wt.%Sr modified experimental alloy #0517 solidified in the SC/HPDC UMSA die under impact and cyclic pressure loading..... 242

Figure 161. Image analysis features: a) D^{min}_{F} AlSi-Co, T_{avg}AlSi-ICB, square which is zoomed out in Figure b), b) D_{avgF} Si-WA, D^{min}_{F}Si-WT.....247

Figure 162. Heating Curve and First Derivative Curve for the 0.15 wt.%Sr modified experimental alloy, previously processed in the SC/HPDC UMSA die under impact and cyclic pressure (38-81) MPa/10c, ref. #0925b. Dissolution of (Q+Θ) eutectic and Q and Θ phase..... 262

Figure 163. LOM, as-cast microstructure for the 0.15 wt.%Sr modified experimental alloy: a) SC/HPDC UMSA sample, solidified under cyclic pressure (38-81) MPa/10c, ref. #0925b, b) test sample after ST at 506 ^{o}C/5 min + 512 ^{o}C/3 min + 530 ^{o}C/2 min, ref. #1022, c) test sample after ST at 506 ^{o}C/6 min + 512 ^{o}C/4 min, ref. #1023, d) test sample after ST at 506 ^{o}C/5 min + 512 ^{o}C/2 min ref. #1024. The samples were quenched in water at 22 ^{o}C after Solution Treatment..... 266

Figure 164. a) HAADF image, b - g) superimposed with HAADF and EDS elemental maps, for the 0.15 wt.%Sr modified experimental alloy, solidified in the SC/HPDC UMSA die, under impact and cyclic pressure (38-81) MPa/10c and heat treated at (ST: 506 ^{o}C/5 min + 512 ^{o}C/2 min,

AA: 200 ^{o}C/10 min). TEM foil was extracted from the subsurface of the sample (20 μm from the edge of the sample), ref. #0925b-AA2..... 267

Figure 165. a) HAADF image, b - g) superimposed with HAADF and EDS elemental maps, for the 0.15 wt.%Sr modified experimental alloy, solidified in the SC/HPDC UMSA die, under impact and cyclic pressure (38-81) MPa/10c and heat treated at (ST: 506 ^{o}C/5 min + 512 ^{o}C/2 min, AA: 200 ^{o}C/10 min). TEM foil was extracted from the center of the sample (9 mm from the edge of the sample), ref. #0925b-AA2..... 268

Figure 166. LOM micrographs with microhardness indentations $HV_{0.1}$; a) Heat treated structure of the Yamaha engine block #Y1, b) As-cast structure of the experimental sample #0925b and c) Solutionized and artificially aged sample #0925b-AA2..... 273

Figure 167. Average Microhardness $HV_{0.1}$ and Standard Deviations for Selected Samples: #0925b-AA1 (ST & AA), #0925b-AA2 (ST & AA), the Yamaha engine block (7 mm, ST & AA), #0429 (As-cast)..... 273

Figure 168. Average HRB Macrohardness and Standard Deviations for Selected Samples: #0925b-AA1 (ST & AA), the Yamaha engine block wall thickness 7 mm and 15 mm (ST & AA)..... 274

Figure 169. Wear profile for the experimental samples after 2000 cycles of applied load 10 N, ref. #0517..... 276

Figure 170. Wear results for selected samples, ref. #0517 (0.15 wt.%Sr modified, impact and cyclic pressure (0-30) MPa/1.5c); #0429 (unmodified, impact and cyclic pressure (48-72) MPa/10c); #0508 (0.10 wt.%Sr modified, solidified at atmospheric pressure)..... 277

Figure 171. SEM micrographs of precipitated particles after heat treatment of the Al-20Si-3Cu alloy; a - c) Yamaha Engine Block, HPDC(100MPa) + ST: 480 °C/240 min and AA: 200 °C/240 min, d - f) SC/HPDC UMSA sample processed under cyclic pressure (38-81) MPa/10c and ST: 507 °C/7 min and AA 200 °C/10 min..... 279

Figure 172. a) HAADF image, b-f) superimposed with HAADF and EDS elemental maps, of the Yamaha HPDC engine block processed at 100 MPa followed by heat treatment; ST: 480 °C/4 h + AA: 200 °C/4 h..... 320
Figure 173. a) HAADF image, b-f) superimposed with HAADF and EDS elemental maps, of the Yamaha HPDC engine block processed at 100 MPa followed by heat treatment; ST: 480 °C/4 h + AA: 200 °C/4 h. (Figure 173 is a higher magnification of Figure 172), ref. #Yamaha engine block..... 321
Figure 174. Bright and dark field images for the Aluminum Copper Magnesium Silicide precipitate $Al_4Cu_2Mg_8Si_7$. Selected Area Diffraction Pattern (SAD), ref. #Yamaha engine block..... 322
Figure 175. Bright and dark field images for the Al_7Cu_2Fe. Selected Area Diffraction Pattern (SAD), ref. # Yamaha engine block..... 322
Figure 176. Bright and dark field images for the Al_2Cu, SAD, ref. # Yamaha engine block..... 323
Figure 177. Bright and dark field images for the Al, SAD, ref. # Yamaha engine block..... 323
Figure 178. Bright and dark field images for the Al-Cu θ" phase, SAD pattern, ref. #Yamaha engine block.. 324
Figure 179. HAADF and EDS elemental mapping, θ" and θ' in the Al-Cu matrix and in the corresponding spectrum, ref. #Yamaha enfine block..... 324
Figure 180. HAADF image showing θ" precipitates oriented towards [002], ref. #Yamaha engine block.....325
Figure 181. High Resolution TEM (HRTEM) and corresponding FFT showing Al-Cu θ" precipitate, ref. #Yamaha engine block..... 325
Figure 182. HR-HAADF (z-contrast) and corresponding FFT showing Al-Cu θ" precipitate, ref.# Yamaha engine block..... 326

LIST OF APPENDICES

Appendix A - S/TEM/EDS Analysis of the Yamaha Engine Block..... 319

Appendix B - Permission from Co-Authors..... 327

LIST OF ABBREVIATIONS/SYMBOLS

A/D	Analogue to Digital
D/A	Digital to Analogue
$SR^{AlSi}_{E,R}$	Al-Si Eutectic Recalescence Solidification Rate, ºC/s
#c	Number of Cycles, #
Δt^{P}_{I}	Pressure Time Interval, s
ΔT^{P}_{Rn}	Pressure Temperature Range (T^{P}_{ST} - T^{P}_{END}), ºC
$2r_c$	Critical dimension for layer extension
AA	Artificial Aging
aASR	Apparent Average SR, ºC/s
ACR	Average Cooling Rate, ºC/s
af_s	Apparent Fraction Solid, %
AlTAP	Aluminum Thermal Analysis Platform
ASR	Average Solidification Rate, ºC/s
aT_{liq}	Apparent Liquidus Temperature, ºC
aT_{sol}	Apparent Solidus Temperature, ºC
BN	Boron Nitride
BSE	Back Scattered Electron
CC	Cooling Curve
CCT	Conventional Casting Technique
CE	Cumulative Energy, J
CE_{liq}	Cumulative Energy in Liquid State = $\Delta CE_{liq1}+\Delta CE_{liq2}$, J
CE_{ss}	Cumulative Energy in Semi-Solid State = $\Delta CE_{ss1}+\Delta CE_{ss2}$, J
DAP	Data Acquisition Processor
DAQ	Data Acquisition System
D_{avg}Si-WA	Average Diameter of Silicon Whiskers and Dendrite Arms
D^{max}_{F}AlSi-Co	Maximum Feret Diameter of Al-Si Colony
D^{min}_{F}AlSi-Co	Minimum Feret Diameter of Al-Si Colony
D^{min}_{F}Si-WT	Minimum Feret Diameter of Silicon Whisker Tip
EB	Electron Beam
ECP	Electric Current Pulse

EDS	Energy Dispersive Spectroscopy
f	frequency, Hz
FD	First Derivative Curve
FS	Fraction Solid Curve
$fs^{\pi Q\Theta}{}_{G}$	Fraction Solid at $T^{\pi Q\Theta}{}_{G}$, %
$fs^{AlSi}{}_{E,END}$	Fraction Solid at $aT^{AlSi}{}_{E,END}$, %
$fs^{AlSi}{}_{E,G}$	Fraction Solid at $T^{AlSi}{}_{E,G}$, %
$fs^{AlSi}{}_{E,MIN}$	Fraction Solid at $T^{AlSi}{}_{E,MIN}$, %
$fs^{CP}{}_{END}$	Fraction Solid when Cyclic Pressure Ends
$fs^{CP}{}_{ST}$	Fraction Solid when Cyclic Pressure Starts
HAADF	High Angle Annular Dark Field
HPDC	High Pressure Die Casting
HR-HAADF	High Resolution High Angle Annular Dark Field
HSR	High Solidification Rate
HT UMSA	High Temperature Universal Metallurgical Simulator and Analyzer
HTM	High Thermal Mass
IIT	Impurity Induced Twinning
IP	Impact Pressure
$ISR_{a,liq}$	Instantaneous Solidification Rate at aT_{liq}, ºC/s
$ISR_{a,sol}$	Instantaneous Solidification Rate at aT_{sol} , ºC/s
ISR^{IP}	Instantaneous Solidification Rate at aT^{IP}, ºC/s
$ISR^{P}{}_{ST}$	Instantaneous Solidification Rate at $T^{P}{}_{ST}$, ºC/s
LB	Laser Beam
LHF	Latent Heat of Fusion
LOM	Light Optical Microscopy
LPDC	Low Pressure Die Casting
LSR	Low Solidification Rate
LTM	Low Thermal Mass
LTP	Low Temperature Pouring
LVDT	Linear Variable Differential Transformer
MA	Master Alloy (Al-Sr)
MCPT	Metal Casting and Post-Processing Technology
MCR	Melt Cooling Rate, $MCR=MC_{Rn}/MCt$, ºC/s
MC_{Rn}	Melt Cooling Range, $MC_{Rn} = T^{M}{}_{SH} - aT_{liq}$, ºC
MCt	Melt Cooling time, (liquidus time - pouring time), s

MMAC	Magnesium Matrix Alumina Composite
MTRT	Melt Thermal Rate Treatment
NA	Natural Aging
NIST	National Institute of Standards and Technology
P_{amp}	Applied Pressure Amplitude, $P_{amp} = (P_{max} - P_{min}) / 2$
P_{MAX}	Maximum Pressure of Cycle, MPa
P_{mean}	Mean Applied Pressure, $P_{mean} = (P_{max} + P_{min}) / 2$
P_{MIN}	Minimum Pressure of Cycle, MPa
PSR	Pressure Solidification Rate, ºC/s
R	Applied Pressure Ratio, $R = P_{min} / P_{max}$
RGT	Restricted Growth Theory
SAD	Selected Area Diffraction Pattern
SC	Squeeze Casting
SC/HPDC UMSA	Squeeze Casting/High Pressure Die Casting Universal Metallurgical Simulator and Analyzer
SDAS	Secondary Dendrite Arm Spacing
SEM	Scanning Electron Microscopy
Si_{EQ}	Silicon Equivalency
$SR^{AlSi}_{E,R}$	AlSi Eutectic Recalescence Solidification Rate = $(\Delta T^{AlSi}_{UC})/(\Delta t^{AlSi}_{UC})$, ºC/s
$SR^{AlSi}_{E,UC}$	AlSi Eutectic Undercooling Solidification Rate = $(\Delta T^{AlSi}_{UC})/(\Delta t^{AlSi}_{UC})$, ºC/s
SR^{CP}	Cyclic Pressure Solidification Rate = $\Delta T^{CP}/\Delta t^{CP}$, ºC/s
SRn	Solidification Range, ºC
SS	Stainless Steel
St	Solidification Time Interval, s
ST	Solution Treatment
STDEV	Standard Deviation
STEM	Scanning Transmission Electron Microscopy
$T^{\pi Q\Theta}_{G}$	πQΘ- Phase Growth Temperature, ºC
TA	Thermal Analysis
$T^{AlSi}_{E,G}$	Al-Si Eutectic Growth Temperature, ºC
$T^{AlSi}_{E,MIN}$	Al-Si Eutectic Minimum Temperature, ºC
$T^{AlSi}_{E,END}$	Apparent Al-Si Eutectic End Temperature, ºC
$t^{AlSi}_{E,UC}$	AlSi Eutectic Undercooling Time = $t_{UC} - t_{liq}$, s
T_{avg}AlSi-ICB	Average Thickness of Al-Si Inter Colony Boundaries

TC	Thermocouple
$TCE_{liq-sol}$	Total Cumulative Energy = $CE_{liq}+CE_{ss}$, J
T^{CP}_{END}	Cyclic Pressure End Temperature, ºC
T^{CP}_{ST}	Cyclic Pressure Start Temperature, ºC
T^{D}_{I}	Die Initial Temperature, ºC
T^{D}_{MAX}	Maximum Melt Temperature Delivered to the Die, ºC
TEM	Transmission Electron Microscopy
T^{IP}	Temperature of Impact Pressure Treatment, ºC
T_{liq}	Liquidus Temperature, ºC
T_{m}	Melting Temperature, ºC
T^{MES}_{MAX}	Maximum Measured Temperature, ºC
T^{M}_{SH}	Melt Superheat Temperature, ºC
T^{P}_{END}	Pressure End Temperature, ºC
T^{PP}_{1}	Plunger 1st Position Temperature, ºC
T^{PP}_{2}	Plunger 2nd Position Temperature, ºC
TPRE	Twin Plane Re-Entrant Edge
T^{PSi}_{G}	Primary Silicon Growth Temperature, ºC
T^{PSi}_{NUC}	Primary Silicon Nucleation Temperature - Liquidus Temperature, ºC
T^{P}_{ST}	Pressure Start Temperature, ºC
T_{sol}	Solidus Temperature, ºC
$T^{\alpha\text{-}Fe}_{G}$	α-Iron Phase Growth Temperature, ºC
$T^{\beta\text{-}Fe}_{G}$	β-Iron Phase Growth Temperature, ºC
UBC	University of British Columbia
UMSA TP	Universal Metallurgical Simulator and Analyzer Technology Platform
USV	Ultrasonic Vibration
UTS	Ultimate Tensile Strength
VHTM	Very High Thermal Mass
wt.%	weight percent
YS	Yield Strength
ΔCE_{liq1}	Cumulative Energy between T^{P}_{ST} and T^{IP}, J
ΔCE_{liq2}	Cumulative Energy between T^{IP} and aT_{liq} , J
ΔCE_{ss1}	Cumulative Energy between aT_{liq} and $T^{AlSi}_{E,MIN}$, J
ΔCE_{ss2}	Cumulative Energy between $T^{AlSi}_{E,MIN}$ and T^{P}_{END} , J
$\Delta T^{AlSi}_{E,R}$	Al-Si Eutectic Recalescence Temperature, ºC
$\Delta t^{AlSi}_{E,R}$	Al-Si Eutectic Recalescence time, s

$\Delta T^{AlSi}_{E,UC}$	AlSi Eutectic Undercooling Temperature $= aT_{liq} - T^{AlSi}_{E,MIN}$, ºC
Δt^{CP}	Cyclic Pressure Time Interval, s
Δt^{P}_{I}	Pressure Time Interval, s
ΔT^{P}_{Rn}	Pressure Temperature Range $= T^{P}_{ST} - T^{P}_{END}$, ºC
ξ	Spacing between added atoms

CHAPTER 1: OBJECTIVES

1. To perform a comprehensive world-wide scientific literature and patent review on the possibility of converting of existing industrial hypereutectic Al-Si-X alloys and development of new alloys with novel Al-Si eutectic as-cast structure(s) with nano and ultra-fine single Si phase(s).

    - To perform a search for an ultra rapid heat treatment technology rendering spheroidized single-phase nano silicon particles.
    - For both as-cast and heat treated structures provide information associated with their engineering characteristics.

    1.1. To review various types of liquid and semi-solid melt process technologies which use chemical and physical means for industrial grade multi-component alloys' structure modification and refinement capable of delivering as-cast nano single Si phase structures.

    1.2. To determine the differences between commercial and ultra-pure alloy processing challenges and consequently metallurgical characteristics.

    1.3. To determine advanced laboratory techniques for control of the primary and eutectic Si morphology that could lead to an as-cast nano structured single phase Si.

    1.4. To review methods for control of the Al-Si cell size and inter-cell boundary characteristics including detrimental Fe-rich phases.

1.5. To determine design requirements for the SC/HPDC UMSA Platform's instrumented die, mini melting furnace and plunger assembly for chemical and automated physical processing of liquid and semi-solid melts.

1.6. To review Thermal Analysis techniques for quantitative characterization of rapidly solidified and heat treated bulk test samples that represent thin walled cast component macro and micro structures.

2. To further develop the SC/HPDC UMSA Platform's novel capabilities allowing for the processing of industrial grade Al-Si-Cu hypereutectic and other alloy(s) generating novel as-cast nano Si whiskers and/or dendrites.

To develop HT UMSA heat treatment(s) generating nano and ultra-fine nodular Si structures free of detrimental primary and eutectic silicon.

2.1. To further advance quantitative Thermal Analysis experimental and solidification characterization capabilities in terms of detection limits and spatial resolution for processed liquid and semi-solid melts.

2.2. To apply chemical modification and ultra rapid dynamic melt treatment for eutectic cell refinement and minimization of the detrimental Fe-rich phase(s) effects.

2.3. Further development of the Thermal Analysis capabilities for the ultra rapid Solution Treatment, Quenching and Artificial Aging treatments.

2.4. To address effective Al-Cu-Mg-Si-Sr rich phase(s) dissolution and Si nano phases fragmentation and spheroidization processes as well as prevention of their coarsening.

2.5. To design novel exploratory SC/HPDC UMSA processing parameters involving melt Sr modification and complementary monotonic, impact and cyclic pressure melt loading during cooling and solidification processes.

2.6. To design procedures and methodologies for comprehensive qualitative interpretation of novel metallurgical phenomena.

2.7. To develop statistically valid models linking fundamental aspects of metallurgical process parameters with Thermal Analysis and structural as well as micro/macro hardness and tribological data.

3. To recommend future scientific and applied engineering directions for the optimum addition of alloying elements, i.e. Cu and Mg that will benefit as-cast and heat treated structures.

3.1. To recommend effective control of the inter-colony boundaries thickness and their supersaturation in alloying and impurity elements.

CHAPTER 2: LITERATURE REVIEW

2.1 Cast Aluminum Alloys

Aluminum is the most commonly used non-ferrous metal in the world. Transportation and other industries are committed to saving energy by utilizing optimized aluminum alloys cast into thin wall components. Pure aluminum does not have the best engineering characteristics, but alloys with an optimized chemistry and technology have mechanical properties comparable with cast iron and lower grade steel. Ultra-fine and homogeneous as-cast and heat treated structures are the key factors that contribute to material and cast component performance. Effective manufacturing of the parts requires optimization of the production processes and the final properties.

Almost 90 % of total aluminum parts are produced by various casting technologies that use Al-Si alloys. Approximately 44 % of automobile parts are cast components like wheels, brackets, brake components, instrument panels, engine blocks and cylinder heads. They have high strength-to-weight ratios, good corrosion resistance, good wear resistance and are fully recyclable [1].

2.1.1 Aluminum-Silicon Equilibrium Phase Diagram and StructureCharacteristics

The silicon content in commercial cast aluminum-silicon alloys is in the range of (5 to 23) wt.%. The properties of a specific alloy depend on physical, chemical and stereological properties of its main phases, minor phases and precipitates, i.e. α-aluminum solid solution, silicon crystals and intermetallic precipitates [3]. The binary Al-Si equilibrium phase diagram has three types of chemistries and respective structures: a-hypoeutectic, b-eutectic, c-hypereutectic, which are presented in Figure 1. The corresponding micrographs are shown in Figure 2.

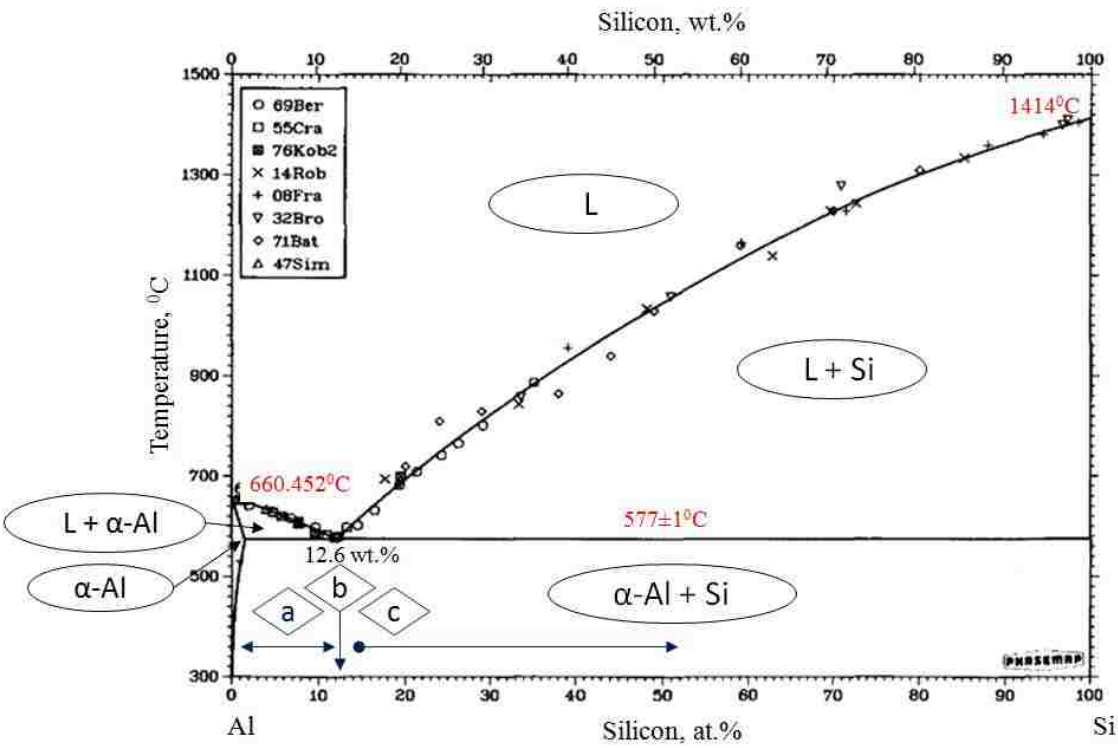

Figure 1. Aluminum-Silicon equilibrium phase diagram and chemical compositions for the a-hypoeutectic (from 1.65 wt.%Si to 12.6 wt.%Si), b-eutectic (12.6 wt.%Si), c-hypereutectic (> 12.6 wt.%Si) phases [2], [3]. Note: The pure Al liquidus temperature according to the NIST standard is 660.323 °C.

Classification of Al-Si Alloys Structures

a) **Hypoeutectic** (from 1.65 wt.%Si to 12.6 wt.%Si): The first to solidify from a liquid is the primary α–aluminum solid solution thus depleting the liquid Al. When the melt reaches the eutectic temperature of 577.25 °C the melt contains 12.6 wt.%Si. Due to the maximum solubility of silicon in the aluminum solid solution being 1.65 wt.%, the eutectic reaction that takes place results in an isothermal solidification of the melt that produces Al-Si eutectic (a mixture of eutectic Si and eutectic aluminum, Figure 2a).

b) **Eutectic** (12.6 wt.%Si): When the cooling liquid reaches 577 °C, a eutectic reaction occurs. The microstructure of the eutectic Al-Si alloy contains eutectic Silicon and the α–aluminum matrix (see Figure 2b).

c) **Hypereutectic** (>12.6 wt.%Si): Primary silicon solidifies from the liquid first, thus depleting the liquid of Si until it reaches the eutectic point where the remaining solidification follows the eutectic reaction (see Figure 2c).

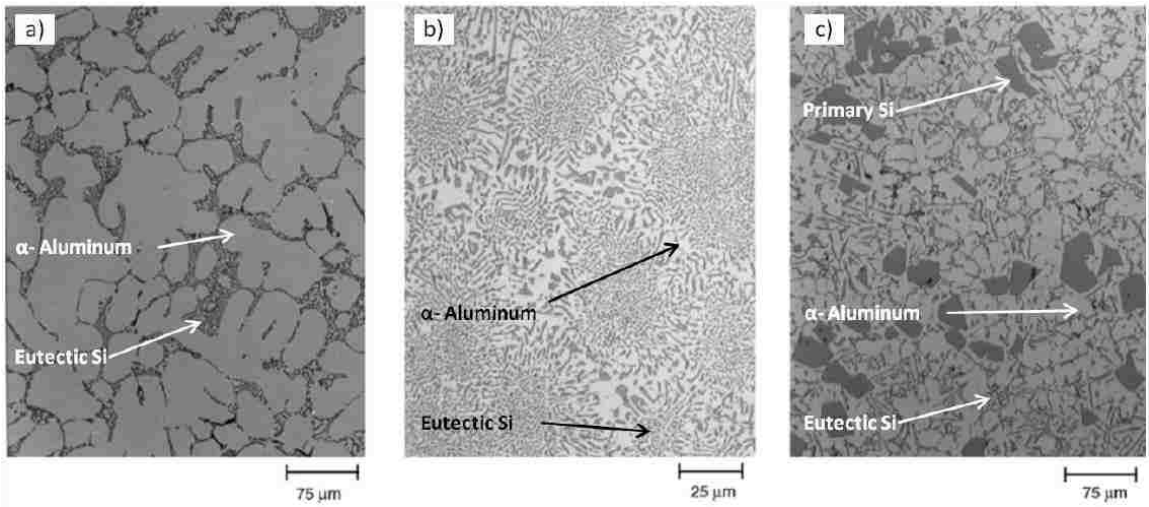

Figure 2. LOM micrographs for commercial cast Al-Si alloys, a) hypoeutectic, 150x, b) eutectic, 400x, c) hypereutectic, 150x [2].

2.1.2 Cast Aluminum and Aluminum Alloy Designation System

The identification system for aluminum and aluminum alloy castings and ingots uses a four digit numerical designation and a decimal point, for dividing alloys into families, see Table 1 [3, 4].

Table 1. Cast Aluminum and Aluminum Alloy Designation System [3, 4].

Code	Description
1xx.x	Aluminum >99.00 wt.%
2xx.x	Aluminum alloys grouped by major alloying element(s): Copper
3xx.x	Silicon, with added Copper and/or Magnesium
4xx.x	Silicon
5xx.x	Magnesium
6xx.x	Unused Series
7xx.x	Zinc
8xx.x	Tin
9xx.x	Other Elements

In the 1xx.x group, series 10x.x is used to designate unalloyed compositions of Aluminum. The last two of the four digits in the designation indicate the minimum aluminum percentage. For 2xx.x through 8xx.x alloys, the alloy group is determined by the alloying element present in the greatest mean percentage. The second two of the four digits in the designation identifies the different alloys in the group. The last digit, after a decimal point, indicates the product form, whether casting (xxx.0) or ingot (xxx.1).

2.1.3 Selected Alloying Elements of Al-Si Alloys

Silicon (Si) is the main alloying element in both the 3XX and 4XX series of alloys. Silicon is added to improve melt and casting characteristics including: fluidity, feeding characteristics hot and tear resistance. Silicon additions decrease shrinkage,

improve wear resistance, reduce specific gravity and the coefficient of thermal expansion of cast components. Commercial alloys contain up to 25 wt.%Si [6], [7]. For slow Solidification Rate processes, such as sand cast, the range is (5 to 7) wt.%Si for permanent mold (7 to 9) wt.%Si and for die casting (8 to 25) wt.%Si. The latent heat of silicon crystallization (50.21 kJ/mol) is approximately 4.7x larger in comparison with Aluminum (10.71 kJ/mol) [8] thus significantly improving melt fluidity [9].

Copper (Cu) is an alloying element in both the 2XX and 3XX series of Al alloys. In the equilibrium binary Al-Cu system the maximum solubility of Copper is 5.65 wt.% in the α-aluminum matrix at a eutectic temperature of 548.2 °C [10]. Copper is the first and most widely used alloying element in aluminum alloys. Al-Cu alloys contain up to 10 wt.%Cu. The addition of Copper provides strength and hardness in the as-cast and heat-treated conditions. It improves machinability of alloys by increasing metal matrix hardness [11] and generally reduces resistance to corrosion, hot tear resistance and decreases castability [12]. Additions of Copper also increase the level of porosity and decrease ductility [13]. Additions of Copper in concentrations from 1 wt.% to 4 wt.% cause a reduction in the SDAS as well as an increase in grain size. Copper will also increase precipitation kinetics and refine certain precipitates during Artificial Aging [14].

Magnesium (Mg) is an alloying element in the 5XX series of Al alloys. In the equilibrium binary Al-Mg system the maximum equilibrium solubility of Magnesium is 18.6 wt.% in the α-aluminum matrix at the eutectic temperature of 450.0 °C [15]. Magnesium provides significant strengthening and improvement of the work hardening of aluminum alloys. Usually Magnesium is used in more complex Al-Si alloys containing Copper, Nickel, and other elements. Binary Al-Mg alloys are used in applications

requiring a bright surface finish and corrosion resistance, as well as desirable combinations of strength and ductility. Common compositions range from 4 wt.% to 10 wt.% Mg and compositions containing more than 7 wt.% Mg are heat treatable. Like Copper, the addition of Magnesium to Al-Si alloys increases strength and reduces ductility. Magnesium reduces the Si Modification Level of Sr modified alloys. The addition of Magnesium to Al-Cu alloys increases the magnitude and rate of natural and Artificial Aging. The preferential precipitation of Magnesium at grain boundaries produces susceptibility to inter-granular cracking and stress corrosion [5].

Manganese (Mn) is a common addition to 3xxx alloys (up to 1.25 wt.%) often in combination with Magnesium. Manganese has quite limited solid solubility in aluminum (1.8 wt.% as a principal alloying element) and will form intermetallics that decrease ductility. Manganese could also be considered an impurity element in casting compositions and is controlled to low levels in most gravity cast compositions [14]. Manganese is used to control the morphology of the iron-rich β-Al_5FeSi phase from its typical platelet/acicular form to a skeleton-like $Al_{15}(MnFe)_3Si_2$ form that provides improved ductility and decreases casting embrittlement [12,13,14].

Nickel (Ni) is usually added in Al alloys together with Copper and forms Al_6Cu_3Ni or $Al_3(Cu,Ni)_2$ phases which are thermally stable and improve the mechanical properties at elevated temperatures. It also reduces the coefficient of thermal expansion [11], [12]. High temperature applications of Aluminum-Silicon alloys contain at least 9 wt.%Si and up to 7 wt.%Ni [19].

Zinc (Zn) is used in 7xxx series aluminum aerospace cast alloys [1]. The addition of Zinc to the aluminum heat treatable or naturally aged alloys is accompanied

by Copper and Magnesium [14]. Al-Zn alloys in the range of (3 to 7.5) wt.%Zn with the addition of Magnesium increases the strength potential of an alloy system. The addition of Copper to the Aluminum-Zinc-Magnesium system, with small amounts of Chromium and Manganese, results in the highest strength aluminum base alloys commercially available [5]. In some cases the addition of Zn at levels of (1 to 2) wt.% to Al-Mg alloys shows higher stress corrosion cracking resistance [11].

Tin (Sn) is used as an alloying addition to Aluminum for concentrations of 0.03 wt.% to several percent in wrought alloys and for concentrations of approx. 25 wt.% in casting alloys. Aluminum-Tin bearing alloys, with additions of other metals such as Copper, Nickel, and Silicon are used where bearings are required to resist high speeds, loads, and temperatures [5]. Sn additions can also be used to improve machinability [14]. In the A356.2 alloy Sn precipitates as Mg_2Sn in the form of Chinese script. The addition of 0.15 wt.%Sn lowers the YS, UTS, and hardness slightly and raises the ductility and toughness of as-cast B319.2 and A365.2 alloys. For the Al-7Si-0.35Mg alloy, 0.05 wt.%Sn is the optimum content of Sn for good mechanical properties of this alloy. The mechanical properties of the heat-treated B319.2 and A356.2 alloys decreased with an increase in the Sn content above 0.05 wt.%, where it acts as a low melting point impurity element that causes incipient melting and leads to the creation of voids in the structure [20].

Lead (Pb) is used in aluminum casting alloys at levels greater than 0.1 wt.% to assist in chip formation for improved machinability [14]. Lead creates low melting constituents and can produce poor mechanical properties and high crack sensitivity on solidification [21]. It was found that a slight variation in both Sn and Pb had an effect on

various solidification events (namely Dendrite Coherency and Al-Si Eutectic Growth Temperatures) as measured by Thermal Analysis. However, the tensile and elongation of the castings (W319 alloy) were unaffected [22].

2.1.4 Selected Silicon Modifying Elements

Strontium (Sr) is used for modification of silicon morphology of the Aluminum-Silicon eutectic and primary Si. Strontium modification can be achieved at very low addition levels; usually a range of (0.007 to 0.050) wt.% is the industry standard. At higher levels Strontium additions are associated with porosity, especially in thick sections of the cast components, where solidification occurs more slowly. Strontium is added to the melt in the form of AlSr master alloys [23]. Some researchers indicate that Strontium increases the hydrogen and consequently the porosity and inclusion content in Al-Si alloys [24] by decreasing the surface tension of the liquid and increasing volumetric shrinkage [25]. Other literature sources indicate that Sr has less effect on porosity than other factors such as local solidification time or dissolved hydrogen [26]. Shabestari et al. [27] reported that Sr modification has no marked effect on hydrogen content in the cleaned melt. Denton et al. [28] stated that Sr enhanced the susceptibility of the alloys to hydrogen pick-up and hydrogen concentration reaching a plateau during a 1hr hold period. Later studies suggest that in order to take advantage of Sr modification it is necessary to apply higher Solidification Rates [29].

Phosphorous (P) is used as a modifier of primary silicon in hypereutectic Al-Si alloys. Phosphorous forms AlP_3 particles, which serve as nucleation sites for primary silicon. A sufficient amount of phosphorus for addition to hypereutectic Al-Si alloys is in

the range of (0.0005 to 0.0025) wt.% (less than 50 % of that added is usually retained in the melt) [30]. Phosphorus diminishes the effectiveness of the common eutectic modifiers sodium and strontium [31]–[33].

Sodium (Na) is used as a modifier of the Aluminum-Silicon eutectic. Less than 0.01 wt.%Na is enough for full modification with a short residence time [34]. Disadvantages of Na modification are the high volatility of Na, which results in low recoveries (10 to 50) %; Na rapidly fades from the melt and is prone to over modification. The addition of Sodium could be a dangerous operation due to its reactiveness with moisture. When added to a melt, sodium tends to form a thick oxide skin on the liquid surface [35]. Sodium interacts with phosphorus and reduces its effectiveness in the eutectic modification of the primary silicon phase. Sodium causes brittleness in aluminum-magnesium alloys [36], [37].

2.1.5 Selected Grain Refining Elements

Titanium (Ti) is used to refine the grain structure of aluminum casting alloys, often in combination with smaller amounts of boron [38]–[43]. The optimum content of Ti is in the range of 0.015 wt.% for effective grain refinement. At higher contents of Ti the grain structure becomes coarser. Titanium is often used at concentrations greater than those required for grain refinement to reduce cracking tendencies [11]. The addition of Ti up to 4 wt.% to the binary Al–Si alloy led to precipitation of the Al_3Ti phase which improved wear resistance of both the as-cast and heat treated alloys [44].

2.1.6 Selected Impurity Elements

Iron (Fe) in an equilibrium binary Al-Fe system has solid solubility in aluminum of (0.03 to 0.05) wt.% at the eutectic temperature of 655 °C and is even lower at room temperature. Most of the iron in Al alloys is present in the form of intermetallic compounds. The β-Al_5FeSi phase (in the form of thin long plates) has the most detrimental effect on mechanical properties, including ductility and fracture toughness. It is necessary to keep iron levels as low as possible due to the negative effect of iron on machinability, shrinkage porosity, flowability and feeding characteristics. To avoid the detrimental influence of iron on mechanical properties, especially ductility, it is necessary to keep iron under critical content which can be calculated by the following formula [16].

$Fe_{crit} = 0.075 \times [\%Si] - 0.05$ (in wt.%)

The negative effect of iron can be eliminated by the addition of Manganese, ultrasonic treatment or by a higher Solidification Rate [45].

Hydrogen (H) has considerable solubility in molten aluminum and decreases rapidly with the temperature. Rejected hydrogen from the liquid aluminum forms rounded gas pores. To avoid the removal of dissolved hydrogen from the molten aluminum alloy it is critical for the production of high quality castings [46].

2.1.7 Silicon Crystal Growth

In Al-Si as-cast components the morphology of the nearly pure Si phase has a significant effect on the mechanical properties. In slowly solidified eutectic Al-Si cast components needle or plate shaped Si crystals are produced (see Figure 2) which result in

low ductility and low tensile strength. By contrast, fast directional solidification results in significantly improved mechanical properties, see Table 2 [47]–[49].

Table 2. Mechanical Properties vs. Silicon Crystal Growth Velocity for Hypoeutectic and Near Eutectic Al-Si Alloys.

Crystal Growth	Ultimate Tensile Strength	Elongation
V (μm/s)	UTS (MPa)	El (%)
20	162	8.7
80	179	15.0
250	190	17.6
600	207	23.8
1000	222	12.5

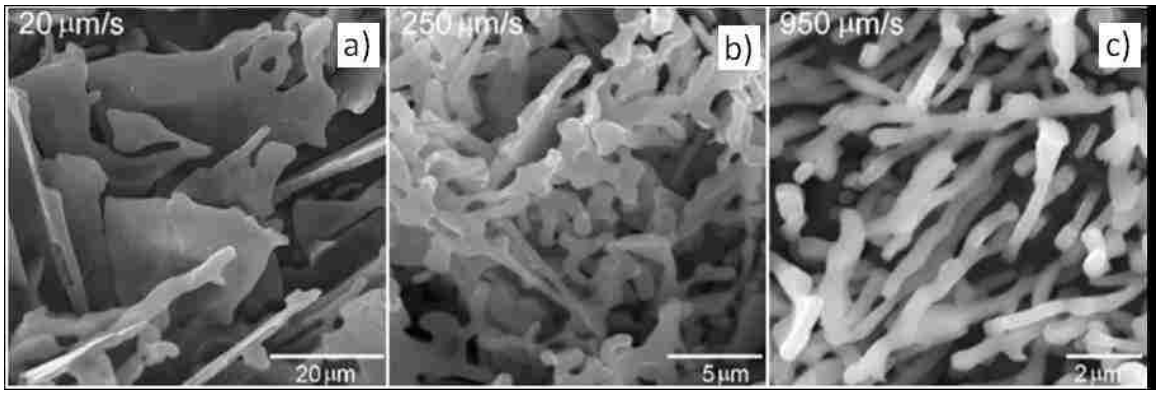

Figure 2. Silicon morphology after directional solidification of an Al-Si near-eutectic alloy (Al-12Si) at velocities of (20, 250 and 950) m/s. These structures represent a) flakes, b) mixed flakes/fibers and c) fiber morphologies. The Al-rich phase has been chemically removed [48], [49].

The main parameter affecting mechanical properties of hypereutectic Al-Si alloys is the morphology of silicon crystals. Therefore, it is very important to understand the silicon dendrite nucleation and growth process.

In the hypereutectic silicon system at temperatures greater than the liquidus, random movement of atoms occurs. Si atom clusters (liquid structure) are created prior to the solidification temperature in a range of (200 to 300) °C [50]. When the temperature decreases to the solidification temperature a primary block of silicon crystals starts to

form. These crystals are not stable. A further decreased melt temperature and its undercooling will be the primary block to forming stable nuclei and solidification of Si crystals starts**.** Silicon crystals grow in an anisotropic diamond cubic structure. The closest packed plane is (111) and the growth rate in the normal direction to the (111) plane is the slowest. There is a strong tendency for growth in the [211] direction. Therefore, the lower surface to volume ratio has less tendency to growth in the [111] direction and results in plate-like shaped crystals. Nucleation and growth of Si crystals is shown in Figure 3.

Instead of a single tetrahedron, the assembly of two tetrahedrals is the primary block to forming a stable nucleus. In this case, a twinning with the (111) twin plane will form, as shown in Figure 3. A mechanism for anisotropic growth of Germanium and Silicon which is known as the Twin Plane Re-entrant Edge Mechanism (TPRE) was proposed in 1960 by Hamilton [9], [51], [52]. The mechanism is schematically shown in Figure 4 and is described in the following steps:

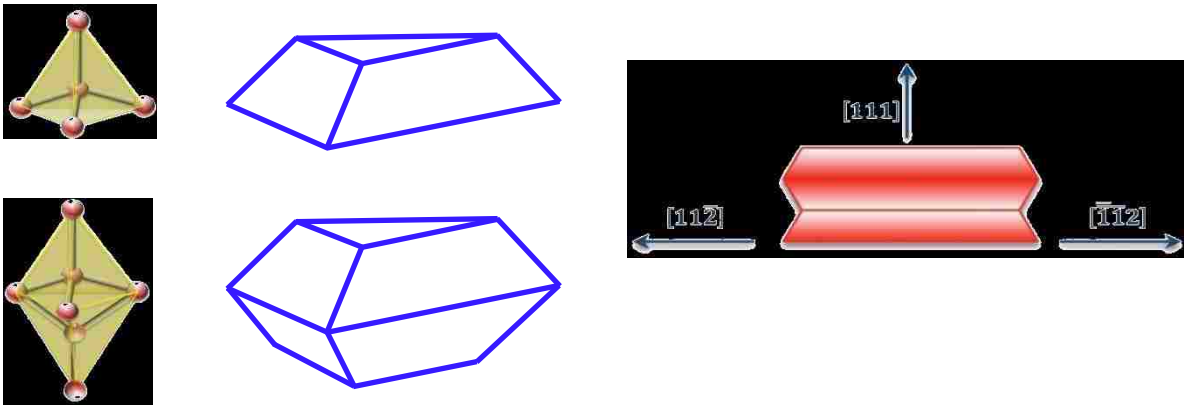

Figure 3. The crystal structure of stable Si nuclei created by the assembly of two tetrahedrals [47]**.**

In Figure 4a) the equilibrium form of Silicon is an octahedron bounded by {111} surfaces. The solid is to be twinned about the plane and is indicated by the dotted line.

In Figure 4b) a twinned crystal is derived from the equilibrium form by reflection across the twin composition plane. The twin plane emerges from the solid in three re-entrant corners, <141° which alternate with ridge structures <219°. Ease of nucleation at the former preferred sites leads at once to three easy growth directions.

In Figure 4c) the trigonal solid is formed if the three re-entrant corner sites in the bi-crystal are allowed to grow. The re-entrant corners vanish and rapid growth stops.

In Figure 4d) a crystal containing two twin planes is found to have six of the favored re-entrant sites, 60° apart located, alternatively, first at one twin plane and then the other. These lead to six equivalent (211) preferred growth directions.

In Figure 4e) at two of the six re-entrant corners of Figure 4d) nucleation events (I) have been allowed to occur. Growth from these has resulted in the development of new corners <109 1/2°, marked as (II). These straddle ridge sites across which nucleation was previously difficult.

In Figure 4f) the growth cycle initiated in Figure 4e) at the original re-entrant corners (I) is completed by growth from the new re-entrant corners (II). The solid is back to its original shape, but has increased in thickness in the directions in which growth was allowed.

In Figure 4g), by allowing an increased nucleation rate, a solid is obtained in which many steps are growing at once. A curved interface could result from these processes. The "flow" of growth steps about the interface is suggested in part of Figure 4g) and shows how the re-entrant corners are maintained by a growth step that "spirals back" on itself [53].

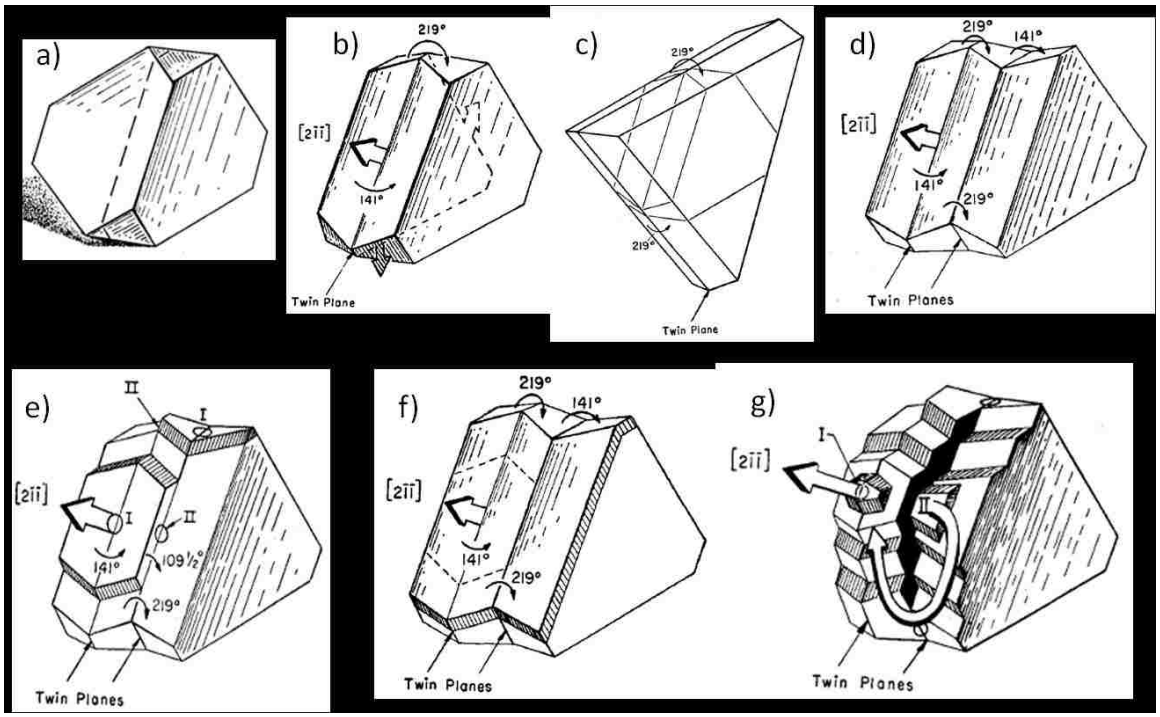

Figure 4. Twin Plane Re-entrant Edge Mechanism. a) The equilibrium form of a germanium crystal, an octahedron bounded by {111} surfaces. The solid is to be twinned about the plane indicated by the dotted line, b) Crystal with a single twin, c) Closure of twins due to ridge formation, d) A crystal containing two twin planes, with six equivalent {211} preferred growth directions, e) Creation of extra re-entrant corners I and II, f) Crystal with two twins, g) Propagation of crystal due to re-entrant corners [51]**.**

Silicon crystals can be categorized by ten basic types depending on the morphology and the shape that correlates with the casting condition(s) [52]. These Si particle types are described in the following section.

Star-like (Five-fold Branched)

Star-like primary silicon (see Figure 5) is usually found in the unmodified hypereutectic Al-Si alloys which solidify under a slow Solidification Rate. Si particles nucleate from the liquid by a heterogeneous mechanism and grow into the undercooled melt of the surrounding aluminum solvent. When local concentration of the solvent reaches a sufficient level, an α-Al phase nucleates, which appears as an Al-halo

surrounding the Si particle (see Figure 5b) [54]–[56]. The effect of undercooling and Si content are illustrated in Figures 6 and 7.

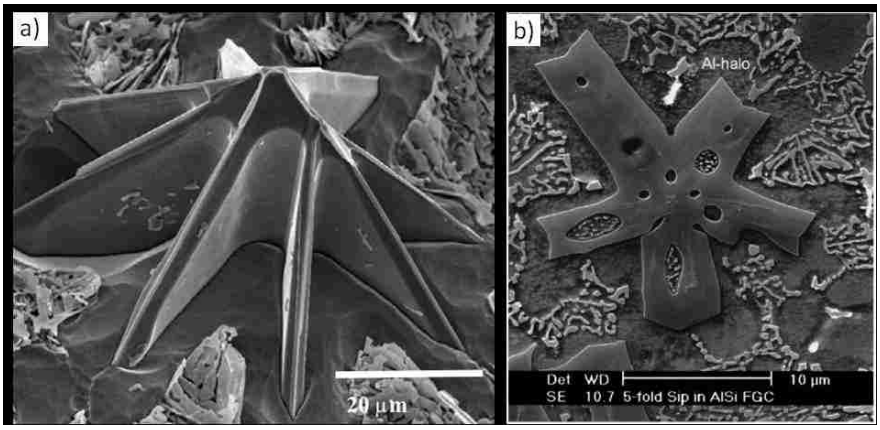

Figure 5. a) SEM deep etched Star-like dendritic morphology of primary silicon [57], [58]**. b) SEM micrograph five-fold branched primary Si particle surrounded by Al-halo and Al-Si eutectic,** [52], [54], [55].

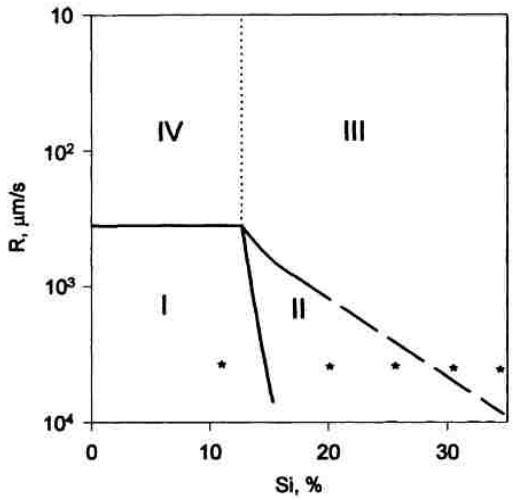

Figure 6. Diagram of the Al–Si alloys microstructure vs. Si concentration and Solidification Rates. I) Fiber-like structures with a primary α–phase. II) A fine-grained eutectic-like structure. III) A flake structure with primary Si crystals. IV) A flake structure with a primary α-phase [59]**.**

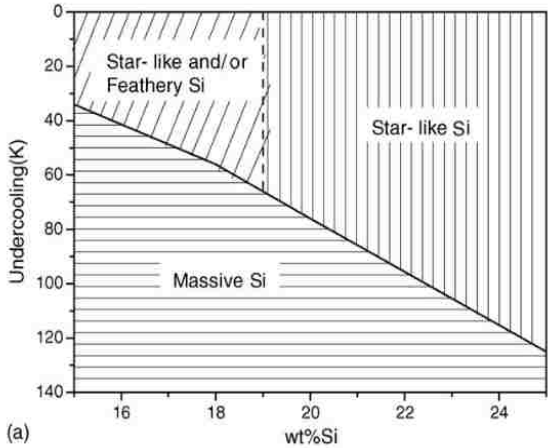

Figure 7. Primary Silicon morphology as a function of undercooling and Si concentration [52]**,** [60]**.**

Feathery Silicon

The feathery or "Fishbone" Silicon structure (see Figure 8) is the result of solidification from a high superheat temperature (150 °C above the liquidus temperature) [60]–[62]. At temperatures above the liquidus Silicon atoms agglomerate and form clusters [63]. The clusters rearrange into a different morphology during Solidification according to the Solidification Rates. The fishbone Silicon morphology has been classified as a pseudo primary phase [64], [65].

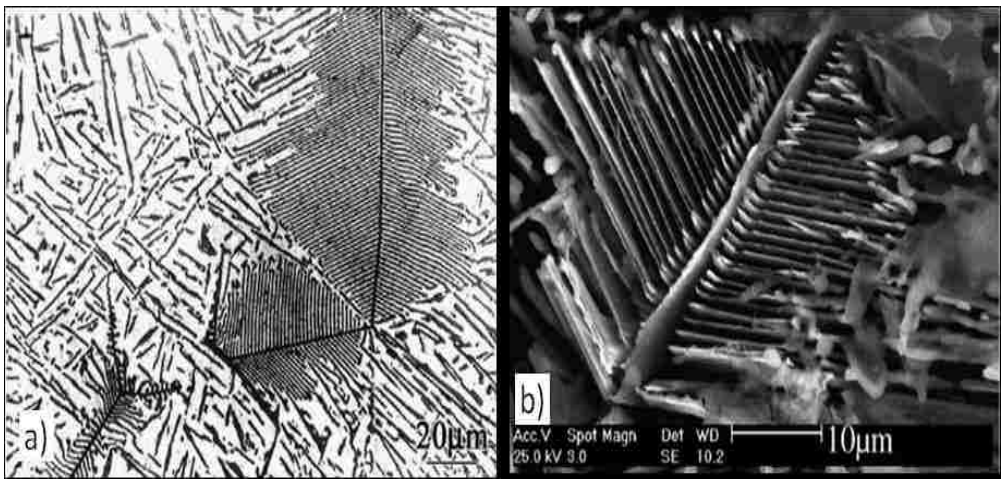

Figure 8. Feathery type Silicon in the hypereutectic Al-17wt.%Si alloy, a) LOM micrograph, b) SEM micrograph of the deep-etched sample [62]**.**

Polyhedral (Octahedral) Silicon

Polyhedral primary Si grows over a wide variety of growth velocities in hypereutectic Al-Si alloys. Studies revealed that primary Si crystallized from the melt at a pouring temperature of 1050 °C (small clusters) and exhibited a polygonal shape when compared to the star-like shape at a pouring temperature of 850 °C (bigger clusters). The basic shape of the polyhedral primary Si is octahedral. Figure 9 illustrates possible shapes of the sectioned primary Si visible after polishing. Octahedral primary Si nucleates heterogeneously in modified alloys or homogeneously in melts solidified at high SR [66], [67].

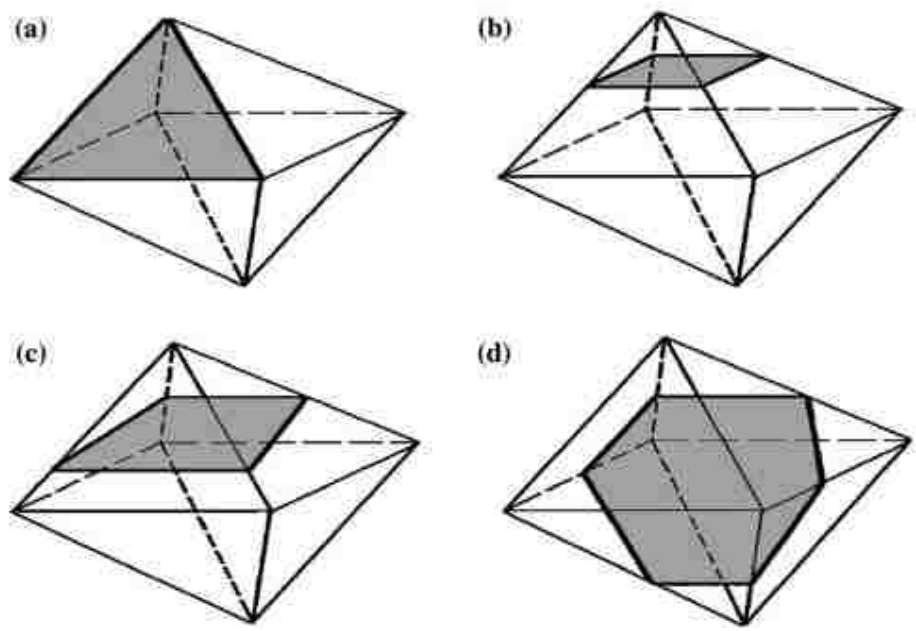

Figure 9. A schematic illustration of the polygonal outline of octahedral primary silicon in the sectioning planes (two dimensional observations), a) triangular outline, b) square outline, c) trapezoidal outline and d) hexagonal outline [66]**,** [67]**.**

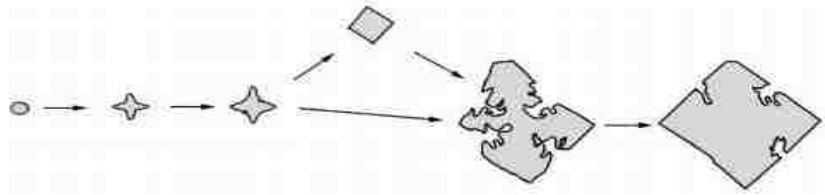

Figure 10. Schematic illustration of growth sequence of octahedral primary Si [66]**.**

Figure 11 illustrates the nucleation and growth sequence of octahedral primary Si. In the initial stage, primary Si creates spherical or round shapes, but as they grow to a critical size, they become unstable and create hillocks on the initial round shape.

The formation of octahedral shapes of primary Si depends on impurity rejection during growth and on the growth velocity of the planes. "Hopper" crystals are created when impurities are rejected by the growing crystal. This causes some parts of the crystal body to be poor in Silicon, see Figure 11b.

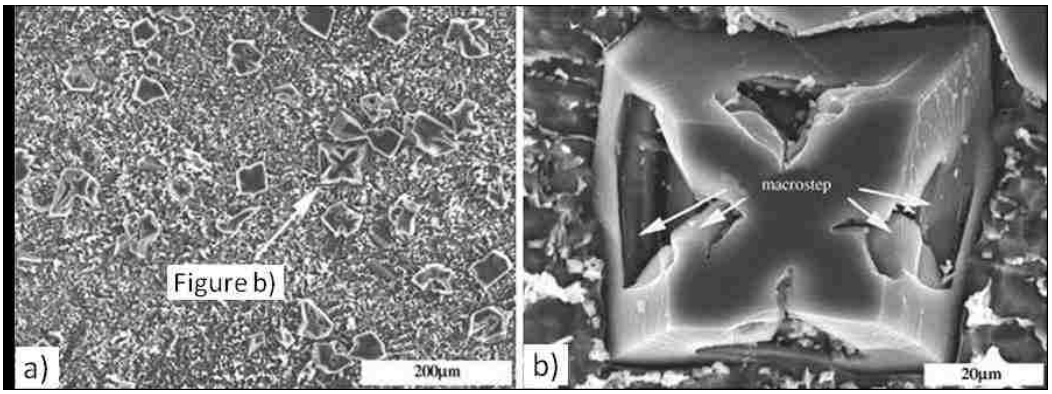

Figure 11. SEM micrographs for the Al-20Si alloy, a) shapes of polygons, b) magnified micrograph of the indicated region (see arrow) in a) - imperfect octahedral primary Si [66]**,** [68]**.**

Dendritic Primary Silicon

The dendritic morphology of primary Silicon is mainly formed in the hypereutectic Al–Si alloys treated with Sr or in the melt solidifying under small undercooling (approx. 10 °C). These types of morphologies are formed by layer growth and are faceted with second, third or higher order branches (see Figure 12) [69]. Sr additions poison the TPRE growth and suppress the growth of primary Silicon which leads to the formation of branches. The accumulation of Sr in front of growth sites will also lead to a decrease in the growth temperature and will thereby suppress the growth of {111} facets. Yilmaz et al. [70] found that at low growth rates Sr accumulation at the Si-liquid interface blocks the advancement of the local growth steps and leads to successive branching and dendritic growth [71], [69].

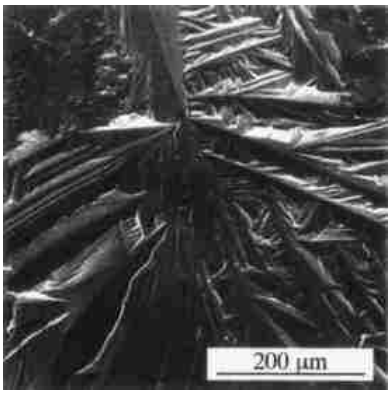

Figure 12. SEM micrograph of dendrite Silicon morphology, the Al-50 at.%Si droplet solidified at the onset of undercooling at 10 °C [69]**.**

Spherical Primary Silicon

The spherical primary Silicon, shown in Figure 13, is a result of Sodium treatment of the hypereutectic Al-Si alloy. This type of Silicon crystal is composed of several pyramidal grains with the tops at the center of the sphere. The Sodium enriched

regions are found at the boundaries of these pyramidal grains and many of these have twin relationships to each other [72].

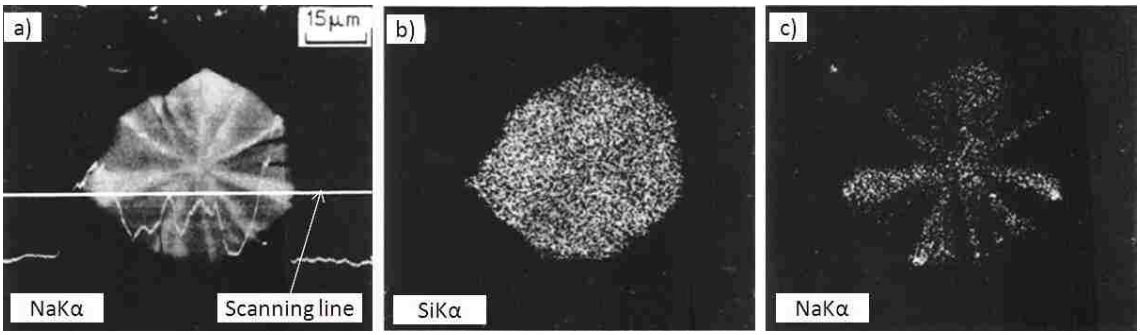

Figure 13. Micrographs of the spherical primary silicon crystal in an Al-16Si alloy treated with Sodium [72]**; a) BSE image; b) Electron Probe Microanalysis for SiKα radiation; c) Electron Probe Microanalysis for NaKα radiation. Note: that the contrast in a) matches the Sodium segregated region revealed in the NaKα micrograph c).**

Plate-like Primary Silicon

Plate-like Primary Silicon nucleates at low Solidification Rates and low undercooling commonly in unmodified hypereutectic alloys (see Figure 14). The primary Silicon particles nucleate and grow isotropically from the liquid by more rapid attachment at certain preferred sites, on the lateral surface. The hexagonal plate grows along the [112] direction by the TPRE growth mechanism. The Silicon crystals grow anisotropically along the less closely packed planes until the crystal is faceted only by {111} facets [72], [73].

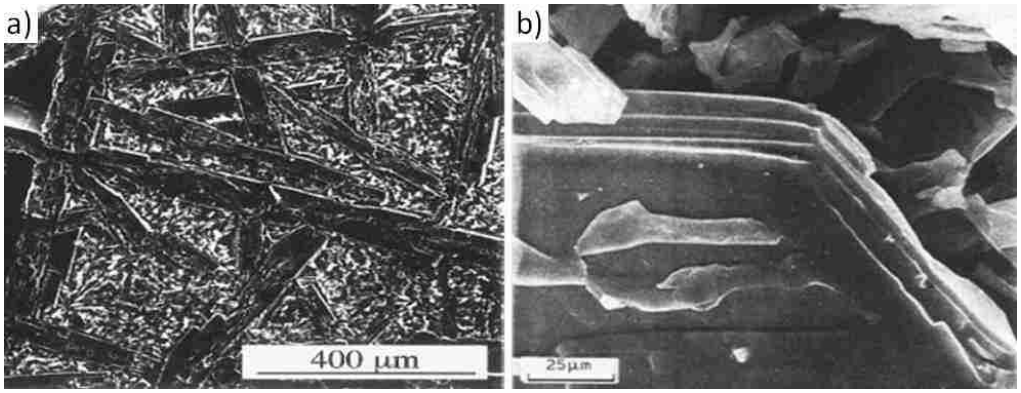

Figure 14. a) SEM micrograph showing the plate-like primary silicon crystals formed at low undercooling, b) SEM micrograph of the growth front of extracted primary Si showing multiple twin traces in the Al-16Si alloy [69]**,** [72]**.**

Plate-like Eutectic Silicon

Plate-like Eutectic Silicon grows as thin flat plates with a growth mode very similar to that of the flat plate primary Silicon. Day and Hellawell [74] defined unmodified Al-Si alloy growth conditions as a growth rate of V ≈ 10 μm/s and a temperature gradient G in a range of (1 to 10) °C/mm. The plates tend to form radiating clusters as shown in Figure 15, sometimes referred to as a "Wheat Sheaf" configuration. A given plate usually grows straight for some distance, then may branch or change direction through a large angle, in response to local conditions at the growth interface. X-ray diffraction images indicate a random crystal orientation of both the Silicon and Aluminum eutectic phases [74]. The driving force for branching is attributed to increased spacing, and therefore the diffusion distance between the Silicon tips is further apart as the radiating flakes grow [75], [76].

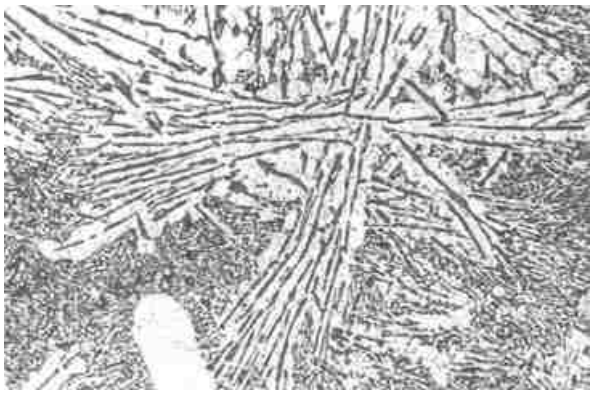

Figure 15. LOM micrograph of the Al-12Si alloy cooled in furnace and quenched after 50 % of the structure has solidified. Flake Silicon eutectic nodules and "Wheat Sheaf" morphology, 240x [75]**.**

Fibrous Silicon

The most significant effect of Silicon modification is a change in the morphology of the eutectic from the flake or plate-like form described above to a highly branched fibrous form (see Figure 16) sometimes called "Seaweed" [75]. Modification can be achieved by the addition of as little as 0.01 wt.% Na, Sr or by a high Solidification Rate.

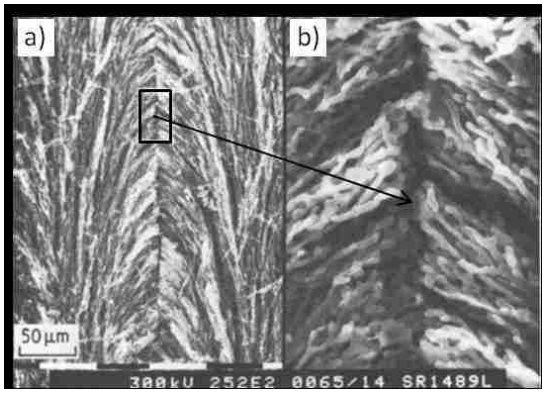

Figure 16. SEM micrographs, deep-etched Al-14Si-0.18Sr alloy, longitudinal section, growth direction bottom to top. V = 89 µm/s. a) Modified eutectic silicon, 242x.b) enlargement of the marked area in a) 1760x [75]**.**

A comparison of the eutectic structure reveals no detectable differences between the modifications produced by Na or S (impurity modification) or by fast solidification (chill modification). Chill modification requires a much higher solid-liquid interface velocity and it may be less effective in improving mechanical properties than impurity modification [77].

Dendritic Silicon

Gesing et al. [78] revealed Silicon Dendrites, which grow like primary Silicon in Aluminum matrix for the Strontium modified hypereutectic Al-20Si-3Cu alloy (see Figure 17). These Silicon dendrites are formed under highly directional solidification conditions. The sample was solidified at an average rate of 150 °C/s, calculated over the semi-solid region. Primary Si dendrites (100 to 200) μm solidified first from the liquid and from the depleting Si melt. A very high Solidification Rate produces non equilibrium and liquid and is depleted from Si lower than the eutectic condition. Interdendritic spaces of liquid contain increased concentrations of Al, Cu and Mg and the last to solidify are the Cu, Mg rich intermetallic phases.

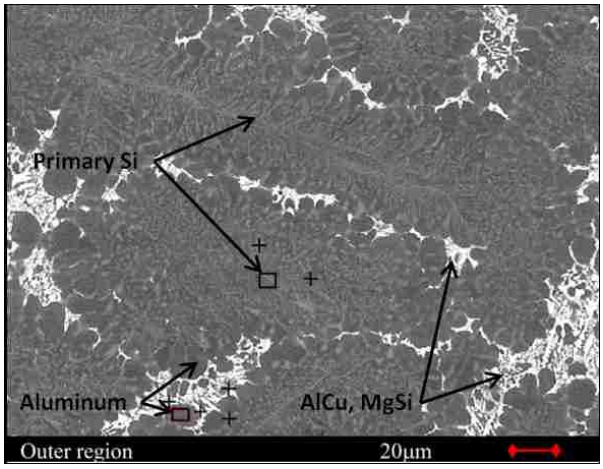

Figure 17. SEM micrograph showing primary Silicon Dendrites in the Aluminum Matrix for the Strontium modified hypereutectic Al-20Si-3Cu Alloy [78]**.**

(Inter-dendritic) Blocky Nano Primary Silicon

Gesing et al. [78] presented another new type of (inter-dendritic) blocky nano primary silicon crystal (see Figure 18), which formed in the 0.15 wt.%Sr modified hypereutectic Al-20Si-3Cu alloy, solidified in the High Temperature Universal Metallurgical Simulator and Analyzer (HT UMSA) Technology Platform at a Maximum Cooling Rate (MCR) of ≈ 400 °C/s. Blocky, equiaxed, sub-micron (0.1 to 0.5) μm primary Si crystals are located inside (3 to 10) μm spheroidal Al grains. Multiple Si crystals inside each Al grain suggest that these Al grains did not nucleate on solid Si but rather engulfed them as they grew. Larger (1 to 2) μm Si grains are located between the Al grains together with the CuAl phase filling the inter-granular space. In larger inter-granular spaces the CuAl phase shows the beginning of dendritic solidification expelling the MgSi phase to the dendrite surface allowing it to coat the interdendritic shrinkage cavities.

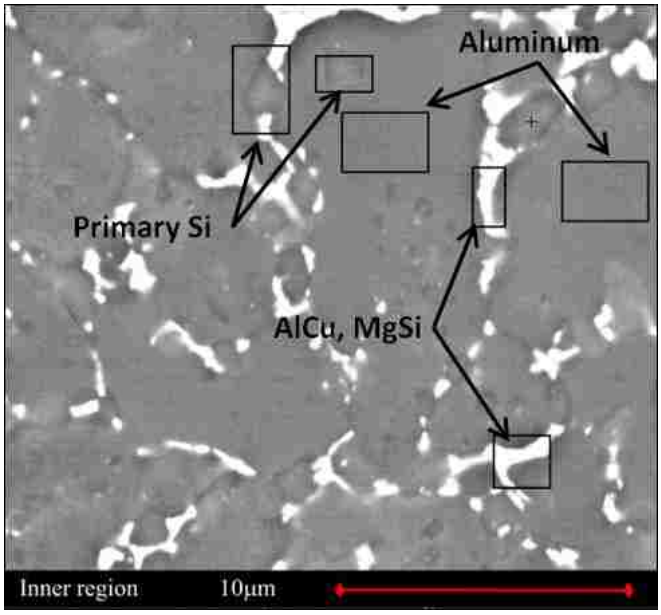

Figure 18. SEM microstructure showing nano blocky primary silicon crystals, which grow like primary silicon in the 0.15 wt.%Sr modified hypereutectic Al-20Si-3Cu alloy, solidified at a MCR of ≈ 400 °C/**s** [78]**.**

2.2 Melt Treatment of Al-Si Alloys

Hypereutectic Al-Si alloys contain more than 12.6 wt.%Si. The structures of the unmodified slowly solidified alloys contain coarse primary and eutectic silicon in an α-Aluminum matrix. The presence of hard primary silicon particles in the strengthened α-Aluminum matrix results in very good wear resistance, which is the most unique property of hypereutectic alloys. At the same time the coarse primary Si particles have a detrimental effect on the machinability, strength and ductility of the alloy. Large unevenly distributed primary Si particles cause greater tool wear than smaller, more uniformly distributed particles [79], [80]. Removing this deficiency is the reason why

researchers attempted to improve the mechanical properties of Al-Si alloys by simultaneously modifying primary and eutectic silicon [30].

Silicon particles can be modified by adding Sr, Na, P, rare earth elements and also by quench modification and by other means such as ultrasound, electric current, electromagnetic stirring and vibration, etc. [82]–[88].

2.2.1 Chemical Modification of Hypoeutectic Al-Si Alloys

The Mechanism of Silicon Modification in Al-Si Alloys

Modification of the eutectic silicon in hypoeutectic Al–Si alloys is implemented extensively in industry to improve mechanical properties, whereby the unmodified needle-like morphology of silicon is changed to a fibrous morphology.

The theory of **Impurity-Induced Twinning (IIT)** of Twin Plane Re-entrant Edge (TPRE) growth of silicon [88], [89], is used to explain the modification of hypoeutectic Al–Si alloys by the addition of small amounts of a suitable element. In the unmodified alloy Silicon flakes exhibit highly anisotropic growth. Modified silicon fibers are crystallographically very imperfect and are able to curve (to bend) and branch. The IIT theory explains that a high density of twinning occurs in silicon in modified alloys because atoms of the modifier are absorbed onto the growth steps of the silicon solid–liquid interface. If the concentration of impurity atoms is sufficient, (distance between impurity atoms -ξ is smaller than the critical one) and creates a “traffic problem” in the step motion thus poisoning the TPRE growth (see Figure 19) [88], [89].

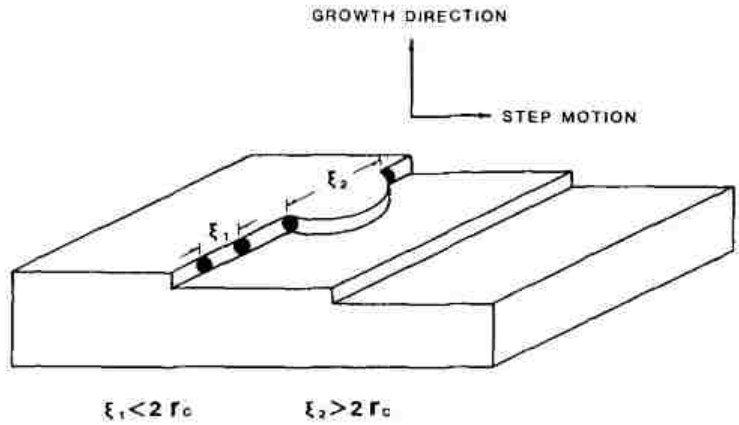

Figure 19. Schematic representation for adsorption of impurity atoms at monolayer steps on a growth interface. Where ξ is the spacing between added atoms, $2r_c$ is a critical dimension for layer extension [89]**.**

A pre-condition for the TPRE theory is that the atomic radius of the modifying element relative to silicon (r/r_{Si}) exceeds 1.65 [89], [90]. Elements including Sr (r/r_{Si} = 1.84), Na (r/r_{Si} = 1.59), Ba (r/r_{Si} = 1.86) have been reported to cause fibrous eutectic modification and all of these elements have an atomic radius ratio close to the theoretical ideal (r/r_{Si} = 1.65) [91], [92].

The Impurity Induced Twining (IIT) mechanism for modification of hypoeutectic Al-Si alloys was studied by using different concentrations of individual additions of Sr, Ba, Yt and rare earth elements [90]–[95]. These studies revealed that in some cases the IIT mechanism does not work. This suggests that some other mechanism is also important for modification of silicon.

The Restricted Growth Theory (RGT) [96] explains modification of Si through the restriction of rapid growth in the [112] direction. Si plates preferred other

growth directions instead of the [112] direction. Modifier atoms are absorbed at re-entrant edges and disrupt the anisotropic growth of Si.

Figure 20 [96] schematically represents a comparison of Impurity Induced Twinning and the Restricted TPRE Growth Theory.

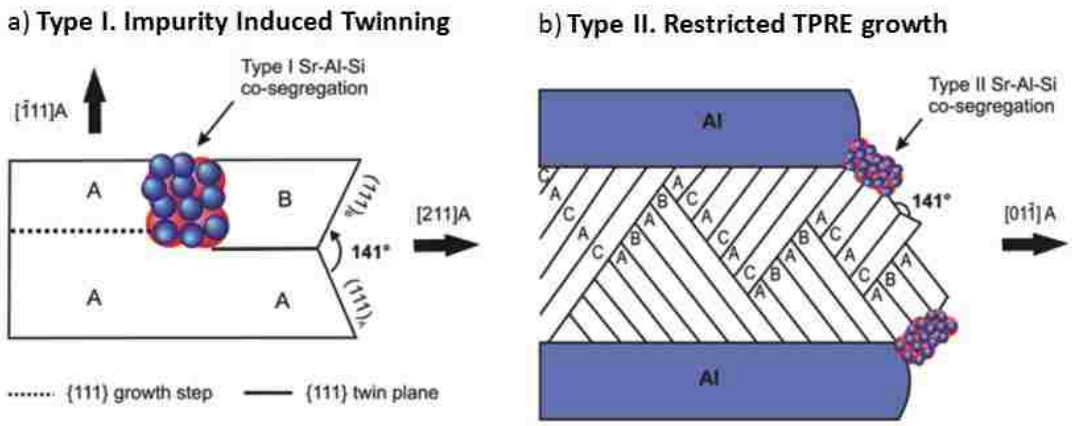

Figure 20. Schematic representation of (011) plane projection of the eutectic Si phase: a) Type I, Sr–Al–Si co-segregation which promotes twinning by changing the stacking sequence. b) Type II, Sr–Al–Si co-segregation within the eutectic Si phase at the re-entrant edges or growing surfaces. A, B and C – represents Si crystals with different orientations [96]**.**

Clapham and Smith [97] developed an Atomic Absorption Spectroscopy (AAS) technique for individual phase analysis of Strontium in Al-Si alloys. The analysis indicates that in the modified Al-Si alloy most of the Strontium segregates to the Silicon phase. This suggests that during solidification the Aluminum phase rejects Strontium which is subsequently incorporated into the Silicon phase. When a modifying impurity element is relatively soluble in solid Aluminum, higher concentrations are required to achieve a change in the Silicon growth.

Elements for Silicon Modification of Hypoeutectic Al-Si Alloys

The most common elements used in the modification of Al-Si alloys are Sr, Na and Sb. These elements produce significant modification at low additions and thus are the only elements widely used in the industry [36].

Sodium (Na) was the first element used to modify hypoeutectic Al-Si alloys commercially. Sodium is an effective modifier in the range (0.005 to 0.010) wt.%, but its recovery is only (20 to 30) % [98]. Due to the disadvantages of Na modification (volatility and reactivity), its use is being reduced in favor of Strontium [34], [35].

Strontium (Sr) added as a modifier to eutectic Al-Si alloys, produces a fibrous eutectic Silicon structure similar to Sodium modified Silicon and also has more advantages than Sodium. Strontium can be added to the melt easily, is effective over a wide concentration range, survives in the melt for long holding times, is less sensitive to over modification than Sodium, and exhibits a high recovery rate [99], [100]. Disadvantages of Sr modification include a relatively high cost and some researchers reported that Strontium increases the gas levels in a melt [25].

The mechanism of Silicon modification of eutectic Al-Si alloys, at different levels of Strontium addition, different SR, and different Silicon content was studied in references [101]–[106].

Experimental studies by Espinoza-Cuadra et al. [107] proved that the combined effect of Sr addition plus the overheating temperature (above 800 $^{\circ}$C) and undercooling cause inhibition of the β-Al_5FeSi phase (needle-like phases are detrimental) in alloys and at the same time support formation of the α-phase (Chinese script) and result in a strong reduction in the stereological characteristics (area, length and width) of the intermetallic

particles in the α-phase. The combined application of Sr modification and squeeze casting of the hypoeutectic Al-11 wt.%Si alloy results in a structure consisting of fine α-phase crystals and fibrous silicon eutectics and allows for the manufacturing of castings which exhibit high mechanical properties: UTS = 270 MPa, A_5 = 16 %, (see Figure 21) [108].

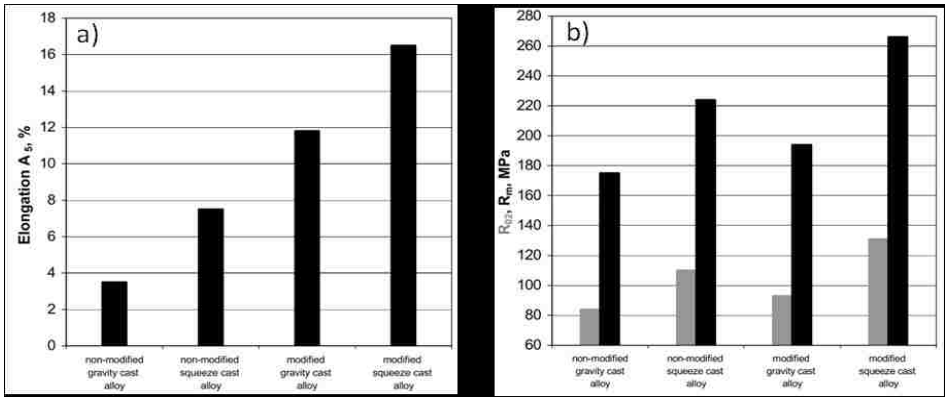

Figure 21. The influence of casting conditions on the properties of the unmodified and 0.05 wt.%Sr modified Al-11Si alloy, a) Elongation, b) Yield (R_{02}) and Ultimate Tensile Strength (R_m) [108]**.**

The most important advantage of using **Antimony (Sb)** as a Silicon modifier is that it does not fade, it is not sensitive to re-gassing and it reduces porosity in parts which are prone to porosity formation. Antimony is a permanent modifier. Disadvantages of Sb modification are that it reacts with Sr and Na and reduces the effectiveness of these modifiers. Sb is less effective than Na and Sr [109]–[112].

Individual modifiers added to Al-Si alloys interact with each other at the same time. The results show that Bismuth (Bi) reduces the efficiency of Si modification by Strontium. Researchers established that the ratio Sr/Bi has to be at least 0.5 for a fully Si modified structure [113], [114] and with respect to **Boron (B)**, a Sr/B ratio exceeding 0.4 is required [115].

Elements like Bismuth, Barium or Rare Earth Elements are not commonly used in industry for Si modification of hypoeutectic Al-Si alloys, but many researchers carried out research with this in mind and reached interesting results.

The effect of **Bismuth (Bi)** addition and the different SR on the eutectic phases in the Al–8.5Si–0.4Mg–0.3Fe alloy was studied by Farahany et al. [109]–[111], [113], [114], [116]–[120]. The addition of Bi (up to 0.5 wt.%) to the base alloy, transformed the morphology of eutectic Si from a flake-like structure to a lamellar structure at a slow SR (0.7 $^{\circ}$C/s). As the SR increased up to 4.0 $^{\circ}$C/s, the morphology of the eutectic Si transformed to a fibrous structure indicating acceleration of the refining effect of Bi addition.

Barium (Ba) can be used as a modifier of hypoeutectic Al–0.35Mg–7.0Si alloys. The microstructure of the alloy after modification by 1.0 wt.%Ba contains α-dendrites and fine fibrous or rod-like eutectic silicon instead of plate-like structures [121].

All **Rare Earth metals – RE** (**Y,** Tb, Dy, Ho, Er, Tm, Yb, Lu, Sc, La, Ce, Pr, Nd, Pm, Sm, Eu, and Gd) have the potential for eutectic modification according to the atomic radius of the modifying element relative to Silicon (r/r_{Si}) = 1.65, [122]–[125].

2.2.2 Chemical Modification of Hypereutectic Al-Si Alloys

For the most part researchers are currently using Phosphorus and Strontium for chemical modification of hypereutectic Al-Si alloys however investigations have also been carried out to determine whether all scales of elements including RE metals can be used for chemical modification of these alloys.

Phosphorous (P) is most often used for chemical modification of hypereutectic Al-Si alloys. The use of Phosphorus additions to modify primary Silicon in hypereutectic Al-Si alloys was patented by Sterner-Rainer [126] in 1933. Phosphorus is an extremely effective modifier requiring only small additions (< 0.007 wt.%) to achieve full modification. Phosphorus added to molten Aluminum forms tiny, insoluble AlP particles which are potent sites for epitaxial nucleation and for the growth of primary Silicon [30]. Phosphorus can be added into the melt in many forms, such as Cu–P, Al–P, Al–Cu/Fe–P master alloys.

Kyffin et al. [127] showed that with the addition of 0.01 wt.%P to the hypereutectic Al-22Si alloy solidified at SR = 25.4 $^{\circ}$C/s, a minimum size of primary Si particles equal to13.1 μm was reached.

Strontium (Sr) is known as a modifier of eutectic and primary Silicon. Tenekedjiev [128] presented experimental data on Sr addition in the range of (0 to 0.2) wt.% to the hypereutectic Al-7Si (A390.1) alloys which resulted in a fibrous eutectic Silicon morphology and a dendritic primary Silicon morphology as well as fragmentation of dendrites. It was determined that the concentration of 0.04 wt.%Sr is sufficient for modification of eutectic silicon and fragmentation of primary Si dendrites. Higher strontium levels promote a more dendritic morphology as well as a reduction of the dendrite size; however the micrographs presented show a primary Silicon size over 100 μm. Thermal Analyses show that the addition of 0.1 wt.%Sr depresses the liquidus temperature by up to 30 $^{\circ}$C for the A390.1 alloy. Mahanti et al. [83] used the addition of 0.2 wt.%$SrCl_2$ for modification of the hypereutectic Al-18Si alloy. Experiments resulted in a reduction in the Silicon size from 100 μm to 20 μm (see Figure 22).

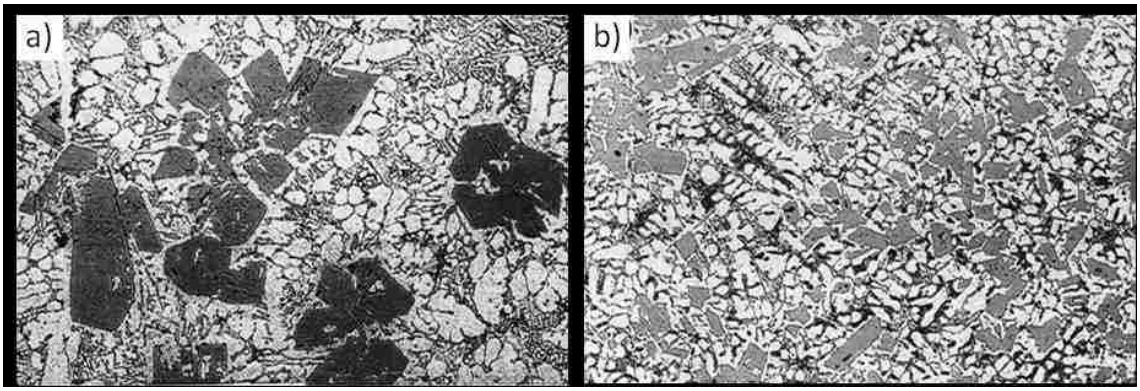

Figure 22. LOM micrographs for the hypereutectic Al-18Si alloy, a) re-melted and cast without melt treatment, b) treated with 0.2 wt.%$SrCl_2$ [83]**.**

The influence of Strontium addition (up to 0.20 wt.%Sr) on the microstructure and properties of the hypereutectic Al-18Si alloy cast into a steel mold, was reported by K. Müller [129]. The author presented modified primary Si dendrites (see Figure 23) corresponding to a minimum Volume Fraction (see Figure 24) reached by adding 0.010 wt.%Sr. The minimum of the average particle size of primary Si (80 μm) was reached by adding 0.08 wt.%Sr.

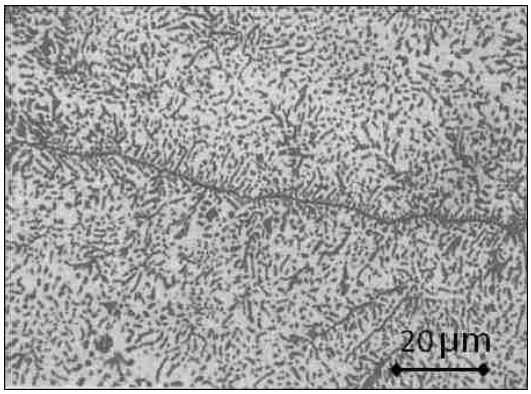

Figure 23. Si dendrite in the hypereutectic Al-18Si alloy modified with 0.01 wt.%Sr [129]**.**

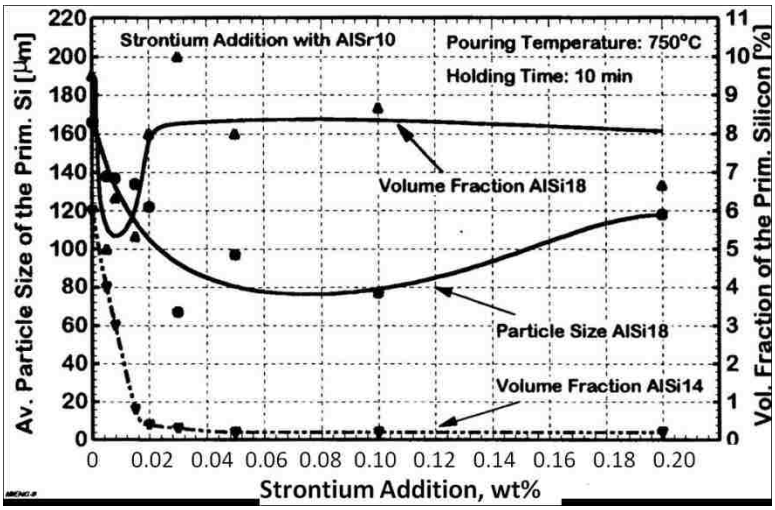

Figure 24. Influence of Sr addition on Average Particles Size and Volume Fraction of the Primary Silicon [129]**.**

Faraji et al. [33] reported that the addition of Sr suppressed the formation of primary Si even in the presence of added P. At a SR of 0.3 °C/s, the addition of 0.2 wt.%Sr to the hypereutectic Al-19Si alloy resulted in a reduction in the nucleation temperature of primary Silicon (liquidus temperature) of 40 °C (from 654 °C to 614 °C) together with a reduction in the number of primary Silicon particles per unit volume N_v by a factor between 20 and 30 times. The best modification was reached by the addition of 0.1 wt.%Sr however the author did not provide the dimensions of the primary Si particles.

Zuo et al. [130] used a combination of 0.06 wt.%P and 0.07 wt.%Sr and reached a modification of Al-30Si for the hypereutectic alloy; the size of the primary Si was reduced from 200 μm to 33 μm, and the eutectic Si was modified to a fibrous form (see Figure 25).

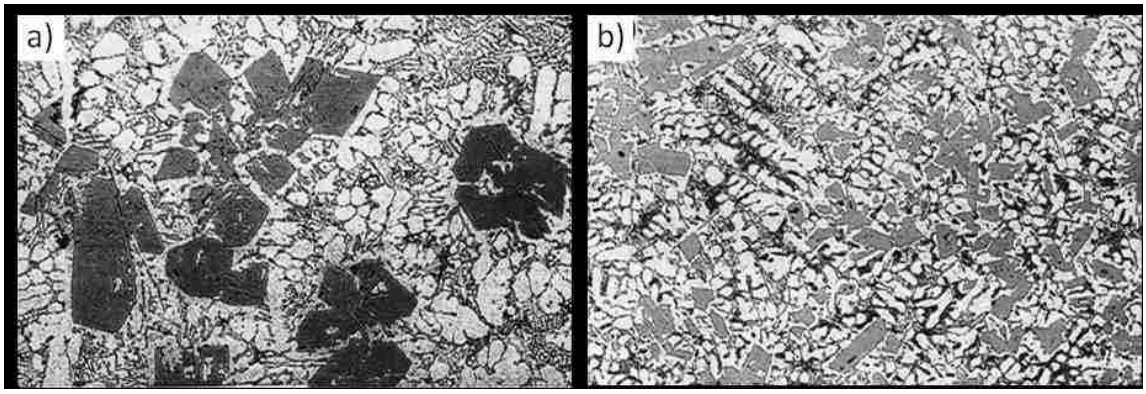

Figure 25. LOM micrographs of the Al-30Si alloy; a) unmodified, b) modified by 0.06 wt.%P and 0.07 wt.%Sr combined [130]**.**

Al-Helal et al. [131] used a solid-liquid duplex casting process to achieve simultaneous modification of primary and eutectic Silicon in hypereutectic Al-Si alloys. In this process the P-treated Al-24Si solid alloy is mixed with the Sr-treated eutectic Al-12.6Si molten alloy to provide an Al-18Si alloy in the Liquid + Primary Si phase field and then cast. By using this process the average particle size of primary Silicon was reduced from 50 μm to 15 μm and the eutectic structure changed from a plate-like structure to a fibrous structure when compared with the conventional casting process (see Figure 26). The Tensile Strength increased by 14 % (from 154 MPa to 175 MPa) and the elongation from 1.64 % to 3.76 %. The improvement in mechanical properties is attributed to the modification of both primary and eutectic silicon [131].

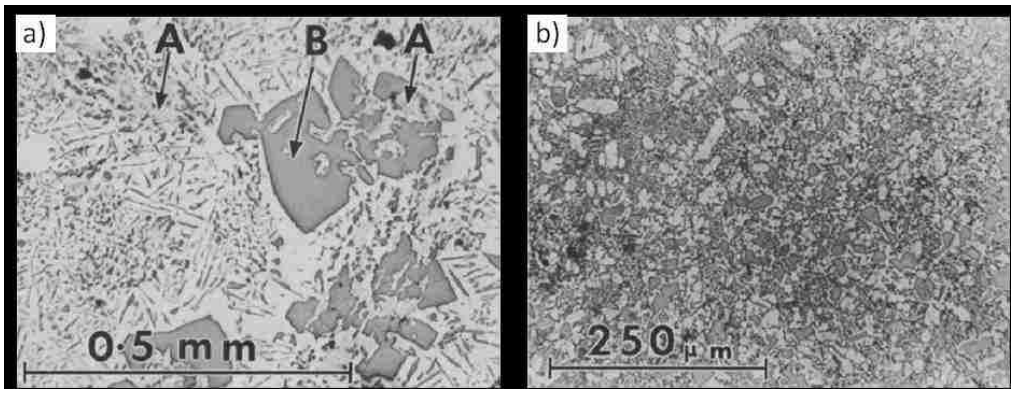

Figure 26. Microstructure of the Al-18Si alloy: a) conventionally cast without additions, b) with the addition of 0.005 wt.%P + 0.02 wt.%Sr and processed by the solid-liquid duplex casting process [131]**.**

Researchers produced very fine Si particles in the cast hypereutectic alloy by powder metallurgy. Delshad-Khatibi et al. [132] used the Solid Assisted Melt Disintegration (SAMD) technique for production of Al-20Si-0.015P powder with reduced primary Si particles to 1.1 μm (for the smallest sieved particles). In this process, melt disintegration was achieved by introducing a solid media (i.e. NaCl or alumina) into the molten alloy and stirring the slurry to produce droplets which form powder particles after solidification.

Shamsuzzoha et al. used Barium as a modifier [133]–[135]. The authors reported that the microstructure of the hypereutectic Al-17Si alloy modified with 3 wt.%Ba and directionally quenched at 17.5 °C/s, contains nano-size fibers from 50 nm to 150 nm without primary Si (see Figure 27). When the authors used the same treated alloy for a small shape casting, without quenching, the microstructure contained primary Si particles of 2 μm to 20 μm. The authors explained simultaneous modification of primary and eutectic Silicon using the expression that "a silicon based solid solution" has a lower melting point than that of pure Si and can effectively shift the corresponding pseudo-eutectic composition towards a higher melting component (Silicon). Barium

forms about 0.5 wt.% solid solution with Si at 900°C, but none with Aluminum [135], [136]. Figure 28 presents the schematically proposed shift of the "original eutectic point" to the higher Si content. The proposed pseudo-binary reaction can then produce a pseudo-eutectic microstructure for the otherwise hypereutectic composition.

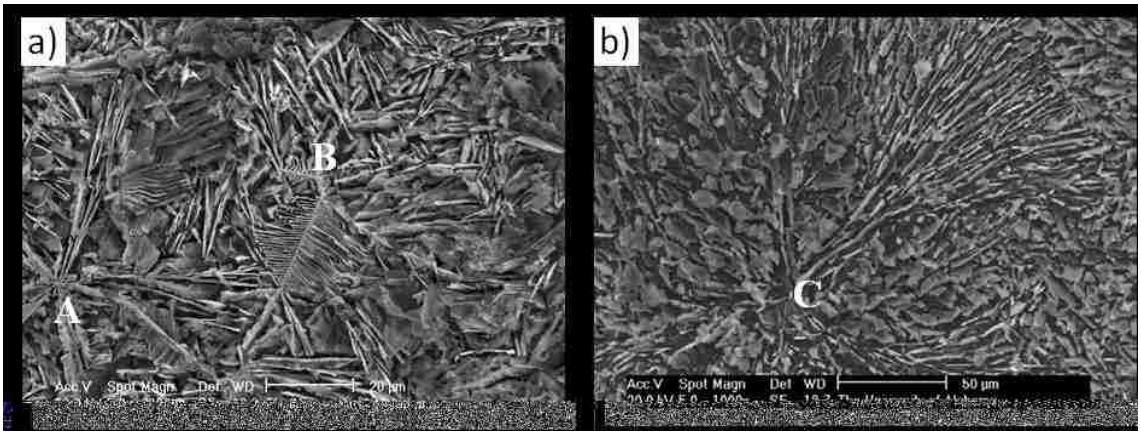

Figure 27. SEM micrographs, deep-etched shape cast Al-17Si-3Ba alloy, a) longitudinal and b) transverse section. Star-like (Points A and C), FishBone (Point B) morphologies of the Si crystal. Point (C) shows the Divergence of Si flakes from a point of origin located at the center of the star-like assembly of the Si crystal [133]**.**

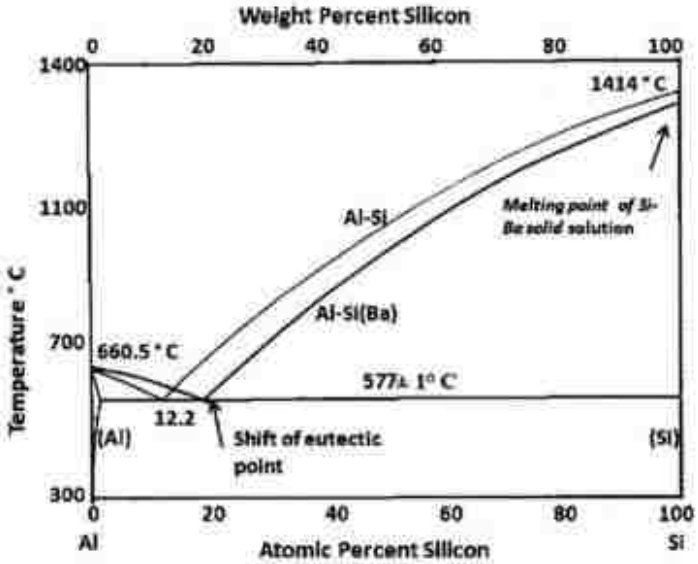

Figure 28. Schematic of the liquidus lines and a eutectic point shift due to the solid solution of Ba in Si as imposed in the Al-Si phase diagram according to reference [135]**.**

The author's explanation of Silicon modification is very mechanistic. In spite of the good experimental results, interpretation of the modification phenomenon using the Al-Si diagram is wrong. The liquidus temperature of pure Si (or of any pure element) is constant and the addition of a third element to the binary eutectic phase system changes the eutectic temperature. For an explanation of the Silicon modification mechanism after the addition of Ba, it is necessary to use a ternary phase diagram for the Al-Si-Ba system.

Ding et al. [137] investigated the effect of Al–5Ti–C master alloy on the microstructure and mechanical properties of the hypereutectic Al–20Si alloy by using the 0.6 wt.% Al–5Ti–C master alloy. The authors reported modification of primary Si crystals from roughly 120 μm to 20 μm and the morphology changes from a coarse star-like and polygonal shape to a blocky shape. Using the master alloy the morphology of eutectic Silicon was changed from a flake-like and acicular shape to a finer fibrous shape.

Chang et al. [138] reported results of modification of the hypereutectic Al-21Si alloys by the addition of different levels of Rare Earth metals (RE) (1, 2 and 3) wt.% in the form of Misch metal (51.9 wt.%Ce, 25.09 wt.%La, 14.25 wt.%Nd, 5.33 wt.%Pr, 1.43 wt.%Fe and 0.12 wt.%Pa) which solidified at different Solidification Rates (130 $^{\circ}$C/s, 73 $^{\circ}$C/s, 45 $^{\circ}$C/s and 33 $^{\circ}$C/s). The results are shown in Figure 29. The authors reported a significant decrease of primary Si size at a maximum CR of 130 $^{\circ}$C/s (cooling rates calculated between the primary reaction and the eutectic reaction temperature) with the addition of 3 wt.% of RE, from 500 μm to 50 μm however, in comparison with the Strontium modified results, RE metals are not effective modifiers of primary Si.

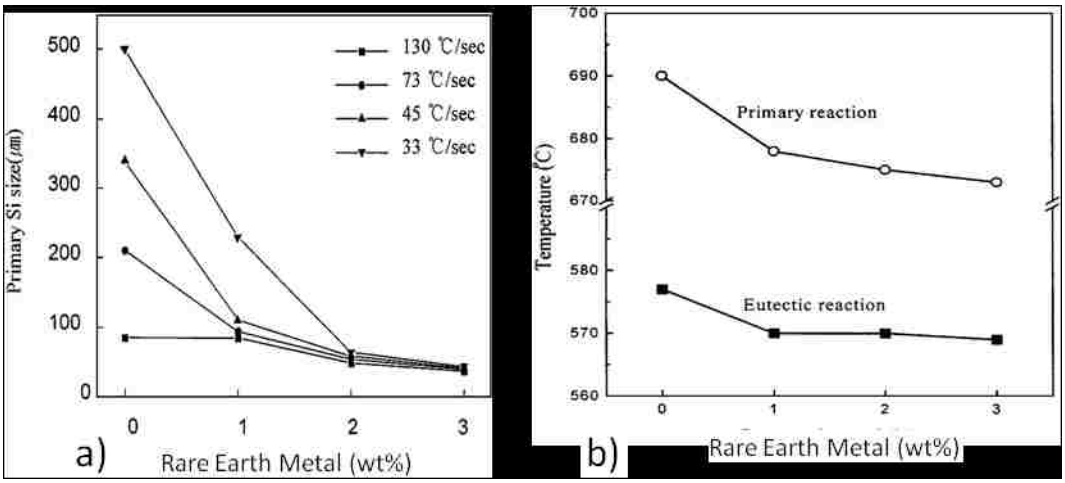

Figure 29. Effect of the RE addition to the Al-21Si alloy on: a) primary Si size and at a different CR (the CR is calculated between the primary reaction and the eutectic reaction temperature), b) Temperature of metallurgical reactions at a CR of 2 °C/min [138]**.**

Aluminum oxide ($A1_2O_3$) nanoparticles (3 wt.%) in the form of sintered Aluminum powder rods and 0.5 wt.% Sodium were used by Cisse et al. [139] for modification of the hypereutectic Al-17Si alloy. The combined addition of $A1_2O_3$ nanoparticles and Na resulted in simultaneous modification of primary and eutectic Silicon (from 250 μm to 50 μm), see Figure 30 (a, b) [139].

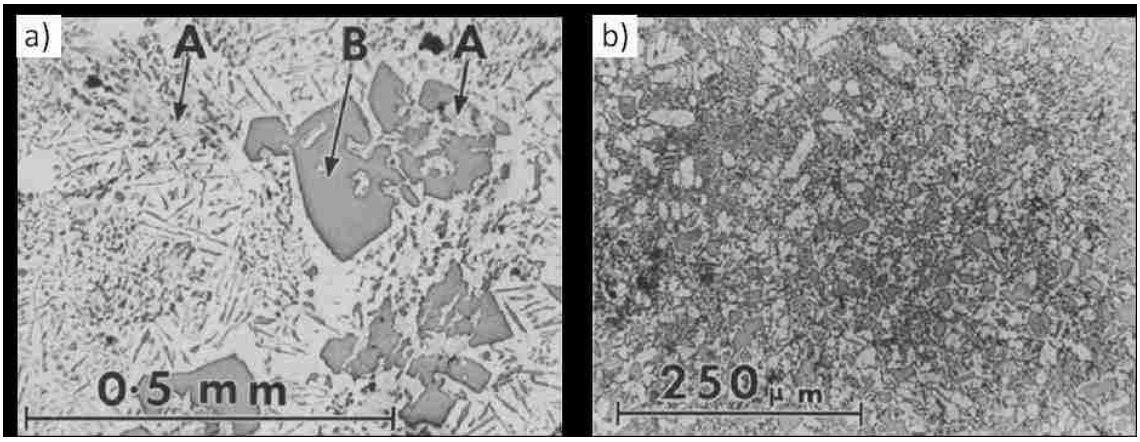

Figure 30. LOM micrographs: a) Al-17Si alloy + 3 wt.%$A1_2O_3$, A-Al_2O_3 particles, B-partially modified primary silicon, b) Al-17Si alloy + 3 wt.%$A1_2O_3$ + 0.5 wt.%Na modified primary and eutectic silicon [139]**.**

Different contents of γ-$A1_2O_3$ nanoparticles for modification of primary Silicon in the hypereutectic Al–20Si alloy were used by Choi et al. [140]. The macroscopic star-shape primary Silicon particles (size: ≈ 250 μm) were modified to small polygons or blocky shapes (size: ≈ 25 μm) with smoother edges and corners. The large plate-like eutectic Si particles were also modified into finer coral-like Silicon particles (see Figure 31). The ductility of the cast hypereutectic Al–20Si–4.5Cu alloy with the addition of 0.5 wt.% γ-$A1_2O_3$ nanoparticles was increased from 0.44 % to 0.98 %, yield strength increased by 5 % and ultimate tensile strength increased by 35 % [141].

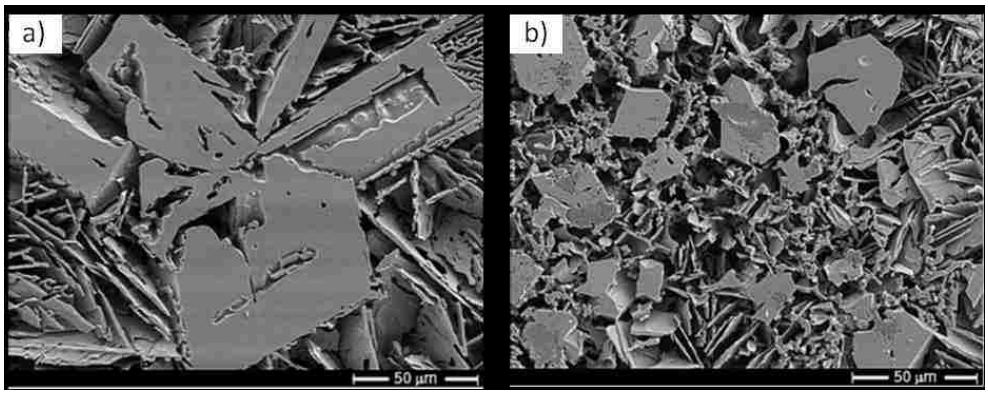

Figure 31. SEM micrographs of the deep-etched Al-20Si alloy, a) unmodified and b) modified with 0.5 wt.% γ-$A1_2O_3$ nanoparticles [140].

2.2.3 Melt Thermal Treatment of Al-Si Alloys (Quench Modification)

Thermal Rate Treatment

The Thermal Rate Treatment of the alloy melt is a technology where the melt is superheated to a very high temperature, usually more than 300 °C above its liquidus, holding the temperature for several minutes, and then cooling it quickly to a pouring temperature.

Bian and Wang [50] reported the results of Thermal Rate Treatment applied to the hypereutectic Al–13Si alloy. The alloy was heated to a superheating temperature and held there for 10 minutes, then cooled quickly to the pouring temperature of 700 °C, and poured into a cast iron mold for examination of the microstructures (see Figure 32).

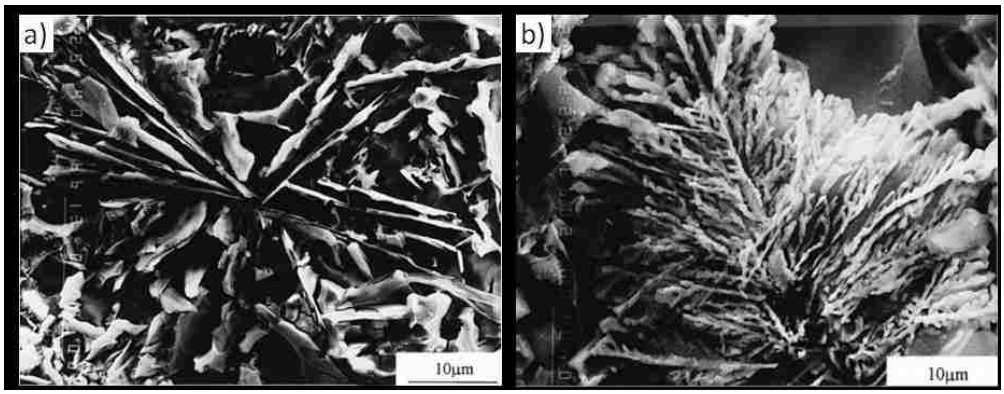

Figure 32. SEM micrographs of the morphology of the Al-13Si, a) without the Thermal Rate Treatment, b) with the Thermal Rate Treatment [50].

Using a high temperature X-Ray diffractometer the mean atomic density - ρ_o (the amount of atoms per unit volume) and the coordination number n_c (number of nearest atoms around one atom) were measured during Solidification. The results are shown in Figure 33.

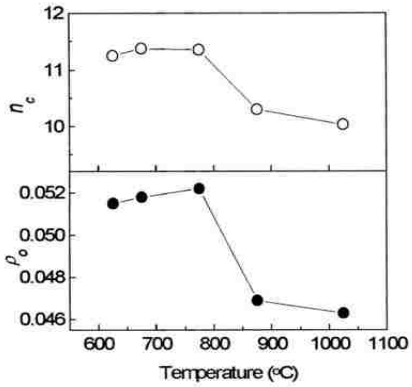

Figure 33. The mean atomic density-ρ_o and coordination number of the alloy-n_c vs. the superheating temperature of the alloy [50]**.**

A sudden change in those parameters (ρ_o and n_c) in the temperature range (775 to 875) °C relates to the dissolution processes of the Si-Si clusters. In this situation, if the amount of Si-Si clusters is decreased, during the solidification process, the number of developing nuclei is also decreased with the result that the Aluminum phase will nucleate at the cost of the Silicon phase. These good conditions for development and growth of Si nuclei are transferred to lower temperatures where diffusion of the Si atoms is more difficult and the result is a finer modified structure. This is how the modified structure can be obtained by Thermal Rate Treatment without any addition of modifying elements. It is not as difficult to modify the eutectic Silicon in hypoeutectic Al-Si alloys (1.65 to 12.6) wt.%Si in comparison with the primary Silicon in hypereutectic Al-Si alloys (>12.6 wt.%Si).

Li et al. [87] performed a similar experiment using the hypereutectic Al-16wt.%Si alloy. The alloy was superheated during remelting in the temperature range (720 to 1050) °C and cooled at 60 °C/s and 150 °C/s to the pouring temperature of 720 °C and then cast into a sand and a metal mold (to provide a different SR).The results are presented in Figures 34 and 35.

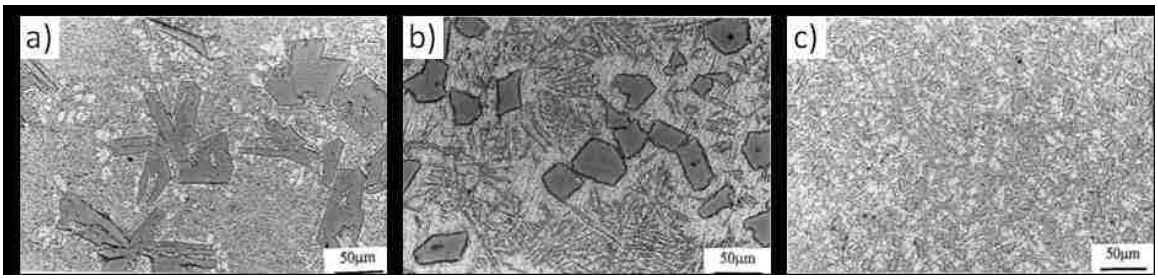

Figure 34. LOM micrographs of the Al-16Si alloy cast into a metal mold at different superheating temperatures and cooling rates, a) The superheating temperature of 720 °C cooled at 60 °C/s, b) 720 °C and 150 °C/s, c) 1050 °C and 150 °C/s [87]**.**

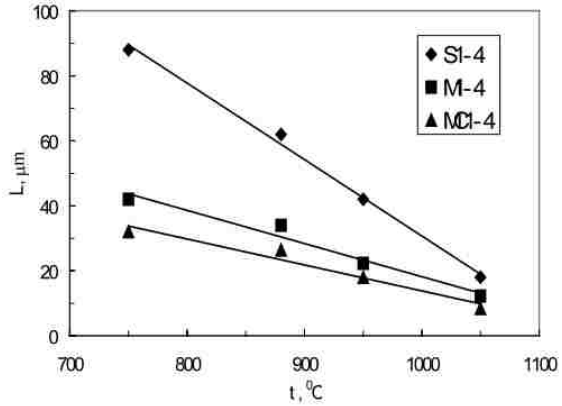

Figure 35. Comparison of the effect of the melt superheating temperature on the Si particle size for the Al–16Si alloy at different CR and SR (sand or metal mold); S-cooled at 60 °C/s and cast into a sand mold, M-cooled at 60 °C/s and cast into a metal mold, MC-cooled at 150 °C/s and cast into a metal mold [87].

Xu et al. [142] investigated the effect of Solidification Rate on the microstructure of the rapidly solidified Al-20Si alloy using a single roller melt spinning technique to manufacture a 40 μm thick melt spun ribbon. At an estimated SR = 1.11 × 10^6 °C/s, the morphologies of primary Silicon in the melt spun ribbon exhibited a fine blocky-shape in the range from 5 μm to 0.5 μm (see Figure 36). Practical utilization of this technique is very limited and SR = 10^6 °C/s is practically non-measurable.

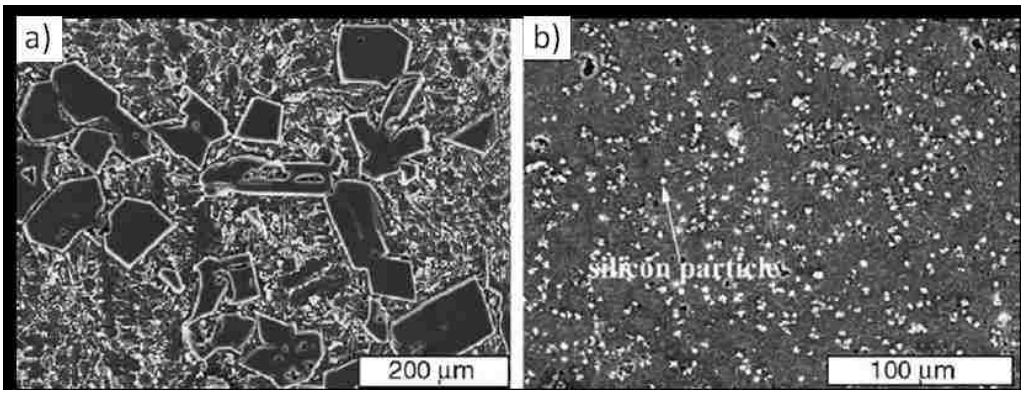

Figure 36. SEM micrographs for the Al–20Si alloy, a) as-cast (SR = 50 °C/s), b) melt spun ribbon at the free surface (SR = 1.11 × 10^6 °C/s) [142].

During rapid solidification the diffusion of Silicon atoms can be very limited, with the result that the growth of primary Silicon in the melt spun Al–20Si alloy is inadequate, and thereby leads to very fine primary Silicon particles. Regarding fine eutectic Silicon, the authors stated that: a) the solidification rate for the Al–20Si melt spun ribbon is so high that most of the added Silicon is retained in the solid solution and b) the growth of eutectic Silicon is slow due to rapid solidification [142].

As was reported in [81], [143]–[146] for complete dissolution of the Si-Si cluster in Al-Si alloys, sufficient superheating temperatures (roughly 300 °C above the liquidus temperature) are necessary. The Si-Si clusters are very stable at a temperature less than 100 °C above the liquidus and are not dissoluble even after a holding time of 3 hours [143]. The clusters, which are the first potential nuclei for primary Si, are dissolved so crystallization of primary Si is partially suppressed. Another factor of concern is that the high CR creates difficulties for diffusion of Silicon which creates nuclei and growth of the Si crystals. A high SR creates conditions for growth of a fibrous crystal instead of blocky Si crystals.

Research on liquid Al-Si melts suggests that thermodynamically stable clusters of atoms exist in the molten state of alloys [147]. Clusters in the eutectic Al-Si and Al-20Si heated and cooled melts show two size populations between 10 to 40 Å and up to 900 Å (0.09 μm). However, the hypereutectic alloy shows the irreversible effect of overheating. The number of larger clusters decreases almost to zero when the alloy is heated to 1200 ºC (and homogenized) but the clusters grow again upon cooling. At the same time the number of smaller clusters increases but they become smaller.

Analysis of the effect of Sr on the liquid structure of the Al-Si hypoeutectic alloys [148] revealed that the addition of Sr significantly alters the structure of the interdendritic liquid and rheological properties, like melt viscosity, so that the nucleation event of the eutectic Si phase is postponed until there is a significant undercooling. This undercooling results in the super saturation of the interdendritic liquid with Si caused by the continual growth of the primary Al dendrites. Addition of Sr delays or inhibits the clustering tendencies of the atoms at temperatures near the nucleation event. Sr not only refines the morphology of the eutectic Si phase but also refines the grains of the eutectic Al.

Other research on clustering in Al-Si alloys states that an increase in the micro and macro levels of homogeneity in the melt converts them into a colloidal system [149]. Research [150] using the empirical electron theory of solid and molecules for non-equilibrium solidification of the Al-22Si melt revealed that Al-Al and Al-Si clusters will precipitate more than Si-Si clusters. The values of the bond energy are (262.7, 60.0 and 53.9) kJ/mol for the Si-Si, Al-Al and Al-Si structure units, respectively.

Researchers [151] found that decomposition of bonds of Si-Si clusters is irrecoverable under electric pulses leading to structure alteration. Work on Al-12.5Si revealed that when the number of Si-Si clusters in the liquid melt decreases, then the number developing into nuclei decreases. Sr weakens the covalent bonds in liquid Al-Si alloys, decreases the number of Si-Si clusters and depresses the nucleation of Si atoms.

Extensive work [152]–[154] on the characterization of the Al-19Si solidification process using in-situ neutron diffraction, the UMSA Platform and microstructure analysis shows a good correlation between these techniques. Neutron diffraction indicated that at

695 °C (the non-equilibrium liquidus temperature is 672 °C) solid Si exceeds 3 %. This phenomenon indicates agglomerations of clusters of primary Si. Similar findings [155] were reported using the 390.1. The Al-Si alloy was quenched from a temperature of 730 °C and analyzed by micro Raman Spectroscopy. The UMSA Platform was used for characterization of the solidification process. Metallography of the UMSA samples revealed that rapid melt quenching (100 °C/s) did not prevent coarsening of the primary Si crystals.

Conclusions drawn from the liquid Al-Si melt atoms clustering research, involving the hypereutectic Al-Si-Cu alloy are as follows:

a) There is a research opportunity for implementation of novel synergetic melt modification with Sr and the dynamic pressure liquid melt treatment that potentially can modify the melt structure and consequently its fundamental solidification characteristics and heat transfer to the die prior to the rapid nucleation of the Al-Si eutectic with nano Si morphologies.

b) Melt superheating to 1200 °C is not a practical solution for industrial operations. For comparison of this strategy's effects, the melt superheating temperature of 850 °C should be used for comparison between the present research and the previous Yamaha R&D program.

The MCPT Group conducted research on the hypereutectic Al-20Si-3Cu alloy to study the effect of melt temperature and Solidification Rate on primary and eutectic Si modification [156]. The reported results are as follows: (see Figure 37)

- Melt temperatures of 785 °C and 850 °C reduced the size and improved distribution homogeneity of the primary Si crystals.

- An increased SR minimized the primary Si crystal size and heterogeneity caused by the melt pre-heating temperature.
- Pouring close to the liquidus temperature (i.e. 730 °C) resulted in coarse primary Si crystals despite the melt high preheating temperature (i.e. 850 °C).
- The melt heated up to 850 °C did not have an effect on the metallurgical reaction during the alloy solidification process.

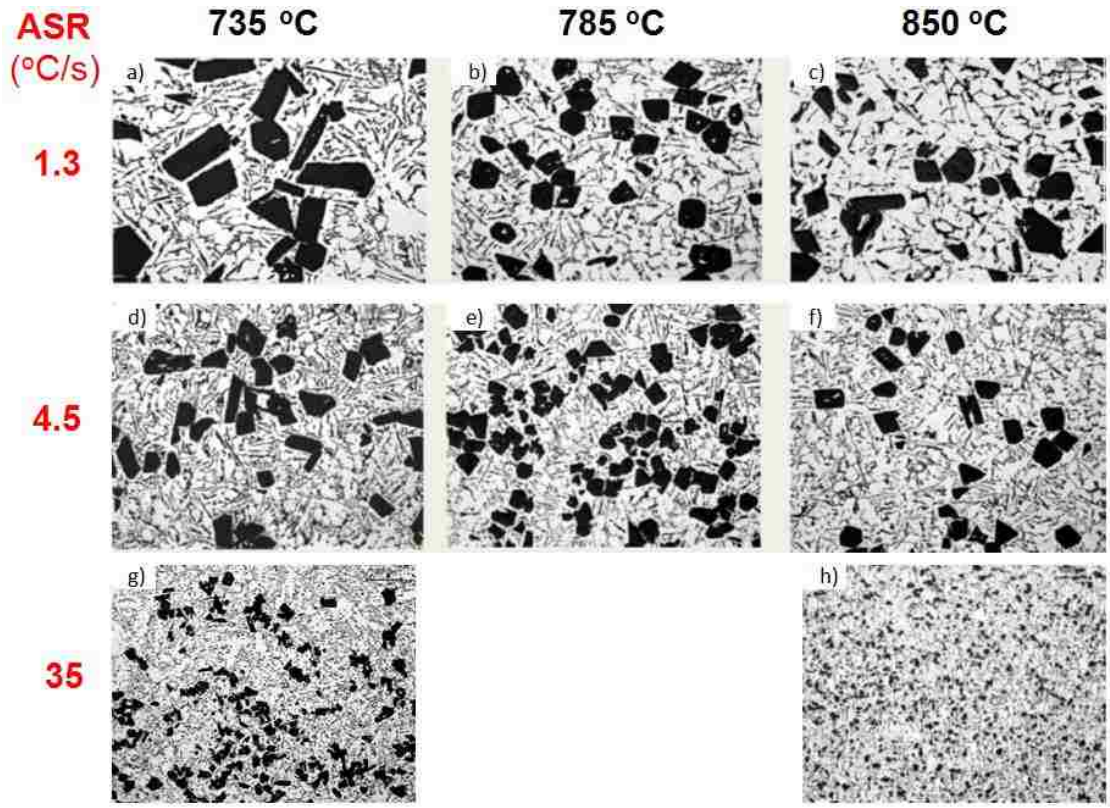

Figure 37. LOM micrographs, hypereutectic Al-20Si-3Cu alloy UMSA test samples superheated to various temperatures (735, 785 and 850) °C solidified under various SR (1. 3, 4. 5 and 35) °C/s.

2.2.4 Physical Treatment of Al-Si Alloys

Physical treatment of a melt is very often used in a semi-solid state where the (temperature range is between the solidus and the liquidus). Semi-solid metal casting is

a near net shape variant of the die casting process which combines the advantages of casting and forging. The metal is treated in a temperature range between the liquidus and the solidus. The most well-known treatments are thixocasting and rheocasting.

Thixocasting is a casting process where induction heating is used to re-heat the billets to the semi-solid state where a non-dendritic microstructure exists and die casting machines are then used to inject this semi-solid melt into steel dies [157]–[160].

Rheocasting is a casting process where semi-solid slurry is produced directly from the molten alloy and is cast in a typical die casting furnace/machine. The rheocasting process in comparison to the thixocasting process is less expensive [161]–[164], [165].

Ultrasonic Vibration Treatment of Al-Si Alloys

During ultrasonic vibration treatment of the liquid metal the alternating pressure creates numerous tiny bubbles in the metal. The bubbles grow and pulsate during a continuous expansion/compression regime and finally collapse. During expansion, the bubbles absorb energy from the melt, undercooling the liquid at the bubble-liquid interface resulting in nucleation at the bubble surfaces [166], [46]. This mechanism is known as **cavitation-enhanced heterogeneous nucleation**. Another explanation to describe cavitation-enhanced heterogeneous nucleation is based on the pressure pulse melting point, where the pressure pulse arising from the collapse of bubbles changes the T_m (Melting Temperature) according to the Clapeyron equation. An increase in T_m is equivalent to increasing the undercooling, so that the nucleation process is enhanced [167], [168]. The first situation only occurs during the bubble expansion stage, while the second occurs during bubble collapse. The bubble collapse develops acoustic streams through the melt, and helps to distribute the nuclei into the surrounding liquid and results

in a significant number of nuclei in the molten alloy. If a solid Volume Fraction is already present in the melt, the first dendritic grains can be broken and distributed in the liquid metal, acting as new nuclei. This mechanism is known as **dendrite fragmentation** which results in eutectic silicon refinement [169]–[171].

The effect of ultrasonic treatment on the microstructure of the hypereutectic Al-17Si alloy was studied by Abramov et al. [172] and Eskin et al. [173].

By applying ultrasonic treatment during the solidification of the hypereutectic Al-17Si alloy, without any additions, primary Silicon crystals were modified from 90 μm to 10 μm. The results are shown in Figure 38.

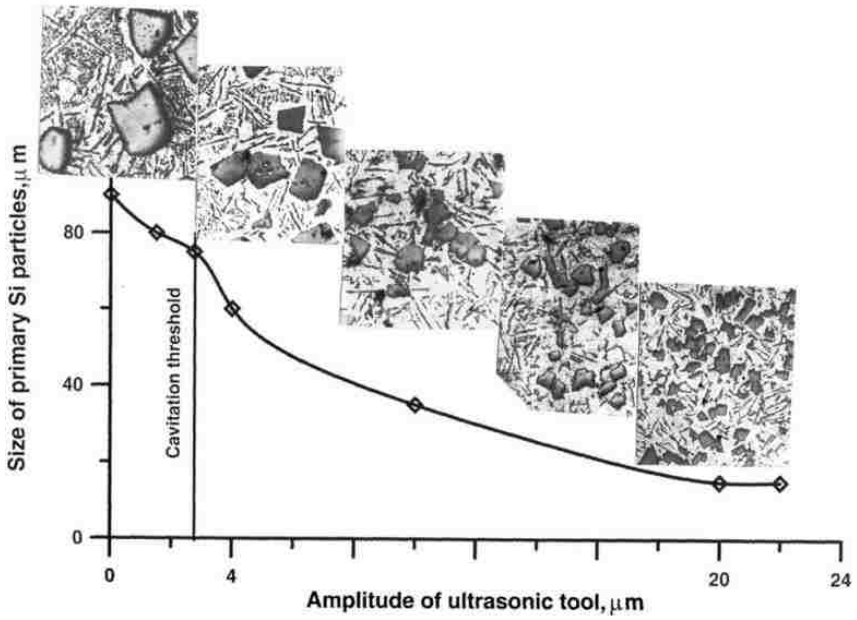

Figure 38. Effect of ultrasonic treatment on the size of primary silicon particles in an Al–17Si alloy without refining additions [173].

Wu et al. [162] investigated the microstructural characteristics of the hypereutectic Al-20Si alloy (0.08 wt.%P was added for Si modification) formed by rheosqueeze casting (Squeeze Casting parameters: pressure applied at 120 MPa, injection speed 50 mm/s, mold preheat temperature at 200 °C, holding time around 20 s) after Ultrasonic Vibration

Treatment, USV, power 1.8 kW, frequency 20 kHz was applied for 90 s at a temperature range from 710 °C to 690 °C). After rheosqueeze casting was reached, refinement of the α-Al dendrites and the average size of the primary Si particles decreased by 43 % from 43 μm to 24.3 μm in comparison with the SC technology without USV (see Figure 39).

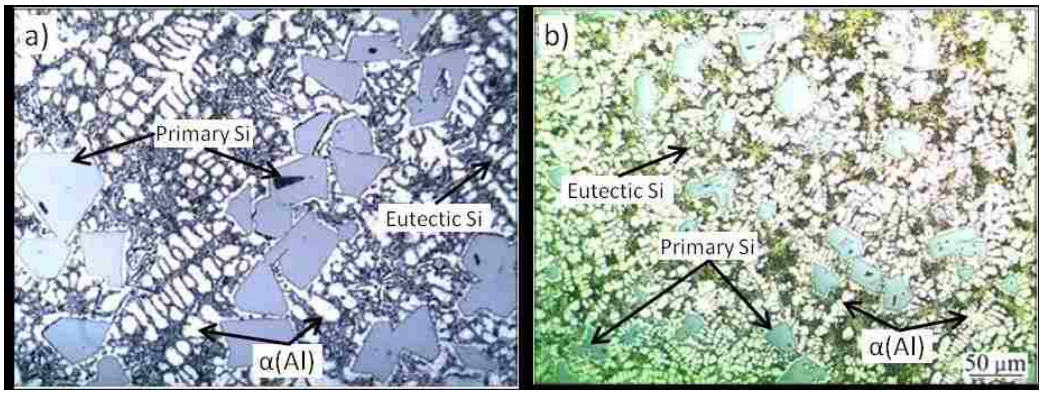

Figure 39. Microstructure of the Al-20Si alloy, a) as-cast by squeeze casting at 760 °C indicating formation of non-equilibrium α-aluminum dendrites, b) semi-solid rheo squeeze casting after USV treatment [162]**.**

Feng et al. [174] reported that after the USV treatment (power 50 W, amplitude 4 μm, during a holding time of 10 min at a temperature range from 680 °C to 700 °C) for the hypereutectic Al-23Si alloy, the hydrogen bubbles in the alloy melt were removed and the morphology of the primary α-Al dendritic crystals was changed to equi-axial crystals, the eutectic lamellar spacing increased and the primary Si particle(s) size was reduced from 500 μm to 180 μm.

Regardless of the positive effects of the USV treatment on the refinement of the α-Al dendritic, and on degassing of the melt, the effect of modification on the primary Si is questionable.

Electromagnetic Vibration Treatment of Al-Si Alloys

Electromagnetic Vibration, in conducting liquid metal, is created by the simultaneous imposition of a stationary magnetic field with a magnetic flux density **B** and an alternating electric field with a current density **J** and a frequency **f** (see Figure 40).

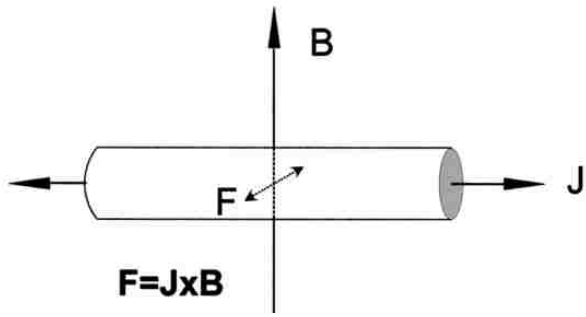

Figure 40. Schematic presentation of vibrating force, developed by the interaction of alternating electric and stationary magnetic fields [175]**,** [176]**.**

Application of electromagnetic vibration to a liquid results in the induction of a vibrating electromagnetic body force with a density of **F** = J x B inside the liquid. This force, which has a frequency equal to that of the applied electric field, vibrates in a direction perpendicular to the plane of the two fields and puts the particles of the conducting liquid into a vibrating motion. The vibrating force **P** (see Equation 1) which generates the electromagnetic pressure, puts the liquid under forces of compression and tension resulting in cavities (a similar process like in ultrasonic vibration as described in the previous section) [175].

$P = B J (V / A) \sin (2\pi ft)$ …….. **Equation 1**

Where: P - Vibrating force, B - magnetic flux density, J - current density, V - volume of the liquid, **A**- area of the surface perpendicular to the direction of the force, f- frequency, t –time.

Radjai and Miwa [175] studied the effects of the intensity and frequency of electromagnetic vibrations on the microstructural refinement of the hypoeutectic Al-7Si alloy. The authors reported that the best refinement of the eutectic structure is achieved at magnetic field 10 T and frequency 1.5 kHz (magnetic pressure 0.093 MPa). Under these parameters the highly columnar α-aluminum dendrites were changed into equiaxed dendrites.

Yu et al. [177] found that a strong static magnetic field up to 10 T (without an electric current) applied to the eutectic Al-12.6Si alloy refines the eutectic structure, but adding an alternating electric current higher than 10^5 A/m^2 makes the eutectic Silicon coarser.

The modification of primary Si in the hypereutectic Al–20wt.%Si alloy by electromagnetic stirring was performed in the semi-solid temperature region (690 to 578) $^{\circ}$C by Dehong et al. [178]. The equivalent diameter of the primary Si particles of 160 μm was reduced to 45 μm by using the stirring current 8 A and the magnetic field intensity ≈ 0.005 T. Better results were achieved by Mizutani et al. [179] who investigated the effect of the intensity and frequency of electromagnetic vibrations on the modification of the primary Silicon in the hypereutectic Al-17Si alloy. The smallest primary Silicon particles (5 μm) were obtained at a magnetic field intensity of 1.6 T and at a vibration frequency near 1 kHz and were applied to the melt at a temperature of 710 $^{\circ}$C during a holding time of 240 s (see Figure 41).

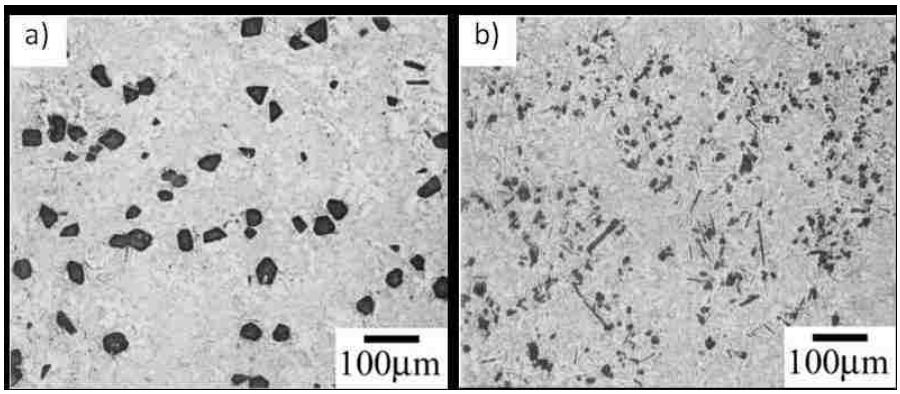

Figure 41. LOM micrographs for the Al-17Si alloy, a) without the magnetic field-electric current (0 T, approximately 60 A, 100 Hz), b) vibrated specimens (1.6 T, approximately 60 A, and frequencies of 1 kHz) [179] **.**

The effect of magnetic field intensity and the effect of holding time on the average particle size are presented in Figure 42.

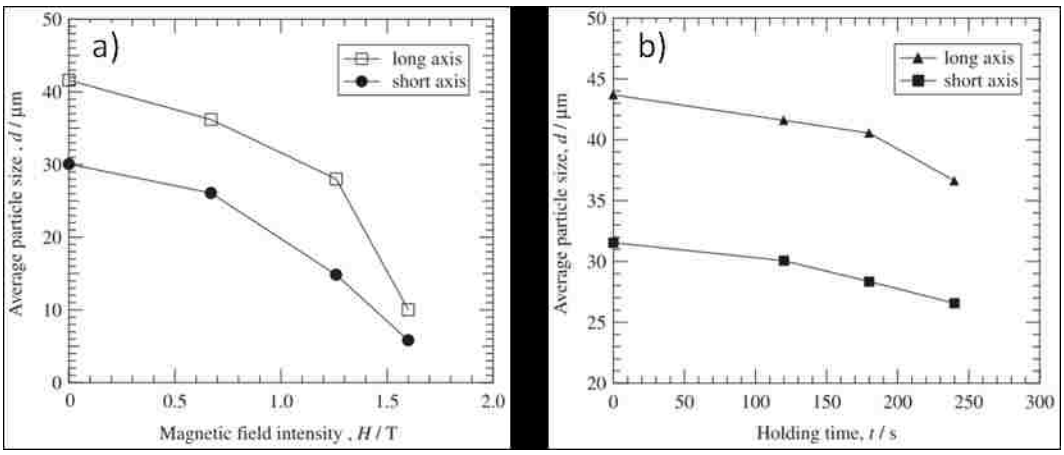

Figure 42. The average size of the primary Silicon particles vs. a) magnetic field intensity and b) holding time at 710 °C (f = 1 kHz, J = 60 A) [179]**.**

Pulse Electric Current Treatment of Al-Si Alloys

The use of the Pulse Electric Current Treatment for modification of primary and eutectic Silicon in the Al-Si alloys was reported in references [180]–[184].

Hongsheng et al. [182] investigated the influence of the Pulse Electric Current Treatment (PECT) on the solidification microstructures and mechanical properties of Al-17Si piston alloys in a liquid state at 675 °C (2 kV at the maximum, 0.24 s charge time, 0.013 s discharge time and 4 Hz frequency). The results showed that the size of the primary Si particles was reduced roughly from 150 μm to 25 μm (see Figure 43).

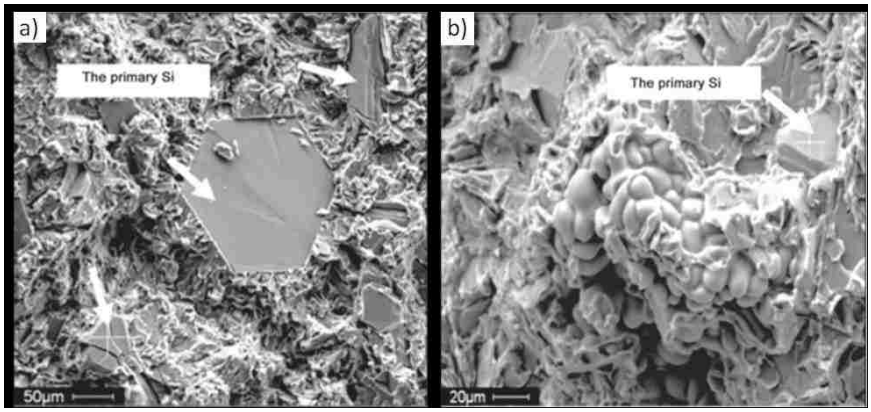

Figure 43. SEM micrographs, morphologies of primary Silicon in the hypereutectic Al-17Si alloy cast at 675 °C, a) without PECT, b) with PECT input voltage 2 kV, frequency 4 Hz [182]**.**

Plotkowski [184] studied the refinement of the cast microstructure for hypereutectic Al-20Si alloys with an applied electric potential of 110 V, at a calculated current of 22 A, with a current density of 500 mA/m^2 through the melt at 825 °C. The size of the large primary Silicon particles was not significantly decreased, but a new population of relatively smaller size primary Silicon particles appeared in the castings solidified under the influence of an applied electric current. The morphology of the eutectic Silicon particles was not affected by applying the electric current during solidification.

Lijia et al. [183] investigated the influence of the Pulse Electric Current Treatment (PECT) on the solidification structure of the hypereutectic Al-25Si (LM-29) alloy. At a temperature of 760 °C, an electric pulse of 800 V, 22 Hz was applied for 2 min. After the treatment, the melt was poured into a metal mold pre-heated to 250 °C. The authors stated that: 1) the average size of primary Silicon was decreased from 153 μm to 78 μm (see Figure 44); 2) the electric pulse increased the dissolution of the metastable Silicon clusters and promoted the structural and compositional homogeneity of the LM-29 alloy melt; 3) by applying electric pulse to the LM-29 melt, the precipitation temperature of the primary Silicon was decreased from 706 °C to 627 °C, which is an important factor for the modification of primary Silicon.

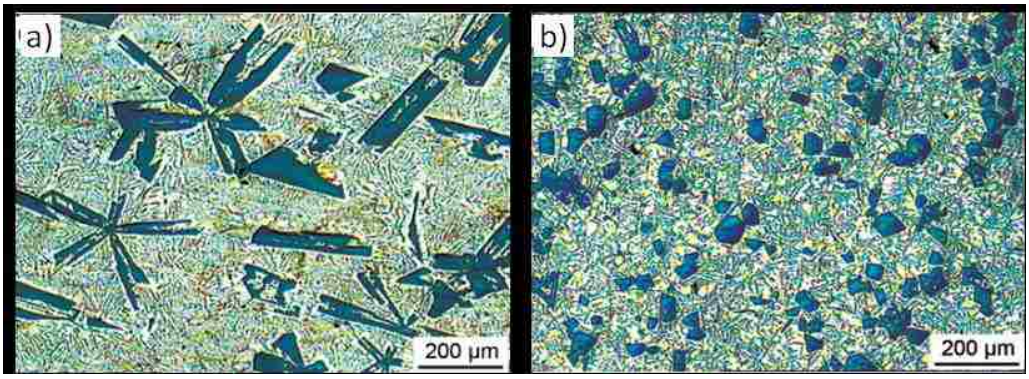

Figure 44. SEM micrographs for the Al-25Si alloy, a) untreated alloy, b) alloy treated by electric pulse (800 V, 22 Hz, at 760 °C, for 2 min.) [183].

Shearing Treatment of Al-Si Alloys in the Semi-Solid State

Lashkari et al. [185] presented the results of microstructure and rheological behavior of the hypereutectic semi-solid Al–17.4Si (A390) alloy under low shear rates compression testing. Semi-solid billets were used for the A390 Al–Si alloy cast in a

permanent mold. The billets were reheated to a semi-solid state (thixocasting method) and held isothermally during parallel plate compression testing. Figure 45 shows the difference in microstructures between the rheocasting and thixocasting processes.

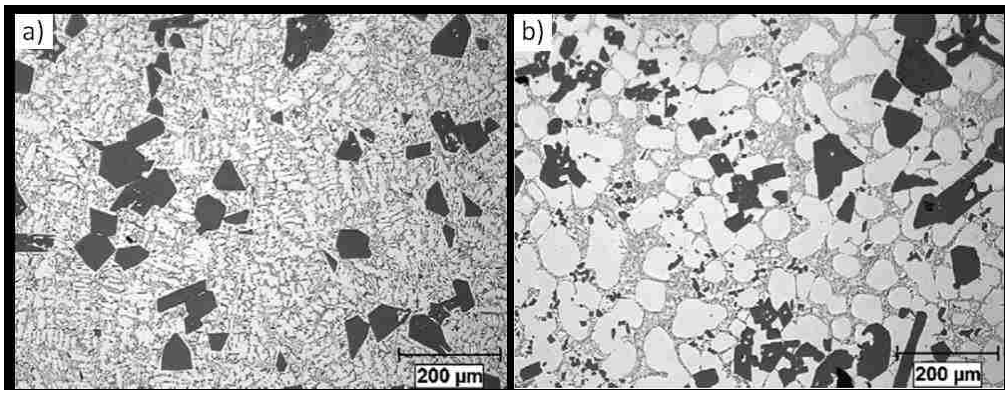

Figure 45. LOM micrographs for the A390 alloy, a) Rheocast, quenched directly from the semi-solid region at 561.5 °C, b) Thixocast, reheated to the semi-solid region at 561.5 °C, and quenched [185]**.**

Barekar et al. [186], [187] investigated the effect of intensive shearing on the morphology of primary Silicon and on the properties of the hypereutectic Al–Si alloy. Shearing processing for the Al-17Si-0.01Sr alloy melt in the liquid state was performed using Melt Conditioning Advanced Shear Technology (MCAST). The melt was sheared at 650 °C, 60 s, at 800 rpm. The initial die temperature was 220 °C. The sheared melt was then cast by using the HPDC process at 12 MPa. A schematic illustration of the MC-HPDC process is shown in Figure 46. The author claimed results indicating that intensive melt shearing can develop a microstructure for the hypereutectic Al-Si alloys that contains finer and equiaxed primary Silicon particles that are relatively uniformly distributed in the Aluminum matrix (see Figure 47). Despite improved tensile properties of the alloy (see Figure 48) the primary Si particle(s) size is in the range of (10 to 60) µm

after the MC-HPDC process (see Figure 47c). This is not a significant improvement in comparison with the microstructure for the conventional HPDC process.

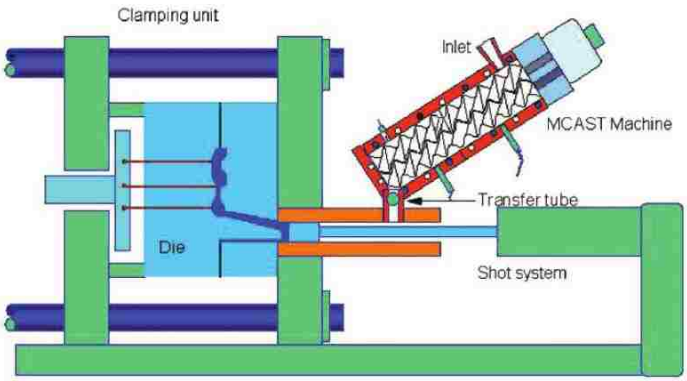

Figure 46. Schematic illustration of the MC - HPDC process [186]**.**

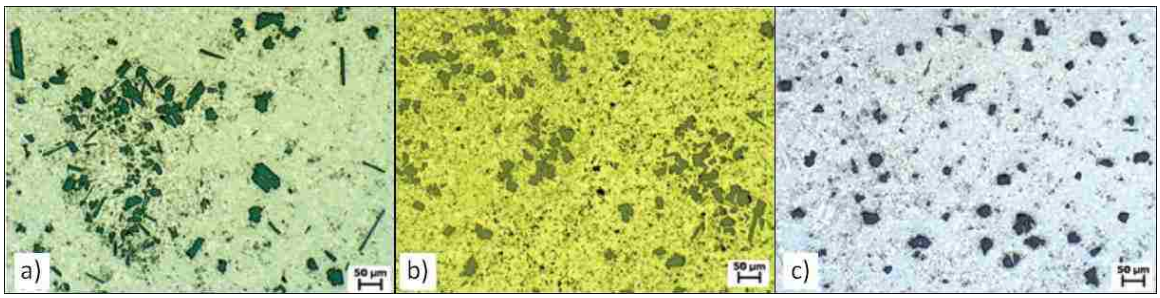

Figure 47. LOM micrographs for the Al-17Si alloy, a) unmodified and conventional HPDC, b) 0.01 wt.%Sr modified and conventional HPDC, c) 0.01 wt.%Sr modified and MC-HPDC [186]**.**

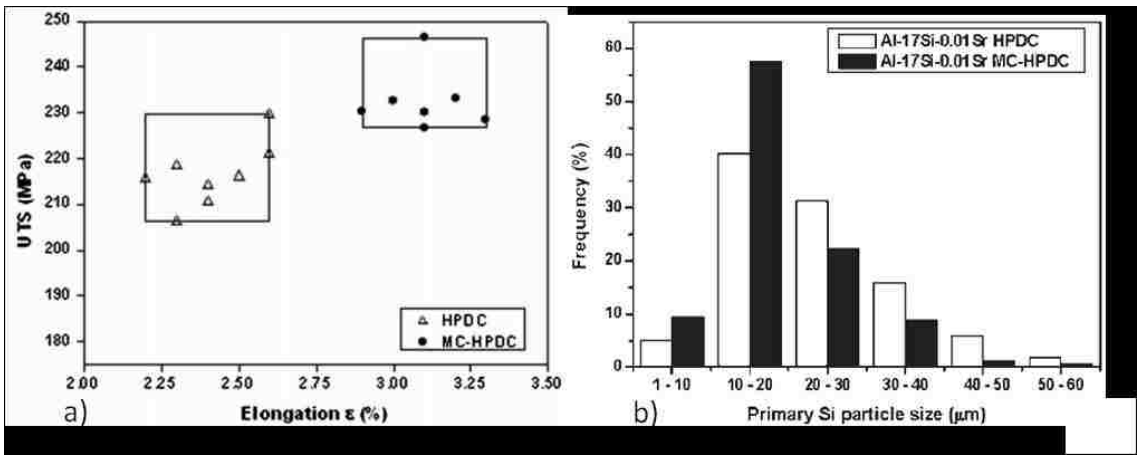

Figure 48. Comparison of the HPDC and MC HPDC technologies applied to the Al-17Si alloy, a) tensile properties, b) Primary Si particle size distribution [187]**.**

Mechanical Vibration Treatment of Al-Si Alloys

Investigation of the effect of low frequency mechanical vibration on macro and micro structures for the eutectic Al-12.3Si (LM6) alloy was performed using vibration at varying frequencies between 15 Hz and 41.7 Hz and amplitudes between 0.125 mm and 0.5 mm during solidification of the melt [188]. The authors reported that using mechanical vibration reduced the shrinkage in the ingot and that eutectic and primary Silicon particles coarsened.

Jayesh [189] studied the effect of mechanical mold vibration on the characteristics of the hypereutectic Al-18Si alloy (B390), using a Mechanical Shaker Table for vibration with frequencies between 8 Hz to 60 Hz and with a maximum amplitude of 2.03 mm. The melt was poured into a crucible at 740 $^{\circ}$C. The experiments produced considerable refinement of the primary Silicon particles and their distribution. The refinement of the primary Si particles was obtained without chemical additives. The size of primary Si particles was reduced from 230 μm to 162 μm.

Electron Beam (EB) Treatment of the Al-Si Alloys Component Surfaces

High Current Pulsed Electron Beam (HCPEB) is a new technology where a high power density electron beam range of (100 to 1000) W/cm^2 is generated within short pulse duration of a few microseconds. HCPEB irradiation induces temperature fields on the surface of a component which generates superfast heating and melting of the surface layer of the component. The fast heating is followed by rapid solidification due to heat conduction towards the center of the component [190].

Surface modification of the hypereutectic Al–20Si alloy by HCPEB using the Electron Beam system working at an accelerating voltage of 23 kV, energy density of 2.5 J/cm^2, number of pulses 25, pulse width 1 μs at a pulse interval of 10 s and a target source distance of 10 cm were presented by Hao et al. [191]. The result of the interaction of 25 pulses of HCPEB was a 4 μm thick remelted layer on the surface of the sample, which is shown in Figure 49.

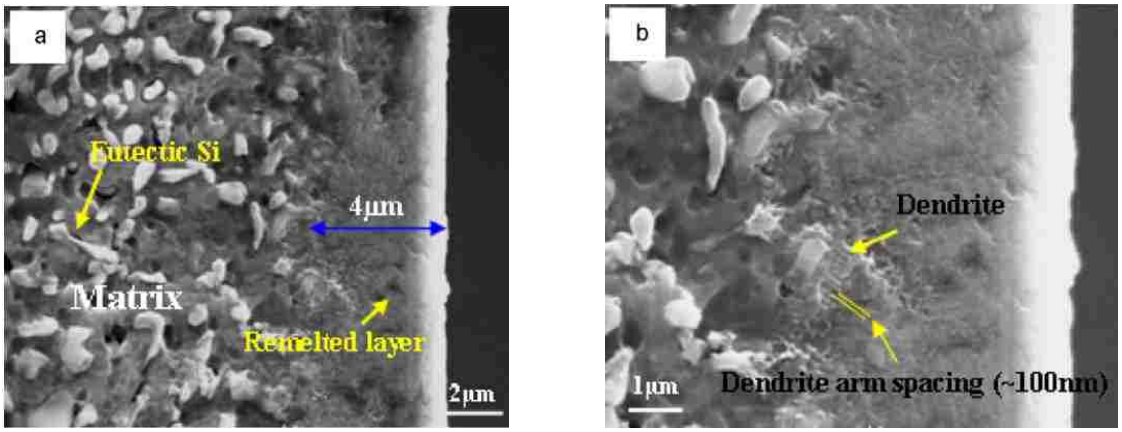

Figure 49. SEM micrographs for the Al-20Si alloy treated by HCPEB, 23 kV, 25 pulses, 25 J/m^2 a) the cross section image after etching, b) local enlargement of a) [191].

During superfast melting and solidification of the surface layer a supersaturated solid solution of Si atoms exists in the Al matrix. EDS analysis reveals that the solid solubility of Si atoms in the Al matrix was increased from 1.59 wt.% (under equilibrium solidification conditions) to the average solid solubility of 8.9 wt.% under non-equilibrium conditions. Hao et al. [192] improved wear resistance of the remelted surface layer of the Al–15Si alloy with a HCPEB treatment by a factor of 9. Raman spectrum analysis of Si on the remelted surface layer caused the structural transformation of Si from a crystalline state to an amorphous state [193]. The authors attributed the higher wear resistance of the HCPEB treated layers to the formation of a supersaturated

solid solution of Si in Al, the formation of nano-crystalline Si and amorphous Si in the surface layer which created a hardening effect and dislocations and residual stresses formed in the microstructure.

Laser Beam Treatment of Al-Si Alloy Component Surfaces

Laser Beam (LB) treatment of the hypereutectic Al–30Si cast alloy was investigated using a CO_2 laser beam with 5 kW of power [194]. The microstructure of the laser remelted layer consisted of fine primary Si particles, a primary α-Al matrix phase and a fine α-Al–Si eutectic phase. The primary Si particles were decreased from 25 μm to 3 μm (see Figure 50). The hardness of the laser remelted layer increased gradually with the decrease of the primary Si particle size. The hardness reached 140 HV at about 5 μm in the Al–30Si layer. The wear resistance of the remelted layer increased with the increased hardness and decreased size of the primary Si particles and was improved by a factor of 9 in comparison to the Al–20Si cast alloy.

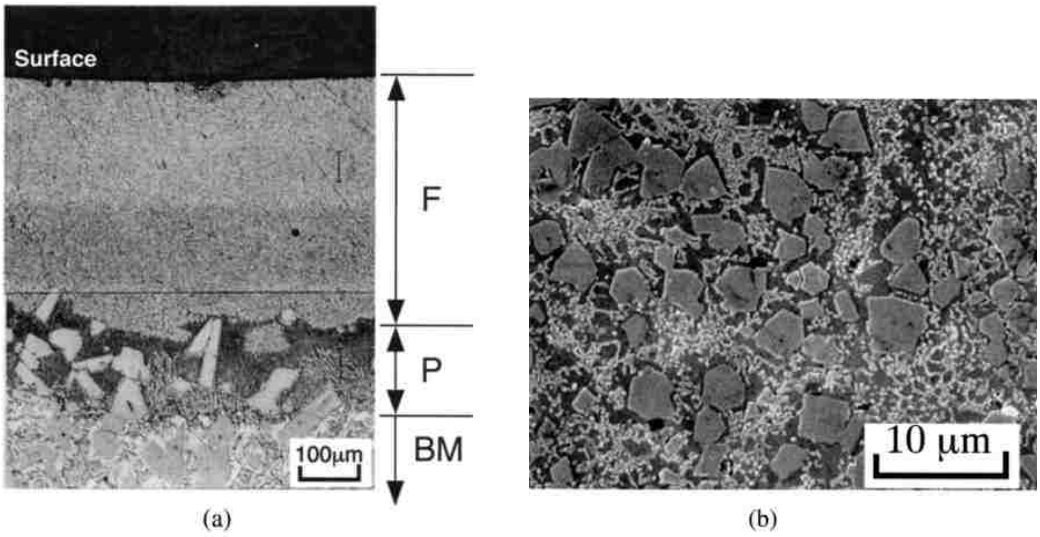

Figure 50. SEM micrographs of the cross section of the laser remelted layer for the Al–30Si cast alloy, a) Cross section of the parent sample and of the remelted layer (F: fully remelted layer, P: partially remelted layer, BM: as-cast structure), b) primary and eutectic Si particles within the fully remelted layer [194].

EB and LB treatments are not suitable for metal structure modification in bulk cast components but research results showed that by using rapid solidification, the primary coarse Si can be substantially modified in the hypereutectic alloys and can improve wear resistance.

2.3 Squeeze Casting

2.3.1 Squeeze Casting Technology

Squeeze Casting (SC) is a technology where liquid and semi liquid melts are poured into a permanent die and solidified under pressure up to 100 MPa. The SC technology is a combination of mold casting and forging technology, based on slower continuous laminar die filling which produces porosity free, near net shape castings with good mechanical properties. SC components are heat-treatable and can also be used in safety applications and are characterized by their higher strength and ductility in comparison with conventional die cast components. SC is an economical casting process suitable for high volume applications and as an alternative to conventional casting processes such as gravity permanent mold, low and high pressure die casting [195], [196]. Mass applications for the SC technology were developed in 1965. SC components are made of cast iron, steel and non-ferrous materials. In 1979 the Toyota Motor Co. Ltd., Japan, introduced an Aluminum automotive wheel. Mass production of heavy duty aluminum alloy pistons also started in the USA [197]. The SC technology is now used for engine blocks, pistons, gears, pulleys, connecting rods, wheels, etc.

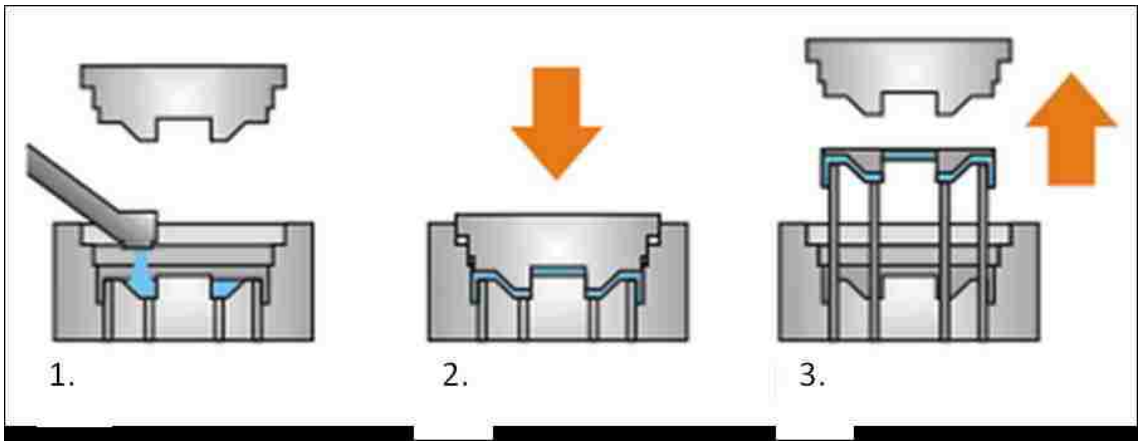

Figure 51. Schematic diagram of the Squeeze Casting Technology [198]**.**

The SC process is schematically presented in Figure 51 and the steps are described below [198], [199]:

1. The melt is poured into a pre-heated die cavity.

2. The melt is pressurized in the die cavity until solidification is completed.

3. The die is opened and the cast component is rejected. The die is lubricated and cooled down for the next cycle.

2.3.2 Effect of Pressure on Solidification of Al-Si Alloys

High pressure and high Solidification Rates applied on a solidifying melt contribute to SC component integrity and a fine as-cast structure. The effect of pressure on the solidification structure formation is expressed by the thermodynamic relationships by Sobczak et al. [200] in the following ways:

1) Mechanical effects related to the physical phenomena at the macro level through elastic and/or plastic deformation, intensification of heat transfer between the casting and the die, high Solidification Rates that affect thermal data characteristics like the liquidus temperature.

2) Thermodynamic and transport phenomena at the micro level through changes in phase diagram characteristics, physical properties, Gibbs free energy, chemical potentials, specific heat, surface tension, diffusion coefficients, etc.

The effect of rapid cooling and the application of 100 MPa pressure on the Al-Si phase diagram characteristics can be seen in Figure 52 [199]–[201].

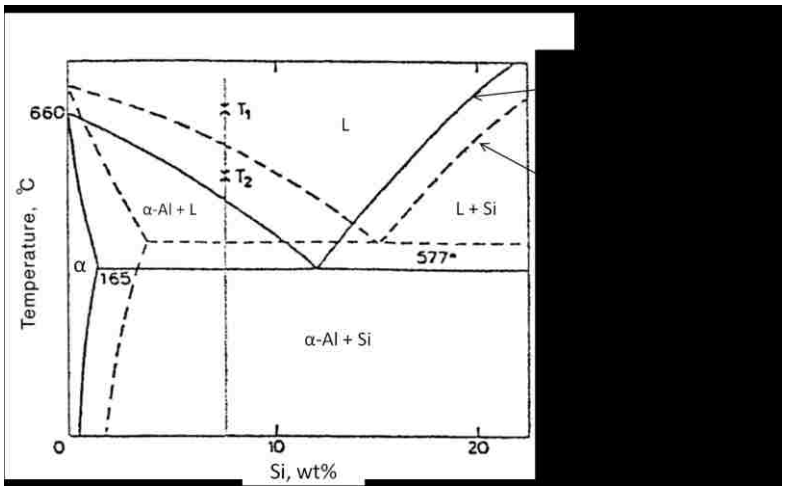

Figure 52. The effect of rapid cooling and the application of 100 MPa pressure on the Al-Si phase diagram [199]**.**

The Clausius-Clapeyron equation (Equation 2) can explain how pressure affects phase relationships in an alloy system.

$\Delta T_{sol} / \Delta P = T_{sol} (V_l - V_s) / \Delta Q_L$ .....**Equation 2**

Where: T_{sol} is the equilibrium solidification temperature, V_l and V_s are the specific volumes of the liquid and solid, respectively, and ΔQ_L is the latent heat of fusion. Substituting the appropriate thermodynamic equation for volume, the effect of pressure on the solidification point may be estimated as follows in Equation 3:

$P = P_0 \exp(-\Delta Q_L / RT_{sol})$……**Equation 3**

Where: P_0, ΔQ_L and R is constant. Therefore, T_{sol} should increase with increasing pressure.

The effect of pressure on the solidification process of Aluminum and its alloys was investigated at pressures up to 5 GPa [202]–[208].

Murray et al. [3] reported that high pressure has an effect on solubility of Si in Al and at atmospheric pressure the solid solubility of Si in Al is 1.5 at.% while at 2.8 GPa the solubility is raised to 7.0 at.%. At 5.4 GPa the solubility is 15.0 at.%. The predicted eutectic point at 5 GPa is at 30.0 at.% Si and 677 °C.

The SC or HPDC industrial processes, however, work with pressures only up to 150 MPa. On the basis of theoretical predictions it was proved that the liquidus temperature increased by 9 °C when the pure Al-Si system was at a pressure of 150 MPa [209].

Pressure has a significant effect on Al-Si alloy solidification due to changes in the diffusion coefficient. The diffusion coefficient of the metal solidified under high pressure can be expressed by the Arrhenius equation [210]:

$D_p = D_0 \exp(-PV/RT)$……**Equation 4**

Where: D_p and D_0 are the diffusion coefficients of solute atoms under high and normal pressures, respectively, R is the gas constant, 8.314 J/molK; T is the temperature of the molten metal, P is the pressure, and V is the initial volume of liquid.

V can be calculated by the following equation:

$V = M/\rho$……**Equation 5**

Where: M is the molar mass; ρ is the density of the molten metal.

The above implies that the diffusion coefficient of atoms in the liquid state under high pressure is reduced when compared with that under normal pressure, so that it is much

more difficult for the solute atoms to diffuse under high pressure. A low value of the diffusion coefficient lowers redistribution of the alloying elements during phase transformation (i.e. solidification) which affects the size and chemical homogenization of the formed crystals [200], [210].

In the SC process, where the effects of pressure and rapid SR act at the same time, it is not easy to determine the contribution of separate effects on the thermodynamic curves in the phase diagram. Ranganathan et al. [211], [212] studied the influence of melt temperature on rapid solidification of the Al-Si alloy system at ambient pressure (Al-18Si, Al-25Si alloys) and investigated only the effect of the SR (the authors claimed that the SR = 2000 °C/s). They expected a non-equilibrium Al-Si phase diagram where the eutectic transformation temperature shifted to lower temperatures (see Figure 54) – as opposed to the results in the references [199]–[201] (see Figure 53).

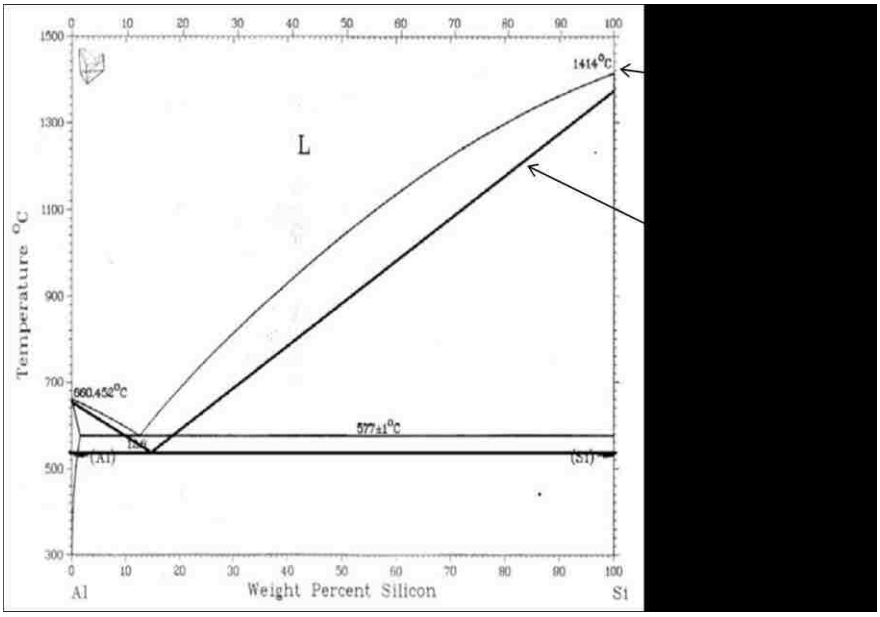

Figure 53. Change of Liquidus and Solidus lines in the binary Al-Si phase diagram following rapid solidification at ambient pressure [212]**.**

Literature source [213] indicates that the lattice parameter of α-Al decreases with increasing pressure as a result of the increased solubility of Si in Al. The amount of Si retained in the Al(Si) solid solution is 1.92 wt.% @ 1 GPa, 5.45 wt.% @ 2 GPa and 6.96 wt.% @ 3 GPa (estimated from the XRD pattern). The equilibrium solid solution limit for the Al-Si alloy is 1.65 wt.% at a eutectic temperature of 577°C and 0.05 wt.% at room temperature under atmospheric pressure. This data indicates that the diffusion coefficient decreases significantly with increasing pressure. When the diffusion of silicon atoms is lower than the movement of liquid–solid interface, the movement of the silicon atoms will be hindered, giving rise to the formation of a supersaturated solid solution in the as-cast alloy. The primary α-Al phase forms at 2 GPa pressure, and its amount increases, while primary Si disappears with increased pressure, Figure 54. This phenomenon indicates that the eutectic point moves to the Si-rich side of the phase diagram with increasing pressure.

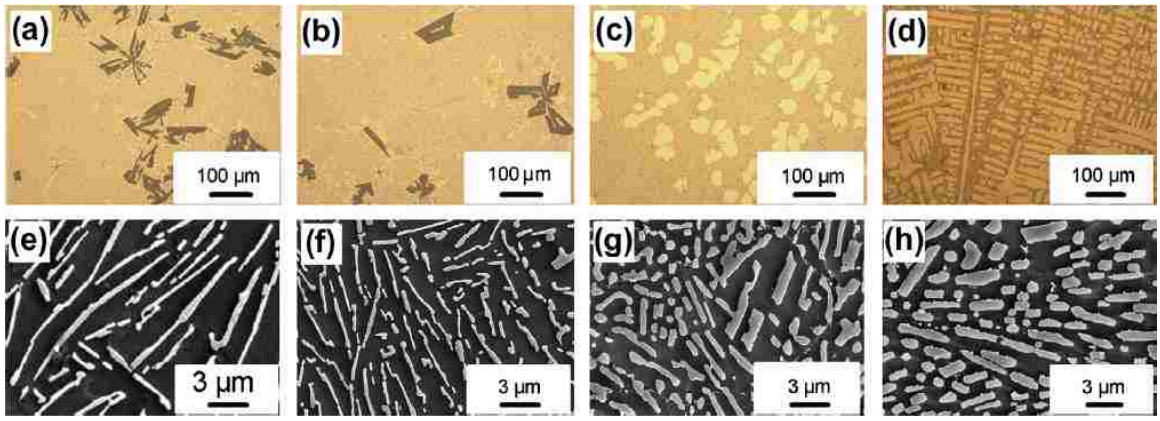

Figure 54. As-cast microstructures for the Al-20Si alloy solidified under: (a, e) ambient pressure, (b, f) 1 GPa, (c, g) 2 GPA and (d, h) 3 GPa. Processed melt temperature: (727 to 877) °C, pressure: kept for 5 minutes, cooling rate 20 °C/s.

At 2 GPa and 3 GPa the hypereutectic Al-20Si alloy transforms to a hypoeutectic α-Al matrix (its volume fraction increases with higher pressure), while primary silicon disappears. Increased pressure results in coarsened (however, still fine) lamellar eutectic Si. The as-solidified structure of the Al-20Si alloy processed under ambient pressure exhibits a stable structure during DSC heating through a temperature range of (127 to 377) °C. Samples processed under (1 to 3) GPa pressures and heated in this range show intensive and increased Si precipitation from the supersaturated α-Al matrix and a coarsening and morphology change between the 152°C and 352 °C range, see Figure 55.

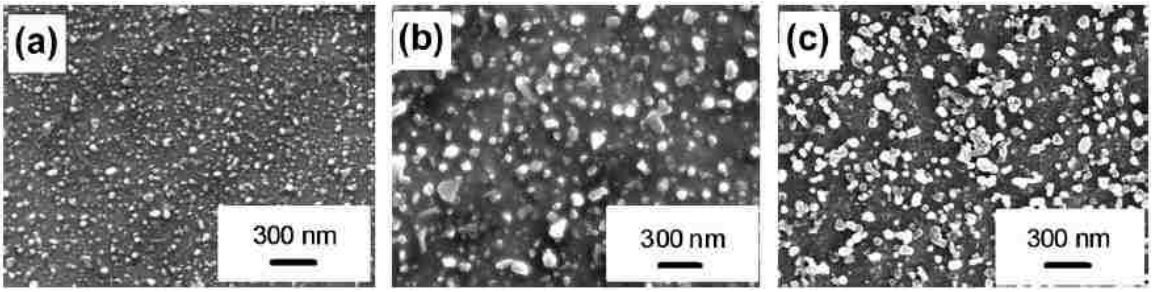

Figure 55. SEM micrographs of Si precipitates in the primary α-Al phase solidified under 3GPa after heating at 5°C/min to (a) 160°C, (b) 230°C and (c) 300°C.

2.4 Solid State Heat Treatment of Al-Si Alloys

Aluminum-Silicon alloys without other alloying elements have good castability and corrosion resistance but are non-heat-treatable alloys; however, in combination with Copper and/or Magnesium, Aluminum produces a precipitation hardening heat treatable alloy. The mechanical properties of Al alloys can be improved by heat treatment. [214]–[222]. Heat treatment is a general term describing heating and cooling operations that are applied for the purpose of improving the structure and consequently mechanical

properties. Aluminum alloy heat treatment usually refers to precipitation hardening, which increases the strength and hardness of precipitation hardenable cast alloys. In the equilibrium phase alloy system, solid solubility significantly depends on the temperature, whereby solubility increases with the increasing temperature (see Figure 56).

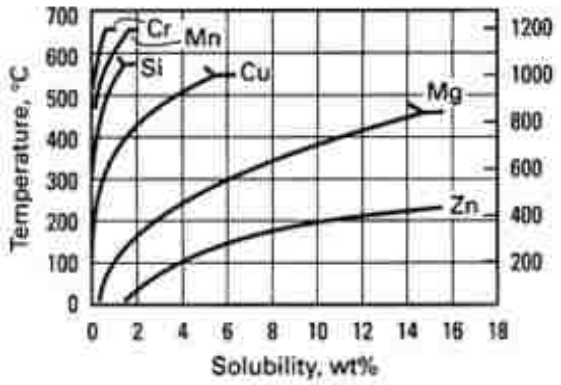

Figure 56. Equilibrium binary solid solubility as a function of the temperature for alloying elements most frequently added to aluminum alloys [5]**.**

The major aluminum alloy systems with precipitation hardening include:

• Al-Cu systems with strengthening from $CuAl_2$ precipitates

• Al-Cu-Mg systems (magnesium intensifies precipitation)

• Al-Mg-Si systems with strengthening from Mg_2Si precipitates

• Al-Zn-Mg systems with strengthening from $MgZn_2$ precipitates

• Al-Zn-Mg-Cu systems [223].

The heat treatment that increases the strength of the Al alloys is carried out in three steps:

1. Solution heat treatment: dissolution of soluble phases.
2. Quenching: development of a supersaturated solid solution.

3. Age hardening: precipitation of solute atoms either at room temperature - Natural Aging (NA) or at an elevated temperature - Artificial Aging (AA) or precipitation heat treatment [223].

2.4.1 Solution Heat Treatment

The Solutionizing Treatment is the first necessary procedure in the heat treatment process for Al alloys. The objective of this procedure is to produce a solid solution containing the maximum amounts of soluble hardening elements in the alloy metal matrix. The process consists of heating the cast component at a sufficiently high temperature and for a time achieving a nearly homogeneous solid solution. During ST the following microstructural changes occur: 1) dissolution of solutes (see Figure 57), 2) spheroidization of eutectic Si, 3) morphological changes of Fe-rich and Cu-rich intermetallics, 4) recrystallization of eutectic grains, and 5) homogenization [214]. The ST temperature is determined by the composition limits of a given alloy. ST is carried out near the solidus temperature. When the ST temperature is too high, (exceeding the eutectic temperature), incipient melting of eutectic phases is involved which has detrimental effects on the mechanical properties. ST at lower than optimum temperatures negatively affects mechanical properties and extends solution times [223].

In order to reduce the solution treatment time for the 319 alloy (Al-7.5Si-3.7Cu), Sokolowski et al. [224] developed a Two-Step Solution Heat Treatment method, which involves a first step at 495 $^{\circ}$C for 2 hours followed by a second step at 515 $^{\circ}$C for 4 hours. The purpose of the first step Solution Treatment, at the lower temperature, is to dissolve the low melting point phase (Al_2Cu), while the objective of the second step, at

a higher temperature, is to increase the homogenization kinetics and reduce the overall solution heat treating time.

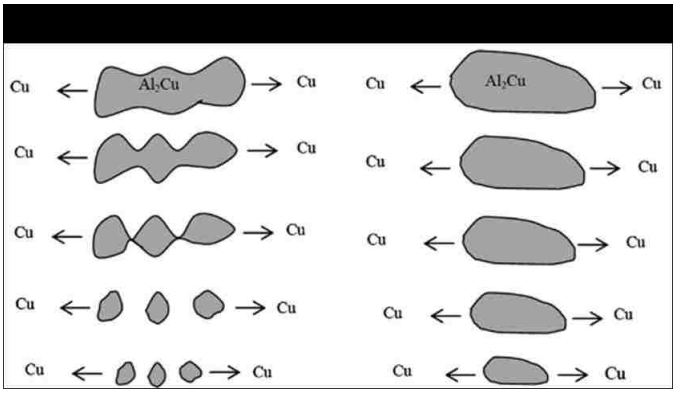

Figure 57. Dissolution process for a) eutectic Al_2Cu and b) blocky Al_2Cu particles [225]**.**

2.4.2 Quenching

Quenching generally follows ST and is the most critical step in the sequence of the heat treating process. Cast components are quenched to a lower temperature with the objective to retain solutes and vacancy concentration (formed at the solution heat treating temperature) at room temperature. It is important to perform quenching with minimum delay during the transportation of the cast components from the furnace to the quench tank. Water is a common quenching medium, but quenching has been accomplished in oil, salt baths, organic solutions and gas [14], [223].

2.4.3 Artificial Aging (AA) and Natural Aging (NA) of Al-Si Alloys

AA is the next step after quenching and is applied to obtain hardening. It occurs at a temperature range of (180 to 250) $^{\circ}$C in a time range of (4 to 48) hours. NA occurs at near room temperature and is completed in a few days depending on the alloy system

[223]. Copper and Magnesium are the most effective alloying elements resulting in precipitation hardening.

The Al-Cu alloy system is often used as the model for precipitation hardening of Al alloys. Decomposition of the supersaturated Al-Cu solid solution (obtained after quenching) results in the formation of the following phases:

$$SSS(\alpha) \rightarrow GPzones\ (discs) \rightarrow \theta''(discs) \rightarrow \theta'(plates) \rightarrow CuAl_2\ (plates)$$

Where: SSS(α) - Supersaturated Solid Solution

GP- Zones consist of 10 nm diameter copper-rich discs on {100} Al planes.

θ”- Phases are also coherent discs 10 nm thick and 150 nm in diameter. These lead to maximum hardening.

θ’- Phase precipitates replace the GP zones as semi-coherent particles. The stage is known as over-aging because the hardness begins to decrease.

θ - ($CuAl_2$) is the equilibrium phase and it has a tetragonal crystal structure and contributes little to hardness.

The aging (precipitation hardening) effect is determined by:

1. The chemical composition of a supersaturated solid solution. This composition is controlled by the cooling/quenching rate and by the initial temperature at which the solid solution was formed.

2. The phase composition of the precipitates forms after the decomposition of the supersaturated solid solution. The precipitate compositions gradually change. Precipitation usually starts with the segregation of the solute atoms in the crystallographic planes of the matrix (GP zones - discs) which later obtain their own crystal lattice

($CuAl_2$ -plates). Spherical solute-rich zones form when the sizes of the solvent and solute atoms are nearly equal (Al-Zn systems). If the difference in atom size is significant (as it is in the Al-Cu system), the GP zones usually form as disks whose planes lie parallel with some low index plane of the matrix lattice.

3. The kinetics of precipitation. The phase precipitation sequence depends on temperature and phase properties. At low temperature precipitates preferentially form coherent GP zones, and at higher temperatures precipitates form semi-coherent metastable phases or stable equilibrium phases.

4. Temperature and time are the most critical parameters that affect kinetics of precipitation.

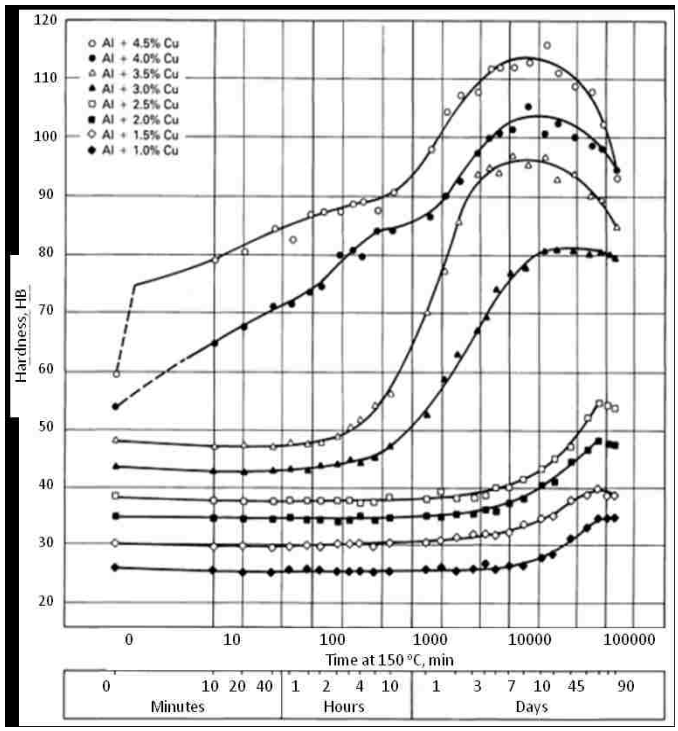

Figure 58. Precipitation hardening curves for binary Al-Cu alloys quenched in water at 100 °C and artificially aged at 150 °C[5].

Precipitation occurs at temperatures between the room and the solvus temperature(s). The precipitates develop sequentially either with increasing temperature or with increasing time (see Figure 58, 59).

5. The properties of precipitated phases include the type of bonding with the matrix, the shape, the composition and the time-temperature stability. It is generally true that the finer precipitates with higher precipitation density give higher strength to the alloy. At the same size and precipitation density, semi-coherent precipitates provide a more effective hardening effect than coherent particles [4], [226].

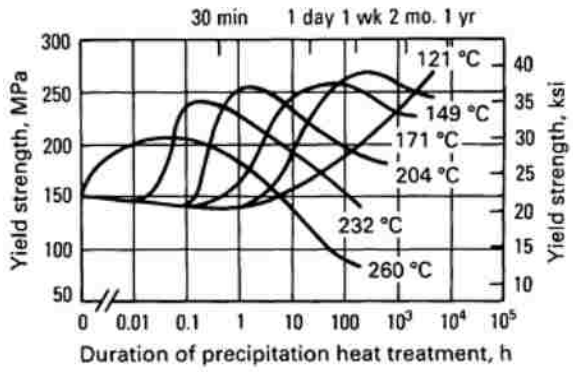

Figure 59. Precipitation Heat Treatment or Artificial Aging curves for the Solution Heat Treated 6061 Aluminum Alloy [5].

2.4.4 Heat Treatment of Hypereutectic Al-Si Alloys

The hypereutectic Al-Si alloys which solidified at low SR and are not modified contain coarse and angular primary Silicon (see Figure 2c), which degrades mechanical properties, generates poor machinability and limits industrial usage. Therefore, these alloys have to be modified to change the angular primary Silicon crystal into small and nodular morphologies.

Zeren, [227], [228] studied the effect of Copper and Silicon content on mechanical properties in Al–Cu–Si–Mg alloys with (1, 3, 4.5, 6) wt.%Cu and (0, 5, 7, 12, 18) wt.%Si. After melting and Na modification, alloys were cast in metal molds at 780 °C and solidified. They were ST at 490 °C for 4 hours and then quenched in water. Samples were aged at 180 °C for (5, 10, 15, 20) hours to observe the effect of aging on the mechanical properties. Any increase of Cu and Si content in Al-Si alloys also results in an increase in hardness and tensile strength accompanied by a decrease in elongation (see Figure 60). The microstructure of the investigated alloy Al–12Si–Cu–Mg is shown in Figure 61.

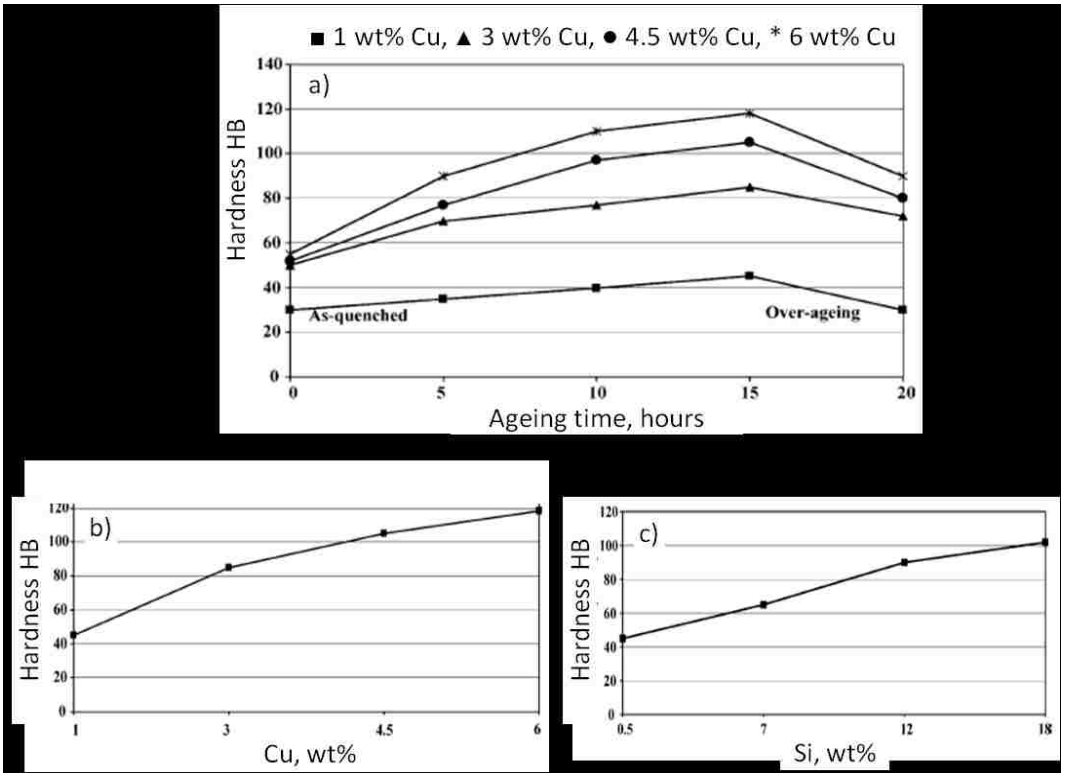

Figure 60. a) Hardness Change vs. Aging Time for the alloys aged at 180 °C, b) Effect of Copper and c) Effect of Silicon content on hardness in the samples aged at 180 °C for 15 hr [227].

Figure 61 shows: a) an as-cast structure containing the blocky primary Si crystals, b) the Sodium modified and heat treated structure, where the authors claim the presence of smaller primary Si crystals however they lost some of their sharp corners (see Figure 61b). In reality ST did not change the primary Si size significantly and spheroidization of the primary Si particles is negligible. It needs to be highlighted that in order to obtain maximum hardness of 120 HB an aging time of 15 hours is required.

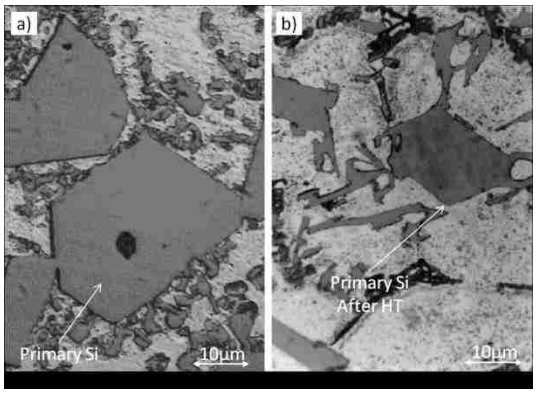

Figure 61. LOM microstructure for the Al–12Si–Cu–Mg Alloy, a) As-cast structure without modification and heat treatment and b) Sodium modified structure after solution heat treatment at 490 ºC/4 hr [227]**.**

The MCPT Group developed an energy efficient heat treatment for linerless hypereutectic Al-Si (20wt.%Si) engine blocks using the Vacuum HPDC Process [6], [7], [229]. The authors reported considerable improvement of the hardness from HRB = 73.5 to 77.2 and a very significant 68 % reduction of the heat treatment duration. The Solution Temperature was increased from 490 °C to 510 °C without risk of incipient melting of the Cu-based phases. The solution time at 510 °C was reduced from 4 hr to 0.5 hr while exceeding the required hardness of 75 HRB and rendering significant thermal modification of the eutectic Si. The aging time at 200 °C was reduced by 50 % (from 4 to 2) hr. The UMSA temperature vs. time heat treatment plots performed for the

Al-20Si engine block and test samples are presented in Figure 62 for: a) T6 Conventional - solution at 490 °C for 4 hr, air quenching and AA at 200 °C for 4hr and b) T6 Modified - rapid solidification arrested at 380 °C, followed by solution at 510 °C for 0.5 hr, air quenching and continuous AA at 200 °C for 4hr.

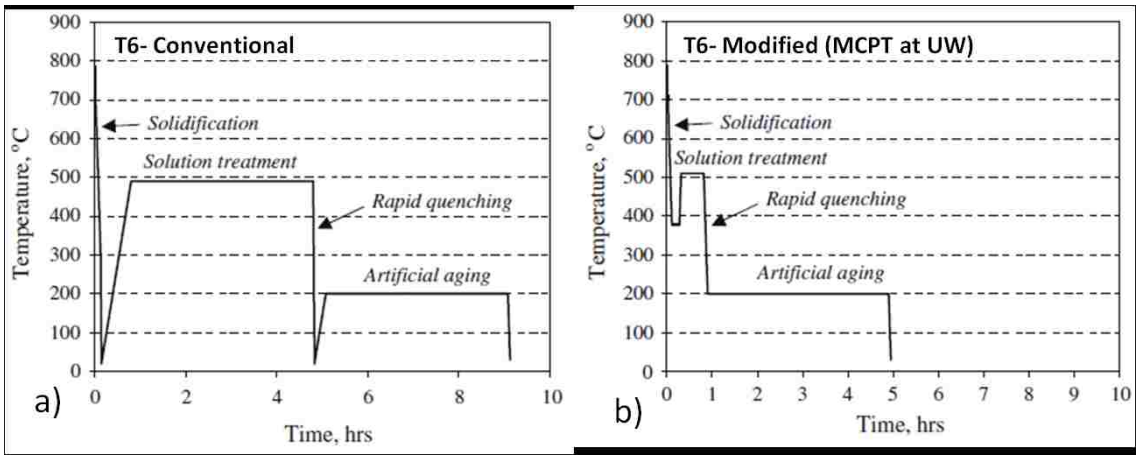

Figure 62. Temperature vs. time heat treatment plots of the UMSA experiments performed for the Al-20Si engine block and test samples: a) T6 Conventional - solution at 490 °C for 4 hr, air quenching and AA at 200 °C for 4hr, b) T6 Modified - rapid solidification arrested at 380 °C, followed by solution at 510 °C for 0.5 hr, air quenching and continuous AA at 200 °C for 4 hr [7]**.**

Metallographic analysis of the as-cast microstructure of the Al-20Si test sample solidified at 20 °C/s contains primary Si particles with an Equivalent Diameter (ED) of approximately 50 μm and fine unmodified Al-Si eutectics (see Figure 63a). When the test sample was subjected to ST at 510 °C for 0.5 hr the microstructure of the sample contained rounded and fragmented eutectic Silicon (see Figure 63b).

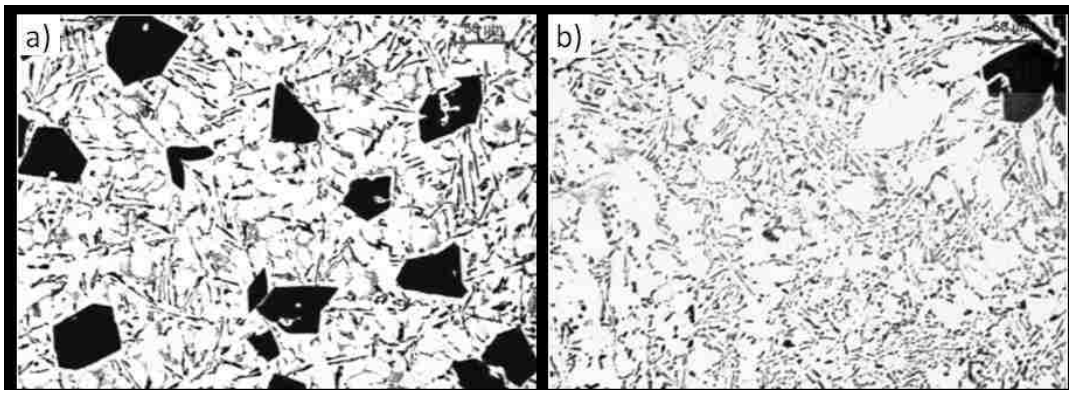

Figure 63. LOM micrographs of the Al-20Si alloy: a) test sample solidified at 20 °C/s, represents the thick section of the HPDC engine block, b) test sample subjected to the Solution Treatment operation at 510 °C for 0.5 hr [6]**.**

2.5 Thermal Analysis (TA) of Hypereutectic Al-Si Alloys

2.5.1 Overview of Thermal Analysis Techniques

Thermal Analysis (TA) investigates the thermo-physical properties of materials as they change with the temperature. Several TA techniques are commonly used for materials characterization and they are distinguished from one another by the property which is measured [230]–[233].

For example in **Differential Thermal Analysis (DTA)** the material being studied and a thermally inert reference are made to undergo identical thermal cycles and recordings are made of the temperature difference between the sample and the reference. Thermocouples measure the temperature difference between the test sample and the reference. When the sample is heated at a programmed rate, the temperatures of both the sample and the reference material increased uniformly when there are no phase changes. If the sample undergoes a phase change, energy is absorbed or emitted, and a temperature

difference (ΔT) between the sample and the reference is detected. A DTA curve plots the temperature difference as a function of temperature (scanning mode) or time (isothermal mode).

Cooling Curve Analysis (CCA), the most widely used method, is based on the fact that thermal events in a cooling process are related to phase transformations occurring in the sample. Temperature changes in a sample are recorded and analyzed through phase transformations in order to determine the solidified sample's metallurgical characteristics [230]–[233].

Commercial TA systems like: ATAS, Foseco and Heraeus [234]–[236] utilize a thermal sensor located in a relatively large rectangular and/or cylindrical solidifying test sample that is held in a Very High Thermal Mass (VHTM) sand test cup predominantly dedicated to the TA of cast iron. These test cups induce complex multi-directional heat transfer and melt convection resulting in a TA signal that is detrimental for high resolution and for a maximum detection limit needed for cooling curve analysis for both non-ferrous and ferrous alloys. However, these types of cups are frequently used by the plants and R&D facilities. An example of the fundamental limitation of using the VHTM test cup is the lack of a cooling curve first derivative "liquid melt arm" that is critical for determination of the Liquidus Temperature and consequently the Base Line that is necessary for calculation of the comprehensive TA characteristics. Figure 64 shows that the first derivative starts at 620 °C, (pouring temperature is 780 °C) and does not have the "liquid melt arm". Therefore, the Liquidus Temperature and other TA characteristics cannot be determined [237]. In addition, commercial and customized TA systems do not have the capability to physically simulate industrial process parameters that have a

profound effect on Solidification and on the heat treated structures that consequently impact the cast component's engineering characteristics.

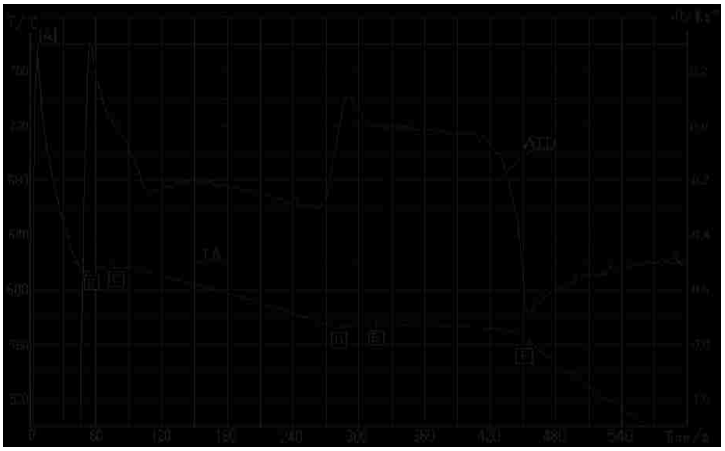

Figure 64. Cooling Curve (TA) and its first derivative (ATD) for the AlSi6 alloy after AlSr10 modification [237]**.**

The MCPT Group have disseminated and applied TA methodologies developed and verified since its inception in 1993. Recently it was observed that more and more researchers developed and advanced TA experimental and analytical procedures, rendering the high resolution thermal data presented in Figure 65 [110]. A recent comprehensive review of patents and journal papers revealed problems associated with some of the above-mentioned TA methodological difficulties. They have only recently been addressed**.**

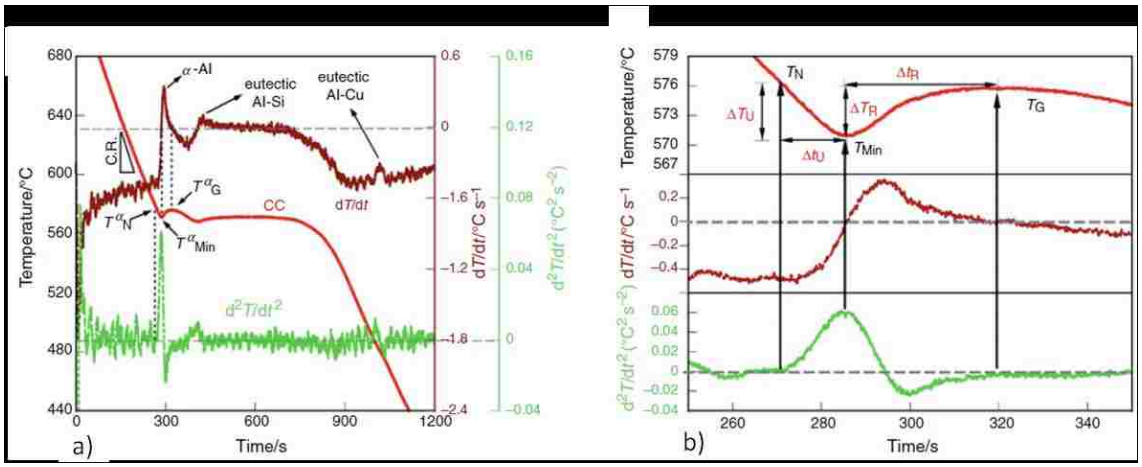

Figure 65. a) The cooling, first and second derivative curves of the alloy containing Bi showing the TA characteristics, b) correlation between the first and the second derivative curves in the Al dendrite arrest region showing the points of interest [110]**.**

TA techniques developed at the University of Windsor are used in the ferrous and non-ferrous industries and in R&D for evaluation and optimization of the melt quality, as-cast structure and other engineering characteristics as well as for optimization of the heat treatment [56], [156], [238], [239]. In contrast to commercial TA systems, the UMSA Technology Platform uses Low Thermal Mass (LTM) "foil containers" for the UMSA sample and thermocouples which contribute to the exceptionally high spatial resolution of the cooling and heating curves and their first derivatives.

2.5.2 Thermal Analysis using the Universal Metallurgical Simulator and Analyzer (UMSA) Technology Platform

The UMSA Technology Platform is a patented physical simulator (US Patent #7,354,491 and Canadian Patent #2,470,127) used for a very wide range of unbiased industrial, scientific and R&D processes and TA of industrial metal casting, forging and heat treatment processes for ferrous and non-ferrous micro and nanostructure materials, composites and components. The UMSA Platform is capable of a wide range of

processing parameters exceeding commercial technologies and uses macro test samples that represent actual components. This Technology Platform is used in scrap recycling, ingot and master alloys and inoculants manufacturing and their applications; melting, melt chemical and physical melt treatments (i.e. SC and HPDC) casting, solidification processes, forging and heat treatment.

The UMSA Platform uses high performance precision and a clean source for heating and cooling/quenching cycles. Comprehensive TA data allows for the correlation of the tested material and the component's simulated metallurgical characteristics with the process parameters.

UMSA testing and analytical methodologies allow for rapid and comprehensive quantification of the characteristics of the materials/components and related processes as well as design and commercialization of new ones. A computer controlled desktop UMSA Platform using a stationary macro test sample (monolithic and/or complex) is automatically processed in the required environment(s).

The UMSA user has the highest degree of freedom in the design and execution of experiments and data interpretation including metallographic/physical and chemical sample characterization [238], [240]–[242]. The Environmental UMSA Platform is depicted in Figure 66. Knowledge generated by the UMSA Platform, to date, challenges the established interpretation of some fundamental solidification and heat treatment phenomena. This new knowledge demonstrates potential technological and consequently significant cast component improvements.

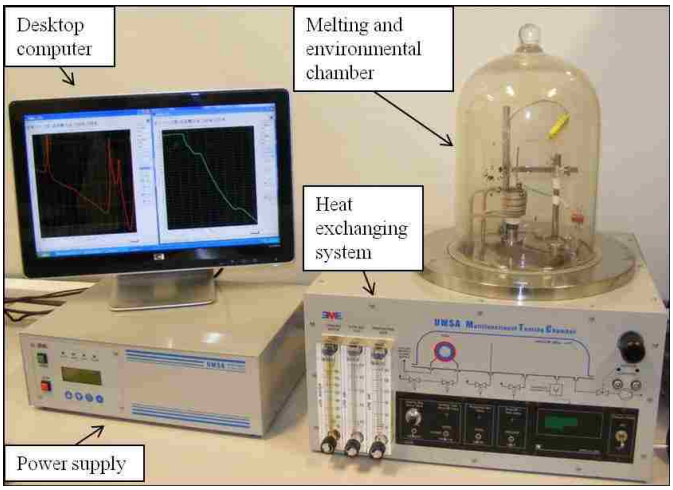

Figure 66. Photograph of the Environmental UMSA Technology Platform's main components.

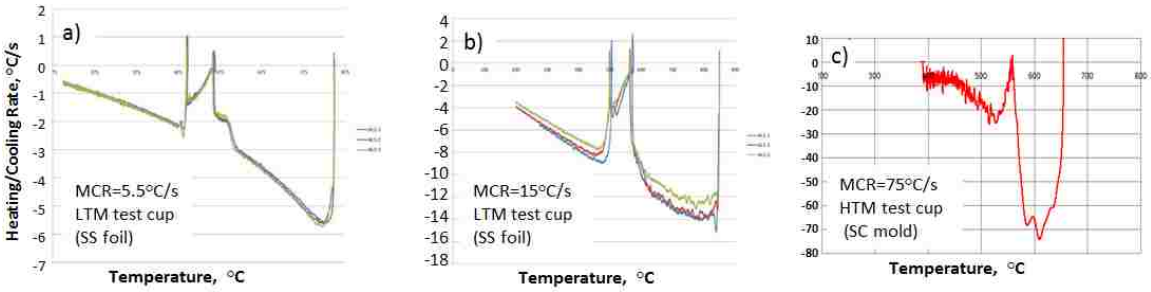

Figure 67. First derivative of the Cooling Curves vs. Temperature for the hypereutectic Al-20Si-3Cu Yamaha alloy solidified in: a) a low thermal mass cup at MCR = 5.5 ºC/s, b) a low thermal mass cup at MCR = 15 ºC/s , c) a high thermal mass cup at MCR = 75 ºC/s.

Examples of the Yamaha alloy's UMSA TA, low thermal mass test cup, low and medium SR, FD liquid and solid state "arms" – T_{liq} and T_{sol}, high thermal mass, high SR are shown in Figure 67 (a, b, c).

The UMSA Technology Platform [243], (described in Chapter 3, Section 3) is capable of collecting in-situ and analyzing on-line the thermal characteristics of metallurgically treated melts and solidifying and heat treated test samples, using precision controlled heating and cooling rates while physically simulating industrial processing conditions [244]–[246].

UMSA heating and cooling curves can be described as the "metallurgical DNA" of the melting and solidification processes. Major and minor thermal events called metallurgical reactions that are thermodynamically strong enough in terms of the latent heat evolution that manifest themselves on the heating and cooling curves as inflection points and slope changes, etc. can be determined. Using the UMSA solidification methodology, the test sample structure and the mechanical properties can be analyzed at any point between the liquidus and solidus or after completion of the solidification process in relation to the metallurgical reaction characteristics. Also, the UMSA test samples subjected to heat treatment can be used for structure and mechanical property analysis [245]. The High Temperature (HT) UMSA Platform is able to work at high temperatures and can simulate heating, heat treatment, homogenization alloying, inoculation, casting, solidification with average and instantaneous heating/cooling rates [243].

2.5.3 UMSA Thermal Analysis of the Hypereutectic Al-20Si-3Cu Alloy

The MCPT Group conducted comprehensive TA and metallographic research on the hypereutectic Al-20Si-3Cu (Al-20wt.%Si-3wt.%Cu) alloy [241], [247], [248]. The Yamaha Motor Co. Ltd., Japan, uses this alloy for the HPDC of high performance monolithic cylinder blocks.

Figure 68 presents an example of the high resolution Al-20Si-3Cu alloy UMSA heating and cooling curves. The alloy was melted at a heating rate of 0.75 $^{\circ}$C/s and solidified under controlled cooling rates of 1.0 $^{\circ}$C/s, 2.8 $^{\circ}$C/s, 4.4 $^{\circ}$C/s, respectively. Definitions of the characteristic points associated with individual non-equilibrium

metallurgical events are summarized in Table 3. The First Derivative Curves (dT/dt, °C/s). vs. Temperature are plotted in Figure 69 and the corresponding metallurgical reactions for different cooling rates are identified and listed in Table 4 [241].

In order to analyze complex features of the heating and cooling curves, the first derivatives (both time and temperature) and their numerical smoothed variations are used to help identify features that are barely detectable on the original curves. In addition, the Fraction Solid curve (pertaining to the specific thermal event) has proven to be very useful in academic and applied research. The Fraction Solid vs. Temperature curve for a 1.0 °C/s SR for the Al-20Si-3Cu alloy is presented in Figure 70.

The temperature shift between two heating and cooling events (the so called "metallurgical hysteresis") is caused by the non-equilibrium heating and solidification processes. This information is of paramount importance since many researchers wrongly use the solidification TA data for optimization of the heat treatment parameters.

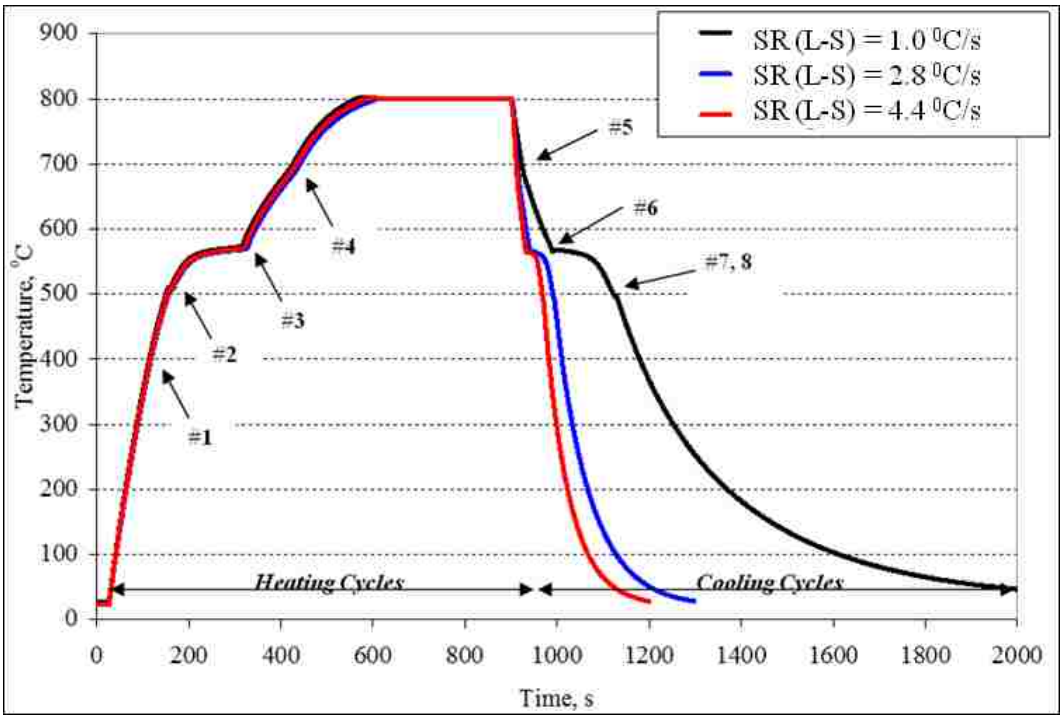

Figure 68. UMSA Time vs. Temperature Heating and Cooling Curves for the Hypereutectic Al-20Si-3Cu Ingot. The test samples were melted at a heating rate of 0.75 °C/s and solidified under controlled conditions at (1, 2.8 and 4.4) °C/s cooling rates, respectively [241]**. The numbers correspond to various metallurgical reactions as shown in Table 3 below** [248]**.**

Table 3. Thermal Characteristics obtained during the Melting and Solidification Processes for the Al-20Si-3Cu Alloy [248]**.**

#	Thermal Characteristics	Temperature, °C ±SD	Fraction Solid, %
1	Apparent start of dissolution of soluble phase(s).	384.7 ± 2.3	
2	Start of the alloy melting process.	502.8 ± 1.3	
3	End of Al-Si eutectic melting.	568.7 ± 1.5	
4	End of the alloy melting process.	710.9 ± 4.3	
5	Nucleation of the Primary Si (Liquidus temperature).	691.0 ± 2.2	0.0
6	Nucleation of the Al-Si eutectic.	567.1± 1.9	21.6
7	Nucleation of the Cu and Mg enriched eutectic(s).	513.6 ± 1.4	93.9
8	End of Solidification (Solidus temperature).	479.9 ± 3.3	100.0

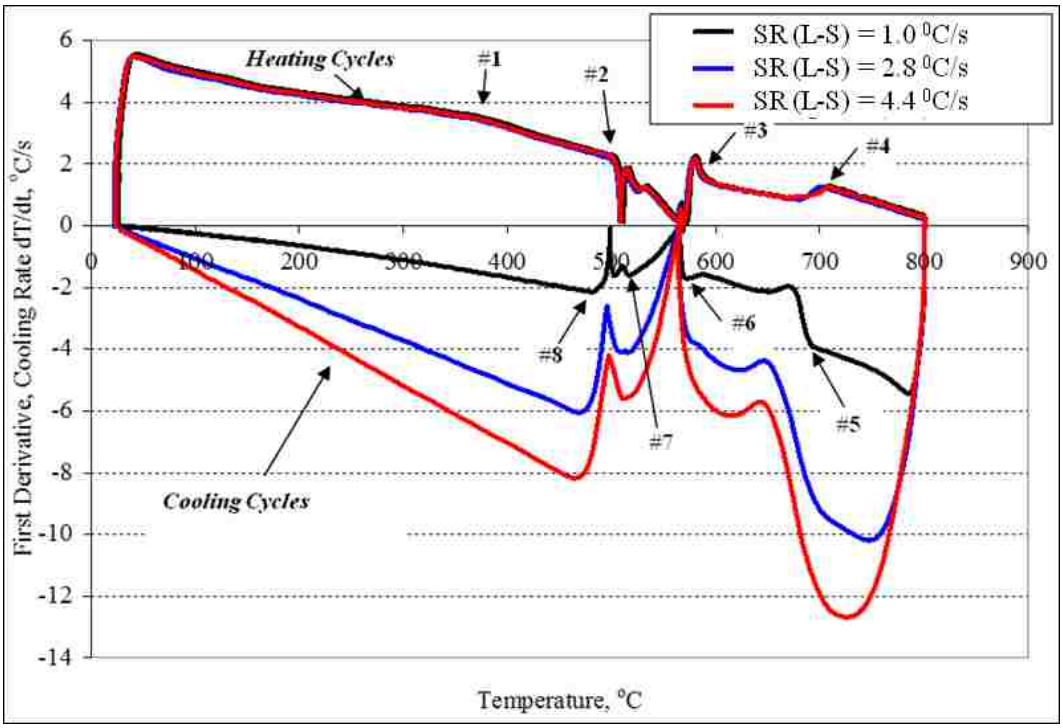

Figure 69. UMSA First Derivative of the Heating and Cooling Curves for the Hypereutectic Al-20Si-3Cu Ingot [241]**.**

Table 4. UMSA Cooling Cycle Thermal Characteristics for the Test Sample taken from the Al-20Si-3Cu Ingot [241]**.**

#	Thermal Characteristics	Temperature, °C	
		SR = 1.0°C/s	SR = 2.8°C/s
5	Nucleation of the primary Si (Liquidus Temperature)	691.2	704.3
6	Nucleation of the Al-Si eutectic	568.4	575.2
7	Nucleation of the Cu, Mg enriched eutectic(s)	513.8	515.7
8	Finish (end) of the Alloy Solidification (Solidus Temperature)	478.5	461.6
	Solidification Range	212.7	242.7

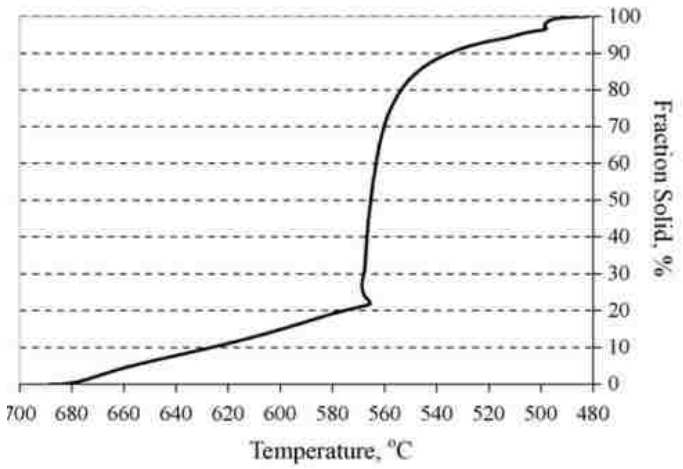

Figure 70. Fraction Solid vs. Temperature Curve for the SR = 1 °C/s for the Al-20Si-3Cu Alloy [248].

The thermal characteristics of the same alloy (Al-20Si-3Cu) but at an elevated ASR (35 °C/s) were investigated by Kasprzak et al. [249] and Marchwica [250]. They performed TA on the Al-20Si-3Cu alloy at an ASR of 80 °C/s (at a peak SR of 360 °C/s). Bäckerud et al. [251] published Solidification reactions and TA characteristics for the hypereutectic B390.1 alloy very similar to the Al-20Si-3Cu alloy (see Table 5) at a slow SR of (0.3, 0.5 and 4.0) °C/s respectively (see Table 6). The metallurgical reactions especially nucleation of primary Si (T_L) and solidification (T_S) are affected by the SR (see Table 6) and generally at higher SR the reactions occurred at lower temperatures. It needs to be mentioned that the determination of the primary Si nucleation temperature (T_L) is imprecise due to the fact that the authors used heavy thermal mass test cups. The authors reported the liquidus temperature in ranges associated with the SR. It is apparent that at a higher SR these ranges are wider (see Table 6).

Table 5. Comparison of the Chemical Compositions for Selected Hypereutectic Alloys

Alloy/ (wt.%)	Si	Cu	Mg	Zn	Fe	Mn	Ni	Ti	P	Al
Al-20Si-3Cu	20	3	0.5	0.1	0.5	0.1	0.1	0.001	0.01	Rest
B390.1	17.5	4.8	0.5	1.0	0.7	0.3	-	0.06	-	Rest

Table 6. Reactions during Solidification of the B390.1 Alloy at different SR [251]**.**

#	Thermal Characteristics	Temperature, °C		
		0.3°C/s	0.5°C/s	4.0°C/s
1	Formation of Primary Silicon –(T_L)	670-663	668-652	665-616
(1-2)		663-557	652-556	616-556
2	Dendritic network of α-Al + Eutectic Si	557-560	556-560	556-557
3a	Liq. →Al+Si+Al_{15}(Mn, Fe)$_3Si_2$ (Script)			
3b	Liq. →Al+Si+Al_5FeSi (Needle)			
3		560-557	560-555	557-549
4	Liq. →Al+Si+Mg_2Si			
(3-5)		557-496	555-496	549-496
5	Liq. + Mg_2Si→Al + Si + Al_2Cu + $Al_5Mg_8Cu_2Si_6$	496-497	496-497	496-494
(5-6)		497-495	-	494-485
6	Liq. →Al + Al_2Cu + $Al_5Mg_8Cu_2Si_6$ + Si -(T_S)	495-484	497-482	485-448

2.6 Silicon Equivalency

In binary aluminum alloys characteristic temperatures like the liquidus and solidus of the Al-Si alloy are determined from the Al-Si phase diagram but it is more

difficult to get accurate liquidus and solidus temperature information when dealing with ternary or high order phase diagrams. This problem could be resolved by using the system known as 'Silicon Equivalency' (Si_{EQ}).

The Si_{EQ} value expresses the chemical composition of major and minor alloying elements in the aluminum melt [252], [253]. 'Equivalent' in this case means that x wt.% of some element will have the same effect on the solidus/liquidus temperatures as y wt.% of silicon (where x and y are variables). Silicon was chosen as the base element for this method since it is common in all 3XX alloys. Si_{EQ} uses information from binary equilibrium phase diagrams between Al and others elements (denoted Xi). The slopes of the liquidus and solidus lines of Al-Xi phase diagrams can be expressed using second order polynomials.

With the silicon equivalents for all component alloys calculated, the overall silicon equivalency value can be expressed using Equation 6 below [240].

$Si_{EQ} = Si + \Sigma Si^{Xi}_{EQ}$, (wt.%)…….. **Equation 6**

This Si_{EQ} value can then be substituted into equations for the characteristic liquidus temperature lower than the eutectic point (see Equation 7) [254].

$T^{Al\text{-}Si\text{-}\Sigma i}_{LIQ} = 660.452 - 6.11 \bullet Si_{EQ} - 0.057 \bullet Si_{EQ}^2$, ($^oC$)...…… **Equation 7**

Equation 8 below is an alternate equation which is applicable for calculating liquidus temperatures in the hypereutectic region [254].

$T^{Al\text{-}Si\text{-}\Sigma i}_{LIQ} = 389.79 + 15.855 \bullet Si - 0.0561 \bullet Si^2 + 3.14 \bullet \Sigma Si^{Xi}_{EQ} + 0.057 \bullet \Sigma (Si^{Xi}_{EQ})^2$, ($^oC$)

…….. **Equation 8**

The Si_{EQ} procedure uses equilibrium phase diagram data and is applicable for very slow SR.

2.7 Literature Summary and Conclusions

Based on the comprehensive literature review containing information from over 260 references out of 1100 sources reviewed the following Conclusions can be made:

- The modification and refinement of hypereutectic Al–Si-X alloys, in industry, reached its limit of applicability. To date, recently known technologies were not able to further improve the Si modification and Al-Si eutectic cell refinement. The Toyota Motor Co. Ltd., a leader in mass production of motorcycle liner less engine blocks, cast using the HPDC technology, produced hypereutectic Al-20Si-3Cu alloy castings with microstructures (after 8 hours heat treatment) that contained eutectic Si particles (≈ 5 μm) and agglomerated primary Si particles (15 μm to 20μm in diameter).
- During the conventional T6 heat treatment process the primary Si particles were thermodynamically stable. These primary Si particles are detrimental to machining operations.
- Various techniques including ultrasound, mechanical and electromagnetic vibrations, chemical modification, thermal treatments, etc. improved modification of primary Si resulting in a change in the size of the particles from 100 μm to 50μm.
- Solidification of hypereutectic Al-Si alloys under ultra high pressure up to 5 GPa results in eutectic Si solidified in the lamellar form and primary Si particles having a diameter of up to 100 μm.
- There are no publications regarding liquid and semi-solid melt process technologies using chemical and physical means for industrial grade multi-component alloy

modification and refinement and associated heat treatment(s) that could possibly lead to the as-cast single Si phase and spheroidized nano Si particles after ST and AA respectively. In addition, there are no Thermal Analysis methodologies for on-line control of melt processing in the liquid and semi-solid states.

2.8 Development Status of Nano and Ultra-fine Structed Cast Alloys – Scientific Research Hypothesis

Development Status

In the last several decades global efforts by the metal casting academic and industrial communities were not fully successful in converting ultra-strength aerospace engineering materials like the B206 Al-Cu alloys or the 7000 series Al-Zn alloys to cast components used by other transportation industries (i.e. automotive). In addition, there is a lack of research on the development of nano and ultra-fine cast Al-Si-Cu materials with characteristics comparable to and/or exceeding ultra-high aerospace ones. Major problems with the first two materials are: corrosion and solidification hot tearing. Attempts aiming at the development of nano aluminum cast alloys are limited to the high purity Al-Si system tested using directional solidification. This methodology is very difficult for mass cast component(s) production in the automotive industry.

One of the reasons contributing to the lack of rapid progress on the above issues is the fact that the engineering community is lacking advanced tools capable of performing rapid fundamental physical simulations of the SC/HPDC industrial processes. The advanced physical simulation tools for industrial alloys and components must be capable of dissecting the technological processes, quantifying and controlling the influential parameters and their interactions on the level of key individual metallurgical reactions (during both solidification and heat treatment). In addition, present global research does not address the new opportunities like multi-pressure profiles applied to the liquid and semi-solid melts treated in a confined environment.

The beta version of the SC/HPDC UMSA Platform is a major milestone in novel R&D physical simulation capabilities. Vital metallurgical process information like the relationship between novel melt pressure treatment parameters is obtained from the feedback provided by the Thermal Analysis system that is capable of quantifying the solidification process and the as-cast nano structures.

The research hypothesis for development of nano Si structures in Al-Si-Cu industrial alloys uses subsurface cylindrical test samples and is based on a comprehensive "set" of process parameters and thermal characteristics of the solidification processes for effective control of the as-cast nano structures.

Quantification of the effect of dynamic melt processing parameters (i.e. pressure profiles) on solidification characteristics (i.e. instantaneous Solidification Rate, evolution of fraction solid of individual reactions) will determine the highest possible as-cast nano-structural characteristics contributing to ultra rapid heat treatment and many other outstanding engineering characteristics.

The proposed methodology for optimization of the SC/HPDC technology will eliminate many major limitations associated with some of the presently used analytical, computer simulations and testing techniques that cannot comprehensively optimize cast alloys, their processing parameters and predictably determine as-cast nano structures and related engineering properties. The proposed solutions are in the category of disruptive innovations that will have a long-term impact on the development and commercialization of new cast aluminum and magnesium alloys, their applications and their manufacturing technologies. Advancements in casting technology and nano materials together with

further demonstration/validation of the novel testing and analytical tools will create opportunities for their routine use by the scientific and engineering communities.

Scientific Research Hypothesis

1. Synergetic melt processing strategies including superheating, chemical modification, dynamic melt loading under confined conditions, high Cooling and Solidification Rates of the liquid and semi-solid hypereutectic Al-Si-Cu alloy will allow for conversion into the as-cast nano and ultra-fine single Si phase(s) ultra-refined Al-Si eutectic colonies and boundaries.

2. Multi-step high Solution Treatment temperature(s) of the as-cast nano-structured single Si phase(s) will allow for ultra-rapid fragmentation and spheroidization. It will also permit control of its stereological characteristics and allow for dissolution of the ultra-fine Al-Cu-Mg rich phases without detrimental incipient melting.

3. Artificial Aging of the Solution Treated nano and ultra-fine structured alloy(s) will allow for ultra-rapid precipitation strengthening which will result in ultra-high micro and macro hardness and significant improvement of wear characteristics.

CHAPTER 3: EXPERIMENTAL METHODOLOGIES

3.1 Experimental Materials

3.1.1 Chemical Composition and Si_{EQ} of the Experimental Ingot

A hypereutectic Al-Si-Cu ingot with the nominal chemical composition presented in Table 7 was utilized in this research project.

Table 7. Nominal Chemical Composition of the Experimental Alloy [6]**.**

Element	Si	Cu	Mg	Zn	Fe	Mn	Ni	Ti	Al	Si_{EQ}
wt.%	20.0	3.0	0.5	0.1	0.5	0.1	0.1	0.001	Balance	21.29

Selection of this complex chemistry is dictated by the fact that only a few researchers have utilized pure Al-Si alloys for the highly sophisticated laboratory demonstration of the feasibility to manufacture an as-cast nano structured Si morphology. However, these researchers did not consider the heat treatment operation. In addition, the highly alloyed melts pose very challenging technological requirements as far as the optimization of both as-cast and heat treated structures. Therefore, in order to demonstrate and overcome these challenges, the above-mentioned commercial alloy (hypereutectic Al-Si-Cu) was selected for this research. Special small ingots having dimensions of 700 mm x 90 mm x 30 mm (see Figure 71) were designed to limit segregation of the primary Si which nucleates first and flows rapidly to the surface. However, the ingot cross-section analysis revealed a considerable as-cast structural gradient with the primary Si floating to the upper region, while eutectic Si is located in the lower region. In order to limit experimental sample-to-sample chemical variability,

the ingot should be re-melted and rapidly solidified in the form of a near-final shape sample(s). This approach was not available since the MCPT Group does not currently have ingot melting capabilities. Therefore, all test samples were extracted from the center of the ingot.

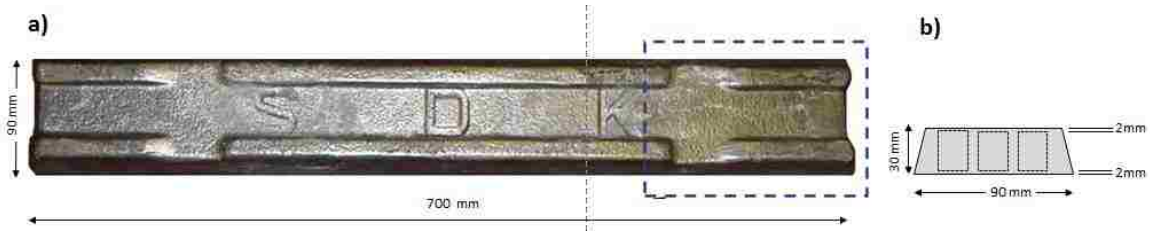

Figure 71. a) Experimental ingot, b) location of the SC/HPDC UMSA and HT UMSA test samples.

HT UMSA thermal analysis of unmodified melt samples using a near-equilibrium Solidification Rate allows for the deterimination of the Liquidus Temperature (T_{liq}), see Figures 89, 91-93. HT UMSA experimental determination of the T_{liq} allows for determination of the alloy's Si equivalent ($Si_{EQ,}$ wt.%), which accounts for Si and other alloying, impurity and modification elements present in the TA test sample [240]. Table 8 shows the values of the UMSA T_{liq} and pertinent Si_{EQ} for the unmodified experimental alloy. As can be seen, for the T_{liq} of 622.8 ºC, Si_{EQ} = 16.55 wt.%. Three HT UMSA experiments were repeated using the unmodified experimental alloy which shows an average T_{liq} = 618.4 ºC and a standard deviation (STDEV) = 5.0 ºC. The alloy with this Si_{EQ}, average chemistry and Lower and Upper Limit (Si_{EQ} in the range of 15.86 wt.% to 16.55 wt.%) is used as the experimental alloy in this project. The Si_{EQ} methodology was also utilized for evaluation of the effects of Sr modification and Cu addition on the test samples' TA characteristics that are presented in Figures 99-103. This approach also

allows for the determination of the effect of modification/alloying elements on the Al-Si eutectic growth temperature ($T^{AlSi}_{E,G}$). These characteristics can be compared with the literature data which is presented in Chapter 2. In future research all processed test samples will be analyzed using the Atomic Absorption Technique.

Table 8. T_{liq}, $T^{AlSi}_{E,\ NUC}$ and Si_{EQ} for unmodified experimental alloy solidified in the HT UMSA Platform at ASR = (0.4 to 1.1) °C.

Sample ref.#	T_{liq} , ºC	$T_{E,NUC}$, ºC	Si, wt.%	Si_{EQ}, wt.%
0808	622.8	566.4	15.26	16.55
1128	613.0	566.5	14.57	15.86
1203	619.3	566.4	15.02	16.31
Average	618.4	566.4	14.95	16.24
STDEV	5.0	0.1	0.35	0.35

3.1.2 Experimental Sr Master Alloy, Pure Calibration Metals and BN Die Lubricoat

KBM AFFILIPS' AlSr10 Master Alloy containing 10 wt.% Sr in the rod form was used for both Primary and Eutectic Silicon modification in the experimental alloy.

Pure Al and Zn were used for calibration of the thermocouples and the Data Acquisition Systems for the HT and SC/HPDC UMSA Platforms.

- **Pure Aluminum -** 99.99 wt.% - NIST standard melting temperature 660.323 ºC [255], in ingot form.
- **Pure Zinc** – 99.99 wt.% - NIST standard melting temperature 419.527 ^{o}C [255], in granular form.

Boron Nitride Aerosol Lubricoat (BN) is an Acetone/Alcohol based aerosol version of Boron Nitride, used for forming a barrier layer to protect the die, the cast sample, the thermocouple, and the graphite seal gate, etc. The BN spray has excellent thermal conductivity (7.4 W/cm.°C) [256] and is not reactive with molten Aluminum. The BN Aerosol Lubricoat Composition is: 87 % BN, 1 % MgO, 2 % SiO_2, the balance is a binder at 2 % Carbon.

3.2 High Temperature (HT) UMSA Technology Platform

The HT UMSA Technology Platform, shown in Figure 72, was utilized in the present study for identification of characteristic temperatures of the metallurgical reactions during rapid heating, natural cooling, for solution treatment, and artificial aging of the aluminum alloys used in this investigation. The HT UMSA Technology Platform was used for calibration of thermocouples using pure zinc and aluminum and for calibration of the Data Acquisition Systems.

The UMSA test sample(s) were used for the performance of comprehensive metallurgical tests including; macrohardness, microhardness and metallographic analysis. Figure 72 shows the HT UMSA Technology Platform which is made up of:

1) Desktop Computer: Used for setup control, data logging and thermal analysis.

2) National Instruments Data Acquisition System: 16-bit system capable of logging temperature/time measurements on two channels simultaneously with a scan rate of up to 100 Hz per channel.

3) Power Supply: Maximum output power of 7.5 kW with the capability to control heating power.

4) Heat Exchange System: The UMSA power supply and the electromagnetic coil must be cooled at all times during operation. The heat exchange system provides a steady flow of coolant to the coil.

5) Environmental Chamber contains an integrated induction heating/cooling coil. The chamber provides the capability to use different heating and cooling modes and rates. Cooling can be performed using either the cooling coil, where gases like argon or nitrogen are blown onto the exterior of the sample, or into the interior of the hollow sample.

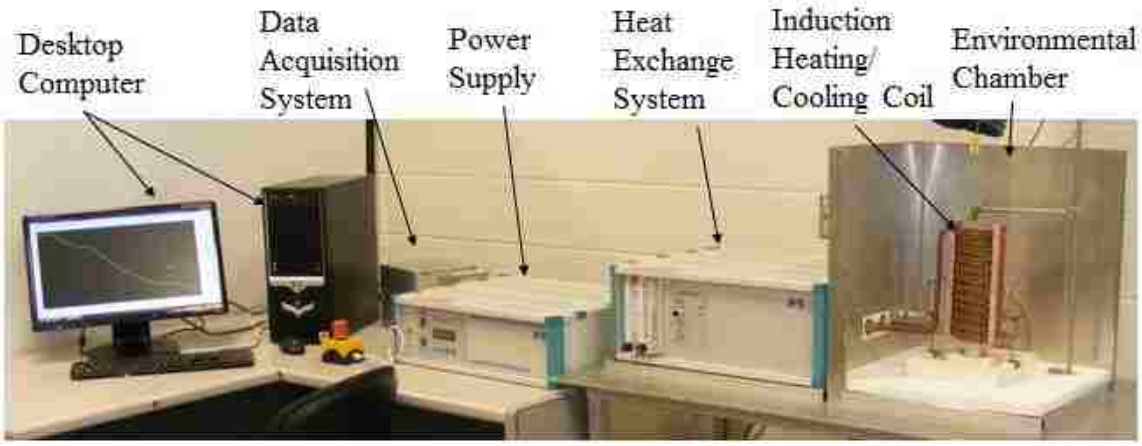

Figure 72. Photograph of the HT UMSA Technology Platform's main components.

UMSA Software consists of:

1) UMSA Control/Monitoring Software is used for experimental control and data logging. It accepts user input in the form of power settings, temperature/time settings, heat treatment paths, etc., and controls the power supply output. If cooling is required, it may also release gas coolants via the integrated cooling coil.

2) UMSA Thermal Analysis Software is the post-processing software used to analyze data logged by the UMSA Control/Monitoring Software. Using the temperature/time data as input the program is capable of calculating information of metallurgical importance, including derivatives, baselines and fraction solid curves as a function of the temperature. The program is well suited for the visualization and comparison of multiple graphs and also has curve smoothing capabilities, which use the Savitzky-Golay algorithms. The data is exportable to any standard spreadsheet program for further off line analysis.

HT UMSA test samples were machined from the ingots. Figure 71 shows the location where the test samples were extracted from the ingot. The dimensions of the samples and the photograph below used for the HT UMSA set-up are shown in Figure 73a and b.

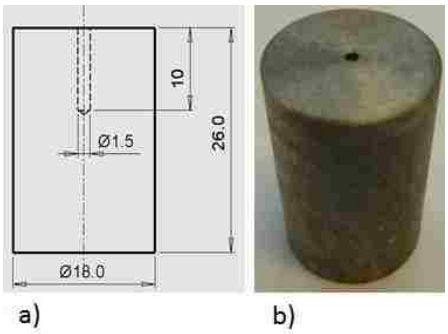

Figure 73. a) HT UMSA test sample drawing and b) picture.

Figure 74. High Temperature UMSA test sample and TA cup assembly.

The crucibles for melting HT UMSA samples were made from stainless steel foil having a thickness of 0.025 mm. The bottom and top caps were machined from stainless steel having a thickness of 0.25 mm, see Figure 74. The minimal thickness of the crucible walls provides minimal thermal mass which is important for unbiased thermal traces. The foils, caps and samples were coated with a very thin film of Boron Nitride spray in order to minimize the reactions with the environment.

3.3 SC/HPDC UMSA Technology Platform

3.3.1 Background

The HT UMSA Technology Platform, as described in Section 3.2, is capable of physically simulating and thermally interpreting metallurgical processes and covers a wide range of research and development on the ferrous and non-ferrous alloys at atmospheric pressure or in a vacuum.

The idea of developing a Squeeze Casting Platform and a High Pressure Die Casting Platform which covers High Pressure Technology parameters including cyclic pressure and high Solidification Rates, was initiated by Dr. J. H. Sokolowski, of the Metal Casting and Post-Processing Technology (MCPT) Group, at the University Windsor, as part of the patented UMSA Technology Platform through incorporation of a tool steel instrumented die into an Instron Mechanical Testing Frame. Some initial work was carried out in collaboration with undergraduate and graduate students and was integrated into the Capstone and/or AUTO21 Projects.

3.3.2 SC/HPDC UMSA Technology Platform's Functional Design

The SC/HPDC UMSA Technology Platform is capable of physically simulating the SC and HPDC solidification processes for a wide range of process parameters. The die was manufactured with the support of CanmetMATERIALS, Natural Sciences and Engineering Research Council of Canada (NSERC), The Foundation for Metal Casting Education (FEF), Gesing Consultants, Inc. and Electro & Metallurgical ENGINEERING (EME), in Poland.

The SC/HPDC UMSA Platform (see Figure 75) utilizes a hydraulic test frame to apply pressure to the liquid/semi-solid melt samples during solidification. The SC/HPDC UMSA Platform can melt alloys at temperatures up to 850 ºC, apply pressure up to 115 MPa using a plunger with a 20.4 mm diameter. The plunger velocity is up to 5 m/s. The parameters of the pressure profile are controlled by the computer. Cast samples have a diameter of 20 mm and a height of 30 mm. A pneumatic cylinder is used for test sample ejection. The initial die temperature can be adjusted up to 350 °C. Water is used for die thermal management. The maximum instantaneous Solidification Rate for pure Aluminum was reached at the liquidus temperature of approximately 294 °C/s. The present Squeeze Casting technology can address a quantitative assessment of the cumulative and individual effects of the solidification process.

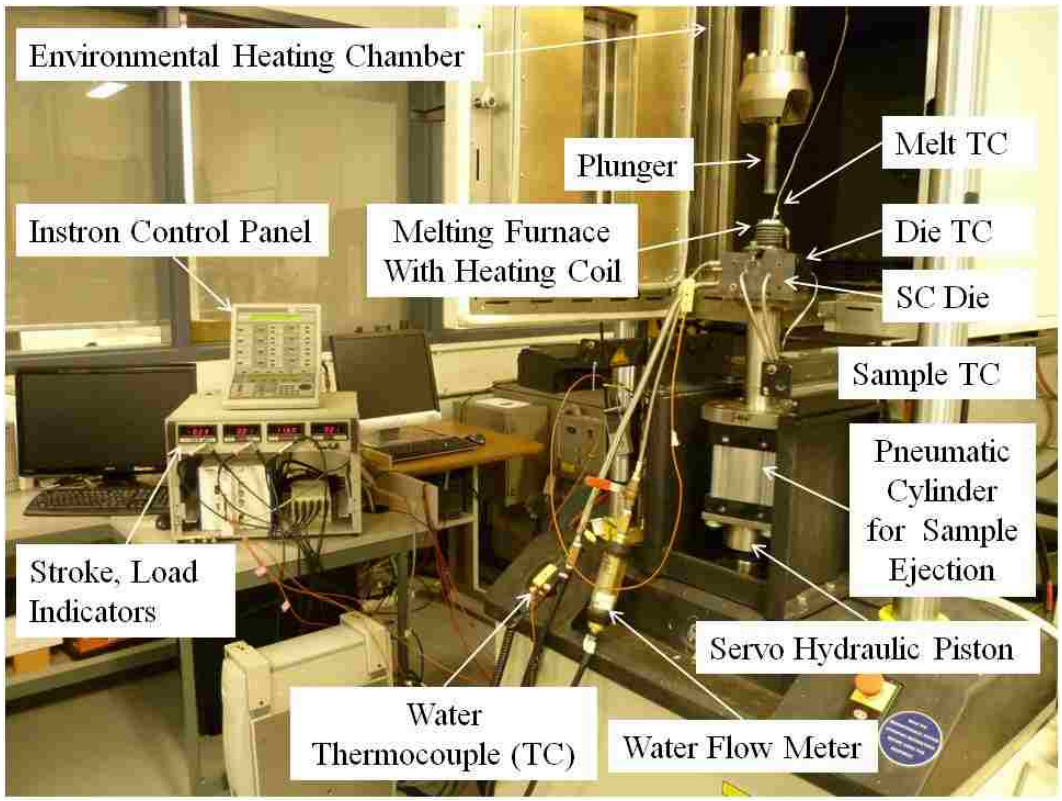

Figure 75. Overall view of the SC/HPDC UMSA Technology Platform.

3.3.3 SC/HPDC UMSA Die

The SC/HPDC UMSA die (see Figures 76 and 77) is designed to produce cylindrical cast test samples. The die assembly consists of a main steel block machined from H13 tool steel. The melting furnace is made of stainless steel (G304), and is capable of handling temperatures up to 1100 ^{o}C, however its tubular resistance heating coil is limited to a maximum of 850 ^{o}C. The die pre-heating system consists of two holes drilled through the die (7.94 mm) for placement of two cartridge heaters. The die cooling system is created by water lines (6.35 mm) drilled through the die block, and two levels of cooling passages within the die. Two holes (1.59 mm) were also drilled diagonally in the die, opposite each other to allow for insertion of the thermocouples. One is through a hole

for temperature measurement of the test sample in the center and the other is a blind hole for measuring the die temperature during the experiments. Passages for the graphite gate and the melting furnace are located on the top part of the die.

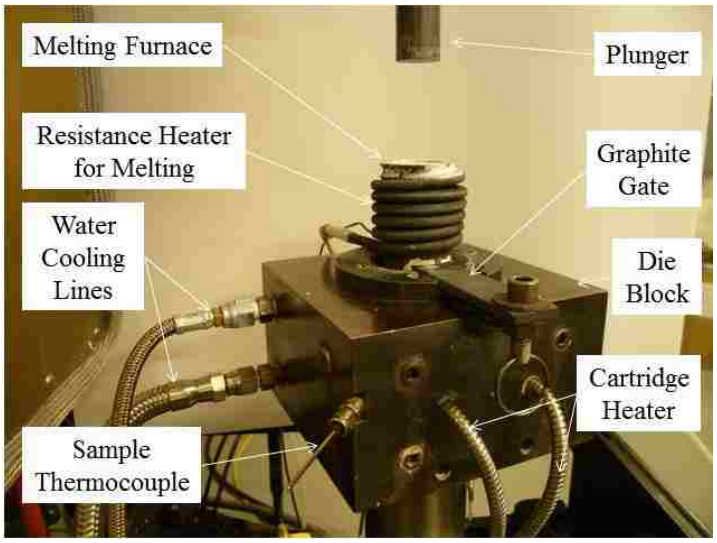

Figure 76. Details of the SC/HPDC UMSA Die assembly.

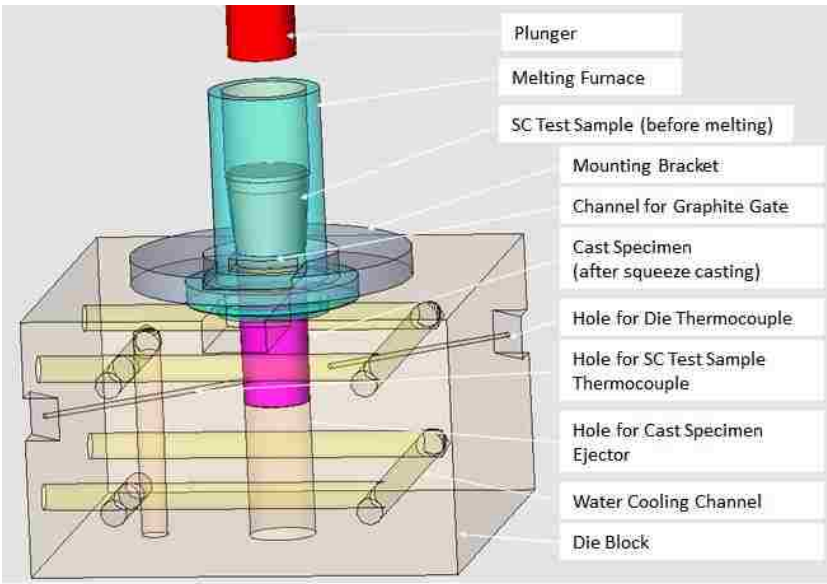

Figure 77. The transparent 3D model assembly for the plunger, melting chamber and die.

3.3.4 SC/HPDC UMSA Test Sample

The UMSA experimental test sample were machined into truncated cone shapes to follow the inside profile of the melting furnace, Figure 78.

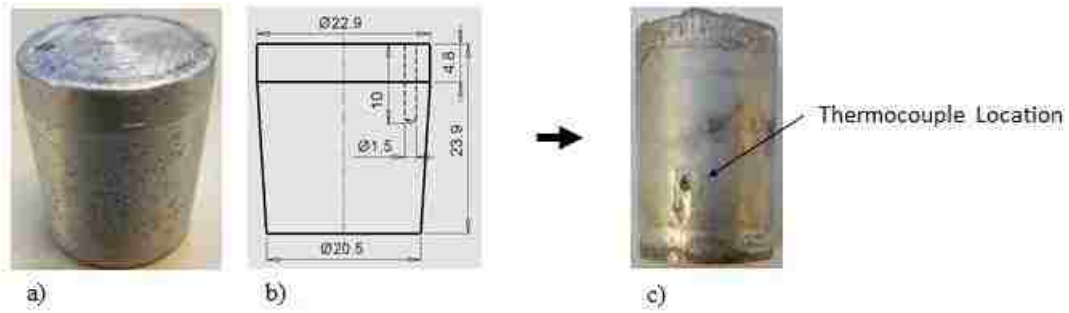

Figure 78. SC/HPDC UMSA test sample; a) picture before SC processing, b) drawing with dimensions (mm) before SC processing, c) UMSA processed as-cast sample.

3.3.5 Processing Parameters for Programmable SC/HPDC UMSA Experiments

Initial Die Temperature

The initial die temperature has an effect on the quality of the cast component and in industrial mass production the initial die temperature is a critical parameter for cycle process duration. A too low initial die temperature may result in premature solidification and it may mean lost energy and longer casting cycles. A too high initial die temperature may cause surface defects as in the case of welding of the casting to the die. In this investigation the initial die temperature was held in the temperature range of (265 ± 18) °C.

Thermocouple, Die and Plunger Coating

The lubricoat Boron Nitride was sprayed onto the thermocouple, the die and the plunger between experiments. The thickness of the protective film was less than 10 μm.

The coating needs to be well dried before the melt is poured into the die cavity to avoid the formation of gas porosity inside the casting due to vaporization of the BN propellant.

Melt Superheating Temperature

Based on previous results from the MCPT Group [156] and in order to reduce the size and improve distribution homogeneity of the primary Si crystals a melt superheating temperature was chosen of (800 ± 15) ^{o}C. Superheating was applied to the melt for a 5 minute homogenization time before its delivery into the die cavity.

Delivered Melt Temperature

The delivered melt temperature has a significant effect on the quality of the cast components, the life of the die, and the overall economy of the casting process. A low casting temperature can cause incomplete die fills and cold laps. A too high casting temperature leads to excessive porosity, shortening of the life of the die, and rising casting costs. In these experiments, the casting temperature was measured in the center of the die cavity and 10 mm from the bottom of the cavity.

Programmable Pressure applied to the Liquid and Solidifying Melt

SC and HPDC commercial technologies utilize static and/or intensified pressure during melt injection and the solidification process [257]. The SC/HPDC UMSA Technology Platform is able to apply pressure in the form of impact, cyclic and fading cyclic loading and combinations thereof (see Figure 79). In this research different pressure loadings were used with maximum pressure up to 115 MPa, with (1 to 45) cycles and at a frequency up to 15 Hz.

The casting pressure was calculated by Equation 9:

P=F/A ……**Equation 9**

Where, F is the force applied by the Instron Machine, and A is the plunger tip area. The maximum force of the SC/HPDC UMSA Platform is 50 kN. The applied force was controlled by the Instron control panel. The diameter of the plunger tip was 20.4 mm. For example: F = 30.0 kN, Diameter of plunger D = 20.4 mm, Area of the plunger tip is $A = \pi (D^2)/4 = 326.0\ mm^2$, therefore pressure P = 91.8 MPa.

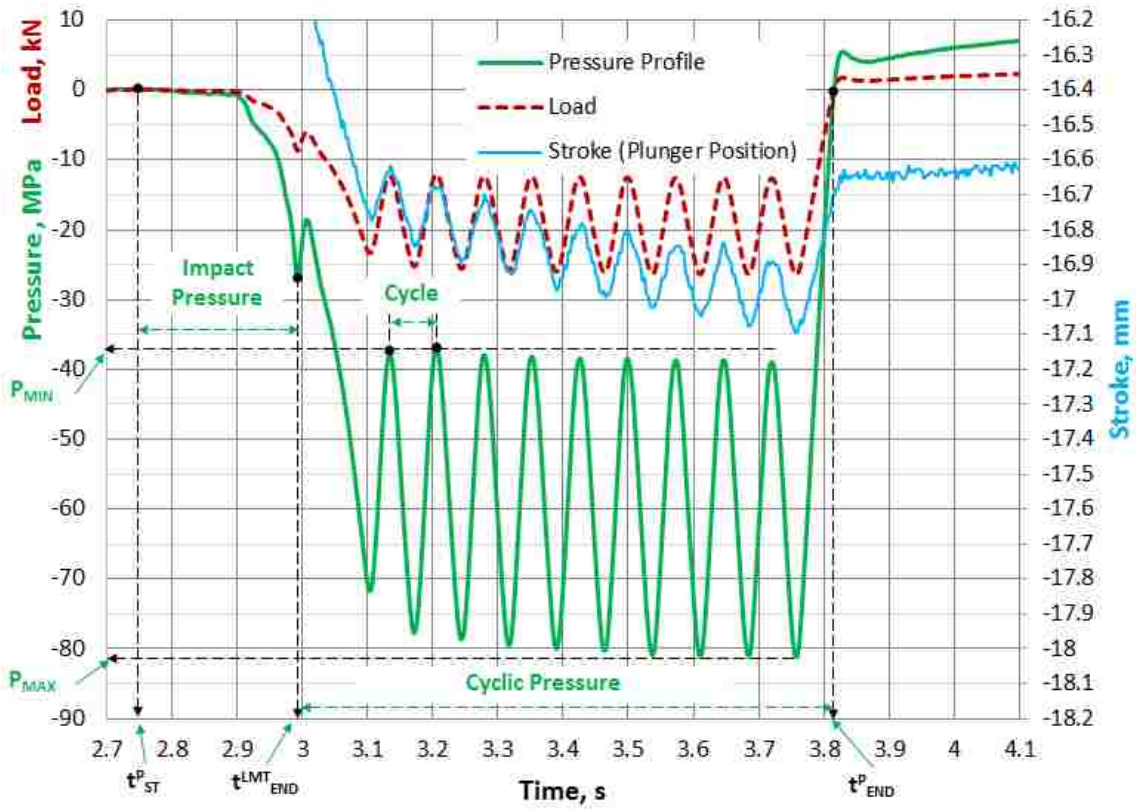

Figure 79. SC/HPDC UMSA processing parameters for the pressure profile, load and stroke curves vs. time.

Plunger Speed and Stroke

In these experiments a safe distance between the plunger and the melt is required to avoid overheating of the plunger. Melt delivery into the die cavity is detected via the sample thermocouple and a two-speed stroke controlled plunger movement was utilized. Initially a rapid approach to the melt surface was followed by a slower impact speed. The fastest approach of the plunger was at 0.15 m/s and was followed by the slower speed of 0.08 m/s. After contact of plunger with the melt the system remains in stroke feedback control but monitors the load and changes the stroke command to achieve a variety of pressure loading modes including cycling loading as shown in Figure 79.

Pressure Start and End Temperatures

The temperatures at which pressure starts and ends are very important parameters in the SC/HPDC UMSA technology. Numerous initial experiments were performed with different pressure start temperatures in a range between the liquid state of 659 $^{\circ}$C and the semi-solid state at 548 $^{\circ}$C. The start temperature and the pressure profile were controlled by the SC/HPDC UMSA computer.

Cumulative Energy

The energy induced into the specimen by the hydraulic system is measured by the work done by the piston force multiplied by the displacement or stroke. In a time history plot of stroke in millimeters and load in kilonewtons, the cumulative energy at any given point in time is the integral of the value of stroke multiplied by load. When both stroke and load increase in the positive direction energy is placed into the treated melt. In the time histories where an "unloading" occurs (compressive load and stroke decrease) energy is withdrawn from the specimen due to "elastic" unloading. The net result with

respect to Figure 129 is that the energy induced into the specimen is represented by the area under the load vs. stroke curve and the "cumulative" energy is the area under the curve at any instance in the time history of the load and the stroke, Figure 80.

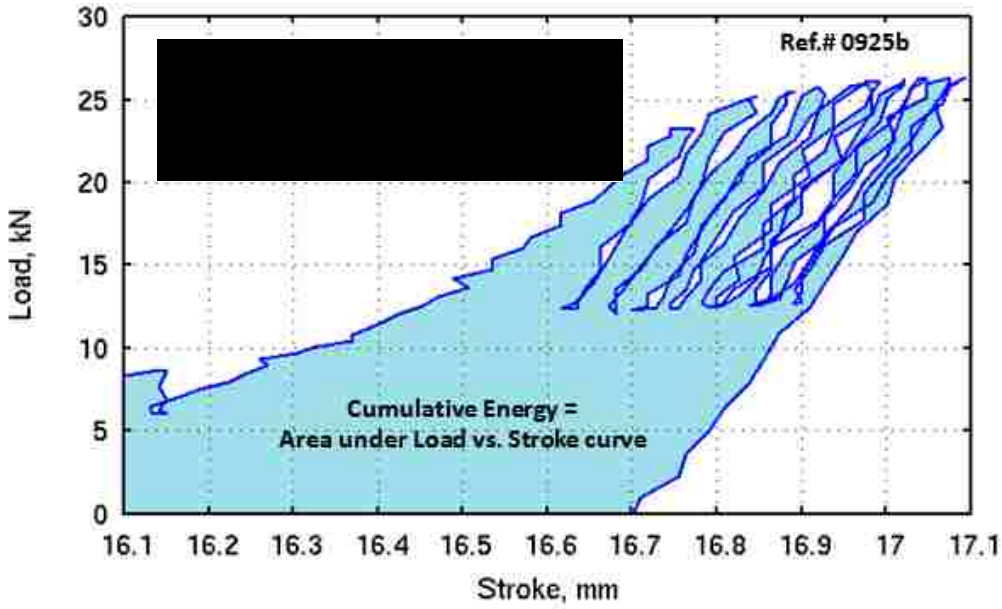

Figure 80. Cumulative energy input expressed as work done by the plunger under impact and cyclic pressure (38 - 81) MPa/10 c applied to the 0.15 wt.%Sr modified experimental alloy processed in the SC/HPDC UMSA die, ref. #0925b.

The above mentioned novel testing and analytical approach for quantification of various pressure profiles was developed and successfully applied in the analytical and statistical analysis of the subsurface of eight test samples.

In order to lower the number of quantified process parameters associated with the pressure profile, Cumulative Energy (CE) was utilized with respect to the melt treatment in the liquid and semi-solid states. As seen in Figure 129, the specific energy delivered into the liquid and semi-solid states (ΔCE_{liq1}, ΔCE_{liq2}, ΔCE_{ss1} and ΔCE_{ss2})

corresponds with the processing temperatures and time ranges determined from the Cooling Curve and its First Derivative for a given test sample:

- ΔT_{liq1}= Start Temperature for the Liquid Melt Pressure Treatment (T^{P}_{ST}) – End Temperature for the Impact Pressure Treatment (T^{IP})
- ΔT_{liq2} = End Temperature for the Impact Pressure Treatment (T^{IP})- Apparent Liquidus Temperature (aT_{liq}),
- ΔT_{ss1} = Apparent Liquidus Temperature (aT_{liq}) - Al-Si Eutectic Minimum Temperature ($T^{Al\text{-}Si}_{E,\ MIN}$) and
- ΔT_{ss2} = Al-Si Eutectic Minimum Temperature ($T^{Al\text{-}Si}_{E,\ MIN}$) – End Temperature for the Pressure Treatment -T^{P}_{END})

Please note that the melt having a residual amount of primary Si particles could result from its natural nucleation process during which the pressure load can be applied. This melt is considered a liquid. In this case, rapid interruption of the natural phase nucleation process by the pressure loading forces establishes the new Apparent $T_{liq.}$ Continuation of the solidification process proceeds, however, further metallurgical reactions can be controlled by additional pressure loading(s).

A summation of all ΔCE values provides the Total Cumulative Energy ($TCE_{liq\text{-}sol}$) delivered to the given test sample.

The above numerical data, the thirteen selected SC/HPDC UMSA Process Parameters for all eight test samples, and their corresponding Thermal Analysis Data and the Structural Data are summarized with the experimental results in Chapter 4.

Analysis of the process parameters, TA data, and consequently the structural data, was conducted using comparative methodologies and statistical analyses.

Derivatives of the process parameters like Cumulative Energy could be divided into two main classes related to:

(1) Experimental equipment involving friction, stroke, air and metallic pressure in the die cavity, transmitting rate of the thermal signal from the test sample interface with the die, transmitting rate of pressure and stroke signals and dynamic formation of the air gap between the test sample and the die.

(2) The testing and analytical procedures like the FD smoothing procedure, a very rapid solidification event affects spatial resolution of the metallurgical reactions. Some of these factors have not been measured, i.e. coefficient of friction. Future TA should include center and edge thermocouples in the sample and other sensors should address the effect of SR on the Heat Transfer Coefficient between the sample and the die.

3.3.6 Test Control Software and Data Collection Procedure for SC/HPDC UMSA Experiments

The SC/HPDC UMSA Technology Platform is controlled by computer software which was developed by Dr. Al Conle as part of an Open Source Fatigue Test Control Software servo hydraulic test control project. The software is a combination of C++, FORTRAN and Linux scripts and runs on a PC computer with a Microstar 840/103 analog to digital (A/D) and digital to analog (D/A) control processor board installed on the PCI bus. The Data Acquisition Processor (DAP) board reads voltages transmitted by Instron Force and displacement transducers and thermocouple signals conditioned by the

National Instruments SCXI-1000 amplifiers. Figure 81 is an overview of the hardware and Figure 82 shows the schematic diagram of the SC UMSA data collection.

Figure 81. SC/HPDC UMSA test setup, data recording and data collection devices.

The control computer software records six Data Channels:

Channel 1 Position of the plunger (stroke): ±10 V

Channel 2 Load: ±10 V

Channel 3 Liquid melt temperature: ±5 V

Channel 4 Solidification temperature of the sample: ±5 V

Channel 5 Outlet temperature of the waterlines: ±5 V

Channel 6 Die temperature near sample chamber: ±5 V

The Instron test controller and the PC DAP test controller measure the conditioned signals, such as stroke, load or temperature, in voltage units. Ram, stroke and load are amplified to be in a range of +/-10 Volts. The NI SCXI - thermocouple conditioner amplifies the temperature generated millivolt signal from the thermocouple to a range of +/-5 V. Data for each channel was recorded in the form of a digital +/-32767 numbering

system which was then scaled for the range of +/-10.000 volts prior to storage on the disk. Since the computer program reads everything in voltages, it was necessary to develop a relationship, through "calibration" between the devices voltage output and the actual signal or variable of interest. The Instron mechanical testing machine was calibrated by the Instron standard such that:

a) Stroke or ram displacement: +/-10.000 V is +/-75 mm

b) Load on +/-10.000 V is +/-50.0 kN

Attached to the system are two PC computer systems, one a UMSA-TAl software system for monitoring of the heating and cooling curves (described in the HT UMSA) and a second Linux based system for test machine control data collection and data analysis.

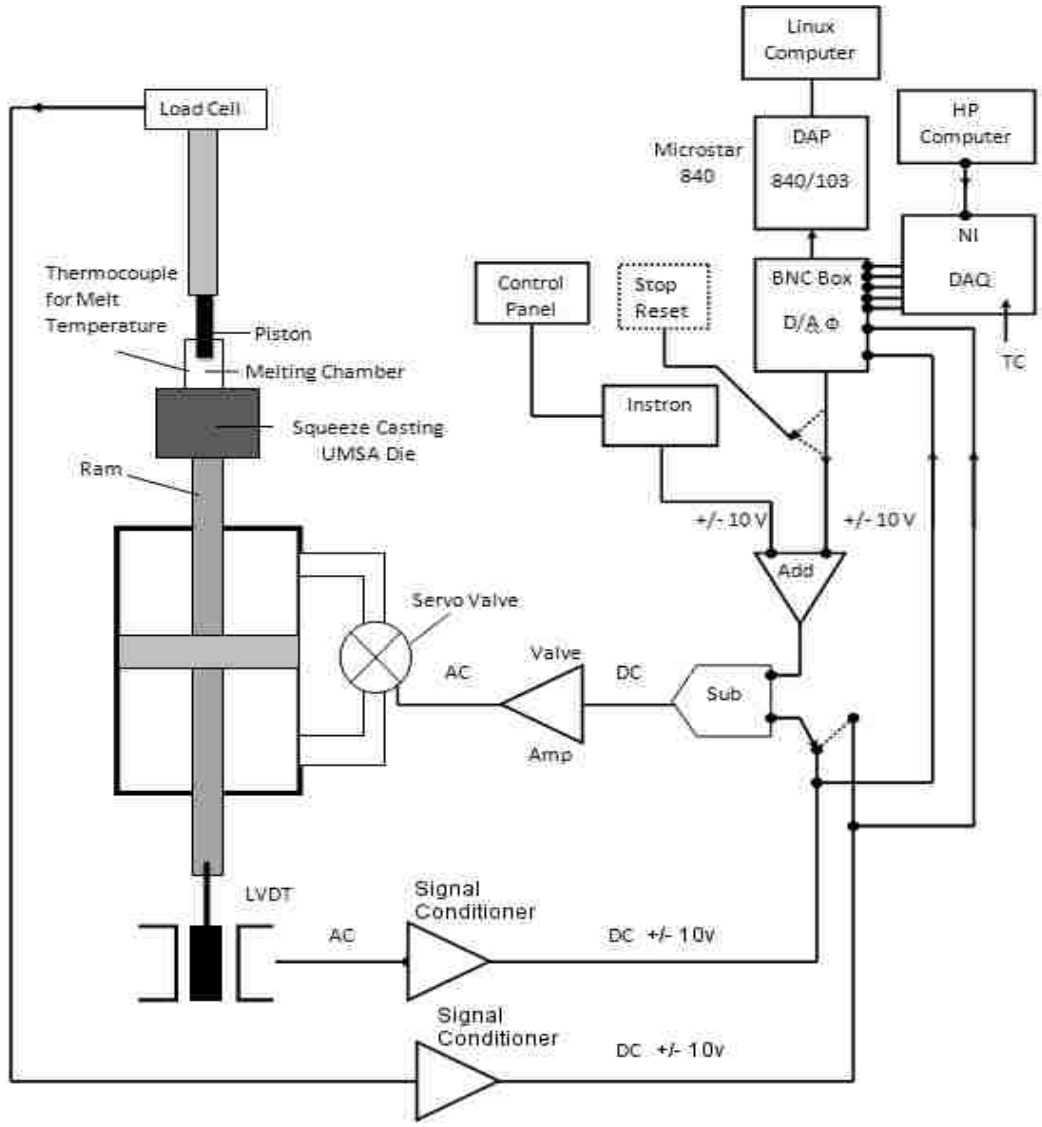

Figure 82. Schematic diagram of SC/HPDC-UMSA data collection.

3.3.7 Procedure(s) used for the SC/HPDC UMSA Experiments

1. Before starting the SC/HPDC UMSA experiments, the die cavity was cleaned with small tools to break off any loose residual metal left from previous experiments. A small vacuum cleaner was used to remove all of the tiny particles.

2. A thermocouple was inserted into a stainless steel sheath, located in the hole that opened into the die cavity. The sheath ended at the cavity wall and the thermocouple tip was centered in the cavity.
3. The interior of the die and the thermocouple (in the center of the cavity) were sprayed with Boron Nitride (BN) and the coating was left to dry.
4. A graphite gate was inserted into the gate channel in order to close the bottom of the melting furnace.
5. The melting furnace and the graphite gate on the bottom of the melting furnace were sprayed with BN and left to dry.
6. The charge Al alloy SC/HPDC UMSA test sample was located in the BN coated melting furnace.
7. A sheathed thermocouple for melt temperature measurement was sprayed with BN and was located in the 1.5 mm hole of the SC/HPDC UMSA melt charge.
8. The Instron piston was set at a position so that the plunger was just above the melting furnace. The environmental chamber was then closed to contain any melted aluminum splash during the test.
9. When all thermocouples were placed in their respective positions, four channels observed and recorded the heating/cooling of the: a) melt test sample, b) die cavity cast specimen, c) cooling water and d) die temperature. The desktop view of the four channels is shown in Figure 83.
10. The cartridge heaters for preheating of the die were turned on. The thermocouple located in the die was used to control the initial temperature of the die. The

cartridge heaters were controlled manually using a 110 VAC dimmer switch and the die temperature was allowed to stabilize at 250 °C ± 10 °C.

11. When the die temperature reached 140 °C, the tubular heater surrounding the melting chamber was switched on. The thermocouple located in the melting chamber wall controlled the heat energy of the tubular heater around the melt.
12. After the melt reached the required superheating temperature, the automated software in the main data control computer collected the data.
13. After 5 min of melt holding at the superheating temperature, the graphite gate was manually opened and the melt flowed into the die cavity. From this part of the experiment to the end of solidification, the process was automatically controlled by the Squeeze Casting Test Control Software: When the melt in the die dropped to the required trigger temperature, the squeezing process was started as programmed (pressure profile-frequency, time and amplitude).
14. The SC/HPDC UMSA test control program works in six stages, and in each stage all six channels of data are recorded to the hard disk at 333 data points/second/channel. The six control stages are:
    - Stage 1: The program monitors the die cavity thermocouple to see when the melt has been delivered to the die cavity. When the thermocouple exceeds 1.5 volts the program concludes that the cavity is filled with melt and Stage 2 begins.
    - Stage 2: The program monitors the die cavity thermocouple's signal to see when a peak temperature is achieved. The computer tracks the voltage on the way up and when a specified voltage drop (0.50) occurs the program

concludes that the peak temperature has been achieved. The volt window is required because the thermocouple signal has inherent noise which, if the window is too small, could trigger an incorrect “peak detected" state. When a peak temperature has been observed Stage 3 begins.

- Stage 3: The program monitors the die cavity thermocouple as the temperatures decrease to see when a user defined post peak temperature trigger has occurred. Then it goes to Stage 4.
- Stage 4: The program gives instruction to move the ram (via outputs onto the D/A) into a predefined position just above the dropped melt at a high ram speed. The ram speed needs to be determined iteratively as overshoot of the target position above the melt is possible. As the ram gets close to the target position the voltage step size is decreased by a factor of 2, to slow the ram. When the Stage 4 ram position is reached, Stage 5 starts.
- Stage 5: The program selects a target load voltage from the program list and changes stroke (ram position) in very small voltage steps to minimize overshoot of the target load. As each of the programmed loads is achieved, the next target load in the list is selected. When the load list is completed, the program proceeds to Stage 6.
- Stage 6: The program monitors and records all six data channels until the stop signal is received.

15. The die cavity thermocouple records solidification process data and verifies the solidification/cooling rate of the test sample.

16. Just after dropping the melt into the die cavity, the water flow is turned on. The outlet water temperature was recorded as one of the data channels.
17. Once the solidification process is completed, the cast specimen is ejected from the die using the pneumatic ejection cylinder activated by way of a detent control valve. The maximum capacity of the air regulator is between 80 psi to 90 psi which is able to eject the test sample out of the die cavity. Prior to the ejection of the sample, an attempt was made to remove the specimen thermocouple from the die, though it was not usually successful. After cooling, the test sample was prepared for metallographic observations through LOM & SEM/EDS.
18. The experimental data was processed by the PC Data Acquisition System (DAS). Final outputs were recorded in a large data log file for computation purposes, which was truncated to the required test data set. Using a Linux Bash script, a set of data files with important variables including time, temperature, stroke, and cyclic pressure was created for data analysis. All data channels were converted from volts to their respective units, e.g., time in seconds, stroke in mm, temperature in ^{o}C, etc.
19. The Savitzky-Golay algorithm was applied twice, each time with a window of 60 points on both sides of each smoothed point. The point window size was larger than that used in the standard UMSA program because the number of samples per second was larger. The Savitzky-Golay code was also used to compute the first derivative of the cooling curves. In parallel to the PC control and record system, the HP computer and its UMSA software was used to obtain heating/cooling curves and the first derivatives.

Figure 83. Desktop view of four channels Labview software for monitoring and recording temperatures of thermocouples in HP computer.

3.3.8 Thermal Analysis, Testing of Analytical Characteristics and Data Interpretation Methodologies

Comprehensive thermal characteristics of the unmodified and modified experimental alloys tested at low and high Solidification Rates, under atmospheric and various pressure profiles in the liquid and semi-solid states were determined using both the HT and SC/HPDC UMSA Platforms. The representative TA characteristics include: the Cooling Curve (CC), its First Derivative (FD) and the Dynamic Base Line (DBL) and Fraction Solid (f_S) Curves vs. Time. Tables 16 and 17 outline HT UMSA Thermal Analysis which is relatively well described in the literature. The Identification Number for specific metallurgical reactions (events), acronyms, detection algorithms and comments as related to the analyzed metallurgical reactions are provided. The TA data presented is based on solidification analysis using HT UMSA TA output and analytical software. Superimposition of both process parameters and thermal data is utilized for determination of their relationship to the as-cast structural characteristics. The literature

review does not offer interpretation methodologies for SC/HPDC UMSA generated TA data for using various melt pressure loading profiles. Therefore these TA methodologies and analysis of experimental variables associated with individual experiments are provided in Chapter 4.

3.4 Calibration of Thermocouples and Data Acquisition Systems for the HT and SC/HPDC UMSA Platform Experiments

3.4.1 Thermocouple Selection and Calibration Requirements

Aluminum alloys used in this research have a solidus temperature of about 486 ^{o}C and a liquidus temperature not more than 633 ^{o}C. The maximum superheating temperature applied in this research was 815 ^{o}C. K type thermocouples (TC) are suitable for this temperature range. Usually the thermocouples are sheathed in stainless steel tubes which provide protection against liquid aluminum dissolution, pressure and vibration. Ungrounded junction thermocouples were selected to improve electrical isolation from electromagnetic signals in the surroundings. Table 9 shows characteristics of the thermocouples used.

A very important characteristic of a thermocouple is its response time; rapid response time is essential for accuracy in a system with fast temperature changes. The response time depends on the physical properties of the thermocouple (thermocouple wire and sheaths: type, materials, dimensions, etc.) and environmental working conditions (temperature, pressure, etc.) Thermocouple response time information is not

provided by manufacturers for high temperatures up to 815 ^{o}C. In addition, thermocouple response time is not provided for cyclic pressure up to 100 MPa. Therefore, comprehensive calibration of the thermocouples and the Data Acquisition Systems need to be performed.

Table 9. Thermocouple Characteristics [258]**.**

	OMEGAS specifications	
Thermocouple	TJ36-CA-XL-116-G-6	K-MQ-SS-020-U-6
Type	K	
Sheath Material	SS 304 (Stainless Steel)	SS 304 (Stainless Steel)
Probe Diameter	1.5 mm	0.5 mm
Junction Type	Grounded (G)	Ungrounded (U)
Probe Length	150 mm	
Wire Diameter	(no clear information)	(not available)
Temperature Range	0 – 1250°C	
ToleranceValue (standard)	2.2°C or 0.75% (whichever is higher)	
Tolerance Value (special)	1.1°C or 0.40% (whichever is higher)	
Response Time	2.1 s	0.9 s

Due to time constraints and experimental conditions, the calibration procedures were limited to the calibration of thermocouples and Data Acquisition Systems for the HT and SC/HPDC UMSA experiments against NIST pure Aluminum and Zinc calibrated solidification temperatures using very slow Solidification Rate under atmospheric pressure conditions.

3.4.2 Calibration Procedures for the Experimental Thermocouples and Data Acquisition Systems

Experimental thermocouples and Data Acquisition Systems were calibrated. National Institute of Standards and Technology (NIST) recommends using fixed solidification temperature pure elements for thermocouple calibration. Pure Al, Zn, Cu,

Sn, among many other elements, are the fixed points of the International Temperature Scale called ITS-90. These pure metals show no thermal reactions during the solidification process. Due to the time constraints, a two point calibration using the Al and Zn procedure was chosen. Solidification temperatures of Al and Zn are 660.323 °C and 419.527 °C, respectively [255], [259]. The thermal mass of both HT and SC/HPDC UMSA test samples are similar.

Calibration was performed using the HT UMSA Platform under atmospheric pressure and natural solidification conditions (see Table 10). Pure Aluminum (#0509) and Pure Zinc (#0626) calibration standards were instrumented with a sheathed K thermocouple having a diameter of 0.5 mm. Calibration involved Al melting to a temperature of 700 °C and melt holding for 5 min for temperature stabilization. After these operations, natural melt cooling and solidification processes started. Figure 84 shows uncalibrated Al melt cooling and a solidification curve which indicates an average Solidification Temperature of 662.216 °C. This temperature is higher than the NIST calibrated standard. Thus the calibration factor of -1.893 °C was applied for the calibrated thermal data presented in Figure 84. As can be observed both the temperature and the First Derivative plateaus are stable during the solidification process and do not indicate any metallurgical reactions.

Table 10. Matrix for Calibration of the Thermocouples, HT and SC/HPDC UMSA Data Acquisition Systems using Pure Aluminum and Zinc.

Runs #	Sample Ref. #	UMSA Platform	Calibration Elements	Applied Pressure, MPa			ASR, °C/s
				P_{min}	P_{max}	Cycles #	
1	**0509**	HT	Al	0.1		N/A	<0.6
2	**0626**		Zn				

An identical calibration procedure was applied for the Zn solidification temperature calibration, Figure 85. The uncalibrated average Solidification Temperature of Zn is equal to 420.056 °C. Therefore the calibration factor of -0.529 °C was applied to the calibrated average Solidification Temperature. Observations to the Cooling/Solidification curve and its First Derivative show that the thermal behavior is similar to the Al experimental data. The uncalibrated and NIST calibrated solidification temperature co-ordinates for Al and Zn were utilized for calculation of the two point linear regression equation (Equation #10), Figure 86. This equation is used for the calibration of the thermal data (Cooling/Solidification Curves, First Derivatives and Fraction Solid) in the required experimental temperature ranges.

Figure 87 shows an example of Cooling/Solidification curves and their First Derivatives from experiments involving calibrated thermocouples utilized for the pure aluminum SC/HPDC UMSA experiments. Aluminum test samples were processed in the die under natural solidification conditions and applied cyclic pressure melt loading (confined environment). As can be observed, the aluminum melt processing parameters have an impact on the average Solidification Temperature. Higher cyclic loading results in higher Average Temperature of Solidification and significant shortening of the solidification time from 6.5 s at 0.1 MPa to 1.2 s at cyclic pressure (53-108)MPa/26 cycles. The pressure treated Al melts exhibit approximately 1°C "undercooling". However this "Apparent Undercooling" is a result of the applied cyclic pressure loading. In addition, cyclic pressure treated aluminum melts exhibit Solidification Rates (SR determined from the FD traces) of approximately 247.0 °C/s and 294.4 °C/s for lower and higher pressure, respectively. These very high SRs are not observed for the

experimental Al-Si-Cu alloy due to its lower thermal conductivity in comparison with pure aluminum. The unpublished highest SRs for this experimental alloy processed under new conditions reached a level of 177.1 °C/s.

$$T_{NISTCalibrated} = 0.994 \bullet T_{HT\ UMSA\ Measured} + 1.837 \quad \text{.....Equation 10}$$

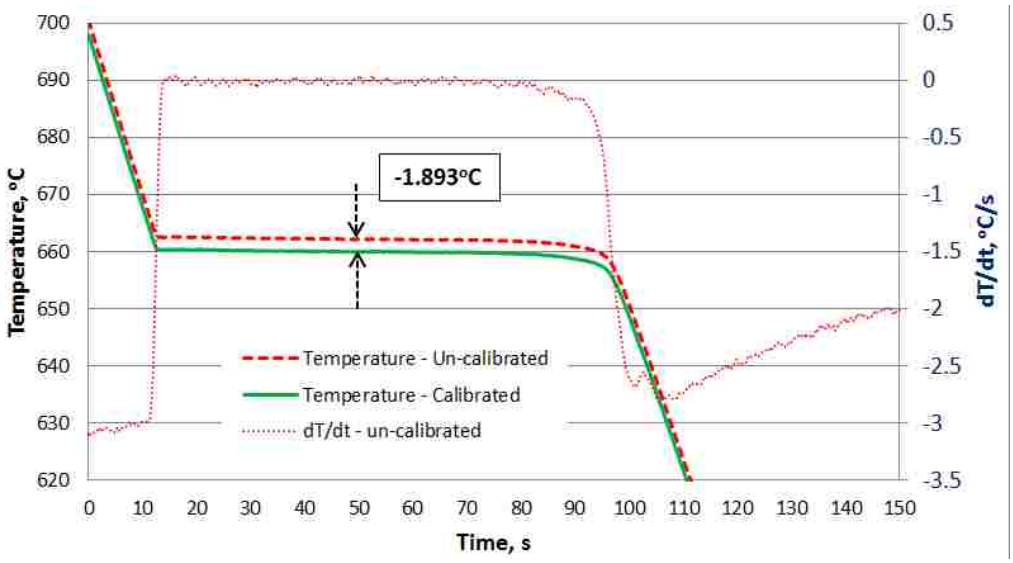

Figure 84. Comparison of calibrated and uncalibrated cooling curves and uncalibrated first derivative curve vs. time for pure Aluminum, solidified in the HT UMSA platform under atmospheric pressure (0.1 MPa).

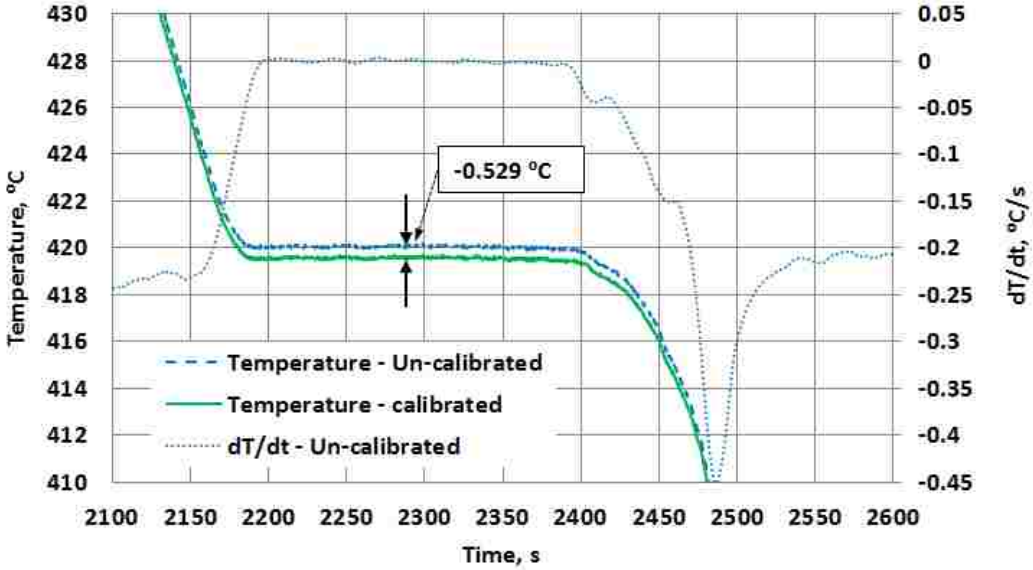

Figure 85. Comparison of calibrated and uncalibrated cooling curves and uncalibrated first derivative curve vs. time for pure Zinc solidified in the HT UMSA die under atmospheric pressure and lower SR ≈ 0.25 °C/s.

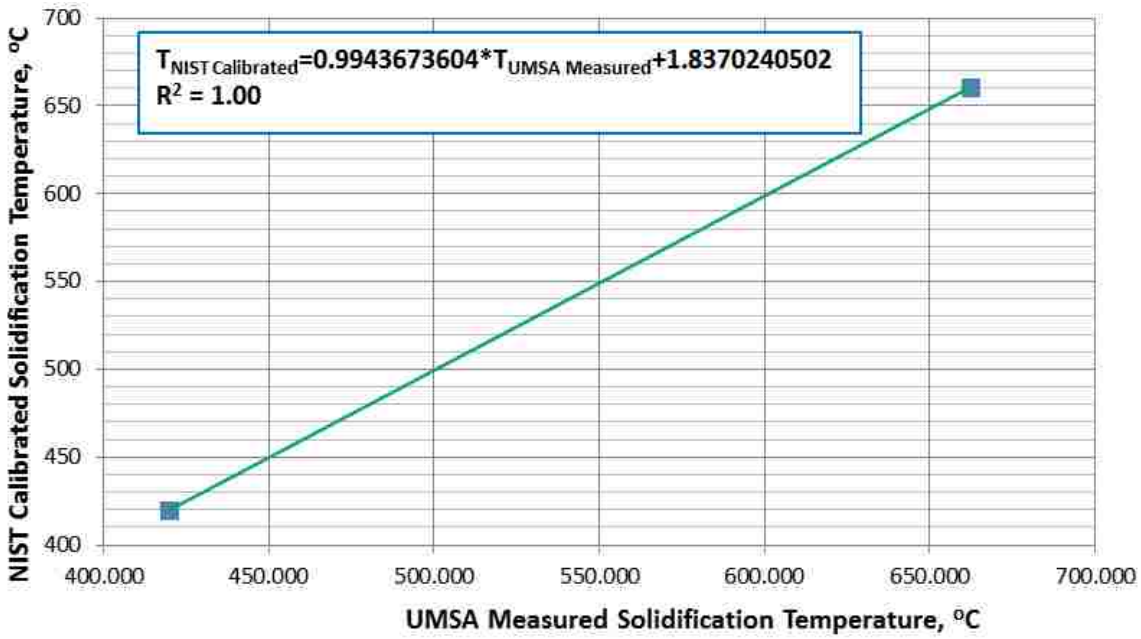

Figure 86. Relationship between UMSA measured solidification temperature and NIST calibrated solidification temperature at 0.1 MPa and ASR ≈ 0.4 °C/s.

3.4.3 Effect of SC/HPDC UMSA Process Parameters on Average Solidification Temperature of Pure Aluminum

Figure 87 provides cooling curves and first derivatives for pure Aluminum test samples processed in the SC/HPDC UMSA under cyclic loading conditions, while Table 11 summarizes the Average Solidification Temperatures.

Table 11. Effect of SC/HPDC UMSA Process Parameters on Average Solidification Temperature for Pure Aluminum.

Runs #	Sample Ref. #	Applied Pressure, MPa			Average Solidification Temperature, ◦C
		P_{min}	P_{max}	Cycles #	
1	**0703b**	40	80	30	663.3
2	**0705**	50	110		664.6

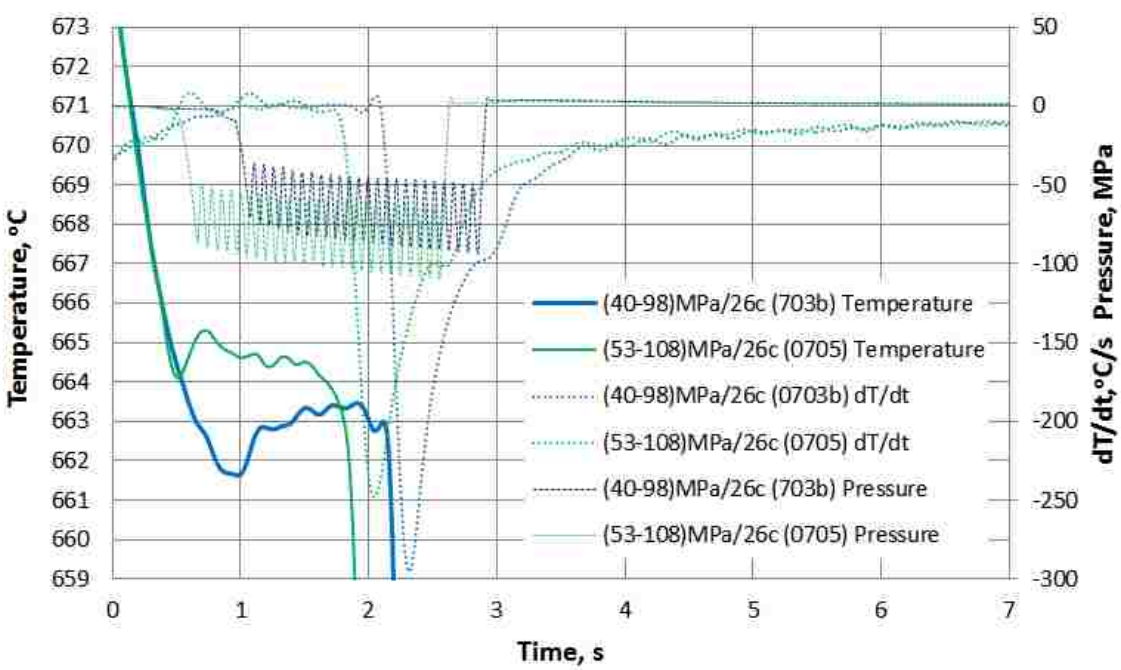

Figure 87. Cooling curves, first derivative curves and cyclic pressure profile curves vs. time for Pure Aluminum processed in the SC/HPDC UMSA die.

3.5 Metallographic Sample Preparation

Cast test samples were cut using a band saw along the longitudinal axis (in some cases in the transverse direction as well). It was possible to observe different microstructures on the top, bottom, edge and center of the cast components. The analytical sections will allow for observation of the gradient of the microstructures. Samples were hot mounted in Diallyl Phthalate at a pressure of 200 MPa and 150 ^{o}C. Samples were ground using a progression of SiC grit papers: 320, 800, 1200, 4000 grit, and polished using water based diamond suspensions Mol R3 DiaPro (3 μm). Water was used as the lubricant for the grinding stages. For final polishing OP-S colloidal silica suspension was used. After the grinding and polishing procedures, the samples were washed in water and finally, ultrasonically cleaned with ethyl alcohol (95 %).

The metallographic samples were used for LOM analysis, SEM, EDS, STEM, analysis and later for measurement of microhardness and macrohardness. LOM and some SEM metallographic observations were performed on the polished, unetched samples. Deep Etching was performed on selected samples using 40 % HCl acid for 3 minutes. The samples were rinsed in water and ethanol, and this was followed by a final ultrasound cleaning in acetone for 2 minutes.

3.6 Light Optical Microscopy (LOM) Analysis

Light Optical Microscopy (LOM) Analysis was performed using a LEICA DMRE microscope connected to a desktop computer and Leica QWin software. The imaging system was calibrated prior to testing to obtain accurate pixel: micron ratios. A stage micrometer with a 2 mm scale, 0.01 mm sub-divisions, a line width of 2.5 µm and accuracy ± 1.5 µm overall for LOM calibration was used.

3.7 Microhardness and Hardness Measurements

Microhardness testing was performed at the Ford Research and Innovation Center, in Michigan. Measurements were made using an Automatic Hardness Testing System (LECO AMH43) with microindentation testing in manual and semi-automatic configurations. The tester was used for indentations of 100 gf with a Vickers indenter according to the Standard Test Method for Knoop and Vickers Hardness of Materials, ASTM International designation E384-11 [260].

Macrohardness measurements were performed on the samples at the University of Windsor using a ROCKWELL Hardness Tester using a 100 kg load and a 1.587 mm diameter ball. Measurements were performed according to the Standard Test Method for Brinell Hardness of Metallic Materials, ASTM International designation E10 [261].

3.8 Scanning Electron Microscopy (SEM) Analysis

SEM Analysis was performed on selected samples at three different research facilities:

a) Silesian University of Technology, Gliwice, Poland

The microstructure investigation was performed using a Scanning Electron Microscope (SEM) **ZEISS Supra 25**. For microstructure evaluation, Secondary Electron (SE) detection was used with accelerating voltage of 5 ÷ 25 KV. Qualitative and quantitative chemical composition analysis in micro areas of the investigated samples was performed using an X-Ray microanalysis system. The samples (reference #0429, #0508, #0517) were analyzed on both the polished and deep etched surfaces.

b) Great Lakes Institute for Environmental Research, University of Windsor

Analysis was carried out using the FEI Quanta 200 FEG Environmental Scanning Electron microscope equipped with a Field Emission Gun (filament) for highest resolution, Everhart-Thornley Secondary Electron Detector, Solid State Backscatter Detector, Large Field Secondary Electron Detector and EDAX Octane Plus SDD Energy Dispersive Spectroscopy (EDS) X-Ray Detector. The samples were studied using the SEM in the polished and deep etched surface state in SE and BSE mode and Elemental analysis of selected experimental samples (Y1, 0925b-AA2, 0925b, 0808, 0618) were performed using EDS.

c) CanmetMATERIALS Technology, Hamilton, Ontario

CanmetMATERIALS provided SEM analysis using the **FEI Nova Nano SEM 650** ultra-high resolution Scanning Electron Microscope. SEM analysis for selected

experimental samples (Yamaha engine block, 0925b-AA2, 0925b) in the polished surface state was performed in SE and BS modes. Elemental analysis was performed using EDS.

3.9 Focused Ion Beam (FIB) Microscopy

The FIB technology provided by CanmetMATERIALS was used for thin foil preparation for transmission electron microscopy analysis**.** The selected test samples and the Yamaha engine block samples were produced using the Helios NANO LAB 650 Dual Beam Electron Microscope. The system contains both the focused Ga+ ion beam and a field emission scanning electron column.

3.9.1 S/TEM Sample Preparation

The samples for Scanning Transmission Electron Microscopy and Transmission Electron Microscopy (S/TEM) analysis were prepared at CanmetMATERIALS using the Helios NANOLAB 650 Dual Beam Electron Microscope. Step by step preparation of the samples is shown in Figure 88.

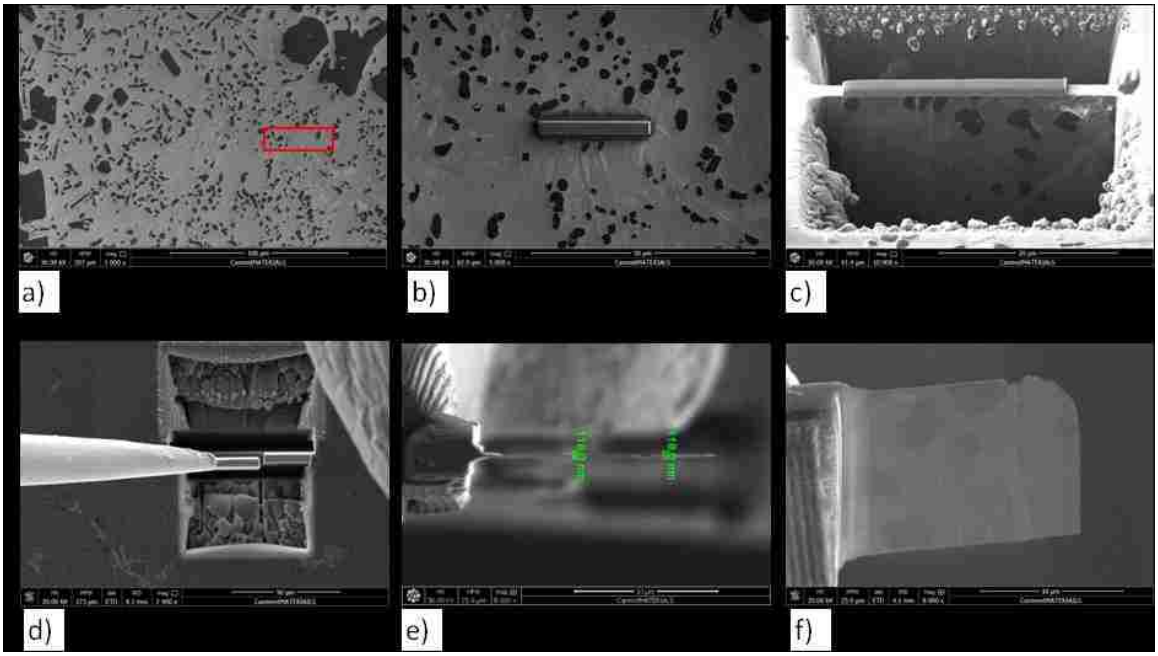

Figure 88. Preparation of the samples for S/TEM analysis; a) the area of interest is marked as a red rectangle, b) deposited platinum strip, c) the bulk material around the Pt strip was removed allowing for formation of the specimen slice, d) the Pt needle welded to the specimen slice allows for cutting and removal from the bulk sample, e) the sample slice was thinned by the ion beam, f) perpendicular view of the thin membrane having a thickness of 200 nm. The thinned specimen was welded to the copper grid for further S/TEM analysis.

3.10 Scanning/Transmission Electron Microscopy (S/TEM) Analysis

S/TEM Analysis on the selected samples (Y1, 0925b-AA2, 0925b) was performed in the CanmetMATERIALS laboratory using the FEI Tecnai Osiris Scanning/Transmission Electron Microscope (S/TEM). The S/TEM operates at 200 kV, in TEM and STEM modes. Mapping was done using a S/TEM in High Angle Annular Dark Field (HAADF) mode. Analysis included Selected Area Diffractions (SAD) and Energy Dispersive X-Ray Spectroscopy (EDS) line scans.

3.11 Design of HT and SC/HPDC UMSA Experiments

In order to quantify the solidification process for the unmodified and 0.15 wt.%Sr modified experimental alloy and relate the TA data to the as-cast structure characteristics, the HT UMSA Platform was used (see Table 12). The ambient pressure and the very low ASR allows for accurate analysis of the main metallurgical reactions needed for future comparison of the TA data rendered by the SC/HPDC UMSA processing samples under a very high SR and under dynamic melt loading conditions.

Table 13 summarizes the SC/HPDC UMSA designed process parameters used for the development of novel structures of the test samples.

The HT UMSA Platform's ultra rapid Solution Treatment and Artificial Aging process parameters are presented in Table 14 and Table 15, respectively.

Table 12. HT UMSA Tests for the Experimental Alloy used for Comprehensive TA Data and Microstructure Analysis.

Runs #	Sample Ref. #	Test Sample	[redacted] MPa	ASR °C/s
1	**0808**	Unmodified Experimental Alloy	0.1	<0.6
[redacted]	**0618**	0.15 wt.% Sr Modified Experimental Alloy		

Table 13. SC/HPDC UMSA Test Processing Parameters for the Development of Novel Structures.

Runs #	Sample Ref. #	Sr wt.%	Applied Pressure, MPa				Temperature, °C			
			Impact	P_{min}	P_{max}	Cycles #	T^D_I	T^P_{ST}	[redacted]	T^P_{END}
1	**0717**	0.00	x	0.1		0	265±18	N/A		
2	**0508**	0.10	x							
3	**0925**	0.15	x							
4	**0429**	0.00	2.0	50	70	10		610	605	570
5	**1009**	0.04	50.0	40	80	10		625	620	570
6	**0925b**	0.15	26.6	40	80	10		620	610	560
7	**0916**		20.0	0	20	1		630	620	620
[redacted]	**0916b**		25.0		25	2		635		605
[redacted]	**0628b**		1.2	40	80	45		660	650	550
10	**0919**		36.6	40	80	10		635	620	565
11	**1002b**		35.7					620	615	560
[redacted]	**0517**		30.0	0	30	1.5	[redacted]	655	630	

Table 14. HT UMSA Processing Parameters using Ultra Rapid Two and Three Step Solution Heat Treatment Tests for the Sr Modified Experimental Alloy.

Runs #	Sample Ref. #	Step 1		Step 2		Step 3	
		Temperature °C	Time min	Temperature °C	Time min	Temperature °C	Time min
1	**1022**	506	5	512	3	530	2
2	**1023**		6		4	x	
3	**1024**		5		2		

Table 15. HT UMSA Processing Parameters for Ultra Rapid Artificial Aging Tests for the Sr Modified Experimental Alloy.

Runs #	Sample Ref. #	Step 1		Step 2	
		Temperature, °C	Time, min	Temperature, °C	Time, min
1	**0925b-AA1**	200	10	110	20
2	**0925b-AA2**			x	

CHAPTER 4: EXPERIMENTAL RESULTS and DATA ANALYSIS

4.1 Thermal and Microstructural Analysis of Experimental Alloy, Sample #0808 – Unmodified Melt Solidified at 0.1 MPa and ASR = 0.4 °C/s

Thermal and microstructural analyses were conducted on the unmodified experimental alloy solidified in the HT/UMSA under atmospheric pressure (0.1 MPa) and a slow SR = 0.4 ºC/s, for identification of the thermal events during solidification and for identification of the as-cast phases. This sample was used as a reference for experimental samples solidified at higher ASR ≈ 10 ºC/s at 0.1 MPa and high ASR ≈ 25 ºC/s and various dynamic pressure melt loading.

4.1.1 HT UMSA Thermal Characteristics for Sample #0808

Experimental melt solidification process was carried out using the HT UMSA Platform. General and detailed TA characteristics for all detected metallurgical events and the analytical/metallurgical interpretation are summarized in Figures 89-96 and in Table 16, while the corresponding representative LOM and SEM structures are presented in Figures 97 (a - f) and 98 (a, b).

According to Figure(s) 89 (a, b) and 90, T_{liq} = 622.8 °C @ SR = 1.9 °C/s signifies the nucleation of the predominantly hexagonal primary Si particles and the lower volume fraction of the primary Si particles having a polyhedral shape with a diameter of (100 to 250) μm (see Figure 97 a, b, c, d), The T^{PSi}_{MIN} and T^{PSi}_{G} temperatures

are practically identical at 585.0 °C and 585.1 °C, respectively. ΔT^{PSi}_{UC} = 37.8 °C, while aT^{PSi}_{END} = 578.3 °C and $at^{PSi}_{END} \approx$ 46.4 s. This length of time associated with the primary Si reaction is due to SR ≈ 0.0 °C/s, associated with the Primary Si Growth Temperature (T^{PSi}_{G}). The Apparent ASR for the primary Si reaction $aASR^{PSi}$ = 0.9 °C/s. The DBL represents the experimental FD of the CC curve that does not go through any metallurgical transformations during the solidification process. It is interesting to note that the calculated ASR using the DBL for this experimental melt shows that if this melt would solidify without the formation of primary Si particles then the $aASR^{PSi}$ would be approx. 1.9 °C/s. This significant difference illustrates the exothermic heat effect during formation of the primary Si phases. A very low SR of primary Si particles allows them to grow to macroscopic size. Deconvolution of the primary Si peak will reveal that the primary Si formation time is even longer. The recalescence temperature of primary Si is negligible and equal to 0.1 °C. Apparent Temperature at the End of the Primary Si reaction (aT^{PSi}_{END}) is approx. 578.3 °C, and this temperature is considered as the Nucleation Temperature of the β-Fe phase ($T^{\beta\text{-}Fe}_{NUC}$). Figure 97 (a – d) presents the primary Si structures, while Figure 97f shows β-Fe needles (β-Al_5FeSi plates in 3D) intertwined with the other phases that nucleate further and use β-Fe needles and/or primary Si particles as the substrate. The Apparent Al-Si Eutectic Nucleation Temperature, $aT^{AlSi}_{E,NUC}$ = 564.2 °C @ SR = -0.2 °C/s, while $T^{AlSi}_{E,MIN}$ = 563.0 °C @ SR = 0.0 °C/s and $T^{AlSi}_{E,G}$ = 563.1 °C @ SR = 0.0 °C/s, see Figures 90-94. Therefore, $\Delta T^{AlSi}_{E,R}$ = 0.1 °C. These TA characteristics suggest the formation of coarse unmodified eutectic Si plates ≈ 5 μm x100 μm as depicted in Figure 97a. Solidus Temperature, T_{sol} = 489.2 °C @ SR = -1.3 °C/s. Solidification Range SRn = 133.6 °C, while the

experimental melt's Solidification Time St = 336.2 s. The processing characteristics summarized above, the TA data, and the respective structural characteristics are used as the baseline for comparison with other processed melts.

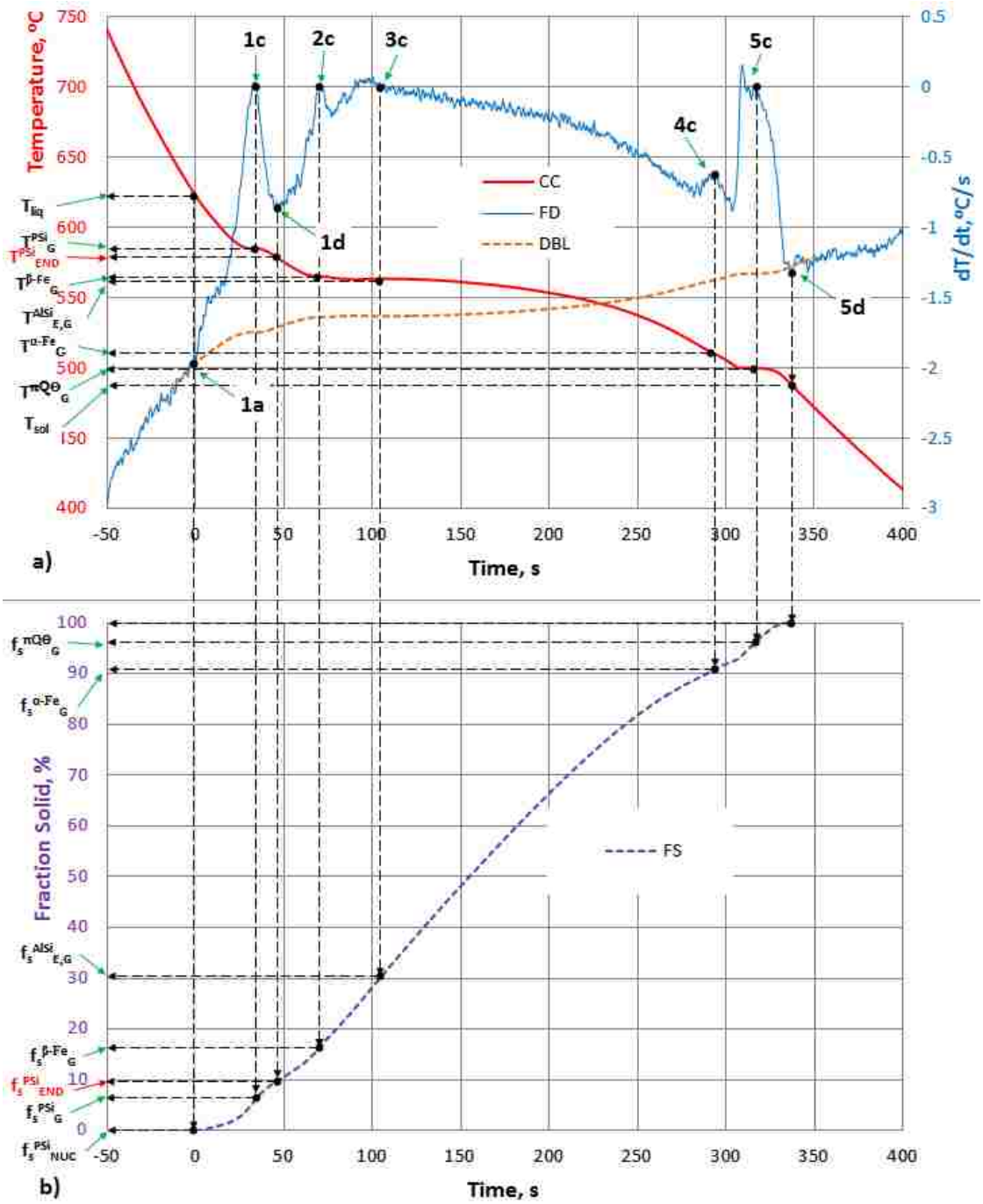

Figure 89. (a, b). a) Cooling/Solidification Curve superimposed with the First Derivative and Dynamic Baseline vs. Time and b) Fraction Solid Curve vs. Time for the unmodified experimental alloy, solidified under atmospheric pressure in the HT UMSA Platform, ASR = 0.4 °C/s, ref. #0808.

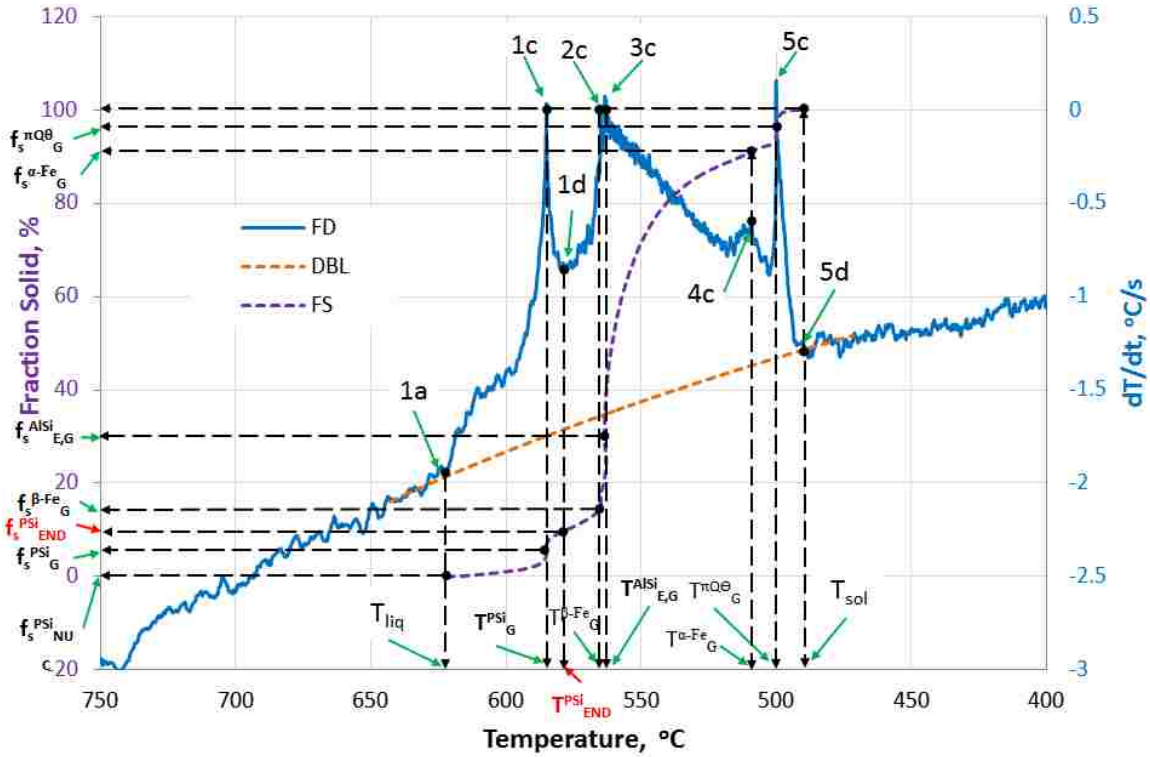

Figure 90. First derivative of the Cooling/Solidification Curve and Fraction Solid Curve vs. Temperature for the unmodified experimental alloy, solidified under atmospheric pressure in the HT UMSA Platform, ASR = 0.4 °C/s, ref. #0808.

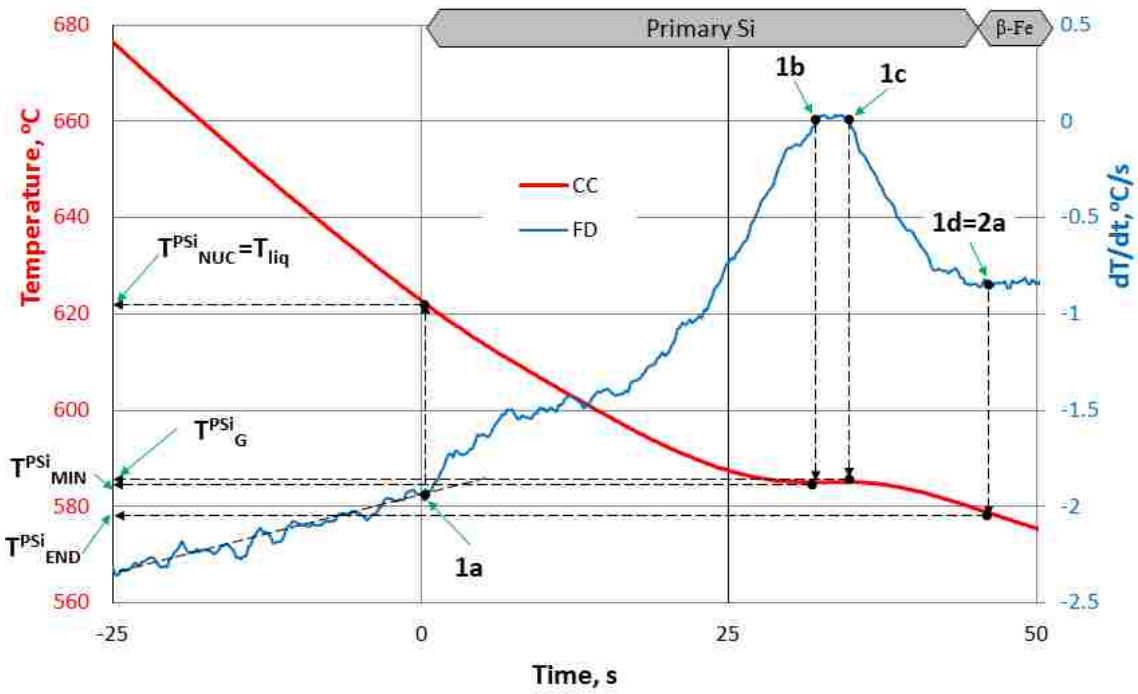

Figure 91. Cooling/Solidification and First Derivative Curves (region of primary Si and β-Fe phase nucleation and growth) vs. Time for the unmodified experimental alloy, solidified under atmospheric pressure in the HT UMSA Platform, ASR = 0.4 °C/s, ref. #0808.

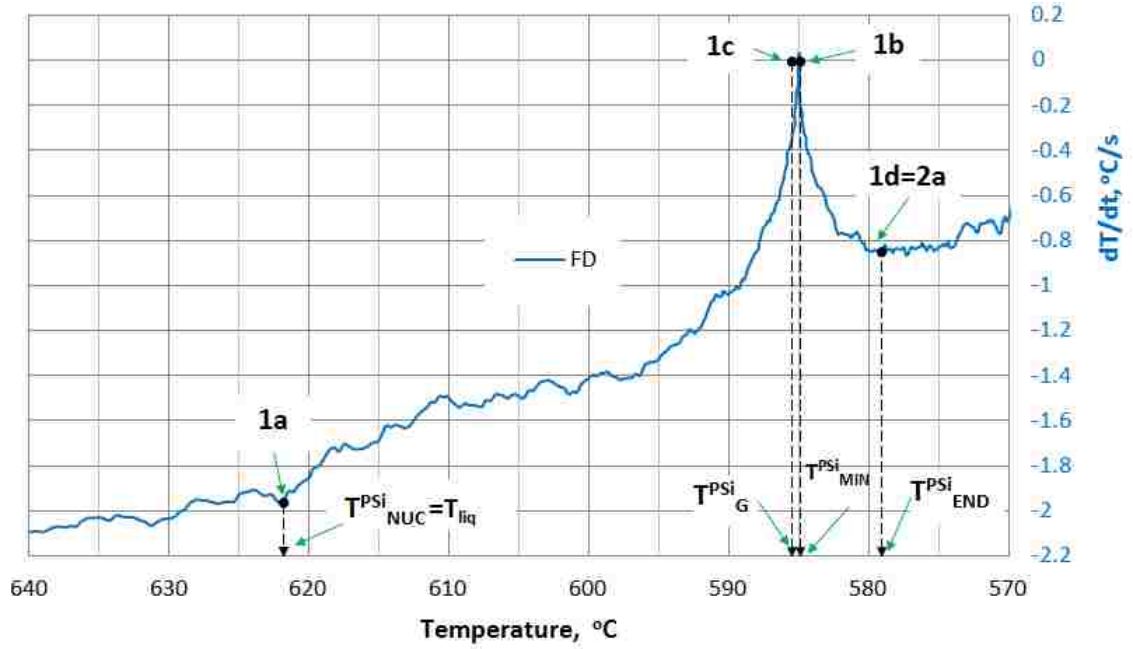

Figure 92. First derivative of the Cooling/Solidification Curve (region of primary Si and β-Fe phase nucleation and growth) vs. Temperature for the unmodified experimental alloy, solidified under atmospheric pressure in the HT UMSA Platform, ASR = 0.4 °C/s, ref. #0808.

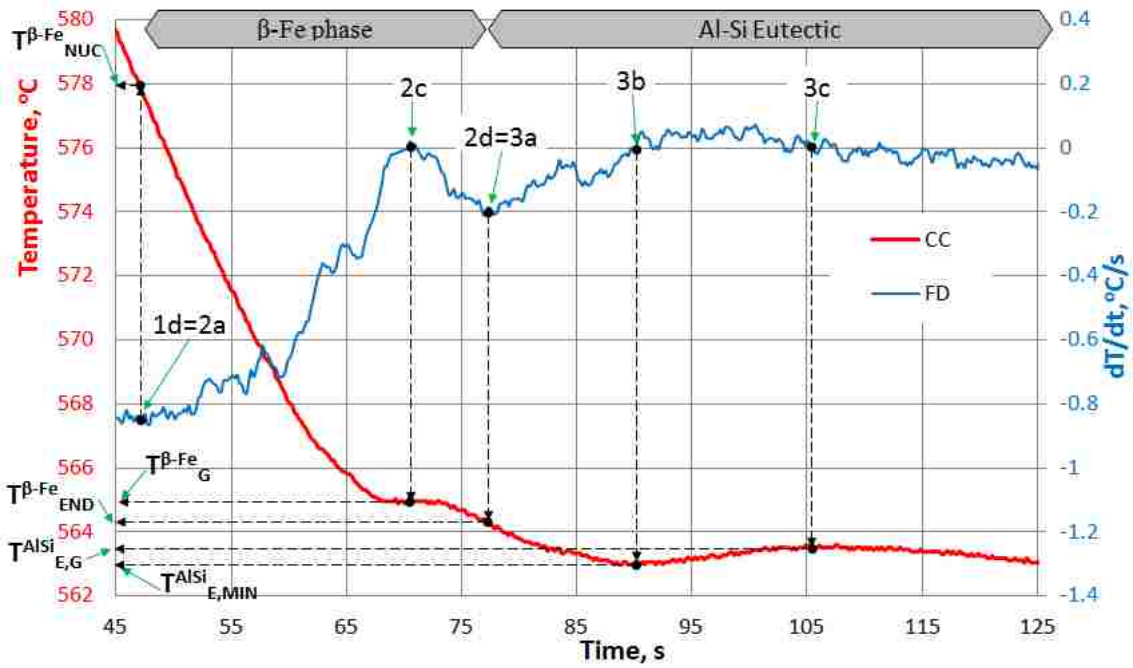

Figure 93. Solidification and First Derivative Curves (region of β-Fe phase and Al-Si Eutectic nucleation and growth) vs. Time for the unmodified experimental alloy solidified under atmospheric pressure in the HT UMSA Platform, ASR = 0.4 °C/s, ref. #0808.

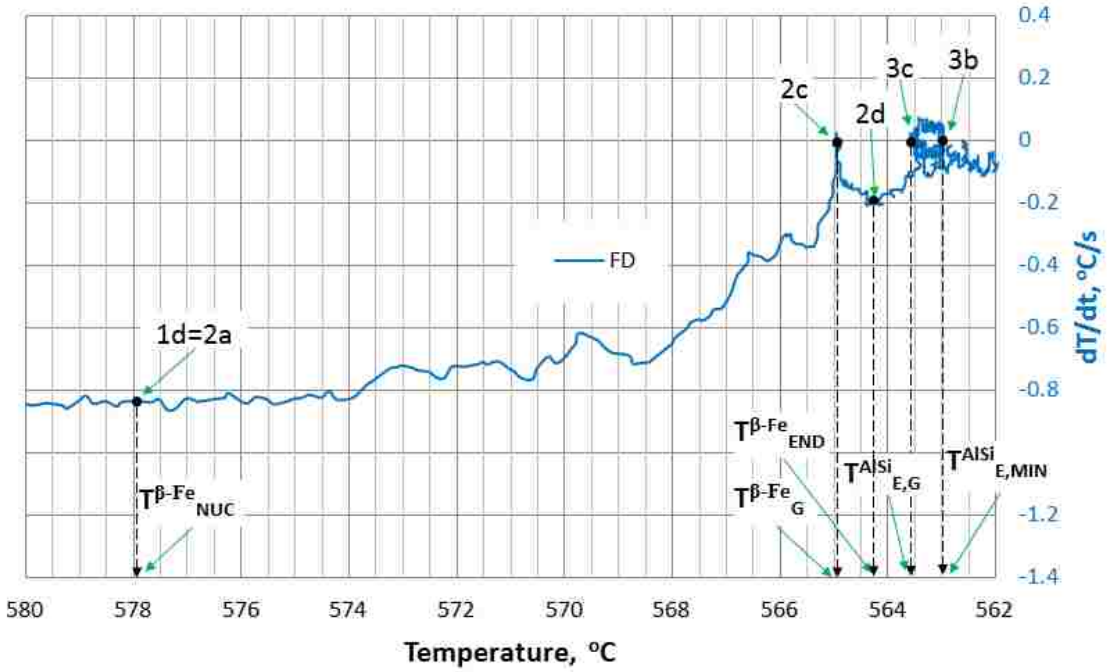

Figure 94. First derivative of the Cooling/Solidification Curve (region of β-Fe phase and Al-Si Eutectic nucleation and growth) vs. Temperature for the unmodified experimental alloy, solidified under atmospheric pressure in the HT UMSA Platform, ASR = 0.4 °C/s, ref. #0808.

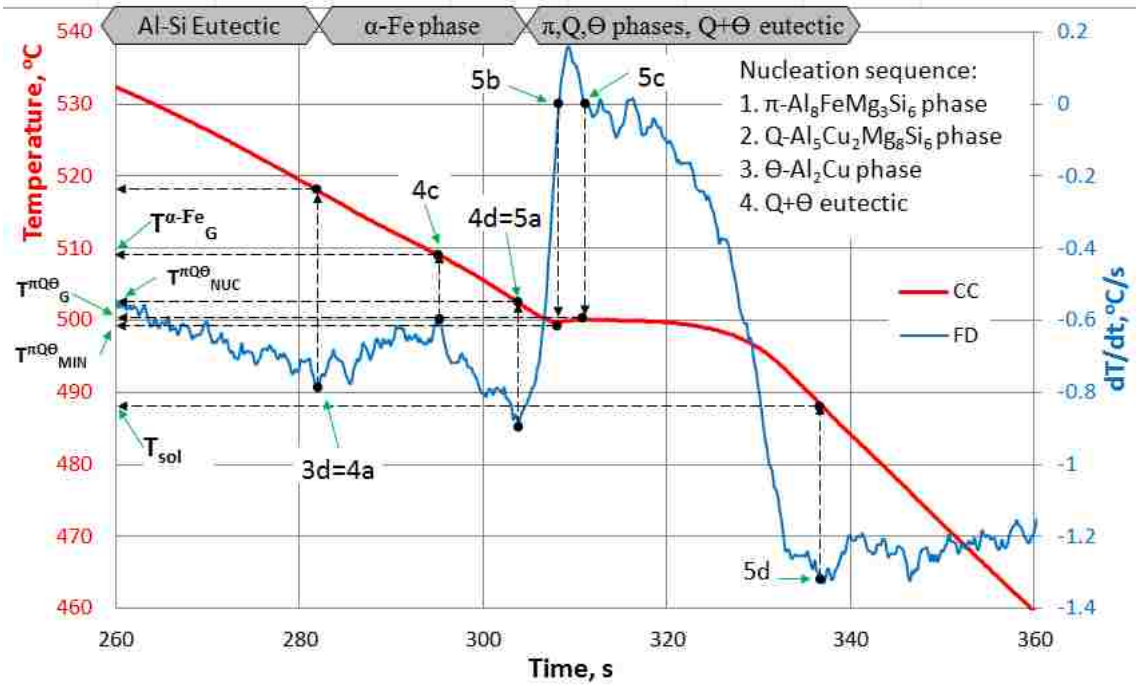

Figure 95. Solidification and First Derivative Curves (regions: Al-Si eutectic, α-Fe, π, Q, Θ phases and (Q+Θ) eutectic nucleation and growth and Solidus temperature) vs. Time for the unmodified experimental alloy, solidified under atmospheric pressure in the HT UMSA Platform, ASR = 0.4°C/s, ref. #0808.

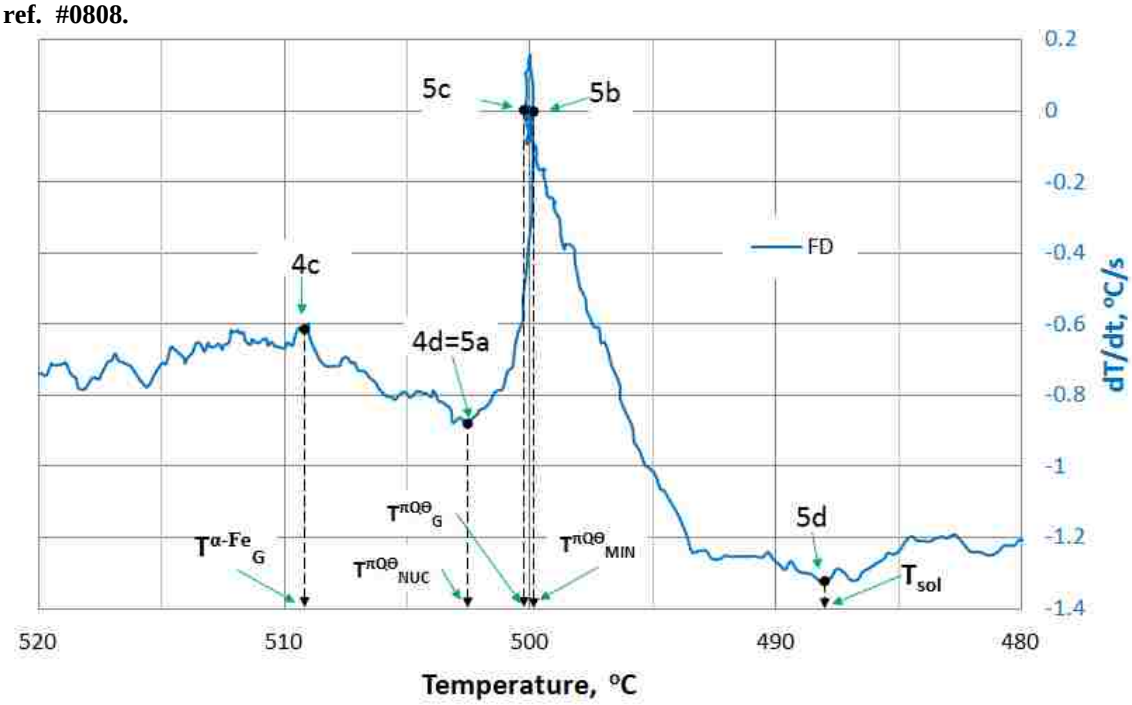

Figure 96. First derivative of the Solidification/Cooling Curve (Regions: Al-Si Eutectic, α-Fe, π, Q, Θ phases & (Q+Θ) eutectic growth and Solidus temperature) vs. Temperature for the unmodified experimental alloy, solidified under atmospheric pressure in the HT UMSA Platform, ASR =0.4 °C/s, ref. #0808.

Table 16. Thermal Analysis Events during Solidification of the Unmodified Experimental Alloy in the HT UMSA Platform under Atmospheric Pressure, ASR = 0.4 °C/s, ref. #0808.

#	Symbol	TA Event	Detection Algorithm	Comments
1a	T^{PSi}_{NUC} = T_{liq}	Primary Si Nucleation Temperature = Liquidus Temperature	At T_{liq} CC changing slope and T_{liq} is detected on FD curve as 1st deflection, and is determined by intersection of the FD with the DBL.	At T_{liq} f_s= 0 %
1b	T^{PSi}_{MIN}	Primary Si Minimum (Undercooling) Temperature	T^{PSi}_{MIN} is the local minimum on the CC and on the FD curve as a 1st point where dT/dt = 0. After passing of the T^{PSi}_{MIN} point the melt temperature increases to a steady state T^{PSi}_{G}.	In this state nucleated Primary Si has grown to such an extent that liberated LH of fusion balances the heat extracted from the test sample.
1c	T^{PSi}_{G}	Primary Silicon Growth Temperature	T^{PSi}_{G} is a local maximum on the CC and on the FD curve as a 2nd zero point where dT/dt = 0. If the FD curve does not intersect the zero line then the $T^{PSi}_{MIN} = T^{PSi}_{G}$ and corresponds to the maximum point on the FD curve.	The time period required to heat up the test sample from T^{PSi}_{MIN} to T^{PSi}_{G} is called recalescence.
	ΔT^{PSi}_{UC}	Undercooling Temperature of Primary Si	$\Delta T^{PSi}_{UC} = T_{liq} - T^{PSi}_{MIN}$	
	Δt^{PSi}_{UC}	Undercooling Duration of Primary Si	$\Delta t^{PSi}_{UC} = t_U - t_{liq}$	
	ΔT^{PSi}_{R}	Recalescence Temperature of Primary Si	$\Delta T^{PSi}_{R} = T^{PSi}_{G} - T^{PSi}_{MIN}$	
	Δt^{PSi}_{R}	Primary Si Recalescence Duration	$\Delta t^{PSi}_{R} = t^{PSi}_{G} - t^{PSi}_{MIN}$	
1d	aT^{PSi}_{END}	Apparent Temperature at the end of the Primary Si Reaction	At the aT^{PSi}_{END} is an inflection point on the CC and this is manifested as the minimum on the FD curve.	It is assumed that the primary Si reaction is completed. Deconvolution provides more accurate data.

Table 16 – Continued				
#	Symbol	TA Event	Detection Algorithm	Comments
1d=2a	$aT^{\beta\text{-Fe}}_{NUC}$	β-Fe phase nucleation Temperature	$aT^{\beta\text{-Fe}}_{NUC}$ is an inflection point on the CC and is manifested as the minimum on the FD curve.	At this temperature the β-Fe phase (ß-Al_5FeSi) is nucleating needles (2D section) and plates in the 3D section.
2c	$T^{\beta\text{-Fe}}_{G}$	β-Fe phase Growth Temperature	$T^{\beta\text{-Fe}}_{G}$ is an inflection point on CC and is manifested as a peak maximum point on the FD curve.	At this temperature a considerable amount of β-Fe phase is being formed.
2d	$aT^{\beta\text{-Fe}}_{END}$	Apparent end of β-Fe Reaction Temperature	$aT^{\beta\text{-Fe}}_{END}$ is signified as an inflection point on the CC and is manifested as the local minimum on the FD curve.	At this point it is assumed that β-Fe reaction is completed. Deconvolution provides more accurate data.
2d=3a	$T^{AlSi}_{E,NUC}$	Al-Si Eutectic Nucleation Temperature	At $T^{AlSi}_{E,NUC}$, CC changing slope and is detected on the FD curve as the local minimum.	At this point a stable nucleation of co-precipitating first eutectic Si crystals and Al from melt begins.
3b	$T^{AlSi}_{E,MIN}$	Al-Si Eutectic Minimum Temperature	$T^{AlSi}_{E,MIN}$ is the local minimum on the CC and on the FD curve the 1st point where dT/dt = 0. After passing of the $T^{AlSi}_{E,MIN}$, melt temperature increases to a steady state $T^{AlSi}_{E,G}$.	At the $T^{AlSi}_{E,MIN}$ the latent heat generated due to the Al-Si eutectic growth equals the heat loss from the test sample.
3c	$T^{AlSi}_{E,G}$	Al-Si Eutectic Growth Temperature	$T^{AlSi}_{E,G}$ is the local maximum on the CC and 2nd zero on the FD curve. If the FD curve does not intersect the zero line then the $T^{AlSi}_{E,MIN} = T^{AlSi}_{E,G}$ and corresponds to the maximum on the FD curve.	The time period required to heat up the test sample from $T^{AlSi}_{E,MIN}$ to $T^{AlSi}_{E,G}$ is called the Al-Si eutectic recalescence.
	$\Delta T^{AlSi}_{E,R}$	Recalescence Temperature of Al-Si Eutectic	$\Delta T^{AlSi}_{E,R} = T^{AlSi}_{E,G} - T^{AlSi}_{E,MIN}$	

Table 16 - Continued				
#	**Symbol**	**TA Event**	**Detection Algorithm**	**Comments**
	$\Delta t^{AlSi}_{E,R}$	Al-Si Eutectic Recalescence Duration	$\Delta t^{AlSi}_{E,R} = t^{AlSi}_{E,G} - t^{AlSi}_{E,MIN}$	
3d	$aT^{AlSi}_{E,END}$	Apparent Temperature at the end of the AlSi Eutectic Reaction	At the $aT^{AlSi}_{E,END}$ is an inflection point on the CC which is manifested as the local minimum on the FD curve.	At this point it is assumed that the AlSi eutectic reaction is completed. Detailed TA data is available from the deconvoluted FD.
3d=4a	$T^{\alpha\text{-}Fe}_{NUC}$	α-Fe phase Nucleation Temperature	At $T^{\alpha\text{-}Fe}_{NUC}$, the CC changing slope is detected on the FD curve as a local minimum.	At this temperature the α-$Al_{15}(FeMn)_3Si_2$ phase is in the form of chinese script nucleating.
4c	$T^{\alpha\text{-}Fe}_{G}$	α-Fe phase Growth Temperature	$T^{\alpha\text{-}Fe}_{G}$ is an inflection point on the CC and the maximum on the FD curve.	At this temperature a considerable amount of α-Fe phase is being formed.
4d	$aT^{\alpha\text{-}Fe}_{END}$	Apparent Temperature at the end of α-Fe phase Reaction	At the $aT^{\alpha\text{-}Fe}_{END}$ is an inflection point on the CC which is manifes-ted as a local mini-mum on the FD curve.	At this point it is assumed that α-Fe phase reaction is completed. Detailed TA data is available from the deconvoluted FD.
4d=5a	$T^{\pi Q\Theta}_{NUC}$	π,Q,Θ phases & Q+ Θ eutectic Nucleation Temperature	At $T^{\pi Q\Theta}_{NUC}$, the CC changing slope is detected on the FD curve as a local minimum.	The following phases nucleate and grow in a narrow temperature range of 503-488ºC under the FD peak #5. The actual nucleation and the end of individual reactions can be determined by de-convolutuion of peak #5. Presently it is assumed that $aT^{\pi Q\Theta}_{NUC}$ of the 1st phase is associated with point #5a. The following phases nucleate under the FD peak #5. π-$Al_8FeMg_3Si_6$ phase, Q-$Al_5Cu_2Mg_8Si_6$ phase, Θ-Al_2Cu phase and , Q+ Θ eutectic.

Table 16 - Continued				
#	**Symbol**	**TA Event**	**Detection Algorithm**	**Coments**
5b	$T^{\pi Q\Theta}_{MIN}$	π,Q,Θ phases & Q+ Θ Eutectic Minimum Temperature	$T^{\pi Q\Theta}_{MIN}$ is the local minimum on the CC and on the FD curve the 1st point where dT/dt = 0. After passing of the $T^{\pi Q\Theta}_{MIN}$, the melt temperature increases to a steady state $T^{\pi Q\Theta}_{G}$.	At the $T^{\pi Q\Theta}_{MIN}$ the latent heat generated due to the AlFeMgCuSi rich phase growth equals the heat loss from the test sample.
5c	$T^{\pi Q\Theta}_{G}$	π,Q,Θ phases & Q+Θ Eutectic Growth Temperature	$T^{\pi Q\Theta}_{G}$ is the local maximum on the CC and the 2nd zero on the FD curve. If the FD curve does not intersect the zero line then the $T^{\pi Q\Theta}_{MIN} = T^{\pi Q\Theta}_{G}$ and corresponds to the maximum on the FD curve.	The maximum point of the recalescence. At this temperature a considerable amount of π-$Al_8FeMg_3Si_6$ phase, Q-$Al_5Cu_2Mg_8Si_6$ phase and Θ-Al_2Cu phases are being formed.
	$\Delta T^{\pi Q\Theta}_{R}$	Recalescence Temperature of π,Q,Θ phases &Q+ Θ Eutectic	$\Delta T^{\pi Q\Theta}_{R} = T^{\pi Q\Theta}_{G} - T^{\pi Q\Theta}_{MIN}$	
	$\Delta t^{\pi Q\Theta}_{R}$	π,Q,Θ phases & Q+ Θ Eutectic Recalescence Duration	$\Delta t^{\pi Q\Theta}_{R} = t^{\pi Q\Theta}_{G} - t^{\pi Q\Theta}_{MIN}$	
5d	$T^{\pi Q\Theta}_{END} = T_{sol}$	Solidus Temperature	At the T_{sol} is an inflection point on the CC which is the local minimum on the FD curve.	Temperature at which full solidification occurs. f_s= 100 %

Note: It is apparent that after the assigned point (#5d) as T_{sol} there is small peak to which a specific phase was not assigned. Further research needs to be conducted in order to determine the specific phase associated with this peak.

4.1.2 Microstructural Characterization of Sample #0808

UMSA thermal data are summarized in Figures 89 (a, b) - 96. Figures 97 (a - f) and 98 (a, b) which show LOM and SEM representative microcgraphs taken from the as-cast HT UMSA samples. The main phases associated with various peaks are as follows:

Peak #1. **Primary Si** nucleates as a first phase (T_{liq} = 622.8 °C, Figures 89a - 92) mostly in polyhedral shaped particles with a diameter of 100-250μm, Figures 97 (a - d). The **Al halo** forms around the Primary Si until the local composition reaches the skewed coupled zone and stable Al-Si eutectics form (see Figures 97 a, c, d). Apparent Fraction Solid (af_s) of Primary Si particles is approx. 9 %.

Peak #2**.** The **β-Al_5FeSi** phase forms needle-like particles (the size is 2 x70 μm) see Figure 97 f. $T^{\beta\text{-Fe}}_G$ = 564.9 °C. The af_s of β-Al_5FeSi phase is approx. 2 %.

Peak #3. The **Al-Si Eutectic** is a mixture of the Al and Si phases which are present in the form of a lamellar structure growing in a faceted manner, (the size is approximately 10 x 150 μm), see Figures 97 f, 98 (a, b). The Eutectic Al phase is the main phase that forms and is initialized by nucleation and growth of the eutectic silicon particles. $T^{AlSi}_{E,G}$ = 563.1 °C. The af_s of Al-Si Eutectic is approx. 70 %.

Peak #4. The **α-$Al_{15}(Mn,Fe)_3Si_2$** phase is commonly known as a Chinese script-like shape (the size is approx. 50 x 80 μm), see Figures 97 e, 98 a. $T^{\alpha\text{-Fe}}_G$ = 509.1 °C. The af_s of α-$Al_{15}(Mn,Fe)_3Si_2$ is approx. 3 %.

Peak #5. **The π-$Al_8FeMg_3Si_6$**, **Q-$Al_5Cu_2Mg_8Si_6$**, **θ-Al_2Cu** phases and **Q+Θ eutectic** nucleate and grow in the temperature range of (503 to 489) ºC under the FD peak #5, see Figures 97 (e, f) and 98 (a, b). The af_s of π-$Al_8FeMg_3Si_6$, Q-$Al_5Cu_2Mg_8Si_6$, θ-Al_2Cu phases and Q+ Θ eutectic is approx. 8 %.

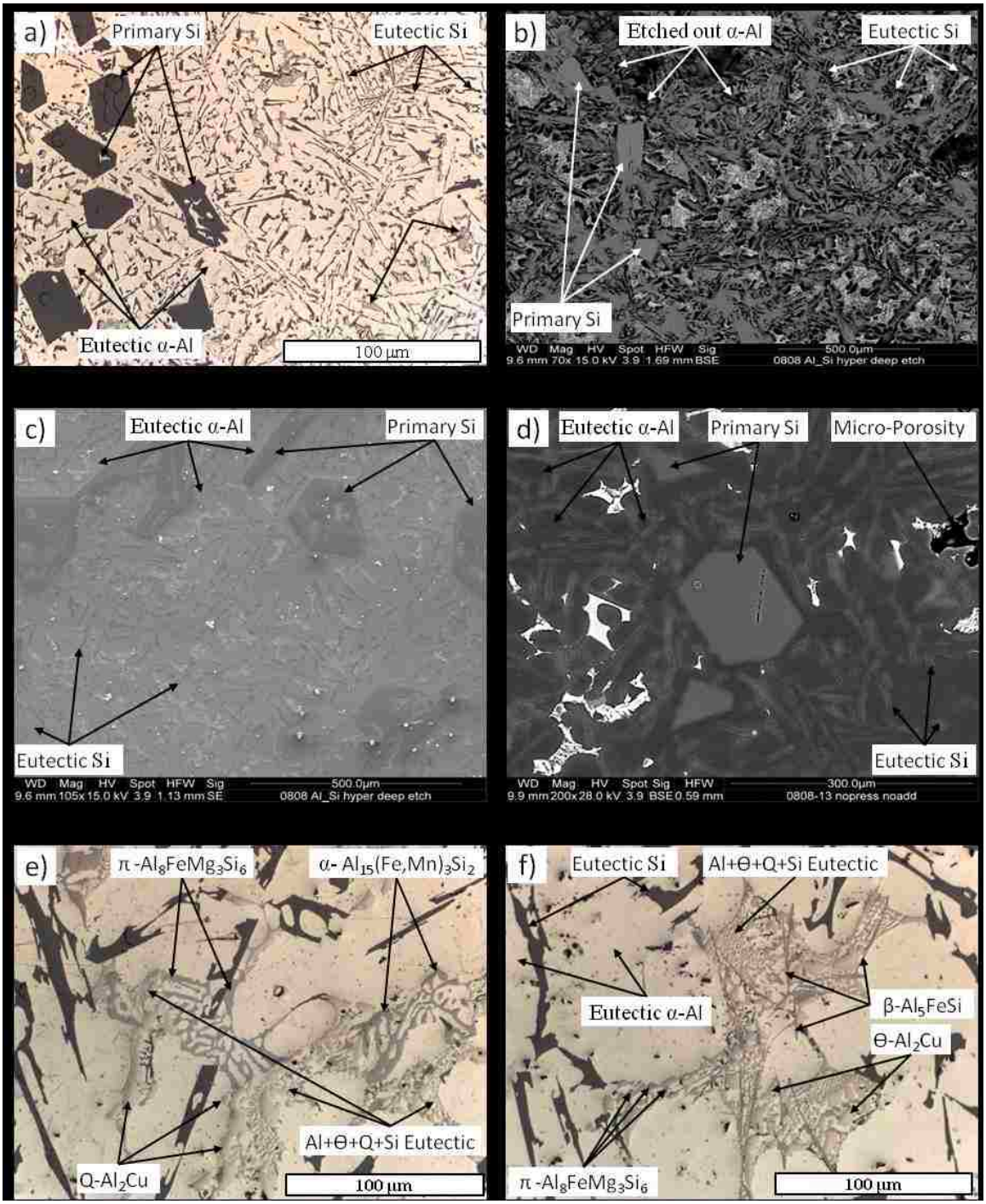

Figures 97. The as-cast micrographs for the unmodified experimental alloy solidified in the HT UMSA Platform under atmospheric pressure and at ASR = 0.4 ^{o}C/s; a,e,f) LOM micrographs/polished, b) SEM micrographs/deep-etched, c,d) SEM micrographs/polished, ref.#0808.

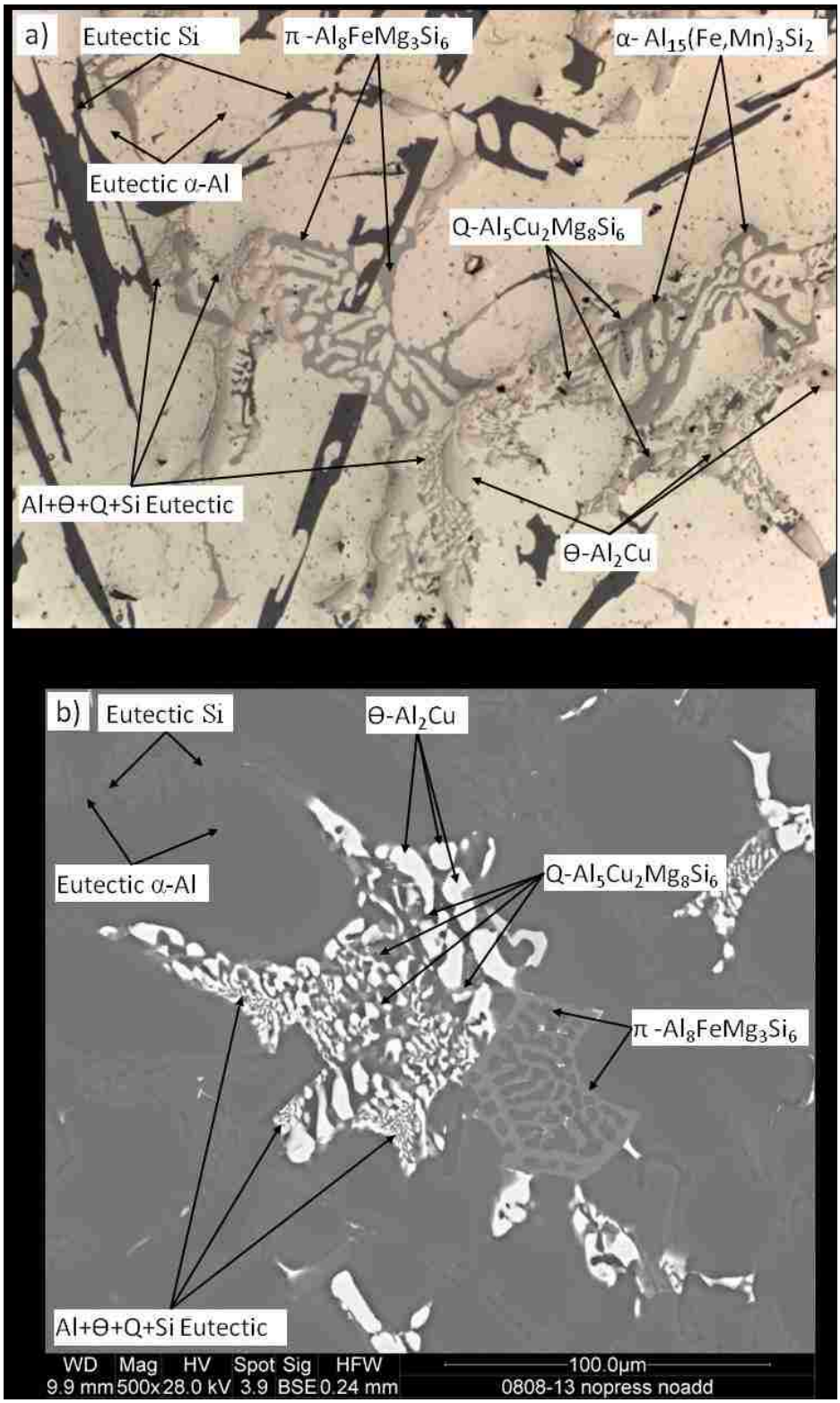

Figure 98. a) LOM and b) SEM micrographs of the polished test sample for the unmodified experimental alloy solidified in the HT UMSA Platform under atmospheric pressure and at ASR = 0.4 ^{o}C/s, ref. #0808.

4.1.3 HT UMSA Thermal Characteristics of Sample #0618

Addition of 0.15 wt%Sr to the experimental melt processed under identical conditions like the unmodified melt resulted in the fundamentally different thermal events and structural characteristics which are presented in Figures 99 (a, b) to 104 and 105-106. Table 17 summarizes the details of the TA events of the solidification process.

The Melt Superheat Temperature was 800.0 °C. Above the experimental melt's Liquidus Temperature, Sr partially reacted with Si and Al forming sparsely distributed $SrSi_2Al_2$ particles; see Figure 105a. Sr rich particles consumed some of the added Sr that did not contribute to the Si modification process. Therefore, the amount of Sr content is called "dead Sr". According to the literature, $SrSi_2Al_2$ particles nucleate at a temperature above the alloys liquidus temperature. The HT UMSA recorded T_{liq} = 606.9 °C and it is associated with the formation of approx. 1 % primary Si particles (significantly lower in comparison with the unmodified melt), see Figures 99 (a, b) - 102. Localized Primary Si particles predominately nucleate on the Al_2O_3 film and/or in its close vicinity. Figure 105c as well as a few Primary Si particles were found near the sample edge, Figure 105 b. Apparent Temperature at the End of the Primary Si Reaction = 568.2 °C @ SR = -1.15 °C/s. This temperature coincides with the Apparent Nucleation of α-Al & β-Fe phases see Figure 101. The α-Al phases nucleate first at the surface of the test sample in the form of semi grains and under developed equiaxed dendrites, while in the center, α-Al dendrites are well developed and are up to 600 μm in length. The β-Fe phase (Al_5FeSi) is present in the 2D needles form having a length of 500 μm; see Figures 105 (e, f) and 106 (a, b). For details of the thermal characteristics please refer to Table 17.

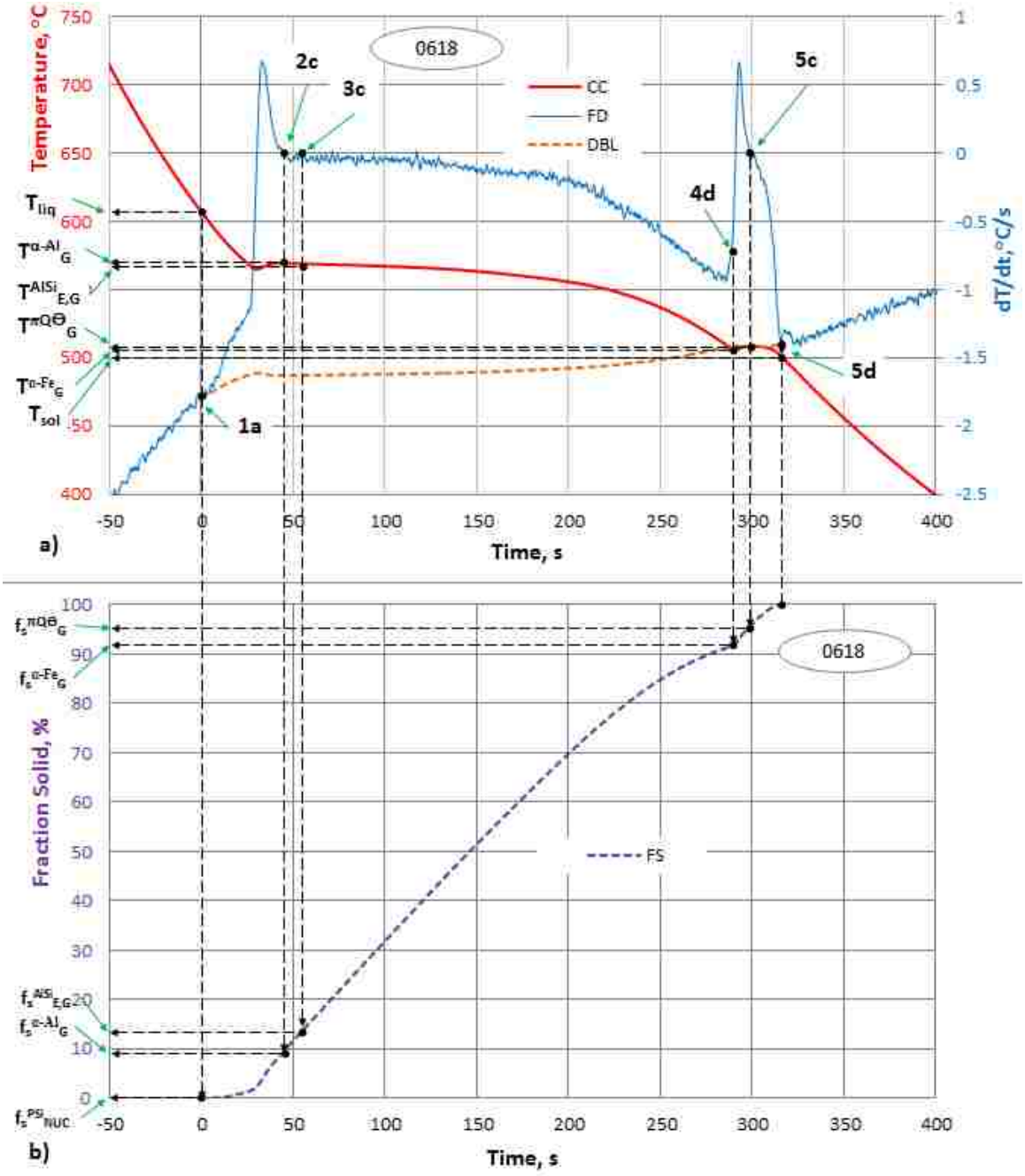

Figure 99. a) Cooling/Solidification Curve superimposed with the First Derivative and the Dynamic Baseline and b) Fraction Solid Curves vs. Time for the 0.15 wt.%Sr modified experimental alloy, solidified under atmospheric pressure in the HT UMSA Platform, ASR = 0.4 °C/s, ref. #0618.

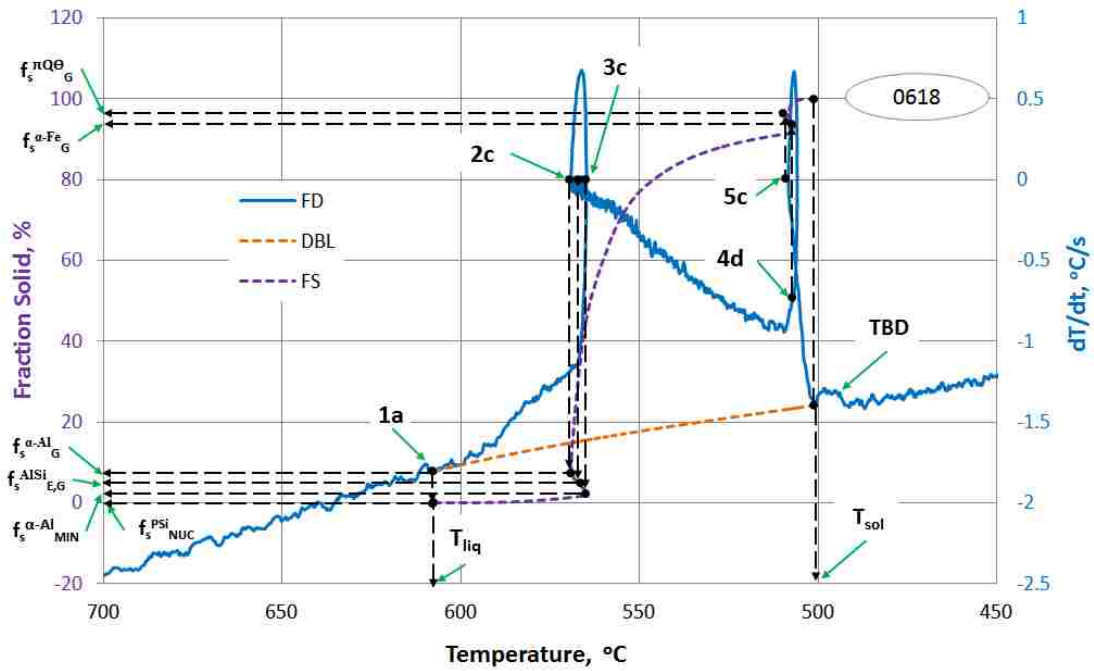

Figure 100. First Derivative of the Cooling/Solidification Curve and Fraction Solid and the DBL Curves vs. Temperature for the 0.15 wt.%Sr modified experimental alloy, solidified under atmospheric pressure in the HT UMSA Platform, ASR = 0.4 °C/s, ref. #0618.

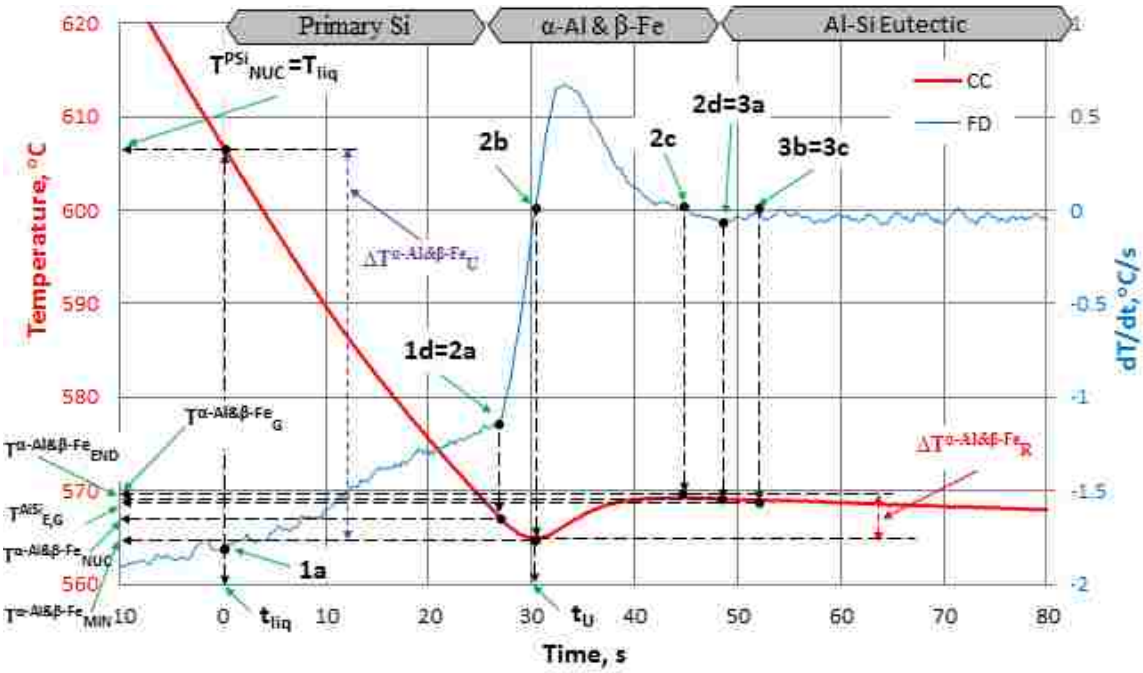

Figure 101. Cooling/Solidification and First Derivative Curves (region of Liquidus and Recalescence and Undercooling Temperatures associated with α-Al Phase Nucleation and Growth) vs. Time for the 0.15 wt.%Sr modified experimental alloy, solidified in the HT UMSA Platform under atmospheric pressure and ASR = 0.4 °C/s, ref. #0618.

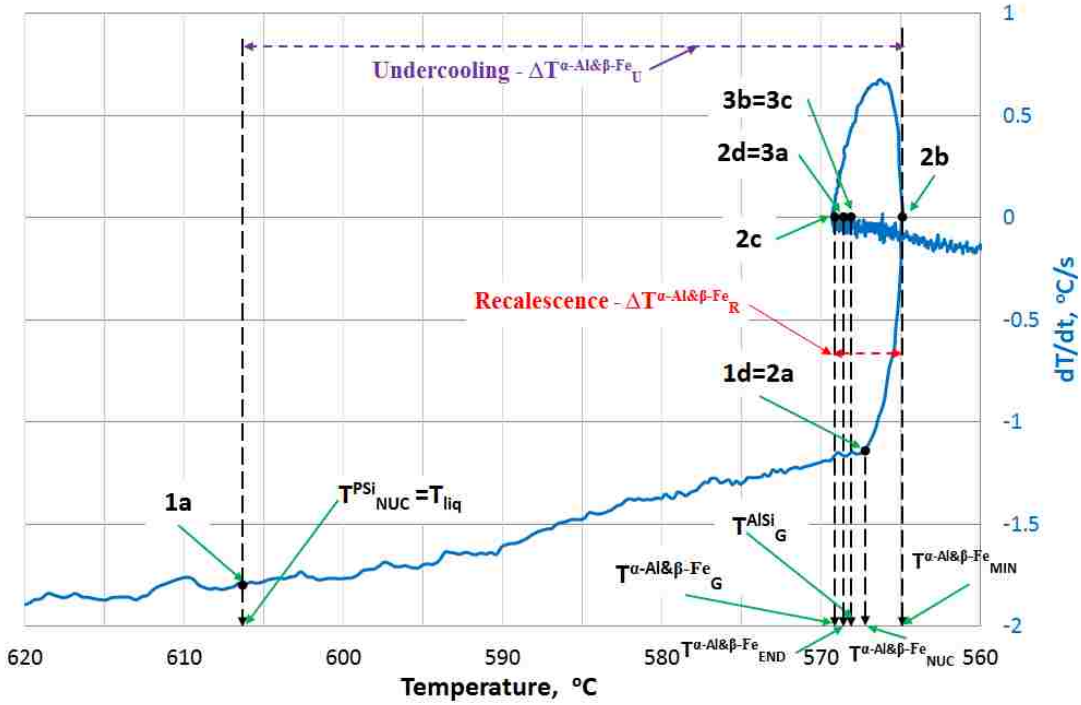

Figure 102. First Derivative Curve (region of liquidus and recalescence and undercooling temperatures associated with α-Al phase nucleation and growth) vs. Temperature for the 0.15 wt.%Sr modified experimental alloy, solidified in the HT UMSA Platform under atmospheric pressure and ASR = 0.4 °C/s, ref. #0618.

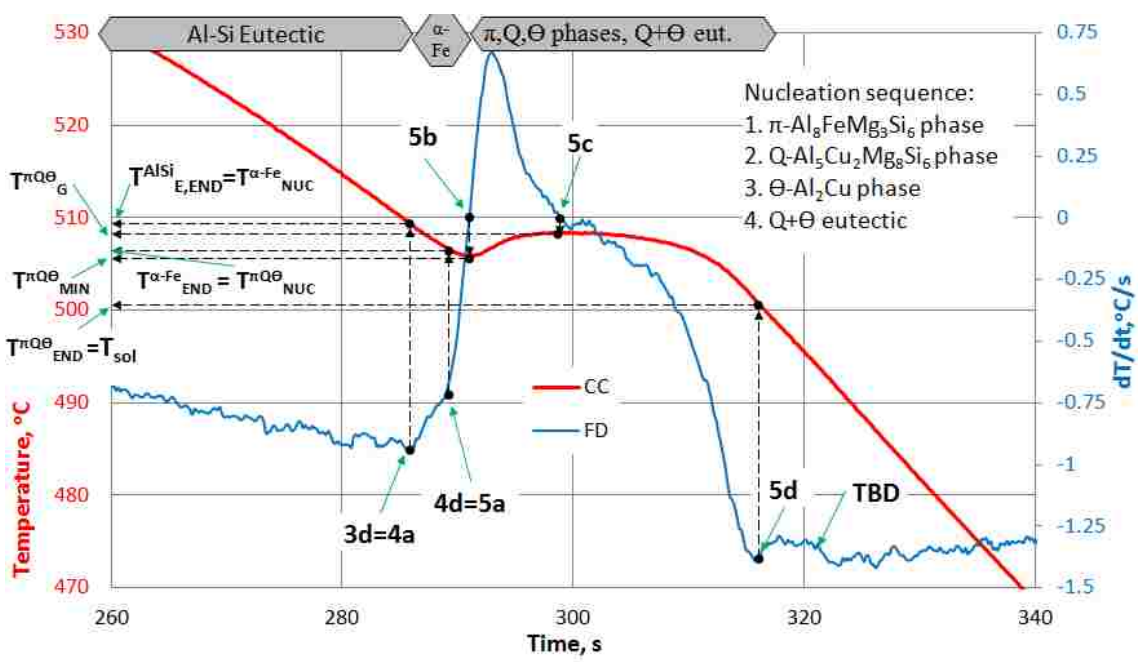

Figure 103. Solidification/Cooling and First Derivative Curves (region of recalescence associated with π, Q, Θ phases & Q+Θ eutectic nucleation and growth and solidus temperature) vs. Time for the 0.15 wt.%Sr modified experimental alloy, solidified in the HT UMSA Platform under atmospheric pressure and ASR = 0.4 °C/s, ref. #0618.

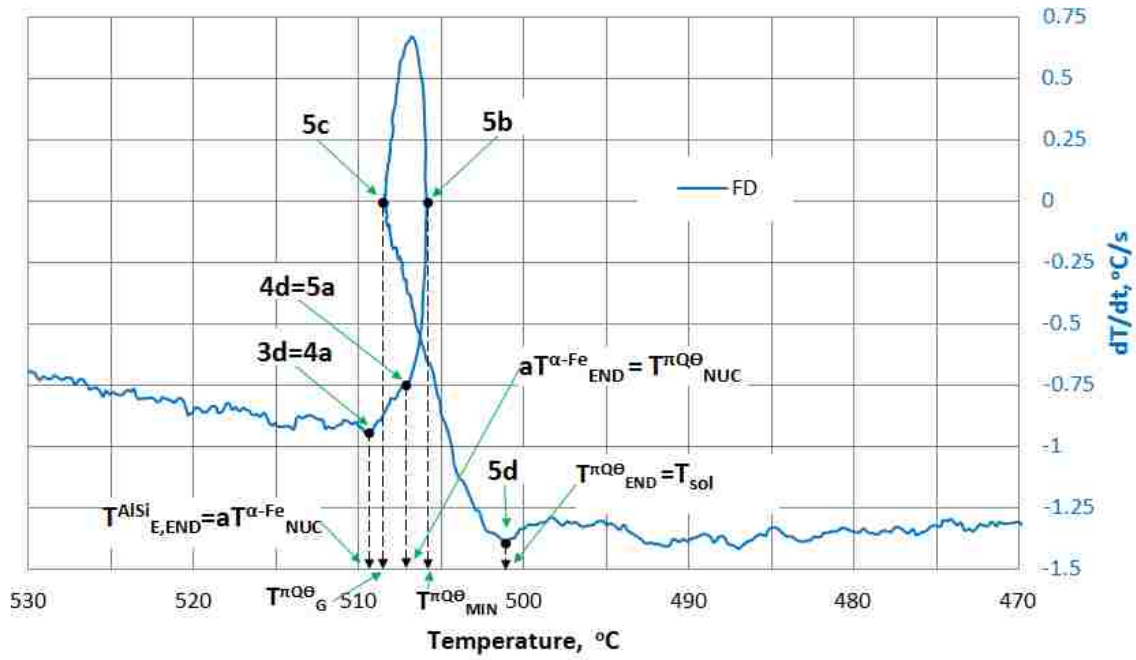

Figure 104. First Derivative Curve (region of recalescence associated with π, Q, Θ phases and Q+Θ eutectic nucleation and growth and Solidus Temperature) vs. Temperature for the 0.15 wt.%Sr modified experimental alloy, solidified in the HT UMSA Platform under atmospheric pressure and ASR = 0.4 °C/s, ref. #0618.

Table 17. Thermal Analysis Events during Solidification for the 0.15 wt.%Sr modified experimental alloy in the HT UMSA Platform under atmospheric pressure, ASR = 0.4 °C/s, ref. #0618.

#	Symbol	TA Event	Detection Algorithm	Comments
1a	T^{PSi}_{NUC} = T_{liq}	Primary Si Nucleation Temperature = Liquidus Temperature	At T_{liq} the CC changes slope and T_{liq} is detected on the FD curve as the 1st deflection and is determined by intersection of the FD with the DBL.	At T_{liq} f_s= 0 % Limited PSi particles nucleates on the oxide film and its vicinity and sparsely on the test cup wall. Evolution details for the PSi reaction can be determined after FD deconvolution.
1d	aT^{PSi}_{END}	Apparent Temperature for the end of the Primary Si Reaction	The aT^{PSi}_{END} is manifested on the FD curve as the intersection of PSi and α-Al tangents.	It is assumed that the primary Si reaction is completed. Deconvolution provides more accurate interpretation (i.e. T^{PSi}_{G}).
1d=2a	$aT^{\alpha\text{-Al}\&\beta\text{-Fe}}_{NUC}$	Apparent α-Al and β-Fe Nucleation Temperature	At $aT^{\alpha\text{-Al}\&\beta\text{-Fe}}_{NUC}$ the CC changes slope and $T^{\alpha\text{-Al}\&\beta\text{-Fe}}_{NUC}$ is detected on the FD curve as the intersection of PSi and α-Al and β-Fe tangents.	At this temperature the α-Al & β-Fe phases (ß-$Al_{15}FeSi$ in the form of needles) - 2D section and in the form of plates - 3D) are nucleating.
2b	$T^{\alpha\text{-Al}\&\beta\text{-Fe}}_{MIN}$	α-Al & β-Fe Minimum Temperature	$T^{\alpha\text{-Al}\&\beta\text{-Fe}}_{MIN}$ is the local minimum on the CC and on the FD curve it is a 1st point where dT/dt = 0. After passing of the $T^{\alpha\text{-Al}\&\beta\text{-Fe}}_{MIN}$ point, the melt temperature increases to a steady state $T^{\alpha\text{-Al}\&\beta\text{-Fe}}_{G}$.	At this state nucleated α-Al and β-Fe have grown to such an extent that the liberated LH of fusion balances the heat extracted from the test sample.

Table 17 - Continued				
#	Symbol	TA Event	Detection Algorithm	Comments
2c	$T^{\alpha\text{-Al}\&\beta\text{-Fe}}{}_{G}$	α-Al & β-Fe Growth Temperature	$T^{\alpha\text{-Al}\&\beta\text{-Fe}}{}_{G}$ is the local maximum on the CC, and on the FD curve it is a 2nd zero point where dT/dt = 0. If the FD curve does not intersect the zero line then the $T^{\alpha\text{-Al}\&\beta\text{-Fe}}{}_{MIN}$ = $=T^{\alpha\text{-Al}\&\beta\text{-Fe}}{}_{G}$ and corresponds to the maximum point on the FD curve.	The time period required to heat up the test sample from $T^{\alpha\text{-Al}\&\beta\text{-Fe}}{}_{MIN}$ to $T^{\alpha\text{-Al}\&\beta\text{-Fe}}{}_{G}$ is called Recalescence.
	$\Delta T^{\alpha\text{-Al}\&\beta\text{-Fe}}{}_{UC}$	Undercooling Temperature of α-Al & β-Fe	$\Delta T^{\alpha\text{-Al}\&\beta\text{-Fe}}{}_{UC}$ = $T_{liq} - T^{\alpha\text{-Al}\&\beta\text{-Fe}}{}_{MIN}$	
	$\Delta t^{\alpha\text{-Al}\&\beta\text{-Fe}}{}_{UC}$	Undercooling Duration of α-Al & β-Fe	$\Delta t^{\alpha\text{-Al}\&\beta\text{-Fe}}{}_{UC}$ = $t_{UC} - t_{liq}$	
	$\Delta T^{\alpha\text{-Al}\&\beta\text{-Fe}}{}_{R}$	Recalescence Temperature of α-Al & β-Fe	$\Delta T^{\alpha\text{-Al}\&\beta\text{-Fe}}{}_{R}$ = $T^{\alpha\text{-Al}\&\beta\text{-Fe}}{}_{G}$ - $-T^{\alpha\text{-Al}\&\beta\text{-Fe}}{}_{MIN}$	
	$\Delta t^{\alpha\text{-Al}\&\beta\text{-Fe}}{}_{R}$	α-Al & β-Fe Recalescence Duration	$\Delta t^{\alpha\text{-Al}\&\beta\text{-Fe}}{}_{R}$ = $t^{\alpha\text{-Al}\&\beta\text{-Fe}}{}_{G}$ - $-t^{\alpha\text{-Al}\&\beta\text{-Fe}}{}_{MIN}$	
2d	$aT^{\alpha\text{-Al}\&\beta\text{-Fe}}{}_{END}$	Apparent Temperature for the end of the α-Al & β-Fe Reaction	At the $aT^{\alpha\text{-Al}\&\beta\text{-Fe}}{}_{END}$ there is an inflection point on the CC and it is manifested as the minimum on the FD curve.	It is assumed that α-Al & β-Fe reaction is completed. Deconvolution can provide more accurate data.
2d=3a	$T^{AlSi}{}_{E,NUC}$	Al-Si Eutectic Nucleation Temperature	At $T^{AlSi}{}_{E,NUC}$, the CC changes slope and is detected on the FD curve as a local minimum.	At this point a stable nucleation of co-precipitating first eutectic Si crystals and α-Al from the melt begins.

Table 17 - Continued				
#	**Symbol**	**TA Event**	**Detection Algorithm**	**Comments**
3b=3c	$T^{AlSi}_{E,G}$	Al-Si Eutectic Growth Temperature	$T^{AlSi}_{E,G}$ is the inflection point on the CC and the local maximum on the FD curve. $T^{AlSi}_{E,MIN} = T^{AlSi}_{E,G}$	At $T^{AlSi}_{E,G}$ a considerable amount of Al-Si eutectic phase is formed. Between $T^{AlSi}_{E,NUC}$ and $T^{AlSi}_{E,G}$ Both the CC temperature and dT/dt values are almost constant.
3d	$aT^{AlSi}_{E,END}$	Apparent Temperature for the End of the AlSi Eutectic Reaction	At $aT^{AlSi}_{E,END}$ there is an inflection point on the CC and it is manifested as the local minimum on the FD curve.	At this point it is assumed that the AlSi eutectic reaction is completed. Detailed TA data is available from the deconvoluted FD.
3d=4a	$T^{\alpha\text{-Fe}}_{NUC}$	α-Fe phase Nucleation Temperature	At $T^{\alpha\text{-Fe}}_{NUC}$ there is an inflection point on the CC and it is manifested as the local minimum on the FD curve.	At this temperature the α-Fe, $(Al_{15}(FeMn)_3Si_2)$ phase forms chinese script that nucleates prior to the following phases π,Q,Θ & Q+Θ eutectic under convoluted peak #5.
4d	$aT^{\alpha\text{-Fe}}_{END}$	Apparent Temperature for the End of the α-Fe Phase Reaction	The $aT^{\alpha\text{-Fe}}_{END}$ is manifested on the FD curve as the intersection of α-Fe and π,Q,Θ and Q+Θ tangents.	It is assumed that the α-Fe reaction is completed. Deconvolution can provide more accurate data.

Table 17 – Continued				
#	**Symbol**	**TA Event**	**Detection Algorithm**	**Comments**
4d=5a	$aT^{\pi Q\Theta}_{NUC}$	π,Q,Θ phases and the Q+Θ Eutectic Nucleation Temperature	At $aT^{\pi Q\Theta}_{NUC}$, the CC changes slope and is detected on the FD curve as the local minimum.	The following phases nucleate and grow in a narrow temperature range of 508-501ºC under the FD peak #5. The actual nucleation and the end of the individual reactions can be determined by deconvolution of peak #5. Presently it is assumed that $aT^{\pi Q\Theta}_{NUC}$ of the 1st phase is associated with point #5a. π-$Al_8FeMg_3Si_6$ phase Q-$Al_5Cu_2Mg_8Si_6$ phase Θ-Al_2Cu phase and Q+ Θ eutectic.
5b	$T^{\pi Q\Theta}_{MIN}$	π,Q,Θ phases & Q+Θ Eutectic Minimum Temperature	$T^{\pi Q\Theta}_{MIN}$ is the local minimum on the CC and on the FD curve the 1st point where dT/dt = 0. After passing of the $T^{\pi Q\Theta}_{MIN}$, the melt temperature increases to a steady state $T^{\pi Q\Theta}_{G}$.	At $T^{\pi Q\Theta}_{MIN}$ latent heat is generated due to the AlFeMgCuSi rich phase growth that equals the heat loss from the test sample.
5c	$T^{\pi Q\Theta}_{G}$	π,Q,Θ phases & Q+Θ Eutectic Growth Temperature	$T^{\pi Q\Theta}_{G}$ is the local maximum on the CC and the 2nd zero on the FD curve. If the FD curve does not intersect the zero line then $T^{\pi Q\Theta}_{MIN} = T^{\pi Q\Theta}_{G}$ and corresponds to the maximum on the FD curve.	The maximum point of recalescence. At this temperature a considerable amount of π-$Al_8FeMg_3Si_6$ phase, Q-$Al_5Cu_2Mg_8Si_6$ phase and Θ-Al_2Cu phase are being formed.

Table 17 - Continued				
#	**Symbol**	**TA Event**	**Detection Algorithm**	**Comments**
	$\Delta t^{\pi Q \Theta}{}_{R}$	π,Q,Θ phases & Q+ Θ Eutectic Recalescence Duration	$\Delta t^{\pi Q \Theta}{}_{R} = t^{\pi Q \Theta}{}_{G} - t^{\pi Q \Theta}{}_{MIN}$	
5d	$T^{\pi Q \Theta}{}_{END} = T_{sol}$	Solidus Temperature	At T_{sol} there is an inflection point on the CC and this is the local minimum on the FD curve.	Temperature at which full solidification occurs. f_s= 100 %

Note: It is apparent that after the assigned point #5d at T_{sol} there is small peak to which a specific phase was not assigned. Further research needs to be conducted in order to determine the specific phase associated with this peak.

4.1.4 Microstructural Characterization of Sample #0618

Figures 105 (a - f) and 106 (a - f) show LOM and SEM representative micrographs taken from the as-cast HT UMSA sample. UMSA thermal data are summarized in Figures 99 (a, b) - 104. The main phases were identified with various associated peaks as follows:

The **$SrSi_2Al_2$** phase solidifies first [262] in the form of diamond crystals (the size is approx. 30 μm x 40 μm), see Figures 105a and 106a or as elongated thin particles (the size is approx. 5 μm x 60 μm), see Figure 106f. The chemical composition of the $SrSi_2Al_2$ phase was proved by EDS analysis. Due to the low volume fraction of the $SrSi_2Al_2$ phase no thermal signal was identified or associated with this reaction.

Peak #1. **Primary Si** solidifies as a first phase (T_{liq} = 606.9 °C, Figures 99 a - 102) in star-like shaped particles having a size of ≈ 250 μm on the periphery of the sample (see Figure 105 b) and in polyhedral shaped particles with a diameter of ≈ 100 μm nucleates on the oxide film (see Figure 105 c). The af_s of Primary Si particles is approx. 2 %.

Peak #2. The **α-Al** dendrites (the size ≈ 250 μm x500 μm) solidify as a second phase (see Figure 105 d) followed by the **β–Al_5FeSi** phase**,** which solidifies in the form of needles (the size is approx. 5 μm x 500 μm), see Figures 105 (e, f) - 106 (a, b). The β–Al_5FeSi phase nucleates almost simultaneously with the α-Al phase, that is shown in Figures 106 (a, b) where the α-Al phase touches the β–Al_5FeSi phase needles on both sides and creates bends on the β–Al_5FeSi phase edges which did not change the growth direction of the β–Al_5FeSi needles. Figures 106 (a, b) show the Sr-rich particle in the β–phase needle that indicates that the Sr-rich particle nucleated the β–phase. $T^{\alpha\text{-Al}\&\beta\text{-Fe}}_{G}$ = 569.3 °C. The af_s of α-Al dendrites and β-Al_5FeSi phase is ≈ 10 %.

Peak #3. The **Al-Si Eutectic** is a mixture of Al and Si phases. Eutectic Si is the leading phase and solidifies in the form of flakes (the size is ≈ 5 μm x 100 μm), see Figures 106 (a, b) or as tree-like dendrites (the size is ≈ 250 μm x 1000 μm), see Figure 106 c or in feathery shaped dendrites (the size is 100 μm x 150 μm), see Figure 106d. $T^{AlSi}_{E,G}$ = 569.0 °C. The af_s of Al-Si Eutectic is ≈ 79 %.

Peak #4. The **α-$Al_{15}(Fe,Mn)_3Si_2$** phase solidifies as Chinese script (the size is 100 μm x 200 μm), see Figures 105 f, 106 (a, d - f). $T^{\alpha\text{-Fe}}_{G}$ = 506.3°C. The af_s of α-$Al_{15}(Mn,Fe)_3Si_2$ is ≈ 1 %.

Peak #5. The **π-$Al_8FeMg_3Si_6$, Q-$Al_5Cu_2Mg_8Si_6$, θ-Al_2Cu** phases and the **Q+Θ eutectic** nucleate and grow in a temperature range of (506 to 501) ºC under the FD peak #5, see Figures 106 (e, f). The af_s of π-$Al_8FeMg_3Si_6$, Q-$Al_5Cu_2Mg_8Si_6$, θ-Al_2Cu phases and Q+Θ eutectic is approx. 8 %.

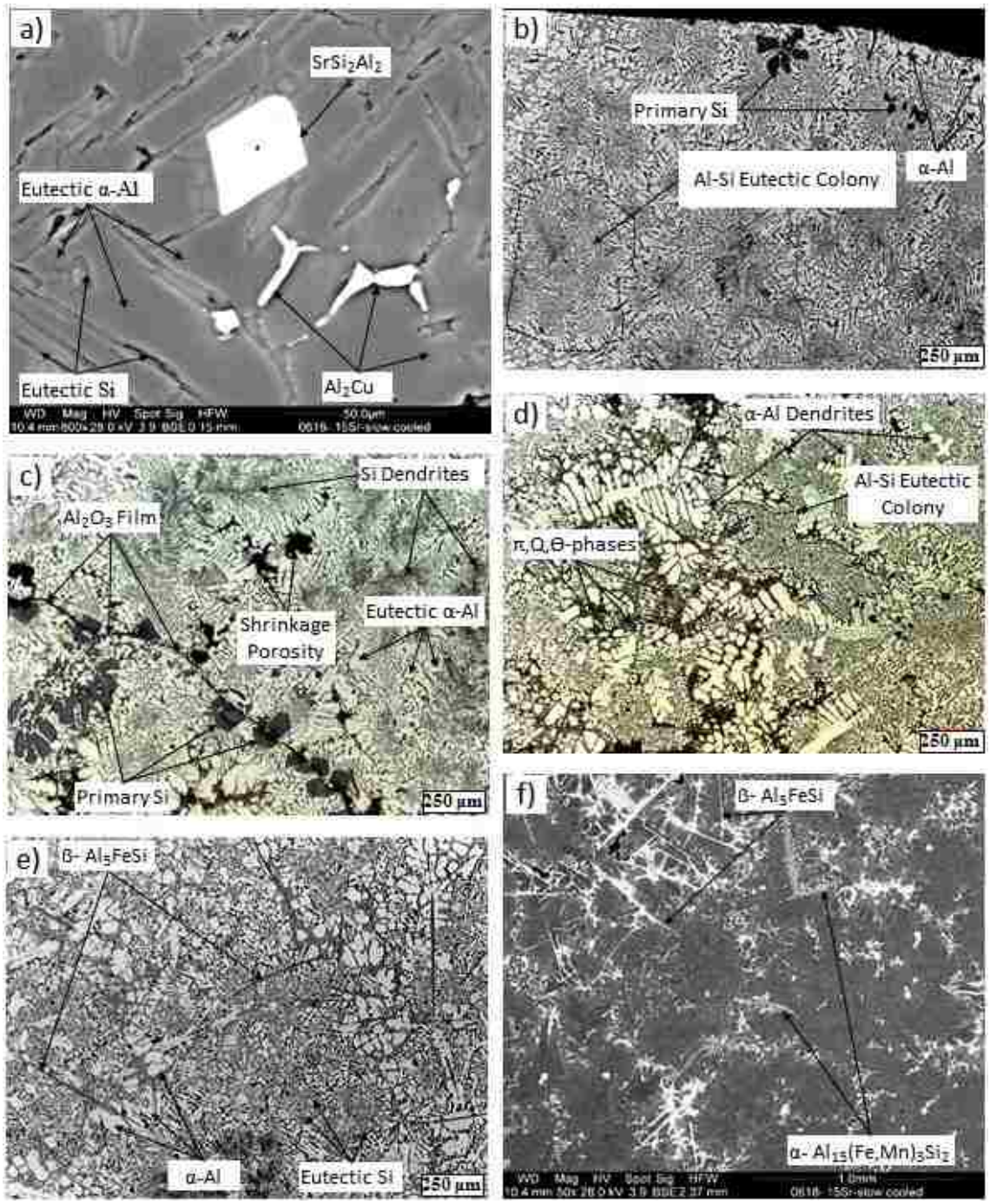

Figure 105. The as-cast micrographs for the 0.15 wt.%Sr modified experimental alloy solidified in the HT UMSA Platform under atmospheric pressure and at ASR = 0.4 ^{o}C/s. b-e) LOM micrographs/polished, a, f) SEM micrographs/polished, ref. #0618.

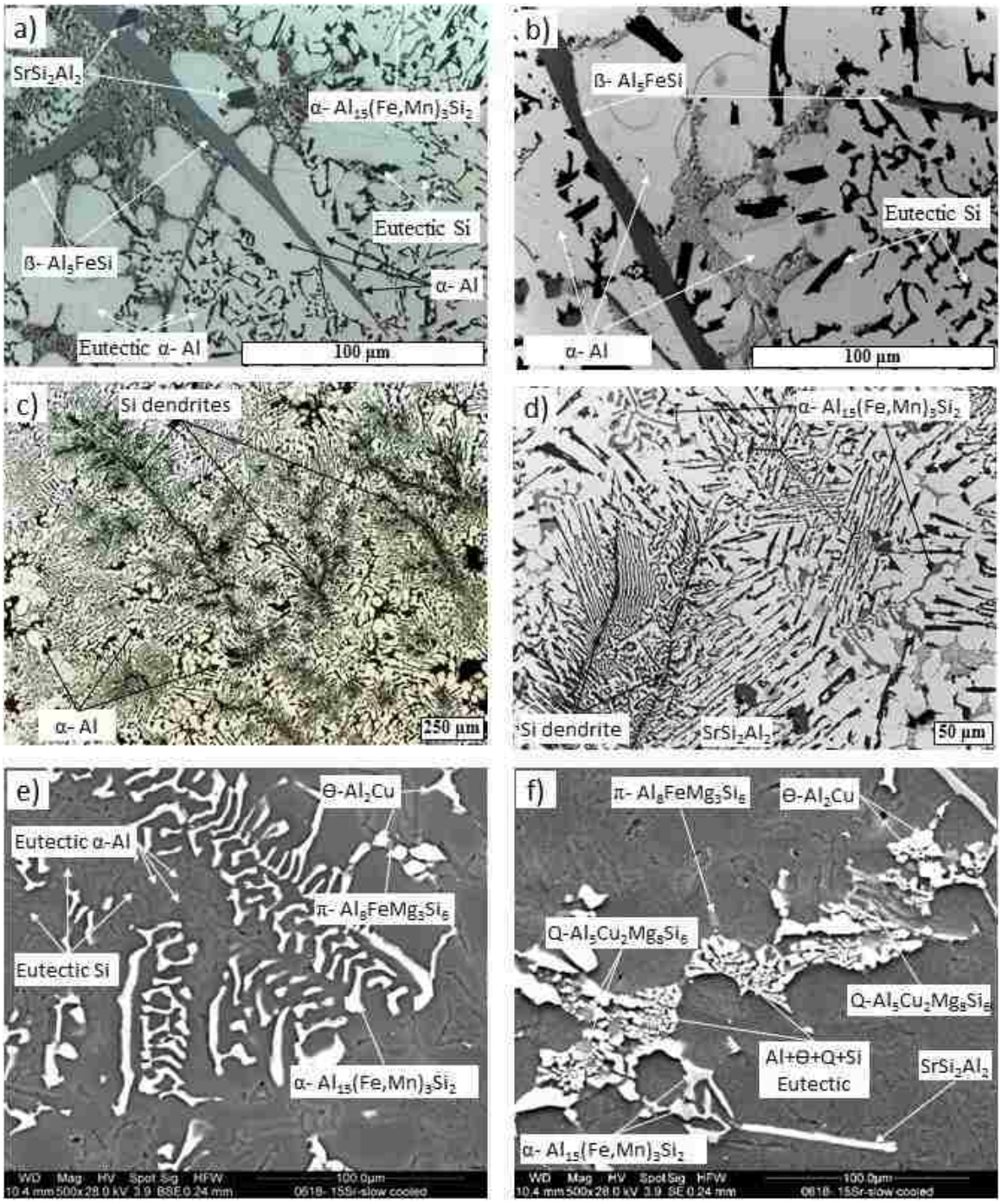

Figure 106. The as-cast micrographs for the 0.15 wt.%Sr modified experimental alloy solidified in the HT UMSA Platform under atmospheric pressure and at ASR = 0.4 ^{o}C/s. a-d) LOM micrographs/polished, e, f) SEM micrographs/polished, ref. #0618.

4.1.5 Summary of Thermal and Microstructural Analysis for the Unmodified and 0.15 wt.%Sr Modified Experimental Alloys Solidified under Atmospheric Pressure and at an ASR of 0.4 ^{o}C/s

Comparison of selected quantitative TA characteristics of the HT UMSA solidified unmodified and 0.15 wt%Sr modified experimental alloy allows for a better understanding of individual metallurgical reactions and their importance to the as-cast structure characteristics. The main objective of the elevated Sr addition is the suppression of the primary Si formation and creation of conditions conducive to the formation of nano and ultrafine structured Si whiskers and dendrites during further melt processing in the SC/HPDC UMSA die.

Superimposed cooling curves, their first derivatives vs. time and temperature, together with Fraction Solid curves are presented in Figures 107, 108 and 109, respectively. This comparative study is limited to the essential data listed below, while more details can be found in Chapters 4.1.1 - 4, Figures 89 - 96, 99 - 104 and Tables 16 and 17.

1. Addition of 0.15 wt%Sr to the melt resulted in the lowering of the T_{liq} from 622.8 ºC to 606.9 ºC and T^{PSi}_{G} from 585.1 ºC to 569.3 ºC while the temperature of other reactions as indicated in Figures 108 and 110 are lower for the unmodified alloy.
2. Addition of 0.15 wt%Sr effectively suppressed f_S^{PSi} from ≈ 9 % to 2 %, while the $f_S^{AlSi}{}_E$ for the modified alloy was increased from ≈ 70 % to 79 %.
3. Suppression of nucleation of the primary silicon in the modified sample resulted in the formation of the aluminum phase, as the leading phase that has positive structural consequences for further melt treatment and solidification in the SC/HPDC UMSA die.

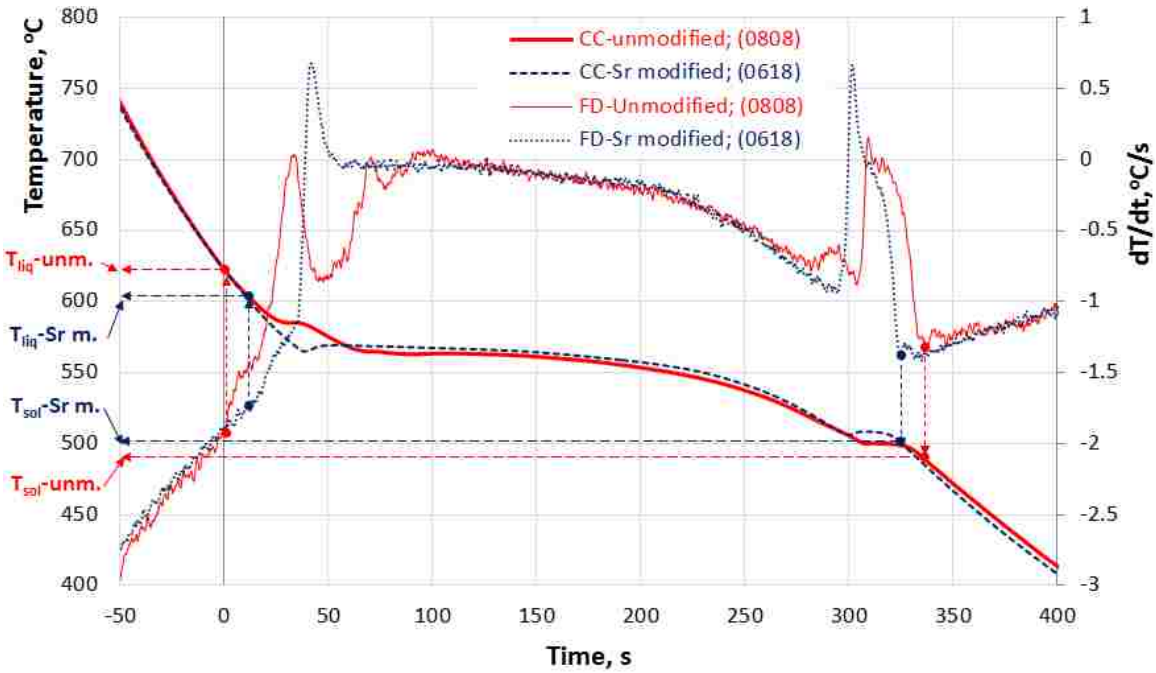

Figure 107. Cooling/Solidification Curves and First Derivative Curves vs. Time for the unmodified and 0.15 wt.%Sr modified experimental alloy solidified in the HT UMSA SS cup under atmospheric pressure, ASR = 0.4 °C/s, ref. #0808 and #0618.

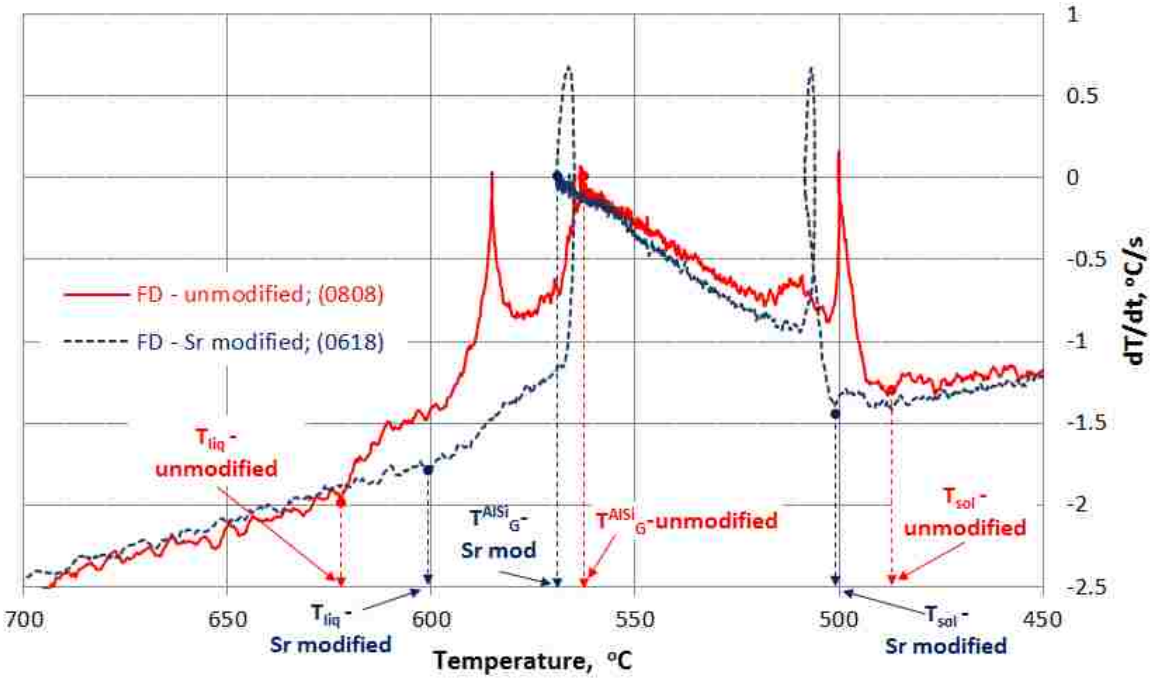

Figure 108. First Derivative Curves vs. Temperature for the unmodified and 0.15 wt.%Sr modified experimental alloy solidified in the HT UMSA SS cup under atmospheric pressure, ASR = 0.4 °C/s, ref. #0808, #0618.

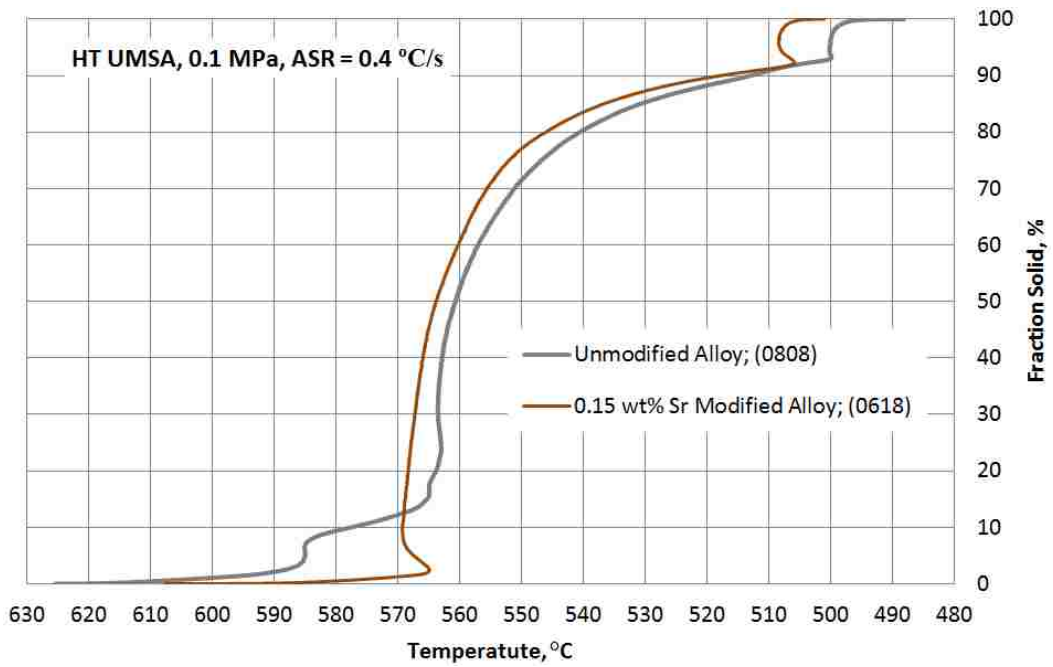

Figure 109. Fraction Solid Curves vs. Temperature for the unmodified and 0.15 wt.%Sr modified experimental alloy solidified in the HT UMSA SS cup under atmospheric pressure, ASR = 0.4 °C/s, ref. #0808 and #0618.

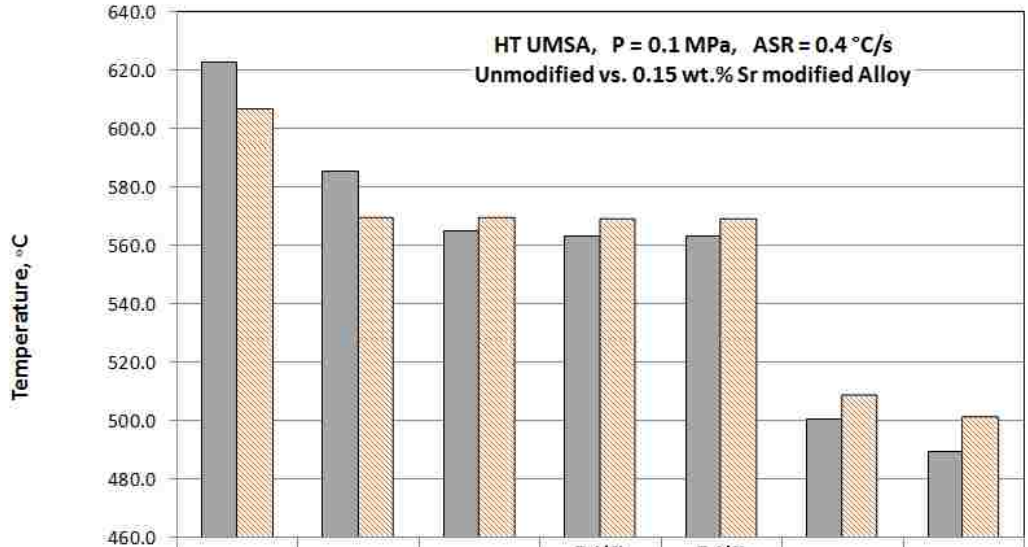

	T liq	T PSi G	T β-Fe G	T AlSi E,MIN	T AlSi E,G	T πQθ G	T sol
Unmodified; (0808)	622.8	585.1	565.0	563.0	563.1	500.1	489.2
0.15wt% Sr Modified; (0618)	606.9	569.3	569.3	569.0	569.0	508.4	501.1

Figure 110. Selected Thermal Characteristics for the unmodified and 0.15 wt.%Sr modified experimental alloy solidified in the HT UMSA SS cup under atmospheric pressure, ASR = 0.4 °C/s, ref. #0808 and #0618.

4.2 SC/HPDC UMSA Thermal and Microstructural Analysis of #0717, #0508 and #0925 Experimental Alloys Solidified at an ASR ≈ 10 °C/s

In order to investigate the effect of Sr modification and higher ASR ≈ 10 ^{o}C/s on the TA characteristics and microstructure of the experimental alloy under atmospheric pressure, three experiments were conducted using the SC/HPDC UMSA Platform and experimental samples #0717 (unmodified), #0508 (0.1 wt.%Sr modified) and #0925 (0.15 wt.%Sr modified). The thermal events for sample #0717 are presented in Figures 111 (a, b) and 112, for sample #0508 in Figures 113 (a, b) and 114 and for sample #0925 in Figures 115 (a, b) and 116. Microstructures for the investigated samples are presented in Figure 117 (a - f) and 118. Table 18 summarizes the thermal characteristics of the above mentioned test samples.

The microstructure of the unmodified experimental alloy ref. #0717 (see Figure 117 (a, b), 0.0 wt.%Sr), solidified in the SC/HPDC UMSA die (ASR = 10.2 ^{o}C/s), under atmospheric pressure contains blocky primary Silicon (the size is ≈ 30 μm x 80 μm), α-Al dendrites, acicular eutectic Si (the size is 5 μm x 100 μm), aluminum eutectic matrix and intermetallic phases located between the dendritic arms of the α-Al dendrites.

The addition of 0.10%Sr to the experimental alloy melt, cast and solidified in the SC/HPDC UMSA die at an ASR = 15.1 ^{o}C/s (ref. #0508), suppressed formation of primary Si, see Figure 117 (c, d). The sample has a very fine structure containing very fine eutectic Si in the eutectic aluminum matrix. Blocky primary Si particles were found very rarely and only in the center of the sample. The intermetallic phase colonies are much finer and interdendritic boundaries are thinner than in the unmodified sample. Higher LOM magnification (see Figure 117 d) and SEM of the deep etched surface,

Figure 118 (a - f) revealed a fibrous (coral-like) morphology of modified silicon. The smallest diameter of Si dendrite arms has a size of ≈ 200 nm, interdendritic space thickness of ≈ 10 μm and the size of Al-Si eutectic cells is ≈ 60 μm.

The addition of 0.15 wt.%Sr to the slowly solidifying experimental alloy (ref. #0925) with an ASR = 9.4 ^{o}C/s, results in a small amount of the primary Si phase nucleating almost simultaneously together with the α-Al phase in the form of dendrites. The Al-Si eutectic colonies that form, from the common origin, are separated by aluminum inter-colony boundaries. In addition, a higher Sr level (in comparison with 0.1 wt.%Sr, #0508) together with higher SR results in the presence of eutectic Si dendrites with ultra-fine arms and trunks, Figure 117 (e, f). These key factors are necessary for future structural modifications and refinement using the SC/HPDC UMSA's new processing parameters including various pressure profiles (i.e. impact pressure, cyclic pressure loading combined with monotonic pressure).

Comparison of the LOM microstructures for the 0.10 wt.%Sr and 0.15 wt.%Sr modified alloy (see Figure 117 (a - f)) shows that the 0.15 wt.%Sr alloy produced the finest silicon structure. The next investigation (see Section 4.4) was extended to apply cyclic pressure during solidification for the 0.15 wt%Sr modified experimental alloy.

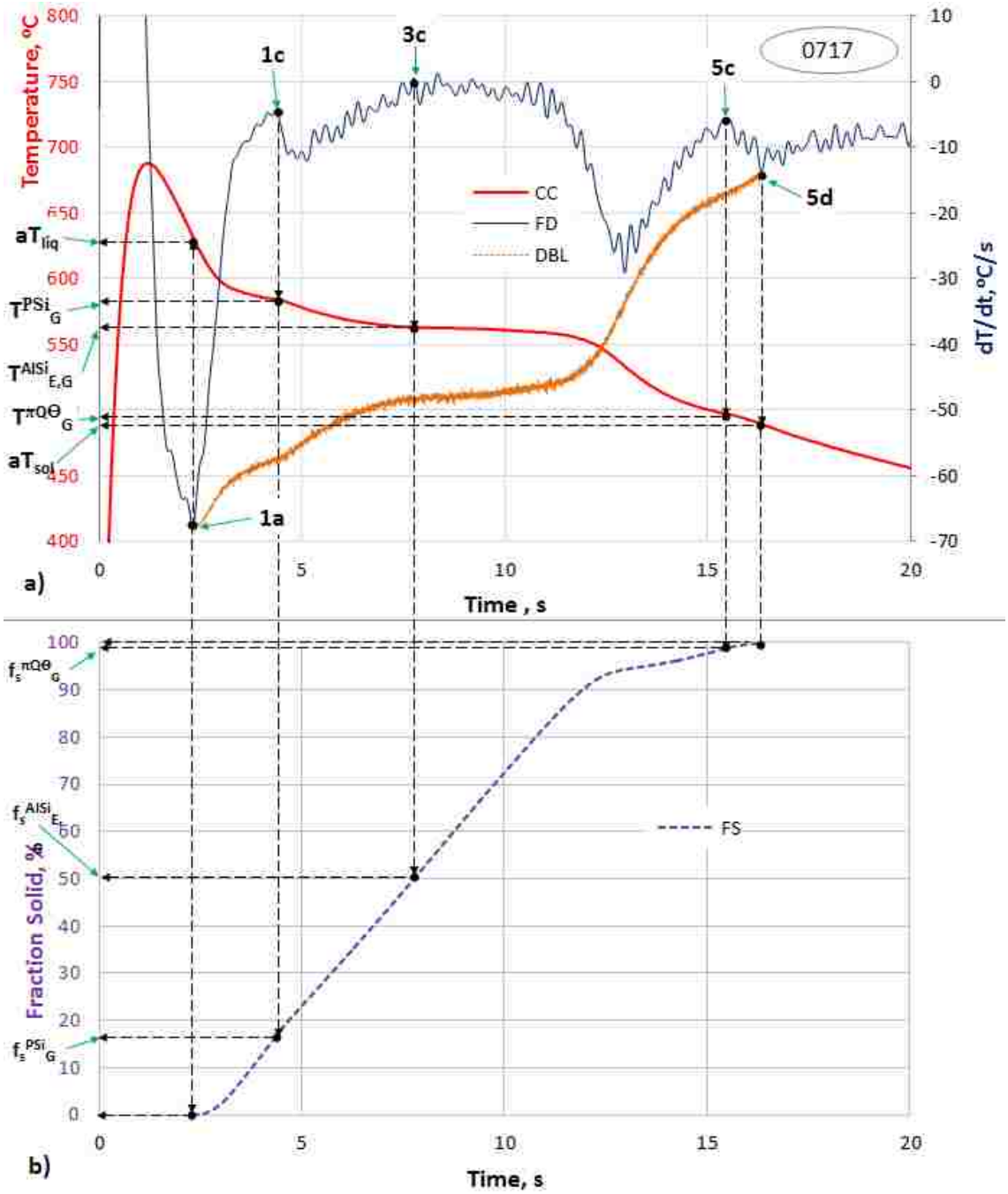

Figure 111. a) Cooling/Solidification Curve superimposed with the First Derivative and the Dynamic Baseline Curve and b) Fraction Solid Curve vs. Time for the unmodified experimental alloy, solidified under atmospheric pressure in the SC/HPDC UMSA die, ASR = 10.2 °C/s, ref. #0717.

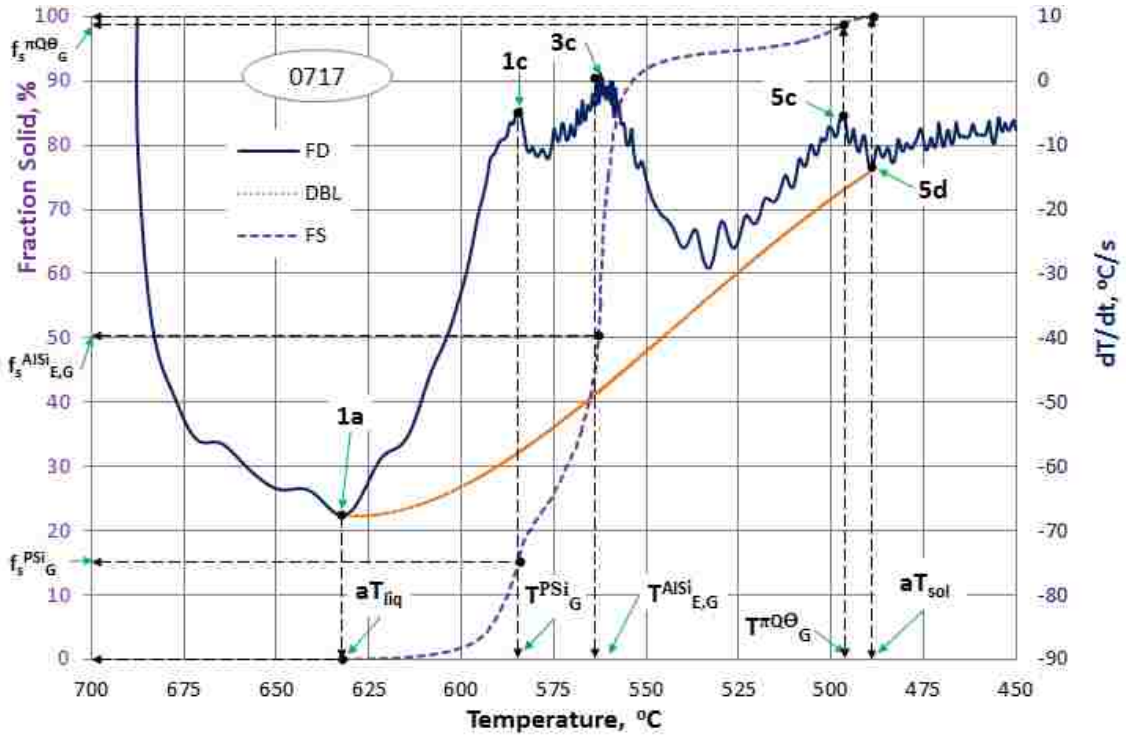

Figure 112. First derivative of the Cooling Curve, Dynamic Baseline Curve and Fraction Solid Curve vs. Temperature for the unmodified experimental alloy, solidified under atmospheric pressure in the SC/HPDC UMSA die, ASR = 10.2 °C/s, ref. #0717.

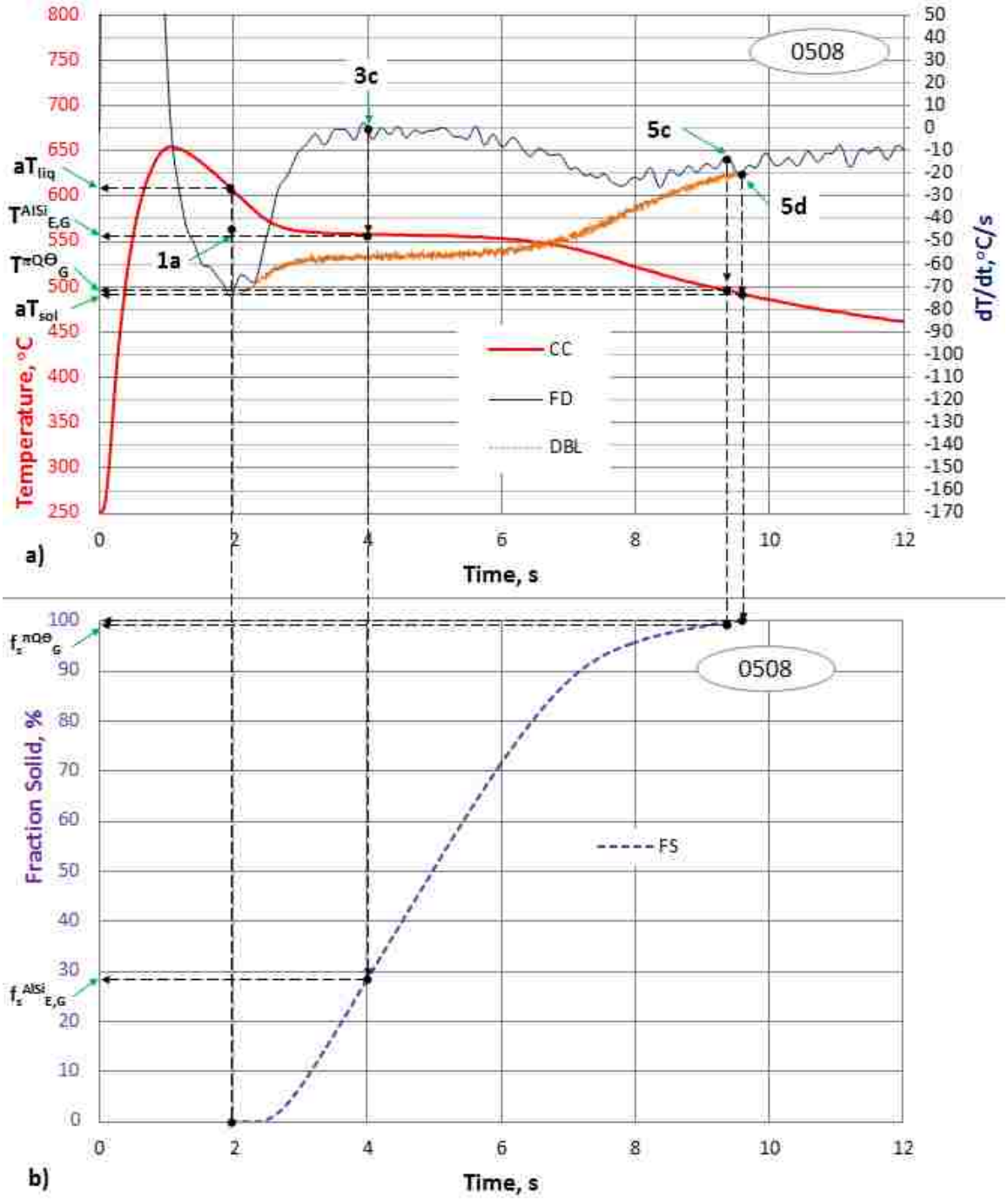

Figure 113. a) Cooling/Solidification Curve superimposed with the First Derivative and the Dynamic Baseline Curve and b) Fraction Solid Curve vs. Time for the 0.1 wt.%Sr modified experimental alloy solidified in the SC/HPDC UMSA die under atmospheric pressure, ASR = 15.3 °C/s, ref. #0508.

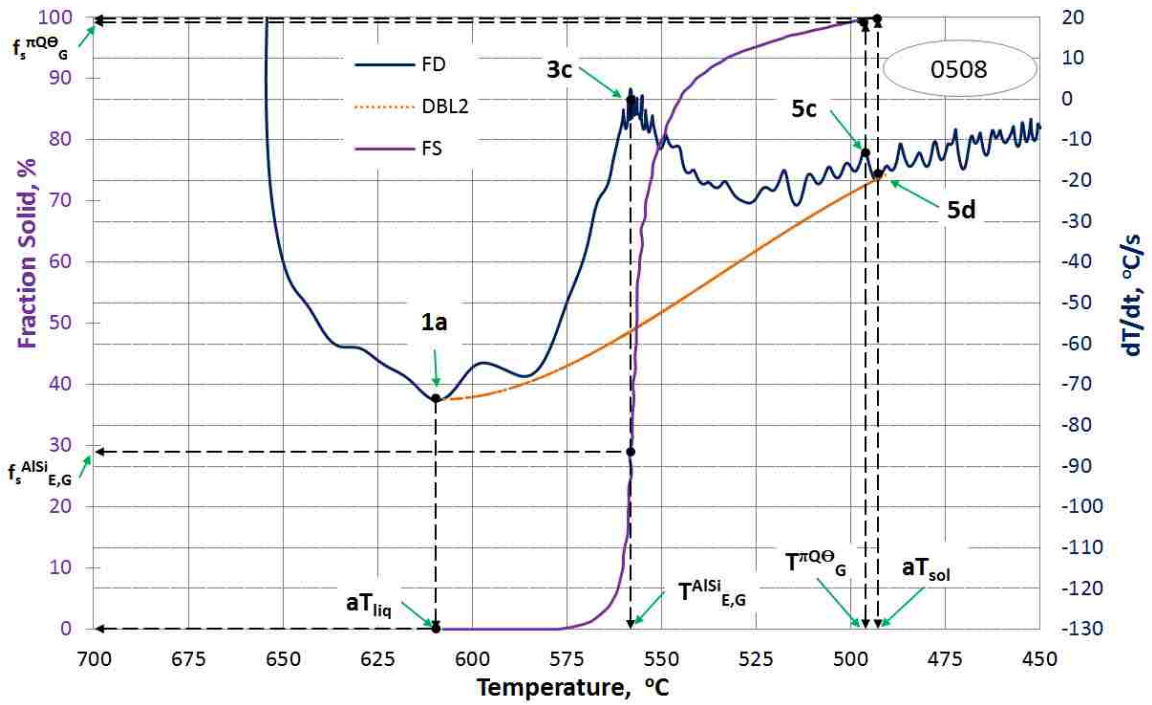

Figure 114. First Derivative of the Cooling Curve and Fraction Solid Curve vs. Temperature for the 0.1wt.%Sr modified experimental alloy solidified in the SC/HPDC UMSA die under atmospheric pressure, ASR = 15.3 °C**/s, ref. #0508.**

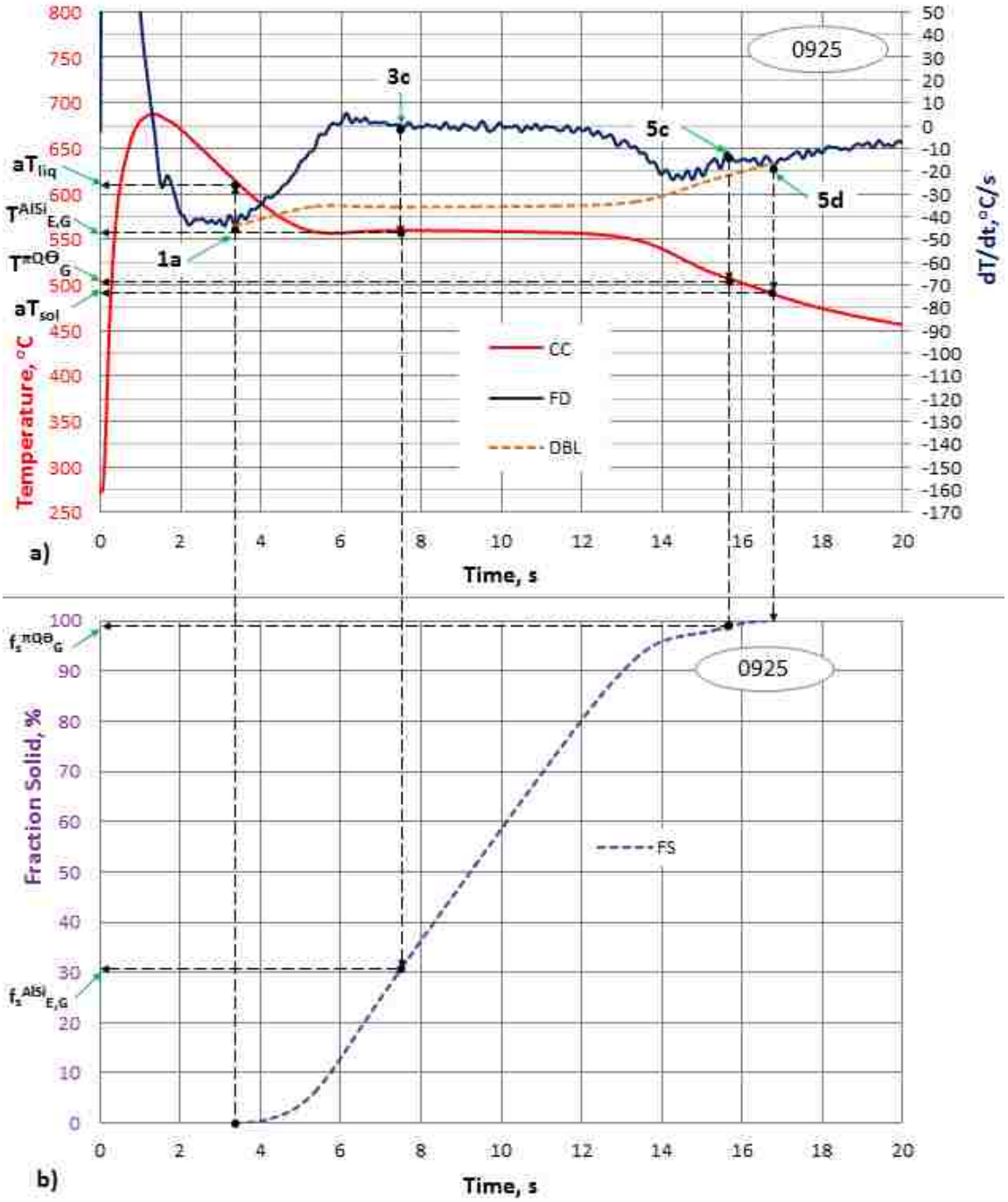

Figure 115. a) Cooling/Solidification Curve superimposed with the First Derivative and the Dynamic Baseline Curve and b) Fraction Solid Curve vs. Time for the 0.15 wt.%Sr modified experimental alloy solidified in the SC/HPDC UMSA die under atmospheric pressure, ASR = 9.3 °C/s, ref. #0925.

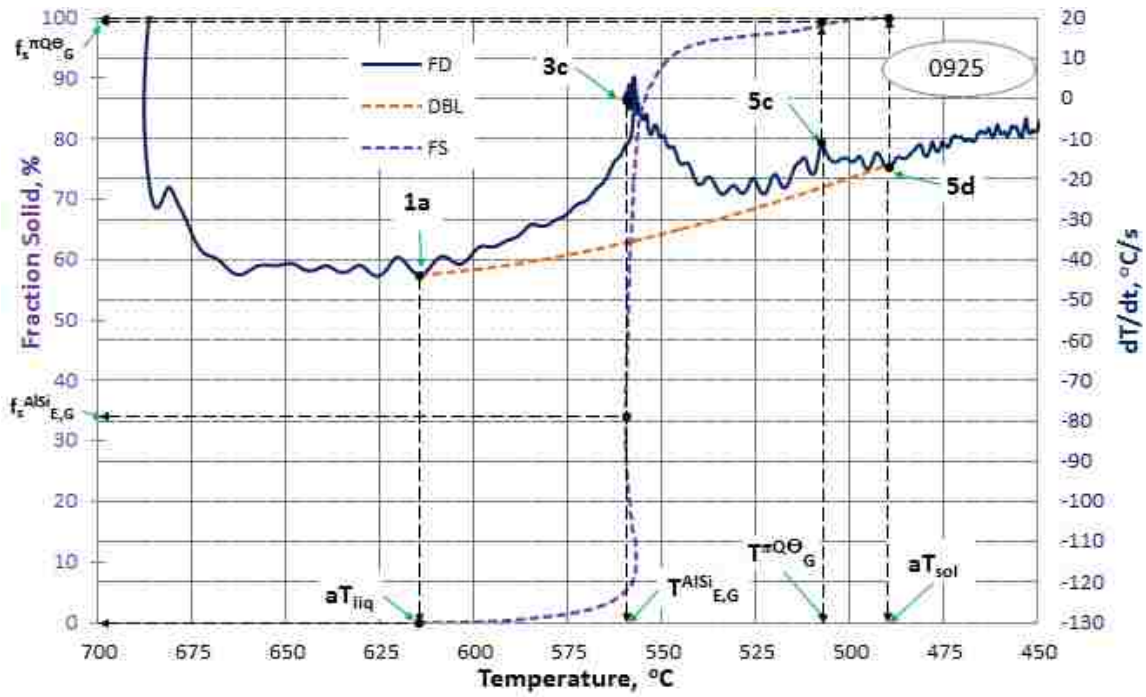

Figure 116. First derivative of the Cooling Curve, Dynamic Baseline Curve and Fraction Solid Curve vs. Temperature for the 0.15 wt.%Sr modified experimental alloy solidified in the SC/HPDC UMSA die under atmospheric pressure, ASR = 9.3 °C/s, ref. #0925.

Table 18. Selected Thermal Characteristics for Test Samples #0717, #0508 and #0925.

Run #	Ref.#	Sr Modif.	T^D_i	T^M_{iH}	T^D_{MAX}	T_{liq}	$T^{AlSi}_{E,MIN}$	$\Delta T^{AlSi}_{E,UC}$	$T^{AlSi}_{E,G}$	$\Delta T^{AlSi}_{E,R}$	$T^{\pi Q\Theta}_G$	T_{sol}	SRn T_{liq}-T_{sol}	St t_{sol} -t_{liq}	ASR	T_{liq}ISR	T_{sol}ISR
		wt.%	°C											s	°C/s		
1	0717	0	264	797.0	688.0	632.1	563.0	69.1	563.1	0.1	496.7	489.2	142.9	14.0	10.2	67.6	13.7
2	0508	0.10	248	790.0	654.4	609.5	557.9	51.6	558.4	0.5	496.4	493.2	116.3	7.6	15.3	73.8	19.9
3	0925	0.15	263	796.0	687.6	614.3	556.8	57.6	559.6	2.8	507.6	489.9	124.4	13.4	9.3	43.7	17.3

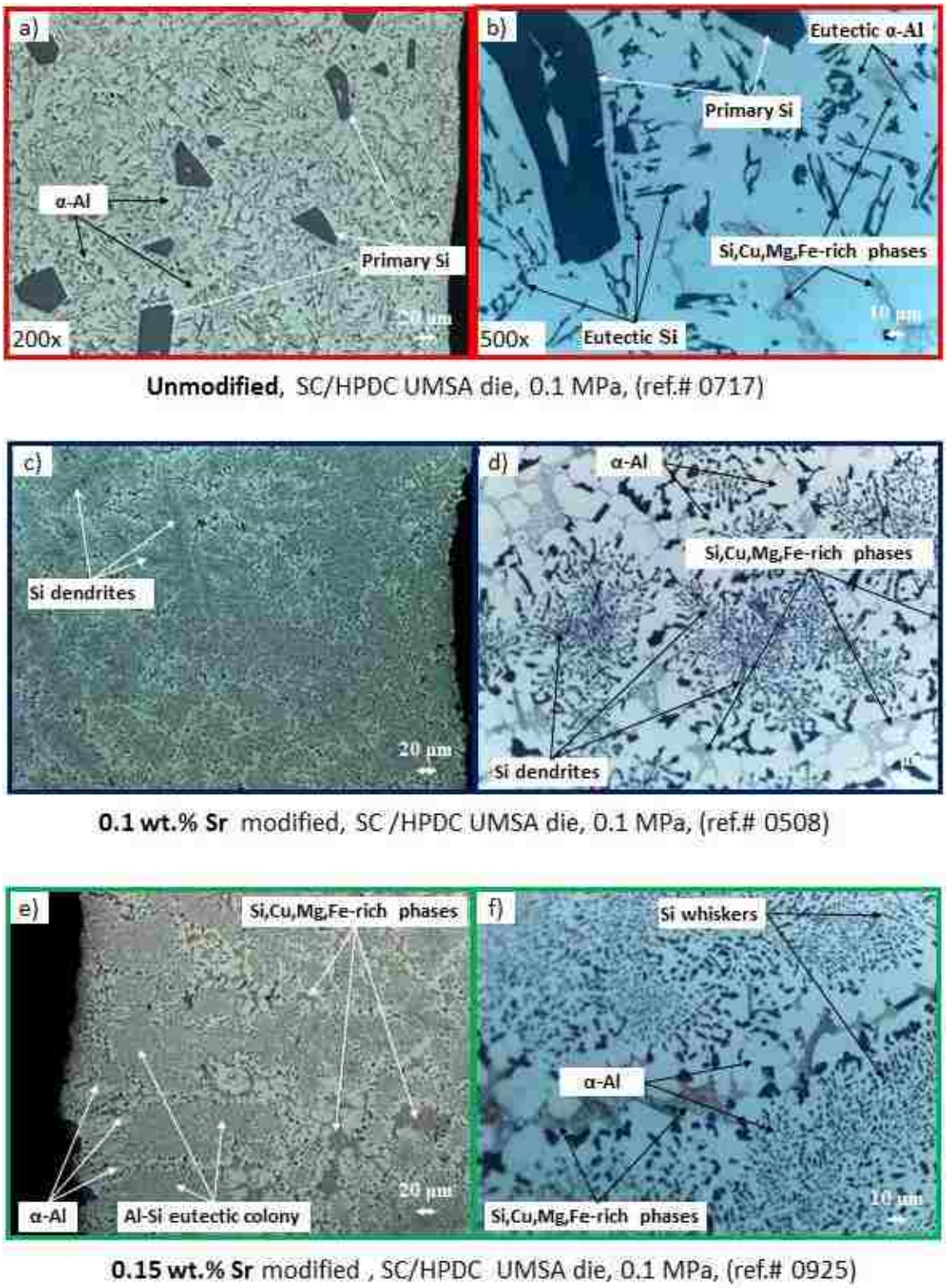

Figure 117. LOM micrographs for the experimental alloy solidified in the SC/HPDC UMSA die under atmospheric pressure: a, b) unmodified, ref. #0717; c, d) 0.1 wt.%Sr modified, ref. #0508; e, f) 0.15 wt.%Sr modified, ref. #0925.

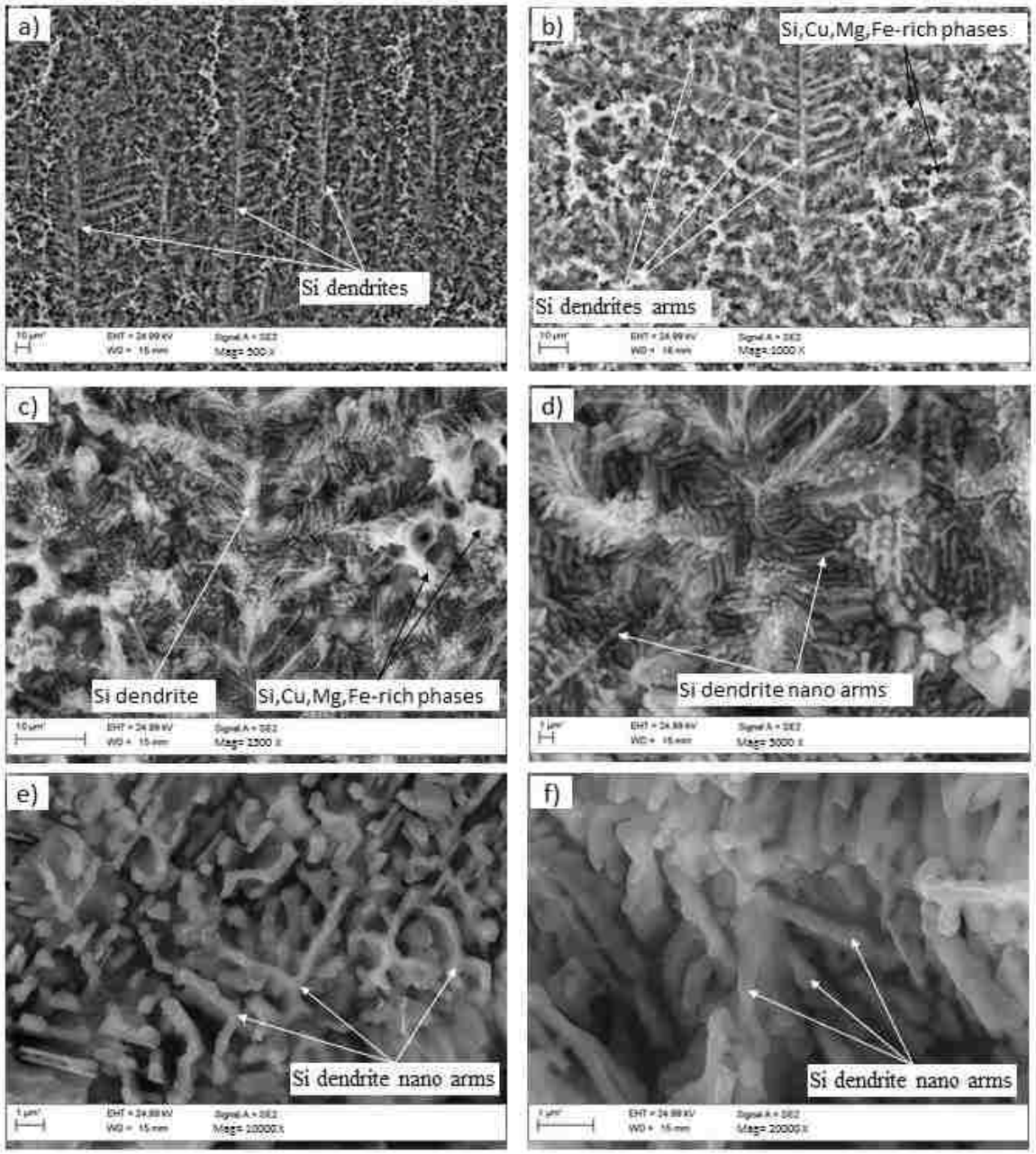

Figure 118 (a - f). SEM micrograph, deep-etched (the α-Al matrix was etched out), 0.1 wt.%Sr modified experimental alloy, solidified in the SC/HPDC UMSA die under atmospheric pressure, ASR = 15.3 ^{o}C/s, ref. #0508.

4.3 Effect of Various Pressure Loading Modes on the Thermal Characteristics and Microstructure of the Experimental Alloy Processed in the SC/HPDC UMSA Die

As mentioned in the Comprehensive Literature Review Summary there are no publications regarding liquid and semi-solid Al-Si-X melt processing technology using chemical, dynamic and monotonic loading profiles in the confined environment for pure or industrial grade multi-component alloy modification and refinement leading to nano and ultra-fine as-cast structures. In addition, there is no information regarding possible heat treatment attempts for laboratory produced ultra-high purity Al-Si alloys with Si whiskers. The as-cast single Si whiskers phase in hypereutectic alloys could lead to ultra rapid fragmentation of the Solution Treatment whiskers and spheroidization together with simultaneous dissolution of the Al, Cu, and Mg rich phases.

Taking into consideration the above-mentioned literature findings and conclusions, the experiments using the SC/HPDC UMSA were designed to explore the opportunity of using Sr for melt modification together with a combination of impact pressure, cyclic pressure and monotonic pressure loading with the aim to further improve modification and refinement of the eutectic cell structures in order to fully control detrimental Fe rich phases.

The unique task of dynamic melt treatment considered the possibility of using cyclic pressure loading including triangular, sinusoidal and square profiles. However, due to time constraints, sinusoidal cyclic pressure profiles were chosen. The melts' sinusoidal cyclic loading, impact and monotonic pressure profiles include:

1. Impact compressive pressure up to 53 MPa.
2. Variable compressive loading in a range of (38 - 82) MPa.
3. Frequency ≈ 10 Hz.
4. Duration up to 5.0 s.
5. Pressure Start temperature treatment T^{P}_{ST} in the range of (659.0 to 610.9) ºC.
6. Pressure End temperature treatment T^{P}_{END} in the range of (619.5 to 547.9) ºC.

   For more information please refer to Table 16.

4.3.1 Development of Novel Al-Si Sandwich (Shell) Dendritic Structure Unmodified Alloy Sample #0429

Development of the novel Al-Si sandwich dendritic structure is based on the hypotheses regarding the formation of the Si shell on the Al dendrite's trunk and dendrite arms during cyclic loading applied during Aluminum dendrite nucleation and growth that competes with Silicon precipitation. In order to fullfil these conditions the $T^{PSi}_{E,G}$ should be approximately equal to $T^{AlSi}_{E,G}$. The Aluminum dendrite trunk and arms formed could be partially thermally fragmented by the heat generated by high latent heat of fusion of the Silicon enriched liquid melt present in the interdendritic space of the Al dendrite arms. Exposed fragments of Aluminum dendrites like the root of the dendrite arms and trunk could be a substrate for nucleation of the Si shell around them. Most likely, thermally activated partial fragmentation could be supported by cyclic loading of the liquid melt being present in the interdendritic regions.

The idea for development of a novel Al-Si sandwich dendritic (shell) structure originated from the discovery of the nucleation of primary α-Aluminum dendrites that can be stimulated by cyclic pressure loading and high Solidification Rates of the

unmodified experimental alloy. The following interpretation of the formation of this novel structure is based on comparative analysis of both the process parameters and the TA data analysis in relation to the as-cast microstructure of the melts processed under various conditions.

The unmodified experimental #0429 alloy processed using SC/HPDC UMSA cyclic loading exhibits a novel Al-Si sandwich dendrite(s) structure that was revealed by deep etching, see Figures 122 (d - f). Therefore, it is necessary to perform comparative analysis with other samples in order to understand the effect of the process parameters, TA data and the resultant structures. The #0429 melt processing parameters, TA data and the corresponding microstructures are presented in Figures 119 - 122. Figures 119 - 121 shows that the melt's aT_{liq} = 618.1 °C @ SR = 72 °C/s which coincides with the short period (estimated to be ≈ 0.5 s) of nucleation and growth of the primary Si phase. This metallurgical reaction overlaps with the formation of the Al dendrites. These two reactions are controlled by two integrated cyclic loadings. Since both the first and second cyclic loading of the experimental melt were applied at temperatures below Liquidus control of the already nucleated unmodified primary Si structure is not feasible. Approximately 0.5 mm from the test sample edge, small primary α-Al dendrites are visible, Figure 122 b. The first cyclic "impact" loading parameters (+1 to -2) MPa/1c were applied to the semi-solid melt at a temperature of approx. 603 °C @ SR = 72 °C/s. At this temperature, the f_S of the primary Si particles was less than 0.2%, (Figure 121).

The first cyclic pressure loading was continuously extended to the second cyclic loading in approximately 0.5 s. The second pressure loading (48-72) MPa/10 cycles was applied to the semi-solid melt at a temperature of 580 °C and where f_S = approx. 9.6 %.

The undercooling temperature is 44.9 °C while there is no recalescence. During the second cycling loading period, the melt temperature stays almost constant (573 °C) for approximately 0.6 s. During this period substantial f_S of the α-Al dendrites nucleated and grew (α-Al dendrite $f_S \approx 5$ %).

The second cyclic loading was applied during progression of the solidification process that includes the interruption of the formation of the primary Si and the nucleation and growth of α-Al and formation of the Al-Si eutectic. During this time a very substantial Latent Heat of Fusion (LHF) is released by the melt. At the same time cycling loading causes increases in the melt temperature. Therefore, both the CC and FD parameters are affected by the melt pressure loading during which two factors need to be considered. Increasing and/or maintaining an instantaneous high SR and consequently Heat Transfer Coefficient with simultaneous release of the LHF are recorded as a "global" TA characteristic. This is a complex phenomenon. Individual effects can be discerned by the comparison of the melt behavior tested under other conditions. The attempt to estimate the rise of the sample temperature as a result of cyclic loading is presented later.

Closer SEM examination of the deep etched as-cast structure revealed the presence of large volume fraction of novel morphology for the "Al-Si sandwich dendrites", see Figures 122 (d-f). In some areas, these sandwich dendrites nucleate on or near the (2D analytical plane) primary Si. Analysis of the SEM micrographs demonstrates that the Si shell nucleates on the Al dendrites which are the perfect substrate because they act as micro chills. In addition, Al dendrites have a very large specific surface area and are excellent heat conductors allowing for nucleation of the Si shell on the surface. In the

next solidification phase, the Si shell becomes the substrate for nucleation of the low solidification temperature phases like π, Q, Θ and (Q+Θ) eutectic in the Si shell interdendritic spaces, see Figures 122 (a-f). Approximate thickness of the Si shell is (1 μm to 5 μm). The #0429 melt's Al-Si eutectic growth temperature is T^{AlSi}_{EG} = 572.1 °C @ f_S = 30.5 % and T_{sol} = 521.1 °C @ SR = 43.6 °C/s. Please note that the T_{sol} is very high for the alloy containing a high amount of Cu.

It is apparent that both pressure cycle loadings together with perfect timing allowed for maintaining of high SRs at T_{liq} and T_{sol} temperatures that resulted in a very short Solidification time of 4.8 s. This contributed to other relatively finer phases in comparison with the unmodified HT UMSA #0808 sample processed under atmospheric pressure. In addition, these observations are consistent with the narrow solidification range $\Delta T = T_{liq} - T_{sol}$ that is equal to 97.0 °C for the #0429 sample. The #0717 SC/HPDC UMSA sample solidified under ambient pressure ΔT = 142.9 °C and the structure exhibits very coarse primary and eutectic silicon and π, Q & θ phases, Figure 123 (c, d).

The as-cast structure of the #0429 (SC/HPDC UMSA cyclic pressure loading) sample shows a significantly smaller size and amount of primary Si particles at the subsurface and center (see Figure 123 (a, b)) in comparison with sample #0717 (SC/HPDC UMSA, 0.1 MPa), Figures 123 (c, d). The density of the Al-Si eutectic in sample #0429 is significantly higher, while the eutectic Si size is significantly smaller in comparison with sample #0717, Figures 123 (a, b). These differences are much greater between sample #0429 and sample #0808 that solidified in the HT UMSA under 0.1 MPa pressure, Figure 123 (e, f). Similar observations also pertain to all other phases π, Q & θ phases and (Q + θ) eutectic.

The HT UMSA sample (ref. #0808) which solidified at a slow ASR = 0.4 °C/s, (St = 336.2 s) exhibits a microstructure containing large blocky Primary Si particles (200 μm x150 μm), lamellar eutectic Si and Cu, Mg, Fe-rich intermetallic phases segregated between the Al-Si grains, (the size is in an order higher than in sample ref. #0717) solidified at ASR = 10.2 °C/s and sample ref.#0429 solidified at ASR = 20.1 °C/s.

Increasing the ASR from 0.4 ^{o}C/s to 21.9 °C/s for the unmodified experimental alloy decreases the size of the primary Si particles from 200 μm to 50 μm and acicular eutectic Si with a wheat morphology (the size is 10 μm x 200 μm) was changed to a finer structure (1 μm x 15 μm). All phases have the same tendency to decrease in size. Comparison of the microstructure for the samples with the slowest and fastest ASR (ref. #0808, #0717, #0429) is shown in Figures 123 (a-f) and approximate dimensions for the present phases are presented in Figure 124.

In summation, the First Derivative of the #0429 Cooling Curve does not show a separate peak associated with the small volume fraction of primary Si particles present in the as-cast structure. The primary Si peak is a part of the FD and is visible as the left hand peak "shoulder", see Figures 119a and 120. This fact indicates that this "Al-Si eutectic like" convoluted First Derivative can be the basis for future work aiming at a "tune-up" of the melt processing parameters and melt chemistry allowing for development and even more effective technology and unique as-cast structures for highly alloyed hypereutectic Al-Si alloys being free of primary Si. The deconvolution of the FD derivative will allow for the precise separation of nucleation and the end of individual reactions and determination of their characteristics. This task will be addressed in future work.

There is an extraordinary opportunity for further development of the cyclic loading technology for unmodified alloys with extraordinarily high T_{sol} even reaching beyond 521.1 °C for high temperature applications.

Even though sample #0429's SR at the Liquidus Temperature reached only 71.8 °C/s due to the low melt temperature delivered to the die cavity (660 °C) the SR at the Solidus Temperature is exceptionally high (43.6 °C/s). This observation strongly suggests that this phenomenon is controlled by the cycling loading process parameters. Test sample solidification time is 4.7 s and ASR = 20.1 °C/s and the unmodified melt solidified in the SC/HPDC UMSA under 0.1 MPa pressure where solidification time is 14.0 s and ASR = 10.2 °C/s, while sample #0808's solidification time is 315.8 s and ASR = 0.4 °C/s. Both samples #0429 and #0717 have similar instantaneous SR at the T_{liq}, however, the SC/HPDC UMSA ambient pressure sample's SR at the T_{sol} is approx. 13.7 °C/s, which reflects on the constituents' nucleation and evolution kinetics, temperature, time and consequently morphological characteristics. This experiment also clearly illustrates the effect of the first cyclic pressure loading on the T_{liq} and its instantaneous SR. The considerably higher untreated melt temperature for the melt delivered to the die cavity, in comparison with the cyclically loaded one (difference = 26.9 °C) shows that very low energy cyclic loading (ΔCE_{ss1} = 2.95 J) can compensate for this difference. The second cyclic loading step very significantly affects SR rates at the T_{sol} and Solidification Time. These process parameters consequently contributed to the fundamentally different solidification kinetics and consequently to the as-cast structures.

Comparison of the #0429 test sample structures for the unmodified experimental alloy processed under very moderate cyclic pressures with ultra high pressures presented

in the literature [263] allows for important Conclusions include the newly developed processing technology that is superior in terms of control of all aspects of the thermal and structural characteristics and required energy as well as simplicity of melt processing that can be rapidly scaled up and commercialized.

The Al-Si sandwich dendritic structure could be ideal for high performance cylinder liner applications. Etched out aluminum dendrites will create complex cavities that can very efficiently retain oil that is necessary to avoid dry engine start.

It can be hypothesized that the Al-Si sandwich dendritic structure could have very high compression strength and wear properties. Since Si forms a continuous shell on the α-Al dendrites, therefore, in a wear environment, it is expected that the morphology will help to significantly outperform other types of Si structures. It would be very interesting to determine the Si shell behavior during heat treatment (i.e. diffusion and possible fragmentation and spheroidization). Experiments using ultra high pressures up to 5GPa using unmodified Al-Si hypereutectic alloys did not demonstrate that the novel Al-Si sandwich type dendrites can be produced. This methodology is capable of a limited decrease in the size and volume fraction of the primary Si particles.

The above analysis for the selected process parameters, TA data and related structures indicates that the thermal characteristics for individual reactions are much more revealing in terms of linking them in a cohesive manner as far as the cause and effect paradigm is concerned.

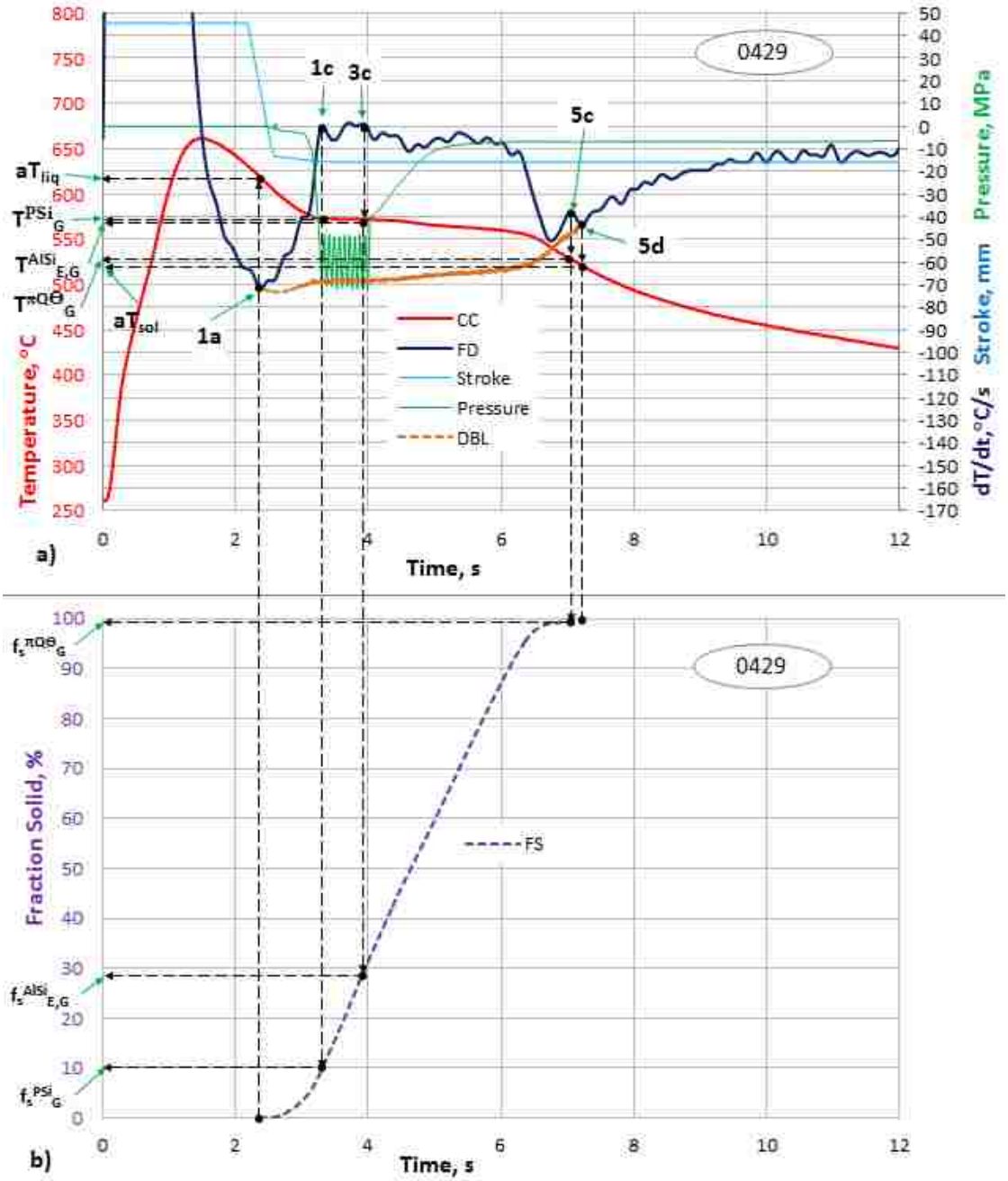

Figure 119. a) Cooling/Solidification Curve superimposed with the First Derivative and Dynamic Baseline and Stroke Curve vs. Time, b) Fraction Solid Curve vs. Time for the unmodified experimental alloy, solidified under impact and cyclic pressure (48-72) MPa/10c in the SC/HPDC UMSA die, ASR = 20.1 °C/s, ref. #0429.

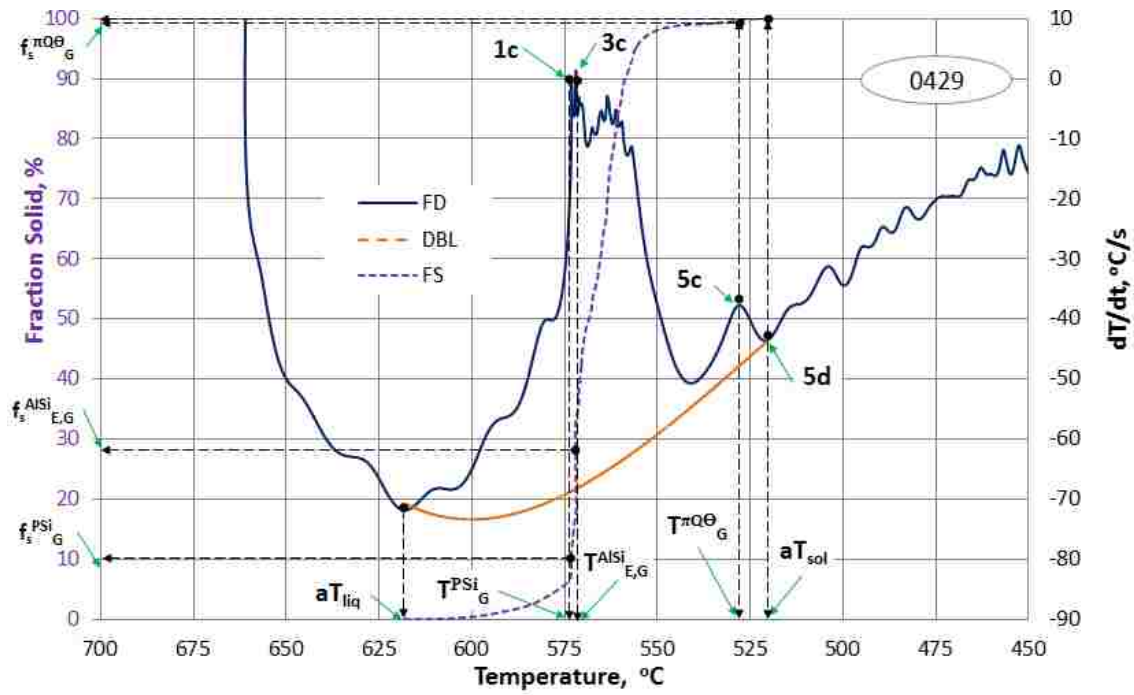

Figure 120. First Derivative Curve, Fraction Solid Curve and Dynamic Baseline vs. Temperature for the unmodified experimental alloy, solidified under impact and cyclic pressure (48-72) MPa/10c, in the SC/HPDC UMSA die, ASR = 20.1 °C/s, ref. #0429.

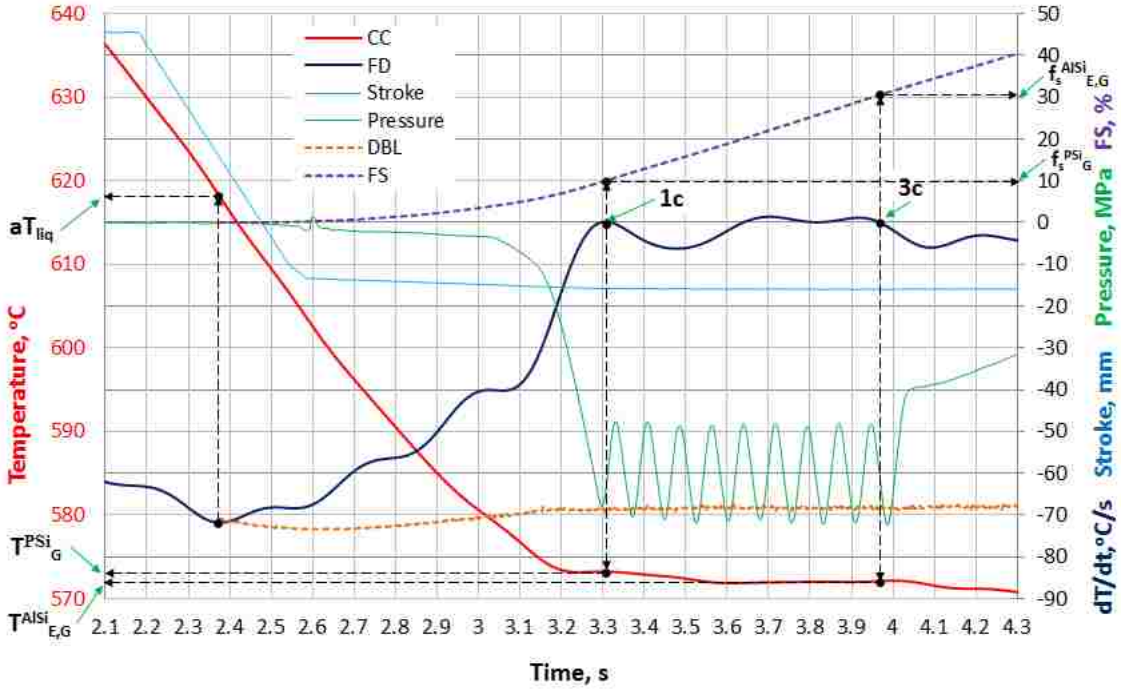

Figure 121. Cooling/Solidification Curve superimposed with the First Derivative and Dynamic Baseline, Fraction Solid and Stroke Curve vs. Time for the unmodified experimental alloy, solidified under impact and cyclic pressure (48-72)MPa/10c in the SC/HPDC UMSA die, ASR=20.1°C/s, ref. #0429.

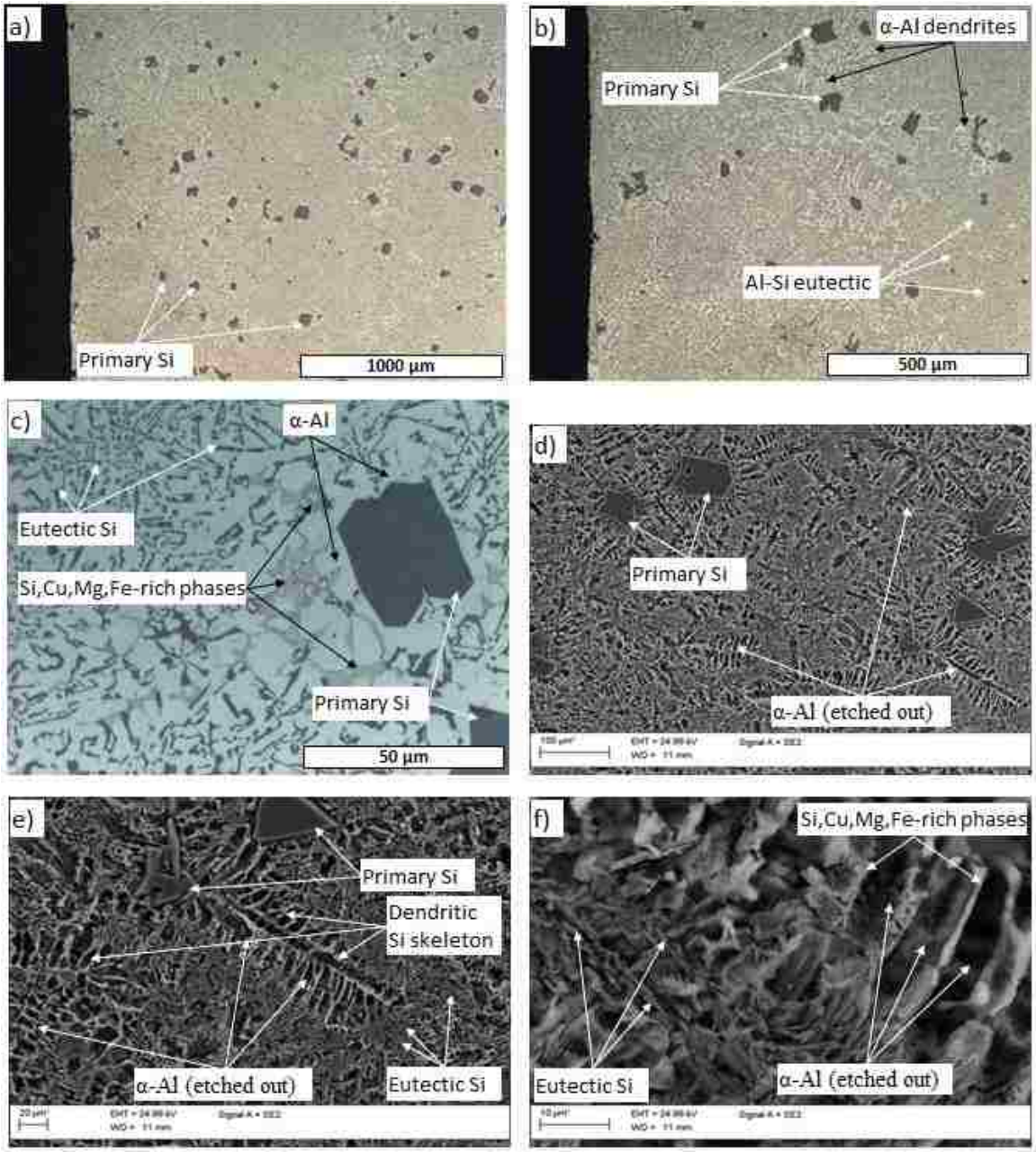

Figure 122. a - c) LOM polished and d - f) SEM deep-etched microstructures for the unmodified experimental alloy processed in the SC/HPDC UMSA die under impact and cyclic pressure (48-72) MPa/10c at ASR = 20.1 ºC/s, ref. #0429.

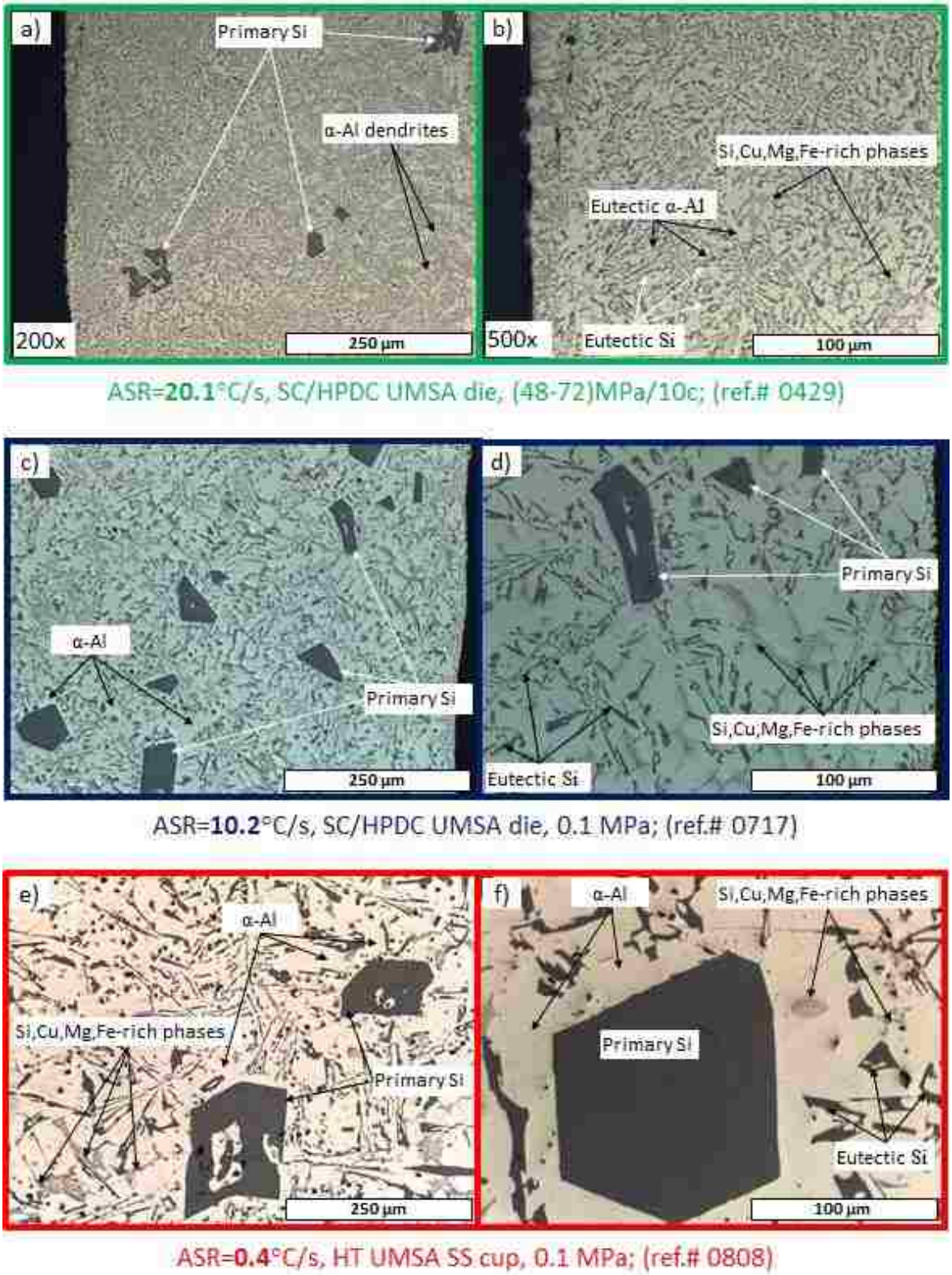

Figure 123. LOM micrographs, (subsurface of the samples) for the unmodified experimental alloy solidified; a - d) SC/HPDC UMSA die under a different ASR and different pressure conditions; e, f) HT UMSA SS cup, ref. #0429, #0717, #0808.

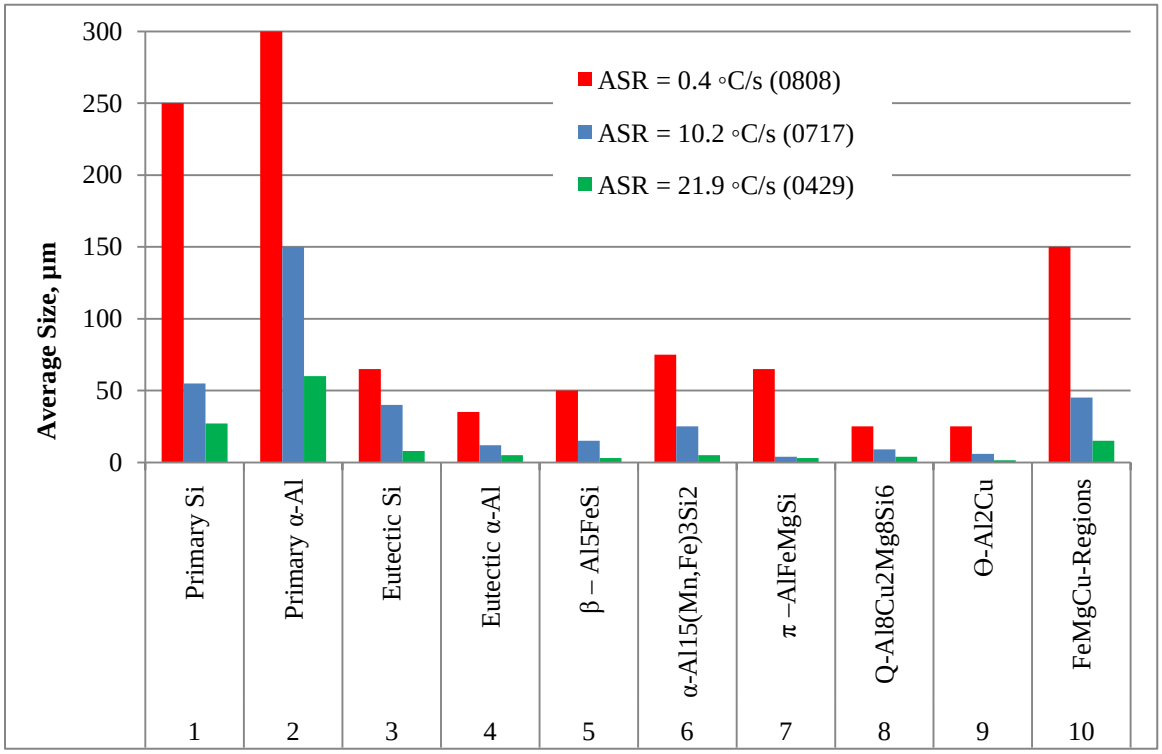

Figure 124. Comparison between the as-cast phases Average Size unmodified experimental alloy, solidified; (Red) in the HT UMSA SS cup under atmospheric pressure at ASR = 0.4 ºC/s, ref. #0808; (Blue) in the SC/HPDC UMSA die under atmospheric pressure at ASR = 10.2 ºC/s, ref. #0717 and (Green) in the SC/HPDC UMSA die under impact and cyclic pressure (48-72) MPa/10c at ASR = 21.9 ºC/s, ref. #0429.

4.3.2 Thermal Data and Microstructure for the 0.04 wt.%Sr Modified Alloy Sample #1009 processed in the SC/HPDC UMSA Platform

This experiment is a part of the initial research aimed at determining the effective Sr level capable of converting the hypereutectic structure into a nano and ultra-fine single Si phase structure using two stage cyclic pressures loading during natural solidification in the die. As can be observed in Figure 125 (a, b) during the natural solidification process at a temperature of 620.4 °C, the first cyclic (impact) pressure loading of 52.9 MPa was applied. The second cyclic loading of (38-82) MPa/10c immediately followed the first one. These two loading cycles resulted in rapid enhancement of the SR from 46.5 °C/s to 106.1 °C/s, which is associated with the apparent liquidus temperature of 597.0 °C. Details about the solidification sequence are provided in Figures 125 (a, b) and 126. Structural analysis of sample #1009, provided below, justified this limited TA data analysis.

Figure 127 (a – f) shows 200x and 1000x LOM micrographs of the subsurface structures of a, b) unmodified and c, d) modified melt using 0.04 wt.%Sr. As can be observed, the addition of 0.04 wt.% Sr to the pressure treated melt considerably improved the as-cast subsurface structure. However, improvements to both the subsurface and the center (primary Si particles are present) are not sufficient to produce the desired as-cast Al-Si eutectic nano Si whiskers that are present in sample #0925b that was modified by the addition of 0.15 wt.%Sr, see Figure 136(e, f).

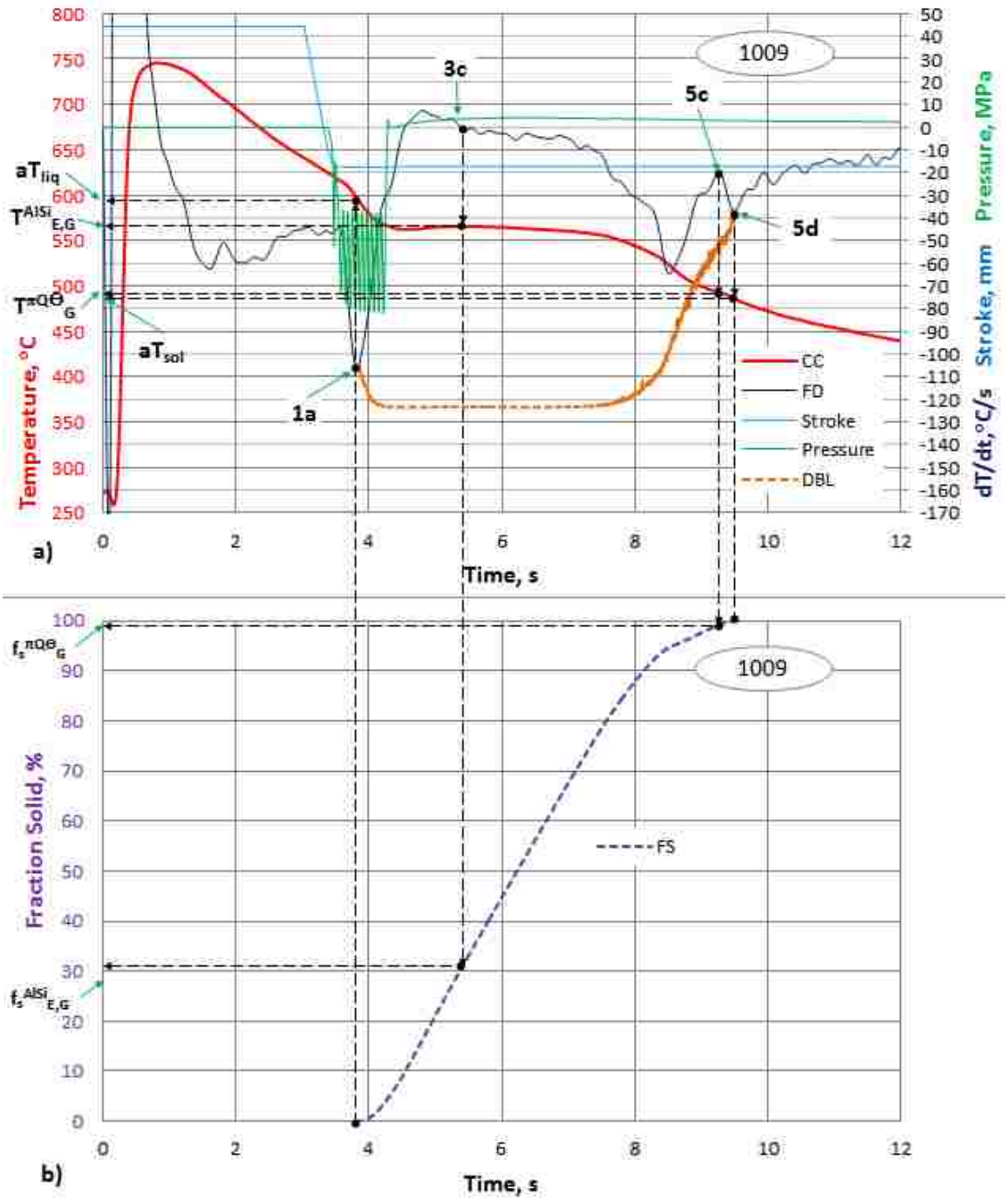

Figure 125. a) Cooling/Solidification Curve superimposed with the First Derivative, Dynamic Baseline, Stroke amd Pressure Profile Curves vs. Time, b) Fraction Solid Curve vs. Time for the 0.04wt.%Sr modified experimental alloy, processed under impact and cyclic pressure (38-82) MPa/10c in the SC/HPDC UMSA die, ASR = 19.5 °C/s, ref. #1009.

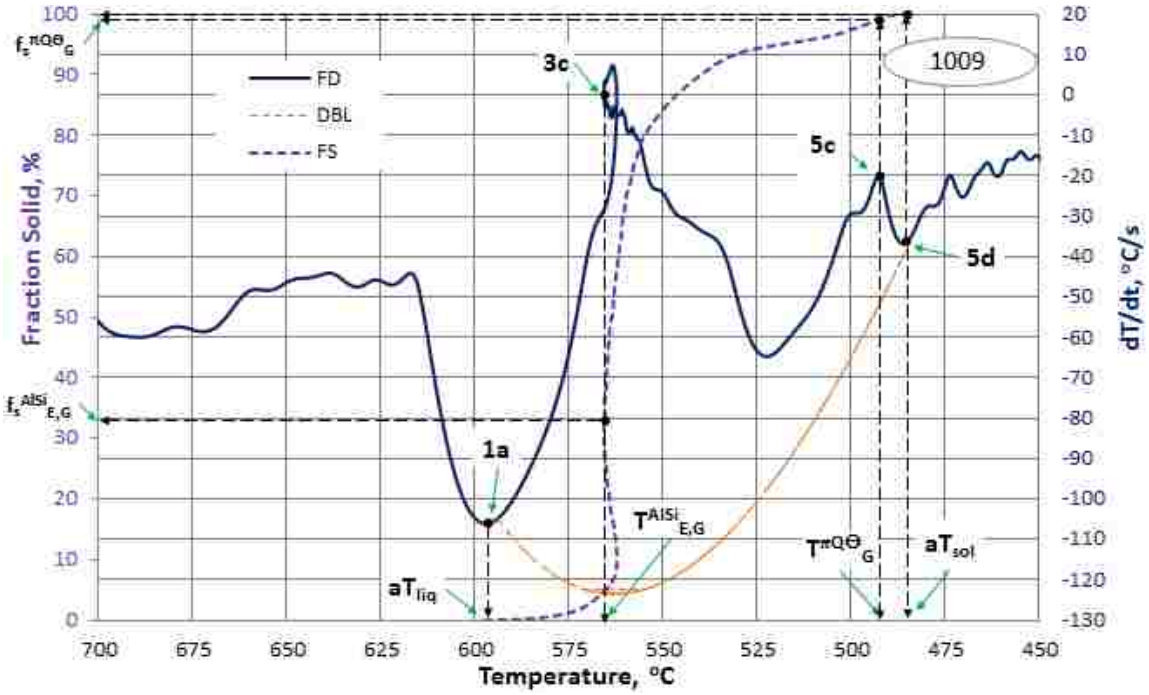

Figure 126. First Derivative Curve, Fraction Solid Curve and Dynamic Baseline vs. Temperature for the 0.04wt.%Sr modified experimental alloy, solidified under impact and cyclic pressure (38-82) MPa/10c, in the SC/HPDC UMSA die, ASR = 19.5 °C/s, ref. #1009.

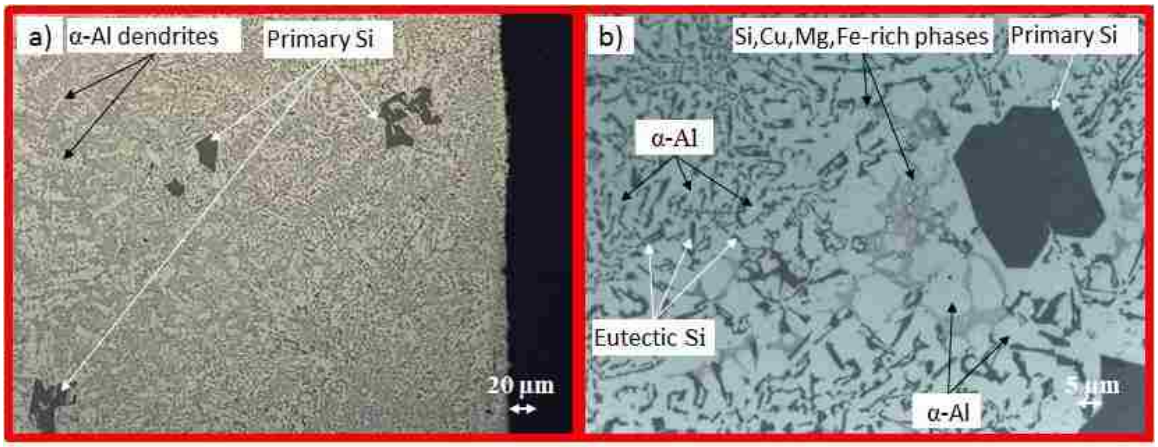

Unmodified, SC UMSA die, (48-72)MPa/10c, (ref.# 0429)

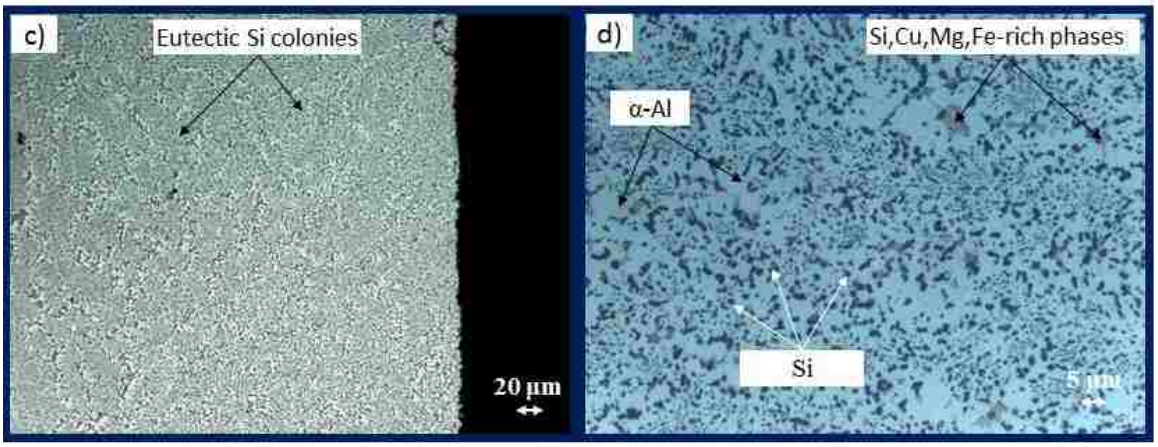

0.04 wt.% Sr, SC UMSA die, (40-80)MPa/10c, (ref.# 1009)

Figure 127. LOM micrographs showing the experimental alloy, processed in the SC/HPDC UMSA die under impact and cyclic pressure (38-81) MPa/10c: a, b) unmodified, ref. #0429, c, d) 0.04 wt.%Sr modified, ref. #1009.

4.3.3 Thermal and Microstructural Analysis for the 0.15 wt.%Sr Modified Alloy Samples processed in the SC/HPDC UMSA Die using Impact and Cyclic Pressure Loadings

Quantitative analysis of cyclic and impact pressure loading under confined and semi-confined conditions is a complex task due to many interrelated processing, testing and analytical factors and techniques that have not been applied in metal casting to date.

Experiments for the 0.15 wt.%Sr modified alloy samples #0925b, #0916, 0916b, #0628b, #0919, #1002b and #0517, respectively were performed according to Table 13, where SC/HPDC UMSA Test Processing Parameters are presented. Figures 128-130, 141-148,151,152,154 and 155 show the Cooling/Solidification Curves, First Derivative Curves, Dynamic Baseline, Stroke Curves, Pressure profiles and Cumulative Energy Curve vs. Time and/or vs. Temperature. In order to illustrate the effect of slowly applied pressure, impact pressure, cyclic pressure and multi-level loading, three melts samples #0925b, #0916 and #0628b were selected for more detailed analysis. The as-cast structures of the tested melts show the best, the second best and the least favourable overall structural characteristics, respectively. Among several other process parameters, the Pressure Start Temperature (T^{P}_{ST}), Cumulative Energy between T^{IP} and aT_{liq} (ΔCE_{liq2}) and associated other TA characteristics have a significant effect on nucleation kinetics and contribute to the final as-cast structure.

Taking into consideration the above-mentioned experimental and analytical limitations it is rewarding to observe that the pressure applied to the molten and semi-solid test sample “instantly” results in acceleration of the SR. Even though the aluminum alloy is a good heat conductor, the sample edge experiences a higher SR, and there is a temperature gradient across the test sample diameter.

4.3.3.1 Sample #0925b (Structure Category #1.1)

Sample #0925b is rated as the best in Structure Category #1.1 having nano Si whiskers, ultrafine Al-Si Eutectic colonies and boundaries as well as ultrafine Al-Cu-Mg-Si and Al-Fe-Cu-Si constituents, see Tables 19, 20, 30, 31 and Figures 135 - 140.

Effect of SC/HPDC UMSA Process Parameters on Alloy's Thermal Characteristics

Sample #0925b with the addition of 0.15 wt% Sr was processed in the SC/HPDC UMSA under impact and cyclic pressure of (28-81) MPa/10c applied to the liquid and semi-solid melt until it reached its Al-Si eutectic minimum ($T^{AlSi}_{E,MIN}$) temperature.

SC/HPDC UMSA Process Parameters and Thermal Analysis Data are presented in Figures 128 and 129 and Tables 21 and 22. Figure 130 shows the details of Figure 128a pertaining to the liquid melt, apparent Liquidus Temperature and semi-solid regions. In addition, Figure 130 provides detailed information about the calculated Cumulative Energy delivered to the dynamically treated melt during its cooling and solidification processes.

The melt was superheated to a temperature of 805 °C and was poured to the SC/HPDC UMSA die having an initial temperature of 262.0 °C. The maximum temperature of the melt, delivered to the die (T^{D}_{MAX}) = 756 °C, was achieved by the rapid opening of the melting furnace bottom gate. During cooling, the melt passed the "natural" Liquidus Temperature of 628 °C @ (2.7 s, ISR = 65.0 °C/s).

At the melt temperature of 619.2 °C @ (2.847 s, ISR^{P}_{ST} = 57.9 °C/s) the plunger started to apply an initial pressure of -0.41 MPa. At a temperature of 609.9 °C single impact treatment pressure of -26.6 MPa was reached at 2.991 seconds (Δt = 0.15 s).

This corresponds with the local minimum of the FD at which the Instantaneous ISR^{IP} = 68.6 °C/s. Cumulative Energy delivered to the liquid melt by the impact pressure ΔCE_{liq1} = 20.9 J. At the melt temperature of 602.9 °C and time = 3.102 s, the first cyclic pressure peak dropped to -71.6 MPa while the ISR = 57.1 °C/s. The consecutive cyclic pressure (38-81) MPa/4c after 0.24 s delivered ΔCE_{liq2} = 10.5 J resulting in an ultra-rapid increase in $ISR_{a,liq}$ = 100.5 °C/s that coincides with the apparent Liquidus Temperature of 584.2 °C ("forced" T_{liq}). At aT_{liq} spontaneous solidification of the dynamically treated melt started. Both applied pressure and the resulting very high SR at aT_{liq} allows for good interface contact between the test sample surface and the die protection BN film. Thus, the heat transfer to the die was very significantly improved. The relationship between the TA characteristics and the sample structure is provided later.

Seamlessly continued cyclic pressure loading of (38-81) MPa/6c through the aT_{liq} to the semi-solid region delivered ΔCE_{ss1} = 4.2 J energy, until the melt temperature reached $T^{AlSi}_{E,MIN}$ = T^{P}_{END} = 560.2 °C @ (3.816 s, $ISR^{AlSi}_{E,MIN}$ = +0.068 °C/s). The total energy delivered to the test sample in both liquid and semi-solid states amounts to $TCE_{liq-sol}$ = 35.5 J. This processing strategy resulted in the best overall structure for sample #0925b/#1.1. Comparison of process parameters, TA characteristics and the structure of sample #0925b with other samples proved that prolonged pressure treatment(s) beyond $T^{AlSi}_{E,MIN}$ is not beneficial and in some cases is detrimental (i.e. #0628b).

The Undercooling Temperature of the Al-Si eutectic reaction $\Delta T^{AlSi}_{E,UC}$ = 23.9 °C, ($\Delta T^{AlSi}_{E,UC}$ = aT_{liq} - $T^{AlSi}_{E,MIN}$), while the Recalescence Temperature of the Al-Si eutectic reaction $\Delta T^{AlSi}_{E,R}$ = 7.1 °C, ($\Delta T^{AlSi}_{E,R}$ = $T^{AlSi}_{E,G}$ - $T^{AlSi}_{E,MIN}$) and the Recalescence time

$\Delta t^{AlSi}_{E,R}$ = 0.95 s which corresponds with the $SR^{AlSi}_{E,R}$ = 7.5 °C/s. Fraction Solid at the Al-Si Eutectic Growth Temperature $f_s{}^{AlSi}_{E,G}$ = 32.1 %.

The total time for both impact and cyclic pressure loading is 0.98 s, while the Temperature Range of Pressure Treatment ΔT^{P}_{Rn} = 59.2 °C. The Solidification Temperature Range SRn = 95.5 °C and Total Solidification Time St = 5.2 s.

As can be observed, the melt processing and related solidification thermal events are of a dynamic nature and substantially change in an ultra short time. Strategically chosen processing parameters very profoundly affect the entire melt's solidification process, all thermal characteristics and consequently the as-cast structures including nano Si whiskers, ultra-fine Al-Si Eutectic colonies and their boundaries as well as ultra-fine Al-Cu-Mg-Si and Al-Fe-Cu-Si constituents.

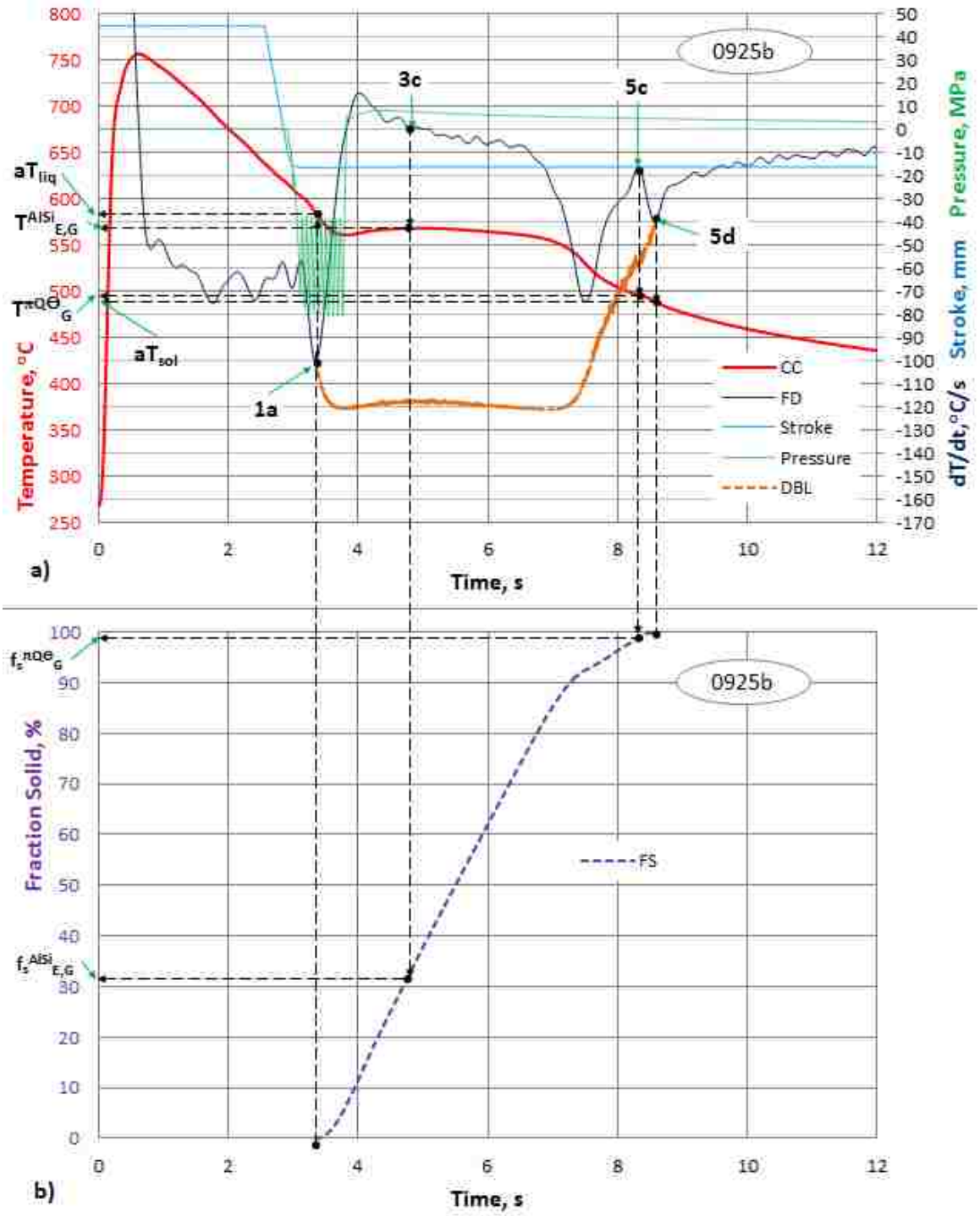

Figure 128. a) Cooling/Solidification Curve superimposed with the First Derivative, Dynamic Baseline, Stroke and Pressure Profile Curves vs. Time, b) Fraction Solid Curve vs. Time for the 0.15 wt.%Sr modified experimental alloy, solidified under impact and cyclic pressure (38-81) MPa/10c in the SC/HPDC UMSA die, ASR = 18.3 °C/s, ref. #0925b.

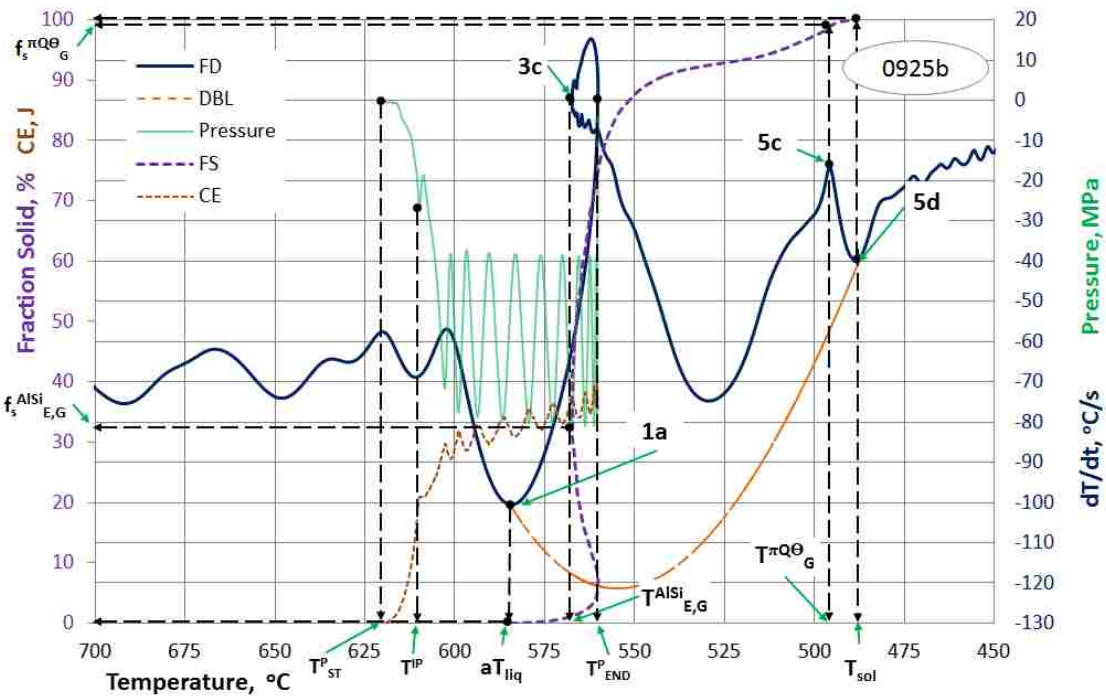

Figure 129. First Derivative Curve, Fraction Solid Curve and Dynamic Baseline vs. Temperature for the 0.15 wt.%Sr modified experimental alloy, solidified under impact and cyclic pressure (38-81) MPa/10c, in the SC/HPDC UMSA die, ASR = 18.3 °C/s, ref. #0925b.

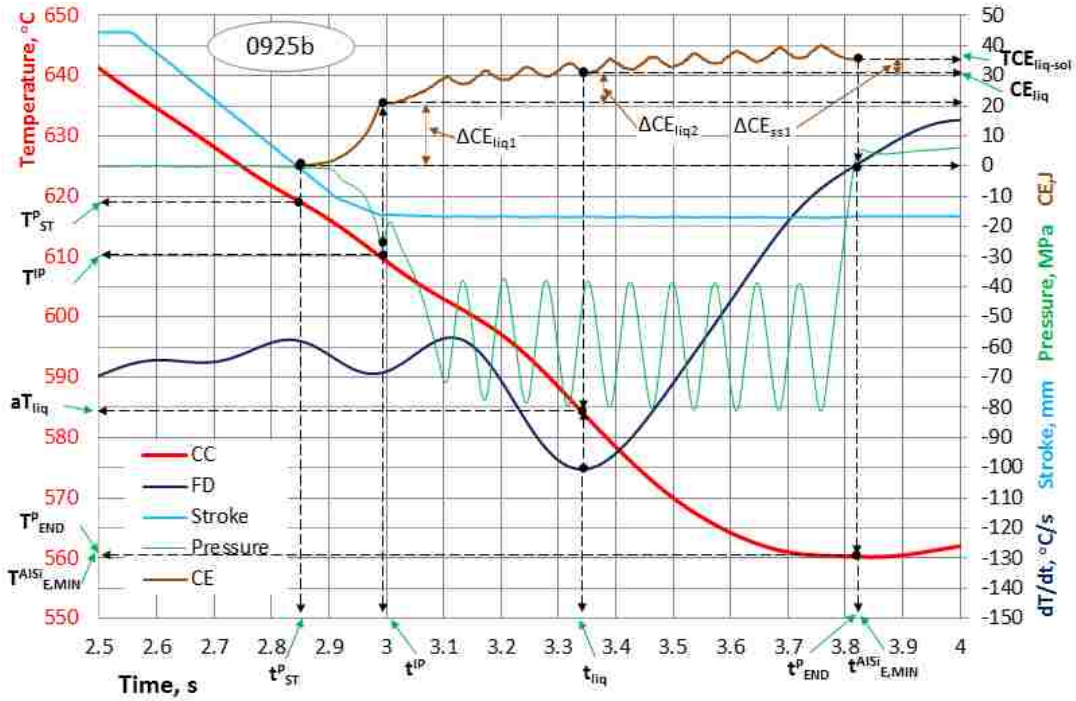

Figure 130. Cooling/Solidification Curve superimposed with the First Derivative Curve, Pressure Profile Curve, Stroke and Cumulative Energy Curve vs. Time for the 0.15 wt.%Sr modified experimental alloy, processed using impact pressure and cyclic pressure (38-81) MPa/10c in the SC/HPDC UMSA die, ASR = 18.3 °C/s, ref. #0925b.

Please note that Figure 129 is very busy in terms of process parameters and thermal characteristics therefore, the FD and the calculated DBL are presented in Figure 131. The Dynamic Baseline equation together with R^2 is presented in the section on De-Convolution of the Cooling Curve's First Derivative.

De-Convolution of the Cooling Curve's First Derivative

The ultra-rapid solidification process for the 0925b melt causes convolution of the thermal peaks in the First Derivative of the Cooling Curve; see Figure 128a. Conversely, the FD of the slowly solidifying melt shows the individual thermal events more clearly; see Figure 89a. The morphology of the "co-existing" as-cast phases associated with the given metallurgical "dynamic" reactions closely resembles the thermal peak convolution phenomenon.

The Dynamic Baseline (DBL) vs. Temperature (T) in the form of the fifth level polynomial function (Equation #11) was developed and fit to the First Derivative data between the melt's liquid and solid states presented in Figure 131.

$R^2 =$ 9.812277666051E-01.

$$DBL = 2.729073782011\ E\text{-}09 \cdot T^5 - 5.939849109264\ E\text{-}06 \cdot T^4 + 5.118218761861\ E\text{-}03 \cdot T^3 - 2.185933745489\ E{+}00 \cdot T^2 + 4.631981607540\ E{+}02 \cdot T - 3.898692374269\ E{+}04$$

…… **Equation 11**

Some additional thermal characteristics of the dynamically treated liquid and semi-solid 0925b melt can be observed in the partially de-convoluted metallurgical reactions recorded on the Cooling Curve First Derivative vs. Time (Figure 132) and consequently Fraction Solid Curve vs. Temperature and Thermal Power Release vs. Temperature plots that are presented in Figures 131 – 134.

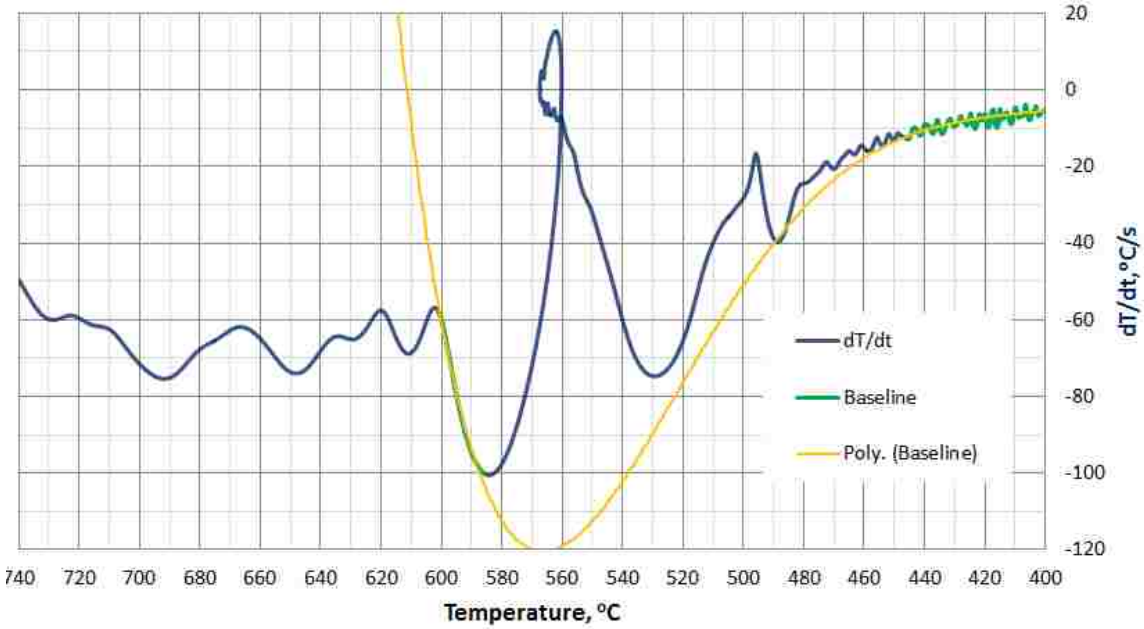

Figure 131. First Derivative Curve and the Calculated Polynomial DBL vs. Temperature for the 0.15 wt.%Sr modified experimental alloy, solidified under impact and cyclic pressure (38-81) MPa/10c, in the SC/HPDC UMSA die, ASR = 18.3 °C/s, ref. #0925b.

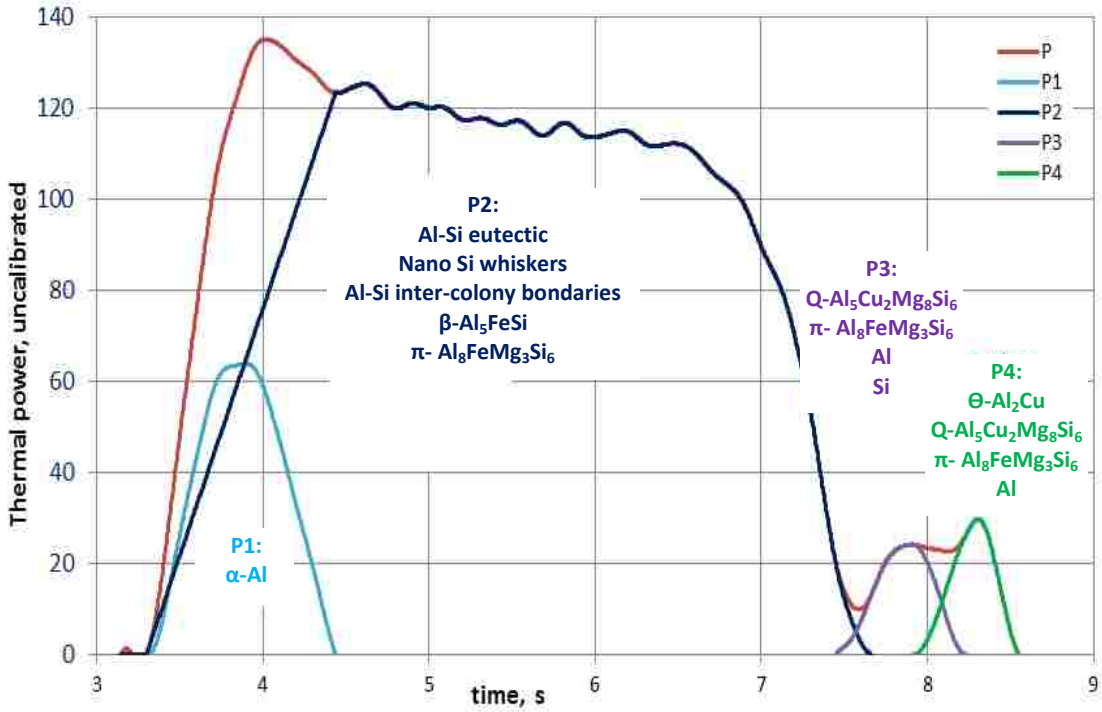

Figure 132. Deconvoluted First Derivative Curves for Individual Thermal Events vs. Time for the 0.15 wt.%Sr modified experimental alloy, solidified under impact and cyclic pressure (38-81) MPa/10c, in the SC/HPDC UMSA die, ASR = 18.3 °C/s, ref. #0925b.

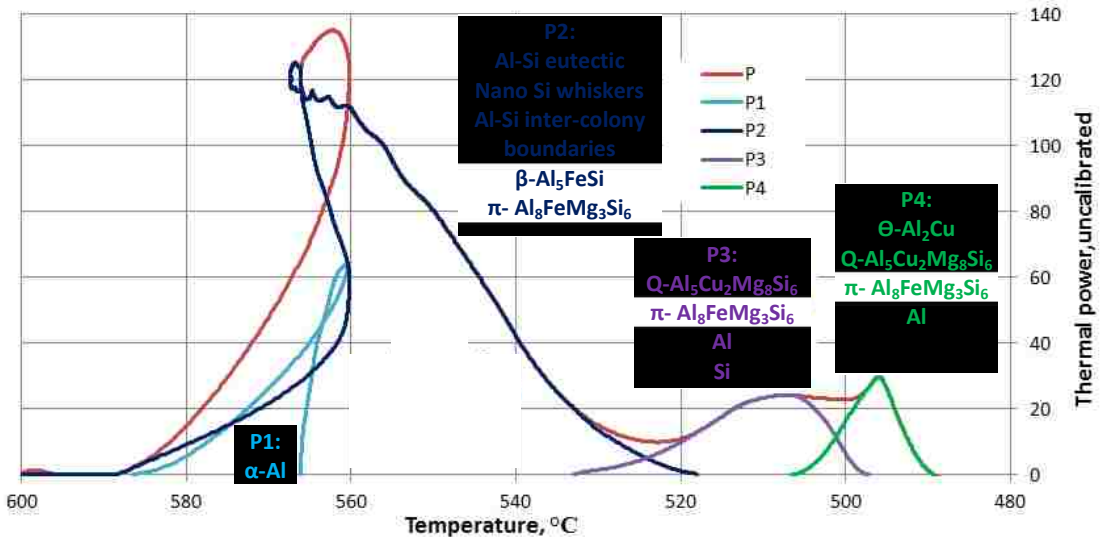

Figure 133. Deconvoluted First Derivative Curves for Individual Thermal Events vs. Temperature for the 0.15 wt.%Sr modified experimental alloy, solidified under impact and cyclic pressure (38-81) MPa/10c, in the SC/HPDC UMSA die, ASR = 18.3 °C/s, ref. #0925b.

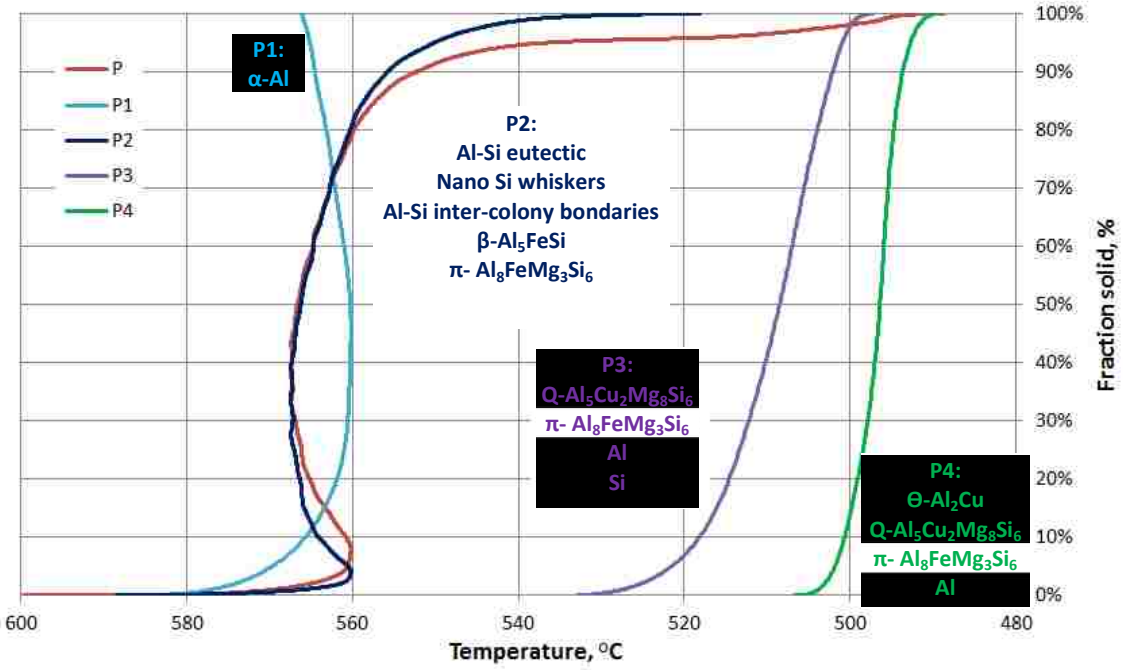

Figure 134. Deconvoluted Fraction Solid Curves for Individual Thermal Events vs. Temperature for the 0.15 wt.%Sr modified experimental alloy, solidified under impact and cyclic pressure (38-81) MPa/10c, in the SC/HPDC UMSA die, ASR = 18.3 °C/s, ref. #0925b.

Metallographic Analysis of As-Cast Sample #0925b

Comprehensive metallographic analysis techniques involving LOM, SEM/EDS, S/TEM/EDS were utilized for characterization of the subsurface and center of the as-cast structure of sample #0925b. Metallographic data collected from the polished and deep etched analytical planes together with thin foils allowed for the gathering of complementary information for determination of the relationship between the process parameters and the TA characteristics.

SC/HPDC UMSA test samples classified as Category #1 include sample #0925b processed using the best parameters, to date, which exhibit novel as-cast nano and ultrafine structures.

Light Optical Microscopy and Scanning Electron Microscopy Characterization of Novel Nano and Ultrafine Structures

Areas of Interest on the Test Sample's Transverse Section

Figures 135 (a and b) show structures observed at 100x magnification on the polished test sample #0925b's transverse section. In the subsurface close to the edge (at the left side of Figure 135a) there is a substantial amount of white α-Al channels extending up to approximately 250 μm. In the adjacent area toward the center, an elongated Al-Si eutectic colony in the form of a "sea star" is visible. This "sea star" extends to approximately 750 μm from the edge of the sample. The transverse analytical plane sections the "sea stars" that are non-uniformly distributed in the 3D space. Some of the "sea stars" are sectioned near the center or close by (see Figures 136 (a and e) and 138 (a and b), however, in a vast majority of cases, the plane is going through the arms of the "sea stars". The structure from the center of the sample, Figure 135b, shows equiaxed

and elongated Al-Si eutectic colonies, the inter-colony boundaries with Cu, Mg, Si and Fe rich phases and residual primary Si particles having a diameter of approx. 25 μm. Table 20 provides the summary of the stereological characteristics from both the subsurface and center of the test samples. In Figures 138 (a and b) the area of equiaxed "sea stars" can be observed. More details of these structures are presented in Figures 136 - 138 and are explained further in the text.

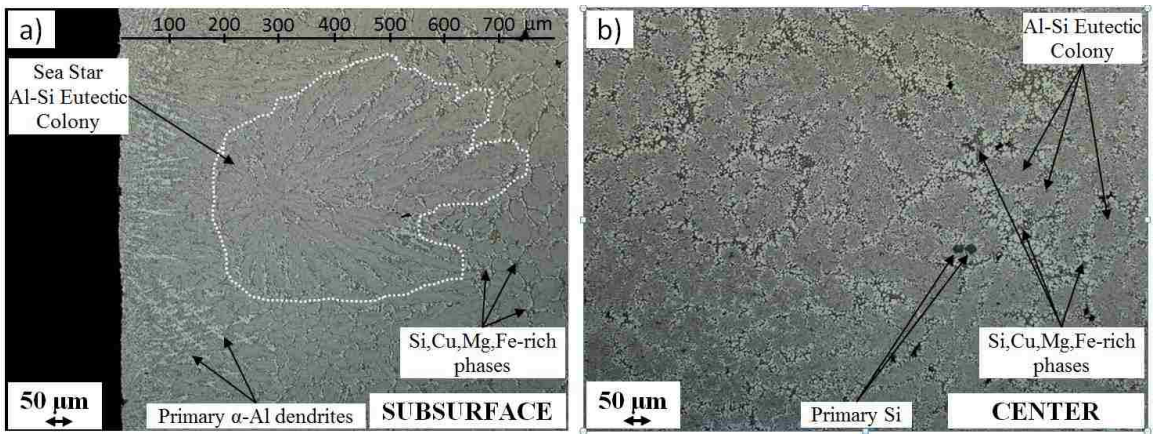

Figure 135. LOM micrographs for the 0.15 wt.%Sr modified experimental alloy, solidified in the SC/HPDC UMSA die, under impact and cyclic pressure (38-81) MPa/10c; a) Subsurface of the sample, b) center of the sample, ref.#0925b, mag. 100x.

Micrographs in Figures 136 (a, b, d and f) show a very significant amount of α-Al phase in the form of channels that are aligned with the heat transfer direction. These rapid heat transfer channels are up to 230 μm in length and are up to 15 μm in width. SEM/EDS determined chemical composition of the subsurface Al channels as follows: Al = 94.77 wt.%, Si = 1.07 wt.%, Cu = 3.40 wt.% and Mg = 0.76 wt.%. Between the aluminum channels very fine Al-Si colonies with nano Si whiskers can be observed.

Figure 136(c) shows elongated Eutectic Al-Si colonies of up to 90 μm in length and 20 μm in width that are located in close vicinity to the α-Al channel circumference layer. The inter colonies average boundary thickness is 2.6 μm.

SEM/BS images as shown in Figures 136 (e and f) revealed morphology of the phases rich in heavier elements like Cu and Fe that are brighter in comparison with Al and Si due to the difference in the atomic numbers. These phases are located in the inter Al-Si colony boundaries.

Figures 137 (a to f) present more structural details including sectioned nano Si whiskers that can be observed in micrographs (c to f).

Figures 138 (a and b) present SEM micrographs of the deeply etched regions near the subsurface exhibiting structures resembling a "sea star" morphology having approximately 26 closely packed Al-Si nano Si whisker colonies located in approximately 10 arms of this analytical plane. These arms are growing outwards from the common origin. The diameter of the "sea star" is approximately 250 μm. Each Al-Si Eutectic colony is made up of nano Si whiskers which originate from the common region.

The SC/HPDC UMSA technology developed in the framework of this PhD project is able to nucleate and grow novel single-phase Si whiskers having an average diameter of 220 nm and Standard Deviation of 48 nm. To date, there is no literature evidence that the single-phase Si whiskers were obtained using the industrial grade hypereutectic as-cast Al-Si-Cu alloy that was utilized in this project. Further discussion about other developed structural features can be found in Section 4.4.

Si whiskers resembling “sea grass” nucleate from the same origin and their growth is not considerably disturbed by the branching process, see Figure 138 (e and f). The edge-to-edge distance between individual whiskers is approximately 400 nm.

The SEM/EDS analysis of the Al-Si eutectic colonies microchemistry revealed their average chemical composition as follows: Al = 80.13 wt.%, Si = 18.00 wt.% and Cu = 2.82 wt.%. Due to the nano structured Si whiskers it can be assumed that this analysis is acceptable. No other elements were detected in these nano-structured features. The content of Cu in the middle of the Al-Si colonies is 2.44 wt.% and on the periphery of the Al-Si colonies is ≈ 3.2 wt.%. This analysis does not mean that Sr will be not detected using more sophisticated techniques like Auger Spectroscopy. The S/TEM analysis of the heat treated sample (ST+AA) identified 0.1 wt.%Sr in the Si particles located in the center of the sample ref.#1029-AA2).

The “sea star” arms are separated by the open-cell Si-X foam-like structure with a large volume fraction of cells filled in by the aluminum. This open-cell Si-X foam-like structure forms the inter Al-Si colony boundaries. Further away from the center of the “sea star” the “thickness” of the open cell Si-X foam is larger. Figures 139, 140 and Tables 30, 31 show the SEM/EDS chemical compositions of these phases. This analysis revealed that 4.4 wt.%Sr and other elements like Al, Cu and Mg are present in this novel structure, while the aluminum droplets filling the “open cell” are enriched with Cu, Si and Mg. The open cell Si-X structure is the substrate for the last solidified Q & Θ phases; (Q-$Al_5Cu_2Mg_8Si_6$) & (Θ-Al_2Cu). Further heat treatment research revealed that the open-cell Si-X foam-like structures together with Q and Θ phases can be ultra rapidly dissolved in the matrix by high temperature Solution Treatment.

The above mentioned and tabulated process parameters control the nucleation and growth of the single-phase Si whiskers and the Al-Si colonies (Feret Diameter = 18.3 μm x 74.9 μm) as well as the inter colony boundaries (average thickness = 2.6 μm) and their chemical make-up. In addition, these powerful process parameters also control morphological features of Fe, Cu and Mg rich phases.

The regions closer to the center of the sample exhibit more semi and individual eutectic nano Si whisker(s) colonies that are separated by the open cell Si-X foam structures, see Figures 138 (c, d and e).

The LOM, SEM/EDS and Thermal Analysis of the discussed as-cast structures indicates that after formation of the Al-Si eutectic nano Si whisker(s) cells, the remaining liquid melt between them is supersaturated with Al, Si, Cu, Mg and Sr. Rapid solidification of this liquid melt most likely nucleated Al "particles" that are a substrate for formation of the open cell Si-X foam structure which nucleates the Θ+Q eutectics.

The spatial resolution and detection limit of the SEM/EDS analysis of the micron range thickness phase can be affected by the electron beam interactions with the surrounding phases, therefore, this data could indicate that the open cell structure could be made of highly alloyed Si. TEM/EDS data will be necessary for future comprehensive chemical and physical characterization of the open cell Si-X alloy structure.

As can be observed in Figure 160 the 100 nm to 1000 nm Al-Cu-Mg (Si) eutectics and nano Si whiskers are very thin and can be rapidly fragmented and dissolved and spheroidized, respectively, during ultra-rapid ST. This chemical data indicates that the dissolved phases located between the Al-Si eutectic cells will significantly increase the level of various elements in these regions. Most likely this phenomenon will result in a

significant increase of the strengthening precipitates formed during aging. It would be of paramount importance to simultaneously optimize the alloy system, its modification, refinement and processing using novel pressure loading profiles.

In order to obtain more information about nucleation and growth of eutectic Al-Si nano Si whisker(s) colonies and the open cell Si-X foam structure it would be necessary to perform 3D structure reconstruction and nano chemical analysis.

Further optimization of both alloy chemistry (i.e. substantially lower Cu levels) and processing parameters (i.e. a more efficient die cooling system and further optimized melt pressure loading parameters) will allow for the production of nano-structured materials with outstanding engineering properties.

A very large number of the SC/HPDC UMSA Processing Parameters, TA characteristics and the resultant structural descriptors indicate the need for statistically designed experiments sufficient for development of the model linking the effect(s) of the process variables and experimental outcomes.

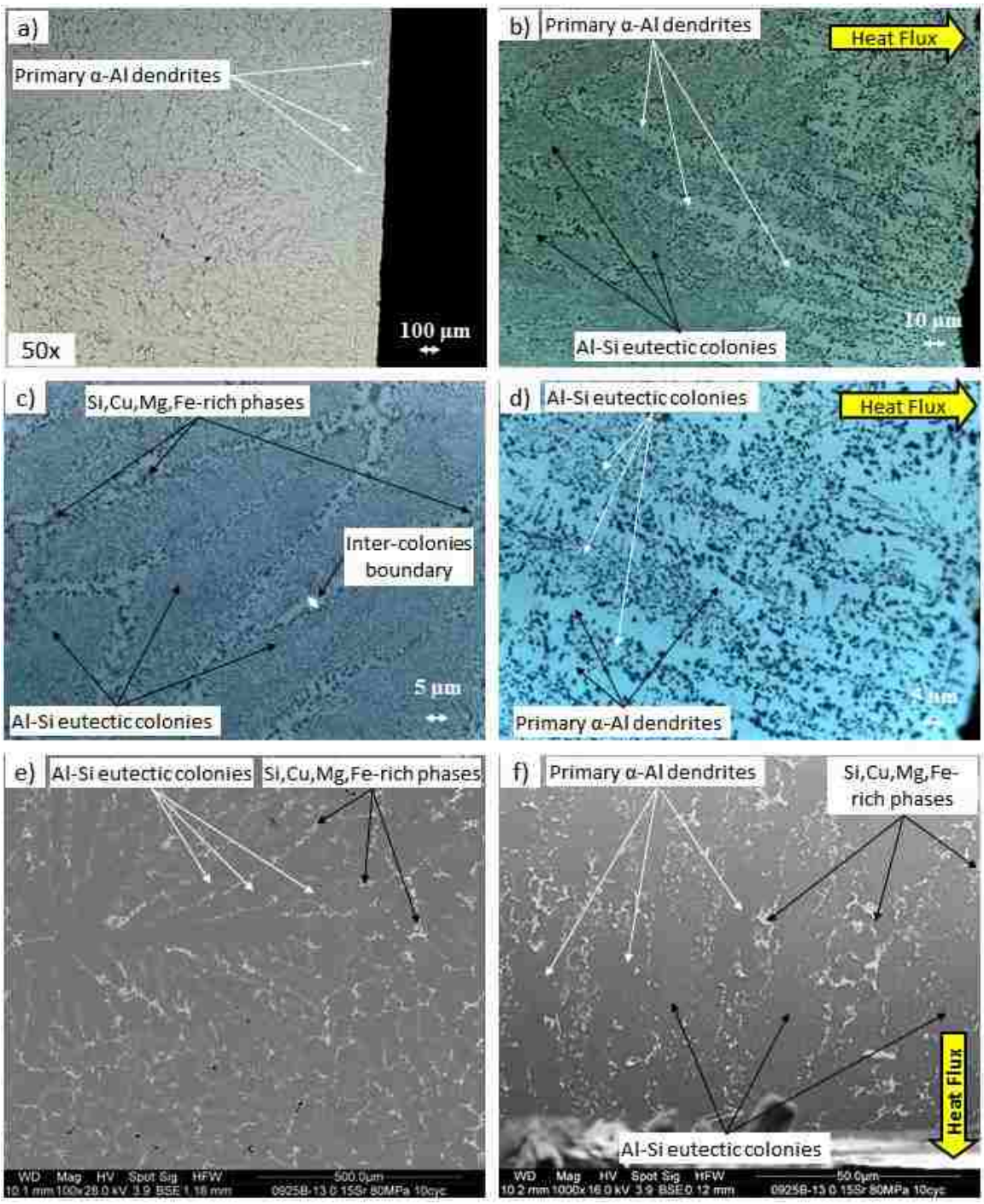

Figure 136. a - d) LOM and e, f) SEM micrographs for the 0.15 wt.%Sr modified experimental alloy, solidified in the SC/HPDC UMSA die under impact and cyclic pressure (38-81) MPa/10c, ref. #0925b.

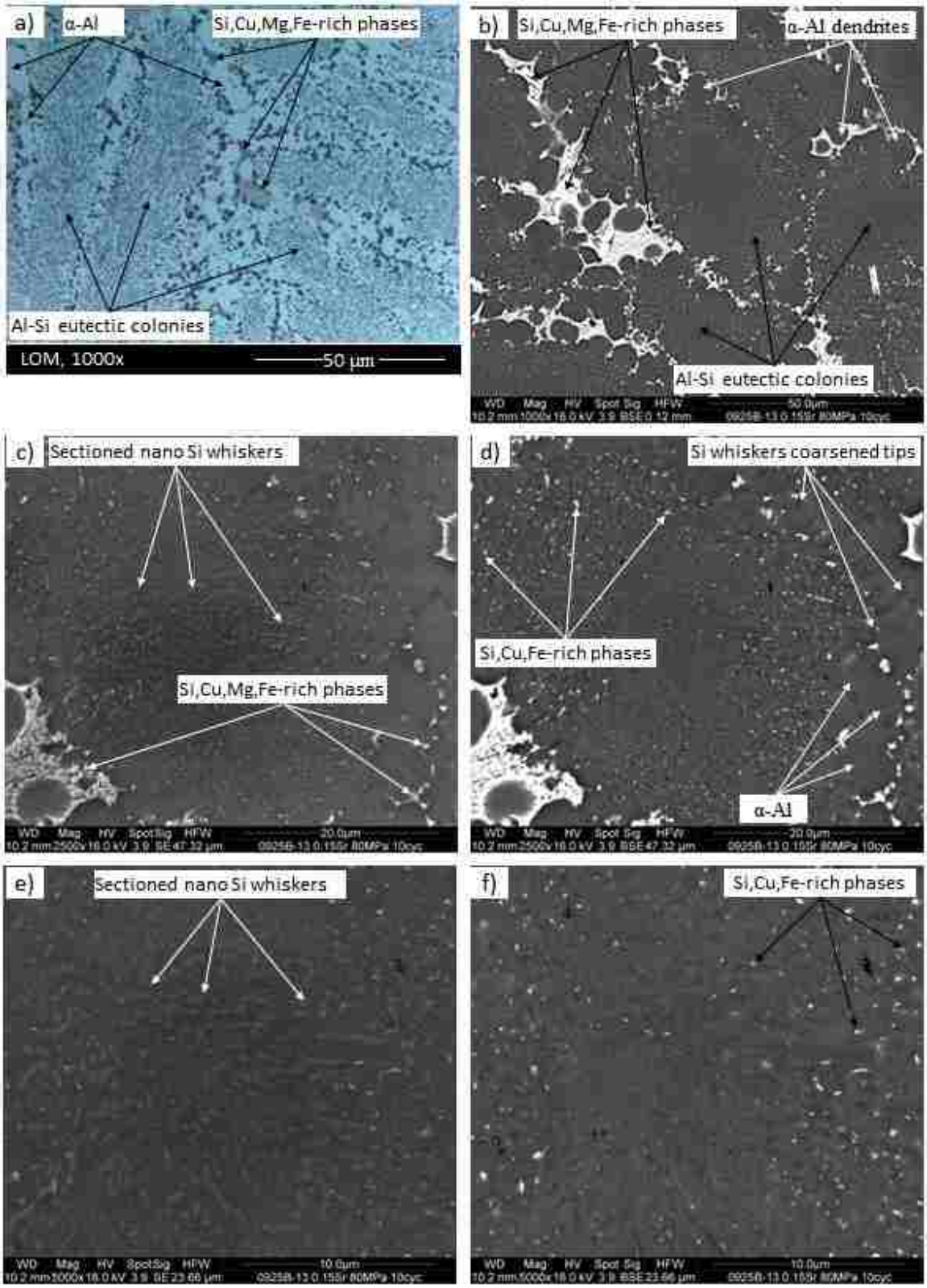

Figure 137. a) LOM and b-f) SEM micrographs for the 0.15 wt.%Sr modified experimental alloy, solidified in the SC/HPDC UMSA die under impact and cyclic pressure (38-81) MPa/10c, ref. #0925b.

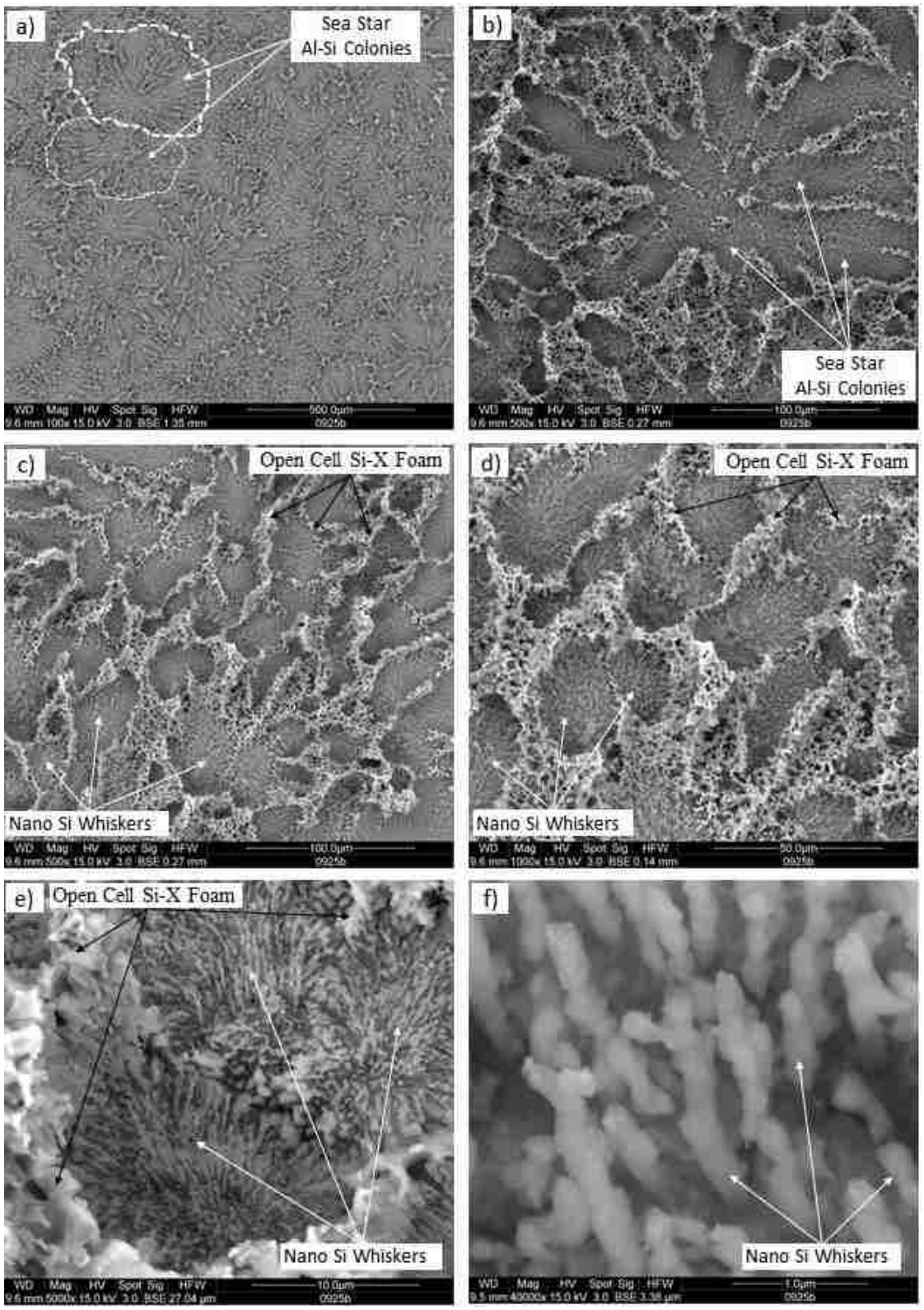

Figure 138. a - f) SEM deep-etched micrographs for the 0.15 wt.%Sr modified experimental alloy, solidified in the SC/HPDC UMSA die under cyclic pressure (38-81) MPa/10c, ASR = 18.3 °C/s, ref. #0925b.

Summary of S/TEM/EDS Analysis of Sample #0925b (Structure Category #1.1)

Figure 139a) presents HAADF image and (b - g) HAADF image and EDS elemental maps for subsurface of the sample #0925b. TEM foil was extracted from the subsurface of the sample, (the distance from the edge of the sample is 20 µm, area of 15 µm x 15 µm). The HAADF image represents very thin boundary area between two Al-Si colonies (center of the figure) where Al_3Cu particles are segragated. The coarsened Si whisker tips in boundary area are visible (in 2D) as coarse particles having a size up to 1.5 µm. Farther from the boundary, Al_3Cu and Si particles (in 2D) are much finer, size up to 500 nm. Elemental maps (see Figures 139 (b - g)) documenting very fine distribution of Si, Cu, Mg, Fe rich phases.

Figure 140a) presents HAADF image and (b - g) HAADF image and EDS elemental maps for the center of the sample #0925b. TEM foil was extracted from the center of the sample, (the distance from the edge of the sample is ≈ 9 mm, area of 15 µm x 15 µm).

S/TEM analysis revealed new stoichiometries of the phases. Comparison between literature references, the Yamaha engine block and experimental sample #0925b's phase stoichiometries and sizes of its structural features, for the subsurface and the center of the SC/HPDC UMSA test sample are documented in Table 24.

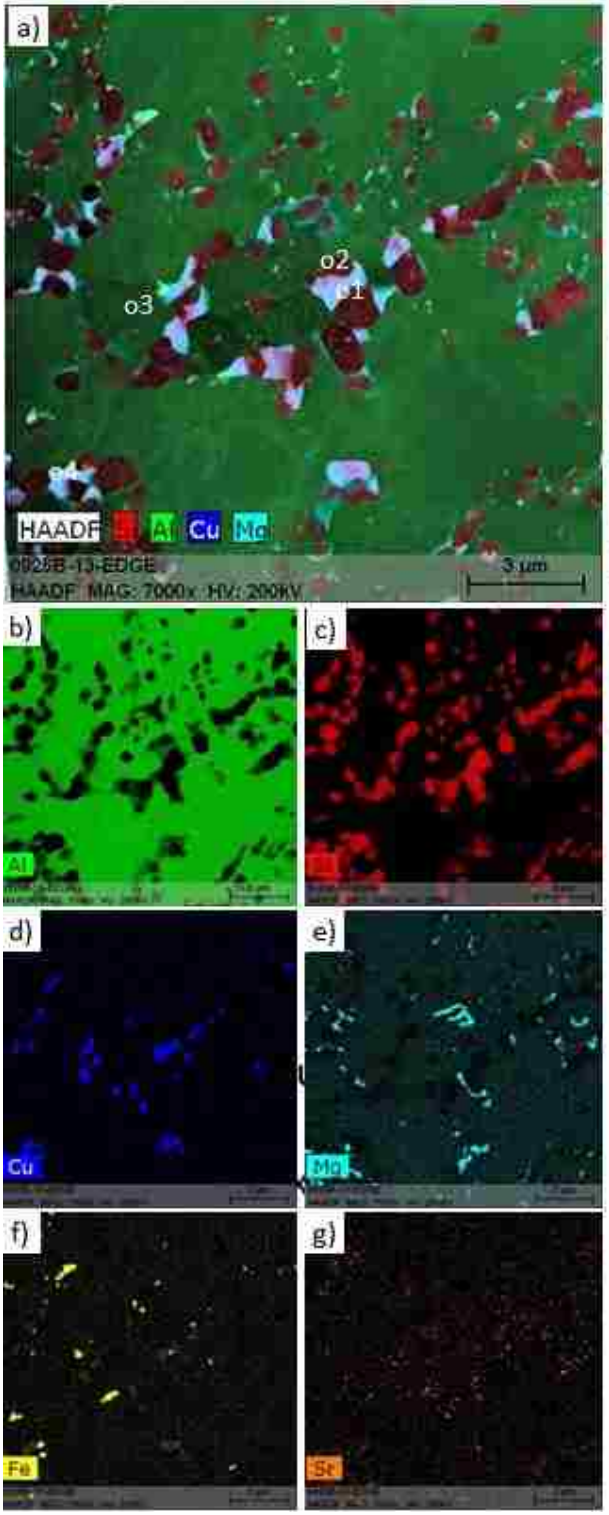

Element	Weight %	Atomic %
# 1: Al_3Cu_2		
Al(K)	41.92	62.56
Si(K)	0.79	1.13
Cu(K)	57.28	36.3
# 2: Si		
Al(K)	2.17	2.28
Si(K)	96.04	96.92
Cu(K)	1.77	0.79
# 3: Al		
Al(K)	96.56	98.37
Si(K)	0.2	0.19
Ti(K)	0.19	0.1
Cu(K)	3.04	1.31
# 4: Al_3Cu_2		
Al(K)	39.96	60.72
Si(K)	0.63	0.92
Fe(K)	0.27	0.19
Ni(K)	0.12	0.08
Cu(K)	59	38.06

Figure 139. a) HAADF image, b - g) superimposed with HAADF and EDS elemental maps, for the 0.15 wt.%Sr modified experimental alloy, solidified in the SC/HPDC UMSA die, under impact and cyclic pressure (38-81) MPa/10c. TEM foil was extracted from the subsurface of the sample (the distance from the edge of the sample is 20 µm), ref. #0925b.

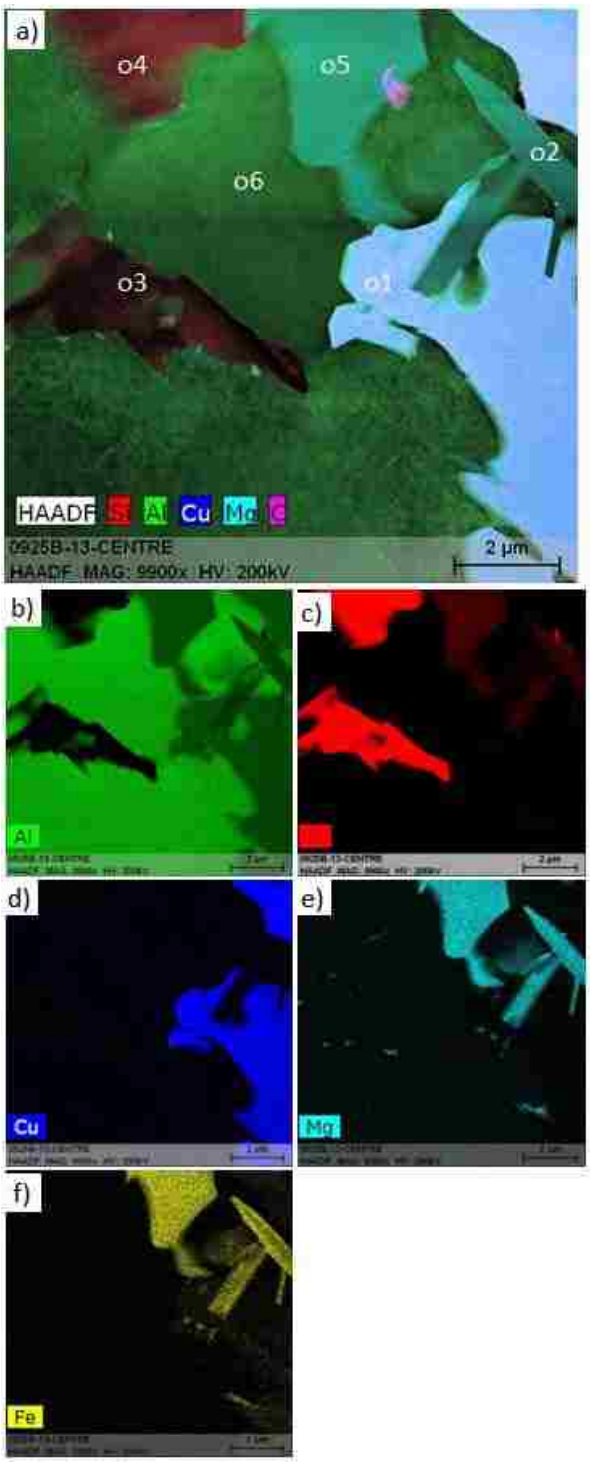

Element	Weight %	Atomic %
# 1: Al_3Cu_2		
Al(K)	38.01	58.73
Si(K)	0.65	0.96
Fe(K)	0.63	0.47
Cu(K)	60.69	39.82
# 2: $Al_{12}Mg_6FeCuSi_6$		
Mg(K)	18.83	22.7
Al(K)	42.44	46.07
Si(K)	22.17	23.11
Fe(K)	7.51	3.94
Cu(K)	9.02	4.16
# 3: Si		
Al(K)	2.68	2.82
Si(K)	95.27	96.26
Cu(K)	2.03	0.91
# 4: Si		
Al(K)	5.48	5.74
Si(K)	93.03	93.59
Cu(K)	1.48	0.65
# 5: $Al_{27}Mg_{12}Fe_3CuSi_{13}$		
Mg(K)	17.5	20.84
Al(K)	45.09	48.37
Si(K)	22.72	23.42
Fe(K)	10.73	5.56
Cu(K)	3.94	1.79
# 6: Al		
Al(K)	95.26	97.7
Si(K)	0.43	0.42
Cu(K)	4.29	1.87

Figure 140. a) HAADF image, b-f) superimposed with HAADF and EDS elemental maps, for the 0.15 wt.%Sr modified experimental alloy, solidified in the SC/HPDC UMSA die, under impact and cyclic pressure (38-81) MPa/10c. TEM foil was extracted from the center of the sample. (the distance from the edge of the sample is ≈ 9 mm), ref. #0925b.

4.3.3.2 Sample #0916 (Structure Category #2.2)

Sample #0916 belongs to the group of samples classified as less structurally advanced than Category #2.2. Figures 141 - 143 present the impact pressure profile, stroke, cooling curve and first derivative. The impact pressure peak started at a low pressure of -0.35 MPa at a temperature of 632.8 °C and an increased pressure up to –1.29 MPa at a temperature of 626.5 °C. In 0.05 s the pressure reached –21.7 MPa. This resulted in a maximum SR = 89.7 °C/s @ a melt temperature of 621.7 °C (the so called "natural" T_{liq}). At this point the pressure rapidly went to a positive value of +3.20 MPa, and the SR at the right "shoulder" of the first FD peak was equal to 51.6 °C/s @ 4.18 s and a melt temperature of 608.6 °C. The further natural melt SR slowed down and after 0.29 s it reached a value of 82.4 °C/s at aT_{liq}.

The first FD peak SR indicates good forced thermal contact established between the test sample and the BN film and the die. Most likely, during natural solidification the loss of thermal contact was exacerbated through the "suctioning up" of the test sample by the positive pressure allowing for an increase in the air gap. This resulted in a rapid decrease of the SR to 51.6 °C/s. After this point, the melt solidified naturally and its aT_{liq} = 589.0 °C and SR = 82.4 °C/s. This example illustrates that even relatively small impact pressure in the liquid state results in a considerably higher SR and can control the T_{liq}. But this effect can be lost if the pressure is elevated to a positive level. It is expected that between the "natural" and the actual "forced" T_{liq} (uninterrupted solidification process) some phase(s) nucleated, while the SR slowed down and therefore the as-cast structures were classified as Category #2.

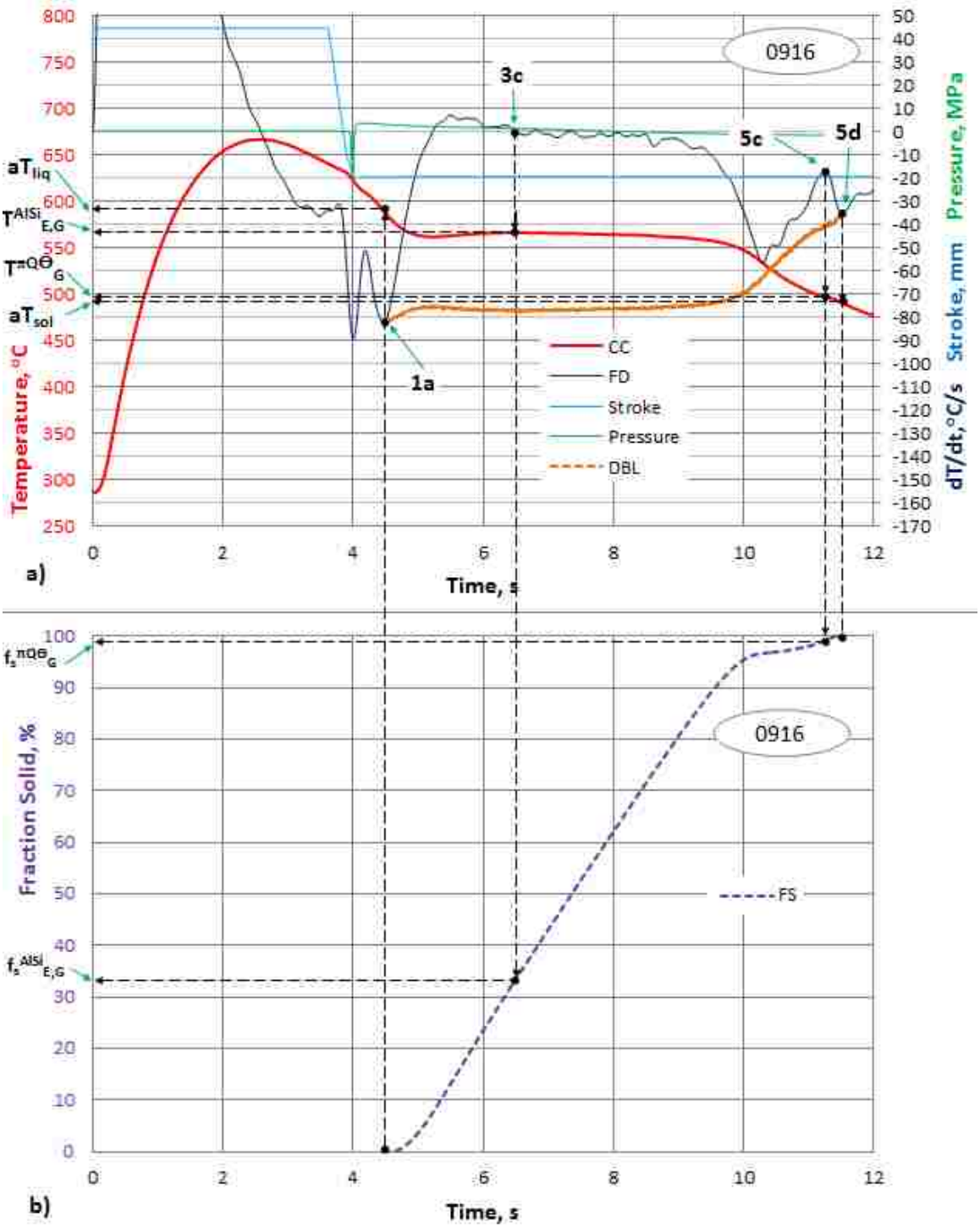

Figure 141. a) Cooling/Solidification Curve with superimposed First Derivative, Dynamic Baseline, Stroke and Pressure Profile Curves vs. Time, b) Fraction Solid Curve vs. Time for the 0.15 wt.%Sr modified experimental alloy, processed under impact pressure (0-22) MPa/1c in the SC/HPDC UMSA die, ASR = 14.1 °C/s, ref. #0916.

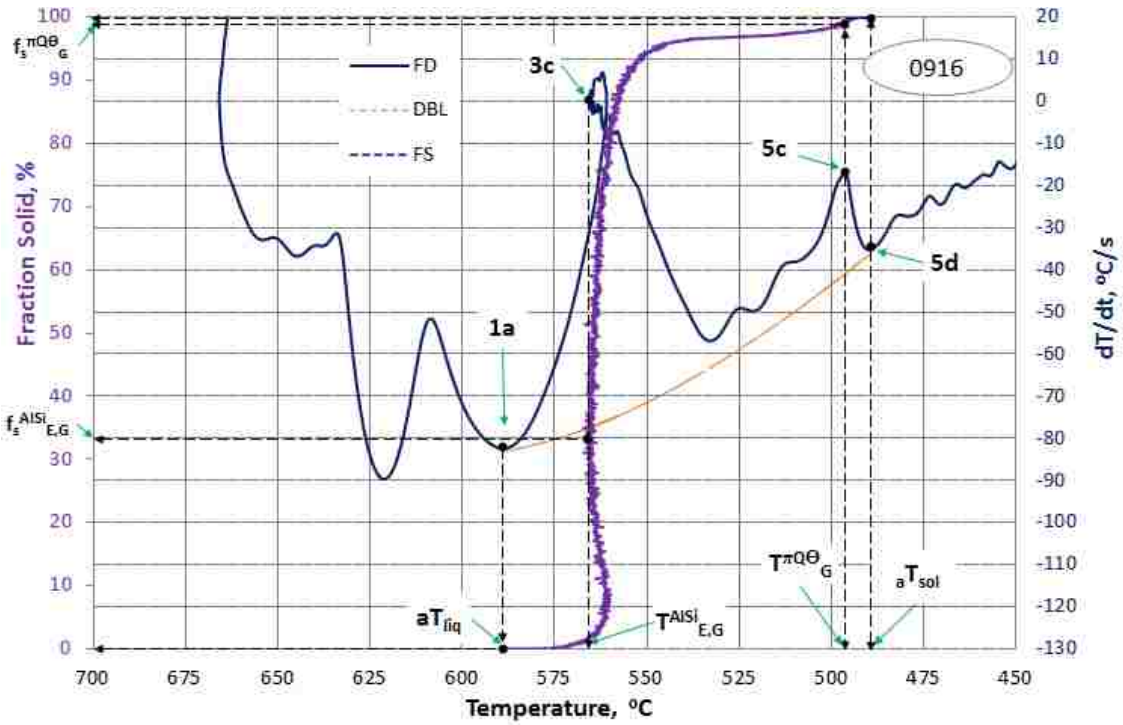

Figure 142. First Derivative Curve, Fraction Solid Curve and Dynamic Baseline vs. Temperature for the 0.15 wt.%Sr modified experimental alloy, solidified under impact pressure (0-22) MPa/1c in the SC/HPDC UMSA die, ASR = 14.1 °C/s, ref. #0916.

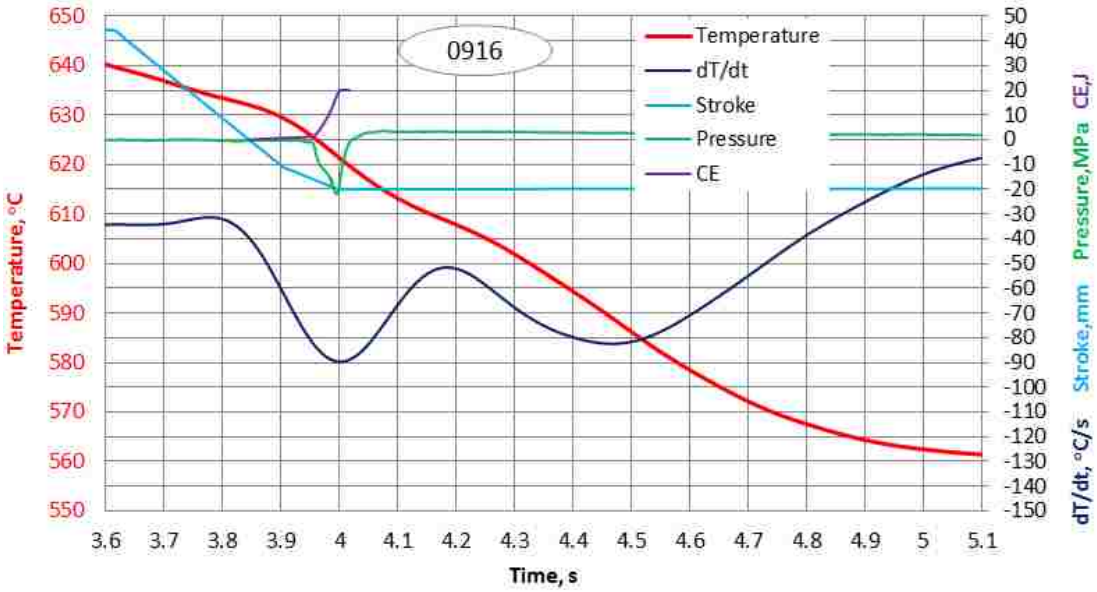

Figure 143. Cooling/Solidification Curve with superimposed First Derivative Curve, Pressure Profile Curve, Stroke and Cumulative Energy Curve vs. Time for the 0.15 wt.%Sr modified experimental alloy, processed under impact pressure (0-22) MPa/1c in the SC/HPDC UMSA die, ASR = 14.1 °C/s, ref. #0916.

4.3.3.3 Sample #0916b (Structure Category #2.1)

Sample #0916b belongs to Category #2 (2.1). For detailed information, please refer to Tables 19, 21 and 22.

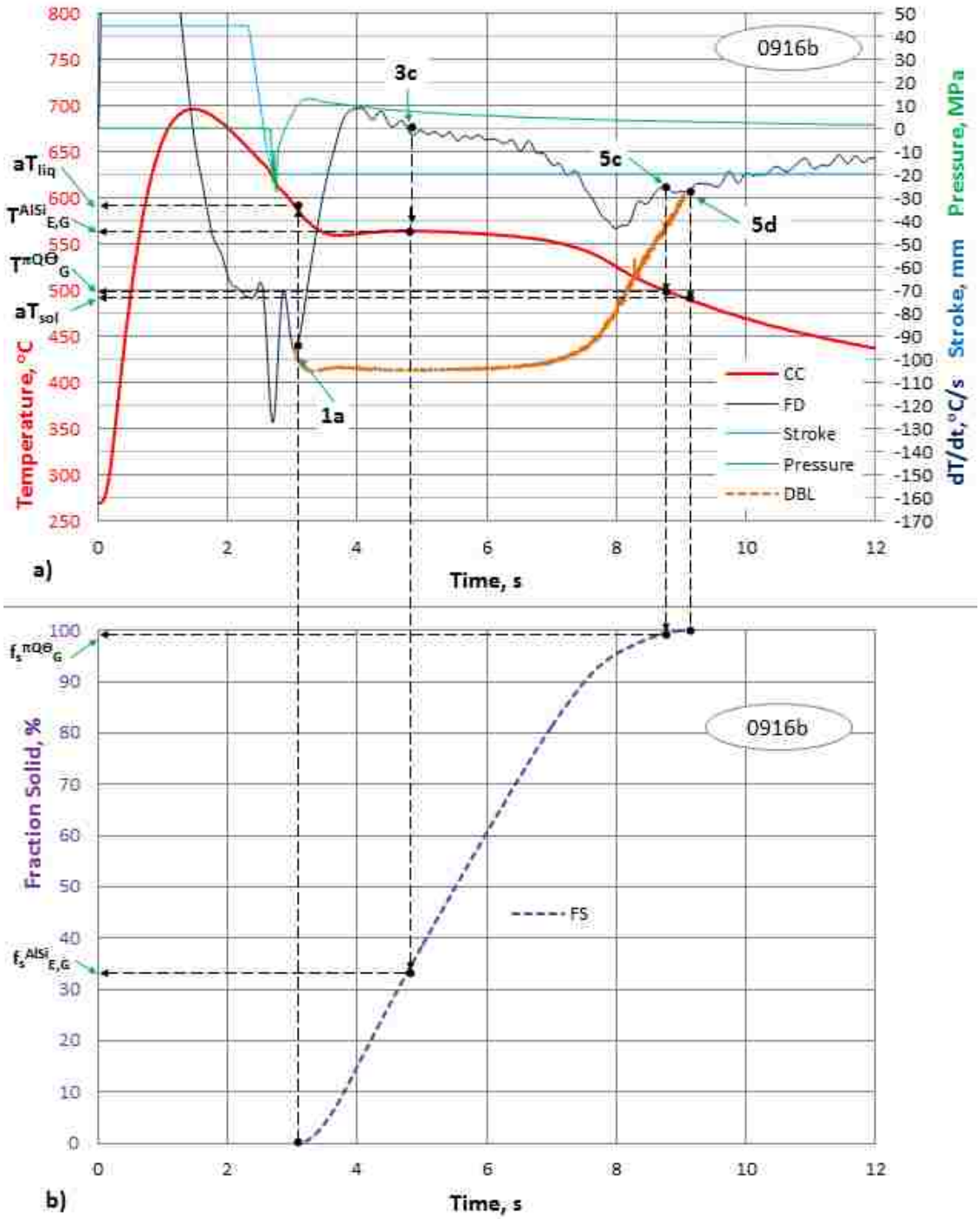

Figure 144. a) Cooling/Solidification Curve with superimposed First Derivative, Dynamic Baseline, Stroke and Pressure Profile Curves vs. Time, b) Fraction Solid Curve vs. Time for the 0.15 wt.%Sr modified experimental alloy, processed under impact/cyclic pressure (0-27) MPa/2c in the SC/HPDC UMSA die, ASR = 16.3 °C/s, ref. #0916b.

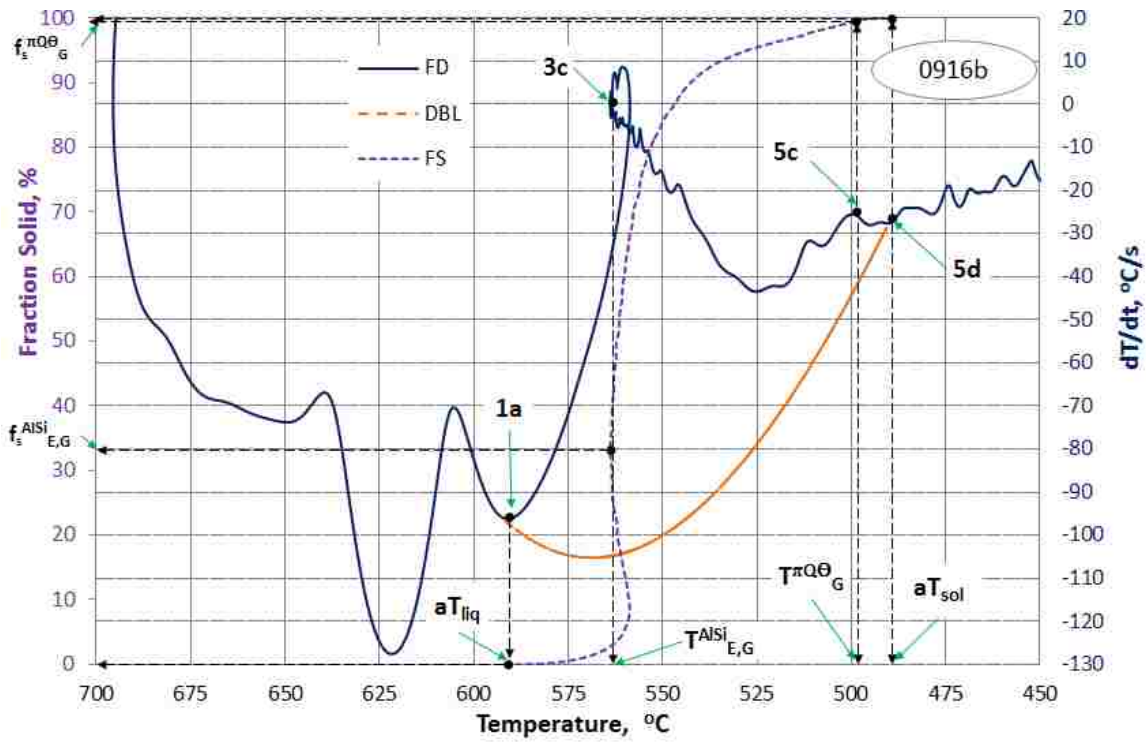

Figure 145. First Derivative Curve, Fraction Solid Curve and Dynamic Baseline vs. Temperature for the 0.15 wt.%Sr modified experimental alloy, solidified under impact/cyclic pressure (0-27) MPa/2c, in the SC/HPDC UMSA die, ASR = 16.3 °C/s, ref. #0916b.

4.3.3.4 Sample #0628b (Structure Category #3)

Sample #0628b is in Category #3, which indicates that some structural attributes do not entirely fulfill the project objectives. However, it is necessary to determine process parameters that contribute to these attributes. Figures 146a - 148 indicate that at the beginning of the applied initial negative pressure of -0.13 MPa (1.2 MPa) the melt temperature was 658.5 °C and the time was 2.73 s. This almost monotonic pressure was maximized at the melt temperature of 632.5 °C at which the SR was significantly slowing down from the peak SR = -112.45 °C/s to -51.1 °C/s.

A very high SR was observed in the first nucleation peak and most likely rapid growth of some phase(s) like primary Si was observed until the second peak reached the maximum SR after 0.55 s. This second FD peak is an aT_{liq} at which the SR was maximized to -135.7 °C/s by cyclic pressure loading (39-82) MPa. However, most likely during 0.17 s between the "natural" T_{liq} (SR = -112.45 °C/s) and the local minimum between the first and second FD peak (SR slowed down to -50 °C/s). The primary Si particles that nucleated in the center of the melt due to an even slower SR become thermally stable and are not able to be converted to a dendritic and/or whiskers structure. In addition, the delay in applying cyclic pressure loading for approximately 0.48 s contributed to interrupted solidification. Therefore, an increased SR to -135.7 °C/s did not affect the already existing primary Si particles and significant coarsening of the Si whiskers tips occurred.

The consequent solidification process was reinforced by cyclic pressure loading at a melt temperature of 632.5 °C and a time of 3.05 s. After first impact of the cyclic loading (39 – 82) MPa @ 45 cycles, the slope of the FD changed and the SR accelerated

to $aT_{liq}ISR$ = -135.7 °C/s. The undercooling of the melt $\Delta T^{AlSi}_{E,UC}$ = 33.6 °C, the recalescence temperature $\Delta T^{AlSi}_{E,R}$ = 3.4 °C, the recalescence time $\Delta t^{AlSi}_{E,R}$ = 0.8 s corresponds with the SR of 4.0 °C/s.

Nucleated primary Si and other thermodynamically stable particles cannot be fragmented and dissolved during high temperature and long time Solution Treatment. Therefore, a fully controlled solidification process using cyclic pressure loading requires carefully chosen process parameters. In-situ TA and processing parameters data are readily available for design and control of this novel technology. This technology allows for ultra rapid acceleration of the SR and forces the melt to start the spontaneous nucleation and solidification process at the optimum temperature.

The best achievable results depend on the Temperature when impact/cyclic pressure starts (T^P_{ST}), the Temperature when impact/cyclic pressure ends (T^P_{END}), the Cyclic Pressure loading parameters, the minimum and maximum Pressure, frequency (f) and the number of cycles (c), expressed by CE_{liq1}, CE_{liq2}, CE_{ss1} and CE_{ss2}.

Cyclic loading of the liquid melt (0.15 wt.%Sr modified alloy, cyclic pressure applied (37-81) MPa/10c) during 1s (at a frequency f = 10 Hz) modification is capable of generating stable undercooling and recalescence as well as very effectively controlling other metallurgical reactions leading to the optimum structure. Dynamic cycling rapidly impacts the melt nucleation kinetics through a significant increase in the Solidification Rate. Dynamic cycling pressure maintains a maximum pressure in the cavity and consequently maintains good contact with the sample die wall (provides good heat flux) during nucleation and at the start stage of solidification. High density of Si nuclei determines the size of the AlSi eutectic colonies. A high SR during AlSi eutectic

transformation maintains the Si whiskers growth in the branching and necking mode with very thin whiskers without coarsening of the Si whiskers tips (which is typical for a slower SR) and consequently the creation of thick inter colony boundaries.

Interdendritic cell boundaries can also be controlled in terms of the width and amount of low melting point phases rich in Al, Cu, Mg, Fe (π, Q, Θ-phases). These phases can be very rapidly dissolved by high temperature ST which does not cause incipient melting which is a common problem in many casting technologies.

In order to fully understand impact solidification rate dependence of the undercooling and recalescence and other TA data leading to nano and ultra-fine structures it is necessary to determine the role of the near liquidus clusters of atoms including Si-Si ones that most likely are affected by cyclic pressure. This task is very challenging since melt processing is carried out in the die.

Sr and Cu markedly affects the as-cast structures of the melt processed using slow and high as well as cyclic pressure loading.

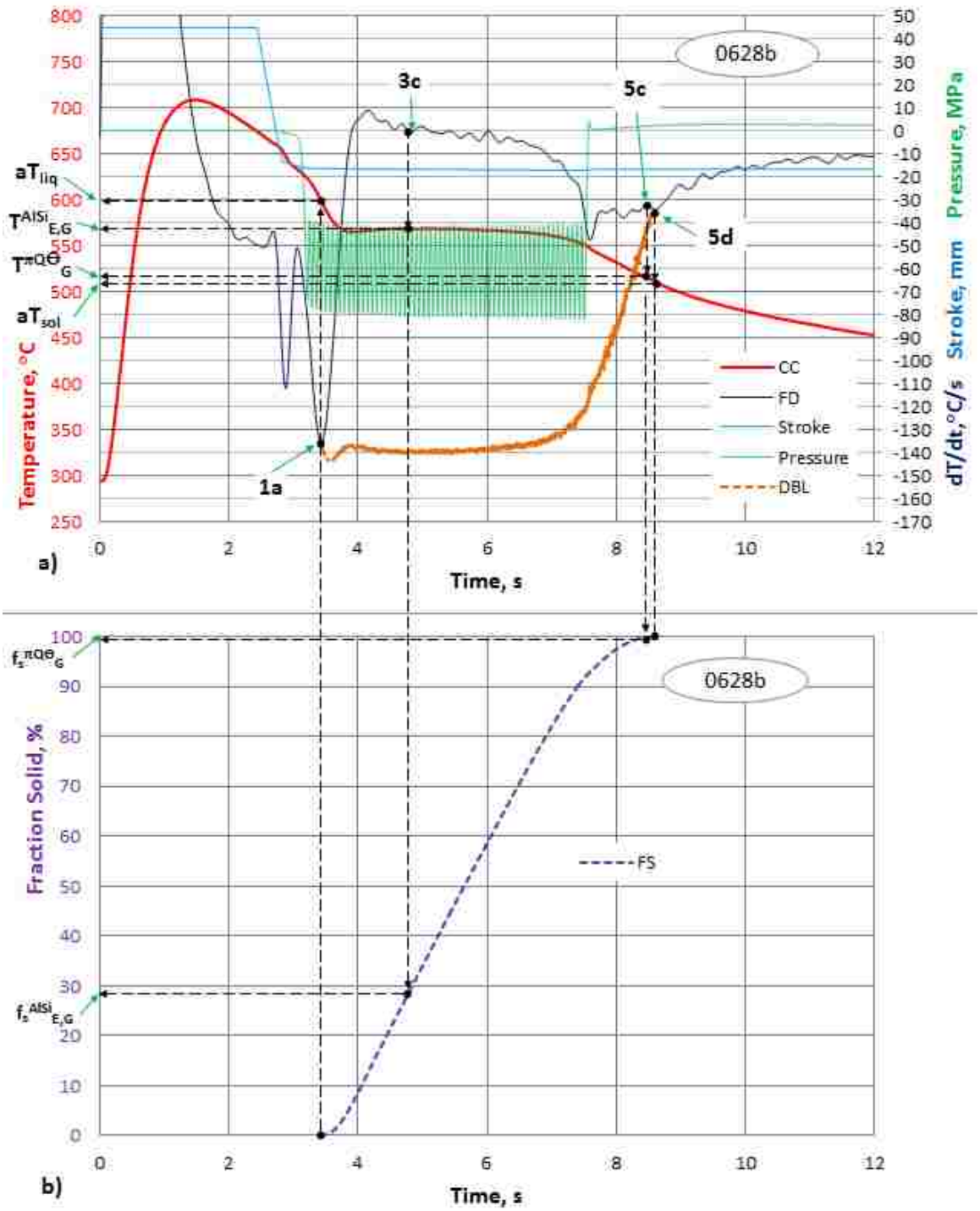

Figure 146. a) Cooling/Solidification Curve superimposed with the First Derivative and Dynamic Baseline, Stroke and Pressure Profile Curves vs. Time, b) Fraction Solid Curve vs. Time for the 0.15 wt.%Sr modified experimental alloy, solidified under impact and cyclic pressure (39-82) MPa/45c in the SC/HPDC UMSA die, ASR = 17.0 °C/s, ref.#0628b.

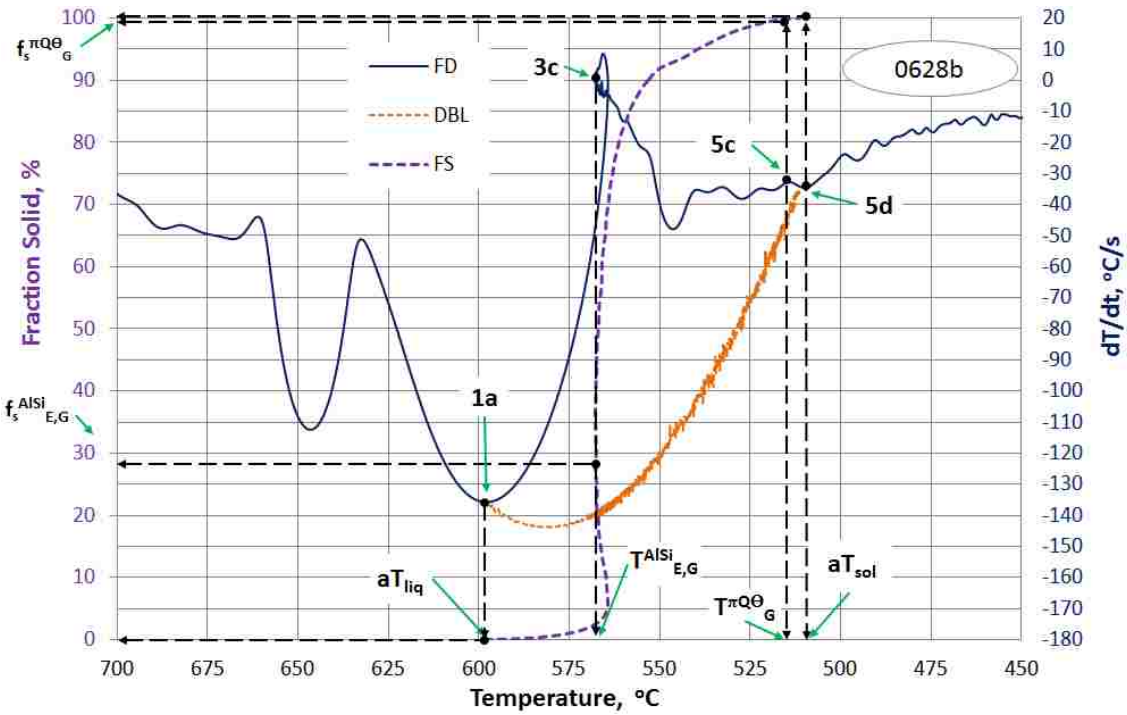

Figure 147. First Derivative Curve, Fraction Solid Curve and Dynamic Baseline vs. Temperature for the 0.15 wt.%Sr modified experimental alloy, solidified under impact and cyclic pressure (39-82) MPa/45c, in the SC/HPDC UMSA die, ASR = 17.0 °C/s, ref. #0628b.

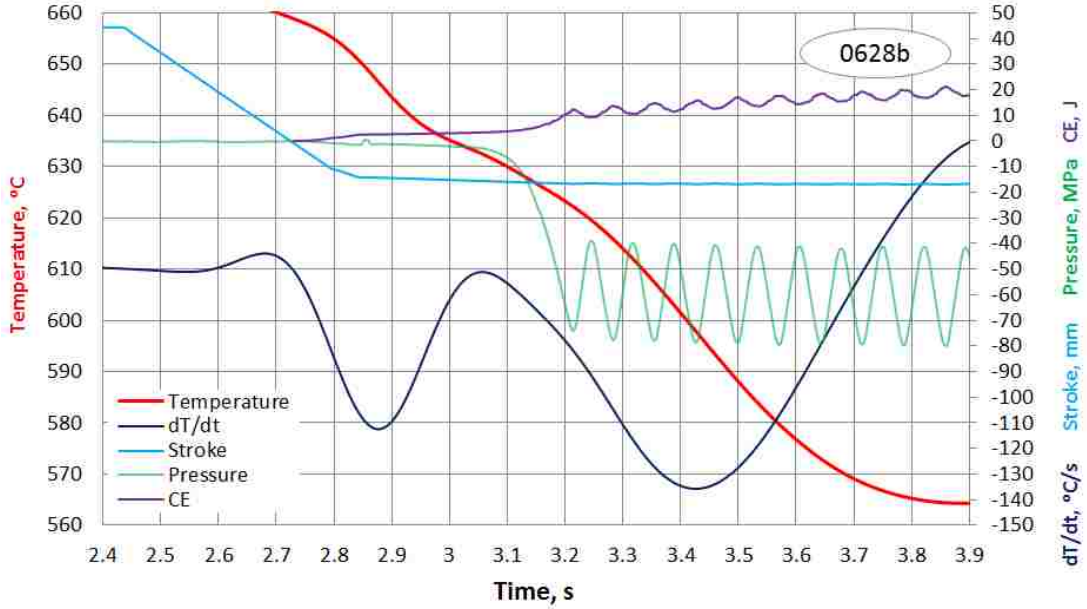

Figure 148. Cooling/Solidification Curve superimposed with the First Derivative Curve, Pressure Profile Curve, Stroke and Cumulative Energy Curve vs. Time for the 0.15 wt.%Sr modified experimental alloy, solidified under impact and cyclic pressure (39-82) MPa/45c in the SC/HPDC UMSA die, ASR = 17.0 °C/s, ref. #0628b.

4.3.3.5 Sample #0919 (Structure Category #1.3)

The SC/HPDC UMSA die temperature profile as a function of time is an influential process characteristic. The Initial Die Temperature and the rate of die temperature heating after filling of the die cavity by the liquid melt has a dominant effect on the SR, solidification kinetics and consequently the as-cast structure. Using both "natural" and forced solidification modes (various pressure profiles) it is critical to determine the optimum capabilities allowing for management of the die temperature profile leading to the desired structures including nano Si whiskers and Si dendrites having nano diameter arms and Al-Si sandwich dendritic structures.

Initial SC/HPDC UMSA experiments showed that samples that solidified without pressure had rounded edges and a convex meniscus. This observation indicates that the Interfacial Heat Transfer Coefficient (IHTC) at the melt/die interface and the corresponding Cooling Rate and SR are not fully controlled in terms of maximization. In addition, BN was used as the die protection and lubricating film. BN has a very high Thermal Conductivity Coefficient (≈ 20 W/mK) (heat flux at metal-mold interface) however it is not wettable by the liquid Al melt. Experiments with various applied pressure profiles indicated that the melt's Cooling Rate and Solidification Rates could be controlled and rapidly significantly increased and in turn render nano and ultra-fine structures. While using pressure, the cast samples (both pressurized air by the die plunger and various hydraulic pressure profiles) showed very sharp corners and sometimes high fluidity of the liquid melt resulted in its flow into the 0.05 mm gap between the plunger and the die (room temperature gap).

Figure 149 (a, b) present superimposed cooling curves, first derivative curves and pressure profile curves for #0919, #1002b and #0925b experiments while Figure 150 presents the measured SC/HPDC UMSA die temperature profile and cooling water temperature profile for these samples. In experiments #0919 (see Figures 151, 152) and #0925b (see Figures 128-130) a water cooling system was used, while for sample #1002b the water cooling system was shut off (see Figures 154, 155). As can be seen the die heating rate from the melt casting operation to the sample's solidus temperature is highest when the water cooling system is shut off. The water cooling temperature profile indicates that after approximately 0.5 s after filling of the die the water starts to boil, thus lowering its capability to maintain the initial die temperature.

More information for samples #0919, #1002b, #0925b relating to Structure Data, Process Parameters and Thermal Analysis data are summarized in Tables 19, 21 and 22, respectively.

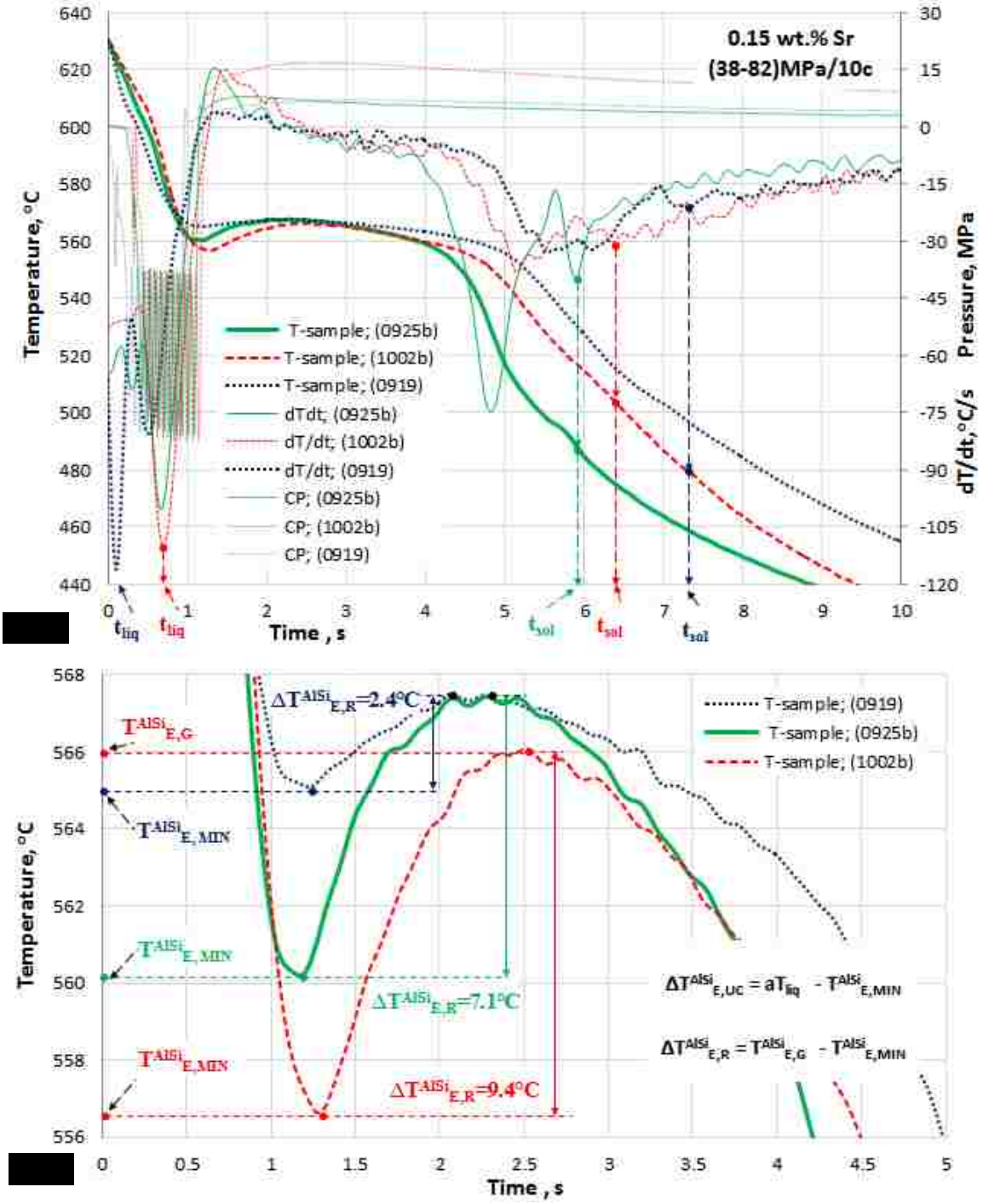

Figure 149. a) Cooling Curves, First Derivative Curves and Pressure Profile Curves for the 0.15 wt%Sr modified experimental alloy processed in the SC/HPDC UMSA die under impact and cyclic pressure (38-82) MPa/10c, at different initial die temperatures; 273 ºC (Blue -ref. #0919), 262 ºC (Green -ref. #0925b) and 267 ºC (Red -ref. #1002b); b) Details for Figure a - undercooling region).

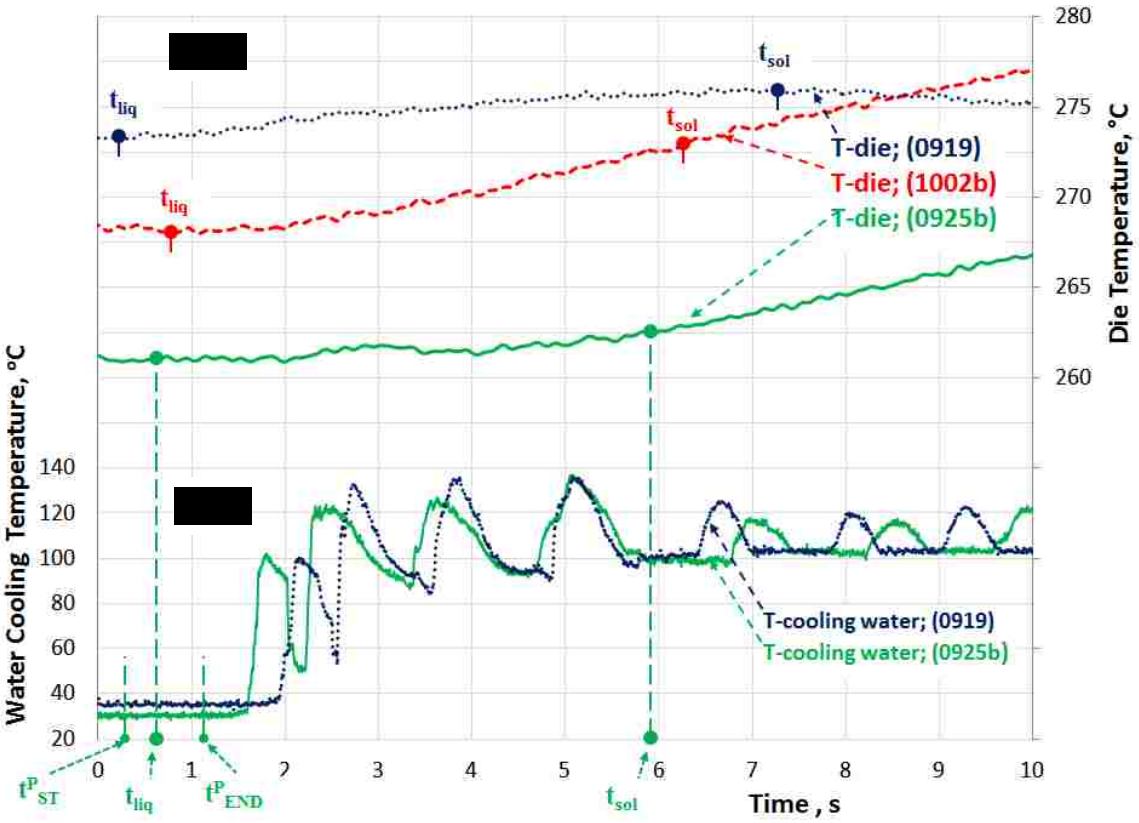

Figure 150. a) SC/HPDC UMSA die temperature profile for #0919, #1002b and #0925b experiments, b) cooling water temperature profile for #0919 and #0925b experiments.

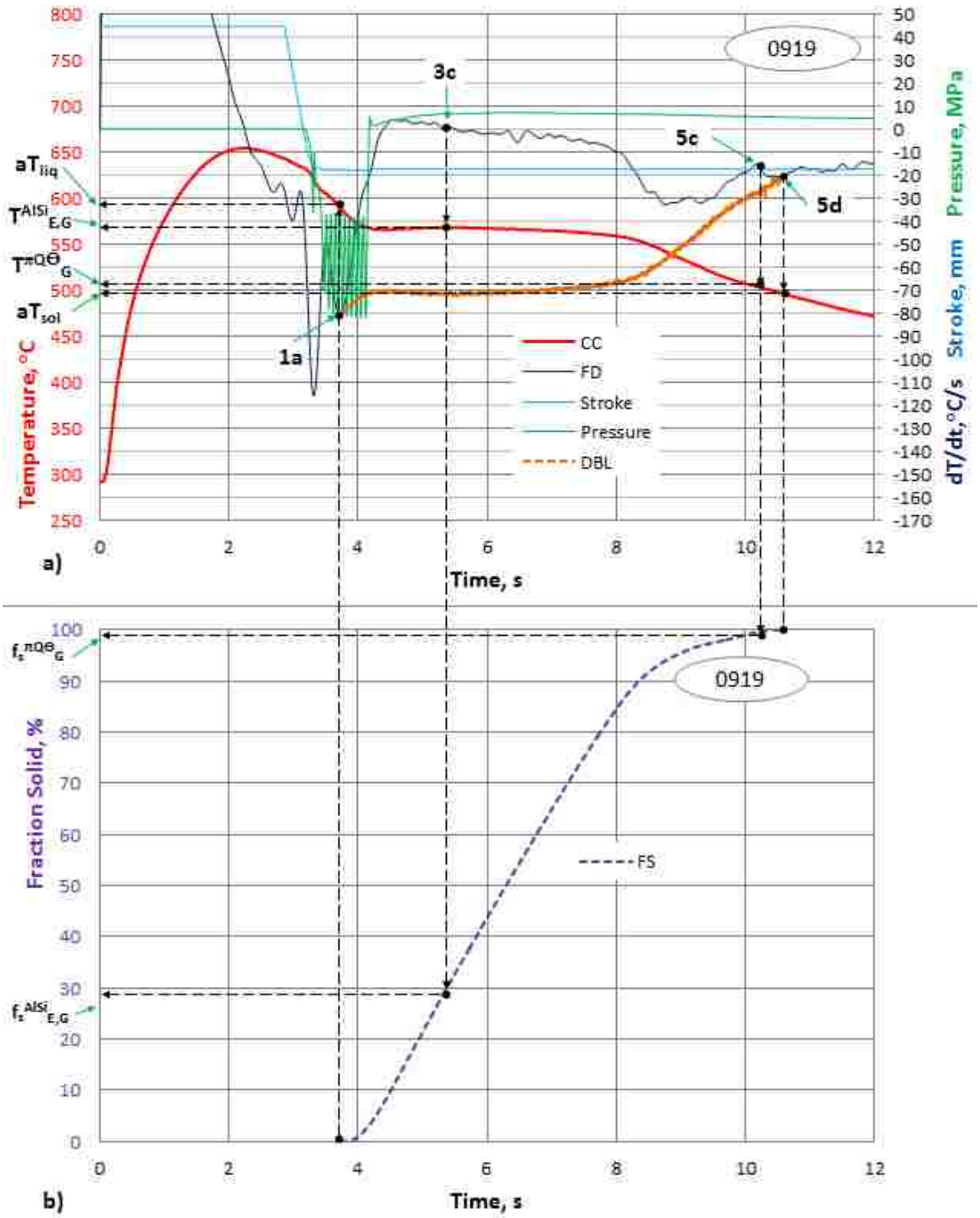

Figure 151. a) Cooling/Solidification Curve superimposed with the First Derivative and Dynamic Baseline, Stroke and Pressure Profile Curves vs. Time, b) Fraction Solid Curve vs. Time for the 0.15 wt.%Sr modified experimental alloy, processed under impact and cyclic pressure (38-82) MPa/10c in the SC/HPDC UMSA die, ASR = 13.6 °C/s, ref. #0919.

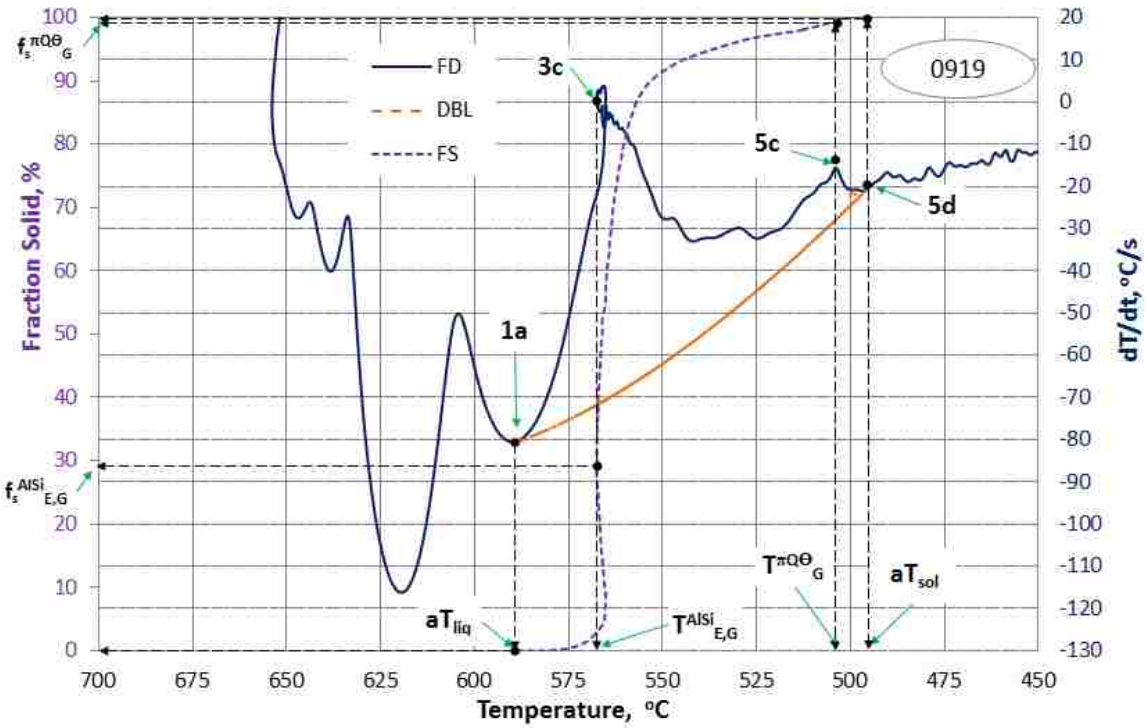

Figure 152. First Derivative Curve, Fraction Solid Curve and Dynamic Baseline vs. Temperature for the 0.15 wt.%Sr modified experimental alloy, solidified under impact and cyclic pressure (38-82) MPa/10c in the SC/HPDC UMSA die, ASR = 13.6 °C/s, ref. #0919.

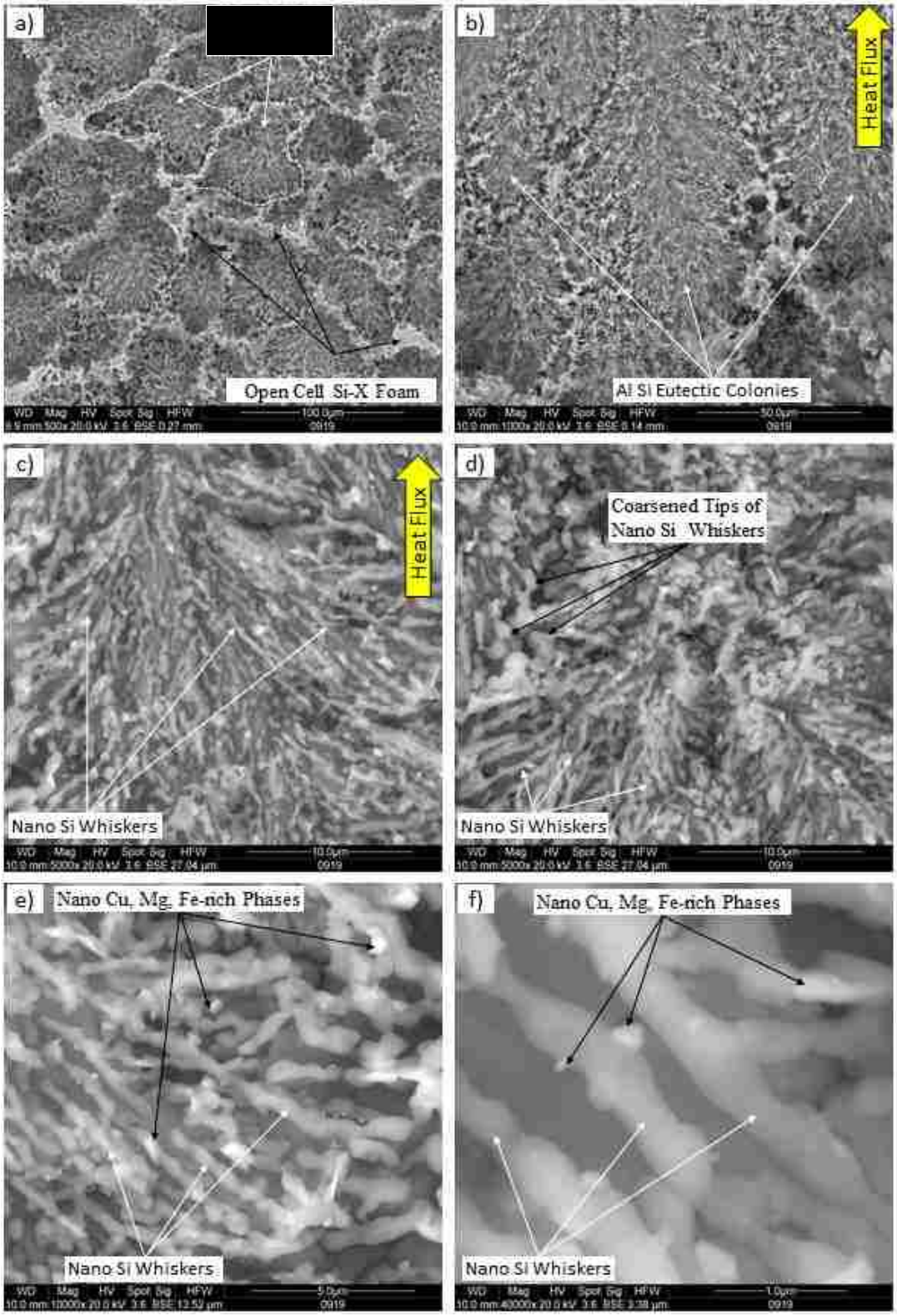

Figure 153. a - f) SEM deep-etched micrographs for the 0.15 wt.%Sr modified experimental alloy, solidified in the SC/HPDC UMSA die under impact and cyclic pressure (38-82) MPa/10c, ASR = 13.6°C/s, ref. #0919.

4.3.3.6 Sample #1002b (Structure Category #1.2)

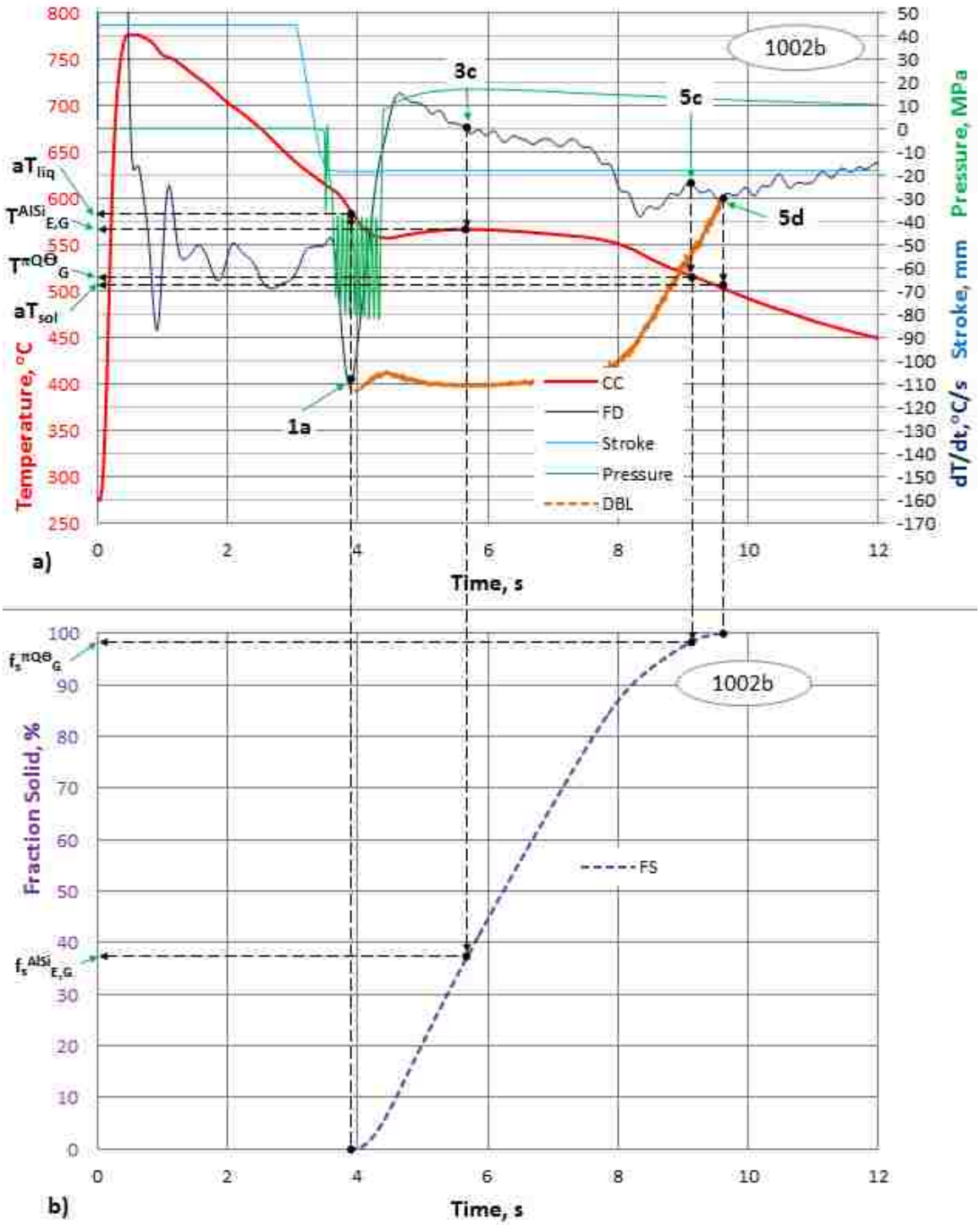

Figure 154. a) Cooling/Solidification Curve superimposed with the First Derivative and Dynamic Baseline, Stroke and Pressure Profile Curves vs. Time, b) Fraction Solid Curve vs. Time for the 0.15 wt.%Sr modified experimental alloy, solidified under impact and cyclic pressure (38-82) MPa/10c in the SC/HPDC UMSA die, ASR = 14.6 °C/s, ref. #1002b.

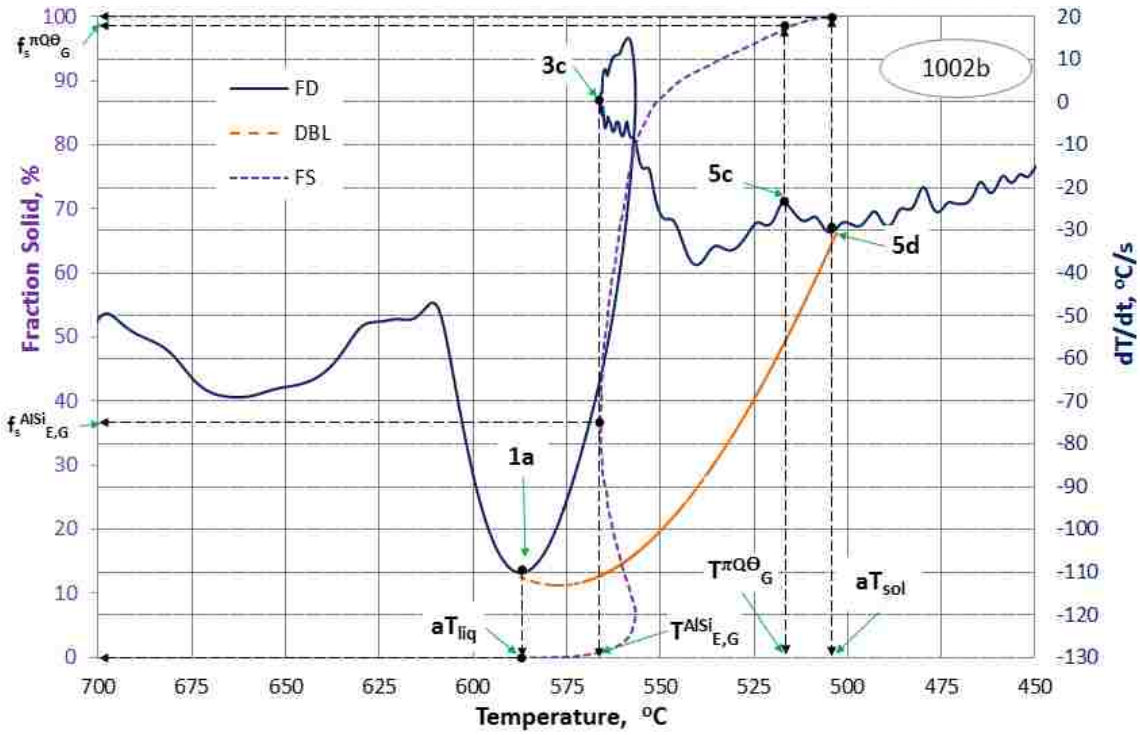

Figure 155. First Derivative Curve, Fraction Solid Curve and Dynamic Baseline vs. Temperature for the 0.15 wt.%Sr modified experimental alloy, solidified under impact and cyclic pressure (38-82) MPa/10c in the SC/HPDC UMSA die, ASR = 14.6 °C/s, ref. #1002b.

More information for sample #1002b relating to Structure Data is found in Table 19. Process Parameters and Thermal Analysis data are summarized in Tables 21 and 22, respectively.

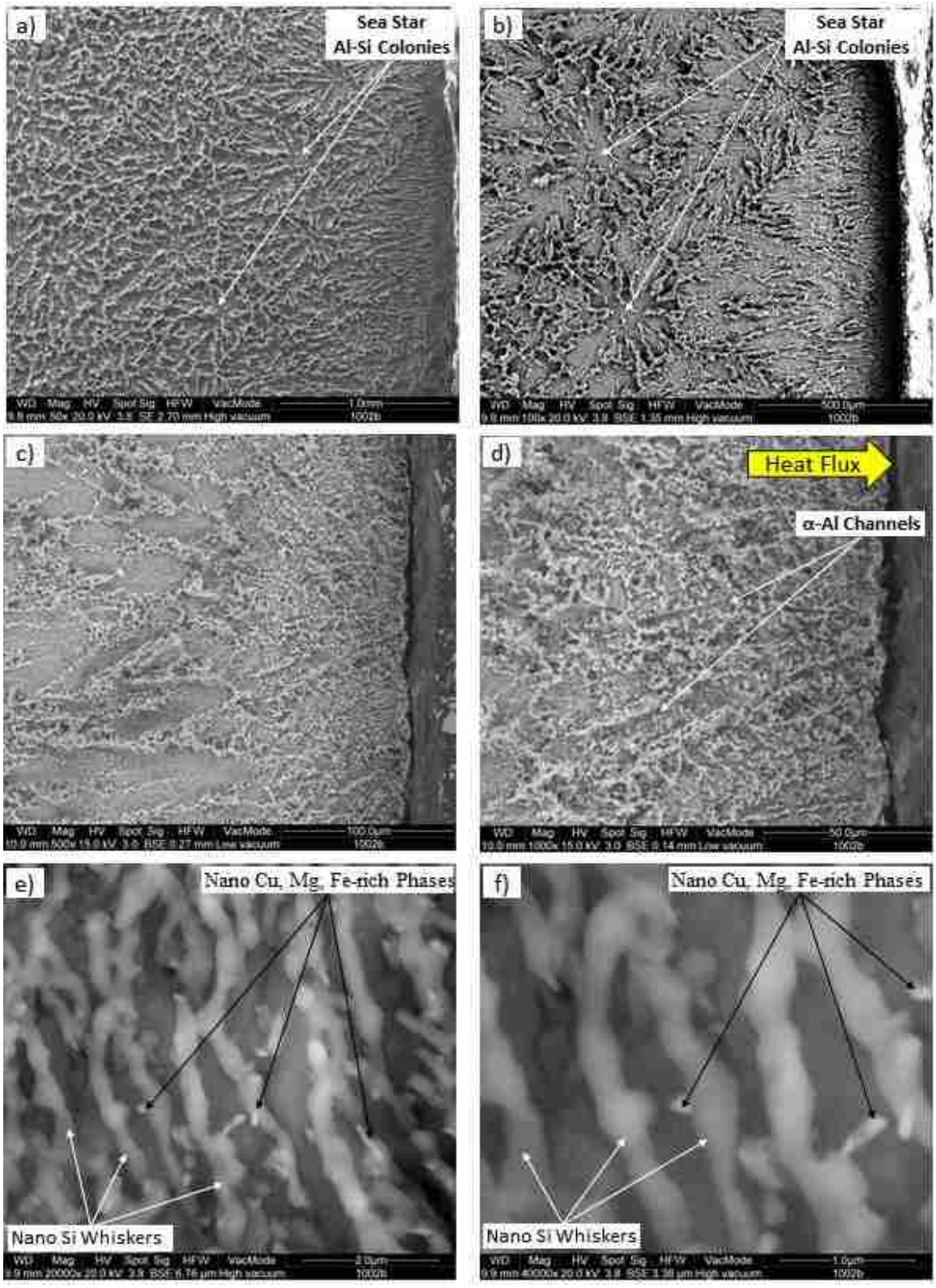

Figure 156. a - f) SEM deep-etched micrographs for the 0.15 wt.%Sr modified experimental alloy, solidified in the SC/HPDC UMSA die under impact and cyclic pressure (38-82) MPa/10c, ASR = 14.6 °C/s, ref. #1002b.

4.3.3.7 Sample #0517 (Structure Category #2.3)

Even though the structure of sample #0517 is in the #3rd place of Structure Category #2 it represents an extraordinary potential for future improvements. This statement is based on the presence of the new hexagonal Si whiskers with an average diameter of 340 nm and whiskers located at the subsurface with an average diameter of 450 nm (see Figure 159). Both hexagonal and cylindrical Si whiskers are very densely packed in the Al-Si eutectic colonies. The hexagonal whiskers did not exhibit the tendency for branching. The cylindrical shaped whiskers show a tendency toward necking and branching. In addition, in this sample, there is a significant amount of Si dendrites with an average diameter of 280 nm for arms and trunks.

Therefore, regardless of some of the differences in shape and cross sections of these Si nano features, high temperature Solution Treatment will be able to fragment and spheroidize them in an extremely short time.

For more details regarding the selected Process Parameters, TA and Structural Data please refer to Tables 21, 22 and 19, respectively.

Figure 157 presents the Cooling/Solidification Curve superimposed with the First Derivative, Dynamic Baseline, Stroke, Pressure Profile Curves and Fraction Solid Curve vs. Time, while Figure 158 presents the First Derivative, Dynamic Baseline and Fraction Solid Curves vs. Temperature for test sample #0517. The most important process parameters and thermal data for sample #0517 are as follows:

1. Initial Die Temperature (T^{D}_{I}) = 272 °C.
2. Die Temperature at the Melt's Solidus Temperature = 292.1 °C.
3. Temperature of Melt Superheat (T^{M}_{SH}) = 811 °C.

4. Maximum Temperature of the Melt delivered to the Die (T^{D}_{MAX}) = 718.5 °C was achieved by rapid opening of the melting furnace's bottom opening.
5. At a temperature of 655.2 °C (T^{P}_{ST}) (55.1 °C above the apparent aT_{liq}), the single impact pressure of 32 MPa was applied and resulted in delivery of energy to the liquid melt ΔCE_{liq1} = 12.1 J. This impact energy allows for rapid acceleration of the SR from 105 °C/s (beginning of natural cooling) to 140.4 °C/s (forced solidification) and establishes a good interface contact between the test sample and the die protection BN film. Thus, the heat transfer was very significantly improved. It is very interesting to observe that after the first impact peak pressure was released to the 0.0 MPa level, the SR at the aT_{liq} was immediately returned to the level of the FD first peak of 140.4 °C/s.
6. After 0.75 s from the impact pressure peak, the pressure becomes positive (approximately +15 MPa) and after approx. 0.2 s at the temperature of 562 °C fading sinusoidal cyclic pressure loading which oscillates around 0.0 MPa with the initial amplitude of approx. -15 MPa to + 12 MPa started. Between aT_{liq} = 600.1 °C and the Al-Si Eutectic Minimum Temperature $T^{AlSi}_{E,MIN}$ = 561.2 °C, ΔCE_{ss1} = 1.4 J was delivered to the melt, see Figures 157a and Table 21. This cyclic pressure faded after 2.5 s at a temperature of 561.5 °C @ F_S = 53.7 %. Between the Al-Si Eutectic Minimum Temperature and the End Treatment Temperature ΔCE_{ss2} = 0.3 J was delivered to the semi-solid melt. The undercooling temperature for the Al-Si eutectic reaction $\Delta T^{AlSi}_{E,UC}$ = 39.1 °C and recalescence $\Delta T^{AlSi}_{E,R}$ = 0.3 °C.
7. The total energy delivered in both the liquid and semi-solid states amounts to 14.1 J.

8. The shapes of the FDs for the tested industrial alloys exhibit various degrees of decline angle as determined by the SRs at the beginning and end of the Al-Si eutectic reaction. The test sample #0517 FD during the Al-Si eutectic reaction (as a function of time) is almost flat, while the SR ≈ 0.0 °C/s. The shape of the #0517 First Derivative presented in Figure 157a is observed only in the solidification processes for pure metals. This explains small and equiaxed Al-Si colonies in the center (D_{avg} AlSi-Co ≈ 60 μm), see Figure 159a.
9. The subsurface structure shows the ultra-fine Si particles nucleating at the edge most likely prior to the aT_{liq} peak. There is the substantial amount of α-Al phase formed in the boundaries of the inter colonies that allows for rapid heat transfer to the die.
10. The Total Pressure Treatment Temperature Range is 93.7 °C.
11. Treated Melt Solidification Range is 80.5 °C and Solidification Time is 5.8 s.
12. Fraction Solid (f_S) at the Al-Si Eutectic Growth Temperature is 19.4 %.

The above mentioned and tabulated process parameters control the nucleation and growth of single phase Si hexagonal whiskers, Si dendrites with nano diameter arms and trunks and Al-Si colonies ($D^{min}{}_{F}$AlSi-Co = 40.6 μm, $D^{max}{}_{F}$AlSi-Co = 135.4 μm) depending on the type of Si whiskers and dendrite type as well as the boundaries of the inter colonies average thickness range = (0.77 to 9.1) μm depending on the type of structural features and their chemical makeup. In addition, these process parameters also control morphological features of Cu, Mg, Fe, Si rich phases (β-Fe, α-Fe, π, Q, Θ –phases and Q+Θ eutectic) located mostly in intercolony regions, see Figure 160.

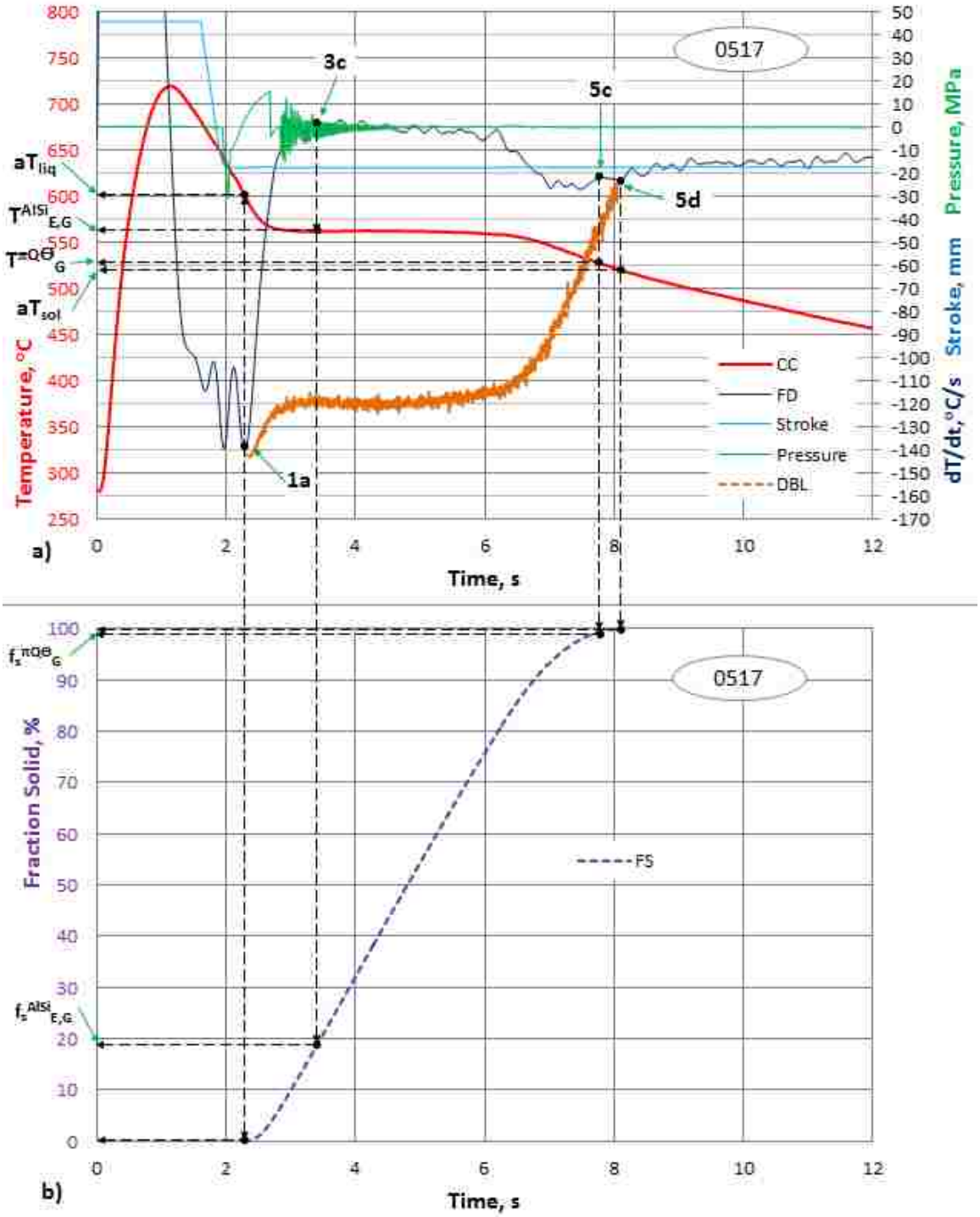

Figure 157. a) Cooling/Solidification Curve superimposed with the First Derivative, Dynamic Baseline, Stroke and Pressure Profile Curves vs. Time, b) Fraction Solid Curve vs. Time for the 0.15 wt.% Sr modified experimental alloy, processed under impact and cyclic pressure (0-30) MPa/1.5c in the SC/HPDC UMSA die, ASR = 13.9 °C/s, ref. #0517.

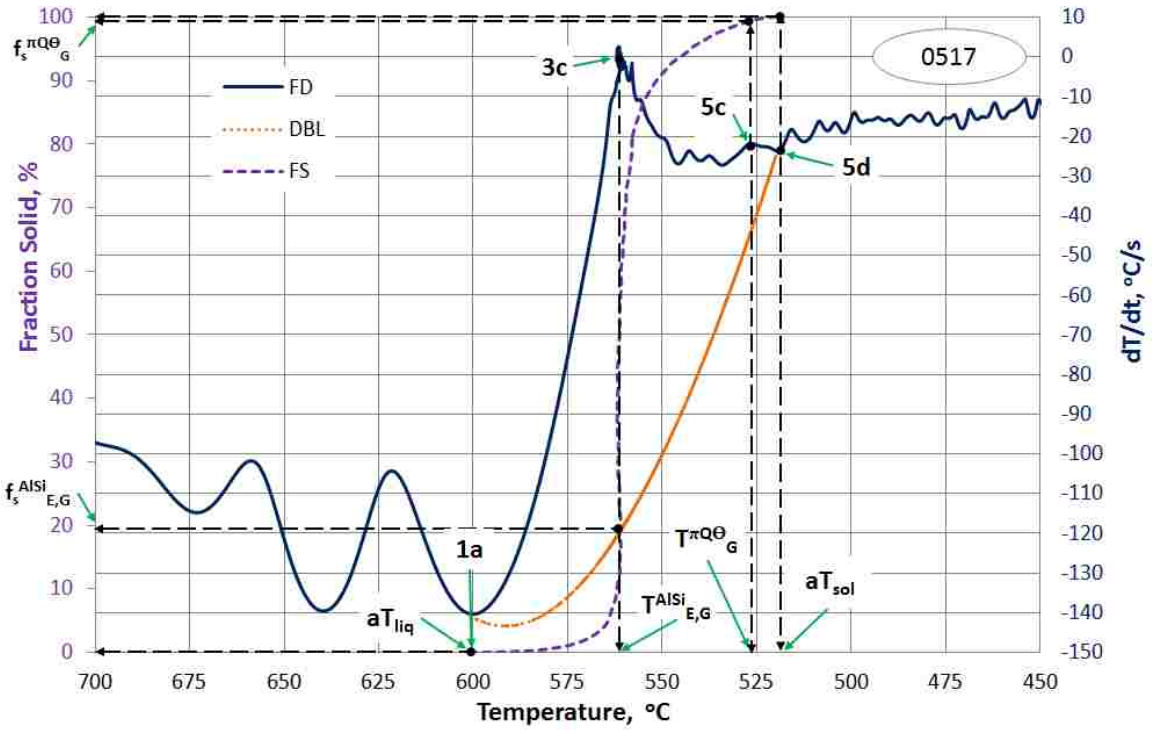

Figure 158. First Derivative Curve, Fraction Solid Curve and Dynamic Baseline vs. Temperature for the 0.15 wt.%Sr modified experimental alloy, solidified under impact and cyclic pressure (0-30) MPa/1.5c, in the SC/HPDC UMSA die, ASR = 13.9 °C/s, ref. #0517.

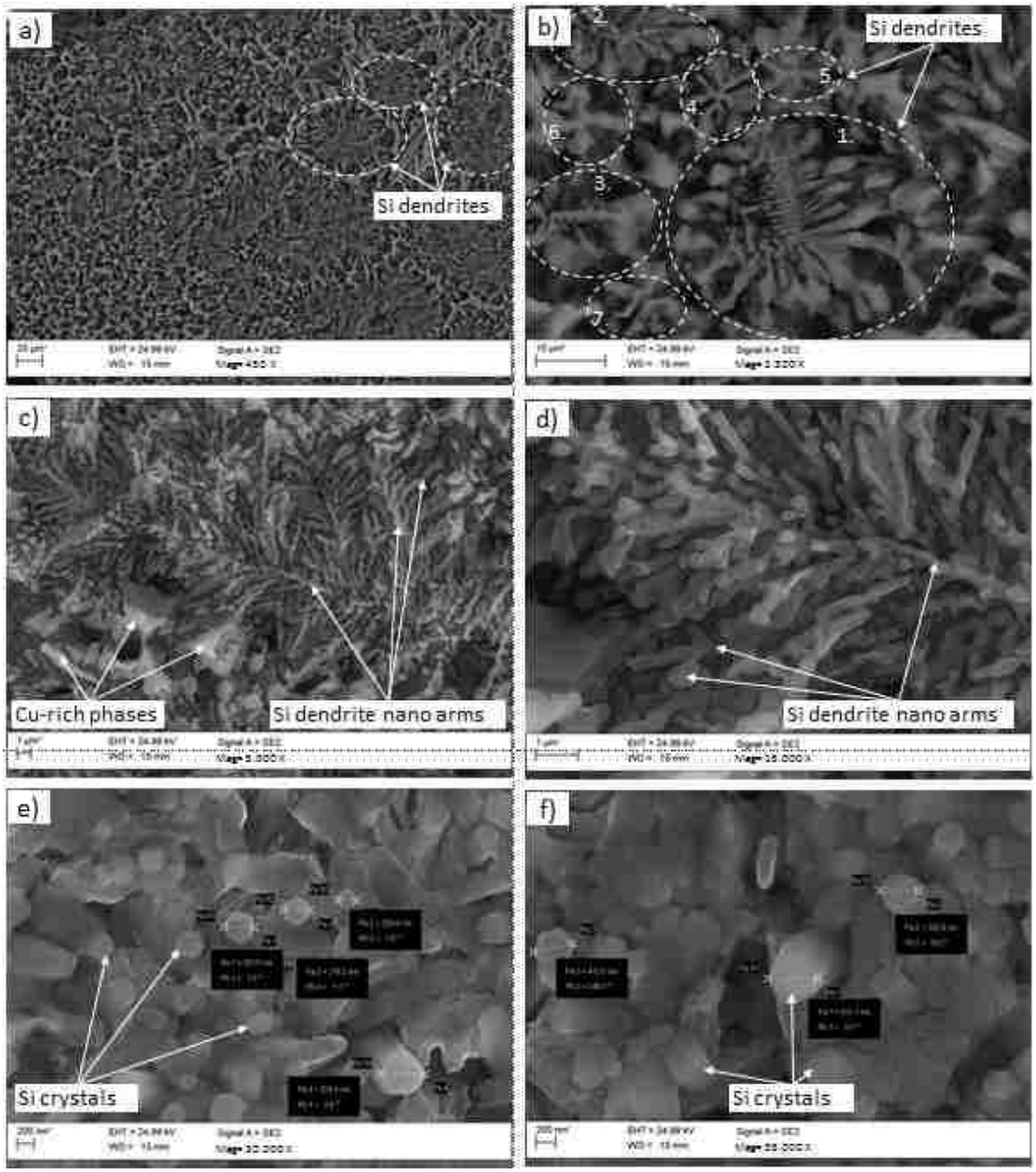

Figure 159. SEM, deep-etched microstructure for the 0.15 wt.%Sr modified experimental alloy, solidified in the SC/HPDC UMSA die under impact and cyclic pressure (0-30) MPa/1.5c; a) Transition from the edge to the center of the sample, b) order of Si dendrite(s) development on the subsurface of the sample; c, d) Si dendrites; e, f) Novel Hexagonal Si Whiskers, ref. #0517.

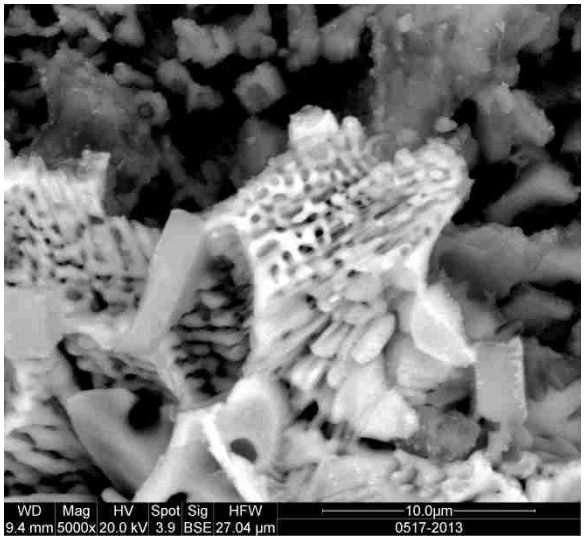

Figure 160. SEM micrograph of the deep etched structure of the (Q+Ɵ) eutectic for the 0.15 wt.%Sr modified experimental alloy #0517 solidified in the SC/HPDC UMSA die under impact and cyclic pressure loading.

4.4 As-Cast Structure Categories for the 0.15 wt%Sr Modified Test Samples processed in the SC/HPDC UMSA

In order to compare the effects of the addition of 0.15 wt%Sr to the experimental alloys and their response to various processing parameters, the unmodified test sample #0925 that solidified in the SC/HPDC UMSA die was used as the baseline.

TA data presented in Sections 4.2 and 4.3.3 and Tables 19, 21 and 22 summarize the processing parameter data for the following samples: #0925b, 1002b, 0919, 0916b, 0916, 0517, 0628b and #0925. Data was continuously collected during each experiment together with the post-process determined TA data.

Superimposed TA data includes recorded characteristics during melting, die filling, application of various pressure loading profiles and solidification as well as post-processing derived TA characteristics. All identified solidification reactions and their characteristics were determined using the identical methodologies used for near equilibrium solidification of the unmodified and modified HT UMSA test samples, see Chapter 4.1, Figures 89-96, 99-104 and Tables 16, 17.

The as-cast structures were characterized using LOM, SEM/EDS, Image Analysis and S/TEM/EDS methodologies and representative results are presented in Tables 20 and 23.

The as-cast structure classification is based on the exploratory research objectives that are given first priority to the technology development of the nano Si structures at the test sample subsurface that represent very thin wall section(s). The temperature gradient across the solidified 20mm diameter test sample resulted in transition from the nano

structures at the subsurface to the coarser structures in the center that will be comprehensively analyzed in future work.

Detailed analysis of the above-mentioned process and thermal data as well as structure data allows for determination of the four distinct test sample Categories #1 to #4. Each category takes into consideration quantitative structural characteristics of the Si phases, Al-Si colonies and inter-colony regions. Category #1 represents the overall best Si modification, Al-Si colony and the inter-colony regions' stereological characteristics. Category #4 represents some outstanding structural features that are not present in commercial HPDC cast components like the Yamaha monolithic engine block.

Based on the comprehensive subsurface as-cast structure analysis data for sample #0925 from Section 4.2 and seven samples from Section 4.3.3, as-cast structures were divided into 4 categories. Samples in Category 1, 2 and 3 were processed using various melt pressure loading profiles, while the sample in Categories #4 solidified under atmospheric pressure.

#1 Best Category Samples include:

#0925b -	the best in this category	-	**#1.1**
#1002b -	the second best	-	**#1.2**
#0919 -	the third best	-	**#1.3**

#2 Category Samples include:

#0916b -	the best in this category	-	**#2.1**
#0916 -	the second best	-	**#2.2**
#0517 -	the third best	-	**#2.3**

#3 Category Samples include:

#0628b - **#3**

#4 Category – Natural Solidification in the SC/HPDC UMSA Die - Baseline Sample

#0925 - **#4**

Summary of structural data associated with the as-cast Subsurface Structure Categories is presented in Table 19.

Table 19. Summary of Subsurface As-cast Structure Data associated with the As-Cast Structure Categories.

#	STRUCTURE DATA, µm	Abbreviations	STRUCTURE CATEGORY							
			1			2			3	4
			1.1	1.2	1.3	2.1	2.2	2.3	3	4
			Sample ref. #							
			0925b	1002b	0919	0916b	0916	0517	0628b	0925
1	Average Diameter of Silicon Whisker	D_{avg}Si-WA	0.22	0.26	0.33	0.3	0.4	0.45	0.3	0.6
2	Minimum Feret Diameter of Silicon Whisker Tip	$D^{min}{}_{F}$Si-WT	0.7	1.8	1.9	1.2	1.7	1.5	1.5	1.7
3	[redacted]	T_{avg}AlSi-ICB	2.6	3.4	6.4	6.2	5.0	9.1	8.1	19.6
4	Minimum Feret Diameter of Al-Si Colony	$D^{min}{}_{F}$AlSi-Co	18.3	40.5	44.0	51.0	27.8	40.6	56.8	51.8
5	Maximum Feret Diameter of Al-Si Colony	$D^{max}{}_{F}$AlSi-Co	74.9	111.6	106.4	133.5	77.7	135.4	169.1	105.0

Table 20 provides complementary information to Table 19 and addresses the characteristics of the subsurface and center of the test sample.

Table 20. Subsurface and Center Characteristics for Eight Test Sample Structure Categories.

Phase	Location	Range of Average size, µm	STRUCTURE CATEGORY			
			Chemical and Physical Melt Tretments			Chemical Melt Treatment
			1	2	3	4
			# 0925b, 1002b, 0919	# 0916b, 0916, 0517	# 0628b	# 0925
Primary Si	Subsurface		none	none	Few particles up to 20x50	Few particles up to 250x250
	Center		Few particles up to 25x25	Few 100x100	Few 25x25	Few 100x100
Eutectic Si	Subsurface	D_{avg}Si-WA	0.22-0.33	0.33-0.45	≈0.30	>0.60
		D^{min}_{F}Si-WT	1.5	1.7	1.5	1.7
		T_{avg}AlSi-ICB	4.1	5.0	8.1	19.6
		D^{min}_{F}AlSi-Co	34.3	39.8	56.8	51.8
		D^{max}_{F}AlSi-Co	97.6	115.5	169.1	105.0
	Center	D_{avg}Si-WA	up to 0.5	up to 0.5	up to 0.5	up to 1.0
		Si Dendrites	none	up to 100x150	none	none
		T_{avg}AlSi-ICB	up to 10	up to 10	up to 15	up to 20
		D^{min}_{F}AlSi-Co	up to 50	up to 60	up to 60	up to 60
		D^{max}_{F}AlSi-Co	up to 100	up to 100	up to 150	up to 200
α-Al	Subsurface	Dendrites	50x150	10x80	none	10x50
	Center		50x150	Few 200x300	none	Few 5x100
β-Fe	Subsurface	size	none			up to 2x40
	Center		none			

The Image Analysis features used for microstructure analysis are defined in Figure 161. Definitions for the structural features measured using the Image Analysis System are as follows:

D_{avg}Si-WA: average diameter of the Si whisker and nano dendrite arms and trunk (in the center of the Si-Al colony area)

D^{min}Si-WT: represents the minimum ferret (caliper) diameter of the Si whisker tip (the coarsened end of the Si whisker)

T_{avg}AlSi-ICB: represents the average thickness of an inter colony boundary – the normal distance between the coarsened Si tips of neighbouring Al-Si colonies.

$D^{min}{}_{F}$AlSi-Co: represents minimum feret (caliper) diameter of the Al-Si colonies – the normal distance between two parallel tangents touching the colony outline.

$D^{max}{}_{F}$AlSi-Co: represents the maximum feret (caliper) diameter of the Al-Si colonies – the normal distance between two parallel tangents touching the colony outline.

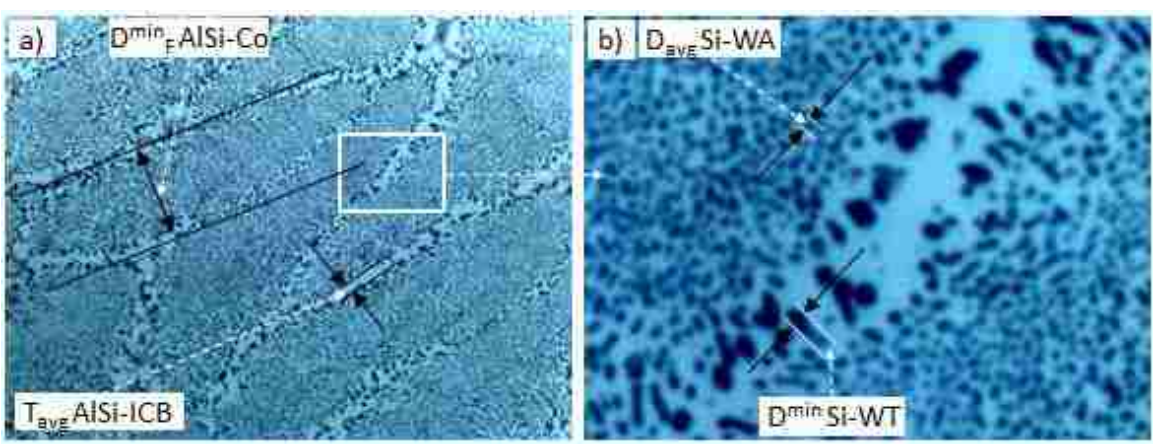

Figure 161. Image analysis features: a) $D^{min}{}_{F}$ AlSi-Co, T_{avg}AlSi-ICB, square which is zoomed out in Figure b), b) D_{avgF} Si-WA, $D^{min}{}_{F}$Si-WT.

4.4.1 Analysis of the Best Category #1, SC/HPDC UMSA processed 0.15 wt% Sr Modified Test Samples #0925b, #0919,#1002b

The SC/HPDC UMSA test samples classified as Category #1 were processed using the best parameters to date and exhibit novel as-cast structures. The deep-etched SEM analytical plane(s) show two distinct types of Al-Si eutectic colony structures, see Figures 138, 153 and 156 which represent experimental samples #0925b, #0919 and 1002b, respetcively. In both cases, each Al-Si eutectic colony made of Si nano whiskers originates from a common region. The SEM/EDS analysis of the Al-Si eutectic colonies (ref. #0925b) revealed the average chemical composition: Al = 80.13 wt.%, Si = 18.00 wt.% and Cu = 2.82 wt.%.

Due to the nano structured Si whiskers it can be assumed that this analysis is acceptable. No other elements were detected in these nano-structural features. The content of Cu in the middle of the Al-Si colonies is 2.44 wt.% and on the periphery of the Al-Si colonies is ≈ 3.2 wt.%. However, this does not mean that Sr will not be detected using more sophisticated techniques like Auger Spectroscopy. The SEM/EDS data indicates that the utilized melt pressure treatment caused a shift in comparison with the eutectic of the slowly solidified of the untreated pressurized alloy. This finding is in agreement with other research in which ultra high pressures up to 5 GPa were used. Auger Spectroscopy analysis is necessary to determine if Sr can be detected in the Al-Si eutectics. However, there is an interesting difference between this project's TA in comparison with the ultra high pressure.

All eight samples (0.15 wt.%Sr modified) SC/HPDC UMSA process parameters and the TA data are summarized in Tables 21 and 22.

4.4.2 Sample #0925/Category #4, 0.15 wt.%Sr Modified, Naturally Solidified in the SC/HPDC UMSA Die

Comparison of the selected structural features and TA data between the Sr modified sample #0925 that naturally solidified at ASR = 9.3 °C/s, the SC/HPDC UMSA die and the SC/HPDC UMSA processed Sr modified test samples #0925b and #0517 provide evidence that novel pressure loading applied during the liquid and semi-solid states profoundly affects the thermal and structural characteristics. For more details please refer to Tables 19 - 21 and Figures 115, 116.

1) Initial Die Temperature, T^D_I = 263 °C.

2) Temperature of Melt Superheat, T^M_{SH} = 796 °C.

3) Maximum Temperature of the Melt delivered to the Die, T^D_{MAX} = 687.6 °C.

4) Natural Solidification T_{liq} = 614.3 °C @ SR = 43.7 °C/s of sample #0925 is significantly lower in comparison with samples #0925b ($ISR_{a,liq}$ = 100.5 °C/s) and #0517 ($ISR_{a,liq}$ = 140.4 °C/s). Therefore, the resultant heat transfer for the naturally solidified sample #0925 will not be as effective in comparison with two other samples. This phenomenon alone will negatively affect metallurgical characteristics of all metallurgical reactions that are indicators of the as-cast structural characteristics. For example SR at the T_{sol} for sample #0925 is 17.3 °C/s, while SR for sample #0517 is 23.7 °C/s and for sample #0925b is 23.7 °C/s. In turn, the Solidification Time (St) for sample #0925 is 13.4 s, while for the other two samples St is in the range of (5.2 to 5.8) seconds. The Solidification Range for sample #0925 is 124.4 °C and for the two compared samples is 80.5 °C to 95.5 °C, respectively. These selected TA parameters explain very significant structural differences between sample #0925 and the two others samples processed using carefully chosen pressure loading parameters. A significantly longer

solidification time and a wider solidification range for sample #0925 resulted in formation of significantly coarser phases like Si and Fe, Cu, Mg rich phases and larger eutectic Al-Si eutectic colonies together with the thick inter colony boundaries, see Figures 117 (e, f), 134 and Table 19.

5) The above mentioned and tabulated process parameters control the nucleation and growth of single-phase Si hexagonal whiskers, Si dendrites with nano diameter arms and trunks and Al-Si colonies (D^{min}_{F}AlSi-Co = 40.6 μm, D^{max}_{F}AlSi-Co = 135.4 μm) depending on the type of Si whiskers and dendrite type as well as the inter colony boundaries' average thickness range (0.77 to 9.1) μm, depending on the type of structural features and their chemical makeup. In addition, the process parameters also control morphological features of Fe and Cu rich phases that are very fine for the best SC/HPDC UMSA processing parameters.

Note: Complementary Environmental UMSA tests using the experimental alloy (0.15 wt%Sr modified) revealed that a MSR of ≈ 400 °C/s is necessary for formation of Si dendrites with nano arms and trunks. To date, the SC/HPDC UMSA was chosen as having the best processing parameters involving various pressure loading profiles that rendered not only the desired dendritic structure but also allowed for the production of novel nano hexagonal Si whiskers and ultra-fine Al-Si eutectic cells with very low thickness of inter cell boundaries for the highly alloyed samples.

4.4.3 Summary of the Process Parameters, TA Data and Resultant As-cast Structure Categories

The summary of process parameters, TA data and as-cast structure categories are presented in Tables 21, 22 and 19.

Table 21. Summary of the Process Parameters and Resultant As-Cast Structure Categories.

#	PROCESS PARAMETERS, UNITS	Abbreviations	STRUCTURE CATEGORY							
			1			2			3	4
			1.1	1.2	1.3	2.1	2.2	2.3	3	4
			Sample ref. #							
			0925b	1002b	0919	0916b	0916	0517	0628b	0925
1	Die Initial Temperature, ◦C	T^{D}_{I}	262	267	273	257	268	272	283	263
2	Melt Superheat Temperature, ◦C	T^{M}_{SH}	805	814	N/A	810	810	811	805	796
3	Delivered Melt Maximum Temperature, ◦C	T^{D}_{MAX}	756.0	776.0	654.0	695.5	665.8	718.5	707.8	687.6
4	Minimum Pressure of Cycle, MPa	P_{MIN}	38	38	38	0	0	0	39	0.1
5	Maximum Pressure of Cycle, MPa	P_{MAX}	81	82	82	27	22	30	82	0.1
6	Pressure Start Temperature, ◦C	T^{P}_{ST}	619.2	621.7	632.6	636.3	632.0	655.2	659.0	
7	Pressure End Temperature, ◦C	T^{P}_{END}	560.2	557.2	567.1	603.8	619.5	561.5	547.9	
8	Number of Cycles, #	#c	10	10	10	2	1	1.5	45	
9	Pressure Time Interval, s	Δt^{P}_{I}	1.0	1.0	1.0	0.3	0.2	2.9	4.8	
10	Pressure Temperature Range (T^{P}_{ST} - T^{P}_{END}), ◦C	ΔT^{P}_{Rn}	59.0	64.5	65.5	32.4	12.5	93.7	111.1	
11	Pressure Solidification Rate, ◦C/s	PSR	60.9	63.1	64.2	97.4	72.1	32.1	23.0	
12	Cumulative Energy between T^{P}_{ST} and T^{LMT}_{END}, J	ΔCE_{liq1}	20.9	13.0	25.2	17.8	18.4	12.1	2.6	0
13	Cumulative Energy between T^{LMT}_{END} and T_{liq}, J	ΔCE_{liq2}	10.5	16.1	15.7	5.6	1.7	0.3	13.1	
14	Cumulative Energy in Liquid State = $\Delta CE_{liq1}+\Delta CE_{liq2}$, J	CE_{liq}	31.3	29.1	40.9	23.4	20.1	12.4	15.7	
15	Cumulative Energy between T_{liq} and $T^{AlSi}_{E,MIN}$, J	ΔCE_{ss1}	4.21	1.43	4.09	0.0	0.0	1.4	2.4	
16	Cumulative Energy between $T^{AlSi}_{E,MIN}$ and T^{P}_{END}, J	ΔCE_{ss2}	0.0	0.0	0.0	0.0	0.0	0.2	29.6	
17	Cumulative Energy in Semi-solid State = $\Delta CE_{ss1}+\Delta CE_{ss2}$, J	CEss	4.2	1.43	3.9	0.0	0.0	1.6	32.1	
18	Total Cumulative Energy = $CE_{liq}+CE_{ss}$, J	$TCE_{liq-sol}$	35.5	30.5	44.8	23.4	20.1	14.1	47.8	

Table 22. Summary of Thermal Analysis Data and Resultant As-Cast Structure Categories.

#	THEMAL ANALYSIS DATA, UNITS	Abbreviations	STRUCTURE CATEGORY							
			1			2			3	4
			1.1	1.2	1.3	2.1	2.2	2.3	3	4
			Sample ref. #							
			0925b	1002b	0919	0916b	0916	0517	0628b	0925
1	Melt Cooling time, (liquidus time - pouring time), s	MCt	3.3	3.9	4.0	3.0	4.5	2.3	3.4	3.36
2	Melt Cooling Range, $MC_{Rn} = T^{M}_{SH} - aT_{liq}$, ◦C	MC_{Rn}	220.8	226.8	N/A	219.0	221.0	210.9	207.1	181.7
3	Melt Cooling Rate, $MCR=MC_{Rn}/MCt$, ◦C/s	MCR	66.1	58.5	N/A	72.3	49.5	92.3	60.4	54.1
4	Apparent Liquidus Temperature, ◦C	aT_{liq}	584.2	587.2	589.7	591.0	589.0	600.1	597.9	614.3
5	[redacted] Solidification Rate at aT_{liq}, ◦C/s	[redacted]	100.5	110.1	140.4	96.2	82.4	140.4	135.7	43.7
6	Al-Si Eutectic Minimum Temperature, ◦C	$T^{AlSi}_{E,MIN}$	560.2	556.6	565.1	558.7	560.9	561.0	564.3	556.8
7	Fraction Solid at $T^{AlSi}_{E,MIN}$, %	$fs^{AlSi}_{E,MIN}$	6.5	6.7	7.8	8.7	7.6	16.4	6.3	9.9
8	AlSi Eutectic Undercooling time = $t_{UC} - t_{liq}$, s	$t^{AlSi}_{E,UC}$	0.5	0.6	0.7	0.7	0.8	1.0	0.5	2.4
9	AlSi Eutectic Undercooling Temperature = $aT_{liq}-T^{AlSi}_{E,MIN}$, ◦C	$\Delta T^{AlSi}_{E,UC}$	23.9	30.5	24.5	32.3	28.0	39.1	33.6	57.6
10	AlSi Eutectic Undercooling Solidification Rate, ◦C/s	[redacted]	50.5	52.7	36.0	45.9	37.1	38.8	70.0	24.3
11	Al-Si Eutectic Growth Temperature, ◦C	$T^{AlSi}_{E,G}$	567.4	566.0	567.5	563.9	565.5	561.2	567.7	559.6
12	Fraction Solid at $T^{AlSi}_{E,G}$, %	$fs^{AlSi}_{E,G}$	32.1	36.6	28.5	33.3	33.0	19.4	27.9	30.3
13	Al-Si Eutectic Recalescence time, s	$\Delta t^{AlSi}_{E,R}$	1.0	1.2	0.9	1.0	1.2	0.1	0.8	1.7
14	Al-Si Eutectic Recalescence Temperature, ◦C	$\Delta T^{AlSi}_{E,R}$	7.1	9.4	2.4	5.2	4.5	0.3	3.4	2.8
15	Al-Si Eutectic Recalescence Solidification Rate, ◦C/s	[redacted]	7.5	7.8	2.6	5.0	3.6	2.0	4.0	1.6
16	Apparent Al-Si Eutectic End Temperature, ◦C	$T^{AlSi}_{E,END}$	495.8	517.1	503.9	499.7	496.4	526.4	514.2	507.6
17	Fraction Solid at $aT^{AlSi}_{E,END}$, %	$fs^{AlSi}_{E,END}$	98.8	98.0	99.5	99.4	99.3	99.5	98.3	98.7
18	πQΘ- Phase Growth Temperature, ◦C	$T^{\pi Q\Theta}_{G}$	495.8	517.1	503.9	499.7	496.4	526.4	514.2	507.6
19	Fraction Solid at $T^{\pi Q\Theta}_{G}$, %	$fs^{\pi Q\Theta}_{G}$	98.8	98.0	99.5	99.4	99.3	99.5	98.3	98.7
20	Apparent Solidus Temperature, ◦C	aT_{sol}	488.7	504.7	496.7	495.0	489.9	519.6	510.0	489.9
21	[redacted] Solidification Rate at aT_{sol}, ◦C/s	[redacted]	39.7	30.5	21.1	28.0	35.3	23.7	34.6	17.3
22	Solidification Time Interval, s	St	5.2	5.7	6.8	5.9	7.0	5.8	5.2	13.4
23	Solidification Range, ◦C	SRn	95.5	82.5	92.9	96.0	99.1	80.5	88.0	124.4
24	Average Solidification Rate, ◦C/s	ASR	18.3	14.6	13.6	16.3	14.1	13.9	17.0	9.3

Table 23. Summary of Novel Structures for the Experimental Alloy.

NOVEL STRUCTURES	STRUCTURE CATEGORY			
	Chemical and Physical Melt [redacted]			Chemical Melt Treatment
	1	2	3	4
	# 0925b, 1002b, 0919	# 0916b, 0916, 0517	# 0628b	# 0925
[redacted]	Nano Silicon Whiskers in Al-Si Eutectic Colonies up to 100 µm			x
	Open-Cell Si-X Foam Morphology at Cell Boundaries			
	[redacted]		x	
	x	Nano Arms and Trunks of Si Dendrites	x	
	x	Hexagonal Nano Whiskers	x	
ST Spheroidized Single Phase Si [redacted] Average Diameter = 590nm	yes	N/A		

4.5 Statistical Analysis of As-cast Structure Categories, TA Data and Process Parameters of Test Samples Presented in Sections 4.3 and 4.3.3

Due to the exploratory nature and complexity of this project's outcomes, statistical analysis includes eight SC/HPDC UMSA experiments that render new scientific and applied engineering knowledge. The selected samples' processing parameters and their thermal data together with structural characteristics are summarized in Tables 19, 21, 22.

Collected data for the three categories of dependent variables (structure) and independent variables (process parameters and resultant thermal data) is very extensive. However, eight experiments allowed for the calculation of predictive model(s) having three independent variables which limits present statistical calculations.

Calculations of the linear regression equations were performed using IBM SPSS Statistics 22 software and were carried out in the Academic Data Centre in the Leddy Library. Two routes were chosen for statistical analysis. The first one deals with the as-cast structural characteristics that are categorized into four groups of individual experiments. As mentioned in Section 4.4, there are four Categories #1 to #4, where #1 includes the best stereological characteristics to date that are associated with the process parameters and consequently with the thermal characteristics. Assignment of the structure to a given category depends on the range of numerical values for the structural characteristics. In the case of the sample structure that naturally solidified in the UMSA die, categorized as #4, this is used as the "base line".

In order to confirm some of metallurgical observations that the Cumulative Energy (CE) delivered by the plunger to the tested melt in liquid (CE_{liq}) and semi-solid (CE_{ss}) states, the relationship between Structure Category (#1 to #4) was modeled. The significance level for both the Cumulative Energies (ΔCE_{liq2} and ΔCE_{ss2}, respectively) and the high $R^2 = 0.970$ indicates a strong and statistically valid relationship between the tested experimental variables, (see Table 24, #1). These CEs are known as the "global process parameters".

Metallurgical observations that the given structural Category depends on are the Start of the Pressure Treatment Temperature (T^P_{ST}) and ΔCE_{liq2} and ΔCE_{ss2}. These were confirmed by the regression equation that was calculated using ΔCE_{ss} for the given processing temperature range according to Tables 24 #1 and #2. The Equation renders very high confidence levels for each predictor and $R^2 = 0.943$ and 0.970 can be observed in Table 24.

Since two valid regression models describe the analyzed relationship, future statistical analysis for a larger experimental population should include these independent variables as input to one comprehensive regression equation.

A regression equation expressing the relationship between the Average Diameter of the nano Si Whiskers and the Si Dendrites Arms - D_{avg}Si-WA, (μm) and process parameters like the Maximum Temperature of the Melt delivered to the Die (T^D_{MAX}), the Start Temperature of the Melt Pressure Treatment (T^P_{ST}) and the Pressure Time Interval (Δt^P_I) is presented in Table 25. Confidence levels for both T^P_{ST} and Δt^P_I are excellent, while for T^D_{MAX} = 91.0 %. $R^2 = 0.978$. Regression equations correlating some other process parameters show very high R^2, but the significance of some predictors were

below 95.0 %, therefore these were not presented. These results indicate that the number of experiments needs to be increased and/or Thermal Analysis data also needs to be considered.

Table 27 provides a regression equation and statistical qualifiers for the relationship between Structural Category (#1 to #4) and Process and Thermal Data. R^2 is 0.969, while the significance level for all independent variables is better than 95 %.

Future research needs to consider a statistically designed experiment(s) approach using variables generated and discovered in this project. In addition, a higher number of experiments will allow for utilization of other variables and determine the effect(s) of interactions between variables for comprehensive regression equations (linear and/or non-linear).

In addition, for rapid analysis of the complex relationships between dependent and independent variables it would be beneficial to also utilize nomograms allowing for fast graphical calculation of the complex regression equations using parallel and other coordinate systems.

Chosen dependent variables (predictors) include the stereological characteristics for the Si whiskers that are summarized in Table 19.

Average diameter of Si whisker(s) and nano dendrite arms and trunk - $\mathbf{D_{avg}Si\text{-}WA}$

Minimum feret (caliper) diameter of Si whisker(s) tip - $\mathbf{D^{min}Si\text{-}WT}$

Average thickness of an inter colony boundary - $\mathbf{T_{avg}AlSi\text{-}ICB}$

Minimum feret (caliper) diameter of Al-Si colonies - $\mathbf{D^{min}{}_{F}AlSi\text{-}Co}$

Maximum feret (caliper) diameter of Al-Si colonies - $\mathbf{D^{max}{}_{F}AlSi\text{-}Co}$

Selected process parameters (i.e. the Maximum Temperature of the Melt delivered to the Die - T^{D}_{MAX} presented in Table 25) have been used in the multiple linear regression analysis as dependent variables for quantification of their effect on both the Thermal Characteristics and the as-cast test samples' structure. Selected Thermal Characteristics can be correlated with both the process parameters and the structural characteristics.

Table 24. Structure Category vs. Process Parameters

#	Predictors	Constant	T^P_{ST}	ΔCE_{liq2}	ΔCE_{ss2}	R^2
1	Coefficients	3.994	-.003	-.077	.066	.970
	Significance Level	.000	.003	.008	.002	
#	Predictors	Constant	T^P_{ST}	ΔCE_{liq2}	CE_{ss}	R^2
2	Coefficients	3.991	-.003	-.086	.063	.943
	Significance Level	.000	.009	.018	.008	

Table 25. D_{avg}Si-WA vs. Process Parameters

Predictors	Constant	T^D_{MAX}	T^P_{ST}	Δt^P_I	R^2
Coefficients	122.815	.086	.063	-3.971	.978
Significance Level	.015	.090	.002	.015	

Table 26. MCRn vs. Process Parameters

Predictors	Constant	T^P_{ST}	ΔCE_{liq2}	Δt^P_I	R^2
Coefficients	181.697	.061	.587	-4.333	.984
Significance Level	.000	.001	.054	.008	

Table 27. Structure Category vs. TA Data & Process Parameters

#	Predictors	Constant	$t^{AlSi}_{E,UC}$	ΔCE_{liq2}	ΔCE_{ss2}	R^2
1	Coefficients	1.085	1.213	-.052	.068	.969
	Significance Level	.021	.003	.046	.002	
#	Predictors	Constant	ΔCE_{liq2}	ΔCE_{ss2}	ASR	R^2
2	Coefficients	5.449	-.085	.075	-.209	.875
	Significance Level	.008	.055	.019	.061	

Table 28. D_{avg}Si-WA vs. Process Parameters & TA Data

Predictors	Constant	CE_{liq}	[redacted]	ΔCE_{ss2}	R^2
Coefficients	0.811	-.004	-.008	.005	.978
Significance Level	.000	.009	.003	.036	

Table 29. D_{maxF}AlSi-Co vs. Process Parameters & TA Data

Predictors	Constant	ΔCE_{ss2}	SRn	[redacted]	R^2
Coefficients	262.400	2.404	-.939	-2.368	.823
Significance Level	.015	.022	.148	.068	

4.6 Ultra-Rapid Si Spheroidization and $Al_5Cu_2Mg_8Si_6$ and Al_2Cu Phases Dissolution Heat Treatment

Solution Treatment (ST) spheroidization of Si whiskers and dissolution of the low melting point of the $Al_5Cu_2Mg_8Si_6$ (Q-phase) and Al_2Cu (Θ-phase) phases are the key factors that control the engineering characteristics (i.e. mechanical, tribological, corrosion, dimensional stability) of novel as–cast nano and ultra-fine structured experimental alloys. The $Al_5Cu_2Mg_8Si_6$ and Al_2Cu phases in deeply etched samples resemble spider web shapes. This 3D structure suggests that the thermally controlled segmentation and dissolution could be performed in an ultra short time. To date there is no information about Heat Treatment addressing the novel materials developed in this PhD project. Therefore, the main objective of the present exploratory research is the determination of the feasibility of the ultra rapid Solution Treatment (ST) and Artificial Aging (AA) resulting in the desired structures and engineering characteristics.

Commercial heat treatment of the industrial grade hypereutectic phosphorus modified Al-Si-Cu HPDC linerless engine block(s) involves eight hours of Solution Treatment (ST) and Artificial Aging (AA) operations [229] that have two inter related objectives. They are: maximization of the dissolution of Q and Θ phases for enhancement of the AA precipitation strengthening process and thermally activated modification of the eutectic silicon. Optimized ST and AA parameters are determined by melt modification and the as-cast thermally unstable phases like Q and Θ and eutectic Si.

Commercially used Heat Treatment technologies involve ST spheroidization of the modified alloy. This approach is capable of partially spheroidizing the eutectic Si. The morphology of the primary Si being a thermodynamically stable phase can be

changed to the extent that rounding of the sharp edges can occur. Q and Θ phases are prone to incipient melting when the ST temperature exceeds approximately 505 °C. Incipient melting causes permanent damage to the integrity of the bulk and subsurface structures through formation of voids and blisters, respectively. Both voids and blisters result from the melting of coarse Cu and Mg phases while the metal matrix stays in the solid state. During ST quenching these liquid phases shrink faster in comparison with the metal matrix causing voids and blisters.

To date, three research teams addressed new rapid heat treatments of cast Al-Si-Cu and Al-Si-Mg-Cu HPDC alloys [264] Si spheroidization in thixo-formed Ba well modified Al-Si alloys [265] and fluidized bed Heat Treatment for the 354 (permanent mold bars) and 319 (cylinder heads) Al-Si-Cu-Mg alloys [214]. The HPDC alloys' truncated ST is performed in 15 min at 490 °C to 505 °C and is followed by AA in a temperature range of (150 to 220) °C [266]. These parameters lead to significant improvements in the tensile properties [264]. Tensile specimens taken from the thixo-formed Al-Si components were placed in the furnace at 540 °C and kept until they reached 500 °C and held for (3 to 5) min and then quenched and AA for 4 h at 160 °C. The 3 min/540 °C ST of as-cast Si coral branches having an approx. 0.5 μm diameter rendered fragmented Si particles with a diameter of approx. 1.2 μm. This structure renders elongation up to 16.7 % and a Yield Strength of approx. 230 MPa. Publication [265] offers analytical modeling of the fragmentation and spheroidization process of the Eutectic coral Si. In the well modified thixo-formed hypoeutectic Al-Si alloys Si disintegrates easily and there is no need for consideration of the potential incipient melting of the low melting phases like AlCuMgSi.

Publication [214] indicates the following: $Al_5Cu_2Mg_8Si_6$ and Mg_2Si phases in the 319 alloy dissolves completely within 45min during ST in the Fluidizing Bed (FB), Al_2Cu blocky particles in the 319 alloy do not dissolve in 2 h ST using the FB and Al_5FeSi and $Al_8FeMg_3Si_6$ phases do not change morphology within 120 min of ST in the FB.

Publication [265] offers analytical modeling of the fragmentation and spheroidization process of the eutectic coral Si. In the well modified thixo-formed hypoeutectic Al-Si alloys Si disintegrates easily and there is no need for consideration of the potential incipient melting of the low melting phases like $Al_5Cu_2Mg_8Si_6$. In contrast, this is a key consideration in ST of the complex Al-Si-Cu hypereutectic alloys. Using the SC/HPDC UMSA technology, nano Si whiskers and Si dendrite arms were formed instead of both primary and eutectic Si phases. Nano Si whisker fragmentation and spheroidization as well as effective dissolution of the $Al_5Cu_2Mg_8Si_6$ and Al_2Cu phases must be performed in a temperature range that is safe for all phases. The response of the structure containing these nano Si whiskers and $Al_5Cu_2Mg_8Si_6$ and Al_2Cu phases to the ST was not examined to date. Therefore, ST process parameters need to be determined for effective fragmentation and spheroidization of the nano Si whiskers and the low melting point phases $Al_5Cu_2Mg_8Si_6$ and Al_2Cu.

Heat Treatment

Figure 162 shows the #0925b test sample HT UMSA heating curve and its FD. Test sample heat of 540 °C was programmed at a heating rate of 1.8 °C/s. As can be observed up to the temperature of 504.7 °C, the heating curve is smooth. Between 504.7 °C and 535.0 °C, the heating curve is no longer smooth and also shows a departure from the programmed curve. This departure is forced by the metallurgical endothermic reactions during which the Latent Heat of Fusion is delivered by the HT UMSA Induction Coil.

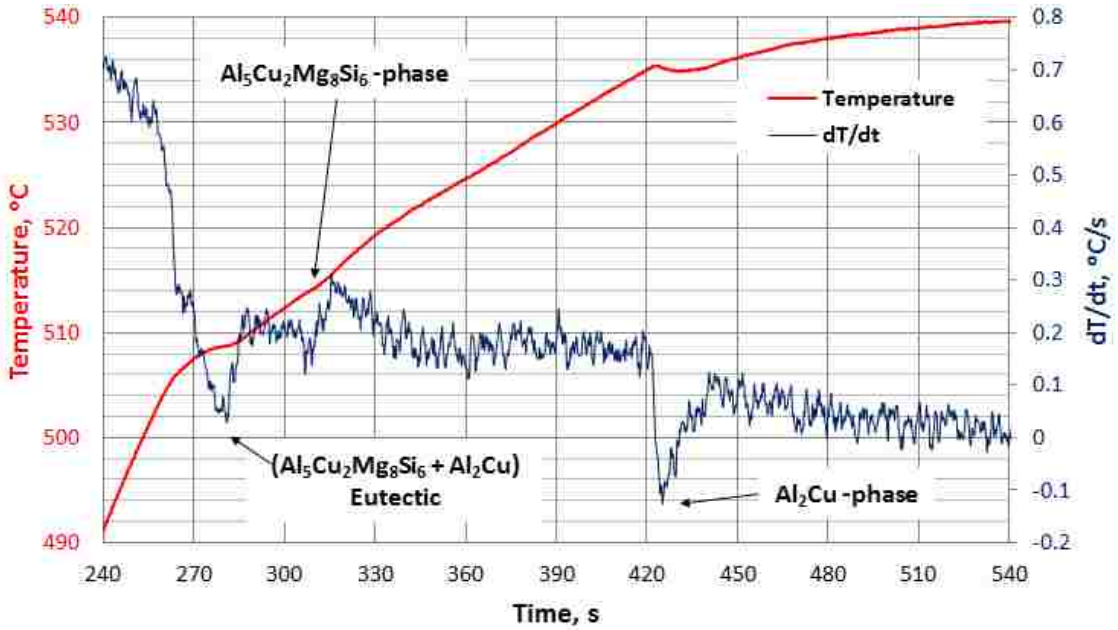

Figure 162. Heating Curve and First Derivative Curve for the 0.15 wt.%Sr modified experimental alloy, previously processed in the SC/HPDC UMSA die under impact and cyclic pressure (38-81) MPa/10c, ref. #0925b. Dissolution of (Q+Θ) eutectic and Q and Θ phase.

The Fitting Heating Curve and its FD above 504.7 °C will allow for a better understanding of the thermally nucleated and controlled process of Q and Θ phases dissolution and Si whisker fragmentation and spheroidization processes. The FD revealed more details about endothermic reactions that start at 504.7 °C @ a Heating

Rate (HR) of 0.61 °C/s. The first peak is convoluted suggesting the presence of overlapping of the two reactions pertaining to (Q+Θ) eutectic and Q-phase. This reaction is finished at a temperature of 516.4 °C @ HR of 0.27 °C/s. After 105 s, the second peak starts a new reaction, which is associated with the Θ-phase at a temperature of 535.08 °C @ a HR of 0.102 °C/s. This reaction ends at a temperature of 535.02 °C @ a HR of 0.035 °C/s. In 105 seconds the smooth FD reaches zero and a programmed temperature of 540 °C.

The zero for the FD heating curve of the sample heated through the Solution Treatment temperature range indicates that there is no detectable amount of phase(s) for further dissolution. However, the TA data of the nano structured experimental alloy shows that dissolution treatment of various phases and fragmentation/spheroidization of Si is ultra rapid. Therefore, future ST research needs to optimize the quenching operation for securing full retention of all dissolved phase(s) in the Al solid solution. Most likely, the most desired direction will be the interrupted quenching method using high quenching rates during the temperature range of AlCuMgSi nucleation and growth, and a slower quenching rate after completion of these reactions. This approach will allow for control of the residual stresses. Since the quenching operation was not addressed in this dissertation, it is conceivable that a very small volume fraction of soluble phases can precipitate during the quenching operation and be detected using the TEM technique.

In comparison with the literature research data [214] the ultra low detection limit of the HT UMSA Thermal Analysis techniques allows for characterization of both the dissolution of the GP zones and dissolution of the soluble phases during Solution Treatment. Based on observations to date it is recommended that in the case of formation

of a very small volume fraction of thermally activated phase(s) precipitation during quenching, the SEM/EDS and TEM/EDS analysis of cryogenically frozen sample(s) right after a given technological operation must complement the Thermal Analysis. This methodology will help to fully understand the heat treatment phenomenon and optimize process parameters, structure and consequently other engineering characteristics.

The detection limit of the Thermal Analysis techniques allows for the determination of the dissolution temperature of the GP zones. However, in the case of formation of a very small volume fraction of precipitates their detection using routine methodologies could be difficult. Therefore, when the FD reaches the zero minute, amounts of precipitates could be present in the structure and detected by TEM.

At the temperature range of (504.7 to 535.08) °C three metallurgical reactions including dissolution of Q and Θ-phases and (Q+Θ) eutectic nano Si whiskers fragmentation and spheroidization as well as Si coarsening could take place. This complex phenomenon can be further quantified by implementation of the UMSA experiments using the nano structured Al-Si alloy and the ultra-fine structured Al-Cu alloy. Both alloys should have similar levels of other elements. This important task should be addressed in the next stages of the research program.

Novel HT UMSA research demonstrates that in seven minutes the above mentioned metallurgical reactions can be completed. Therefore, it was concluded that these processes are ultra fast. In addition, the HT UMSA thermal characteristics of the Si nano whiskers fragmentation and spheroidization as well as dissolution of the AlCuMg rich phases are superior in comparison with the literature data. These ultra short reaction times relate to the nano structured Si whiskers and ultra-fine Al-Si cells and inter cell

boundaries and consequently the AlCuMg morphologies. This complex industrial secondary Al-Si-Cu experimental alloy test sample response to the ST is extremely fast and its commercialization requires an adequate technology. In this respect, the concept of utilization of solidification heat as a part of the flash ST could be considered.

Figure 163 presents preliminary optimization of solution treatment process for experimental sample #0925.

The HAADF image superimposed with HAADF and EDS elemental maps and phase stoichiometry at the subsurface and center of the sample #0925b after heat treatment (ST: 506 ºC/5 min + 512 ºC/2 min, AA: 200 ºC/10 min), (marked as #0925b-AA2) is presented in Figures 164 and 165. TEM foil was extracted from the subsurface of the sample (the distance from the edge of the sample is 20 μm) (see Figure 164). TEM foil was extracted from the center of the sample (9 mm from the edge of the sample (see Figure 165).

Comparison between literature references, the Yamaha engine block and experimental sample #0925b's phase stochiometries and the sizes of its structural features are provided in Table 30. Table 31 presents the comparison between the chemical composition (wt.%) of the main phases and the Yamaha engine block and sample # 0925b under as-cast and heat treated conditions.

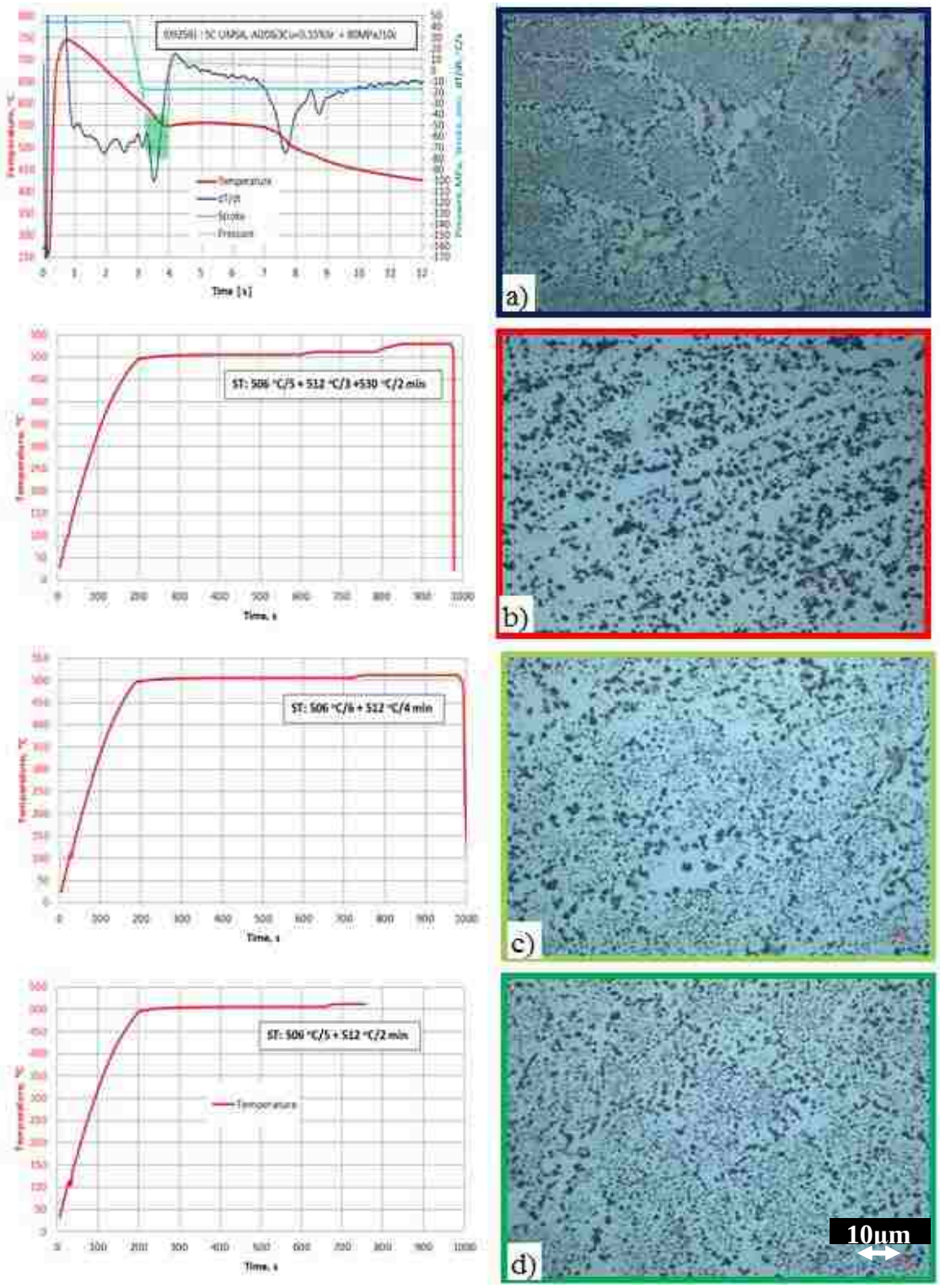

Figure 163. LOM, as-cast microstructure for the 0.15 wt.%Sr modified experimental alloy: a) SC/HPDC UMSA sample, solidified under cyclic pressure (38-81) MPa/10c, ref. #0925b, b) test sample after ST at 506 °C/5 min + 512 °C/3 min + 530 °C/2 min, ref. #1022, c) test sample after ST at 506 °C/6 min + 512 °C/4 min, ref. #1023, d) test sample after ST at 506 °C/5 min + 512 °C/2 min ref. #1024. The samples were quenched in water at 22 °C after Solution Treatment.

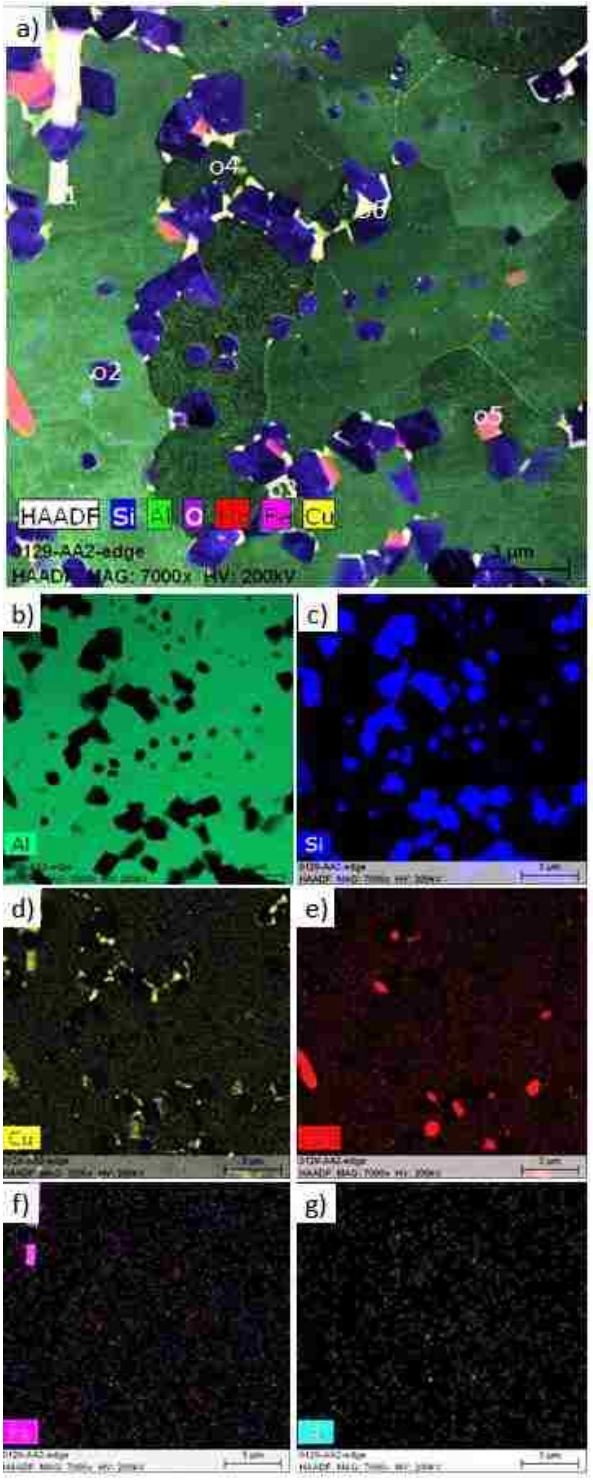

Element	Weight %	Atomic %
1: $Al_{11}Cu_3Fe$		
Al(K)	57.77	75.47
Si(K)	0.42	0.53
Fe(K)	10.58	6.68
Cu(K)	31.2	17.3
# 2: Si		
Al(K)	2.28	2.4
Si(K)	96.13	96.89
Cu(K)	1.57	0.7
# 3: $Al_4Cu_2Mg_8Si_3$		
O(K)	0.99	1.89
Mg(K)	31.28	38.97
Al(K)	16.05	18.01
Si(K)	27.42	29.57
Cu(K)	24.22	11.54
# 4: Al		
Al(K)	93.33	96.58
Si(K)	0.88	0.87
Cu(K)	5.78	2.54
# 3: $Al_4Cu_2Mg_8Si_3$		
Mg(K)	32.39	40.36
Al(K)	16.86	18.92
Si(K)	27.47	29.62
Cu(K)	23.25	11.08
# 6: Al_3Cu_2		
Al(K)	41.11	60.91
Si(K)	2.49	3.55
Fe(K)	0.66	0.47
Cu(K)	55.72	35.05

Figure 164. a) HAADF image, b - g) superimposed with HAADF and EDS elemental maps, for the 0.15 wt.%Sr modified experimental alloy, solidified in the SC/HPDC UMSA die, under impact and cyclic pressure (38-81) MPa/10c and heat treated at (ST: 506 ^{o}C/5 min + 512 ^{o}C/2 min, AA: 200 ^{o}C/10 min). TEM foil was extracted from the subsurface of the sample (20 µm from the edge of the sample), ref. #0925b-AA2.

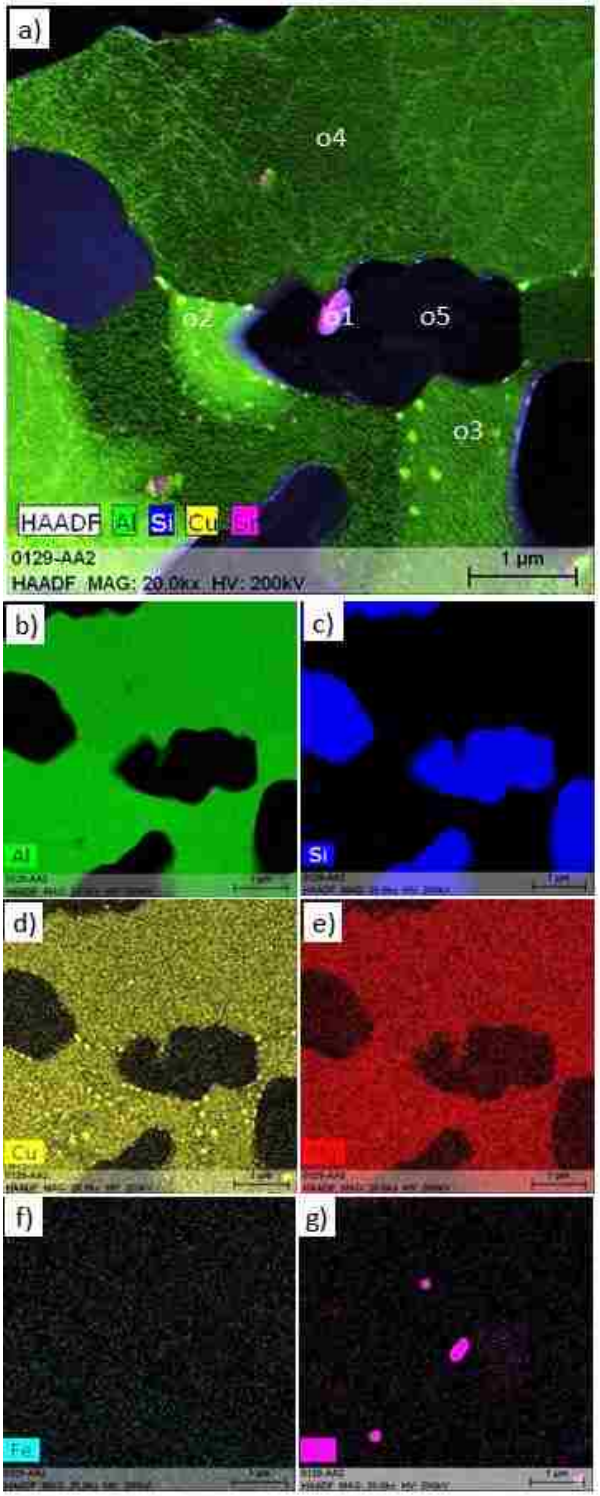

Element	Weight %	Atomic %
# 1: $Al_{22}Si_{23}Sr_6Cu$		
Al(K)	33.02	42.46
Si(K)	36.3	44.83
Ti(K)	0.06	0.04
Cu(K)	3.54	1.93
Sr(K)	27.05	10.71
# 2: Al		
Al(K)	94.63	97.47
Si(K)	0.32	0.32
Cu(K)	5.03	2.2
# 3: Al		
Al(K)	96.69	98.41
Si(K)	0.23	0.22
Ti(K)	0.18	0.1
Cu(K)	2.88	1.24
# 4: Al		
Mg(K)	0.88	1.01
Al(K)	92.09	95.35
Si(K)	0.92	0.91
Ti(K)	0.22	0.13
Cu(K)	5.87	2.58
Sr(K)	0	0
# 5: Si		
Al(K)	2.13	2.24
Si(K)	95.72	96.81
Cu(K)	2.01	0.9
Sr(K)	0.12	0.03

Figure 165. a) HAADF image, b - g) superimposed with HAADF and EDS elemental maps, for the 0.15 wt.%Sr modified experimental alloy, solidified in the SC/HPDC UMSA die, under impact and cyclic pressure (38-81) MPa/10c and heat treated at (ST: 506 ^{o}C/5 min + 512 ^{o}C/2 min, AA: 200 ^{o}C/10 min). TEM foil was extracted from the center of the sample (9 mm from the edge of the sample), ref. #0925b-AA2.

Table 30. Comparison between literature references, the Yamaha engine block and experimental sample # 0925b's phase stochiometries and sizes of its structural features.

Literature Reference	Yamaha Engine Block	#0925b			
	HPDC/HT	**As Cast**		**SC/HPDC UMSA/HT**	
	Stat.Pres.100MPa	Cyclic Pressure (38-82)MPa/10c			
	ST:480°C/4h AA: 200°C/4h			ST: 506°C/5min+512°C/2min AA: 200°C/10min	
	Subsurf./ Center	**Subsurface**	**Center**	**Subsurface**	**Center**
Al_2Si_2Sr size, nm	P modified	$Al_8Si_{27}Sr$ $Al_{22}Si_{31}Sr$ <100	none	$Al_{55}Si_9Sr_3Cu$ <50	$Al_{22}Si_{23}Sr_6Cu$ $Al_{33}Si_{11}Sr_2Cu$ $Al_7Si_7Sr_2Cu$ $Al_8Si_8Sr_3Cu$ 50-150
β–Al_5FeSi	none				
α-$Al_{15}(Fe,Mn)_3Si_2$ size, nm	$Al_{87}Cu_{30}F_{12}Si$ up to 6000	$Al_{34}Cu_2Fe_2Si$ 200-1000	none	$Al_{11}Cu_3Fe$ 500-1500	$Al_{10}CuFe_2Si_6$ 400-500
π-$Al_8FeMg_3Si_6$ size, nm	none	none	$Al_{12}Mg_6FeCuSi_6$ $Al_{27}Mg_{12}Fe_3CuSi_{13}$ up to 10 000	none	none
Q-$Al_5Cu_2Mg_8Si_6$ size, nm area fraction	$Al_3Cu_2Mg_7Si_5$ $Al_{11}Cu_5MgSi$ up to 2000 considerable amount	$Al_2CuMg_4Si_9$ up to1000 small amount	none	$Al_2CuMg_4Si_3$ $Al_{16}CuMg_4Si_7$ <300 small amount	none
θ-Al_2Cu size, nm area fraction	Al_3Cu Al_4Cu <500 small amount	Al_3Cu_2 Al_9Cu <500 small amount	Al_3Cu_2 up to 3000 N/A	Al_3Cu_2 Al_6Cu <400 small amount	Al_5Cu Al_7Cu $Al_{17}Cu$ <50 small amount
GP zones size, nm	GP zones -AlCu <30	none		GP zones -AlCu <25	GP zones -AlCu <10
θ"-AlCu size, nm	θ"-AlCu 80-120			θ"-AlCu 25-50	θ"-AlCu 15-30

*The amount of phases was estimated on a single STEM/HAADF/EDS micrograph.

Table 31. Comparison of the Chemical Composition (wt.%) of the Main Phases between the Yamaha Engine Block and Sample # 0925b under As-cast and Heat Treated Conditions.

Major Elements Present in the Phase, wt.%	Yamaha	#0925b			
	HPDC/HT	As Cast		SC/HPDC UMSA/HT	
	Stat.Pres.100MPa	Cyclic Pressure (38-82)MPa/10c			
	ST:480°C/4h AA: 200°C/4h			ST: 506°C/5min+512°C/2min AA: 200°C/10min	
	Subsurf./ Center	Subsurface	Center	Subsurface	Center
Si(Al,Cu,Sr)	**92.1**(1.5, 5.8, 0.0)	**96.9**(2.3, 0.8, 0.0)	**95.3**(2.7, 2.0, 0.0)	**96.1**(2.3, 1.6, 0.0)	**95.7**(2.1, 2.0, 0.1) **97.3**(1.0, 1.8, 0.0) **96.9**(1.3, 1.8, 0.0)
α-Al(Si,Cu,Sr)	**94.6**(0.3, 4.2, 0.0)	**98.4**(0.2, 1.3, 0.0)	**95.3**(0.4, 4.3, 0.0)	**93.3**(0.9, 5.8, 0.0) **87.6**(4.7, 3.2, 4.5)	**94.6**(0.3, 5.0, 0.0) **96.7**(0.2, 2.9, 0.0) **92.1**(0.9, 5.9, 0.0)

4.7 Microhardness and Macrohardness for Selected Experimental Samples vs. the Yamaha Engine Block

The first objective of this task was to determine the average microhardness of as-cast, Sr modified and unmodified test samples as well as the heat treated nano structured Al-Si eutectic and conventional Al-Si eutectic present in the Yamaha heat treated engine block. The second objective was to determine the macrohardness HRB (100kg-1/16 ball) for the heat-treated sample #0925b and to compare it with the Yamaha engine block. This information is useful for exploratory research and needs to be expanded to all analyzed phases in future programs.

The eight preliminary comparative μHV100g microhardness measurements were conducted on the experimental samples #0429, #0925b, #0925b-AA1, #0925b-AA2, and on the Yamaha monolithic engine block. The μHV measurements were conducted at the Ford Scientific Research Laboratory in Dearborn, Michigan. A microhardness tester (LECO AMH43 Automatic Hardness Testing System) was used.

The μHV measurements include all randomly located constituents on the straight testing line between the primary Si particles, present in the Yamaha sample, see Figure 166b. Figure 166a presents the indentations into the heat treated Yamaha engine block sample. Figures 166 a and c presents the indentations into as-cast and heat treated SC/HPDC UMSA sample #0925b, respectivelly. This 'rough' data will provide some information about the response of the tested materials to Sr modification and heat treatment. Unmodified primary Si is thermodynamically stable during Solution Treatment during which only "rounding of corners" could be achieved. Please note that the average

μHV value from eight measurements on each sample is indicated as the numerator and the standard deviation is indicated as the denominator.

The as-cast sample #0925b (Category 1.1) having the $\mu HV_{0.1}$ = 119.6/2.1 was subjected to two heat treatment cycles:

AA1: ST @ 506 °C/7 min and AA @ 200 °C/10 min + 110 °C/20 min resulted in μHV = 178.0/6.0.

AA2: ST @ 506 °C/7 min and AA @ 200 °C/10 min resulted in μHV = 172.1/2.6.

The Yamaha HPDC monolithic engine block's 7.0 mm section exhibits $\mu HV_{0.1}$ = 145.5/2.7 after a long heat treatment ST @ 480 °C/240 min and AA @ 200 °C/240 min. The as-cast sample #0429 with the sandwich Al-Si dendrite(s) structure has similar microhardness to the Yamaha heat treated Al-Si eutectic structure, $\mu HV_{0.1}$ = 144.1/4.8.

The average $\mu HV_{0.1}$ and the standard deviations are presented in Figure 167. As can be observed sample #0925b, after AA1 ultra rapid heat treatment has a 22.2 % higher $\mu HV_{0.1}$ in comparison with the Yamaha heat treated engine block. The heat treatment of the #0925b sample improved its nano structured Al-Si eutectic μHV to 48.8 %.

Macro HRB hardness for the #0925b ultra rapid AA1 heat treatment is 86.2, while the Yamaha monolithic block section 7.0 mm has a HRB = 77.8 and a section thickness of 15 mm HRB = 72.0 (see Figure 168). This data indicates that HRB of the nano structured #0925b-AA1 sample is 19.8% higher than the Yamaha 15.0 mm section and 10.8 % higher than the Yamaha 7.0 mm section.

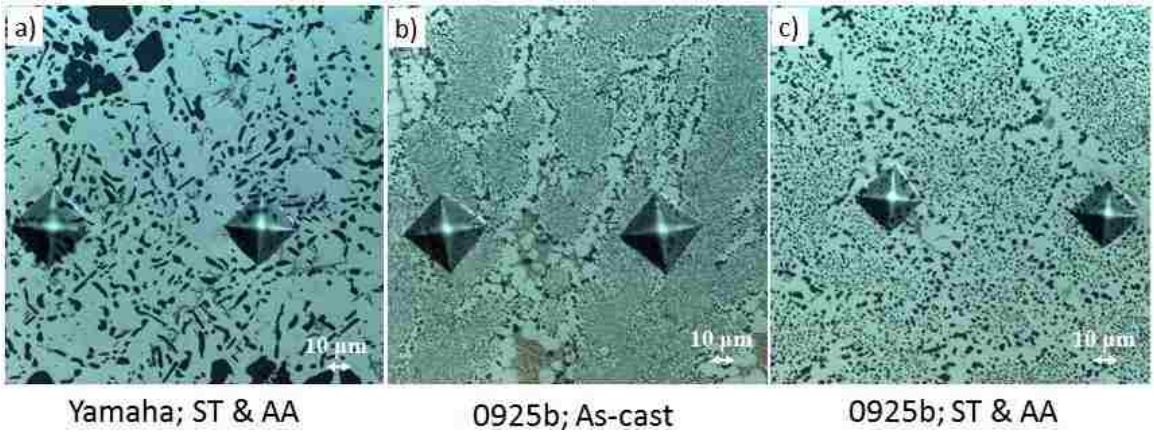

Figure 166. LOM micrographs with microhardness indentations $HV_{0.1}$; a) Heat treated structure of the Yamaha engine block #Y1, b) As-cast structure of the experimental sample #0925b and c) Solutionized and artificially aged sample #0925b-AA2.

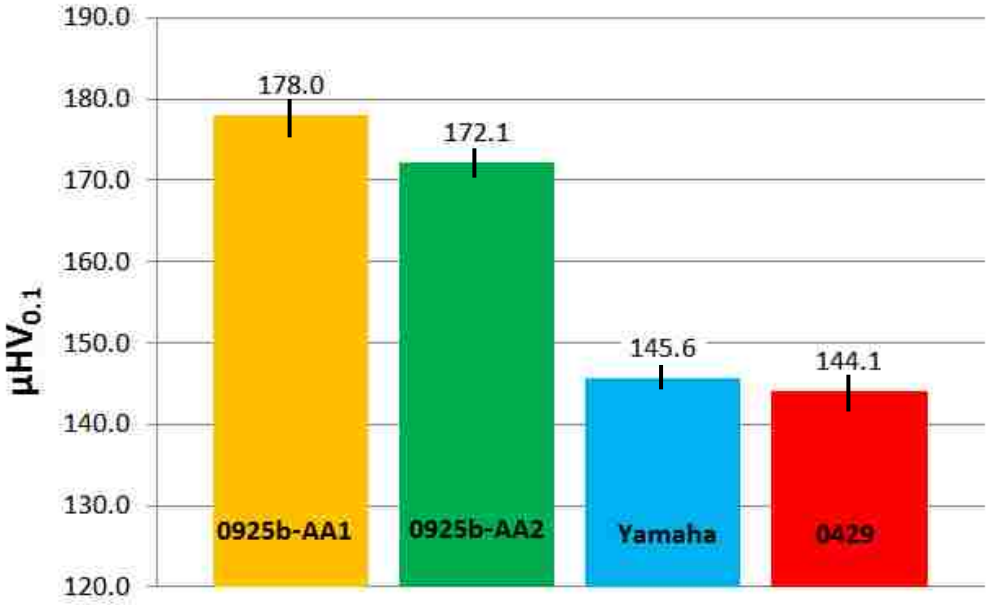

Figure 167. Average Microhardness $HV_{0.1}$ and Standard Deviations for Selected Samples: #0925b-AA1 (ST & AA), #0925b-AA2 (ST & AA), the Yamaha engine block (7 mm, ST & AA), #0429 (As-cast).

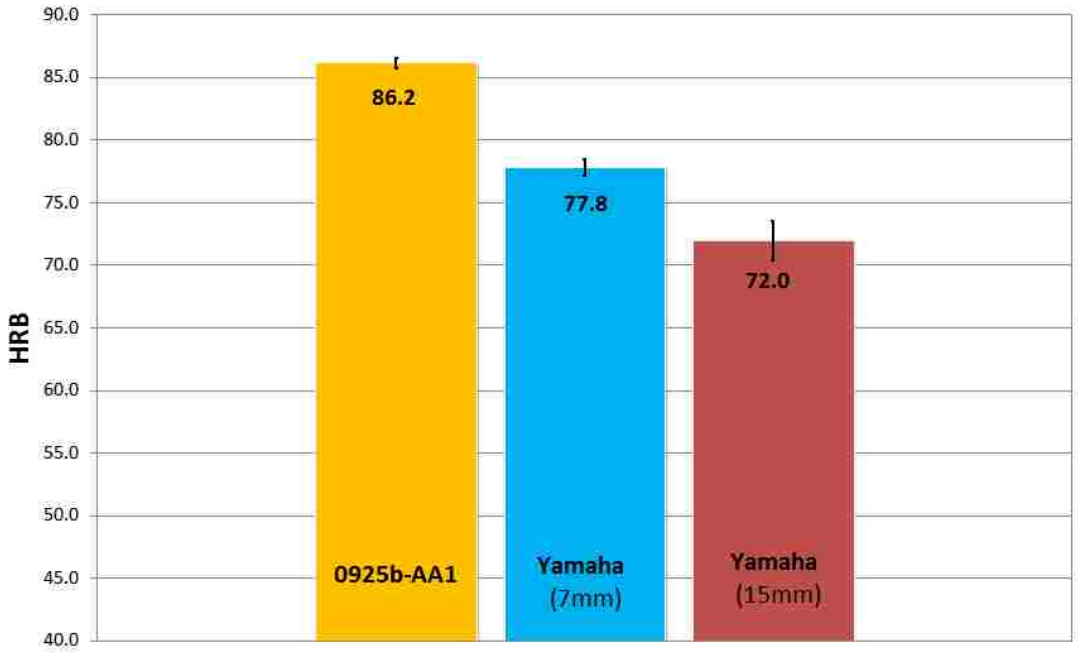

Figure 168. Average HRB Macrohardness and Standard Deviations for Selected Samples: #0925b-AA1 (ST & AA), the Yamaha engine block wall thickness 7 mm and 15 mm (ST & AA).

4.8 Wear Performance of Selected Test Samples

Due to time constraints only three as-cast test samples were tested for determination of the effects of Sr addition and the melt pressure treatment on wear performance. The following test samples were selected: #0517, #0429 and #0508 for wear testing.

Wear was investigated by measurement of the sample wear track profile after applying cyclic force on the surface of the tested samples. Wear Testing conditions: Tribometer Module/Version 4.4M, Acquisition: Linear Mode, Trajectory: Sinus, 1/2 Amplitude: 2.50 mm, Max Lin. Speed: 4.00 cm/s, Frequency: 2.55 Hz, Normal Load: 10.00N, Length: 20.00 m, Acquisition Rate: 20.0 Hz, Ball diameter: 6.00 mm, Temperature 25.0 ^{o}C, Humidity 0.00%.

Figure 169 shows the wear profile for the experimental samples after 2000 cycles of applied load 10 N. Wear performance data are presented in Figure 170. As can be observed the addition of 0.15 wt.%Sr and impact and cycle pressure treated (0-30) MPa/1.5c, $TCE_{liq\text{-}sol}$ = 14.1 J at ASR = 13.9 °C/s sample #0517 shows the lowest wear of 65 μm; followed by sample #0429 which has not been modified with Sr, but was pressure impact and cyclic treated (48-72) MPa/10c, $TCE_{liq\text{-}sol}$ = 14.9 J, ASR = 20.1 °C/s and exhibits 101 μm wear. The worst performance of 132 μm wear is observed in sample #0508 with 0.10 wt.%Sr and solidified under atmospheric pressure and ASR = 15.3°C/s. These tests strongly indicate that the as-cast nano structured alloy has 103.1 % higher wear performance in comparison with the 0.10 wt.% Sr modified, non-pressurized melt.

Both hardness and wear tests provided further confidence that the nano structured pressure treated experimental alloys (with a lower Si level in comparison with the Yamaha alloy) significantly out performs the commercial HPDC engine block having an equivalent wall thickness lower than the experimental alloy sample. In addition, this data proved that the developed novel pressure loading parameters are instrumental for control of the as-cast structures and consequently heat treated engineering material characteristics. Even though the hardness and wear studies were not completed on the entire population of as-cast and heat treated test samples, this limited data gives evidence that further development of the nano structured materials will continue to deliver novel ultra-high performance alloys.

Figure 169. Wear profile for the experimental samples after 2000 cycles of applied load 10 N, ref. #0517.

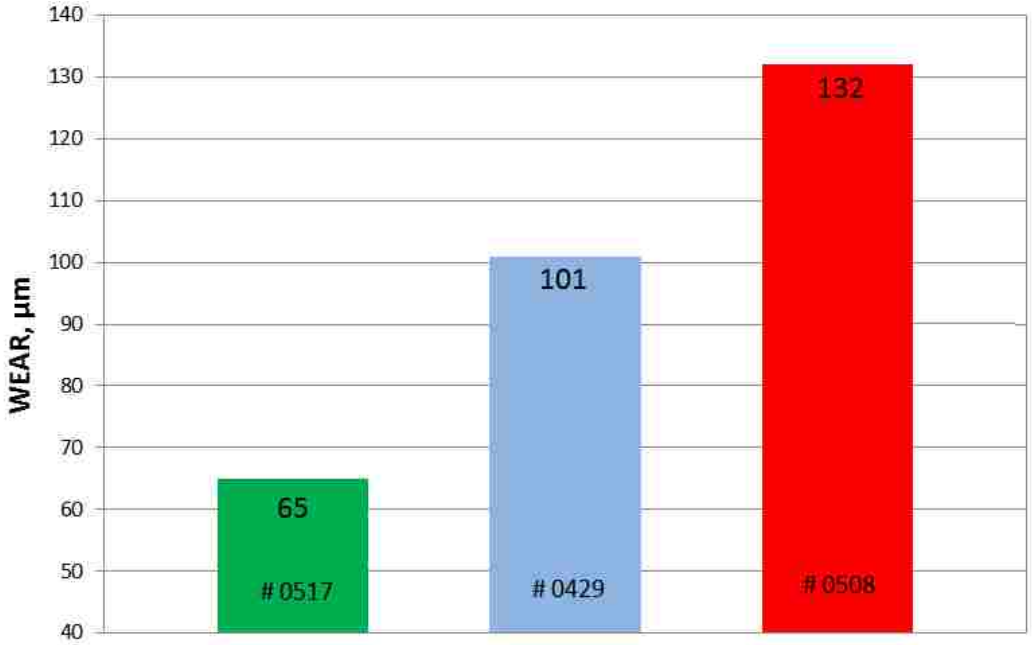

Figure 170. Wear results for selected samples, ref. #0517 (0.15 wt.%Sr modified, impact and cyclic pressure (0-30) MPa/1.5c); #0429 (unmodified, impact and cyclic pressure (48-72) MPa/10c); #0508 (0.10 wt.%Sr modified, solidified at atmospheric pressure).

4.9 Comparison of the Yamaha Engine Block Structure vs. the SC/HPDC UMSA Sample (Category 1.1) (# 0925b-AA2 Heat Treated)

Figure 171 shows deep-etched structures for the heat treated Yamaha Engine block (a – c) and UMSA sample Category 1.1 (# 0925b-AA2) (d – f). In Figure 171 (a, b) undissolved primary Si agglomerates (approx. 80 µm diameter) are present and thermally modified eutectic Si particles (up to 20 µm in length) are visible. In Figure 171 (d – f) the single phase spheroidized Si particles having an average diameter of 590 nm are presented.

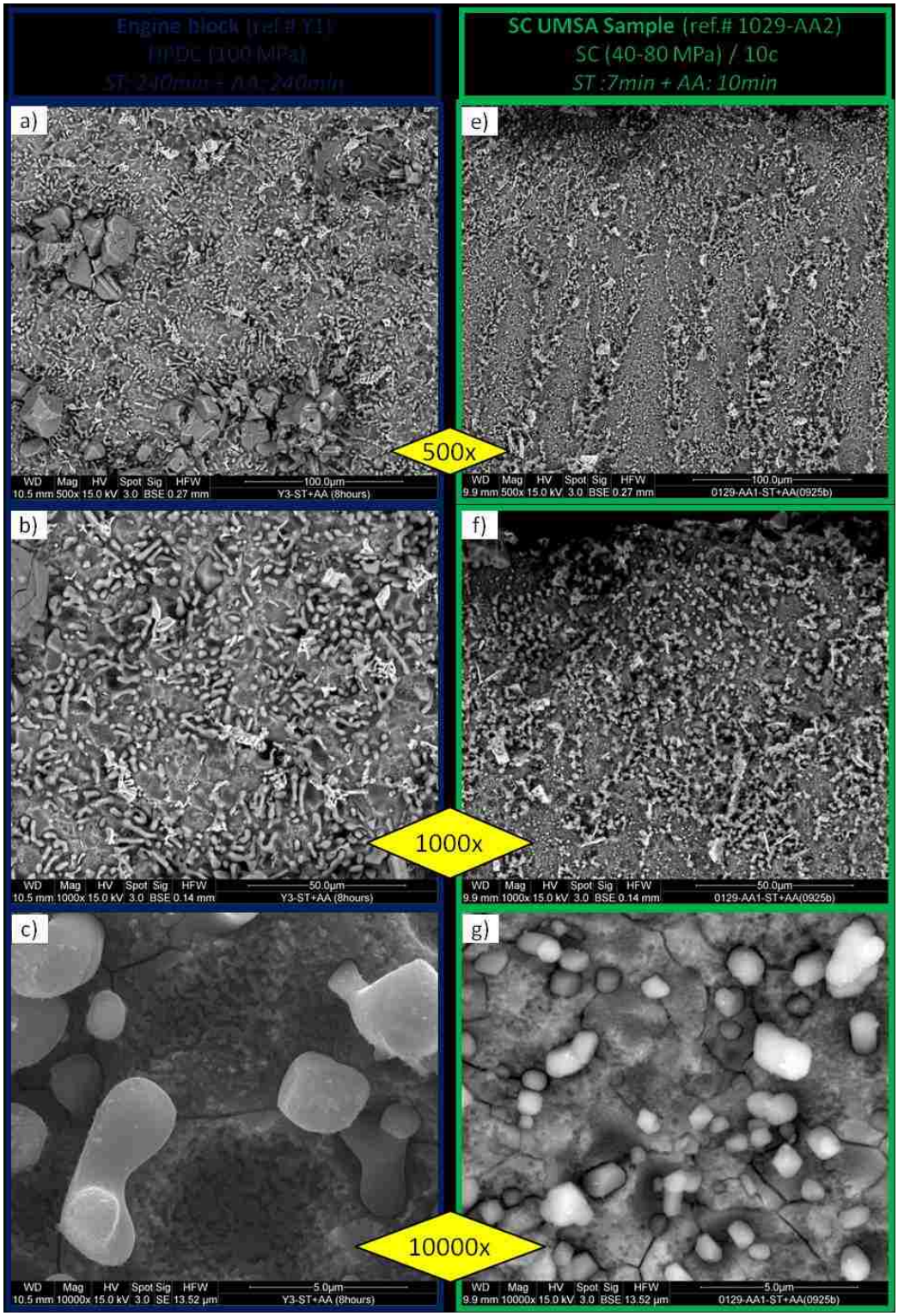

Figure 171. SEM micrographs of precipitated particles after heat treatment of the Al-20Si-3Cu alloy; a - c) Yamaha Engine Block, HPDC(100MPa) + ST: 480 °C/240 min and AA: 200 °C/240 min, d - f) SC/HPDC UMSA sample processed under cyclic pressure (38-81) MPa/10c and ST: 507 °C/7 min and AA 200 °C/10 min.

4.10 Development of Nano and Ultra-Fine Structured Aluminum Alloys and Composites that are not reported in this Dissertation

Limited time and the volume of this dissertation did not allow for the full disclosure of the entire work conducted by the PhD Candidate. Therefore, a concise Summary of the Candidate's additional work is presented below. At the present time a patent related to the development of novel nano materials and technologies together with the preparation of papers for publication are in the process.

In addition to the reported work in this dissertation, the PhD candidate carried out exploratory research aimed at the development of novel bulk nano and ultra-fine structured industrial as-cast Aluminum alloys and composites beyond the Al-Si-Cu ones that have been reported. This work involved collaboration with researchers from the University of British Columbia (UBC) and from the Silesian University of Technology, in Poland. The unreported research scope involved testing of industrial grades of hypereutectic 390 Al-Si-Cu alloys with the addition of nano alumina particles, B206 (Al-Cu) and 7000 series (Al-Zn) alloys. In addition, the possibility of incorporating wettable and non-wettable strengthening particles into the Al alloys and improving the coefficient of friction particles were also tested.

The B206 and 7000 series alloys are not used by the automotive industry due to corrosion and other manufacturing challenges. The motivation for this research stemmed from the partially proven expectations that these materials will significantly improve component properties including: mechanical (i.e. hardness, strength, tensile ductility, fatigue, corrosion, wear and high temperature dimensional stability. These characteristics are critically important for future generations of high performance materials for the

transportation industry and beyond. Presently, bulk materials with these desired properties do not exist. Progress on vehicle component lightening and significant lowering of fuel consumption and gas emissions cannot be realized. Complex SC/HPDC UMSA experiments and characterization of these alloys resulted in the development of as-cast nano structures and significantly improved solid solubility of alloying elements thus allowing for future ultra short heat treatment. Incorporation of non-wettable and wettable nano ceramic strengthening particles used for simultaneous constituent(s) modification and grain refining and the addition of small particles for improvement of the coefficient of friction were extremely successful. The B206 alloy has been used by the aerospace industry thanks to its ultra high mechanical properties however, this alloy exhibits detrimental corrosion performance (even after 30hrs of Solution Treatment), which precludes it from being used by the automotive industry. Research on the B206 commercial alloy cast into a steel mold resulted in significant improvement of corrosion resistance while maintaining ultra high mechanical properties. An ultra-fine grain structure results in homogeneous distribution of precipitates that will eliminate corrosion problems. The SC/HPDC UMSA technology proves the possibility of converting the 7000 series aerospace wrought alloys to cast alloys used for ultra high mechanical property applications.

CHAPTER 5: DISCUSSION REGARDING SELECTED EXPERIMENTAL OUTCOMES AND COMPARISON WITH THE LITERATURE INFORMATION

In most cases the industrial HPDC melt modification of the hypereutectic Al-Si-Cu alloys is limited to detrimental primary Si. Phosphorus is used as a Si modifier. Commercial thermal modification during Solution Treatment is beneficial for eutectic Si morphology however it is not capable of converting the primary Si and eutectic Si phases into nanostructured Si whiskers and dendrites. In addition, conventional technologies are not capable of fully controlling the Al-Si eutectic colonies (grains) morphology (size and distribution) and the boundary size of the inter colonies and the morphology of various phases located inside these boundaries. In general, commercial Si modification and grain refinement technologies (if used) are costly, melt treatment effects fade during melt holding and melt quality control is not adequate for on-line operations.

To date, limited worldwide laboratory research addressing the development of nano Si whiskers and/or microscopic Si dendrite arms in hypereutectic alloys are limited to pure Al-Si binary alloys [49, 129, 135]. The directional solidification techniques predominately used cannot be easily applied in an industrial environment.

Comprehensive work by Dr. K. Müller on the improved hypereutectic super pure Al 14 wt.%Si and 18wt.%Si alloys modified with an addition of up to 2200 ppm (0.22 wt.%) Sr cast 30 mm diameter test samples at room temperature for the steel die revealed that there are significant differences in the as-cast structures and properties. These differences depend on the Si level and on the Sr additions as well as other

processing parameters. The volume fraction of primary silicon particles is 6 % to 0.3% and 9.5 % to 5.3 % for 14 wt.%Si and 18 wt.%Si, respectively. The primary Si particles size is in the range (80 to 165) µm. The degree of eutectic Si modification is up to 5.8 levels for both alloys. The size of the eutectic cells of the Al-14Si alloy is (1.1 to 2.6) mm. The Si dendritic arms diameter is ≈ 1 µm and significant coarsening is visible at the eutectic cell boundaries. The Al-14Si alloy's Ultimate Tensile Strength in the untreated state is ≈ 132 MPa while for the 150 ppm Sr addition it is 152 MPa. The wear coefficient for the Sr modified alloy is considerably lower in comparison with the unmodified alloy [129]. Thermal Analysis was not used for in-depth quantification of the solidification processes and correlation with structural characteristics. In addition, Thermal Treatment was not used in this research.

In this research the best sample (#0925b) in Structure Category #1 does not contain any Primary Si particles at the subsurface and in the center of the sample there are a few Si particles that have a size of approx. 25 µm x 25 µm. The Al-Si eutectic colonies have an Average Size of approx. 35 µm x 98 µm. Average Si whiskers and dendrite arms D_{avg}Si-WA = 220 nm, D_{minF}AlSi-Co = 34.3 µm, D_{maxF}AlSi-Co = 97.6 µm.

The inability to industrially manufacture and/or convert the existing cast alloys into bulk hypereutectic nanostructured alloys has a severely negative impact on heat treatment outcomes such as maximization of the engineering characteristics that would otherwise benefit from ultra rapid ST operations. Therefore, taking into consideration the above limitations of the commercial processing technologies it is of paramount importance to develop SC/HPDC UMSA hypereutectic Al-Si-Cu alloy(s) with nano Si whiskers and/or silicon dendrites with nanostructured arms and trunks as well as ultra-refined Al-Si

eutectic colonies. This Chapter presents in-situ and "simultaneous" melt modification and refinement treatment technologies together with the associated scientific analysis of the critical relationships between process parameters and the HT UMSA thermal data for the solidification process and consequently for the as-cast structure as well as the Solution Treatment operation. Ultra rapid heat treatment is addressed in Section 4.6

The worldwide literature lacks information about technologies that are capable of manufacturing in-situ nano and ultra-fine as-cast structures and Thermal Analysis methodologies for online control of melt processing in the liquid and semi-solid states. Therefore, this research is based on a series of carefully designed exploratory experiments with a very wide range of processing parameters and combinations of processing parameters. This monumental and complex task requires very significant technical and analytical resources as well as a long-term scientific program. A single PhD project cannot address an unexplored scientific field. Therefore, the development of these novel technologies and materials needs to be continued by many future generations of researchers.

Traditional statistically designed experiments are not beneficial for development of new knowledge therefore were not utilized in this research. In addition, experience to date revealed that future generations of the SC/HPDC UMSA Platforms need to be further instrumented to include additional thermocouple(s) for TA data collection from the edge of the sample.

The addition of 0.15 wt.%Sr to the slowly solidifying experimental alloy (ref. #0925) with an ASR = 9.4 ^{o}C/s, results in a small amount of the primary Si phase nucleating almost simultaneously together with the α-Al phase in the form of dendrites.

The Al-Si eutectic colonies that form, from the common origin, are separated by aluminum inter-colony boundaries. In addition, a higher Sr level (in comparison with 0.1 wt.%Sr, #0508) together with higher SR results in the presence of eutectic Si dendrites with ultra-fine arms and trunks, see Figure 117 (e, f). These key factors are necessary for future structural modifications and refinement using the SC/HPDC UMSA's new processing parameters including various pressure profiles (i.e. impact pressure, cyclic pressure loading combined with monotonic pressure).

A residual percentage of primary Si particles could be present in the high SR processed melt in the UMSA die since cyclic pressure loading, in most cases, has been applied after impact pressure (i.e. by pressurized air) that interrupts natural nucleation of the solidification process (after the natural T_{liq} has been passed). In some experiments, two FD "negative peaks" are present after natural nucleation occurred. (The time difference between the Natural Liquidus Temperature - T_{liq} reached and the Apparent Liquidus Temperature - aT_{liq} = 0.6 s). However, due to the small amount of the phase a separate primary Si peak is not present in the rapidly solidified SC/HPDC UMSA test samples.

In addition, a very high SR resulted in a rapid slope change of the FD liquid "arm" that formed the negative peak, see Figures 127a. In comparison with slow solidification, in Figure 115 (#0925) accurate establishment of the T_{liq} of alloys that solidify rapidly requires deconvolution of the FD curve, see Figures 130 - 133. This "new" T_{liq} is slightly shifted to the lower temperature. PhD project time limitations did not allow for completion of this time consuming task.

Figures 130 - 133 show examples of TA data resulting from deconvolution of the FD. A residual amount of primary Si particles formed between the natural and forced T_{liq} is going to grow very slightly due to a very short time lapse. Potential primary Si growth is also controlled by the solidification sequence and by the amount of Al phase that controls primary Si morphology and volume fraction.

Please note that the nuclei of the primary Si are thermodynamically active and do not behave like oxides in the liquid melt.

The above described methodology is justified after the aT_{liq} CC and FD curves exhibited continuous solidification processes during which various melt pressure loading profiles were utilized. However, future research should address the new scientific challenges mentioned above.

CHAPTER 6: MAIN FINDINGS and CONCLUSIONS

1. All three scientific research hypotheses were fully proven through developed novel experimental strategies, thermal analysis, metallurgical structure characterization and statistical analysis. In addition, novel structures and precipitates were developed and characterized for the unmodified alloy having the potential for applications like high temperature and compressive loading and wear.

2. A comprehensive worldwide review of books, journals and conference papers as well as patents revealed that there is not a single piece of information about the industrial grade Al-Si-X hypereutectic alloys' technology capable of manufacturing in-situ nano and ultra-fine as-cast structures having a single silicon phase in various forms of whiskers and dendritic arms.

2.1 There is no information about effective control of the Al-Si eutectic colonies and detrimental iron rich phase characteristics.

2.2 There is no information about ultra rapid Solution Treatment capable of simultaneously fragmenting and spheroidizing Si whiskers and dendritic arms rendering nano and ultra-fine single phase silicon particles.

2.3 There is no information about technologies capable of converting aerospace ultra high strength materials like the 7000 series, and the B206 alloy into engineering materials applicable to as-cast automotive components that must be corrosion resistant among other requirements.

2.4 There is no information about as-cast nano and ultra-fine structured alloys and their technology optimization.

2.5 There is no information about the instrumented equipment for melt processing technology utilizing various forms of impact, cyclic pressure like loading during liquid and semi-solid states in a confined or semi-confined environment.

2.6 There is no information about utilization of the high resolution and low detection limit Thermal Analysis (TA) systems for metallurgical quantification of the bulk test samples' solidification process using dynamic melt loading treatment and rapid Solution Treatment. TA data is critical for a statistically valid relationship between processes and as-cast and heat-treated structures and material/component engineering characteristics.

The above findings indicate that the PhD project objectives addressed unexplored scientific and technical fields.

3. The SC/HPDC UMSA Platform's novel technological and Thermal Analysis capabilities will be further developed and will include synergetic melt chemical treatment(s) and dynamic liquid and semi-solid melt loading which renders as-cast nano and ultra-fine structures for the industrial grade hypereutectic Al-Si-Cu and other tested but unpublished aluminum alloys.

3.1. The relationship developed between the SC/HPDC UMSA process parameters and the Thermal Analysis and metallographic characteristics concluded that the most influential factors for the 0.15 wt% Sr modified experimental as-cast Al-Si-Cu test samples with nano (subsurface up to 4 mm) and ultra-fine

(center) Si whiskers and dendritic arms required for the given Structure Category #1 to #3 are as follows:

- General Requirement for **all Structural Categories #1 to #3:**

$$\mathbf{T^{P}_{ST} > aT_{liq}}$$

- Requirement for **Structure Category #1**:

$$\mathbf{T^{P}_{END} \geq T^{AlSi}_{E,MIN}}$$

- Requirement for **Structure Category #2**:

$$\mathbf{T^{IP} = T^{P}_{END} < T^{AlSi}_{E,MIN}}$$

- Requirement for **Structure Category #3**:

$$\mathbf{T^{P}_{END} < T^{AlSi}_{E,\ MIN}}$$

3.2. Versatility of the Advanced Capabilities for the SC/HPDC/HT UMSA Platform and Dynamic Melt Treatment Technology.

Novel nano and ultra-fine structured Al-Si alloys and their processing technologies were developed and yielded a variety of novel structures and exceptional engineering materials characteristics including hardness, micro-hardness and wear performance and ultra rapid Solution and Artificial Aging Treatments.

Unpublished SC/HPDC UMSA data from the processed nano and ultra-fine structured alloys and composites using various dynamic melt treatment methods creates the opportunity for engineering of the existing and novel materials with ultra high properties designed for specific functional applications.

SC/HPDC/HT UMSA processing and thermal data together with the supporting analytical evidence allows for an understanding and for quantification of the statistical relationship between the process parameters, melt solidification and heat treatment metallurgical reactions and nano/ultra-fine structured materials characteristics. This new knowledge will permit future development of on-line advisory software.

4. The novel phases' stoichiometry and morphology, as developed, resulted from various SC/HPDC UMSA' applied loading modes to the unmodified and Sr modified liquid and semi-solid melts and indicates that nucleation and growth of these phases during solidification is a dynamic process. Future comprehensive work needs to address the establishment of a relationship between the utilized exploratory experimental parameters and nucleation and growth dynamics. These key dynamic control factors relate to both solidification reactions (and consequently as-cast structures) and reactions pertaining to phase formation during Solution Treatment and Artificial Aging. These control factors allow for unprecedented primary and eutectic Si modification (and Fe and Cu rich phases) together with the refinement of the Al-Si eutectics on the nano and macro levels without using refining particles like TiB_2. Cu rich and other precipitate(s) characteristics were also altered.

CHAPTER 7: RECOMMENDATIONS FOR FUTURE RESEARCH

During the SC/HPDC UMSA process the melt is delivered into the die cavity using gravity pouring from the melting furnace. Automation of the furnace bottom gate will accelerate this operation and allow for the high temperature melt to be delivered to the die cavity. Computer aided tools like MAGMAsoft should be further utilized for optimization of the design of the new die cast test sample geometry, (i.e. allowing for structure and mechanical characterization), the solidification process and the SC/HPDC UMSA operating parameters. Experimental verification of simulation results (i.e. using DOE techniques) together with metallurgical analysis of trial test samples needs to be carried out in order for the developed technology to fulfill engineering requirements. Application of low and especially high vacuum levels during HPDC of aluminum alloys capable of rapidly evacuating the die cavity during filling could be considered. An applied vacuum level must be optimized and monitored together with the melt cleanliness through the entire melt processing and delivery to the die cavity. Improvements to the SC/HPDC UMSA Platform and its processing parameters can be realized by utilization of various techniques and sensors capable of quantifying some parameters related to cast component metallurgical characteristics including various nano and ultra-fine structural features, mechanical properties, etc. Utilization of more temperature sensors will assure higher quality of the test sample by development of a statistically valid functional relationship between the as-cast structure, solidification thermal data and process variables.

The established relationship between the in-cavity pressure loading profile, Solidification Rates and the heat transfer efficiency revealed that the improved efficiency of the heat transfer due to controlled pressure impact is of paramount importance. Therefore, a higher melt temperature and application of given pressure loading control after the cavity filling process is complete will result in an increase in peak values and further solidification heat flux values during the process. Increased spatial resolution of the Cumulative Energy delivered to the melt will help with the generation of new knowledge and both metallurgical analysis of the relationship between process parameters, thermal characteristics and as-cast structure characteristics. Utilization of thermal imaging for evaluation of the effect of the die's thermal process variables can be a useful tool for process and test sample quality control improvements. Thermography technology could be utilized for monitoring of the die's thermal balance during multiple die filling cycles, the design of a more efficient die cooling system and spraying operations leading to property improvements in the sample.

Various SC/HPDC UMSA operations (i.e. melt, die and cooling channels temperature, solidification characteristics) are monitored and controlled using thermocouples. More stringent requirements for these sensors like microsecond response time, linearity, minimal error, and easy and stable calibration need to be developed. Utilization of a heat transfer coefficient gauge will allow for demonstration of the influences of range parameters on peak heat transfer rates. A fast surface heat flux sensor can be used for monitoring of the rapid solidification process and future correlation with the UMSA ultra-fine thermal sensor data.

Selection of high performance tool steel for the SC/HPDC UMSA die and its components includes: a high level of resistance to thermal shock and fatigue, good high temperature toughness, good machinability and good dimensional stability. There are several types of highly alloyed steels suitable for die applications including Orvar Superior, etc. In order to prevent premature wear, the die surface needs to be nitrocarburized. Improved tolerances would be beneficial and this can be achieved by purchasing the die components from a professional tool making shop.

The new SC/HPDC UMSA Platform allows for determination of over 50 high resolution thermal and metallurgical characteristics during melt heating and sample solidification cycles including comprehensive characteristics of individual reactions, fraction solid evolution, and solidification rates, etc. It is necessary to utilize key thermal characteristics as the process control variables.

Design a new SC/HPDC UMSA test sample for assessment of the as-cast, heat treated structure and many engineering characteristics should allow for simultaneous quantification of thermal characteristics for the sample's variable wall thickness from 0.5 mm to 10.0 mm. This sample should also allow for the performance of liquid and semi-solid squeeze casting operations using the innovative pressure loading parameters.

Proposed improvements can effectively address the quantitative assessment of the cumulative and individual effects of the processing parameters on the as-cast and heat treated sample structures and consequently development of the technology and material(s) with disruptive characteristics required by the transportation industries and beyond.

REFERENCES/BIBLIOGRAPHY

[1] "NADCA, North American Die Casting Association." [Online]. Available: http://www.diecasting.org/. [Accessed: 20-Jan-2014].

[2] M. Warmuzek, "Aluminum-Silicon Casting Alloys, Atlas of Microfractographs." ASM International, 2004.

[3] J. L. Murray and A. J. McAlister, "The AI-Si (Aluminum-Silicon) System," *Bull. Alloy Phase Diagrams*, vol. 5, no. 1, pp. 74–84, 1984.

[4] D. S. Mackenzie and E. G. Totten, *Handbook of Aluminum, vol. 1, Physical Metallurgy and Processes*. CRC Press, 2003.

[5] *ASM Handbook, vol. 2, Properties and Selection: Nonferrous Alloys and Special-Purpose Materials*. ASM International, 1992.

[6] W. Kasprzak, J. H. Sokolowski, H. Yamagata, and H. Kurita, "Development of Energy Efficient Heat Treatment Processes for Light Weight Automotive Castings," in *Heat Treating: Proceedings of the 25th ASM*, 2009.

[7] W. Kasprzak, J. H. Sokolowski, H. Yamagata, M. Aniolek, and H. Kurita, "Energy Efficient Heat Treatment for Linerless Hypereutectic Al-Si Engine Blocks Made Using Vacuum HPDC Process," *J. Mater. Eng. Perform.*, vol. 20, no. 1, pp. 120–132, Apr. 2010.

[8] "Periodic Table of the Elements," 2014. [Online]. Available: http://kinetics.nist.gov/janaf/periodic_table.html. [Accessed: 10-Jan-2014].

[9] J. W. Lee and J. R. Morris, "Effects of twin boundaries on crystal growth," in *NIST Workshop on Wires, Whiskers and Walls: Energy Applications at the Nanoscale*, 2010.

[10] L. A. Willey, "The Al-Cu (Aluminum-Copper) System," *Bull. Alloy Phase Diagrams*, vol. 1, no. 1, pp. 27–33.

[11] R. S. Rana, R. Purohit, and S. Das, "Reviews on the Influences of Alloying Elements on the Microstructure and Mechanical Properties of Aluminum Alloys and Aluminum Alloy Composites.," *Int. J. Sci. Res. Publ.*, vol. 2, no. 6, pp. 1–7, 2012.

[12] Madhavan Manivannan, “Improving the Corrosion Resistance of a High-Strength Aluminum-Copper Casting Alloy,” MASc thesis, University of Windsor, Canada, 2009.

[13] A. M. Samuel and F. H. Samuel, “A Metallographic Study of Porosity and Fracture Behavior in Relation to the Tensile Properties in 319.2 End Chill Castings,” *Metall. Mater. Trans. A*, vol. 26, pp. 2359–2372, Sep. 1995.

[14] *ASM Handbook, vol. 15, Casting*. ASM International, 1988.

[15] H. Okamoto, “AI-Mg (Aluminum-Magnesium),” *J. Phase Equilibria*, vol. 19, no. 6, p. 598, 1998.

[16] S. Seifeddine, “The Influence of Iron on the Micro-structure and Mechanical Properties of Cast Al-Si Alloys,” Jonkoping University The School of Engineering Component Technology, Sweden, 2007.

[17] X. J. Liu, I. Ohnuma, R. Kainuma, and K. Ishida, “Thermodynamic assessment of the Aluminum-Manganese (Al-Mn) binary phase diagram,” *J. Phase Equilibria*, vol. 20, no. 1, pp. 45–56, Jan. 1999.

[18] S. Seifeddine and I. L. Svensson, “The influence of Fe and Mn content and cooling rate on the microstructure and mechanical properties of A380-die casting alloys,” *Metall. Sci. Technol.*, vol. 27, no. 1, pp. 11–20, 2009.

[19] G. D. Scott, B. S. Shabel, and A. Morales, “Aluminum Alloy Suitable for Piston,” U.S. Patent 5,162,065, Nov. 10,1992.

[20] A. M. A. Mohamed, F. H. Samuel, A. M. Samuel, H. W. Doty, and S. Valtierra, “Influence of Tin Addition on the Microstructure and Mechanical Properties of Al-Si-Cu-Mg and Al-Si-Mg Casting Alloys,” *Metall. Mater. Trans. A*, vol. 39, no. 3, pp. 490–501, Jan. 2008.

[21] “How and why alloying elements are added to aluminum.” [Online]. Available: http://www.alcotec.com/us/en/education/knowledge/qa/How-and-why-alloying-elements-are-added-to-aluminum.cfm. [Accessed: 10-Jun-2014].

[22] R. I. Mackay, “Development of a New Durable Al-Si Alloy for the Next Generation of Engine Block Casting,” 2003.

[23] “KBM AFFILIPS Master Alloys,” 2012. [Online]. Available: http://www.kbmaffilips.com/. [Accessed: 10-Apr-2014].

[24] E. Diagram, B. C. B. Alcock, V. P. P. Itkin, and C. B. Alcock, “The Al-Sr (Aluminum-Strontium) System,” *Bull. Alloy Phase Diagrams*, vol. 10, no. 6, pp. 624–630, 1989.

[25] D. Emadi, J. E. Gruzleski, and J. M. Togurt, “The Effect of Na and Sr Modification on Surface Tension and Volumetric Shrinkage of A356 Alloy and their Influence on Porosity Formation,” *Metall. Trans. B*, vol. 24, no. 12, pp. 1055–1063, 1993.

[26] Ö. Savaş and R. Kayikci, “Application of Taguchi’s methods to investigate some factors affecting microporosity formation in A360 aluminium alloy casting,” *Mater. Des.*, vol. 28, no. 7, pp. 2224–2228, Jan. 2007.

[27] S. G. Shabestari, S. M. Miresmaeili, and S. M. A. Boutorabi, “Effects of Sr-modification and melt cleanliness on melt hydrogen absorption of 319 aluminium alloy,” *J. Mater. Sci.*, vol. 38, pp. 1901–1907, 2003.

[28] J. R. Denton and J. A. Spittle, “Solidification and susceptibility to hydrogen absorption of AI-Si alloys containing strontium,” *Mater. Sci. Technol.*, vol. 1, no. 4, pp. 305–311, 1985.

[29] G. E. Byczynski and D. A. Cusinato, “The effects of strontium and grain refiner additions on the fatigue and tensile properties of industrial Al-Si-Cu-Mg alloy castings produced using the Ford Motor Company - Cosworth precision sand process,” *Int. J. Cast Met. Res.*, vol. 14, pp. 315–324, 2002.

[30] J. Jorstad and D. Apelian, “Hypereutectic Al-Si Alloys: Practical Casting Considerations,” *Int. J. Met.*, vol. 3, no. 3, pp. 13–33, 2009.

[31] Y. H. Cho, H. C. Lee, K. H. Oh, and A. K. Dahle, “Effect of Strontium and Phosphorus on Eutectic Al-Si Nucleation and Formation of β-Al5FeSi in Hypoeutectic Al-Si Foundry Alloys,” *Metall. Mater. Trans. A*, vol. 39, no. 10, pp. 2435–2448, Jul. 2008.

[32] K. Nogita and A. K. Dahle, “Eutectic Growth Mode in Strontium, Antimony and Phosphorus Modified Hypoeutectic Al-Si Foundry Alloys,” *Mater. Trans.*, vol. 42, no. 3, pp. 393–396, 2001.

[33] M. Faraji, I. Todd, and H. Jones, “Effect of Phosphorus and Strontium Additions on Formation Temperature and Nucleation Density of Primary Silicon in Al-

19Wt%Si Alloy and their Effect on Eutectic Temperature," *Metall. Mater. Trans. A*, vol. 40, no. 7, pp. 1710–1715, Jul. 2009.

[34] M. Abdulwahab, I. A. Madugu, S. A. Yaro, and A. P. I. Popoola, "Degradation Behavior of High Chromium Sodium-Modified A356.0-Type Al-Si-Mg Alloy in Simulated Seawater Environment," *J. Miner. Mater. Charact. Eng.*, vol. 10, no. 6, pp. 535–551, 2011.

[35] J. Campbell, *Castings*. 2003.

[36] "Modification of Foundry Al-Si Alloys, Comalco Aluminium Limited," Brisbane Queensland, Australia, 1997.

[37] A. K. M. B. Rashid, "The Treatment of Liquid Aluminium-Silicon Alloys, Lecture 16." Dhaka, pp. 1–22, 2010.

[38] W. Youdelis, "Alloy Structure Refinement by Microalloying," Windsor, ON.

[39] W. Reif, "Melt Treatment Practice of Aluminum and Al-Alloys," in *Advanced Light Alloys and Composites*, R. Ciach, Ed. Cracow, Poland: Kluwer Academic Publisher, 1998, p. 191.

[40] H. Liao, Y. U. Sun, and G. Sun, "Effect of Al-5Ti-1B on the microstructure of near-eutectic Al-13.0% Si alloys modified with Sr," *J. Mater. Sci.*, vol. 37, pp. 3489–3495, 2002.

[41] H. C. Liao, M. Zhang, J. J. Bi, K. Ding, X. Xi, and S. Q. Wu, "Eutectic Solidification in Near-Eutectic Al-Si Casting Alloys," *J. Mater. Sci. Technol.*, vol. 26, no. 12, pp. 1089–1097, Dec. 2010.

[42] D. G. Mallapur, "Influence of grain refiner and modifier on the microstructure and mechanical properties of A356 alloy," *Int. J. Eng. Sci. Technol.*, vol. 2, no. 9, pp. 4487–4493, 2010.

[43] S. Haro-Rodríguez, R. E. Goytia-Reyes, D. K. Dwivedi, H. Flores-Zúñiga, and M. J. Perez-Lopez, "On influence of Ti and Sr on microstructure, mechanical properties and quality index of cast eutectic Al-Si-Mg alloy," *Mater. Des.*, vol. 32, pp. 1865–1871, 2011.

[44] N. Saheb, T. Laoui, A. R. Daud, M. Harun, S. . Radiman, and R. Yahaya, "Influence of Ti addition on wear properties of Al–Si eutectic alloys," *Wear*, vol. 249, no. 8, pp. 656–662, Aug. 2001.

[45] G. Zhong, S. Wu, J. Huawen, and A. Ping, “Effect of ultrasonic vibration on the iron-containing intermetallic compounds of high Si Al alloy with 2%Fe,” *J. Alloys Compd.*, vol. 492, pp. 482–487, 2010.

[46] H. Xu, Q. Han, and T. T. Meek, “Effects of ultrasonic vibration on degassing of aluminum alloys,” *Mater. Sci. Eng. A*, vol. 473, no. 1–2, pp. 96–104, Jan. 2008.

[47] J. H. Jeffrey and P. Saidi, “Molecular Dynamics Study of Solidification in the Aluminum-Silicon System.” 2013.

[48] T. Hosch, L. G. England, and R. E. Napolitano, “Analysis of the high growth-rate transition in Al–Si eutectic solidification,” *J. Mater. Sci.*, vol. 44, no. 18, pp. 4892–4899, Jul. 2009.

[49] T. Hosch and R. E. Napolitano, “The effect of the flake to fiber transition in silicon morphology on the tensile properties of Al–Si eutectic alloys,” *Mater. Sci. Eng. A*, vol. 528, no. 1, pp. 226–232, Nov. 2010.

[50] X. Bian and W. Wang, “Thermal-rate treatment and structure transformation of Al–13 wt.% Si alloy melt,” *Mater. Lett.*, vol. 44, no. 1, pp. 54–58, May 2000.

[51] D. R. Hamilton and R. G. Seidensticker, “Propagation Mechanism of Germanium Dendrites,” *J. Appl. Phys.*, vol. 31, no. 7, p. 1165, 1960.

[52] V. V. K. Narayan Prabhu, “Review of Microstructure Evolution in Hypereutectic Al–Si Alloys and its Effect on Wear Properties,” *Trans. Indian Inst. Met.*, vol. 67, no. 1, pp. 1–18, Aug. 2013.

[53] V. H. Guthy, “Evolution of the Eutectic Microstructure in Chemically Modified and Unmodified Aluminum Silicon Alloys,” 2002.

[54] Y. T. Pei and J. T. M. De Hosson, “Five-fold branched Si particles in laser clad AlSi functionally graded materials,” *Acta Mater.*, vol. 49, no. 4, pp. 561–571, Feb. 2001.

[55] Y. T. Pei and J. T. M. De Hosson, “Functionally graded materials produced by laser cladding,” *Acta Mater.*, vol. 48, no. 10, pp. 2617–2624, Jun. 2000.

[56] F. C. Robles Hernández and J. H. Sokolowski, “Thermal analysis and microscopical characterization of Al–Si hypereutectic alloys,” *J. Alloys Compd.*, vol. 419, no. 1–2, pp. 180–190, Aug. 2006.

[57] R. E. Napolitano, H. Meco, C. Jung, and M. J. Kramer, “Mechanistic Selection in Faceted Crystal Growth.” pp. 2–3.

[58] R. E. Napolitano, H. Meco, and C. Jung, “Faceted Solidification Morphologies in Low-Growth-Rate Al-Si Eutectics,” *JOM*, Apr. 2004.

[59] S. P. Nikanorov, M. P. Volkov, and V. N. Gurin, “Structural and mechanical properties of Al–Si alloys obtained by fast cooling of a levitated melt,” *Mater. Sci. Eng. A*, vol. 390, pp. 63–69, 2005.

[60] H. S. Kang, W. Y. Yoon, K. H. Kim, M. H. Kim, and Y. P. Yoon, “Microstructure selections in the undercooled hypereutectic Al–Si alloys,” *Mater. Sci. Eng. A*, vol. 404, no. 1–2, pp. 117–123, Sep. 2005.

[61] F. C. Robles Hernández and J. H. Sokolowski, “Comparison among chemical and electromagnetic stirring and vibration melt treatments for Al–Si hypereutectic alloys,” *J. Alloys Compd.*, vol. 426, no. 1–2, pp. 205–212, Oct. 2006.

[62] R. P. Liu, D. M. Herlach, M. Vandyoussefi, and A. L. Greer, “Morphologies of Silicon Crystals Solidified on a Chill Plate,” *Metall. Mater. Trans. A*, vol. 35, pp. 1067–1073, Mar. 2004.

[63] H. Yi and D. Zhang, “Morphologies of Si phase and La-rich phase in as-cast hypereutectic Al–Si–xLa alloys,” *Mater. Lett.*, vol. 57, no. 16–17, pp. 2523–2529, May 2003.

[64] B. Korojy and H. Fredriksson, “On solidification of hypereutectic Al-Si alloys,” *Trans. Indian Inst. Met.*, vol. 62, pp. 361–365, Oct. 2009.

[65] O. A. Atasoy, F. Yilmaz, and R. Elliott, “Growth structures in aluminium-silicon alloys I. The coupled zone,” *J. Cryst. Growth*, vol. 66, no. 1, pp. 137–146, Jan. 1984.

[66] C. L. Xu, H. Y. Wang, C. Liu, and Q. C. Jiang, “Growth of octahedral primary silicon in cast hypereutectic Al–Si alloys,” *J. Cryst. Growth*, vol. 291, no. 2, pp. 540–547, Jun. 2006.

[67] C. L. Xu and Q. C. Jiang, “Morphologies of primary silicon in hypereutectic Al–Si alloys with melt overheating temperature and cooling rate,” *Mater. Sci. Eng. A*, vol. 437, no. 2, pp. 451–455, Nov. 2006.

[68] R. Wang, W. Lu, and L. M. Hogan, “Faceted growth of silicon crystals in Al-Si alloys,” *Metall. Mater. Trans. A*, vol. 28, no. 5, pp. 1233–1243, May 1997.

[69] R. P. Liu, D. M. Herlach, M. Vandyoussefi, and A. L. Greer, “Undercooling and Solidification of Al-50At.%Si Alloy by Electromagnetic Levitation,” *Metall. Mater. Trans. A*, vol. 35, no. 2, pp. 607–612, Feb. 2004.

[70] F. Yilmaz, O. A. Atasoy, and R. Elliott, “Growth structures in aluminium-silicon alloys II. The influence of strontium,” *J. Cryst. Growth*, vol. 118, no. 3–4, Apr. 1992.

[71] F. Yilmaz and R. Elliott, “The microstructure and mechanical properties of unidirectionally solidified Al-Si alloys,” *J. Mater. Sci.*, vol. 24, pp. 2065–2070, 1989.

[72] K. Kobayashi, P. H. Shingu, and R. Ozaki, “Crystal growth of the primary silicon in an A1-16.wt % Si alloy,” *J. Mater. Sci.*, no. 10, pp. 290–299, 1975.

[73] L. L. Ge, R. P. Liu, G. Li, M. Z. Ma, and W. K. Wang, “Solidification of Al–50 at.% Si alloy in a drop tube,” *Mater. Sci. Eng. A*, vol. 385, no. 1–2, pp. 128–132, Nov. 2004.

[74] M. G. Day and A. Hellawell, “The Microstructure and Crystallography of Aluminium-Silicon Eutectic Alloys,” *Proc. R. Soc. London. Ser. A, Math. Phys.*, vol. 305, no. 1483, pp. 473–491, 1968.

[75] K. F. Kobayashi and L. M. Hogan, “The crystal growth of silicon in Al-Si alloys,” *J. Mater. Sci.*, vol. 20, pp. 1961–1975, 1985.

[76] K. Kobayashi, P. H. Shingu, and R. Ozaki, “Crystallographic study on eutectic microstructure of Al-Si system.” 1979.

[77] S. C. Flood and J. D. Hunt, “Modification of AI-Si eutectic alloys with Na,” *Met. Sci.*, vol. 15, pp. 287–294, Jul. 1981.

[78] A. J. Gesing, P. C. Marchwica, S. Lackie, and J. H. Sokolowski, “Quantitative X-Ray Fluorescence Determination of Elemental Composition of Micro-Constituents Smaller than the Electron Probe Volume,” in *The Minerals, Metals & Materials Society*, 2013, vol. 1.

[79] P. Chen, “Mechanical Properties and Machining of Al-Si Alloys Modified by Bi or Sn,” MASc thesis, University of Windsor, Canada, 2012.

[80] S. Hong and C. Suryanarayana, “Mechanical Properties and Fracture Behavior of an Ultrafine-Grained Al-20 wt.% Si Alloy,” *Metall. Mater. Trans. A*, vol. 36, pp. 715–723, Mar. 2005.

[81] Q. Wang, S. Zhang, Z. Zhang, X. Yan, and H. Geng, “Study of Melt Thermal-Rate Treatment and Low-Temperature Pouring on Al-15%Si Alloy,” *JOM*, vol. 65, no. 8, pp. 958–966, Jun. 2013.

[82] K. G. Basavakumar, P. G. Mukunda, and M. Chakraborty, “Influence of melt treatments on sliding wear behavior of Al–7Si and Al-7Si-2.5Cu cast alloys,” *J. Mater. Sci.*, vol. 42, pp. 7882–7893, 2007.

[83] R. K. Mahanti, K. Lal, and A. N. Sinha, “A Novel Technique for Hyper Eutectic Aluminum-Silicon Alloy Melt Treatment,” *Mater. Trans.*, vol. 34, no. 12, pp. 1207–1211, 1993.

[84] G. I. Eskin, “Broad prospects for commercial application of the ultrasonic (cavitation) melt treatment of light alloys.,” *Ultrason. Sonochem.*, vol. 8, no. 3, pp. 319–25, Jul. 2001.

[85] Q. Wang, H. Geng, S. Zhang, H. Jiang, and M. Zuo, “Effects of Melt Thermal-Rate Treatment on Fe-Containing Phases in Hypereutectic Al-Si Alloy,” *Metall. Mater. Trans. A*, vol. 45, no. 3, pp. 1621–1630, Nov. 2014.

[86] J. Campbell, “Discussion of Effects of Melt Thermal-Rate Treatment on Fe-Containing Phases in Hypereutectic Al-Si Alloy,” *Metall. Mater. Trans. A*, vol. 45, no. 10, pp. 4193–4193, Sep. 2014.

[87] P. Li, V. I. Nikitin, E. G. Kandalova, and K. V. Nikitin, “Effect of melt overheating, cooling and solidification rates on Al–16wt.%Si alloy structure,” *Mater. Sci. Eng. A*, vol. 332, no. 1–2, pp. 371–374, Jul. 2002.

[88] S. Lu and A. Hellawell, “Modification of Al-Si Alloys: Microstructure, Thermal Analysis and Mechanisms,” *JOM*, vol. 47, no. 2, p. 38, Feb. 1995.

[89] S. Lu and A. Hellawell, “The Mechanism of Silicon Modification in Aluminum-Silicon Alloys: Impurity Induced Twinning,” *Metall. Trans. A*, vol. 18, pp. 1721–1733, Oct. 1987.

[90] K. Nogita, H. Yasuda, M. Yoshiya, S. D. McDonald, K. Uesugi, A. Takeuchi, and Y. Suzuki, “The role of trace element segregation in the eutectic modification of

hypoeutectic Al–Si alloys," *J. Alloys Compd.*, vol. 489, no. 2, pp. 415–420, Jan. 2010.

[91] A. K. Dahle, K. Nogita, and J. W. Zindel, "Eutectic Nucleation and Growth in Hypoeutectic Al-Si Alloys at Different Strontium Levels," *Metall. Mater. Trans. A*, vol. 32, pp. 949–960, Apr. 2001.

[92] K. Nogita and A. K. Dahle, "Determination of Eutectic Solidification Mode in Sr-modified Hypoeutectic Al-Si Alloys by EBSD," *Mater. Trans.*, vol. 42, no. 2, pp. 207–214, 2001.

[93] K. Nogita, J. Drennan, and A. K. Dahle, "Evaluation of Silicon Twinning in Hypo-Eutectic Al-Si Alloys," *Mater. Trans.*, vol. 44, no. 4, pp. 625–628, 2003.

[94] K. Nogita, S. D. McDonald, and A. K. Dahle, "Eutectic Modification of Al-Si Alloys with Rare Earth Metals," *Mater. Trans.*, vol. 45, no. 2, pp. 323–326, 2004.

[95] K. Nogita, H. Yasuda, K. Yoshida, K. Uesugi, A. Takeuchi, Y. Suzuki, and A. K. Dahle, "Determination of strontium segregation in modified hypoeutectic Al–Si alloy by micro x-ray fluorescence analysis," *Scr. Mater.*, vol. 55, no. 9, pp. 787–790, Nov. 2006.

[96] M. Timpel, N. Wanderka, R. Schlesiger, T. Yamamoto, N. Lazarev, D. Isheim, G. Schmitz, S. Matsumura, and J. Banhart, "The role of strontium in modifying aluminium–silicon alloys," *Acta Mater.*, vol. 60, no. 9, pp. 3920–3928, May 2012.

[97] L. Clapham and R. W. Smith, "Segregation behaviour of strontium in modified and unmodified Al-Si alloys," *J. Cryst. Growth*, vol. 92, pp. 263–270, May 1988.

[98] J. E. Gruzleski and B. M. Closset, *The Treatment of Liquid Aluminum-Silicon Alloys*. American Foundrymen's Society, Inc., Des Plains, IL, USA, 1990.

[99] P. C. Wiggen and J. K. Belgraver, "Advanced addition practices with AlSr rod for accurate and cost effective modification in the Casthouse and Aluminium Foundry," pp. 979–984, 2001.

[100] L. Liu, A. M. Samuel, and F. H. Samuel, "Influence of oxides on porosity formation in Sr-treated Al-Si casting alloys," *J. Mater. Sci.*, vol. 38, pp. 1255–1267, 2003.

[101] S. D. McDonald, K. Nogita, and A. K. Dahle, "Eutectic nucleation in Al–Si alloys," *Acta Mater.*, vol. 52, no. 14, pp. 4273–4280, May 2004.

[102] L. Liu, A. M. Samuel, and F. H. Samuel, “Characteristics of α-dendritic and eutectic structures in Sr-treated Al-Si casting alloys,” *J. Mater. Sci.*, vol. 39, 2004.

[103] Z. Chen and R. Zhang, “Effect of strontium on primary dendrite and eutectic temperature of A357 aluminum alloy,” *CHINA FOUNDRY*, vol. 7, no. 2, pp. 149–152, May 2010.

[104] M. Makhlouf, “On the Mechanism of Modification of the Aluminium-Silicon Eutectic by Strontium: The Role of Nucleation,” *Int. J. Met.*, vol. 10, pp. 47–51, 2010.

[105] R. Aparicio, C. Gonzalez, G. Barrera, and G. Trapaga, “Newton Thermal Analysis of Al-Si Alloys with Different Sr Content,” in *METAL 2010, Roznov pod Radhostem, Czech Republic*, 2010.

[106] M. Timpel, “Einfluss von Strontium auf die Mikrostruktur von Aluminium-Silizium Legierungen,” Dr. Ing. dissertation, Institut für Angewandte Materialforschung, Berlin, 2012.

[107] J. Espinoza-Cuadra, P. Gallegos-Acevedo, H. Mancha-Molinar, and A. Picado, “Effect of Sr and solidification conditions on characteristics of intermetallic in Al-Si 319 industrial alloys,” *Mater. Des.*, vol. 31, 2010.

[108] A. Zyska, Z. Konopka, M. Łągiewka, and M. Nadolski, “The influence of modification and squeeze casting on properties of AlSi11 alloy castings,” *Arch. Foundry Eng.*, vol. 11, no. 2, pp. 153–156, 2011.

[109] S. Farahany, A. Ourdjini, M. H. Idris, and S. G. Shabestari, “Evaluation of the Effect of Bi, Sb, Sr and Cooling Condition on Eutectic Phases in an Al-Si-Cu Alloy (ADC12) by In-situ Thermal Analysis,” *Thermochim. Acta*, 2013.

[110] S. Farahany, A. Ourdjini, M. H. Idris, and S. G. Shabestari, “Computer-aided cooling curve thermal analysis of near eutectic Al–Si–Cu–Fe alloy,” *J. Therm. Anal. Calorim.*, vol. 114, no. 2, pp. 705–717, Feb. 2013.

[111] M. M. Barzani, S. Farahany, N. M. Yusof, and A. Ourdjini, “The Influence of Bismuth, Antimony, and Strontium on Microstructure, Thermal, and Machinability of Aluminum-Silicon Alloy,” *Mater. Manuf. Process.*, vol. 28, no. 11, pp. 1184–1190, Nov. 2013.

[112] M. Abdulwahab, I. A. Madugu, F. Asuke, O. S. I. Fayomi, and F. A. Ayeni, “Effect of thermal ageing treatment on the mechanical properties of antimony-modified A356.0-type Al-Si-Mg alloy,” *J. Mater. Environ. Sci.*, vol. 4, no. 1, pp. 87–92, 2013.

[113] S. Farahany, A. Ourdjini, A. Bakar, T. Asma, and M. H. Idris, “A new approach to assess the effects of Sr and Bi interaction in ADC12 Al–Si die casting alloy,” *Thermochim. Acta*, vol. 575, pp. 179–187, Jan. 2014.

[114] S. Farahany, A. Ourdjini, M. H. Idris, and L. T. Thai, “Effect of bismuth on microstructure of unmodified and Sr-modified Al-7Si-0.4Mg alloys,” *Trans. Nonferrous Met. Soc. China*, vol. 21, no. 7, pp. 1455–1464, Jul. 2011.

[115] K. Nogita, S. D. McDonald, and A. K. Dahle, “Effects of Boron-strontium Interactions on Eutectic Modification in Al-10 mass % Si Alloys,” *Mater. Trans.*, vol. 44, no. 4, pp. 692–695, 2003.

[116] S. Farahany, A. Ourdjini, A. B. T. Asma, and M. H. Idris, “Authors’ Reply to Discussion of ‘“On the Refinement Mechanism of Silicon in Al-Si-Cu-Zn Alloy with Addition of Bismuth,”’” *Metall. Mater. Trans. A*, pp. 22–23, Aug. 2014.

[117] S. Farahany, A. Ourdjini, M. H. Idris, A. V Takaloo, and L. T. Thai, “Combined effect of bismuth content and cooling rate on microstructure and mechanical properties of Al–8.5Si – 0.4Mg -0.3Fe alloy,” *Can. Metall. Q.*, vol. 52, no. 2, pp. 208–216, 2013.

[118] S. Farahany, A. Ourdjini, T. A. A. Bakar, and M. H. Idris, “Communication on the Refinement Mechanism of Silicon in Al-Si-Cu-Zn Alloy with Addition of Bismuth,” *Metall. Mater. Trans. A*, pp. 1–4, Jan. 2014.

[119] S. Farahany, A. Ourdjini, T. A. A. Bakar, and M. H. Idris, “Role of Bismuth on Solidification , Microstructure and Mechanical Properties of a Near Eutectic Al-Si Alloys,” *Met. Mater. Int.*, vol. 20, no. 5, pp. 929–938, 2014.

[120] S. Farahany, A. Ourdjini, and M. H. Idris, “The usage of computer-aided cooling curve thermal analysis to optimize eutectic refiner and modifier in Al–Si alloys,” *J. Therm. Anal. Calorim.*, vol. 109, no. 1, pp. 105–111, Jun. 2012.

[121] X. H. Zhang, G. C. Su, C. W. Ju, W. C. Wang, and W. L. Yan, “Effect of modification treatment on the microstructure and mechanical properties of Al-0.35%Mg-7.0%Si cast alloy,” *Mater. Des.*, vol. 31, pp. 4408–4413, 2010.

[122] M. Zhu, Z. Jian, L. Yao, C. Liu, G. Yang, and Y. Zhou, “Effect of mischmetal modification treatment on the microstructure, tensile properties, and fracture behavior of Al-7.0%Si-0.3%Mg foundry aluminum alloys,” *J. Mater. Sci.*, vol. 46, pp. 2685–2694, 2011.

[123] B. Li, H. Wang, J. Jie, and Z. Wei, “Microstructure evolution and modification mechanism of the ytterbium modified Al-7.5%Si-0.45%Mg alloys,” *J. Alloys Compd.*, vol. 509, pp. 3387–3392, 2011.

[124] B. Li, H. Wang, J. Jie, and Z. Wei, “Effects of yttrium and heat treatment on the microstructure and tensile properties of Al–7.5Si–0.5Mg alloy,” *Mater. Des.*, vol. 32, no. 3, pp. 1617–1622, Mar. 2011.

[125] W. Zhang, Y. Liu, J. Yang, J. Dang, H. Xu, and Z. Du, “Effects of Sc content on the microstructure of As-Cast Al-7wt.% Si alloys,” *Mater. Charact.*, vol. 66, pp. 104–110, Apr. 2012.

[126] R. Sterner-Rainer, “Aluminium Silicon alloy with a Phosphorus content of 0.001 to 0.1%,” 1933.

[127] W. J. Kyffin, W. M. Rainforth, and H. Jones, “Effect of phosphorus additions on the spacing between primary silicon particles in a Bridgman solidified hypereutectic Al-Si alloy,” vol. 6, pp. 2667–2672, 2001.

[128] N. Tenekedjiev, “Strontium Treatment of Aluminum-17% Silicon Casting Alloys,” MASc thesis, McGill University, Montreal, Quebec, 1989.

[129] K. Müller, “Improved Hypereutectic Al-Si Cast Alloys: Microstructure and Properties,” in *Advanced Light Alloys and Composites*, 2nd ed., R. Ciach, Ed. Institute of Metallic Materials — Physical Metallurgy, Technical University of Berlin, Berlin, Germany, 1998, pp. 233–241.

[130] M. Zuo, D. Zhao, X. Teng, H. Geng, and Z. Zhang, “Effect of P and Sr complex modification on Si phase in hypereutectic Al–30Si alloys,” *Mater. Des.*, vol. 47, pp. 857–864, Jan. 2013.

[131] K. Al-Helal, I. C. Stone, and Z. Fan, “Simultaneous Primary Si Refinement and Eutectic Modification in Hypereutectic Al-Si Alloys,” *Trans Indian Inst Met*, vol. 65, no. 6, pp. 663–667, 2012.

[132] P. Delshad-Khatibi and F. Akhlaghi, “Ultrafine Primary Silicon Particles in Phosphorus-Modified Hypereutectic Al-Si Alloy Powders Produced By SAMD Method,” *Int. J. Mod. Phys. B*, vol. 22, pp. 3304–3310, Jul. 2008.

[133] M. Shamsuzzoha, “Refinement of Primary and Eutectic Silicon Phases in Shape Casting of Hyper-eutectic Al-Si Alloys.,” in *Light Metals 2012, The Minerals, Metals & Materials Society*, 2012.

[134] M. Shamsuzzoha, F. R. Juretzko, and A. Hague, “Development of High Strength Hypereutectic Al-Si Alloys by Nano-Refining the Constituent Si Phases,” in *The Minerals, Metals & Materials Society*, 2008, pp. 207–211.

[135] M. Shamsuzzoha, L. Nastac, and J. Berry, “Development of Nano-fibrous Eutectic and Primary Silicon Phases in Al-Si Cast Alloys for High Strength Structural Applications,” *Int. J. Met.*, pp. 27–34, 2012.

[136] B. N. Rygalin, V. K. Prokofeva, L. M. Pavlova, and E. B. Sokolov, “Experimental study and thermodynamic analysis of phase equilibria in the silicon-rich part of the Si-Sr and Si-Ba systems,” *Inorg. Mater.*, vol. 46, no. 2, pp. 97–103, Feb. 2010.

[137] W. Ding, T. Xia, W. Zhao, and Y. Xu, “Effect of Al–5Ti–C Master Alloy on the Microstructure and Mechanical Properties of Hypereutectic Al–20%Si Alloy,” *Materials (Basel).*, vol. 7, no. 2, pp. 1188–1200, Feb. 2014.

[138] J. Chang and I. Moon, “Refinement of cast microstructure of hypereutectic Al-Si alloys through the addition of rare earth metals,” vol. 3, pp. 5015–5023, 1998.

[139] J. Cisse, G. F. Bolling, and H. W. Kerr, “Simultaneous Refinement of Primary and Eutectic Silicon in Hypereutectic AI-Si Alloys,” *Metall. Trans. B*, vol. 6 B, pp. 195–197, Mar. 1975.

[140] H. Choi, H. Konishi, and X. Li, “Al2O3 nanoparticles induced simultaneous refinement and modification of primary and eutectic Si particles in hypereutectic Al–20Si alloy,” *Mater. Sci. Eng. A*, vol. 541, pp. 159–165, Apr. 2012.

[141] H. Choi and X. Li, “Refinement of primary Si and modification of eutectic Si for enhanced ductility of hypereutectic Al–20Si–4.5Cu alloy with addition of Al2O3 nanoparticles,” *J. Mater. Sci.*, vol. 47, no. 7, pp. 3096–3102, Nov. 2011.

[142] C. L. Xu, H. Y. Wang, F. Qiu, Y. F. Yang, and Q. C. Jiang, “Cooling rate and microstructure of rapidly solidified Al–20wt.% Si alloy,” *Mater. Sci. Eng. A*, vol. 417, no. 1–2, pp. 275–280, Oct. 2006.

[143] R. Zhang, Q. Cao, S. Pang, Y. Wei, and L. Liu, “Dissolution kinetics of primary silicon in hypereutectic Al–Si melt,” *Sci. Technol. Adv. Mater.*, vol. 2, no. 1, pp. 3–5, Mar. 2001.

[144] Y. Sun, Q. Wang, and H. Geng, “Effects of complex modificating technique on microstructure and mechanical properties of hypereutectic Al–Si alloys,” *J. Mater. Sci.*, vol. 47, pp. 2104–2109, Nov. 2012.

[145] C. Guan, Y. Jianwei, F. Hengzhi, and Y. Jianwel, “Influence of the melt heat history on the solid / liquid interface morphology evolution in unidirectional solidification,” *J. Mater. Sci. Lett.*, vol. 1, no. 8, pp. 1571–1573, 1999.

[146] A. H. Ahmad, S. Naher, and D. Brabazon, “The Effect of Direct Thermal Method, Temperature and Time on Microstructure of a Cast Aluminum Alloy,” *Mater. Manuf. Process.*, vol. 29, no. 2, pp. 134–139, Mar. 2014.

[147] U. Dahlborg, M. Besser, M. Calvo-Dahlborg, G. Cuello, C. D. Dewhurst, M. J. Kramer, J. R. Morris, and D. J. Sordelet, “Structure of molten Al–Si alloys,” *J. Non. Cryst. Solids*, vol. 353, no. 32–40, pp. 3005–3010, Oct. 2007.

[148] P. Srirangam, M. J. Kramer, and S. Shankar, “Effect of strontium on liquid structure of Al-Si hypoeutectic alloys using high-energy X-ray diffraction,” *Acta Mater.*, vol. 59, no. 2, pp. 503–513, 2011.

[149] K. V. Nikitin, a. B. Finkel’shtein, O. a. Chikova, and I. Y. Timoshkin, “Influence of the structure of the AlSi20 foundry alloy on the microstructure and viscosity of the Al-6% Si model silumin in solid and liquid states,” *Russ. J. Non-Ferrous Met.*, vol. 54, no. 4, pp. 314–319, Sep. 2013.

[150] J. Wang, L. He, C. Lin, and D. Cang, “EET research on the Al-22%Si alloy under the action of electric pulses,” *Sci. China, Ser. E Technol. Sci.*, vol. 51, no. 50674054, pp. 1930–1938, 2008.

[151] B. Xiufang, W. Weimin, Y. Shujuan, and Q. Jingyu, “Structure factors of modified liquid Al - Si alloys,” *Sci. Technol. Adv. Mater.*, vol. 2, pp. 19–23, 2001.

[152] W. Kasprzak, D. Sediako, M. Sahoo, M. Walker, and I. Swainson, “Characterization of hypereutectic Al-19% Si alloy solidification process using in-situ neutron diffraction and thermal analysis techniques,” 2010.

[153] W. Kasprzak, D. Sediako, M. Walker, M. Sahoo, and I. Swainson, “Solidification Analysis of an Al-19 Pct Si Alloy Using In-Situ Neutron Diffraction,” *Metall. Mater. Trans. A*, vol. 42, no. 7, pp. 1854–1862, Apr. 2011.

[154] D. Sediako, W. Kasprzak, I. Swainson, and O. Garlea, “Solidification analysis of Al-Si alloys modified with addition of Cu using in-situ neutron diffraction.” 2011.

[155] F. C. Robles Hernandez, J. H. Sokolowski, and J. Cruz Rivera, “Micro-Raman Analysis of the Si Particles Present in Al-Si Hypereutectic Alloys in Liquid and Semi-Solid States,” *Adv. Eng. Mater.*, vol. 9, no. 1–2, pp. 46–51, Feb. 2007.

[156] J. H. Sokolowski, “UMSA Quantification of the Effect of Melt Temperature on Microstructure,” 2008.

[157] Y. Tsunekawa, M. Okumiya, and T. Motomura, “Semisolid casting with ultrasonically melt-treated billets of Al-7mass%Si alloys,” *China Foundry*, vol. 9, no. 1, pp. 78–83, 2012.

[158] A. Lowe, “Thixoforming.” [Online]. Available: http://www.azom.com/article.aspx?ArticleID=1373. [Accessed: 23-May-2014].

[159] Y. Birol, “Semisolid processing of near-eutectic and hypereutectic Al–Si–Cu alloys,” *J. Mater. Sci.*, vol. 43, no. 10, pp. 3577–3581, Mar. 2008.

[160] Y. Birol, “Cooling slope casting and thixoforming of hypereutectic A390 alloy,” *J. Mater. Process. Technol.*, vol. 207, no. 1–3, pp. 200–203, Oct. 2008.

[161] S. Wu, G. Zhong, L. Wan, P. An, and Y. Mao, “Microstructure and properties of rheo-diecast Al-20Si-2Cu-1Ni-0.4Mg alloy with direct ultrasonic vibration process,” *Trans. Nonferrous Met. Soc. China*, vol. 20, pp. 7963–767, 2010.

[162] S. Wu, G. Zhong, P. An, L. Wan, and H. Nakae, “Microstructural characteristics of Al–20Si–2Cu–0.4Mg–1Ni alloy formed by rheo-squeeze casting after ultrasonic vibration treatment,” *Trans. Nonferrous Met. Soc. China*, vol. 22, no. 12, pp. 2863–2870, Dec. 2012.

[163] X. Jian and Q. Han, “Formation of hypereutectic silicon particles in hypoeutectic Al-Si alloys under the influence of high-intensity ultrasonic vibration,” *China Foundry*, vol. 10, no. 2, Mar. 2013.

[164] M. Ramadan and N. Fathy, “Microstructure of Hyper-Eutectic Al–Si alloy Processed in Semi-Solid State,” *Int. J. Res. Eng. Technol.*, vol. 1, no. 4, pp. 238–241, 2012.

[165] M. Tebib, J. B. Morin, F. Ajersch, and X. Grant Chen, “Semi-solid processing of hypereutectic A390 alloys using novel rheoforming process,” *Trans. Nonferrous Met. Soc. China*, vol. 20, no. 9, pp. 1743–1748, Sep. 2010.

[166] H. Puga, J. Barbosa, S. Costa, S. Ribeiro, A. M. P. Pinto, and M. Prokic, “Influence of indirect ultrasonic vibration on the microstructure and mechanical behavior of Al-Si-Cu alloy,” CT2M - Centre for Mechanical and Materials Technologies Universidade do Minho, Azurém.

[167] M. Qian, A. Ramirez, and A. Das, “Ultrasonic refinement of magnesium by cavitation: Clarifying the role of wall crystals,” *J. Cryst. Growth*, vol. 311, no. 14, pp. 3708–3715, Jul. 2009.

[168] A. Das and H. R. Kotadia, “Effect of high-intensity ultrasonic irradiation on the modification of solidification microstructure in a Si-rich hypoeutectic Al–Si alloy,” *Mater. Chem. Phys.*, vol. 125, no. 3, pp. 853–859, Feb. 2011.

[169] G. I. Eskin, “Cavitation mechanism of ultrasonic melt degassing,” *Ultrason. Sonochemistry*, vol. 2, no. 2, p. 137, 1995.

[170] X. Jian, H. Xu, T. T. Meek, and Q. Han, “Effect of power ultrasound on solidification of aluminum A356 alloy,” *Mater. Lett.*, vol. 59, pp. 190–193, Oct. 2005.

[171] G. I. Eskin, G. S. Makarov, and Y. P. Pimenov, “Effect of Ultrasonic Processing in Molten Metal, Eskin,” *Adv. Perform. Mater.*, vol. 2, pp. 43–50, 1995.

[172] V. O. Abramov, O. V. Abramov, B. B. Straumal, and W. Gust, “Hypereutectic Al–Si based alloys with a thixotropic microstructure produced by ultrasonic treatment,” *Mater. Des.*, vol. 18, pp. 323–326, Jul. 1997.

[173] G. I. Eskin and D. G. Eskin, “Production of natural and synthesized aluminum-based composite materials with the aid of ultrasonic (cavitation) treatment of the melt.,” *Ultrason. Sonochem.*, vol. 10, no. 4–5, pp. 297–301, Jul. 2003.

[174] H. K. Feng, S. R. Yu, Y. L. Li, and L. Y. Gong, “Effect of ultrasonic treatment on microstructures of hypereutectic Al–Si alloy,” *J. Mater. Process. Technol.*, vol. 208, no. 1–3, pp. 330–335, Nov. 2008.

[175] A. Radjai and K. Miwa, “Effects of the Intensity and Frequency of Electromagnetic Vibrations on the Microstructural Refinement of Hypoeutectic Al-Si Alloys,” *Metall. Mater. Trans. A*, vol. 31, pp. 755–762, Mar. 2000.

[176] Jacek Ohl, “Development of Novel System Used for the Electromagnetic Treatment of Aluminum Alloys During the Solidification Process,” MASc thesis, University of Windsor, Canada, 2002.

[177] J. Yu, Z. Ren, W. Ren, K. Deng, and Y. Zhong, “Solidification structure of eutectic Al-Si alloy under a high magnetic field-aid-electromagnetic vibration,” *Acta Metall. Sin. (English Lett.*, vol. 22, no. 3, pp. 191–196, Jun. 2009.

[178] D. Lu, Y. Jiang, G. Guan, R. Zhou, Z. Li, and R. Zhou, “Refinement of primary Si in hypereutectic Al–Si alloy by electromagnetic stirring,” *J. Mater. Process. Technol.*, vol. 189, no. 1–3, pp. 13–18, Jul. 2007.

[179] Y. Mizutani, S. Kawai, K. Miwa, K. Yasue, T. Tamura, and Y. Sakaguchi, “Effect of the Intensity and Frequency of Electromagnetic Vibrations on Refinement of Primary Silicon in Al-17%Si Alloy,” *Mater. Trans.*, vol. 45, no. 6, pp. 1939–1943, Apr. 2004.

[180] H. Shuxian, W. Jun, and S. Bao-de, “Effect of high density pulse electric current on solidification structure of low temperature melt of A356 alloy,” *Trans. Nonferrous Met. Soc. China*, vol. 12, no. 3, pp. 414–418, 2002.

[181] Y. Zhang, C. Song, L. Zhu, H. Zheng, H. Zhong, Q. Han, and Q. Zhai, “Influence of Electric-Current Pulse Treatment on the Formation of Regular Eutectic Morphology in an Al-Si Eutectic Alloy,” *Metall. Mater. Trans. B*, vol. 42, no. 3, pp. 604–611, Jun. 2011.

[182] D. Hongsheng, Z. Yong, J. Sanyong, C. Ruirun, Z. Zhilong, G. Jingjie1, X. Daming, and Fu Hengzhi, “Influences of pulse electric current treatment on solidifi

cation microstructures and mechanical properties of Al-Si piston alloys," *China Foundry*, vol. 6, no. 1, 2008.

[183] H. Lijia, W. Jianzhong, Q. Jingang, D. Huiling, and Z. Zuofu, "Influences of electric pulse on solidification structure of LM-29 Al-Si alloy," pp. 1–4, May 2010.

[184] A. J. Plotkowski, "Refinement of the Cast Microstructure of Hypereutectic Aluminum-Silicon Alloys with an Applied Electric Potential," Grand Valley State University, 2012.

[185] O. Lashkari, F. Ajersch, A. Charette, and X.-G. Chen, "Microstructure and rheological behavior of hypereutectic semi-solid Al–Si alloy under low shear rates compression test," *Mater. Sci. Eng. A*, vol. 492, no. 1–2, pp. 377–382, Sep. 2008.

[186] N. S. Barekar, N. H. Babu, B. K. Dhindaw, and Z. Fan, "Effect of intensive shearing on morphology of primary silicon and properties of hypereutectic Al–Si alloy," *Mater. Sci. Technol.*, vol. 26, no. 8, pp. 975–980, Aug. 2010.

[187] N. S. Barekar, B. K. Dhindaw, and Z. Fan, "Improvement in silicon morphology and mechanical properties of Al–17Si alloy by melt conditioning shear technology," *Int. J. Cast Met. Res.*, vol. 23, no. 4, pp. 225–230, Aug. 2010.

[188] K. Kocatepe and C. F. Burdett, "Effect of low frequency vibration on macro and micro structures of LM6 alloys," *J. Mater. Sci.*, vol. 35, pp. 3327–3335, 2000.

[189] D. Jayesh, "The Effect of Mechanical Mold Vibration On the Characteristics of Aluminum Alloys," MASs thesis, Worcester Polytechnic Institute, Worcester, USA, 2006.

[190] B. Gao, Y. Hao, G. Tu, W. Shi, F. Yu, and S. Li, "Compounded Surface Modification of ZK60 Mg Alloy by High Current Pulsed Electron Beam + Micro-Plasma Oxidation," *Plasma Sci. Technol.*, vol. 12, no. 1, pp. 1–4, Feb. 2010.

[191] Y. Hao, B. Gao, G. F. Tu, S. W. Li, S. Z. Hao, and C. Dong, "Surface modification of Al–20Si alloy by high current pulsed electron beam," *Appl. Surf. Sci.*, vol. 257, no. 9, pp. 3913–3919, Nov. 2010.

[192] Y. Hao, B. Gao, G. F. Tu, S. W. Li, C. Dong, and Z. G. Zhang, "Improved wear resistance of Al–15Si alloy with a high current pulsed electron beam treatment,"

Nucl. Instruments Methods Phys. Res. Sect. B, vol. 269, no. 13, pp. 1499–1505, Apr. 2011.

[193] T. A. Harriman, D. A. Lucca, J.-K. Lee, M. J. Klopfstein, K. Herrmann, and M. Nastasi, "Ion implantation effects in single crystal Si investigated by Raman spectroscopy," *Nucl. Instruments Methods Phys. Res. Sect. B*, vol. 267, no. 8–9, pp. 1232–1234, Jan. 2009.

[194] S. Tomida, K. Nakata, S. Shibata, I. Zenkouji, and S. Saji, "Improvement in wear resistance of hyper-eutectic Al-Si cast alloy by laser surface remelting," *Surf. Coatings Technol.*, vol. 169–170, pp. 468–471, Jun. 2003.

[195] Z. Brown, C. Barnes, J. Bigelow, and P. Dodd, "Squeeze Cast Automotive Applications and Design Considerations," *La Metall. Ital.*, pp. 1–4, Mar. 2009.

[196] A. Iyer, "Squeeze Casting: The Future," *International Specialised Skills Institute*, pp. 1–48, Apr-2011.

[197] S. Rajagopal, "Squeeze Casting: A Review and Update," *J. Appl. Met. Work.*, vol. 1, no. 4, pp. 3–14, 1981.

[198] "Aluminium Casting Techniques - Sand Casting and Die Casting Processes." [Online]. Available: http://www.azom.com/article.aspx?ArticleID=1392. [Accessed: 20-Jun-2014].

[199] M. R. Ghomashchi and A. Vikhrov, "Squeeze Casting: An Overview," *J. Mater. Process. Technol.*, vol. 101, pp. 1–9, May 2000.

[200] J. J. Sobczak, L. Drenchev, and R. Asthana, "Effect of pressure on solidification of metallic materials," *Int. J. Cast Met. Res.*, vol. 25, no. 1, pp. 1–14, Jan. 2012.

[201] H. Bengt and S. Jochen, "A simple approach to pressure dependence, exemplified in the Al-Mg-Si system." [Online]. Available: http://www.calphad.org/meetings/2004/a/2/2-8.htm. [Accessed: 30-Jul-2014].

[202] E. Brosh, G. Makov, and R. Z. Shneck, "Application of CALPHAD to high pressures," *Calphad*, vol. 31, no. 2, pp. 173–185, Jun. 2007.

[203] H. Gotou, T. Yagi, T. Okada, R. Iizuka, and T. Kikegawa, "A simple opposed anvil apparatus for high pressure and temperature experiments above 10GPa," *High Press. Res.*, vol. 31, no. 4, pp. 592–602, Dec. 2011.

[204] J. F. Cannon, “Behavior of the elements at high pressures,” *J. Phys. Chem. Ref. Data*, vol. 3, no. 3, pp. 781–824, 1974.

[205] P. Wasilewski, *Siluminy - Modyfikacja i jej Wplyw na Strukture i Wlasciwosci*. Katowice: Polish Academy of Sciences Department Katowice Foundry Commission, 1993.

[206] L. X. Li, H. T. Zong, and M. Li, “Microstructure of Al-Si alloy solidifíed under high pressure,” *High Temp. Press.*, vol. 41, pp. 69–77, 2012.

[207] S. Wang, D. He, W. Wang, and L. Lei, “Pressure calibration for the cubic press by differential thermal analysis and the high-pressure fusion curve of aluminum,” *High Press. Res.*, vol. 29, no. 4, pp. 806–814, Dec. 2009.

[208] R. C. Liebermann, “High Pressure Research: An Multi-anvil, high pressure apparatus: a half-century of development and progress,” *High Press. Res. An Int. J.*, pp. 37–41, Nov. 2011.

[209] G. Smith, “Squeeze casting of pure Al/Si alloys,” Ph.D. dissertation, University of Southampton, UK, 1986.

[210] Y. Zhang, Y. Li, B. Han, F. Zhang, and L. Qian, “Microstructural characteristics of Hadfield steel solidified under high pressure,” *High Press. Res.*, vol. 31, no. 4, pp. 634–639, Dec. 2011.

[211] S. Ranganathan, “Rapid solidification behaviour of Fe and Al based alloys,” KTH-Royal Institute of Technology, Stockholm, Sweden, 2009.

[212] S. Ranganathan and H. Fredriksson, “Influence of melt temperature on rapid solidification of Al-Y and Al-Si alloy system,” *Trans. Indian Inst. Met.*, vol. 62, no. 4–5, pp. 515–519, Oct. 2009.

[213] P. Ma, C. M. Zou, H. W. Wang, S. Scudino, B. G. Fu, Z. J. Wei, U. Kühn, and J. Eckert, “Effects of high pressure and SiC content on microstructure and precipitation kinetics of Al–20Si alloy,” *J. Alloys Compd.*, vol. 586, pp. 639–644, Feb. 2014.

[214] S. K. Chaudhury and D. Apelian, “Fluidized Bed Heat Treatment of Cast Al-Si-Cu-Mg Alloys,” *Metall. Mater. Trans. A*, vol. 37A, pp. 2295–2311, Jul. 2006.

[215] G. Y. Liu, “Effect of Ageing Heat Treatment on the Hardness and Tensile Properties of Aluminum A356.2 Casting Alloy,” MASc. thesis, McMaster University, Hamilton, Canada, 2009, 2009.

[216] F. Pisek, L. Jenicek, and P. Rys, *Nauka o materialu, nezelezne kovy*. ACADEMIA, Praha, 1966.

[217] S. G. Shabestari and F. Shahri, “Influence of modification, solidification conditions and heat treatment on the microstructure and mechanical properties of A356 aluminum alloy,” *J. Mater. Sci.*, vol. 39, no. 6, pp. 2023–2032, Mar. 2004.

[218] F. H. Samuel, “Incipient melting of Al5Mg8Si6Cu2 and Al2Cu intermetallics in unmodified and strontium-modified Al–Si–Cu–Mg (319) alloys during solution heat treatment,” *J. Mater. Sci.*, vol. 33, no. 9, pp. 2283–2297, May 1998.

[219] M. A. Moustafa, F. H. Samuel, and H. W. Doty, “Effect of solution heat treatment and additives on the microstructure of Al-Si (A413.1) automotive alloys,” *J. Mater. Sci.*, vol. 38, pp. 4507–4522, 2003.

[220] F. J. Tavitas-Medrano, J. E. Gruzleski, F. H. Samuel, S. Valtierra, and H. W. Doty, “Effect of Mg and Sr-modification on the mechanical properties of 319-type aluminum cast alloys subjected to artificial aging,” *Mater. Sci. Eng. A*, vol. 480, no. 1–2, pp. 356–364, May 2008.

[221] M. A. C. Services, “A Guide to Aluminum Casting Alloys.” pp. 1–8.

[222] J. C. C. Benedyk, “Aluminum alloys for lightweight automotive structures,” *Woodhead Publ. Ltd.*, 2010.

[223] ASM International, *ASM Handbook, vol. 4, Heat Treating*. 1991.

[224] J. H. Sokolowski, M. B. Djurdjevic, C. A. Kierkus, and D. O. Northwood, “Improvement of 319 aluminum alloy casting durability by high temperature solution treatment,” *J. Mater. Process. Technol.*, vol. 109, no. 1–2, pp. 174–180, Feb. 2001.

[225] E. Sjölander and S. Seifeddine, “The heat treatment of Al–Si–Cu–Mg casting alloys,” *J. Mater. Process. Technol.*, vol. 210, no. 10, pp. 1249–1259, Jul. 2010.

[226] J. M. Silcock, T. J. Heal, and H. K. Hardy, “Structural Ageing Characteristics of Binary Aluminium-Copper Alloys,” *J. Inst. Met.*, vol. 82, pp. 239–248, 1953.

[227] M. Zeren, “Effect of copper and silicon content on mechanical properties in Al–Cu–Si–Mg alloys,” *J. Mater. Process. Technol.*, vol. 169, no. 2, pp. 292–298, Nov. 2005.

[228] M. Zeren, “The effect of heat-treatment on aluminum-based piston alloys,” *Mater. Des.*, vol. 28, no. 9, pp. 2511–2517, Nov. 2006.

[229] W. Kasprzak, H. Kurita, J. H. Sokolowski, and H. Yamagata, “Energy-Efficient Tempers for Aluminum Motorcycle Cylinder Blocks,” *Adv. Mater. Process.*, pp. 24–27, Mar. 2010.

[230] S. Anandhan, “Thermal Analysis.” 2001.

[231] T. Hatakeyama and F. X. Quinn, *Thermal Analysis: Fundamentals and Applications to Polymer Science*. John Wiley & Sons, Inc, 1999.

[232] T. Ozawa, “Thermal analysis-review and prospect,” *Thermochim. Acta*, vol. 355, pp. 35–42, Jul. 2000.

[233] M. E. Brown, *Introduction to Thermal Analysis Techniques and Applications*. Kluwer Academic Publishers, Dordrecht, The Netherlands, 2001.

[234] Heraeus Electro-Nite International N.V., “Thermal Analysis of Cast Iron.” Houthalen, Belgium.

[235] “ATAS Perlit.” [Online]. Available: http://www.powershow.com/view/14cfc5-OTk5Z/Adaptive_Thermal_Analysis_System_powerpoint_ppt_presentation. [Accessed: 15-Sep-2014].

[236] “Foseco Home.” [Online]. Available: http://www.foseco.com/se/end-markets/foundry/foseco-home/. [Accessed: 02-Aug-2014].

[237] J. Piatkowski and B. Gajdzik, “Testing Phase Changes in Al-Si Alloys with Application of Thermal Analysis,” *Metalurgija*, vol. 52, no. 4, pp. 469–472, 2013.

[238] J. H. Sokolowski, “Universal Metallurgical Simulator and Analyzer (UMSA) Platform,” 2002.

[239] H. Yamagata, W. Kasprzak, M. Aniolek, H. Kurita, and J. H. Sokolowski, “The effect of average cooling rates on the microstructure of the Al–20% Si high pressure die casting alloy used for monolithic cylinder blocks,” *J. Mater. Process. Technol.*, vol. 203, no. 1–3, pp. 333–341, Apr. 2008.

[240] P. C. Marchwica, J. H. Sokolowski, and W. T. Kierkus, “Fraction Solid Evolution Characteristics of AlSiCu Alloys – Dynamic Baseline Approach,” *J. Achiev. Mater. Manuf. Eng.*, vol. 47, no. 115–136, 2011.

[241] M. Aniolek, W. Kasprzak, and J. H. Sokolowski, “Heat Treatment Project Conducted for the Yamaha Motor Co. Ltd.,” Windsor, 2004.

[242] J. H. Sokolowski, “UMSA Thermal Analysis Results for Phosphorus Modified Hypereutectic Al-Si Alloys Solidified under Semi and Non-Equilibrium Conditions.”

[243] J. H. Sokolowski, W. T. Kierkus, M. Kasprzak, and W. Kasprzak, “Method and Apparatus for Universal Metallurgical Simulation and Analysis,” US 2005/0151306 A1, Jul. 14,2005.

[244] J. H. Sokolowski and M. Kasprzak, “Universal Metallurgical Simulator and Analyzer (UMSA) Platform for the Advanced Simulation of Melting and Solidification Processes, Software Information.” 2002.

[245] J. H. Sokolowski and M. Kasprzak, “Universal Metallurgical Simulator and Analyzer (UMSA) Platform for the Advanced Simulation of Melting and Solidification Processes, Hardware Information,” 2002.

[246] J. H. Sokolowski, “Novel Opportunities for Disruptive Analysis , R & D and QC of Alloys, Melts, Cast Components and Heat Treatment Processes based on Physical Simulations,” 2009.

[247] H. Yamagata and H. Kurita, “The Controlling Factors of the Size and Distribution of Si Particles in the Hypereutectic Al-20%Si Linerless Die-Cast Cylinder Block,” *JD*, pp. 221–228, 2008.

[248] H. Yamagata, W. Kasprzak, M. Aniolek, H. Kurita, and J. H. Sokolowski, “Thermal and metallographic characteristics of the Al–20% Si high-pressure die-casting alloy for monolithic cylinder blocks,” *J. Mater. Process. Technol.*, vol. 203, no. 1–3, pp. 84–90, Apr. 2008.

[249] W. Kasprzak, M. Sahoo, J. H. Sokolowski, H. Yamagata, and H. Kurita, “The Effect of the Melt Temperature and the Cooling Rate on the Microstructure of the Al-20%Si Alloy used for Monolithic Engine Blocks.,” *Int. J. Met.*, vol. 3, no. 3, pp. 55–72, 2009.

[250] P. C. Marchwica, “Microstructual and Thermal Analysis of AlSi and MgAl Alloys Subjected to High Cooling Rates,” MASc. thesis, University of Windsor, Canada, 2012.

[251] L. Bäckerud, G. Chai, and J. Tamminen, *Solidification Characteristics of Aluminum Alloys, Vol 2-Foundry Alloys*. American Foundry Society, 1990.

[252] M. B. Djurdjevic, B. Duric, A. Mitrasinovic, and J. H. Sokolowski, “Modelling of Casting Processes Parameters for the 3XX Series of Aluminum Alloys using the Silicon Equivalency Algorithm,” *Metal. Metall.*, 2003.

[253] M. B. Djurdjevic, S. Manasijević, Z. Odanović, and N. Dolić, “Calculation of Liquidus Temperature for Aluminum and Magnesium Alloys Applying Method of Equivalency,” *Adv. Mater. Sci. Eng.*, vol. 2013, pp. 1–8, 2013.

[254] F. C. R. Hernandez, M. B. Djurdjevic, W. T. Kierkus, and J. H. Sokolowski, “Calculation of the liquidus temperature for hypo and hypereutectic aluminum silicon alloys,” *Mater. Sci. Eng. A*, vol. 396, no. 1–2, pp. 271–276, Apr. 2005.

[255] H. Preston-Thomas, “The International Temperature Scale of 1990 (ITS-90),” 1990.

[256] “Boron Nitride (BN) - Mechanical Properties.” [Online]. Available: http://www.ioffe.ru/SVA/NSM/Semicond/BN/mechanic.html. [Accessed: 10-Jul-2014].

[257] M. S. Dargusch, G. Dour, N. Schauer, C. M. Dinnis, and G. Savage, “The influence of pressure during solidification of high pressure die cast aluminium telecommunications components,” *J. Mater. Process. Technol.*, vol. 180, no. 1–3, pp. 37–43, Dec. 2006.

[258] “Sensors, Thermocouple, PLC, Operator Interface, Data Acquisition, Rtd,” 2014. [Online]. Available: http://www.omega.ca/.

[259] W. J. Boettinger, U. R. Kattner, and J. H. Perepezko, *DTA and Heat-flux DSC Measurements of Alloy Melting and Freezing*. U.S. Government Printing Office, Washington, 2006.

[260] *Standard Test Method for Knoop and Vickers Hardness of Materials, E384-11*. 2012, pp. 1–43.

[261] ASTM, *Standard Test Method for Brinell Hardness of Metallic Materials*. 2012, pp. 1–32.

[262] E. Sato, N. Kono, I. Sato, and H. Watanabe, “Study on the phase diagram of Al-Si-Sr ternary alloy system,” vol. 35, no. 2, 1984.

[263] F. F. Wu, S. T. Li, G. A. Zhang, and F. Jiang, “Microstructural Evolution and Mechanical Properties of Hypereutectic Al-Si Alloy Processed by Liquid Die Forging,” *Bull. Mater. Sci.*, vol. 37, no. 5, pp. 1153–1157, Aug. 2014.

[264] R. N. Lumley, I. J. Polmear, and P. R. Curtis, “Rapid Heat Treatment of Aluminum High-Pressure Diecastings,” *Metall. Mater. Trans. A*, vol. 40, no. 7, pp. 1716–1726, May 2009.

[265] E. Ogris, A. Wahlen, H. Lüchinger, and P. J. Uggowitzer, “On the silicon spheroidization in Al–Si alloys,” *J. Light Met.*, vol. 2, no. 4, pp. 263–269, Nov. 2002.

[266] K. He, F. Yu, D. Zhao, and L. Zuo, “Characterization of precipitates in a hot-deformed hypereutectic Al-Si alloy,” *J. Alloys Compd.*, vol. 539, pp. 74–81, 2012.

APPENDICES

Appendix A - S/TEM/EDS Analysis of the Yamaha Engine Block

The samples were observed using TEM FEI's Tecnai Osiris equipped with a Super X field emission gun (FIG) and ChemiSTEM™ X-ray detection technology (for EDS analysis) operating at 200 kV for characterization and identification phases. For the Scanning TEM (STEM) mode three different detectors were used to collect different types of electrons: a bright field detector for transmitted electrons, a dark field detector located farther from the center to collect low angle scattered electrons that have gone through diffraction, and a donut shaped High Angle Annular Dark Field (HAADF) detector located even farther from the center to collect high angle scattered electrons that are scattered by the atoms nuclei.

High Angle Annular Dark Field (HAADF) in the STEM mode was used to form images and perform EDS analysis. Esprit software was used for elemental mapping. Quantification of point EDS in the STEM/HAADF mode was used in phase identification along with diffraction techniques.

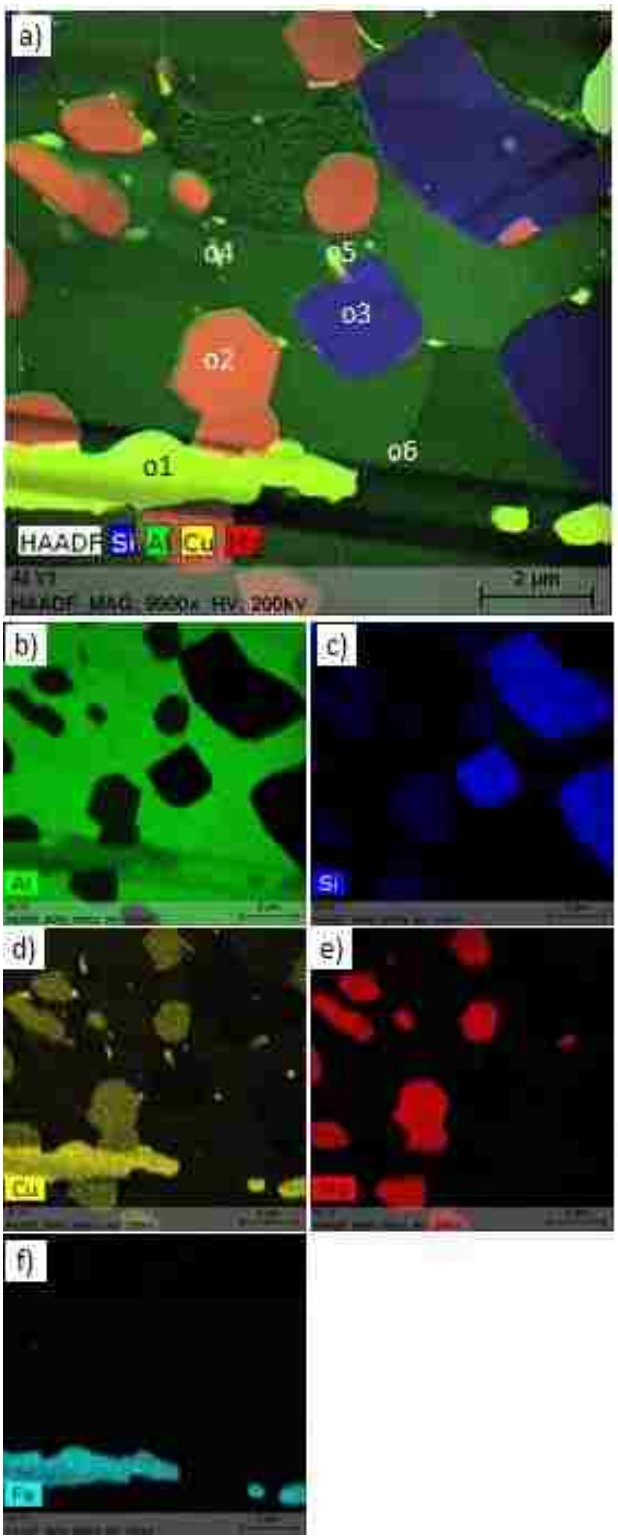

Element	Weight %	Atomic %
# 1: Al_7CuFe_2		
Al(K)	47.35	66.86
Si(K)	0.56	0.77
Fe(K)	13.68	9.33
Ni(K)	0.33	0.21
Cu(K)	38.05	22.81
# 2: $Al_4Cu_2Mg_8Si_7$		
O(K)	1.34	2.52
Mg(K)	30.7	38.01
Al(K)	16.99	18.95
Si(K)	27.39	29.34
Cu(K)	23.56	11.16
# 3: Si		
O(K)	0.65	1.16
Al(K)	1.54	1.62
Si(K)	94.96	95.94
Cu(K)	2.82	1.26
# 4: Al_2Cu		
O(K)	1.3	2.71
Al(K)	64.3	79.27
Cu(K)	34.38	18
# 5: Al_2Cu		
O(K)	1.21	2.54
Al(K)	63.48	78.63
Si(K)	0.39	0.46
Cu(K)	34.9	18.35
# 6: Al_2Cu		
O(K)	1.3	2.96
Al(K)	52.47	70.39
Si(K)	0.43	0.56
Cu(K)	45.77	26.07

Figure 172. a) HAADF image, b-f) superimposed with HAADF and EDS elemental maps, of the Yamaha HPDC engine block processed at 100 MPa followed by heat treatment; ST: 480 °C/4 h + AA: 200 °C/4 h.

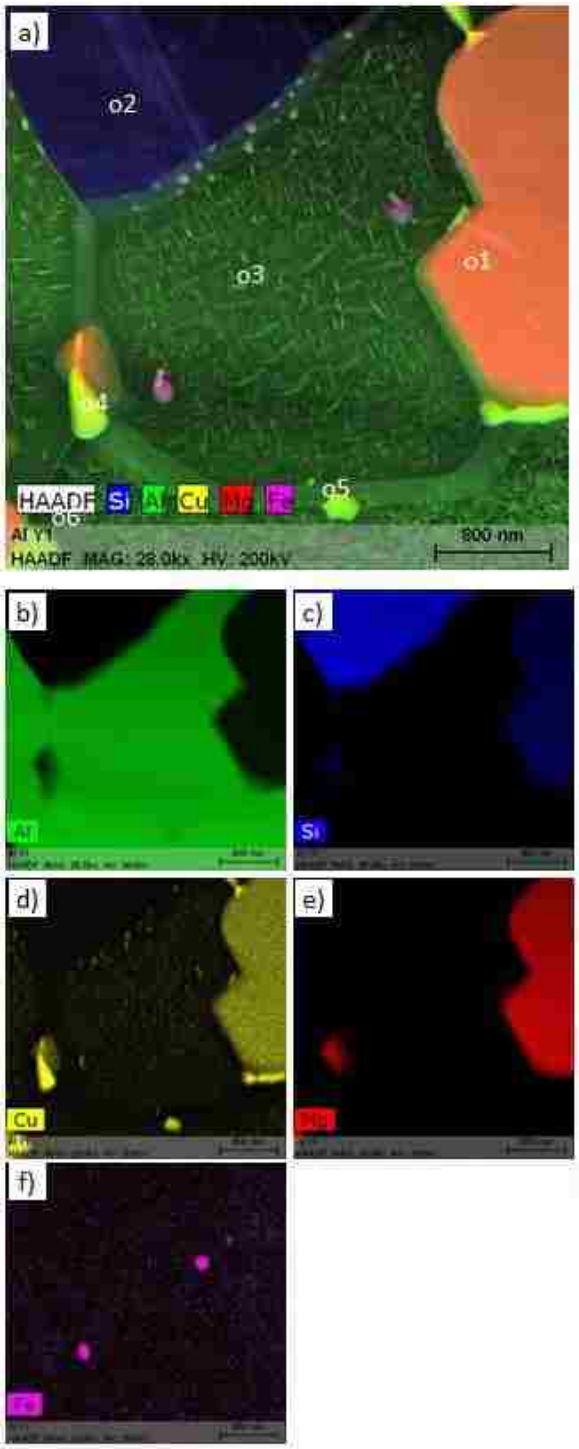

Element	Weight %	Atomic %
# 1: $Al_4Cu_2Mg_8Si_7$		
O(K)	1.24	2.34
Mg(K)	30.19	37.36
Al(K)	16.91	18.85
Si(K)	28.44	30.46
Cu(K)	23.18	10.97
# 2: Si		
O(K)	0.54	0.98
Al(K)	1.53	1.64
Si(K)	92.08	94.72
Cu(K)	5.83	2.65
# 3: Al		
O(K)	0.83	1.42
Al(K)	94.59	96.4
Si(K)	0.33	0.32
Cu(K)	4.24	1.83
# 4: Al_2Cu_3MgSi		
O(K)	1.28	2.87
Mg(K)	5.02	7.4
Al(K)	44.05	58.55
Si(K)	4.41	5.64
Cu(K)	45.23	25.52
# 5: Al_2Cu		
O(K)	1.13	2.19
Al(K)	74.63	85.82
Si(K)	0.23	0.25
Cu(K)	23.99	11.71
# 6: Al_2Cu		
O(K)	1.46	3.3
Al(K)	52.82	70.57
Si(K)	0.26	0.34
Cu(K)	45.44	25.77

Figure 173. a) HAADF image, b-f) superimposed with HAADF and EDS elemental maps, of the Yamaha HPDC engine block processed at 100 MPa followed by heat treatment; ST: 480 °C/4 h + AA: 200 °C/4 h. (Figure 173 is a higher magnification of Figure 172), ref. #Yamaha engine block.

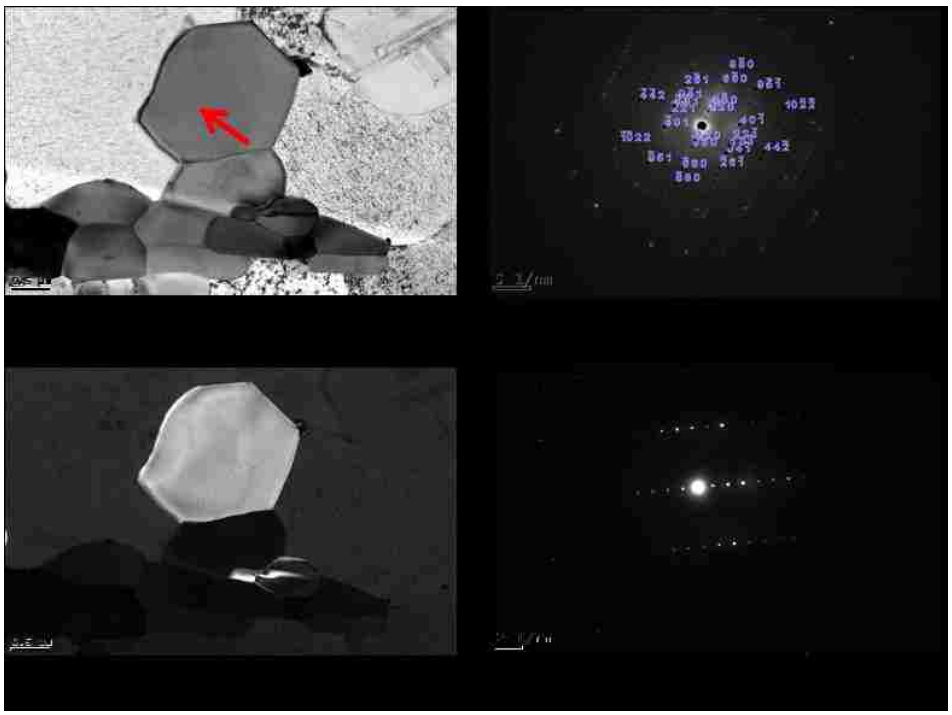

Figure 174. Bright and dark field images for the Aluminum Copper Magnesium Silicide precipitate $Al_4Cu_2Mg_8Si_7$. Selected Area Diffraction Pattern (SAD), ref. #Yamaha engine block.

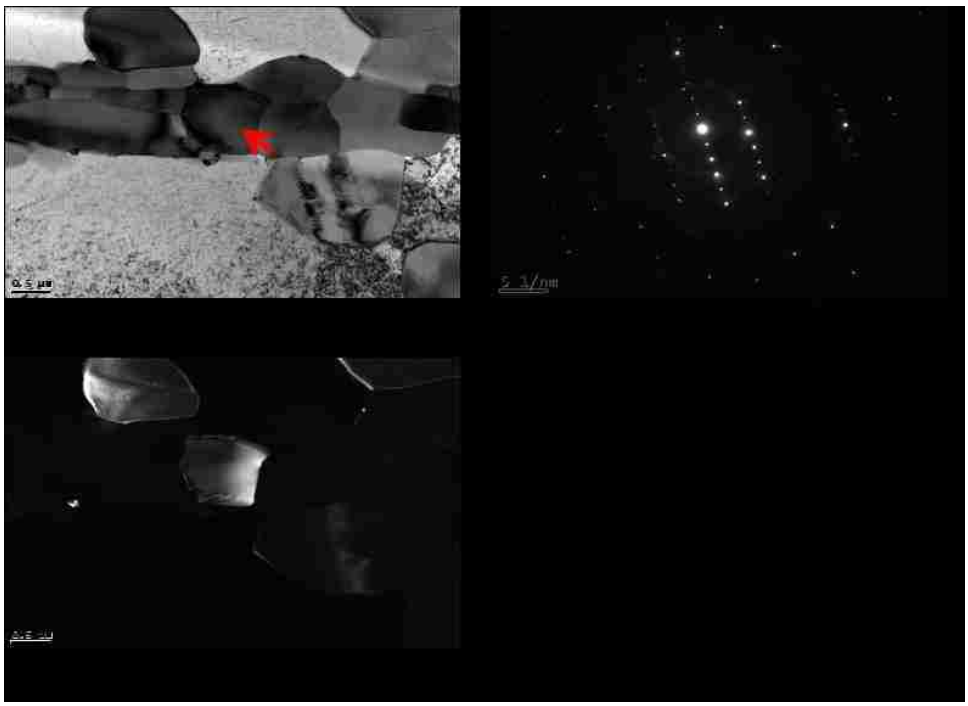

Figure 175. Bright and dark field images for the Al_7Cu_2Fe. Selected Area Diffraction Pattern (SAD), ref. # Yamaha engine block.

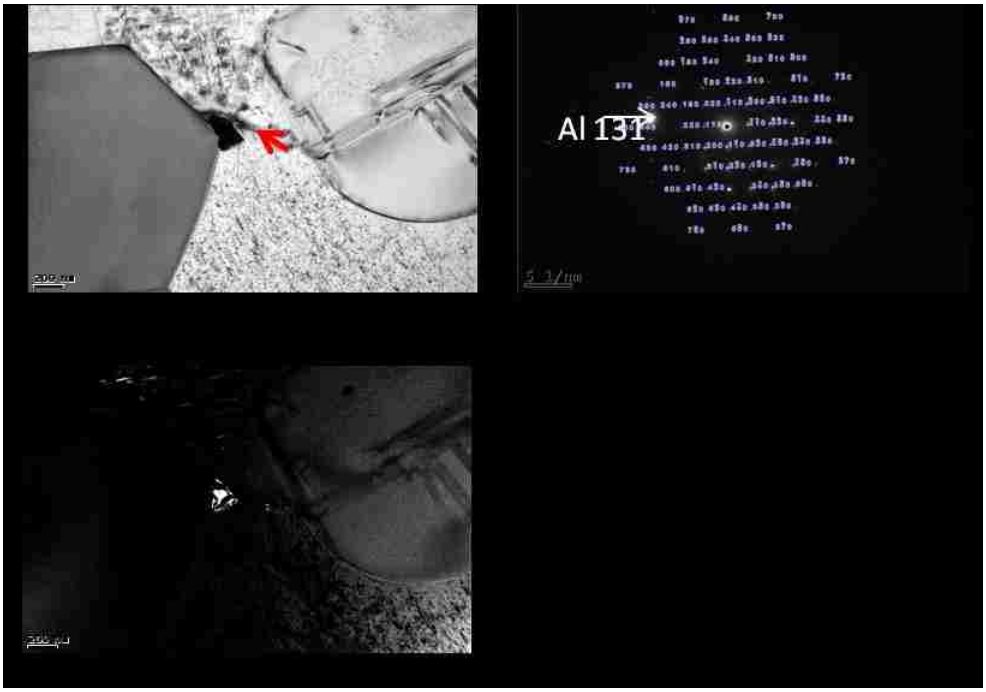

Figure 176. Bright and dark field images for the Al_2Cu, SAD, ref. # Yamaha engine block.

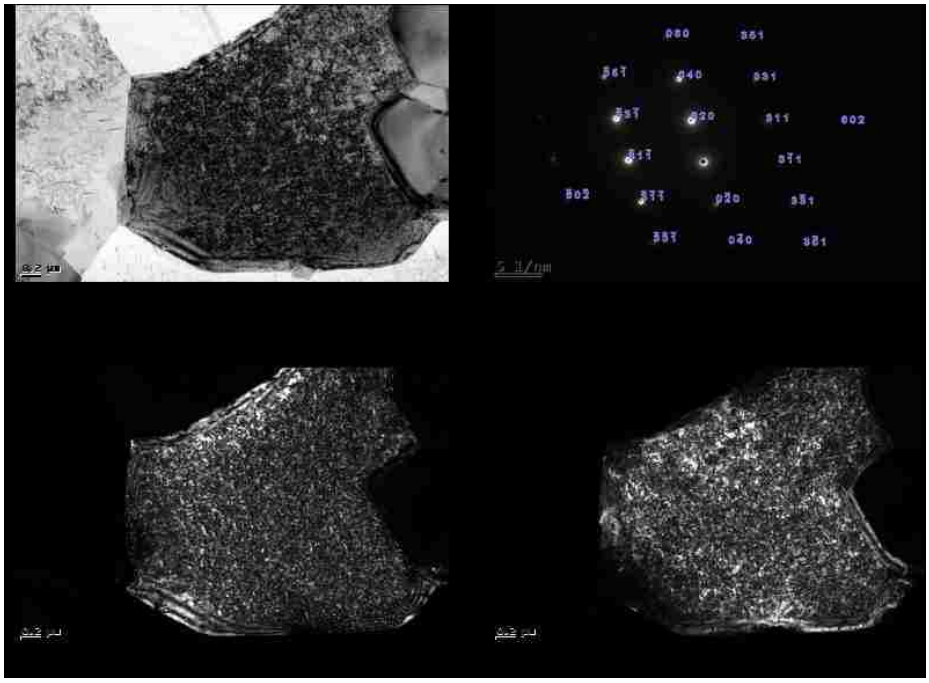

Figure 177. Bright and dark field images for the Al, SAD, ref. # Yamaha engine block.

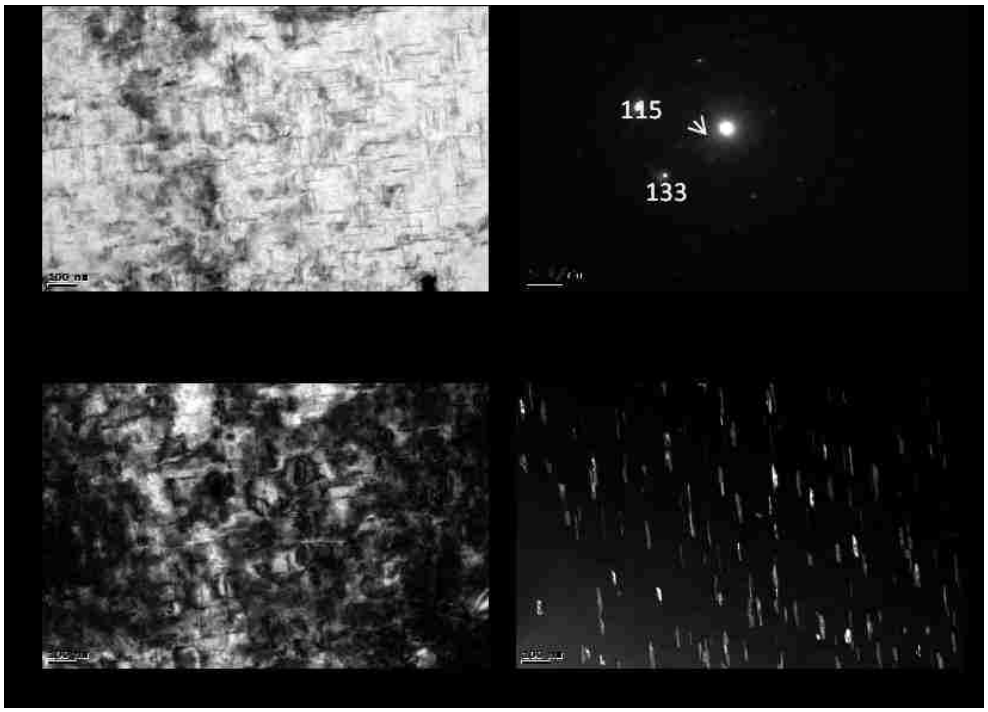

Figure 178. Bright and dark field images for the Al-Cu θ" phase, SAD pattern, ref. #Yamaha engine block.

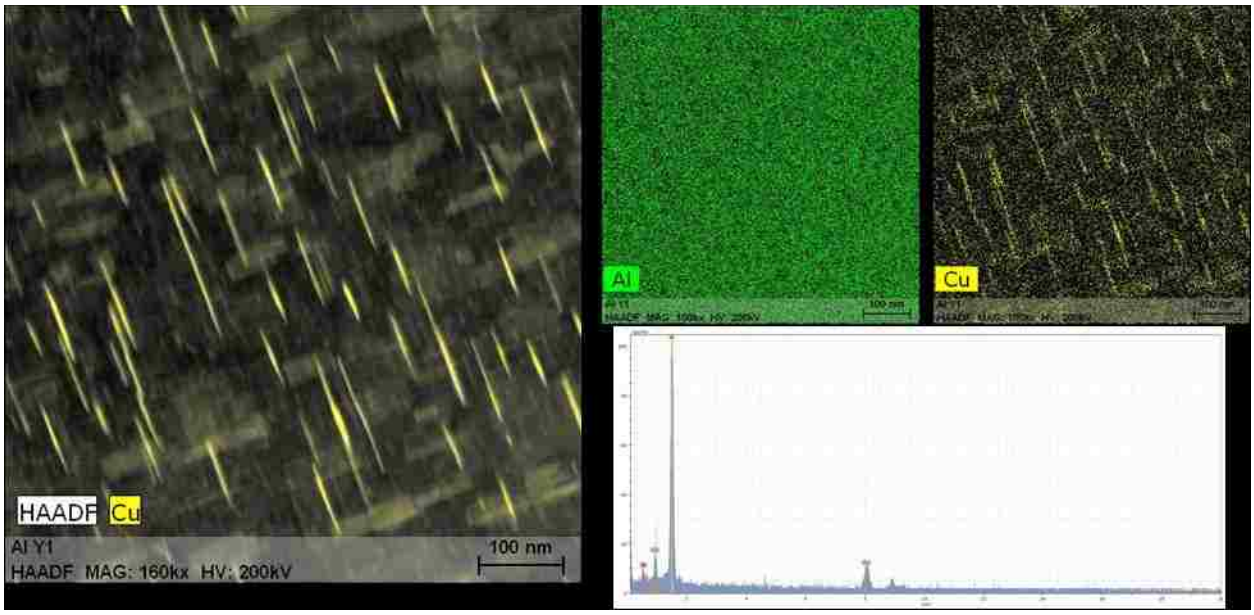

Figure 179. HAADF and EDS elemental mapping, θ" and θ' in the Al-Cu matrix and in the corresponding spectrum, ref. #Yamaha enfine block.

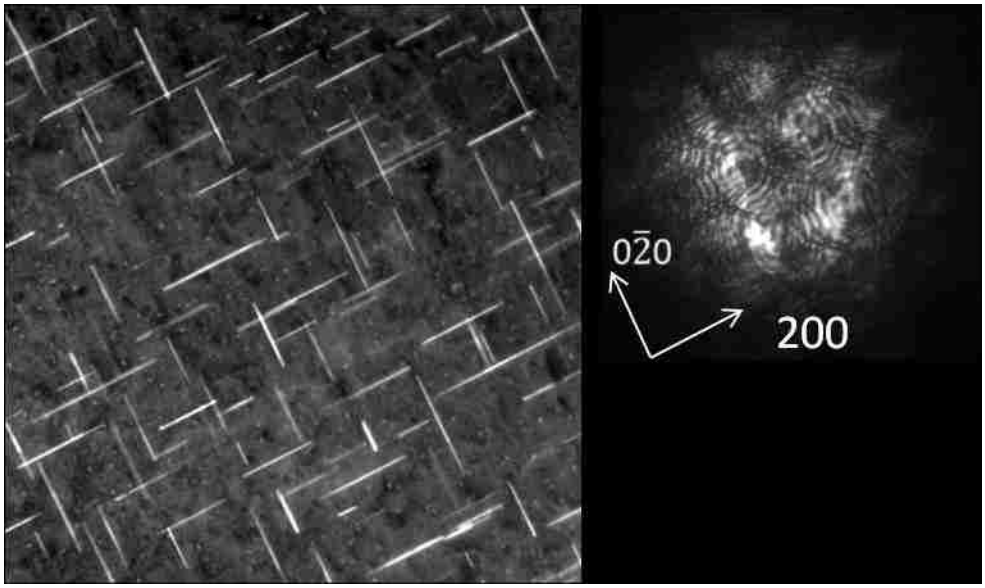

Figure 180. HAADF image showing θ" precipitates oriented towards [002], ref. #Yamaha engine block.

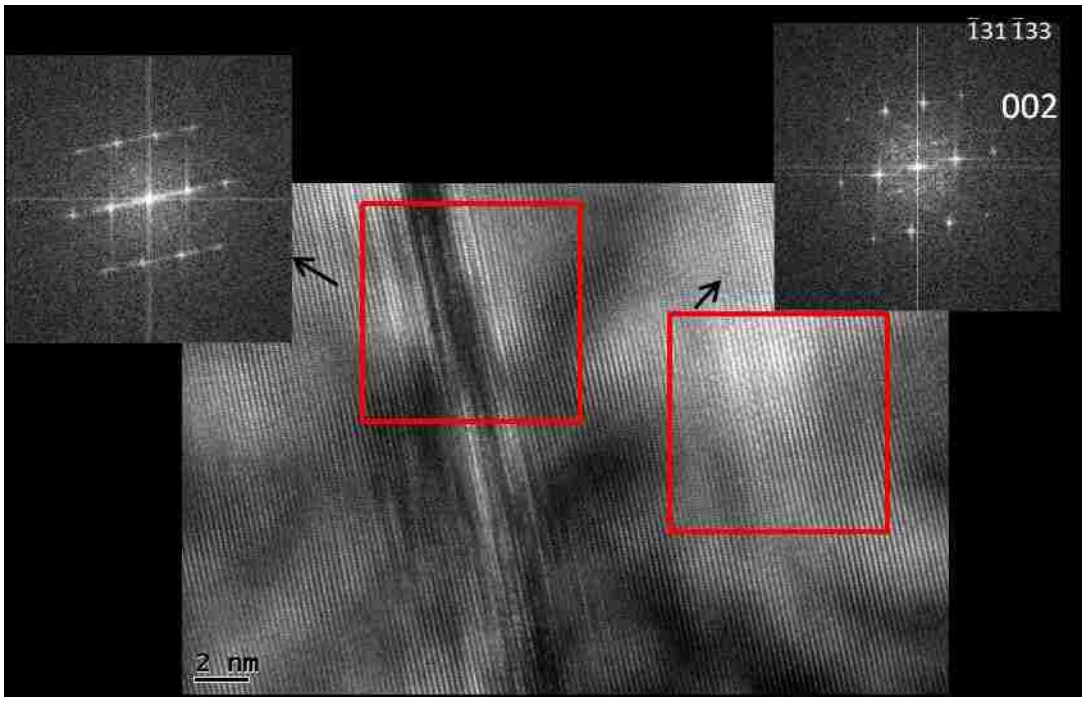

Figure 181. High Resolution TEM (HRTEM) and corresponding FFT showing Al-Cu θ" precipitate, ref. #Yamaha engine block.

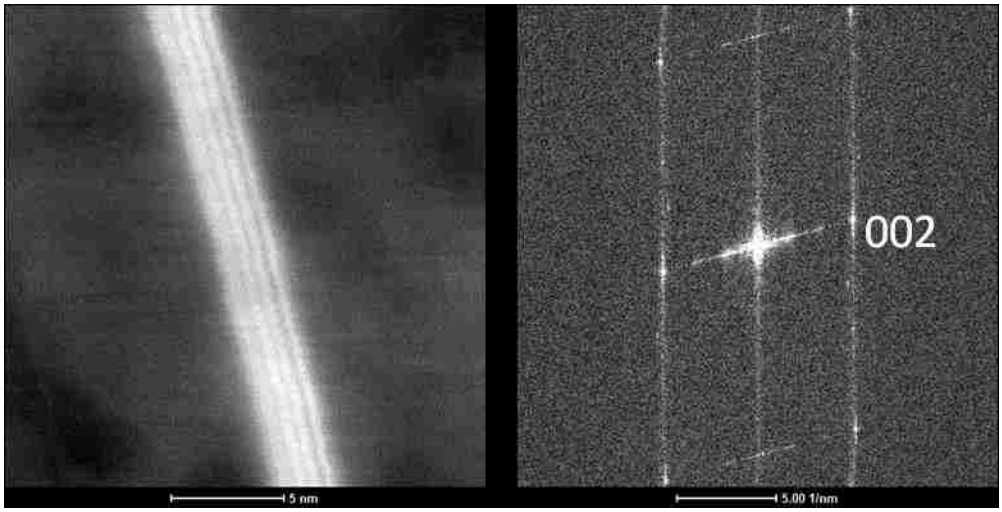

Figure 182. HR-HAADF (z-contrast) and corresponding FFT showing Al-Cu θ" precipitate, ref.# Yamaha engine block.

Appendix B - Permission from Co-Authors

Hello Dr. Al Conle,

During my all experiments I used software for Process Parameters Programming, Control and some Results Analysis which you developed. You provide me with description of the software and Data Collection Procedure for SC/HPDC UMSA Experiments.

I am asking for you to grant me permission so that I can include these results and software description in my PhD dissertation.

.....
Peter Guba, March 9, 2015

.....
Dr. Al Conle, March 9, 2015

Hello Dr. Adam Gesing,

During our cooperation, using my experimental sample #0925b, you did partial the de-convolution of first derivative curve of the cooling/solidification curve, using Excel and applying the methodology which you developed. You provided me with the Excel file containing graphs of the first derivative of cooling /solidification curves vs. temperature and vs. time, de-convoluted first derivative curves for individual thermal events vs. temperature and de-convoluted fraction solid curves for individual thermal events vs. temperature.

This information is very valuable for me and would fit very well into my thermal analysis, being applied into sample #0925b.

I am asking for you to grant me permission so that I can include these graphs and calculations in my PhD dissertation.

.....
Peter Guba, March 15, 2015

.....
Dr. Adam Gesing, March 15, 2015

VITA AUCTORIS

NAME: Peter Guba

PLACE OF BIRTH: Trebisov, Slovakia

YEAR OF BIRTH: 1962

EDUCATION: Special Secondary School of Metallurgy,Kosice, Slovakia, 1981

Technical University of Kosice, M.Sc., Kosice, Slovakia, 1985

Technical University of Kosice, Ph.D., Kosice, Slovakia, 1989